Co-Mineralization of Alkaline-Earth Carbonates and Silica

Dissertation

zur Erlangung des Grades

Doktor der Naturwissenschaften (Dr. rer. nat.)

der Naturwissenschaftlichen Fakultät IV

Chemie und Pharmazie

Universität Regensburg

vorgelegt von

Matthias Kellermeier

Regensburg 2011

Promotionsgesuch eingereicht am: 03. März 2001
Promotionskolloquium am: 01. April 2011

Die Arbeit wurde angeleitet von Prof. Dr. Werner Kunz.

Prüfungsausschuss:

Vorsitzender: Prof. Dr. Dominik Horinek
1. Gutachter: Prof. Dr. Werner Kunz
2. Gutachter: Prof. Dr. Juan Manuel García-Ruiz
3. Gutachter: Prof. Dr. Arno Pfitzner

Preface

"Was lange währt, wird endlich gut" – this famous German saying (or its English equivalent "Good things come to those who wait") probably applies very well to most doctoral studies and, in particular and hopefully, also to the present work. One of the main difficulties in the course of a PhD thesis is indeed to recognize the point at which enough or as much details as reasonably possible have been gathered on a subject and the time has come to start writing the results down. Certainly, open questions will always remain and bother a researcher, but this is actually what the fascination of science is all about.

This thesis is part of the outcome of studies performed between November 2005 and February 2011 at the Institute of Physical and Theoretical Chemistry of the University of Regensburg. Some of the work presented in the following was done during several stays of the author at the Laboratorio de Estudios Cristalográficos (LEC) in Granada, Spain, a research institute belonging to the Spanish council of science (IACT-CSIC) as well as the University of Granada. The thesis was written in a way that each chapter serves as a manuscript draft which has either been already published in a shortened form as an article in a scientific journal, or is intended to be submitted in the near future. Therefore, individual chapters have their own abstract, introduction, and conclusion. This main body of the work (Chapters 2-9) is preceded by a section devoted to gradually guide the reader to the topic, define the central goals of the work, and provide background information required to understand the implications of the results (Chapter 1). Eventually, the major conclusions drawn in each chapter are recapitulated and suggestions for possible future studies are given (Chapter 10).

The achievements made in the course of this PhD project would not have been possible without the valuable help of many people who became involved in terms of experimental work and/or by advancing the development and formulation of concepts. It was a pleasure to cooperate with all of them and it is a natural must to acknowledge their contributions.

First of all, I wish to thank my supervisor Prof. Dr. Werner Kunz for the opportunity to work in his group and the confidence to allow me to work independently and pursue my

own ideas, as well as the financial support over the years. I truly appreciate his ongoing interest in the progress of the different projects and enthusiasm about the results, his eagerness to look across the borders of the topic and his ability to pinpoint essentials when things got complicated.

Likewise, I owe a great debt of gratitude to Prof. Dr. Juan Manuel García-Ruiz (LEC Granada) who, though usually being far away, always had an open ear for my questions, invited me to come to Granada and let me benefit from his enormous expertise concerning silica biomorphs and crystal growth in general. He helped a lot in the ongoing evaluation and interpretation of the many data collected, largely enhanced my understanding of precipitation phenomena, and often motivated me to proceed with the work. Also, I would like to thank Dr. Emilio Melero-García for the innumerable discussions we had, which kept me thinking hard and often led to new perspectives and theories that are reflected in the text and conclusions of this thesis. In particular, Emilio provided some of the microscopy data presented in Chapter 6 and contributed substantially to the writing of Chapter 8 as well as the design of the methodical approach described therein, but I wish to thank him too simply for being a friend. Moreover, I am indebted to JuanMa, Emilio and the whole staff of LEC for their hospitality during my stays, the great time we had, and assistance during the experiments conducted in their lab. Special thanks thereby go to Dr. Duane Choquesillo-Lazarte for acquiring XRD data and the staff at the electron microscopy unit of the University of Granada for measurement time and support.

Further acknowledgement is addressed to Dr. Denis Gebauer and Prof. Dr. Helmut Cölfen (University of Konstanz) for collaborating in the field of pre-nucleation clusters and their brightness in developing the model of aggregation-based nucleation. In this context, I am also utterly grateful to Antje Völkel for performing the ultracentrifugation experiments.

In addition, I would like to thank Dr. Anna Carnerup and Prof. Dr. Stephen Hyde (Australian National University, Canberra) for introducing me to the world of biomorphs in the course of my visit to ANU during my diploma thesis, and the helpful advice they provided when elaborating the role of additives in biomorph formation.

Beyond that, the numerous different techniques employed throughout this thesis required a number of cooperations with experts in the corresponding areas, which I honestly appreciate. In particular, I thank Dr. Reinhard Rachel (University of

Regensburg) for teaching me how to operate a transmission electron microscope and granting generous access to his machine, as well as for preparing thin sections of biomorphs. Dr. Markus Drechsler (University of Bayreuth) is acknowledged for the vast amount of time he spent on cryo-TEM analyses of the many samples with which I came to him. I also wish to express my gratitude to Prof. Dr. Ishi Talmon and his co-workers Drs. Judith Schmidt and Ellina Kesselman at the Technion Haifa for carrying out excellent cryo-TEM studies on $CaCO_3$ clusters. Further thanks go to Benjamin Gossler, Martina Heider and Werner Reichstein (University of Bayreuth) who allowed me to regularly use their superior scanning electron microscope and provided valuable support during the measurements. Prof. Dr. Lorenz Kienle (University of Kiel) and his team helped with sophisticated high-resolution TEM, EDX and electron diffraction studies on both calcium carbonate and biomorph samples. Dr. Heiner Santner (Anton Paar GmbH, Graz) acquired SAXS spectra of cluster solutions and accomplished primary data handling. I am furthermore pleased to thank Dr. Martina Andratschke and Prof. Dr. Arno Pfitzner for powder diffraction measurements, Dr. Thomas Burgemeister and Fritz Kastner for collecting NMR spectra, and Hannes Krauss as well as Dr. Rainer Müller for help concerning IR measurements (all University of Regensburg).

Another crucial brick in the construction of this thesis was the access to different synchrotron radiation facilities. In this respect, I would like to thank the evaluation committees of HASYLAB/DESY (Hamburg) and ELETTRA (Trieste) for allocating beamtime and Drs. Edmund Welter, Thomas Wroblewski (both HASYLAB), Alberto Cassetta, and Luisa Barba (both ELETTRA) for technical support at the beamlines. I am greatly indebted to Dr. André Rothkirch (HASYLAB) for his interest in our research and for providing a software tool that enabled automated evaluation of EDXRD data. Roger Kutta (University of Regensburg) is acknowledged for programming routines which facilitated data processing and graphical illustration. I also thank Prof. Dr. Wolfgang Bensch and his group (University of Kiel) for kindly introducing us to the EDXRD setup at DESY and assistance in the design and setup of the experiments.

Cordial thanks are devoted to all colleagues at the Institute of Physical and Theoretical Chemistry for the pleasant working climate and ongoing socializing in the course of the time I spent there. In particular, I would like to thank my lab mate Fabian Glaab for the congenial, though not always calm atmosphere we had in our office and the unhesitant help he offered me whenever I needed it. Likewise, I wish to acknowledge Josef

Eiblmeier for assisting with experiments and other issues during the final stages of this thesis, Alexander Stoppa for support in various aspects, Alina Voinescu for fruitful collaboration in the field of silica biomorphs, Björn Bartel for performing SEM and EDX analyses, Martin Fleischmann for the preparation of biomorphs and the acquisition of some of the SEM images shown in this work, as well as the staff of the mechanical and electronic workshops for their technical help. Aside from the topics addressed in the following chapters, the research performed in the framework of this thesis was concerned also with thematically distinct projects. In this context, I would like to thank Regina Klein, Dr. Oliver Zech and Dr. Rainer Müller for their excellent cooperation in the fields of surfactants, ionic liquids and alginate hydrogels. Special thanks further go to Hannes Krauss for useful advices regarding graphics and design.

This work was partially funded by the Fonds der Chemischen Industrie and I appreciate their granting of a two-year scholarship.

Finally, I would like to thank Prof. Dr. Juan Manuel García-Ruiz and Prof. Dr. Arno Pfitzner for their willingness to be examiners of this thesis.

Warmest thanks are reserved for my family and friends, with whom I spent wonderful and relaxing hours away from work. Above all, I owe deepest gratitude to Regina and my parents, who always took care of me in whatever respect and gave me strength to carry on. This thesis would probably never have been completed without their support, and it is therefore dedicated to them.

Matthias Kellermeier, Regensburg, February 2011.

Table of Contents

Chapter 1 General Background

1.1 Introduction

The variety and structural complexity of forms displayed by mineralized inorganic matter in Nature have ever been a rich source of fascination. Traditionally, the morphologies of minerals may be divided with respect to their origin into those produced by living organisms (biominerals), and those prevailing in purely inorganic, non-living environments (e.g. geological scales), as illustrated in Fig. 1-1. The latter are usually featured by classical crystal-like shapes, i.e. show angular facets and more or less strictly obey certain symmetrical restrictions. By contrast, biominerals frequently exhibit elaborate architecture beyond any crystallographic restraints and hardly reflecting the atomic order of the underlying crystal phase, with sinuous surfaces of smooth curvature often characterizing the appearance of the mineral rather than sharp edges. Such delicate rounded shapes are commonly, and by intuition, associated with the presence of life.

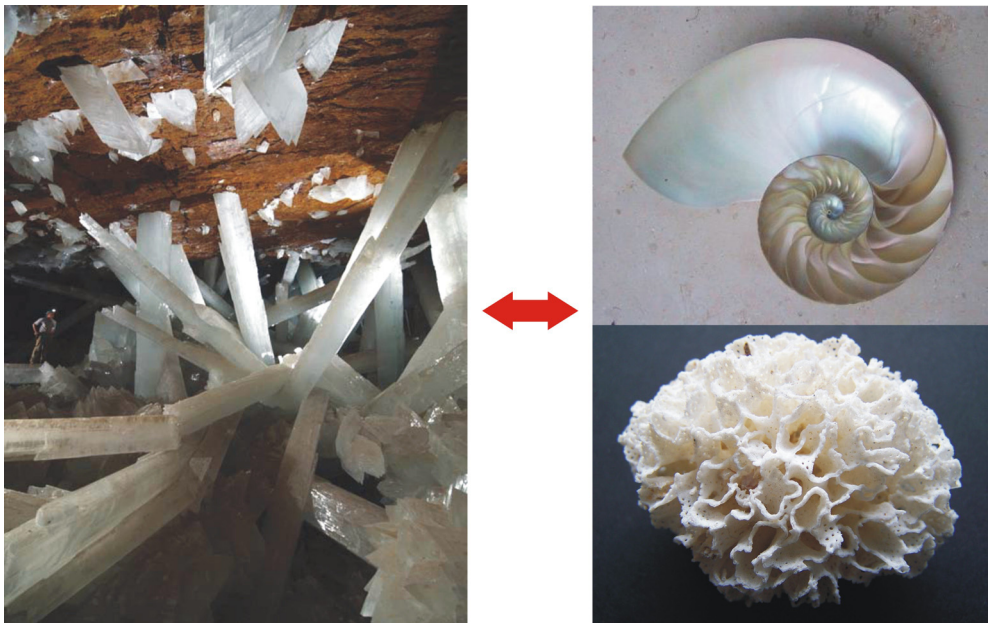

Fig. 1-1: "Inorganic" vs. "organic" morphology. Left: Geological gypsum megacrystals found in caves of the Naica mine near Chihuahua in Mexico, displaying well-defined euhedral prismatic faces (adapted from [1]). Right: Photographs of a nacreous hemishell of the cephalopod *Nautilus* (top) and a natural coral collected on the Eastern Australian seaside (bottom), both delineating smoothly curved forms lacking any distinct kind of crystallographic symmetry (reproduced from [2] and [3]).

Although the regularity of "classical" crystal habits is by no doubt impressive, the sheer unlimited morphological diversity and aesthetic form realized by organisms during biomineralization has particularly intrigued scientists from virtually any field and even inspired artists and philosophers. This is manifest, amongst many others, in the landmark works of Pieter Harting and Ernst Haeckel in the late 19th and beginning 20th century (see Fig. 1-2),[4,5] or the pioneering ideas on the evolution of morphology in biological systems published by D'Arcy Thompson in his famous book "On Growth and Form".[6]

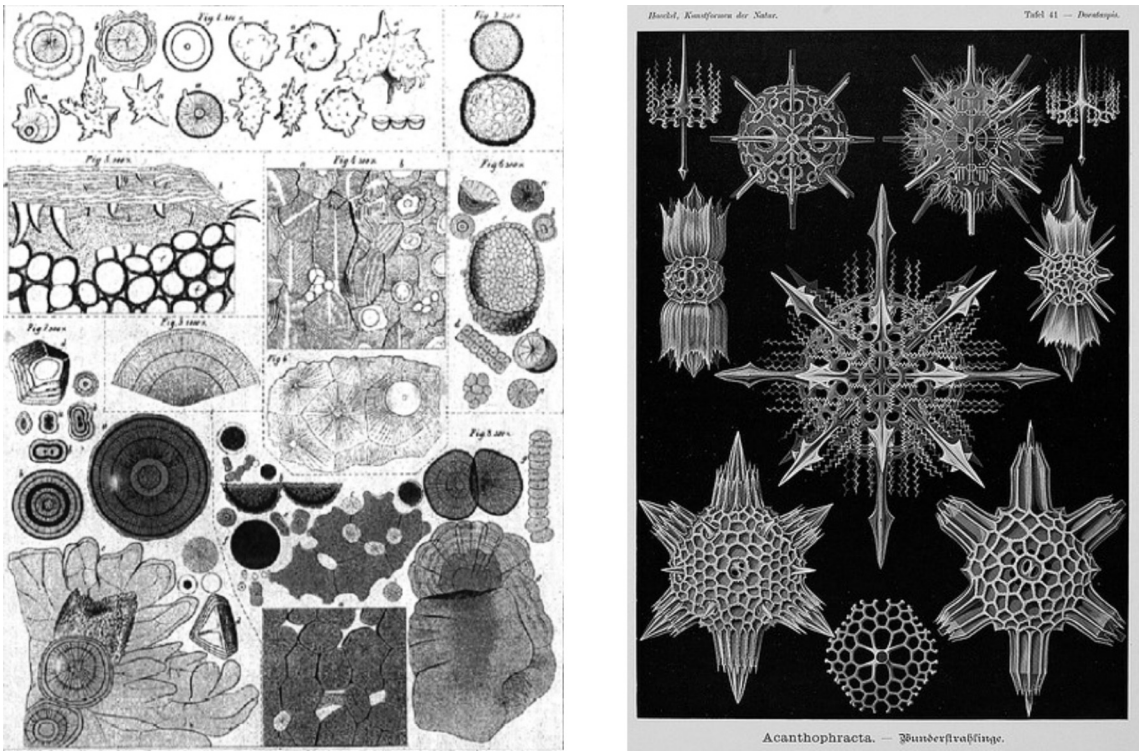

Fig. 1-2: The fascination of life-like form. Right: Harting's original drawing of "calcospherites", precipitates which he obtained by mineralizing inorganic salts in the presence of organic matter (reproduced from [4]). Left: Schematic table depicting the morphological beauty and variety of natural radiolarians, adapted from Haeckel's "Art Forms from Nature" [5].

Harting was one of the first to recognize that a fundamental concept being at the heart of natural biomineralization is to benefit from the influence of organic matter during the crystallization, or precipitation, of the inorganic phase.[4] Since then, numerous studies have been devoted to shed light on the detailed morphology and mode of construction of certain biominerals (see Fig. 1-3), and to unravel by which mechanisms these inorganic-organic hybrid materials are generated.[7-20] It soon became clear that, as Nature is indifferent to aesthetics, functionality and superior properties must be the crucial goals in the determination of morphology and structure in biogenic minerals.[11]

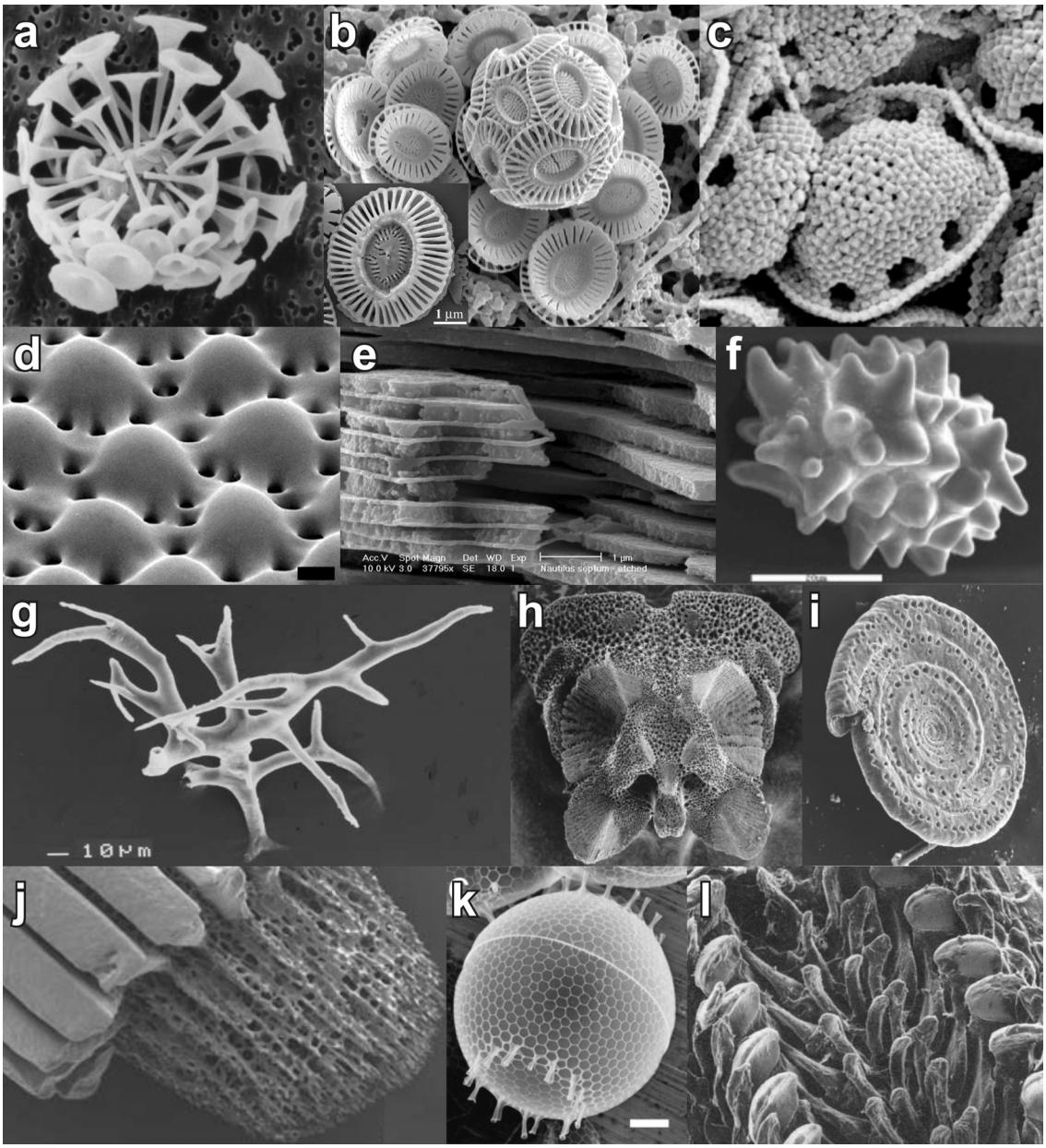

Fig. 1-3: Gallery of scanning electron micrographs visualizing the structural and morphological diversity of common biominerals. (a-c) Exoskeletons of coccolithophorids, a group of marine algae. The mineralized parts of the organisms consist of an array of calcite single crystals, which may adopt hammerheaded forms as in the case of the coccosphere of *Emiliana Huxleyi* (b) or simple rhombohedral shapes as observed for the holococcolith *Calyptrosphaera pirus* (c) (images adapted from [11-13]). (d) Calcitic photoreceptors of the brittlestar *Ophiocoma wendtii* (reproduced from [14]). (e) Close-up view of the aragonite plates in *Nautilus* nacre (adapted from [15]). (f) Cystolith from the leaves of of *Ficus microcarpa*, and (g) an antler spicule of the ascidian *Pyura pachydermatina*, both being composed of stable biogenic amorphous calcium carbonate (ACC) (reproduced from [16, 17]). (h-j) Examples of crystalline $CaCO_3$ biominerals which are believed to form *via* a transient ACC precursor: vertebra of the brittlestar *Ophiocoma wendtii* (h), shell of the foraminifera *Spirillina* (i), growing tip of sea urchin spine (j) (adapted from [18, 19]). (k) Cell walls of the diatom *Stephanopyxis turris*, consisting of biogenic amorphous silica (reproduced from [20]). (l) Teeth of the chiton *Acanthopleura haddoni*, composed of calcium phosphate and iron oxides (adapted from [9]).

Nacre is a prime example in this context. Due to its composite texture, consisting of three-dimensionally ordered calcium carbonate plates sandwiched between thin layers of organic macromolecules (see Fig. 1-3e), this material exceeds the toughness of its constituent mineral aragonite in pure state by a factor of around 3000.[10] Further functions identified to be performed by biominerals include skeletal support of living tissues[7] or the sensing of the Earth's magnetic field required for the migration of magnetotactic bacteria.[21] The design principle found in nacre highlights another key feature of many biomineralized frameworks: control over structure is retained in a highly hierarchical manner over multiple length scales, from the arrangement of atoms on the Ångström level (polymorphism) over the integration and alignment of building units at mesoscopic dimensions (nm to μm) to the appearance of the mineral from a macroscopic standpoint.

Among the around 60 types of biominerals known to date, calcium carbonate-based materials are most abundant, although silica (especially in marine environments) and calcium phosphate are also relatively widespread inorganic components in biogenic sources (cf. Fig. 1-3).[10] In general, calcium carbonate is a polymorphic compound which can exist in five distinct crystalline modifications. Of these, the anhydrous phases calcite, aragonite and vaterite are most common, with calcite representing the thermodynamically stable form under ambient conditions and vaterite being least stable.[22] A further, nowadays well-established polymorph is amorphous calcium carbonate (ACC) which, due to its inherent metastability, was yet found to be short-lived in synthetic systems unless stabilized.[23] Nevertheless, all of these phases were confirmed to be segregated specifically in living tissues, partially even in separate but adjacent domains under virtually identical physicochemical circumstances as in the case of the calcite-prism and aragonite-nacre layers in mollusk shells[24] or the vaterite-aragonite distinction accomplished in fish otholiths.[25] Likewise, mineral architectures entirely consisting of long-term stabilized ACC (Fig. 1-3f-g) have been reported,[16,17] while the skeletons of certain ascidians and calcareous sponges were shown to comprise both stable ACC and calcite.[26] Beyond that, there is increasing evidence that some organisms use ACC as a precursor during the mineralization process.[16,18] This is documented in comparably great detail for the formation of sea urchin larval spicules[27] and adult spines (cf. Fig. 1-3j),[19] the convoluted shapes of which develop by the initial deposition of an amorphous phase that later transforms into a coherent single crystal while maintaining the original morphology. These observations emphasize that Nature

is adept at precisely selecting crystal modifications according to the actual demands and required functions, and playing with polymorphism in order to facilitate morphogenesis of complex form. Though still inadequately understood at present, such intimate guidance of crystal structure and morphology appears to rest upon the interactions between complicated biomolecules and the evolving inorganic phase, usually combined with concerted variations of local conditions in terms of, for example, the concentrations of both involved and foreign ions as well as other parameters like the pH or temperature. In addition, mineralization often takes place in specialized compartments established for instance by single lipid vesicles, macromolecular networks, or larger reaction chambers defined by membraneous envelopes of many cells, confining an inner volume in which the flux of ions, state of supersaturation, and exchange of water is carefully regulated.[7-10] Within these micro-environments, growth of the mineral occurs under the influence of solubilized biopolymers which potentially affect the habit of forming single crystals (e.g. by face-specific adsorption) or stabilize small crystal building units that subsequently self-organize to construct elaborate polycrystalline architectures. In turn, nucleation of the inorganic phase and, with it, polymorph selection and crystal alignment are supposed to be frequently directed by immobilized parts of the organic matrix, acting as structured substrates which provide preferential sites for oriented nucleation.[28] Finally, cellular control over global morphology may be achieved by moulding of the mineral with the walls of a compartmentalized mineralization space or pre-assembled cells serving as templates.[10]

The search for possible mechanisms underlying the formation of biominerals has however not been motivated by aspects of basic science alone or the enthusiasm about their structural manifoldness and aesthetic beauty. Rather, the finding that these materials often exhibit extraordinary properties by far surmounting the performance of man-made counterparts has stimulated the endeavor to mimic them as close as possible *in vitro* and thus generate solids with advanced features for practical applications. The emerging fields of “biomimetic” materials chemistry and bio-inorganic morphosynthesis have received an enormous deal of attention in the past two decades, and innumerable studies were performed for the sake of designing novel materials with special morphologies and structure.[29,30] Selected examples where the artificial reproduction of biomineral textures or their imitation by laboratory approaches have been realized successfully and in a striking fashion are shown in Fig. 1-4.

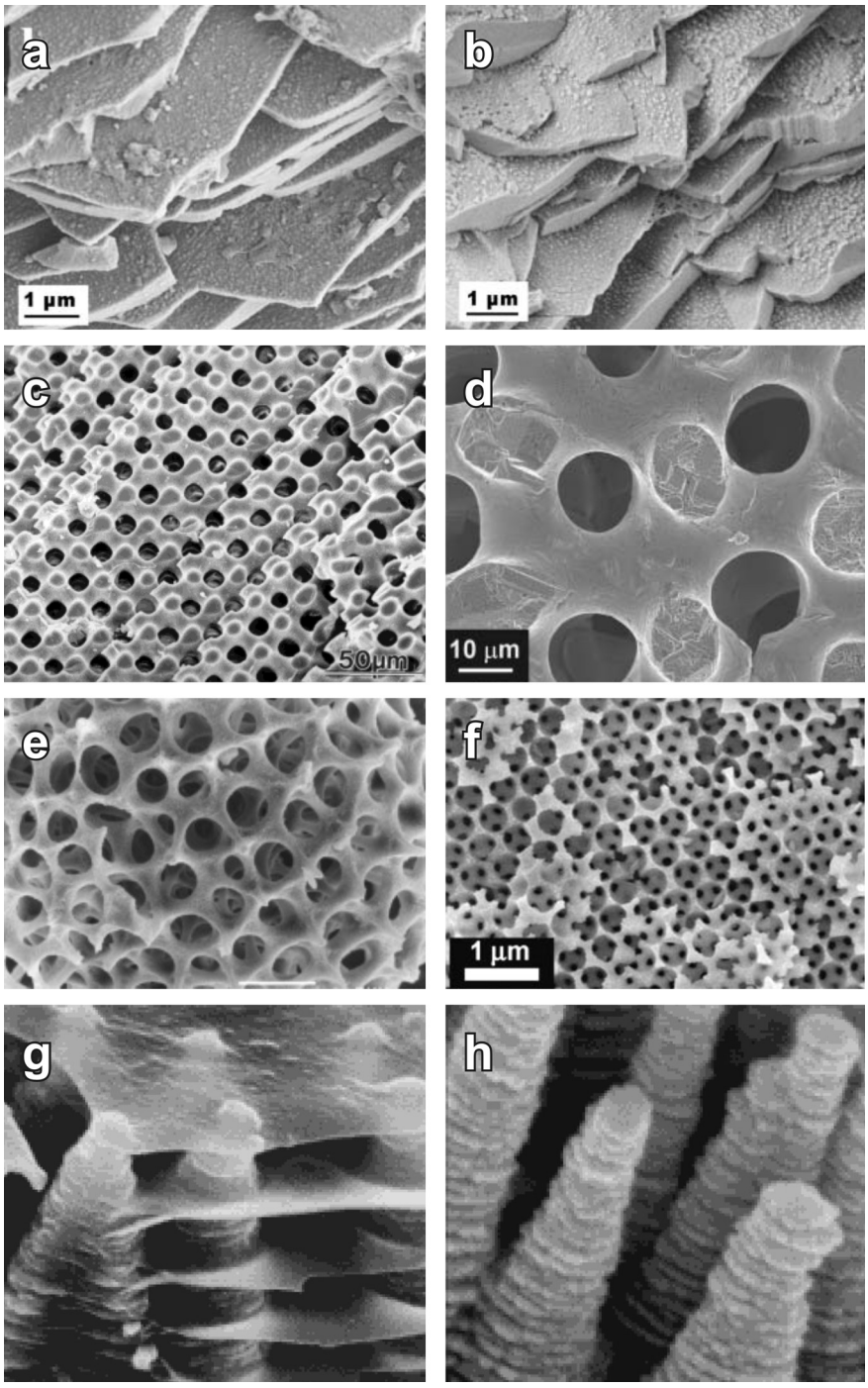

Fig. 1-4: Biomimetic mineralization. (a) Fracture edge of the nacreous layers in *Haliotis laevigata* and (b) structure obtained by crystallization of $CaCO_3$ in the presence of the extracted insoluble organic matrix (adapted from [31]). (c) Cross-section of a sea urchin test and (d) macroporous copper network prepared by electrochemical deposition in a polymeric replica of the biological structure (reproduced from [33]). (e) "Vesicle foam"-like pattern of amorphous silica characterizing the shell of radiolarians (adapted from [11]) and (f) a calcite single crystal with ordered pores synthesized by infiltrating a 3D array of polymeric particles with an ACC precursor phase and subsequent recrystallization (reproduced from [34]). (g) Nacreous columns and layers at the growing tip of *Haliotis rufescens* and (h) columnar zinc oxide architectures achieved by crystallization from solutions containing citrate ions and hexamethylenetetramine (adapted from [35]).

A straightforward, though experimentally often difficult pathway to mimic biomineralization is to extract the "organic matrix" from living tissues and use it in crystallization experiments. This may afford information on the role of associated biomolecules in the natural process,[15,24,26] and occasionally allow for more or less accurate retrosynthesis of the material (Fig. 1-4a-b).[31,32] Another promising concept is modeled upon the templating effect envisaged for at least some biological membranes and compartments. When mineralization is carried out within a volume bearing geometrical resemblance to biological structures, the final crystal(s) will adopt a similar morphology if the initially precipitated phase can be shaped into that volume. For this purpose, amorphous precursor particles have proven to be versatile tools,[32,34] and prominent templates employed include replica of sea urchin tests (Fig. 1-4c-d)[33] or colloidal crystals (Fig. 1-4e-f).[34]

Such "top-down" methodology is evidently capable of yielding inorganic matter with peculiar morphologies, but in turn necessitates elaborate preparation of a suitable template and moreover does usually not account for the ordered microstructure displayed by many biominerals. Therefore, it is desirable to develop "bottom-up" strategies for the design of biomimetic materials, that is, synthetic routes which enable the formation of complex architectures based on the self-assembly of preferably simple compounds. To that end, a vast amount of effort has been spent on investigating the influence of various soluble additives on the crystallization of distinct minerals. In some cases, noticeable morphological effects could already be observed upon introduction of foreign ions (Fig. 1-5), which were ascribed primarily to substitutions in the crystal lattice or adsorption on specific planes, modifying relative growth rates, the final habit and potentially also polymorphism.[36-38] However, in view of the principles learned from biomineralization, additive species of organic nature are a more obvious choice in the quest for crystal growth modifiers. Indeed, experiments with substances like citric acid confirmed that such small organic molecules can have a remarkable impact on the progress of crystallization, for instance producing dumbbell-like shapes in the case of calcium carbonate as a consequence of specific adsorption (see Fig. 1-6a). Delicate crystal aggregates of both $CaCO_3$ (Fig. 1-6b) and ZnO (Fig. 1-4g-h), with the latter being somewhat reminiscent of growth fronts found in nacre, were moreover obtained with comparatively simple molecules, although morphogenetic aspects of these peculiar nanoparticle superstructures have remained obscure up to date.[35,40]

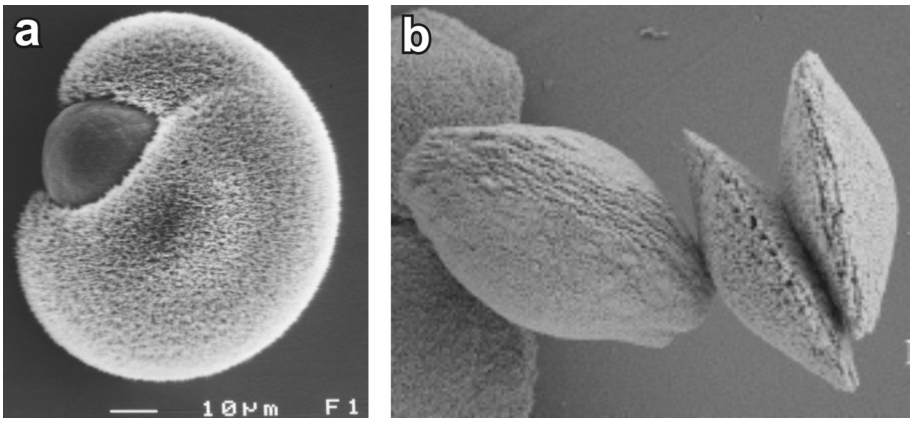

Fig. 1-5: The effect of foreign ions on the crystallization of calcium carbonate. (a) Rounded morphology grown upon addition of Mg^{2+} ions, consisting of a magnesian calcite core and a polycrystalline envelope of aragonite (adapted from [37]). (b) Lens-shaped superstructures of oriented vaterite nanoparticles, obtained under the influence of ammonium ions (reproduced from [38]).

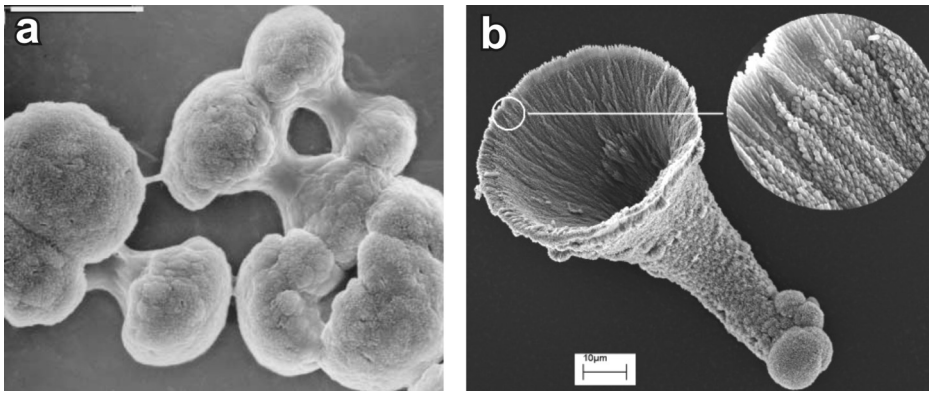

Fig. 1-6: Morphosynthesis based on small organic molecules. (a) Dumbbell-shaped calcite morphologies generated by the cooperative action of citric acid and Mg^{2+} ions (adapted from [39]). (b) Self-assembled polycrystalline calcite "microtrumpet", synthesized by addition of 1,2-diamino-2-hydroxypropane-*N*,*N*,*N'*,*N'*-tetraacetic acid (reproduced from [40]).

Apart from these certainly interesting examples of structure induction by means of ions and small molecules, the vast majority of biomimetic approaches to the design of novel materials has been focused on the beneficial influence of large organic polyelectrolytes or different kinds of surfactants on crystallization scenarios. This is because polymers, on the one hand, may be regarded as simplified and easy-to-handle model compounds imitating the role of biological macromolecules. Surfactants, on the other, and in particular supramolecular assemblies like micelles, vesicles or microemulsion droplets could simulate lipid bilayers and membrane-delineated compartments in biomineralization. The effects provoked by these additives are extremely manifold and there is an almost unmanageable number of studies available in literature on this

topic.[30,31,41-59] Galleries of some of the most intriguing morphologies and structures synthesized with the aid of polymers and surfactants are reproduced in Fig. 1-7 and Fig. 1-8.

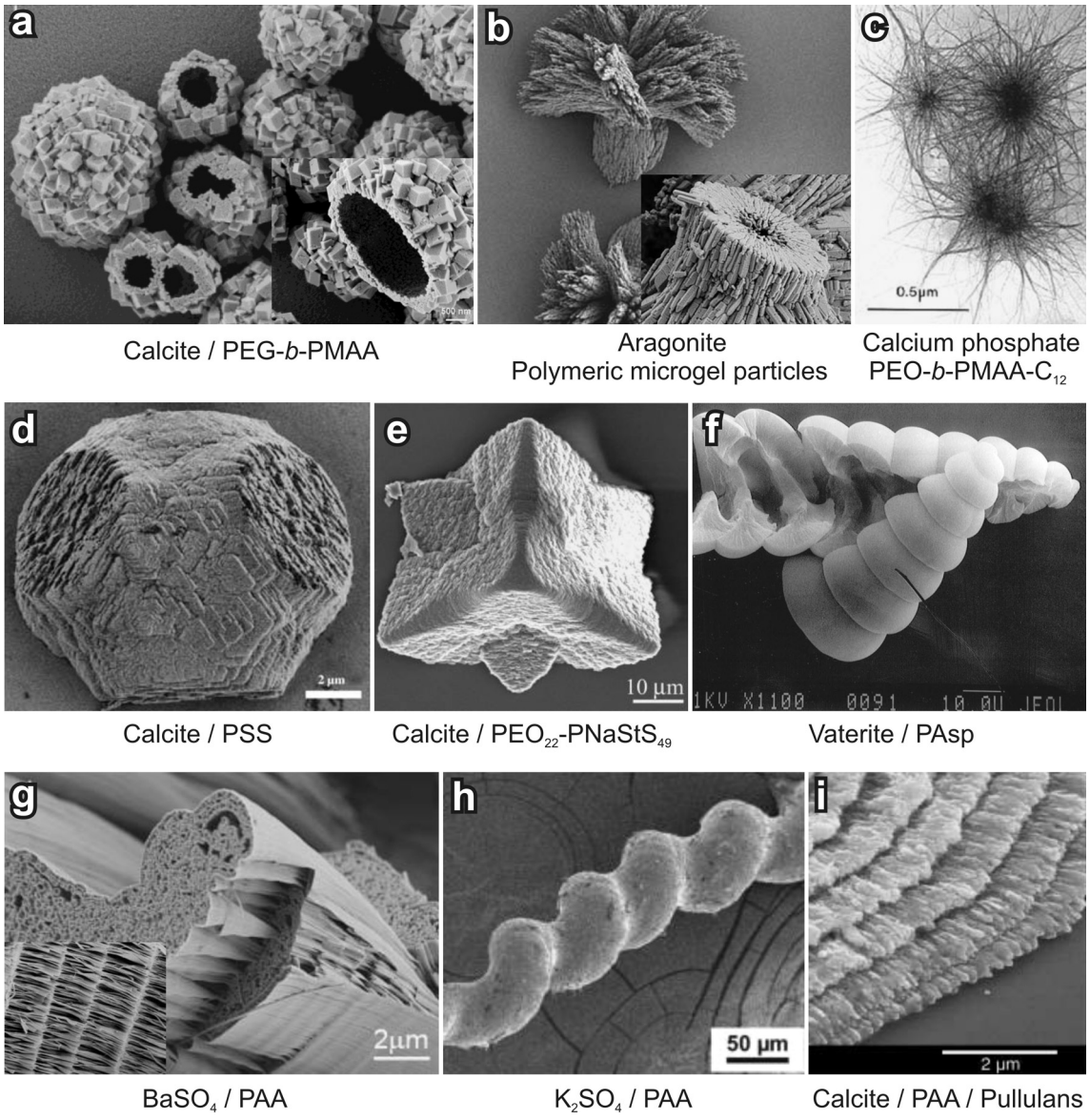

Fig. 1-7: Selected examples of polymer-controlled crystallization. The mineral phase constituting the architectures and the additive employed for their preparation are outlined below the respective micrographs. Images were adapted from (a) [44], (b) [45], (c) [41], (d) [47], (e) [30], (f) [48], (g) [31], (h) [49], and (i) [50]. Abbrevations: PEG-*b*-PMAA – Poly(ethylene glycol)-*block*-poly(methacrylic acid); PEO-*b*-PMAA-C_{12} – Poly(ethylene oxide)-*block*-dodecyl functionalized poly(methacrylic acid); PSS – Poly(styrene sulfonate); PEO-*b*-PSS – Poly(ethylene oxide)-*block*-poly(styrene sulfonate); PAsp – Poly(*α*,*L*-aspartate); PAA – Poly(acrylic acid). The microgel particles used for the synthesis of the aragonite superstructure shown in (b) were composed of a triblock copolymer of diethylaminoethyl methacrylate, *N*-isopropylacrylamide, and methacrylic acid. Pullulans are natural polysaccharides consisting of maltotriose units.

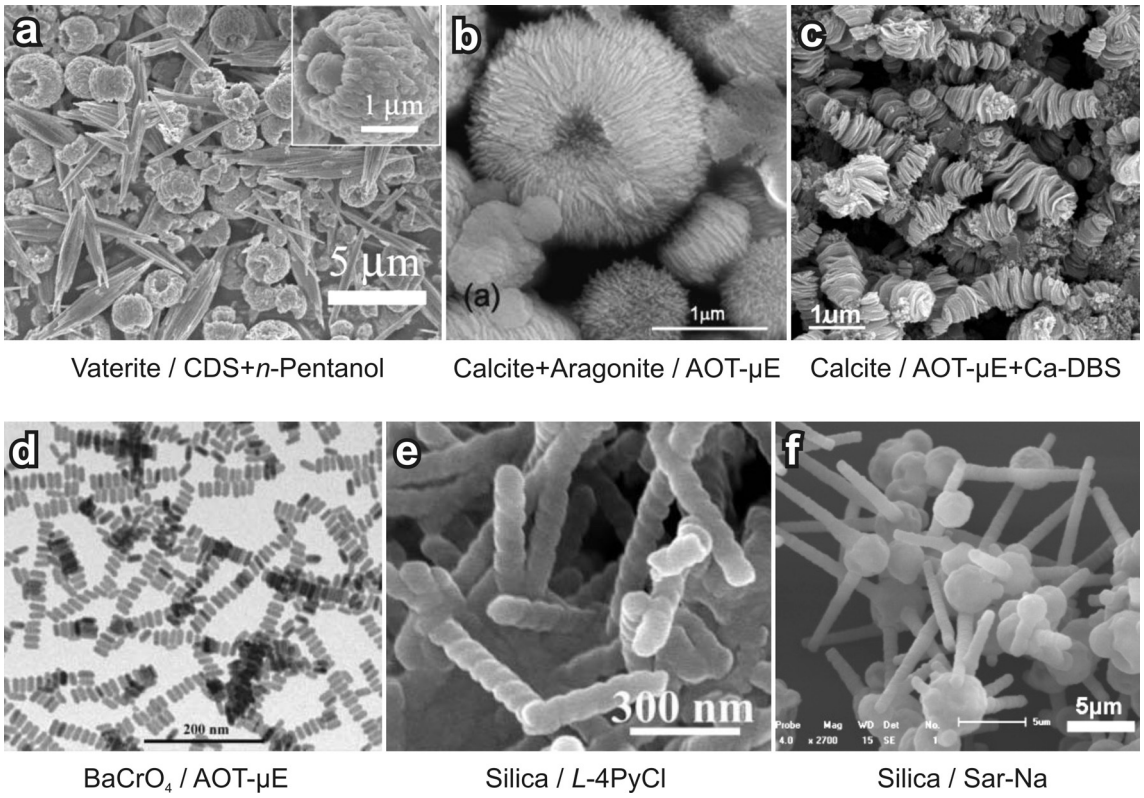

Fig. 1-8: Surfactant-based morphosynthesis of inorganic minerals, reproduced from (a) [51], (b) [52], (c) [53], (d) [54], (e) [55], and (f) [56]. Abbreviations: CDS – Calcium dodecylsulfate; AOT - Bis(2-ethylhexyl) sulfosuccinate; µE – Microemulsion; Ca-DBS – Calcium dodecyl-benzenesulfonate; *L*-4PyCl - Pyridinium-based cationic surfactant derived from *L*-isoleucyl-aminooctadecane; Sar-Na – Sodium *N*-lauroylsarcosine.

Charged polymers can for instance interfere with the crystallization process by sequestering ions involved in precipitation and thereby alter the effective supersaturation and growth kinetics. In turn, binding of ions increases their concentration locally, which may render the vicinity of the polymer a favorable site for nucleation. If, in addition, the polymer has a suitable conformation in terms of its functional groups and charge distribution, and further provides an interface (which is for example the case when the polymer is adsorbed to surfaces like glass walls), it can direct nucleation and hence possibly control phase selection and crystal orientation (cf. Fig. 1-7b and i). In analogy to what has been suggested for ions and simple molecules, polymeric additives were shown to interact specifically and often in a much more efficient way with distinct crystal planes. This can lead to drastic habit changes of growing single crystals, but may also result in a stabilization of relatively small crystal units and the generation of superstructures *via* their aggregation (cf. Fig. 1-7b-e and g-i). Likewise, the occurrence of metastable modifications such as amorphous particles can be promoted in the presence of polymers, and their delayed transformation into

crystalline phases is frequently found to be accompanied by the formation of most unusual architectures (Fig. 1-7a and f). Similar functions are generally attributed to the behavior of added surfactants. Here, the self-organization of the amphiphilic species in water or water/oil mixtures and the dimensions of corresponding surfactant aggregates however also play essential roles. For example, polymerization of silica in media containing ordered surfactant assemblies can yield in a transcription of the solution structure to the emerging solid phase (Fig. 1-8e). On the other hand, the spatial confinement of the aqueous micro-environment prevailing in water-in-oil and bicontinuous microemulsions as well as reverse micelles factually determines the size and shape of the precipitating mineral and can thus afford well-defined particles with micron- or nanoscale sizes. Their aggregation and arrangement into higher-order ultrastructures as those shown in Fig. 1-8b-c is then mediated by surfactant molecules in a manner related to the action of polymers (see below). Another factor contributing to morphogenesis in such systems is the existence of polar-nonpolar interfaces at which mineralization may preferentially take place. In this case, selective solidification of the phase boundaries results in hollow frameworks with various morphologies (cf. Fig. 1-8f and Fig. 1-9a). Eventually, combining the shaping effect of microemulsions with that of externally imposed templates can produce architectures with superior structural hierarchy (Fig. 1-9b).

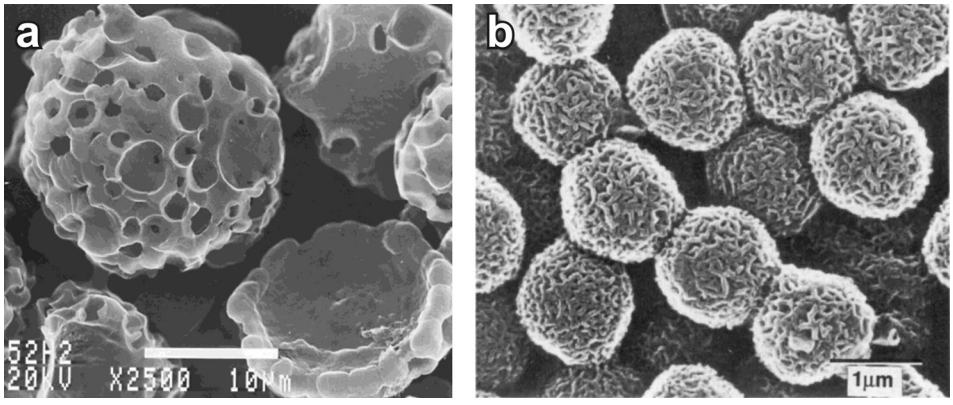

Fig. 1-9: Biomimetic mineralization in microemulsions. (a) Hollow sponge-like vaterite spheroids grown from a microemulsion of water in octane with sodium dodecylsulfate as surfactant. Patterning of the surface is due to microbubbles caused by degassing of CO_2 from the inner supersaturated calcium bicarbonate solution (adapted from [58]). (b) Aragonite shells with porous texture, synthesized by spreading a film of a bicontinous microemulsion consisting of water, tetradecane, and didodecyldimethylammonium bromide surfactant over micron-sized polystyrene beads (reproduced from [59]).

Essentially, the diverse studies conducted in the past years on biological and biomimetic mineralization have highlighted that the formation of a crystal does not necessarily proceed along the pathway envisaged by classical theories, that is, via incorporation of single ions or molecules to an existing particle and concurrent growth by unit-cell replication (see Fig. 1-10, pathway (a)). Instead, pre-formed nanoparticles can serve as building blocks, opening alternative reaction channels which may be summarized under the label "non-classical crystallization".[41,47,60,61] In the absence of additives, primary particles can agglomerate and mutually arrange such that merging in a common crystallographic register becomes possible and a single crystal is formed (Fig. 1-10, pathway (b)); this process is called "oriented attachment".[62]

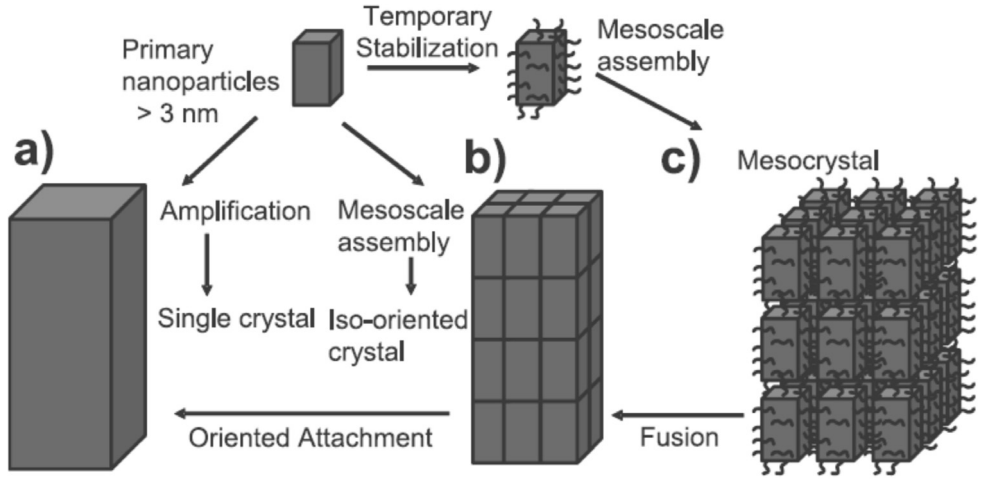

Fig. 1-10: Schematic comparison of (a) classical and (b) non-classical crystallization. Pathway (c) illustrates how additives like polymers or surfactants can stabilize individual nanoparticle units and trigger the formation of a mesocrystal (adapted from [41]).

In turn, adsorption of suitable additive species on the nanoparticle units can prevent their fusion and the interactions between the molecules covering the surface will govern particle aggregation under these circumstances. This is nicely visualized by the chain-like structures of prismatic barium chromate crystals obtained in AOT microemulsions (Fig. 1-8d), where interdigitated bilayers of the surfactant mediate co-orientation.[55] However, even such additive-decorated hybrid particles can aggregate in a way that they are perfectly aligned with respect to their crystallographic axes in all three dimensions of space, yielding an ordered mesoscale assembly which scatters like a single crystal but still consists of multiple individual units (Fig. 1-10, pathway (b)). Examples for these so-called "mesocrystals" are the architectures shown in Fig. 1-7d, e and g as well as Fig. 1-8a. It is obvious that this alternative route of crystallization is capable of generating pseudo-single crystals with remarkable morphologies. Depending

on the detailed interactions between the adsorbed layers, possible re-ordering phenomena during aggregation, and the occurrence of amorphous precursors, mesoscale integration of the building blocks can likewise produce polycrystalline superstructures as those displayed in Fig. 1-7b and Fig. 1-8b-c, which lack crystallographic lock-in of the components and exhibit extraordinary complexity. A highly delicate situation arises when an additive adsorbs selectively on distinct faces of anisotropic particles and thereby encodes their self-assembly. This accounts for the formation of twisted K_2SO_4 morphologies in concentrated polyelectrolyte solution (cf. Fig. 1-7h),[49] and was moreover realized for barium carbonate with the aid of a double-hydrophilic block copolymer (see Fig. 1-11).[63] In the latter case, specific adsorption of the sterically demanding polymeric additive on certain planes at the tips of elongated $BaCO_3$ crystallites causes a staggered arrangement of the building blocks and allows incoming units to differentiate between the lateral faces during their attachment, which eventually facilitates the formation of helical morphologies.

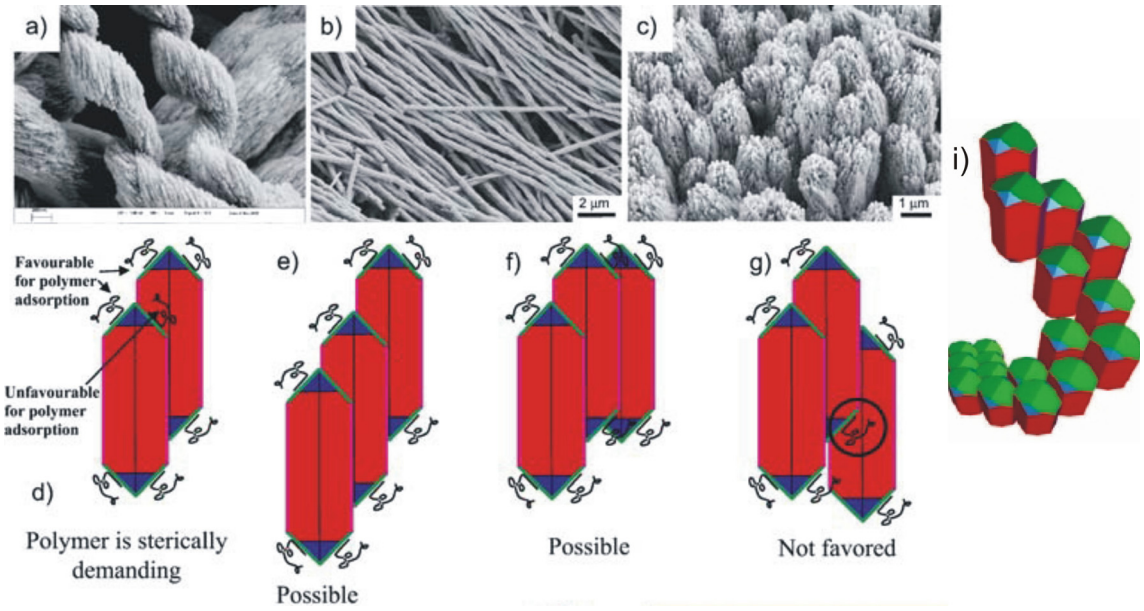

Fig. 1-11: "Programmed" higher-order self-assembly of inorganic nanoparticles. (a-c) SEM images of tectonic $BaCO_3$ aggregates obtained upon crystallization from solutions containing a phosphonated block copolymer. The architectures show helical forms of variable pitch (a-b) and consist of parallel and largely aligned nanocrystals. (d-i) Schematic representations explaining the origin of helicity in the system. Face-selective adsorption of the polymer on (110) planes and sterical hindrance (d) promote staggered particle aggregation along a common growth direction (e-f) and inhibit other arrangements (g). Integration of building blocks occurs by epitaxial attachment to the uncovered lateral faces (020) and (011). Upon continued aggregation, the latter can be differentiated by approaching particles and become divided into favorable and unfavorable sites for attachment. This introduces an either right- or left-handed turn in the assembly (i) and propogates helical winding (adapted from [41]).

The above examples clearly point out the considerable progress recently made in the realms of bio-inspired material synthesis and additive-controlled crystallization. The work performed in the framework of this thesis affords further contributions to these exciting areas of research, yet with a fundamental distinction to most of the previously reported studies: the present experiments were focused on the effect of added silica on the mineralization of alkaline-earth carbonates and, thus, the systems in the scope of investigation were *purely inorganic*. This may appear a bit odd at first glance in the context of biomineralization and common approaches to emulate related phenomena *in vitro*, which – except for experiments with simple ions like Mg^{2+} (cf. Fig. 1-5) or different phosphate species[64,65] – all rely on the influence of more or less elaborate *organic* (macro)molecules and/or supramolecular matrices. However, on the one hand, silica is abundant in Nature, both by itself as a mineral and dissolved in natural waters, and could hence have an impact on alkaline-earth carbonates crystallizing in its environment. On the other hand, in the late 1970s, Juan Manuel García-Ruiz discovered highly unusual crystal architectures which formed upon precipitation of strontium or barium carbonate in silica gels at high pH.[66-68] Spontaneously and in the absence of any organic matter, complex structures including twisted ribbons, regular helicoids, and diversely shaped sheets were produced (see Fig. 1-12 and Fig. 1-13), each of which was confirmed to be composed of myriad nanocrystallites in a somewhat ordered array.

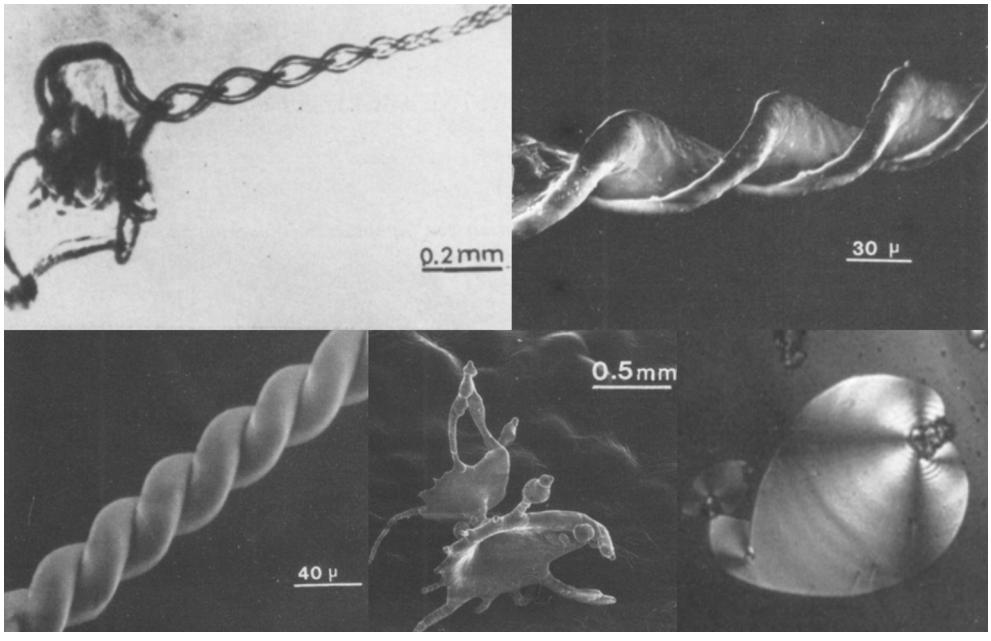

Fig. 1-12: Barium and strontium carbonate crystal aggregates grown from alkaline silica gels, reported by García-Ruiz in his original work in 1981.[67]

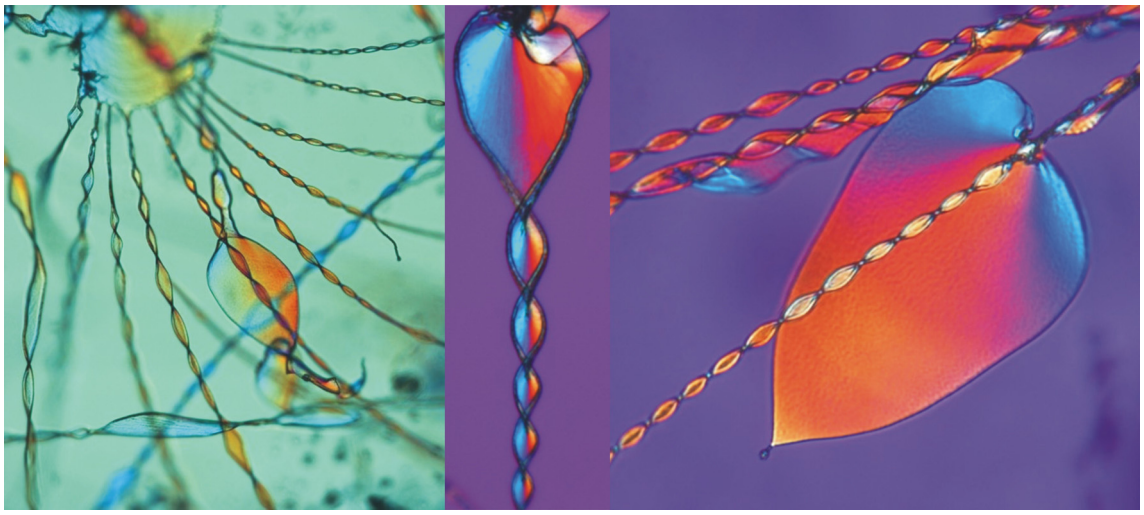

Fig. 1-13: Optical micrographs of twisted and sheet-like $BaCO_3$ architectures obtained upon crystallization in silica-containing environments at high pH (image courtesy of Prof. Dr. Juan Manuel García-Ruiz).

This finding was revolutionary in a sense that the interplay of completely abiotic components was for the first time shown to potentially yield crystal aggregates with curved morphologies devoid of crystallographic symmetry and hence an appearance thought to be exclusive to the animate nature. In their later studies, García-Ruiz *et al.* extended this notion by revealing a striking morphological convergence between some of the as-prepared inorganic precipitates and putative microfossils as well as certain living beings (see Fig. 1-14).[69-72] On that basis, it was concluded that there can be no strict classification of form into "inorganic and organic symmetry" as suggested in Fig. 1-1 and, in turn, that an identification of biogenicity by morphological aspects alone may be misleading.

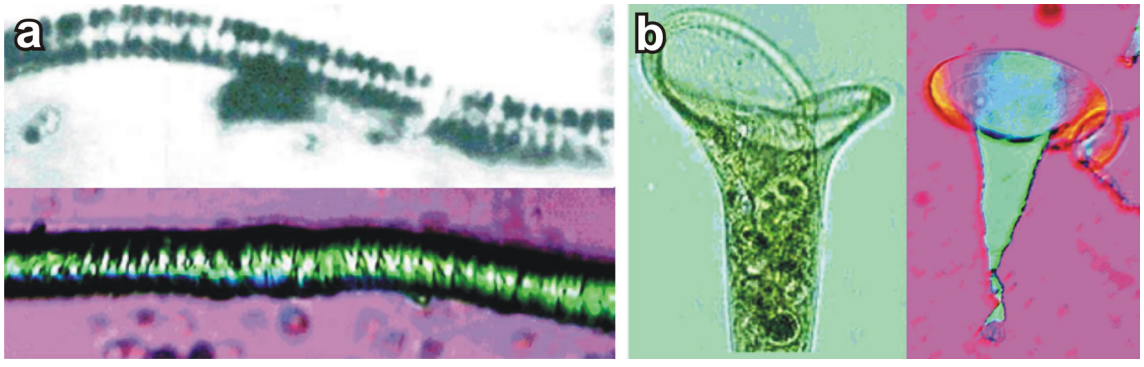

Fig. 1-14: Abiotic emulation of biological morphology. (a) Comparison of a purported Precambrian microfossil (top) and an inorganic "biomorph" (bottom). (b) Optical micrographs of the modern protist *Stentor roeseli* (left) and a $BaCO_3$ aggregate grown in the presence of silica (right). Adapted from [71].

Such non-crystallographic carbonate aggregates grown from silica-rich media were named “biomorphs” in an attempt to express the emulation of biological form by an inanimate system. Apart from obvious implications for fields like paleontology, the structural organization found in biomorphs is impressive and mimics hierarchical principles inherent in many biominerals, despite the simplicity of the components involved. Therefore, biomorphs are interesting laboratory models for the design of bottom-up strategies towards advanced functional materials via concerted self-assembly, which may at the same time yield valuable information on concepts at work during the construction of (truly) biogenic and biomimetic minerals. To further illustrate the broad panoply of curved morphologies accessible by silica-directed crystallization of $BaCO_3$, a compilation of selected electron micrographs is given in Fig. 1-15.

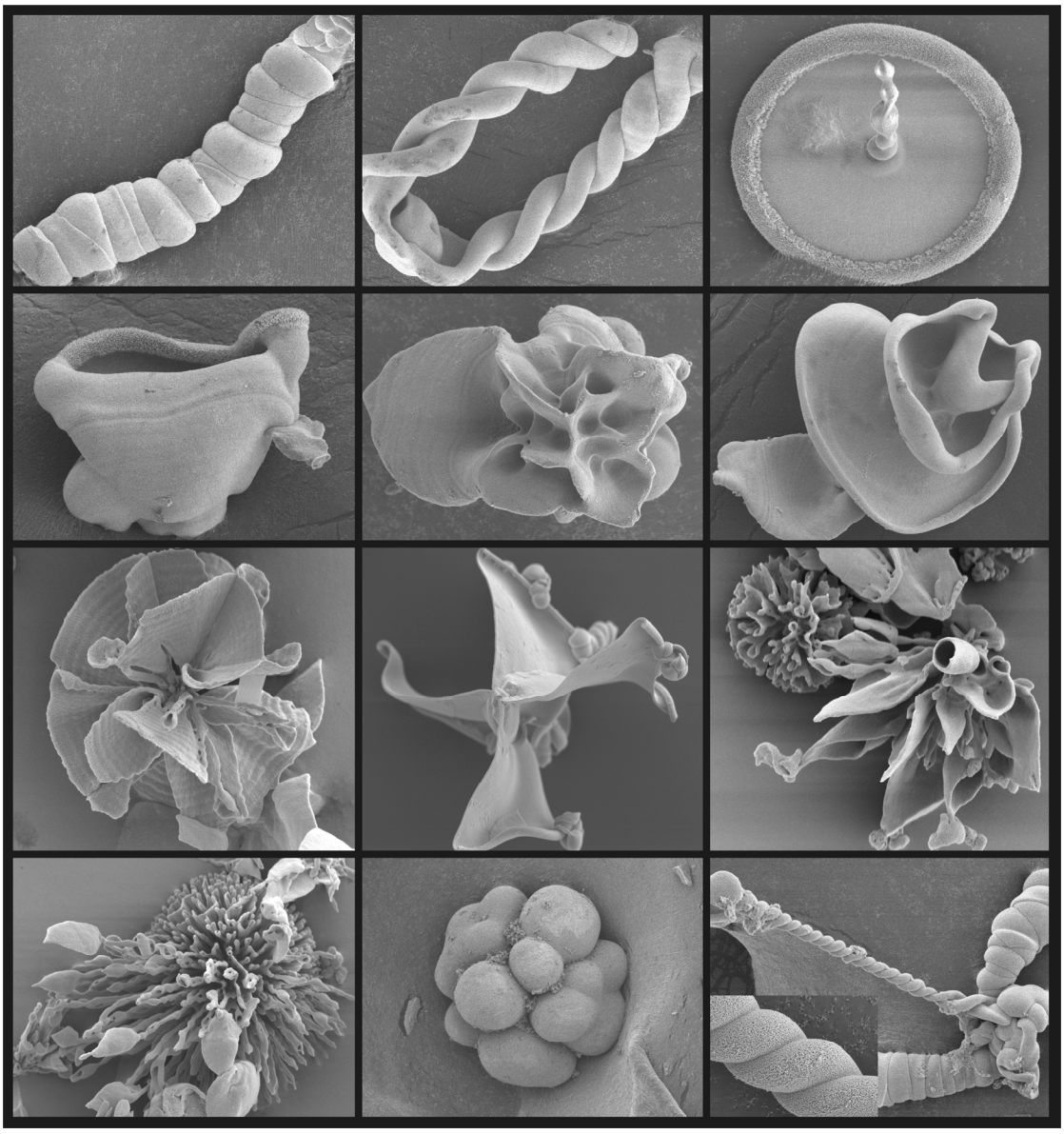

Fig. 1-15: Complex materials from simple chemistry: a selection of images visualizing the structural diversity of silica biomorphs.

1.2 Aim of the Thesis

Inspired by these findings, the aim of the present thesis was to generally explore in more detail the processes occurring when alkaline-earth metal carbonates are crystallized under the influence of dissolved silica as an additive. This problem was addressed by two substantially different approaches. On the one hand, emphasis was placed on understanding the interactions between the species from a fundamental point of view and deciphering at which stages of crystallization the silica may interfere. These studies were carried out predominantly with calcium carbonate, as it is technologically much more relevant than the higher homologues and since the phenomena encountered during its precipitation from solution are comparably well-characterized. Moreover, related experiments were performed exclusively in systems at high supersaturation, that is, crystallization was induced by directly mixing the corresponding ions, so as to provide sufficient amounts of sample for proper analysis and, simultaneously, imitate precipitation conditions applying for many practical situations. Thus, the main goal of this part of the work was to shed light on the effects of silica on nucleation and growth of $CaCO_3$ particles as well as possible polymorphic transformations, rather than deliberately provoking structured crystallization and preparing biomimetic materials. Results obtained from these experiments are presented in Chapters 2-5 of this dissertation.

On the other hand, given the scarce knowledge available on the formation mechanism of silica biomorphs at the beginning of the thesis, a second major line of research was devoted to investigating the growth behavior and particular morphogenetic features of these fascinating crystal aggregates. Here, barium carbonate was the mineral of choice, as it yields biomorphic architectures more readily than calcium carbonate and the most intriguing morphologies, such as helicoids, could to date not be realized with $CaCO_3$. As opposed to the work described in the first part, this section of the thesis is hence concerned with the directed self-organization of inorganic matter and the interplay between carbonate and silica under conditions of relatively slow and ordered crystallization. In general, the performed studies were aimed at gaining insight into the distinct forces driving self-assembly on different length scales, namely the silica-mediated formation and stabilization of nanometric carbonate crystallites, their oriented arrangement over mesoscale dimensions, and the development of curved shapes from a global perspective. Further, the growth kinetics of these unique materials were examined, and means were sought by which the morphology of the aggregates may be

tuned. The outcome of the numerous experiments conducted with silica biomorphs and essential implications for morphogenetic scenarios are summarized in Chapters 6-9.
Before discussing in detail the data collected during this thesis, basics on calcium carbonate precipitation required to understand the conclusions drawn in the following chapters as well as the state-of-the-art in the field of biomorphs shall be addressed.

1.3 Calcium Carbonate Precipitation

Interest in the crystallization of calcium carbonate from solution does not only originate from its abundance as inorganic component in the hybrid structures of many biominerals, but also from its large occurrence as geological scales in rocks and ocean sediments,[73] and related implications for the natural CO_2 cycle and Earth's climate.[74] Further fundamental relevance derives from its wide industrial application for instance as a filler or ingredient of construction materials,[75] as well as from the long-standing problems caused by incrustation and scaling due to spontaneous precipitation at elevated temperatures.[76]
Classical theories treat crystallization predominantly from a thermodynamic viewpoint and assume that crystal growth proceeds from a nucleus by amplification of the unit cell. The final morphology of the crystal is then considered to be the consequence of energetic differences between the distinct planes, that is, faces with a high surface energy grow fast and eventually vanish while energetically favored ones become expressed (Wulff rule).[77] The role of additives is well accommodated within this model, as adsorption of suitable species on high-energy faces can lower interfacial potentials and thus alter relative growth rates and the resulting morphology.[31] However, such conceptualization often fails to explain the phenomena encountered in biological and biomimetic mineralization. This is because, especially for a polymorphic compound as calcium carbonate, there exists an alternative pathway for crystallization which is controlled by kinetics rather than thermodynamics (see Fig. 1-16). In this case, the mineral does not crystallize directly in its thermodynamically stable modification but, beforehand, may undergo multiple phase transitions along a series of intermediates towards increasing stability. This observation is reflected in Ostwald's rule of stages, which states that during sequential precipitation the least stable and commonly most soluble polymorph is formed first and, in succession, converted preferentially to phases that are structurally and/or energetically closest.[78] Whether or not crystallization takes place under kinetic control and which of the metastable polymorphs occur in such a

multi-step process depend on modulations of the activation energies ΔG^* associated to nucleation (N) and growth (G) of the initially precipitated phase and transformations (T) in-between the distinct stages (cf. Fig. 1-16). In principle, polymorph interconversions can be mediated either through solid-state transitions or by a dissolution-reprecipitation mechanism, the latter scenario apparently being favored in most cases due to the considerable energetic effort needed for solid-phase re-ordering.[31,79,80]

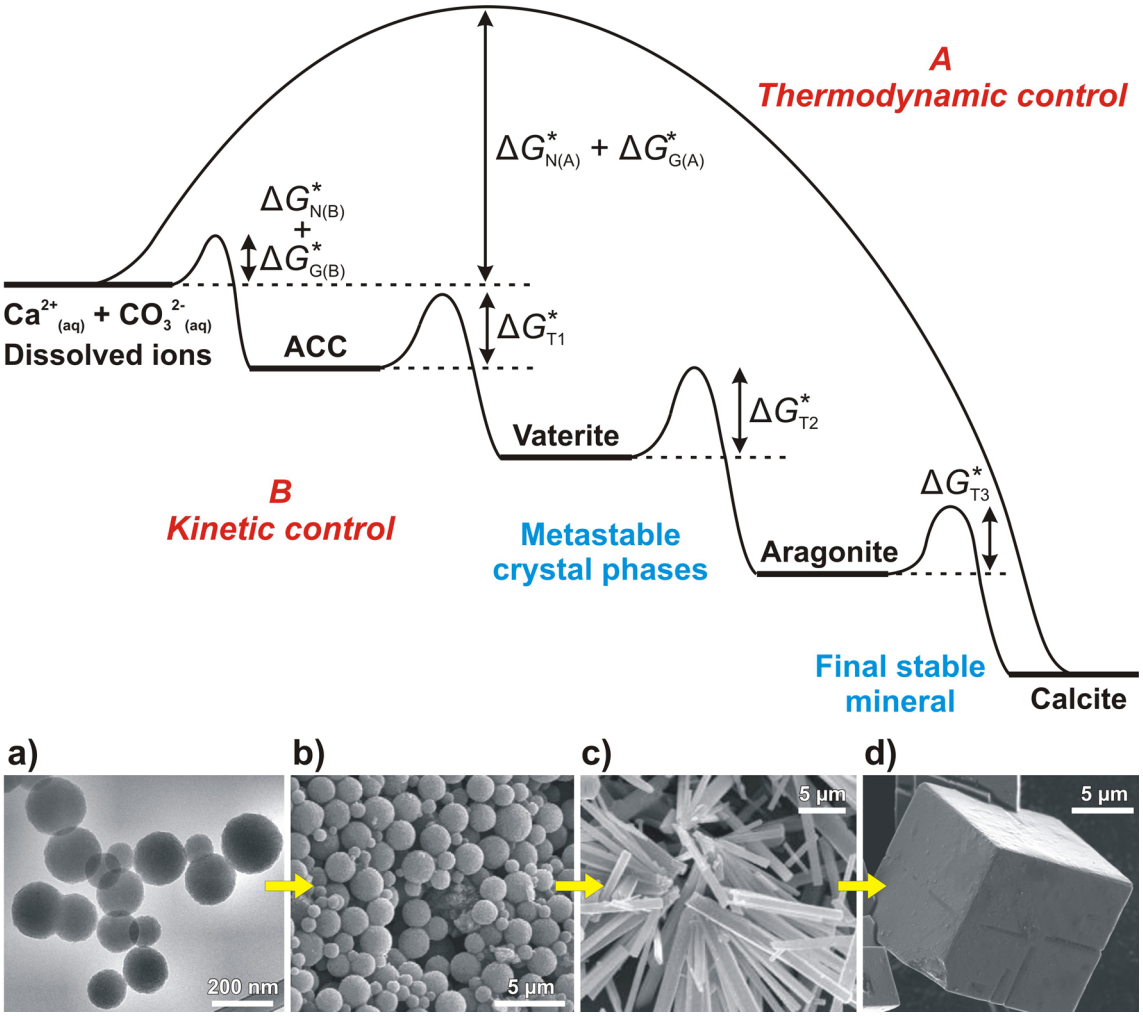

Fig. 1-16: Top: Scheme depicting the crystallization of calcium carbonate under thermodynamic (A) and kinetic control (B). The activation barriers to be overcome for nucleation (N), growth (G), and phase interconversion (T) essentially determine which of the two possible pathways is traveled and whether a certain metastable polymorph is observed in sequential precipitation under given conditions or not. Bottom: Electron micrographs showing typical morphologies of (a) ACC, (b) vaterite, (c) aragonite, and (d) calcite. Images (b) and (c) were adapted from [81] and [82], respectively, and the scheme was in part re-drawn after [61].

For calcium carbonate, Ostwald's law would imply a kinetic phase sequence according to ACC → vaterite → aragonite → calcite under ambient conditions, when neglecting the much less common hydrated crystalline polymorphs ikaite ($CaCO_3 \cdot 6H_2O$) and

monohydrocalcite ($CaCO_3 \cdot H_2O$). In fact, experimental studies have confirmed that kinetically driven crystallization is particularly promoted in systems at high supersaturation and that the first solid phase usually generated under these circumstances is ACC.[23,64] At room temperature, subsequent transformation was found to yield vaterite, which was converted in the following to calcite without involving aragonite as a further intermediate stage.[83,84] In turn, on heating, the fractions of metastable vaterite traced during crystallization under kinetic control decreased systematically, while the temporary occurrence of aragonite was enhanced.[85] This shows that synthesis parameters play an important role in the choice of the particular precipitation pathway. Another means to influence this process is to introduce additives which interact with one or more of the kinetic intermediates and hence potentially affect their interconversions. For example, adsorption of additive species on the surface of the metastable particles can impede dissolution and thus increase their temporal stability. This seems to be accomplished *in vivo* by specialized biomolecules (as mentioned in Section 1.1), but has likewise been realized synthetically, in the case of ACC for instance by adding phytic acid as inhibitor (see Fig. 1-17).[86]

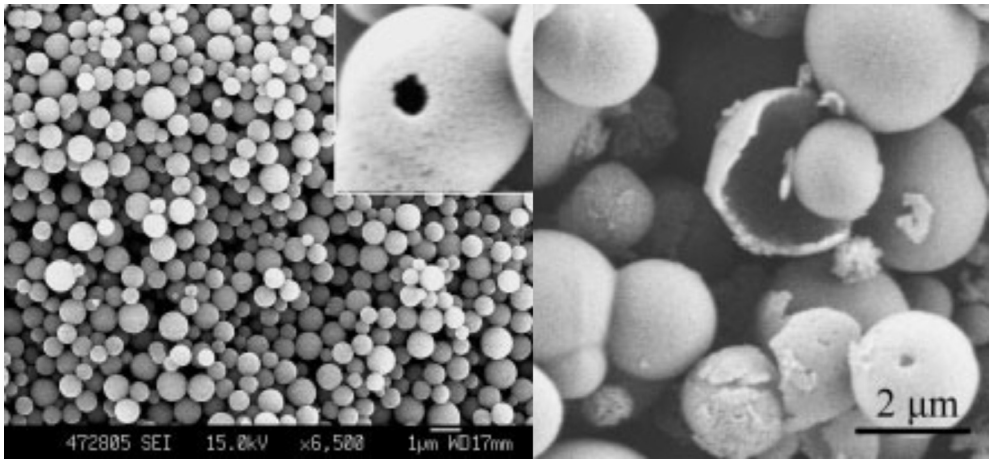

Fig. 1-17: Hollow spheroids of ACC prepared by precipitation of $CaCO_3$ in the presence of phytic acid, a sixfold phosphonated derivative of inositol. The particles remained amorphous even when left in contact with the mother solution for three months (reproduced from [86]).

On a similar basis, also vaterite[87] and aragonite[88] could be stabilized *in vitro* against energetically favored transformation and, thereby, obtained more or less selectively upon precipitation from solution. Evidently, this concept allows for controlling to a certain extent the crystal or amorphous modification retrieved from an experiment and thus has great potential for the preparation of $CaCO_3$ powders for various applications –

given that polymorphism defines, together with other factors such as particle size or morphology, macroscopic material properties.[89]

In this regard, the present experiments were intended to study the progress of $CaCO_3$ crystallization under conditions of kinetic control and especially to examine the effect of silica on the endurance of different polymorphs in the system. For this purpose, samples with various silica contents were prepared and characterized concerning their temporal evolution by quenching the process at distinct times and analyzing formed precipitates. Chapter 2 provides a summary of the results gained for the interactions between silica and initially nucleated ACC particles, and highlights how silica is capable of stabilizing this precursor phase. In Chapter 3, the mode in which temporarily silica-protected ACC is converted to crystalline polymorphs with time is outlined, with special focus on how the additive interferes with growth of calcite and provokes unusual single- and polycrystalline morphologies. The work described in Chapter 5 was in turn founded on a different methodical approach, in that $CaCO_3$ crystallization was in this case monitored *in situ* rather than by discontinuous sample drawing. To that end, the diffraction of particle suspensions obtained by mixing reagents was recorded as a function of time utilizing synchrotron radiation. These experiments shed particular light on the behavior and relative stability of the metastable crystalline polymorphs vaterite and aragonite in the presence of silica.

Another issue under severe debate for more than a century is the actual onset of precipitation from solution, that is, nucleation. Principally, common theories distinguish between homogeneous and heterogeneous nucleation. While the former occurs spontaneously in the bulk volume of a supersaturated solution, the latter involves extrinsic interfaces such as impurities or tube walls where the free energy required to generate a new surface is reduced. In the classical picture, homogeneous nucleation is interpreted to result from an association of ions which randomly form clusters in the solution, which either grow or disintegrate again.[90,91] This process is thought to be a stochastic phenomenon and therefore such clusters are expected to be a rare species. Whether a cluster grows or not is essentially governed by the counter-play of two opposing contributions to the overall free energy of cluster formation ΔG_{Nucl}, namely the positive term of the surface energy ΔG_{S} (which is proportional to the square of the cluster radius r in case of spherical geometry) and the negative input originating from the win in bulk energy due to the development of a crystal lattice ΔG_{B} (scaling with the

volume, and thus ~ r^3) (see Fig. 1-18). Once the cluster reaches a certain critical size r^*, surface and bulk contributions become balanced and any further growth leads to a gain in the net free energy. Thus, the activation barrier for nucleation ΔG_{Nucl}^* (being a function of both temperature and supersaturation) is overtraveled and a so-called critical crystal nucleus is achieved, which can grow by unit-cell replication.

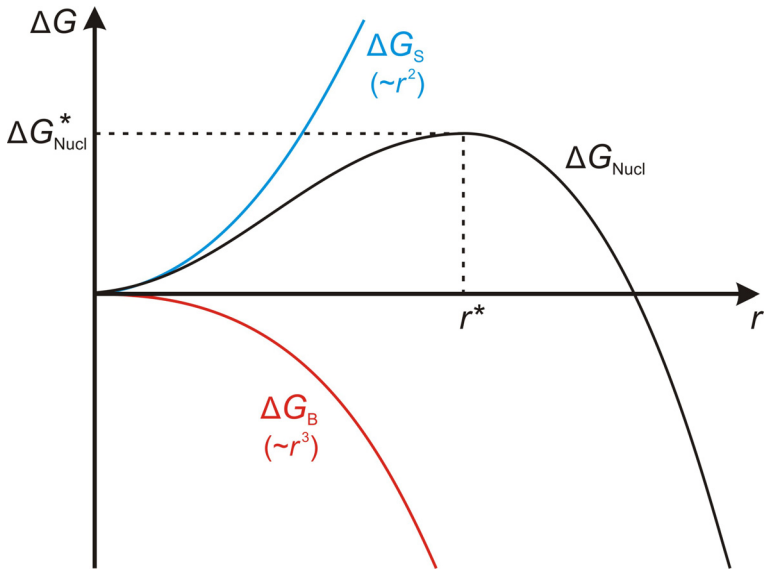

Fig. 1-18: Plot of the Gibbs free energy ΔG for the formation of a nucleation cluster as a function of the cluster radius r, according to classical nucleation theory. The balance between the cost in energy for creating a new surface (ΔG_S) and the gain due to attractive forces in the emerging lattice (ΔG_B) provoke a maximum in the net curve (ΔG_{Nucl}), which defines the critical cluster size r^* and the corresponding activation energy for nucleation ΔG_{Nucl}^*.

However, this fairly simplistic model fails to describe experimental data accurately, basically because it assumes that smallest nuclei behave like the corresponding macroscopic phase. In turn, even advanced nucleation theories cannot explain processes observed in non-classical crystallization and do neither allow evaluation of the state of a solution before nucleation. Very recent work has painted a thoroughly distinct picture of the very early stages of $CaCO_3$ crystallization. By titrating carbonate buffers at constant pH with $CaCl_2$ solutions and concurrently measuring the Ca^{2+} activity in the system, Gebauer *et al.* evidenced that substantial amounts of the present Ca^{2+} and CO_3^{2-} ions are not free in solution prior to nucleation, but rather appear to be bound (see Fig. 1-19).[92] This finding was ascribed to the pronounced formation of ion clusters, which were traced independently also by analytical ultracentrifugation. Considering the progression of the recorded titration curves and their pH dependency, it was concluded that these so-called pre-nucleation clusters are thermodynamically stable and exist in equilibrium

with the dissolved ions, both in the under- and supersaturated region. This is in sharp contrast to the critical clusters proposed in classical models, which are metastable and underlie the laws of kinetics (see Fig. 1-20). Further, it was shown that these ion clusters are on average neutral and consist of around 35 units of $CaCO_3$.

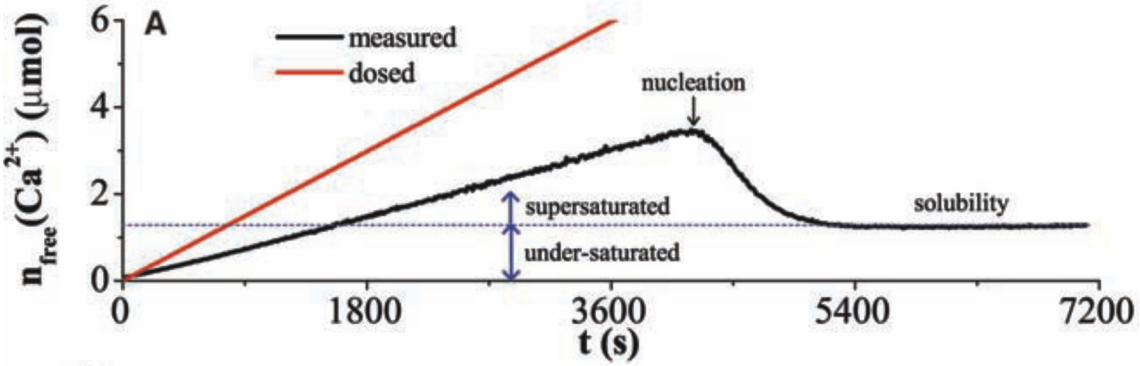

Fig. 1-19: Development of the concentration of free Ca^{2+} ions in carbonate buffer at a constant pH of 9.25 upon continuous titration with $CaCl_2$ solution, as reported by Gebauer *et al.* in [92]. The detected amount of Ca^{2+} (black) in the pre-nucleation stage is considerably lower than the dosed one (red), indicating that the ions are bound with carbonate in stable clusters.

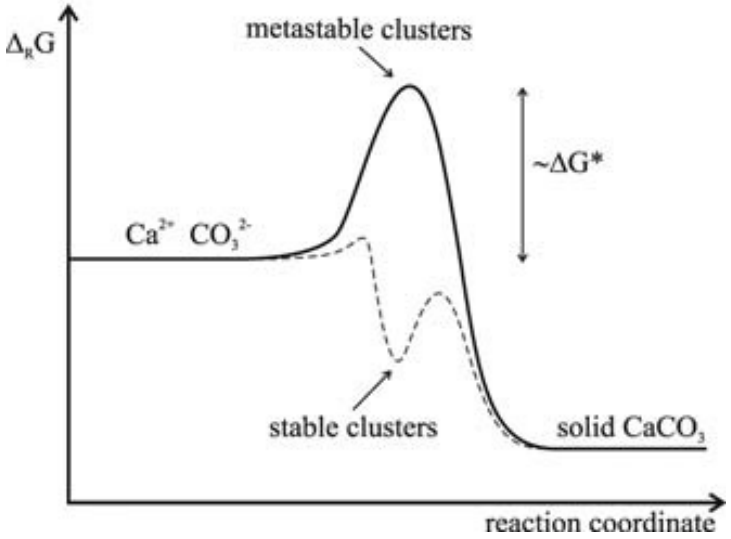

Fig. 1-20: Comparison of the reaction free energy envisaged for nucleation by classical theories (full line) and in light of the occurrence of stable pre-nucleation clusters (dashed line) (adapted from [92]). In the former case, critical clusters are metastable and the product of kinetically controlled processes that premise a certain activation barrier to be overcome. According to the novel view, clusters present in the pre-nucleation phase are stable species existing in a minimum of free energy. Note that this finding adds another, i.e. earlier, precursor stage to the sequential diagram shown in Fig. 1-16.

Another essential outcome of the work by Gebauer *et al.* was that the newly discovered clusters have a solute-like character and there is no true interface between them and the

surrounding solution. This is reflected in the linear increase of the free Ca^{2+} concentration before nucleation (cf. Fig. 1-19), and the fact that an equilibrium constant can be assigned to cluster formation, instead of a solubility product as for a solid phase (which would cause a constant Ca^{2+} activity, as observed in the curves after nucleation).[92] Thus, these pre-nucleation clusters may be regarded as solute complexes rather than particles with a distinct surface tension – again unlike the classical critical clusters and as expressed by the following equilibrium:

$$z\,Ca^{2+}_{(aq)} + z\,CO^{2-}_{3(aq)} \rightleftharpoons \{CaCO_3\}_{z(aq)}$$

Beyond that, there were furthermore indications that there is a correlation between the binding strength and hence the structure of the clusters and the short-range atomic order prevailing in the ACC particles that were initially nucleated in the experiments, as well as the crystalline polymorph into which the ACC phase transformed subsequently. This suggests that a certain degree of pre-structuring is inherent already prior to nucleation and that this earliest ordering may be somehow conveyed to the post-nucleation stage. These fascinating novel ideas on the onset of $CaCO_3$ precipitation are depicted by a comprehensive sketch in Fig. 1-21.

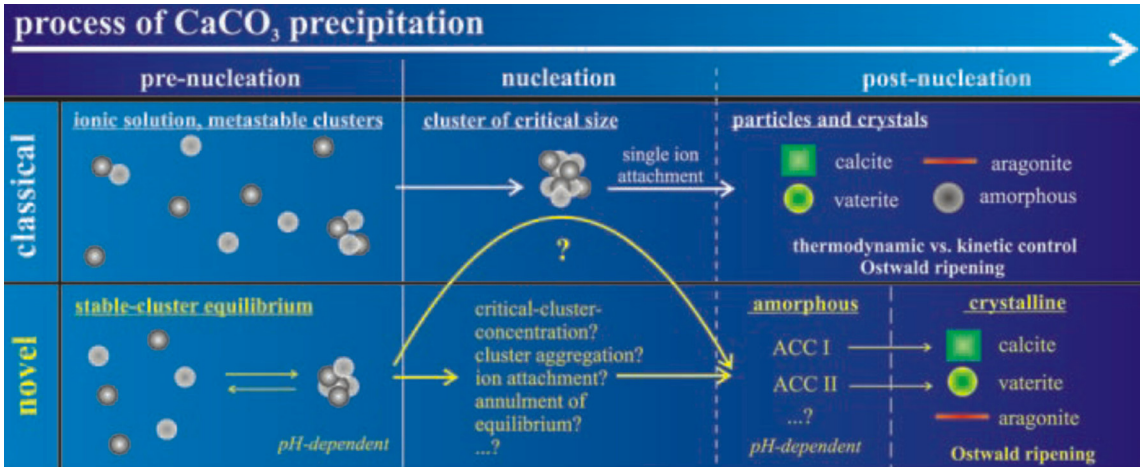

Fig. 1-21: Classical (top path) vs. novel (bottom path) picture of the formation of calcium carbonate polymorphs from supersaturated solutions. The existence of stable pre-nucleation clusters challenges the model of stochastic ion clustering and critical nuclei, and raises exciting questions on the mechanism of nucleation and possible pre-ordering phenomena (reproduced from [92]).

Sommerdijk and co-workers were the first to factually image these precursors in their native state by means of cryogenic transmission electron microscopy (cryo-TEM).[93] Starting from drop of a calcium bicarbonate solution which was placed directly on the

TEM grid, outgassing of CO_2 led to a gradual increase in supersaturation with respect to $CaCO_3$ and thus provoked relatively slow crystallization. Images acquired from samples that were vitrified more or less immediately after preparation of the solution showed a multitude of individual cluster units (see Fig. 1-22), the average diameter of which was determined to vary within a range of about 0.6-1.1 nm.

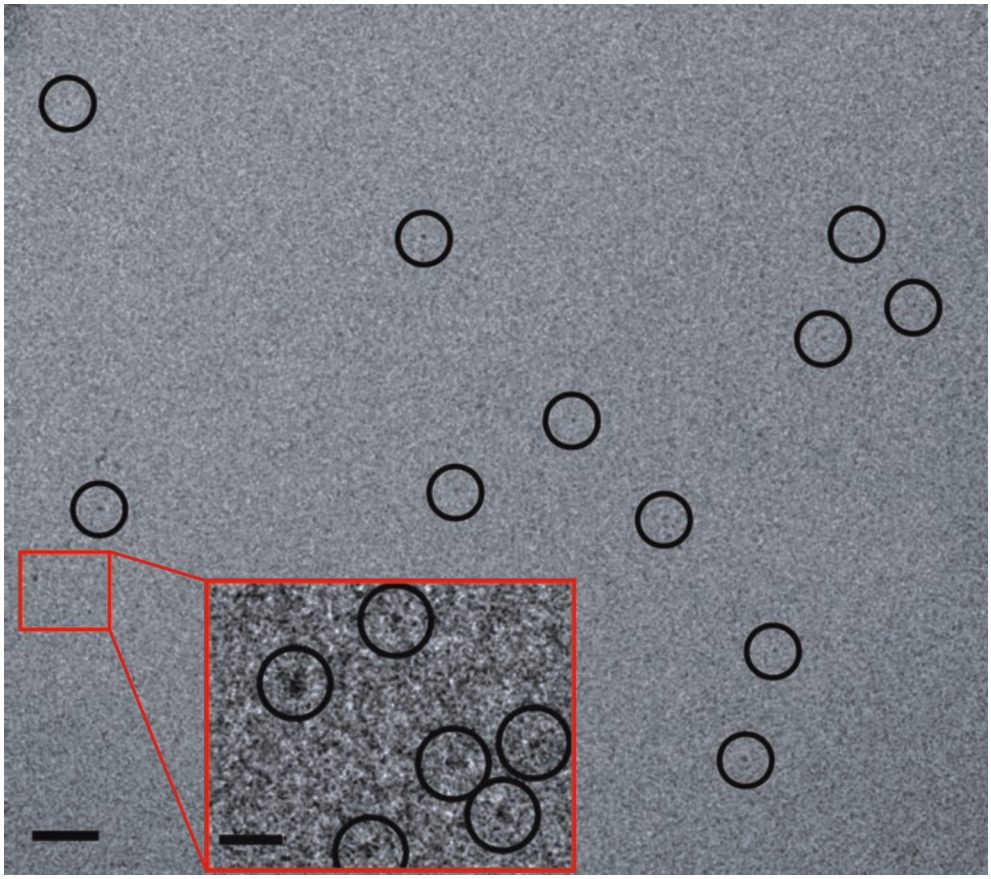

Fig. 1-22: Cryo-TEM micrograph of a fresh $Ca(HCO_3)_2$ solution, showing numerous nanosized objects (highlighted by black circles) which were identified as $CaCO_3$ pre-nucleation clusters (adapted from [93]). The scale bars of the main image and the inset are 20 and 5 nm, respectively.

Time-dependent cryo-TEM studies on heterogeneous nucleation and growth of particles on self-assembled monolayer templates proved that the first solid phase succeeding these clusters were ACC nanoparticles which had a quite narrow size distribution centered around 30 nm.[93] Based thereon, the authors speculated that aggregation of pre-nucleation clusters due to Brownian motion might be responsible for the formation of these particles. This was tentatively supported by ultracentrifugation data, which indicated the occurrence of a population with sizes slightly larger than single clusters in the system. Moreover, it was reported that cluster-like species were present in solution also after nucleation, which confirms the notion that equilibrium thermodynamics

govern their formation and suggests that particle growth could proceed by incorporation of cluster units rather than simple monomer addition.

In view of these findings, a central question yet remains: how do the clusters transform into ACC, that is, which are the processes that underlie nucleation of calcium carbonate? Indeed, cluster aggregation has been put forward as a feasible explanation for this step in previous work, but concrete evidence or direct insight into such phenomena could not yet be achieved. An answer to this fundamental question is provided in Chapter 4 of this thesis, where the role of added silica in the pre-nucleation stage of $CaCO_3$ precipitation and its interactions with ion clusters are described.

1.4 Silica Biomorphs

In contrast to the stunning complexity of the crystal morphologies and structures displayed by silica biomorphs, their preparation is utterly simple. In the early works, conventional setups comprised a silica gel body at a pH of about 10-10.5, in which carbonate crystallization was induced either by counter-diffusion of the reactants (usually barium chloride and sodium carbonate) in a U-shaped cassette, or by covering a gel already containing a certain amount of pre-dissolved carbon dioxide with a concentrated solution of alkaline-earth metal cations, followed by unidirectional in-diffusion.[66-68] In both cases, gradual precipitation produced biomorphic aggregates throughout the gel matrix, the detailed morphology, size and number of which yet depended on the respective location relative to the gel-solution interface. Later on, it was found that virtually identical architectures can be obtained also by directly mixing metal salt with dilute silica sol and exposing the resulting solutions to the atmosphere.[72,94] At SiO_2 contents of 250-1000 ppm and Ba^{2+} concentrations of 0.005-0.5 M, continuous uptake of CO_2 under the chosen alkaline conditions (pH 8.5-11) provoked the formation of carbonate species in the system and resulted in the mineralization of characteristic forms. This technique was applied predominantly in the experiments performed in the present work. The particular pH at which crystallization is carried out was soon revealed to play a most decisive role in the morphological evolution of the aggregates. Generally speaking, crystal architectures exhibiting delicate sinuous shapes were formed in solutions exclusively at pH levels well above 10, whereas lower values yielded cauliflower-like dendrites instead.[70,94,95] This observation was related to the chemistry and solubility of carbonate and silicate in aqueous media, which both are intimately sensitive to the pH. During the studies conducted in the

framework of this thesis, samples with an initial pH of ~11 were in the focus of interest, as the interplay between the components affords a superior degree of self-assembly under these circumstances. From a corresponding experiment, three distinct types of micron-scale morphologies are commonly isolated: filamentous helicoids (Fig. 1-23a), thicker worm-like braids (Fig. 1-23b), and extended flat sheets (Fig. 1-23c).

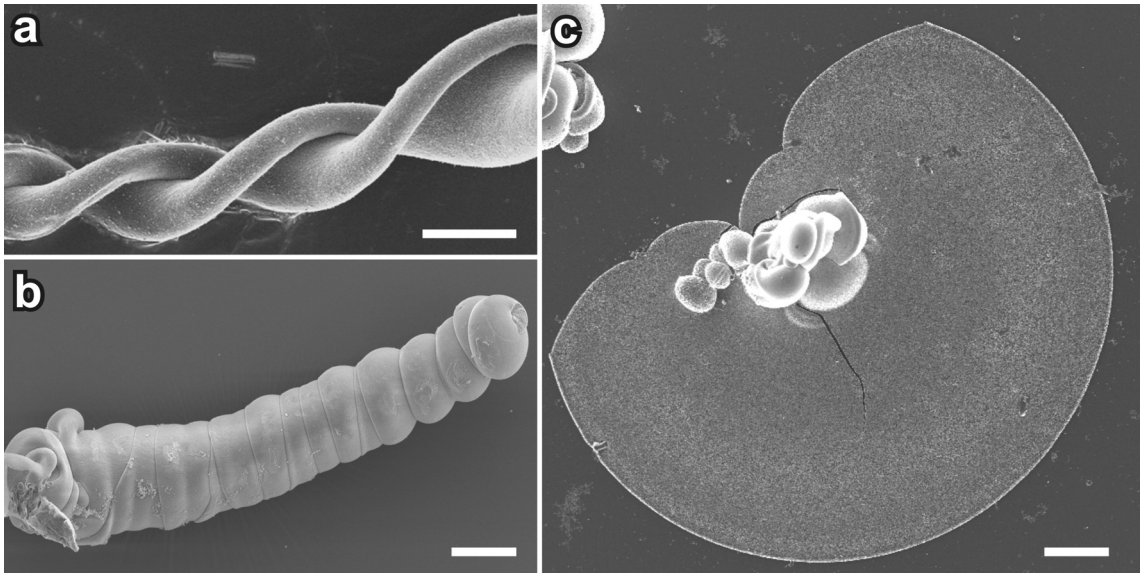

Fig. 1-23: Principal morphologies obtained from a typical synthesis of silica biomorphs in solution ([$BaCl_2$] = 5 mM, [SiO_2] = 8.9 mM, $pH_{initial}$ = 11). Scale bars are 20 μm.

Analyses of the as-formed precipitates have shown that the delicate ultrastructures adopted by silica biomorphs are made up of a polycrystalline core established by a multitude of individual nanometric crystallites exhibiting the pseudohexagonal rod-like habit typical for witherite (barium carbonate) (see Fig. 1-24).[71,72,96]

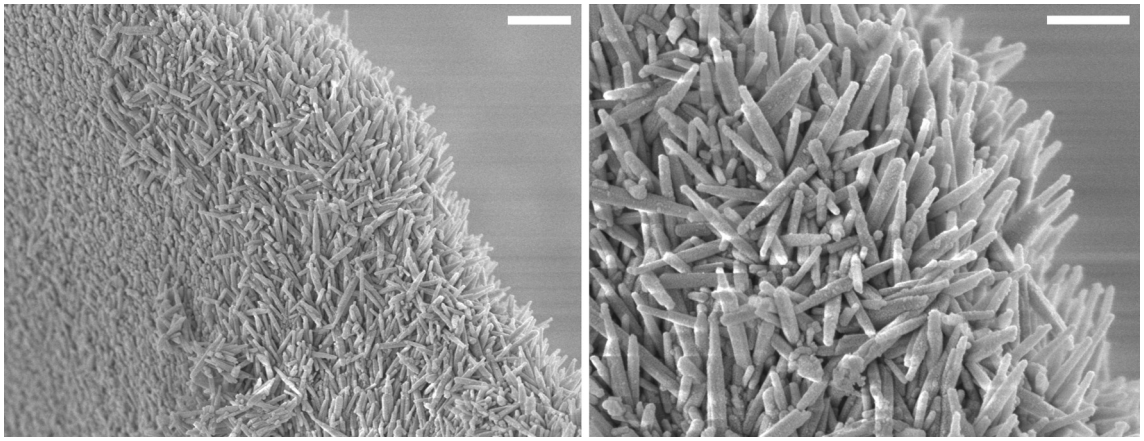

Fig. 1-24: Close-up views of the surface of a biomorph, illustrating that the precipitates are crystal aggregates composed of myriad witherite nanorods. Scale bars are 1 μm (left) and 500 nm (right).

Beyond that, previous studies have pointed out that the orientation of these nanocrystals is not at all random within the assemblies, but follows a distinct long-range order on the mesoscale.[96] In fact, adjacent rods are arranged almost parallel to one another with respect to their crystallographic *c*-axis (which is the long axis of the rods) and yet maintain a slight but coherent mutual misalignment. Thus, the building units describe an orientational field with constantly varying vector, which becomes obvious when viewing sheet-like morphologies between crossed polarizers or performing X-ray diffraction on confined areas of individual aggregates (see Fig. 1-25).

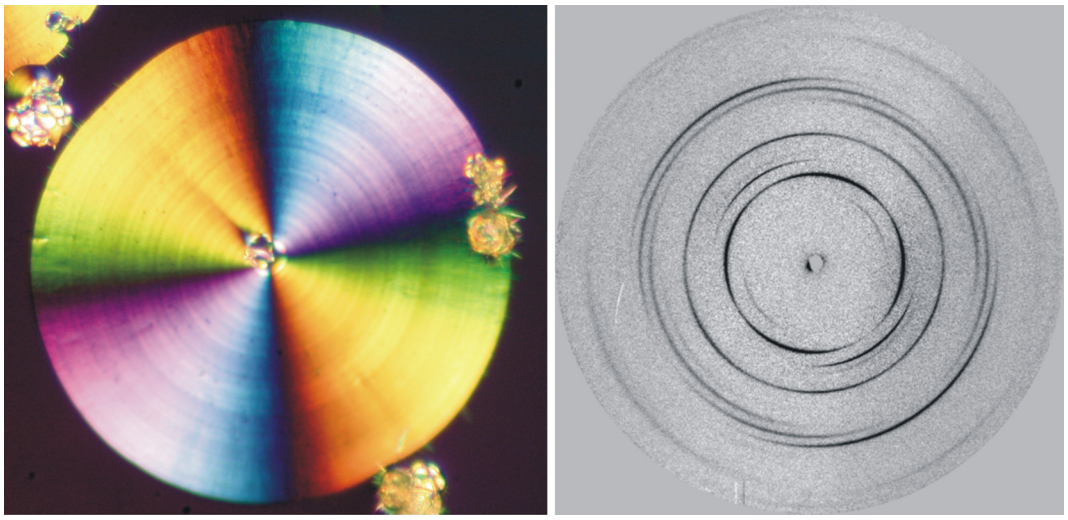

Fig. 1-25: Orientational ordering. Left: Polarized optical micrograph of a circular sheet. The characteristic Maltese-cross extinction pattern indicates an alignment of the anisotropic witherite crystallites radially outwards from a common origin. Right: Microfocus X-ray diffraction pattern collected from a distinct part of a sheet. The occurrence of arc-like reflections suggests preferential and locally varying orientation of the nanocrystals.

In addition to this well-ordered crystalline carbonate phase, biomorphs were moreover confirmed to always contain a certain fraction of co-precipitated amorphous silica.[66-72,94-98] On occasion, the entire carbonate core was found to be sheathed by spacious layers of silica, which in turn consisted of densely agglomerated siliceous nanospheres.[96,99] The presence of these external silica skins could be verified unequivocally for selected aggregates by immersion in dilute acid, which caused selective dissolution of the labile carbonate component and left a hollow framework – referred to as silica "ghost" – that still displayed the original morphology of the biomorphic architecture (cf. Fig. 1-26). Other work suggested that also single carbonate crystallites in the core may be enveloped by silica, and that such a coating of individual rods could mediate their stabilization against ripening.[97] These results illustrate that

biomorphs are dual composites of crystalline barium carbonate and amorphous silica, with an apparent intergrowth of the species over multiple length scales.

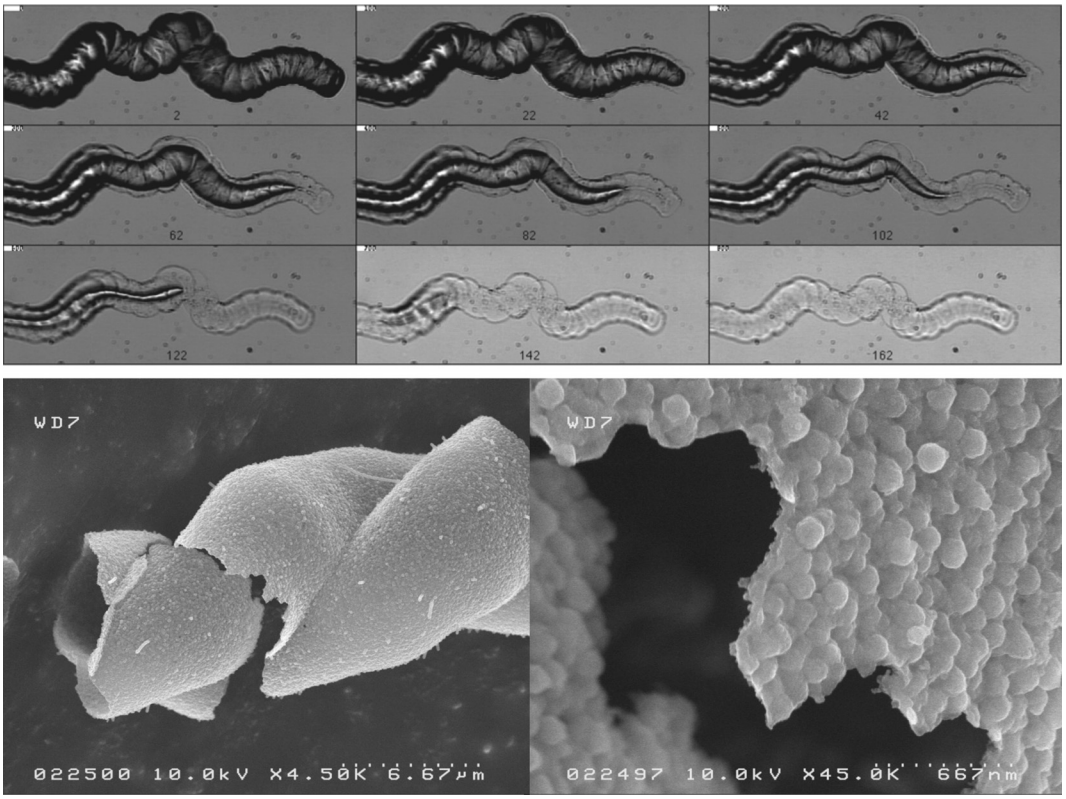

Fig. 1-26: Selective carbonate dissolution. Top: Image sequence illustrating the gradual disappearance of the witherite core of a worm-like aggregate upon treatment with acetic acid (frame interval: 100 s). The initial morphology is conserved in the remaining silica "ghost" (adapted from [71]). Bottom: SEM micrographs of the hollow silica membrane left after exposure to acid. The material apparently consists of aggregated colloidal silica spheroids (image courtesy of Prof. Dr. Stephen Hyde).

Experiments in which barium was replaced by strontium basically gave similar crystal architectures,[98,100] which is reasonable when considering that strontianite ($SrCO_3$) and witherite are isomorphic minerals. For growth of strontium carbonate in silica gels at high pH, Terada *et al.* reported petal-like morphologies (Fig. 1-27a), from the tips of which helical filaments sprouted in the following (Fig. 1-27b).[100] Indeed, floral ultrastructures could be achieved likewise with $BaCO_3$, practically by raising the concentration of alkaline-earth metal salt in the syntheses.[96] However, the subunits constructing the biomorphs in the case of $SrCO_3$ were shown to be fibrous rather than rod-shaped (Fig. 1-27c) and, essentially, it was experimentally demonstrated that they were covered individually by a nanoscale siliceous sheath.[100] The amount of silica incorporated into the carbonate core was in general quite high as compared to $BaCO_3$ counterparts (up to 50% Si relative to Sr), as evidenced by the continuous three-

dimensional structure of pure silica obtained when treating the specimens with acid (cf. Fig. 1-27d).

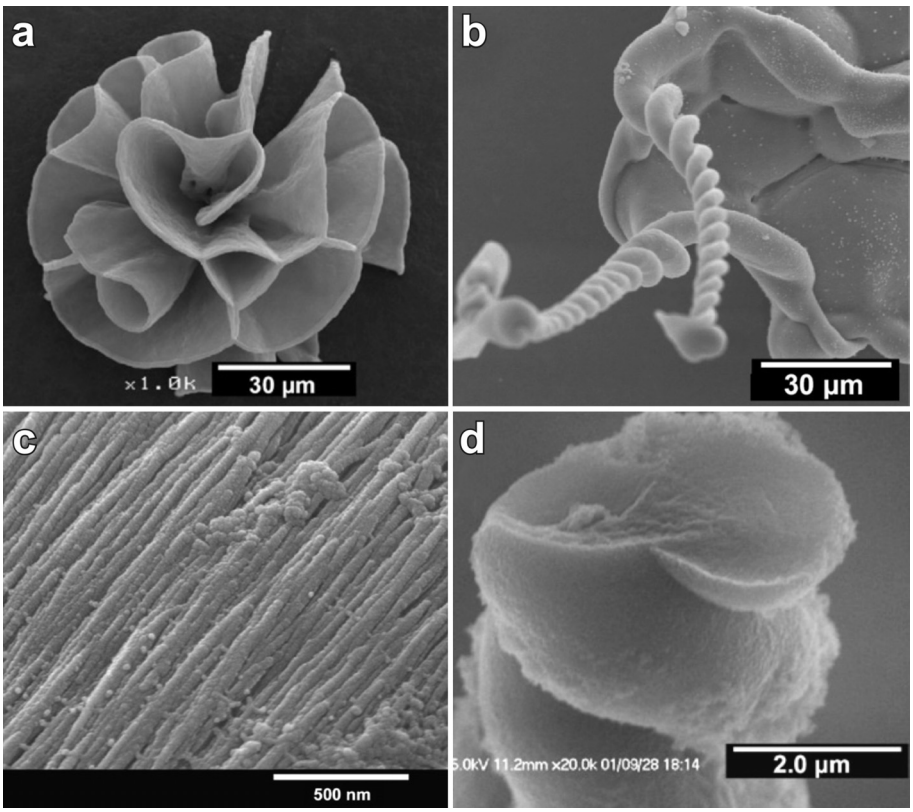

Fig. 1-27: Strontium carbonate biomorphs prepared in silica gels at pH 10.5. (a) Petal-shaped aggregate from which (b) helicoids emerged as growth proceeded. (c) Texture of the obtained crystal aggregates. (d) Silica framework remaining after the precipitates had been immersed in acid (reproduced from [100]).

For calcium carbonate, crystallization in silica-rich media has long failed to produce materials that meet the actual definition of biomorphs (i.e. crystal aggregates with life-like appearance and complex curved morphologies). Nevertheless, the growth behavior of calcite observed in silica gels was likewise highly delicate, yielding for instance non-crystallographic finger-like structures[68] as well as bundles reminiscent of natural sheaf of wheat (see Fig. 1-28a), as reported by Dominguez-Bella and García-Ruiz.[101,102] The latter were composed of cleaved calcite rhombohedra aligned with their *c*-axis pointing in direction of the fiber length and self-assembled to build laminar aggregates with rhythmic banded patterns (Fig. 1-28b). Alongside, other non-banded sheaf-of-wheat morphologies were isolated which had a different textural design and organization of the rhombohedral building blocks. These included fibers consisting of three ribs arranged at angles of ~120° (Fig. 1-29a) as well as more complicated ones lacking a threefold symmetry axis, which appeared to comprise regular dome-like units oriented in a somewhat helical motif (Fig. 1-29b).

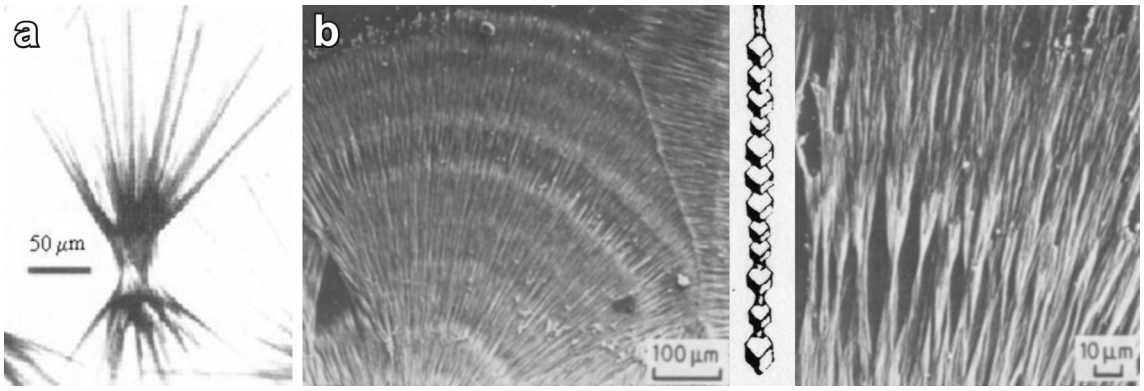

Fig. 1-28: $CaCO_3$ crystallization in the presence of silica. (a) Single sheaf-of-wheat morphology of calcite grown in silica gel at pH 10. (b) Planar aggregate of multiple, radially arranged micro-sheaves. The inserted schematic drawing illustrates how the bundles are constructed by individual aligned calcite crystals (adapted from [102]).

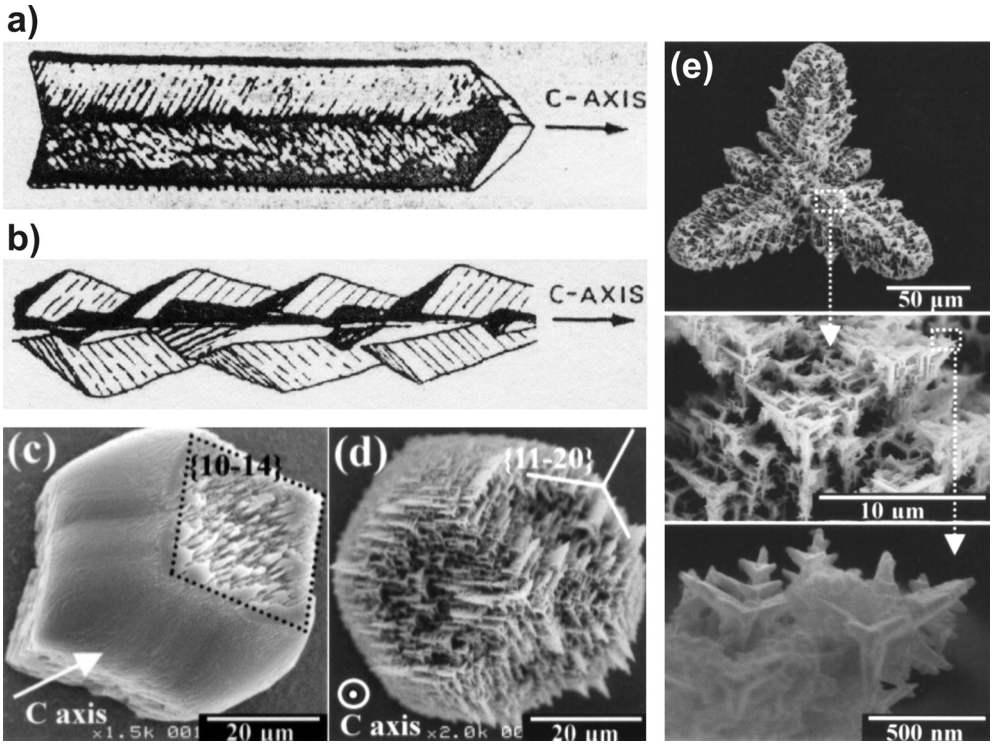

Fig. 1-29: Complex calcite crystals produced with the aid of silica. (a-b) Serrated fibers exhibiting (a) threefold symmetry and (b) a screw axis, characteristic of sheaf-of-wheat aggregates without banding pattern (reproduced from [102]). (c-e) Evolution of a self-similar single-crystalline calcitic ultrastructure in silica gel at pH 10.5, triggered by preferential adsorption of silicate oligomers on the {110} faces parallel to the crystallographic *c*-axis. The hierarchy of the architecture is evident from the zoom sequence shown in (e) (adapted from [103]).

In a more recent study, Imai and co-workers described a morphologically related kind of calcite crystals grown in alkaline silica gels.[103] Again, architectures with threefold rotational symmetry (3*m*) were generated (see Fig. 1-29c-e), which however proved to

be of single-crystalline nature rather than representing aggregates of smaller subunits. Morphogenesis was shown to start from a regular rhombohedral crystal which successively became roughened on its {104} faces and elongated along the *c*-axis (Fig. 1-29c). In the following, many small projections developed from the basal crystal and took the form of three-pointed stars in cross-section. Thereby, the orientation of the three wings coincided with that of the {110} planes in the calcite lattice (Fig. 1-29d). This led to the conclusion that silicate species were selectively adsorbed onto these faces, altering growth rates and causing the traced habit changes. Variations in the composition of the system due to ongoing precipitation of $CaCO_3$ (that is, a continuous increase in the ratio of silicate to carbonate) were finally assumed to be responsible for the hierarchy of the structure, which was characterized by a consistent miniaturization of three-pointed star-like units with proceeding growth (cf. Fig. 1-29e). Calcite crystals with similar features were obtained also from the precipitation experiments conducted in the present work, as will be discussed in detail in Chapter 3 of this thesis.

The main difference between calcium carbonate on the one hand and barium and strontium carbonate on the other is their mineralogy. While $CaCO_3$ is a polymorphic compound and occurs preferentially in its stable calcite modification under ambient conditions, both $BaCO_3$ and $SrCO_3$ can only crystallize in the orthorhombic aragonite-type lattice due to the larger size of the metal ions. However, the design principle innate to silica biomorphs seems to be strictly bound to the crystal structure of aragonite and/or the anisotropic elongate shape of corresponding twinned crystallites. Coherently, aragonitic precipitates isolated as a by-product along with calcite from silica gels at high pH in the investigations by Imai *et al.* displayed unusual biomimetic forms, including porous spheres and coral-like morphologies (Fig. 1-30a).[104] The frequency of such architectures could be dramatically enhanced when the gel was seeded with prefabricated aragonite needles. Inspection of structural details revealed that these materials were aggregates of at first fibrous nanoscale constituents that later developed into platy units. Again, each of these crystallites was enveloped by a skin of amorphous silica and specific adsorption phenomena were claimed to account for the shape of the nanocrystals, while the morphological behavior was proposed to arise from "fluctuations" at the growth site.[104] Voinescu *et al.* succeeded in preparing complex assemblies of $CaCO_3$ from dilute silica solutions by increasing the temperature to 80°C in order to favor the formation of aragonite over calcite.[105] In this case, overall spherical entities strongly reminiscent of natural coral (Fig. 1-30b) as well as dumbbell-shaped

particles with flower-like appearance were obtained. Unlike the structures reported by Imai *et al.*, these precipitates were shown to consist of a core of uniform aragonite nanorods describing a long-range orientational field (cf. Fig. 1-30b) and an outer silica membrane sheathing the assembly.

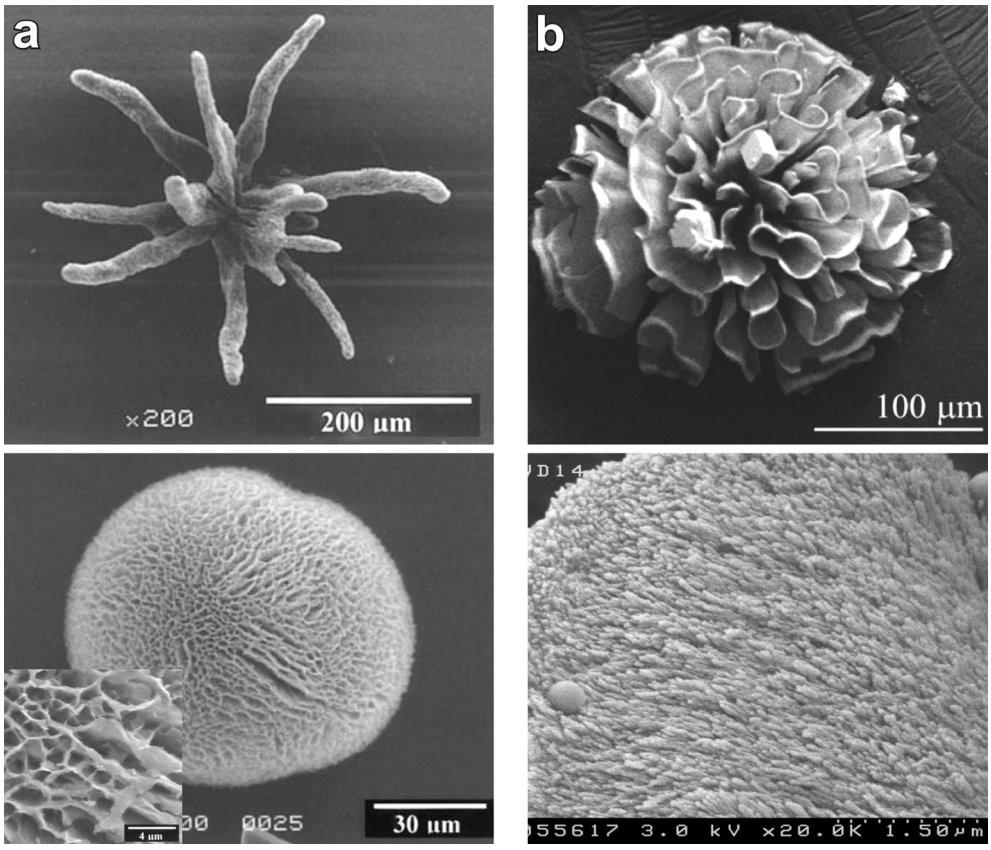

Fig. 1-30: Calcium carbonate biomorphs. (a) Aragonite crystal aggregates showing coral-like (top) and cellular spheroidal ultrastructures (bottom), produced in silica gel at pH 10.5. The inset in the lower image illustrates the platy nature of the subunits constituting the assemblies (reproduced from [104]). (b) Coralline morphology synthesized in dilute silica sol at elevated temperature (top). The architecture is composed of individual aragonite nanorods that show orientational ordering (bottom) (image courtesy of Alina Voinescu).

Moreover, the coralline aggregates were made up of partially interconnecting sheet-like domains exhibiting sinuous and smoothly varying curvature. In this sense, these architectures can be regarded as "true" silica biomorphs. However, despite explicit effort, crystallization of calcium carbonate under these circumstances has never afforded the most characteristic morphologies observed for $BaCO_3$ and $SrCO_3$ biomorphs, that is, regular shapes such as twisted ribbons or helical filaments. A possible reasoning explaining this behavior is given in Chapter 9 of this thesis.

Apart from such structural modulations, the presence of silica was shown to be also capable of directly affecting $CaCO_3$ polymorphism. For example, silica dissolved in sols

of the protein casein enabled the synthesis of vaterite hemispheres,[106] whereas the combined effect of silica and polyvinylalcohol or chitosan-coated surfaces provoked preferred mineralization of aragonite.[107,108] By contrast, in the absence of any further additives, silicate species were found to propel growth rates of calcite and thus shift polymorphic ratios for its benefit.[109] This will be of particular importance in Chapter 5, where the influence of silica on polymorph selection and kinetic stability is outlined.

Though discovered already more than thirty years ago, central morphogenetic aspects and the physical origin underlying the formation of silica biomorphs have remained puzzling until recently. Work of García-Ruiz *et al.* unraveled that, in the "standard" $BaCO_3$ system (cf. Fig. 1-23), the growth process can be divided into two fundamental stages which are run through sequentially on the basis of temporally changing conditions.[110] It was demonstrated that the manifold morphologies displayed by biomorphs all arise from an initial micron-sized carbonate crystal which is nucleated in the alkaline mixtures after some delay. Upon growth, this single-crystalline core becomes subject to poisoning by silicate species, which results in a splitting of the rod at its tips and the outgrowth of tilted projections emanating at non-crystallographic angles from the parent crystal,[94] as depicted in Fig. 1-31.

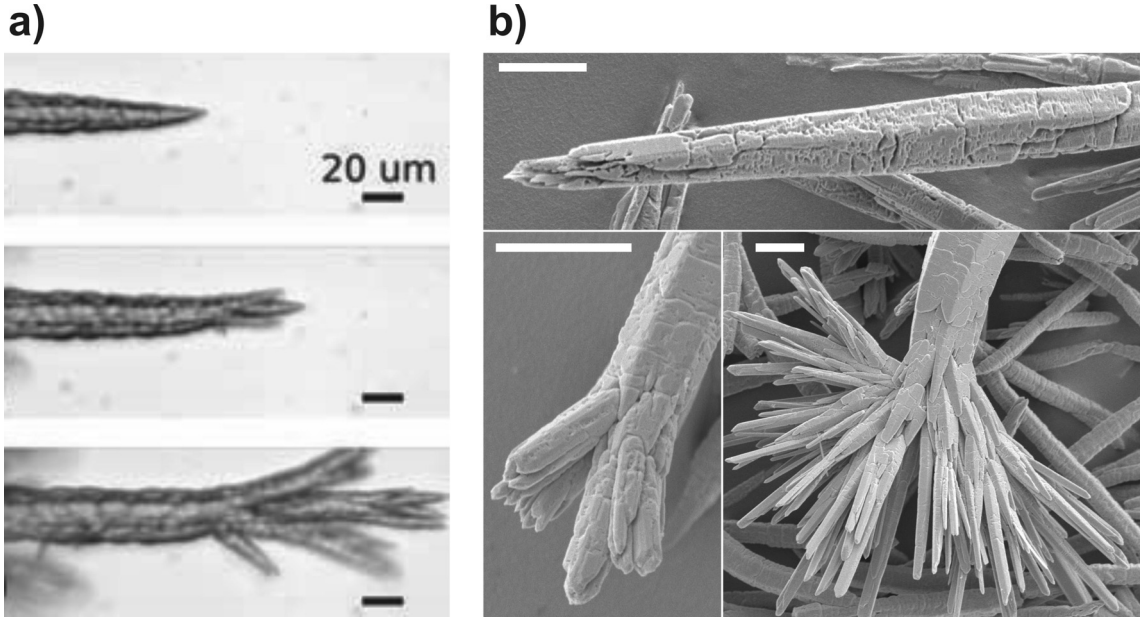

Fig. 1-31: (a) Optical and (b) SEM micrographs illustrating the splitting of a rod-like barium carbonate crystal at its tips induced by the presence of impurities (images in (a) are reproduced from [110], the scale bars in (b) correspond to 5 μm).

This phenomenon is caused by the action of non-adsorbable polymeric silica impurities, creating two-dimensional "islands" which are slightly misoriented relative to the original crystal lattice.[111] As growth proceeds, poisoning is sustained and the crystal becomes increasingly bifurcated. Consequently, dumbbell-shaped particles are generated first which, with time, develop into spacious cauliflower-like structures or closed spherulitic architectures (depending on the mode and intensity of branching), both enclosing the incipient pseudohexagonal seed in their center (Fig. 1-32).

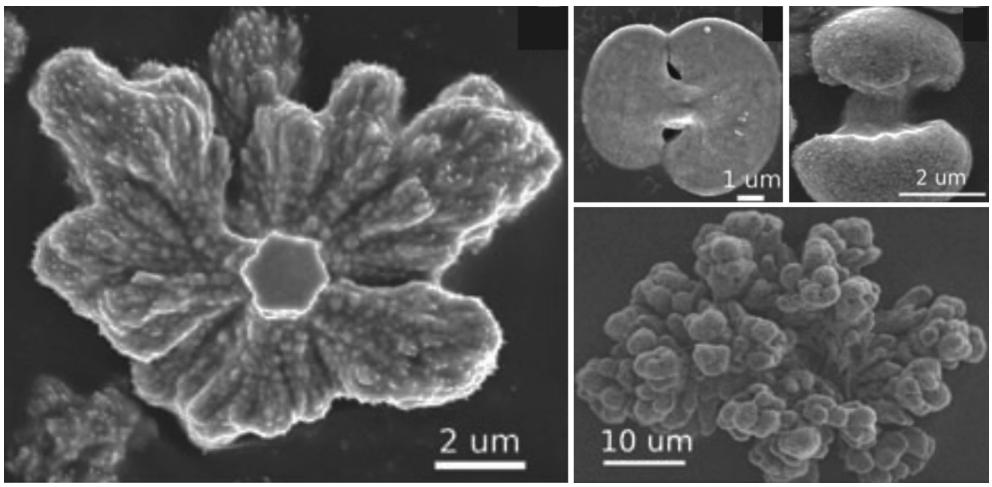

Fig. 1-32: Dumbbell- and cauliflower-like particles formed from a pseudohexagonal single-crystal core as a result of silica-mediated crystal splitting (adapted from [110]).

Similar growth patterns have been reported for fluorapatite, which underwent a "rod-to-dumbbell-to-sphere" morphological transformation in the presence of gelatin due to successive crystal ramification in a self-similar branching motif (Fig. 1-33).[112]

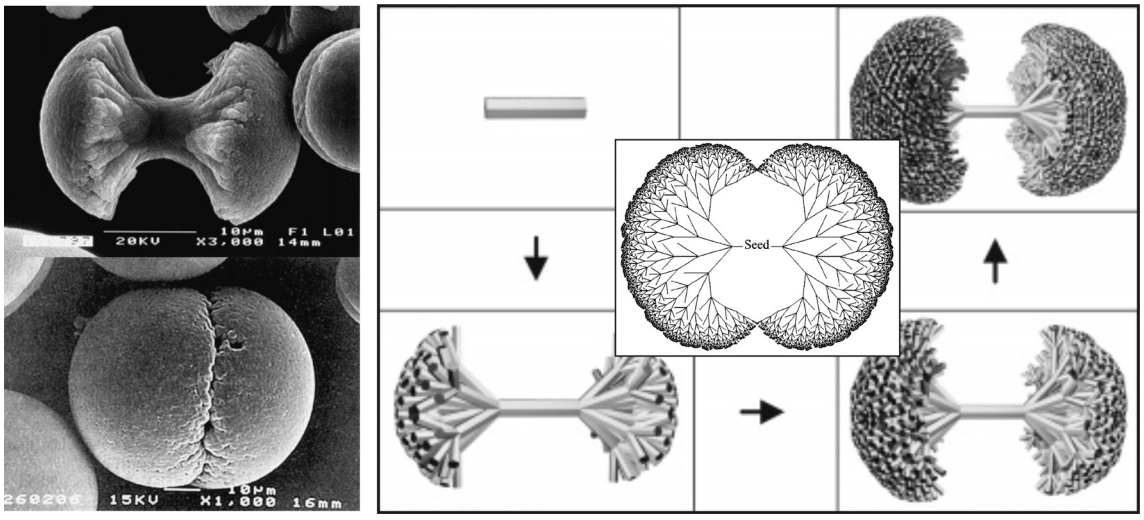

Fig. 1-33: Hierarchical fluorapatite architectures with dumbbell- and notched-sphere-like morphologies grown in gelatin matrix (left), and schematic drawings visualizing their proposed formation mechanism by self-similar fractal branching (right) (adapted from [112]).

This first stage of morphogenesis and the subsequent development described below were confirmed in the studies performed in this work, as described in Chapter 7 of the thesis. At the end of the fractal route, the silica has effectively locked up any active sites for further addition of carbonate units, such that the branched architecture can no longer grow. Since the system is still supersaturated at this point, the carbonate is forced to re-nucleate and a multitude of new crystallites are generated in a three-dimensional nucleation event all over the surface of the existing fractal structure, where precipitation barriers are reduced. This step, called "fibrillation", brings about a fundamental change of the growth mechanism: the initial single-crystalline front gives way to polycrystalline mineralization in the form of numerous nanocrystals, which is characteristic of the second stage of morphogenesis. Essentially, García-Ruiz *et al.* proposed that the stabilization of nanoscale crystallites and their continuous production over prolonged timeframes are mediated by a dynamic, pH-based coupling of the equilibria of carbonate and silicate in solution.[110] This scenario relies on the sensitivity of the speciation of both components to pH fluctuations at the front of aggregates evolving in alkaline media and opposite trends in solubility of silica and barium carbonate with pH. A sketch illustrating the envisaged co-precipitation phenomena is presented in Fig. 1-34. Basically, growth of carbonate crystallites is thought to be accompanied by dissocation of bicarbonate ions in their vicinity, seeking to restore the CO_3^{2-}/HCO_3^- equilibrium ratio at the given pH. This should induce a local decrease in pH, which will shift the silica speciation towards a higher degree of protonation and thus facilitate condensation reactions. Consequently, silica polymerizes around the developing crystals and forms coating layers which prevent growth beyond nanometric dimensions (Fig. 1-34a). Continued silica oligomerization under these circumstances in turn provokes a gradual increment in pH, since acidic silanol groups (Si-OH) vanish in the course of condensation (2 Si-OH $\rightarrow$ Si-O-Si + H_2O). As a result, the local concentration of carbonate ions nearby previously mineralized domains increases and new nucleation can occur (Fig. 1-34b). In this manner, a loop process is initiated during which the components are alternately precipitated (Fig. 1-34c), yielding uniform nanorods that, by a yet unknown mechanism, self-assemble in a concerted fashion into ordered arrays with preferential but slowly varying orientation (Fig. 1-34d). Taken together and speaking figuratively, the proposed interplay comprises an acid and a base (i.e. hydrogen carbonate and silicate) which are successively subject to neutralization, the latter being directly linked to precipitation.[113]

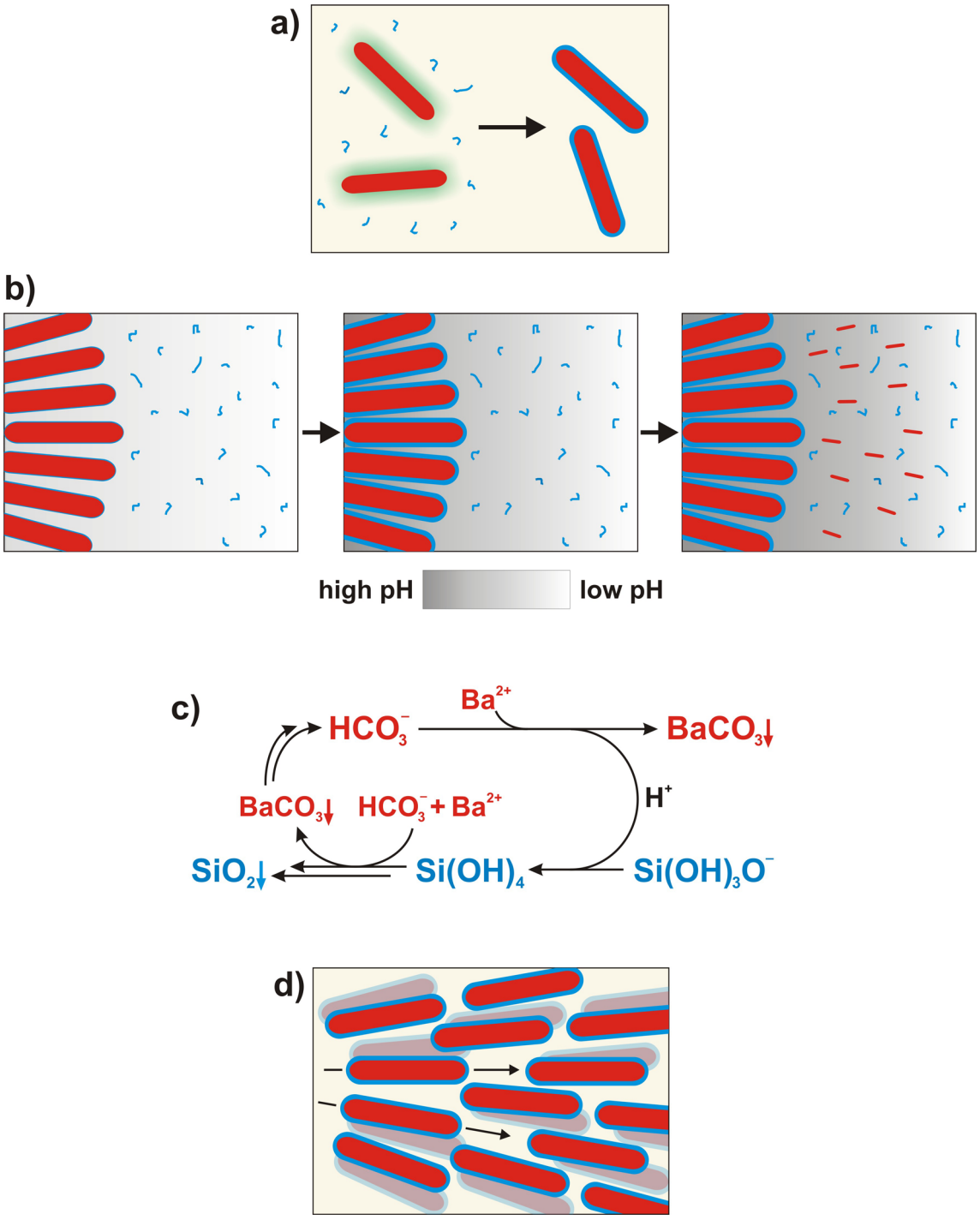

Fig. 1-34: The concept of chemical coupling. (a) Rod-like carbonate nanocrystals (red) become enveloped by a skin of silica (blue) as dissociation of bicarbonate ions provokes a local drop in pH (green) and triggers silica polymerization. (b) Ongoing silica condensation re-elevates the pH at the front of the crystal aggregate, thus raising the supersaturation of barium carbonate in the local vicinity and causing a novel event of nucleation. (c) Representation of the chemical processes underlying the pH-based coupling of silica and carbonate precipitation. (d) Alternating carbonate crystallization and silica polymerization lead to the continuous formation of silica-coated crystallites, which arrange with a mutual incremental tilt and hence establish orientational order throughout their assembly.

Neutralizing one leads to local conditions under which the other is suddenly out of equilibrium – a situation somewhat reminding of the famous Belousov-Zhabotinsky reaction.[114] Silica thereby acts, *via* precipitation, as an inhibitor for continued crystal growth first, to stimulate renewed nucleation later on.

Though being comprehensive and reasonably explaining the driving force governing the formation of silica biomorphs, the concept introduced by García-Ruiz *et al.* still has largely theoretical character. In this sense, the model of chemically coupled co-precipitation was in the focus of interest throughout the analysis and interpretation of the data acquired in this work, and effort was made to collect evidence for its validity. A crucial point in this context was to clarify whether pH-induced interactions between the components can indeed excite silica precipitation around growing carbonate particles. An answer to this question is given in Chapter 2 for the case of calcium carbonate, while corresponding results for silica biomorphs are summarized in Chapter 6. Finally, the experiments described in Chapters 7 and 8 were intended, *inter alia*, to provide an indirect proof-of-concept for the proposed model.

While such dynamic phenomena may steer growth of silica biomorphs on a microscopic level, even more delicate factors appear to govern the morphological evolution of the crystal aggregates towards sinuous shapes on a global scale. Previous studies have illustrated that self-assembly proceeds at first by developing quasi-2D laminar sections with radial symmetry that sprout outwards from their parent fractal crystal with virtually equal growth rates in all directions, initially forming a more or less perfectly circular disc (cf. Fig. 1-23c, Fig. 1-25, and Fig. 1-35a).[71,110,113] Strikingly, the advancing flat aggregates happen to become scrolled either up- or downwards at some point around their rim (Fig. 1-35b). This curling introduces smooth curvature to the system and gives birth to the diverse complex morphologies typical for silica biomorphs. Once initiated, such curls were found to be propagated along the perimeter of the sheet-like aggregates in a manner reminiscent of a surfing wave (Fig. 1-36). Thus, a novel growth front is opened which progresses orthogonally to the advancement of still uncurled sheet segments and continually abandons radial enlargement. Commonly, two or more of these curls occur on a single sheet and the competition of their propagation essentially decides which shape the laminar aggregate will finally adopt. When, for instance, two segments bent to the same side of the sheet counter-propagate along the border (as in Fig. 1-36), an overall leaf-like or cardioid contour will result with a cusp signifying the position where the two lips collided.

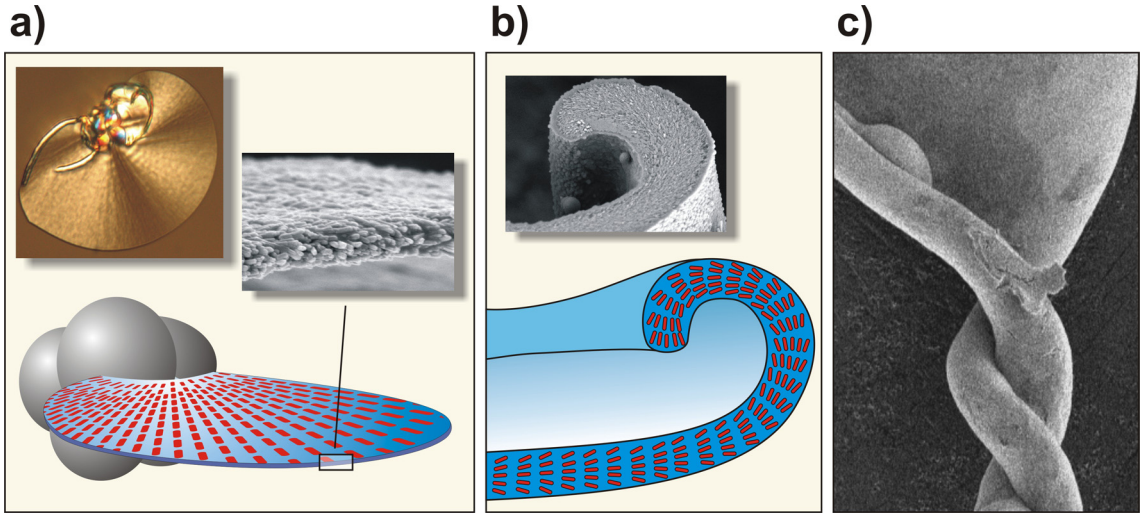

Fig. 1-35: The phenomenological growth mechanism of silica biomorphs. (a) In the initial stages of polycrystalline growth, nanorods generated by chemical coupling attach preferentially along a thin path over the surface of the fractal architecture (indicated as grey globules), leading to the extrusion of virtually flat, leaf-like sections in which the building blocks (red bars) are radially aligned. (b) Laminar growth continues until the leaves become scrolled at certain points around their border. The emergent curvature is fueled by propagation of the as-generated curl along the rim. (c) Collision of two oppositely curled segments at a cusp of a sheet can create a twist, which is maintained by mutual winding of the lips. SEM images in (a) and (b) were kindly provided by Dr. Anna Carnerup and Prof. Dr. Stephen Hyde.

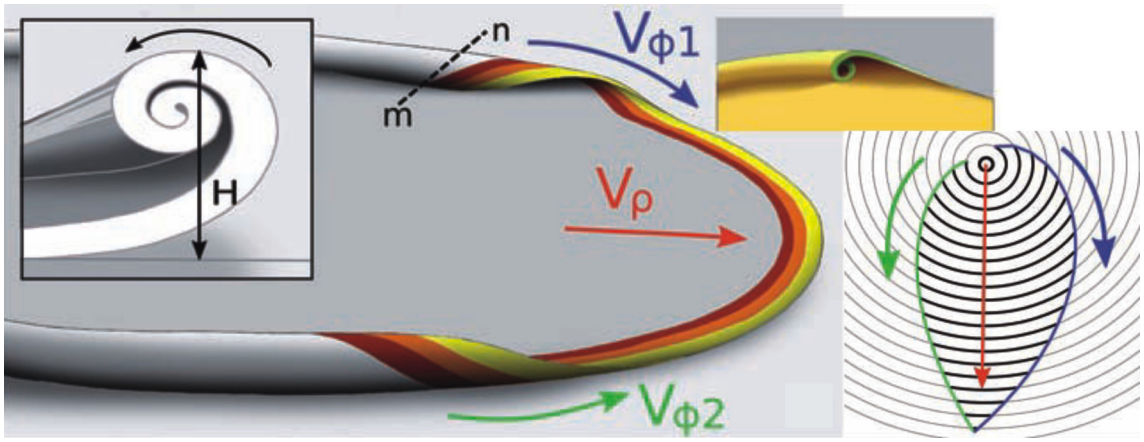

Fig. 1-36: Sheet curling as the origin of curved form in silica biomorphs. The generation of scrolled lips initiates tangential growth along the sheet perimeter, which progressively overrides and thus arrests radial advancement of the structure. The detailed shape of the final leaf is determined by the azimuthal ($V_{\varphi 1}$ and $V_{\varphi 2}$) and radial (V_{ρ}) growth velocities, usually leading to cardioid morphologies (see rightward panel). In turn, the occurrence of twisted morphologies is moreover governed by the relative handedness of two distinct curls and their heights H (adapted from [110]).

The physical model described by García-Ruiz *et al.* does however not only explain the characteristic shape of sheet-like biomorphs, but also accounts for the morphogenesis of

curved and twisted forms. In fact, their work revealed that the emergence of helicoids and worms can likewise be ascribed to curling and may be regarded as special cases – or accidents – of the same mechanism. Key parameters in the determination of which morphology arises were thereby identified to be the relative directionality of distinct curled segments, their height, as well as respective growth and propagation velocities (cf. Fig. 1-36).[110] For the formation of a helicoid (cf. Fig. 1-23a), two approaching waves must be situated on opposite sides of the sheet surface and have a similar height and tangential velocity. Upon collision, the two segments intertwine and wind around each other (Fig. 1-37). Subsequent outgrowth preserves the induced twist (cf. Fig. 1-35c), and the ratio of azimuthal and radial advancement rates distinguishes the resulting helical patterns between regular braids and less tightly wound ribbons.[110]

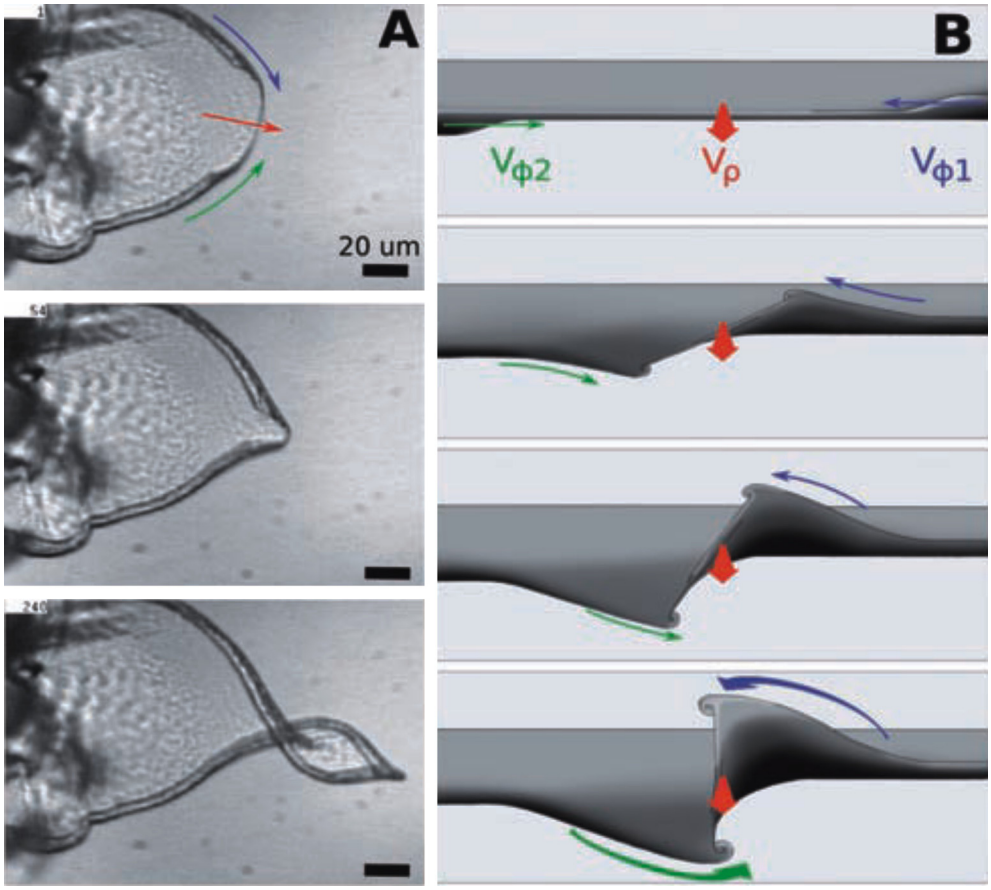

Fig. 1-37: Morphogenesis of a helicoid. (a) Sequence of optical micrographs granting a face-on view of a laminar aggregate on which two curls with equal handedness gradually approach (upper curl bent towards the camera, lower curl bent downwards), meet at a cusp, and eventually lock in to produce a twisted morphology. (b) Schematic edge-on view of the same situation. The azimuthal velocities $V_{\varphi 1}$ and $V_{\varphi 2}$ as well as, most importantly, the height of the two waves must be similar in order to allow for a regular helicoid to be generated (reproduced from [110]).

In turn, the development of a worm-like morphology (cf. Fig. 1-23b) necessitates a situation in which one of the curls is significantly larger and travels faster than the other, such that it will ultimately coil onto itself rather than intertwining.

Clearly, the findings described above have substantially improved our understanding of the formation of silica biomorphs from a phenomenological point of view. However, central steps in the proposed scenario for the evolution of the crystal assemblies on the micron-scale have not yet been elucidated. For example, what is the reason for the traced initial two-dimensionality of the aggregates, that is, why do the crystallites at first prefer to grow in flat layers rather than building whatever 3D architecture? The second mystery in this context refers to the actual origin of curvature. Why do the sheets curl and thus induce sinuous morphologies? Further questions can be raised regarding the structural features found at mesoscopic length scales. Which is the driving force provoking orientational ordering among the nanocrystals and why do adjacent rods maintain a coherent misalignment? Work addressing these issues has been carried out in the framework of this thesis. Possible answers to the posed questions are given in Chapter 6 and, particularly, Chapter 7. Apart from that, it should be noted that the morphologies displayed by silica biomorphs are not restricted to those mentioned in the previous discussion of the formation mechanism. For instance, flower-like shapes were grown under different conditions with barium carbonate,[96] and related structures moreover characterize the appearance of typical calcium carbonate biomorphs.[105] Such architectures are not readily accounted for by the morphogenetic pathways documented in literature and, therefore, their origin deserves further exploration. An attempt to unify the effect of experimental parameters and certain secondary additives on the growth process with the reported phenomenological model is made in Chapter 9 of this thesis.

1.5 References

(1) García-Ruiz, J. M.; Villasuso, R.; Ayora, C.; Canals, A.; Otálora, F. *Geology* **2007**, *35*, 327.

(2) Available from http://en.wikipedia.org/wiki/Nautilus.

(3) Voinescu, A. E. *Biomimetic formation of $CaCO_3$ particles showing single and hierarchical structures*; PhD thesis, University of Regensburg, Regensburg, Germany, 2008.

(4) Haeckel, E. *Kunstformen der Natur*; Prestel Verlag: Munich/New York, 2005.

(5) (a) Harting, P. *Q. J. Microsc. Sci.* **1872**, *12*, 118. (b) Harting, P. *Recherches de morphologie synthétique sur la production artificielle de quelques formations calcaires organiques*. Verhandelingen der Koninklijke Akademie: Amsterdam, 1872.

(6) Thompson, D. W. *On growth and form*; Cambridge University Press: Cambridge, 2004.

(7) Lowenstam, H. A.; Weiner, S. *On biomineralization*; Oxford University Press: New York, 1989.

(8) Simkiss, K.; Wilbur, K. M. *Biomineralization: cell biology and mineral deposition*; Academic Press: San Diego, 1989.

(9) Addadi, L.; Weiner, S. *Angew. Chem. Int. Ed.* **1992**, *31*, 153.

(10) Mann, S. *Biomineralization: principles and concepts in bioinorganic chemistry*; Oxford University Press: Oxford, 2001.

(11) Mann, S. *Angew. Chem. Int. Ed.* **2000**, *39*, 3392.

(12) Cusack, M.; Freer, A. *Chem. Rev.* **2008**, 108, 4433.

(13) Young, J. R.; Davis, S. A.; Bown, P. R.; Mann, S. *J. Struct. Biol.* **1999**, 126, 195.

(14) Aizenberg, J.; Tkachenko, A.; Weiner, S.; Addadi, L.; Hendler, G. *Nature* **2001**, *412*, 819.

(15) Addadi, L.; Joester, D.; Nudelman, F.; Weiner, S. *Chem. Eur. J.* **2006**, *12*, 981.

(16) Addadi, L.; Raz, S.; Weiner, S. *Adv. Mater.* **2003**, *15*, 959.

(17) Levi-Kalisman, Y.; Raz, S.; Weiner, S.; Addadi, L.; Sagi, I. *J. Chem. Soc., Dalton Trans.* **2000**, 3977.

(18) Weiner, S.; Sagi, I.; Addadi, L. *Science* **2005**, *309*, 1027.

(19) Politi, Y.; Arad, T.; Klein, E.; Weiner, S.; Addadi, L. *Science* **2004**, *306*, 1161.

(20) Sumper, M.; Brunner, E. *Adv. Funct. Mater.* **2006**, *16*, 17.

(21) Blakemore, R. *Science* **1975**, *190*, 377.

(22) Meldrum, F. C. *Int. Mater. Rev.* **2003**, *48*, 187.

(23) (a) Brecevic, L.; Nielsen, A. E. *J. Cryst. Growth* **1989**, *89*, 504. (b) Radha, A. V.; Forbes, T. Z.; Killian, C. E.; Gilbert, P. U. P. A.; Navrotsky, A. *Proc. Natl. Acad. Sci. U.S.A.* **2010**, *107*, 16438.

(24) (a) Belcher, A. M.; Wu, X. M.; Christensen, R. J.; Hansma, P. K.; Stucky, G. D.; Morse, D. E. *Nature* **1996**, *381*, 56. (b) Falini, G.; Albeck, S.; Weiner, S.; Addadi, L. *Science* **1996**, *271*, 67.

(25) Tohse, H.; Saruwatari, K.; Kogure, T.; Nagasawa, H.; Takagi, Y. *Cryst. Growth Des.* **2009**, *9*, 4897.

(26) (a) Aizenberg, J.; Lambert, G.; Addadi, L.; Weiner, S. *Adv. Mater.* **1996**, *8*, 222. (b) Aizenberg, J.; Lambert, G.; Weiner, S.; Addadi, L. *J. Am. Chem. Soc.* **2002**, *124*, 32.

(27) Beniash, E.; Aizenberg, J.; Addadi, L.; Weiner, S. *Proc. R. Soc. Lond. Ser. B* **1997**, *264*, 461.

(28) Heywood, B. R.; Mann, S. *Adv. Mater.* **1994**, *6*, 9.

(29) Mann, S. *Biomimetic materials chemistry*; Wiley-VCH: New York, 1995.

(30) Meldrum, F. C.; Cölfen, H. *Chem. Rev.* **2008**, *108*, 4332.

(31) Xu, A. W.; Ma, Y.; Cölfen, H. *J. Mater. Chem.* **2007**, *17*, 415.

(32) Gehrke, N.; Nassif, N.; Pinna, N.; Antonietti, M.; Gupta, H.; Cölfen, H. *Chem. Mater.* **2005**, *17*, 6514.

(33) (a) Seshadri, R.; Meldrum, F. *Adv. Mater.* **2000**, *12*, 1149. (b) Lai, M.; Kulak, A. N.; Law, D.; Zhang, Z.; Meldrum, F. C.; Riley, D. J. *Chem. Commun.* **2007**, 3547.

(34) Li, C.; Qi, L. *Angew. Chem. Int. Ed.* **2008**, *47*, 2388.

(35) Tian, Z. R.; Voigt, J. A.; Liu, J.; Mckenzie, B.; Mcdermott, M. J. *J. Am. Chem. Soc.* **2002**, *124*, 12954.

(36) Sims, S. D.; Didymus, J. M.; Mann, S. *J. Chem. Soc., Chem. Commun.* **1995**, 1031.

(37) Raz, S.; Weiner, S.; Addadi, L. *Adv. Mater.* **2000**, *12*, 38.

(38) Gehrke, N.; Cölfen, H.; Pinna, N.; Antonietti, M.; Nassif, N. *Cryst. Growth Des.* **2005**, *5*, 1317.

(39) Meldrum, F. C.; Hyde, S. T. *J. Cryst. Growth* **2001**, *231*, 544.

(40) Mukkamala, S. B.; Powell, A. K. *Chem. Commun.* **2004**, 918.

(41) Cölfen, H. *Top. Curr. Chem.* **2007**, *271*, 1.

(42) Mann, S. *Nature Mater.* **2009**, *8*, 781.

(43) Gower, L. B. *Chem. Rev.* **2008**, *108*, 4551.

(44) Yu, S. H.; Cölfen, H.; Antonietti, M. *J. Phys. Chem. B* **2003**, *107*, 7396.

(45) Nassif, N.; Gehrke, N.; Pinna, N.; Shirshova, N.; Tauer, K.; Antonietti, M.; Cölfen, H. *Angew. Chem. Int. Ed.* **2005**, *44*, 6004.

(46) Antonietti, M.; Breulmann, M.; Göltner, C. G.; Cölfen, H.; Wong, K. K. W.; Walsh, D.; Mann, S. *Chem. Eur. J.* **1998**, *4*, 2493.

(47) Cölfen, H.; Antonietti, M. *Angew. Chem. Int. Ed.* **2005**, *44*, 5576.

(48) Gower, L. A.; Tirrell, D. A. *J. Cryst. Growth* **1998**, *191*, 153.

(49) Oaki, Y.; Imai, H. *Langmuir* **2005**, *21*, 863.

(50) Sugawara, A.; Ishii, T.; Kato, T. *Angew. Chem. Int. Ed.* **2003**, *42*, 5299.

(51) Shen, Q.; Wang, L.; Huang, Y.; Sun, J.; Wang, H.; Zhou, Y.; Wang, D. *J. Phys. Chem. B* **2006**, *110*, 23148.

(52) Thachepan, S.; Li, M.; Davis, S. A.; Mann, S. *Chem. Mater.* **2006**, *18*, 3557.

(53) Viravaidya, C.; Li, M.; Mann, S. *Chem. Commun.* **2004**, 2182.

(54) Li, M.; Schnablegger, H.; Mann, S. *Nature* **1999**, *402*, 393.

(55) Yang, Y.; Suzuki, M.; Owa, S.; Shirai, H.; Hanabusa, K. *J. Mater. Chem.* **2006**, *16*, 1644.

(56) Wang, J.; Xiao, Q.; Zhou, H.; Sun, P.; Li, B.; Ding, D.; Chen, T. *J. Phys. Chem. C* **2007**, *111*, 16544.

(57) Xu, A. W.; Dong, W. F.; Antonietti, M.; Cölfen, H. *Adv. Funct. Mater.* **2008**, *18*, 1307.

(58) Walsh, D.; Mann, S. *Nature* **1995**, *377*, 320.

(59) Walsh, D.; Lebeau, B.; Mann, S. *Adv. Mater.* **1999**, *11*, 324.

(60) Cölfen, H.; Antonietti, M. *Mesocrystals and non-classical crystallization*; Wiley: Chichester, 2008.

(61) Cölfen, H; Mann, S. *Angew. Chem. Int. Ed.* **2003**, *42*, 2350.

(62) Penn, R. L.; Banfield, J. F. *Science* **1998**, *281*, 969.

(63) Yu, S. H.; Cölfen, H.; Tauer, K.; Antonietti, M. *Nature Mater.* **2005**, *4*, 51.

(64) (a) Clarkson, J. R.; Price, T. J.; Adams, C. J. *J. Chem. Soc., Faraday Trans.* **1992**, *88*, 243. (b) Sawada, K. *Pure Appl. Chem.* **1997**, *69*, 921.

(65) Katsifaras, A.; Spanos, N. *J. Cryst. Growth* **1999**, *204*, 183.

(66) García-Ruiz, J. M. *Teoría del crecimiento de cristales en geles. Precipitación polimorfica y agregados cristalinos de morfología inducida*; PhD thesis, Universidad Complutense, Madrid, 1980.

(67) García-Ruiz, J. M.; Amorós, J. L. *J. Cryst. Growth* **1981**, *55*, 379.

(68) García-Ruiz, J. M. *J. Cryst. Growth* **1985**, *73*, 251.

(69) García-Ruiz, J. M. *Origins Life Evol. Biosphere* **1994**, *24*, 451.

(70) García-Ruiz, J. M. *Geochemical scenarios for the precipitation of biomimetic inorganic carbonates*; in: *Carbonate sedimentation and diagenesis in the evolving Precambrian world*; Grotzinger, J. P. and James, N. P., Eds., Special Publication of the Society for Sedimentary Geology (Darlington, US), Vol. 67, pp. 75-89, 2000.

(71) García-Ruiz, J. M.; Carnerup, A.; Christy, A. G.; Welham, N. J.; Hyde, S. T. *Astrobiology* **2002**, *2*, 353.

(72) García-Ruiz, J. M.; Hyde, S. T.; Carnerup, A. M.; Christy, A. G.; Van Kranendonk, M. J.; Welham, N. J. *Science* **2003**, *302*, 1194.

(73) Lippmann, F. *Sedimentary carbonate minerals*; Springer-Verlag: Berlin, 1973.

(74) Zeebe, R. E.; Zachos, J. C.; Caldeira, K.; Tyrell, T. *Science* **2008**, *321*, 51.

(75) Tegethoff, W.; Rohleder, J.; Kroker, E. *Calcium carbonate: from the cretaceous period to the 21st century*; Birkhäuser Verlag: Basel, 2001.

(76) (a) Rieger, J. *Tenside Surf. Det.* **2002**, *39*, 6. (b) MacAdam, J.; Parsons, S. A. *Rev. Environ. Sci. Biotechnol.* **2004**, *3*, 159.

(77) Wulff, G. *Z. Kristallogr.* **1901**, *34*, 449.

(78) (a) Ostwald, W. *Z. Phys. Chem.* **1897**, *22*, 289. (b) Nyvlt, J. *Cryst. Res. Technol.* **1995**, *30*, 443.

(79) (a) Rieger, J.; Thieme, J.; Schmidt, C. *Langmuir* **2000**, *16*, 8300. (b) Wolf, S. E.; Leiterer, J.; Kappl, M.; Emmerling, F.; Tremel, W. *J. Am. Chem. Soc.* **2008**, *130*, 12342. (c) Xu, A. W.; Dong, W. F.; Antonietti, M.; Cölfen, H. *Adv. Funct. Mater.* **2008**, *18*, 1307.

(80) Peric, J.; Vucak, M.; Krstulovic, R.; Brecevic, L.; Kralj, D. *Thermochim. Acta* **1996**, *277*, 175.

(81) Wei, H.; Shen, Q.; Wang, H.; Gao, Y.; Zhao, Y.; Xu, D.; Wang, D. *J. Cryst. Growth* **2007**, *303*, 537.

(82) Sarkar, A.; Mahapatra, S. *Cryst. Growth Des.* **2010**, *10*, 2129.

(83) Ogino, T.; Suzuki, T.; Sawada, K. *Geochim. Cosmochim. Acta* **1987**, *51*, 2757.

(84) Rieger, J.; Frechen, T.; Cox, G.; Heckmann, W.; Schmidt, C.; Thieme, J. *Faraday Discuss.* **2007**, *136*, 265.

(85) (a) Wang, L.; Sondi, I.; Matijevic, E. *J. Colloid Interf. Sci.* **1999**, *218*, 545 (b) Zhao, D.; Zhu, Y.; Li, F.; Ruan, Q.; Zhang, S.; Zhang, L.; Xu, F. *Mater. Res. Bull.* **2010**, *45*, 80.

(86) Xu, A. W.; Yu, Q.; Dong, W. F.; Antonietti, M.; Cölfen, H. *Adv. Mater.* **2005**, *17*, 2217.

(87) (a) Cölfen, H.; Antonietti, M. *Langmuir* **1998**, *14*, 582. (b) Tsuno, H.; Kagi, H.; Akagi, T. *Bull. Chem. Soc. Jpn.* **2001**, *74*, 479.

(88) (a) Berner, R. A. *Geochim. Cosmochim. Acta* **1975**, *39*, 489. (b) Jiang, F.; Yang, Y.; Huang, L.; Chen, X.; Shao, Z. *J. Appl. Polym. Sci.* **2009**, *114*, 3686.

(89) (a) Richter, A.; Petzold, D.; Hoffmann, H.; Ullrich, B. *Chem. Tech.* **1995**, *47*, 306. (b) Kitamura, M.; Konno, H.; Yasui, A.; Masuoka, H. *J. Cryst. Growth* **2002**, *236*, 323. (c) Somani, R. S.; Patel, K. S.; Mehta, A. R.; Jasra, R. V. *Ind. Eng. Chem. Res.* **2006**, *45*, 5223.

(90) Becker, R.; Döring, W. *Ann. Phys.* **1935**, *24*, 719.

(91) Volmer, M. *Kinetik der Phasenbildung*; Steinkopff-Verlag: Dresden, 1939.

(92) Gebauer, D.; Völkel, A.; Cölfen, H. *Science* **2008**, *322*, 1819.

(93) Pouget, E. M.; Bomans, P. H. H.; Goos, J. A. C. M.; Frederik, P. M.; de With, G.; Sommerdijk, N. A. J. M. *Science* **2009**, *323*, 1455.

(94) García-Ruiz, J. M. *Geology* **1998**, *26*, 843.

(95) Baird, T.; Braterman, P. S.; Cheng, P.; García-Ruiz, J. M.; Peacock, R. D.; Reid, A. *Mater. Res. Bull.* **1992**, *27*, 1031.

(96) Hyde, S. T.; Carnerup, A. M.; Larsson, A. K.; Christy, A. G.; García-Ruiz, J. M. *Physica A* **2004**, *339*, 24.

(97) (a) Bittarello, E.; Aquilano, D. *Eur. J. Mineral.* **2007**, *19*, 345. (b) Bittarello, E.; Massaro, F. R.; Aquilano, D. *J. Cryst. Growth* **2010**, *312*, 402.

(98) Voinescu, A. E.; Kellermeier, M.; Carnerup, A. M.; Larsson, A. K.; Touraud, D.; Hyde, S. T.; Kunz, W. *J. Cryst. Growth* **2007**, *306*, 152.

(99) Hyde, S. T.; García-Ruiz, J. M. *Actual. Chim.* **2004**, *275*, 4.

(100) Terada, T.; Yamabi, S.; Imai, H. *J. Cryst. Growth* **2003**, *253*, 435.

(101) Dominguez-Bella, S.; García-Ruiz, J. M. *J. Cryst. Growth* **1986**, *76*, 236.

(102) Dominguez-Bella, S.; García-Ruiz, J. M. *J. Mater. Sci.* **1987**, *22*, 3095.

(103) Imai, H.; Terada, T.; Yamabi, S. *Chem. Commun.* **2003**, 484.

(104) Imai, H.; Terada, T.; Miura, T.; Yamabi, S. *J. Cryst. Growth* **2002**, *244*, 200.

(105) Voinescu, A. E.; Kellermeier, M.; Bartel, B.; Carnerup, A. M.; Larsson, A. K.; Touraud, D.; Kunz, W.; Kienle, L.; Pfitzner, A.; Hyde, S. T. *Cryst. Growth Des.* **2008**, *8*, 1515.

(106) Voinescu, A. E.; Touraud, D.; Lecker, A.; Pfitzner, A.; Kienle, A.; Kunz, W. *J. Phys. Chem. C* **2008**, *112*, 17499.

(107) Valiyaveettil, S.; Lakshminarayanan, R. *Polym. Mater. Sci. Eng.* **2001**, *84*, 798.

(108) Kotachi, A.; Miura, T.; Imai, H. *Cryst. Growth Des.* **2004**, *4*, 725.

(109) (a) Kitano, Y.; Okumura, M.; Idogaki, M. *Geochem. J.* **1979**, *13*, 253. (b) Lakshtanov, L. Z.; Stipp, S. L. S. *Geochim. Cosmochim. Acta* **2010**, *74*, 2655.

(110) García-Ruiz, J. M.; Melero-García, E.; Hyde, S. T. *Science* **2009**, *323*, 362.

(111) Keith, H. D.; Padden, F. J. *J. Appl. Phys.* **1963,** *34*, 2409.

(112) Busch, S.; Dolhaine, H.; DuChesne, A.; Heinz, S.; Hochrein, O.; Laeri, F.; Podebrad, O.; Vietze, U.; Weiland, T.; Kniep, R. *Eur. J. Inorg. Chem.* **1999**, 1643.

(113) Kunz, W.; Kellermeier, M. *Science* **2009**, *323*, 344.

(114) Zaikin, A. N.; Zhabotinsky, A. M. *Nature* **1970**, *225*, 535.

Chapter 2 Stabilization of Amorphous Calcium Carbonate in Silica-Rich Environments

2.1 Abstract

The crystallization of calcium carbonate is a process that has long and extensively been studied due to both its complexity and importance for various fields of research. Recent insight in the formation mechanisms of certain biogenic minerals has revealed that organisms repeatedly take advantage of polymorphism, often stabilizing a specific phase that is most suitable for a given demand. In particular, the lifetime of usually transient amorphous calcium carbonate (ACC) often seems to be thoroughly regulated by the organic matrix, so as to potentially use it either as intermediate storage depot or directly as structural element in a permanently stable state. In this chapter, it is shown that the temporal stability of ACC can be influenced in a deliberate manner also in much simpler purely abiotic systems. To illustrate this, the progress of calcium carbonate precipitation at high pH from solutions containing different amounts of sodium silicate was monitored. It was found that growing ACC particles provoke spontaneous polymerization of silica in their vicinity, which is proposed to result from a local decrease of pH nearby the surface. This leads to the deposition of hydrated amorphous silica layers on the ACC grains, which arrest growth and alter the size of the particles. Depending on the silica concentration, these skins have different thickness and exhibit distinct degrees of porosity, therefore impeding to varying extents the dissolution of ACC and energetically favored transformation to calcite. Under the given conditions, crystallization of calcium carbonate was slowed down over tunable periods or completely prevented on timescales of years, even when ACC coexisted side by side with calcite in solution.

2.2 Introduction

The hard parts of living organisms often feature intriguing morphologies, textures and an elaborate hierarchical structure designed to fulfill a wide range of specific tasks, from protection to gravity perception and balance sensing. These materials usually consist of an inorganic mineral and an intimately associated organic matrix of biological macromolecules, which control the mineralization process leading to complex hybrid structures.[1] One of the most common minerals in biogenic sources is calcium carbonate, which mainly occurs in the form of the crystalline polymorphs calcite and aragonite.

Prominent examples include mollusk nacre, or the coccoliths produced by certain marine algae.

In recent years, an increasing amount of evidence has been collected suggesting that amorphous calcium carbonate (ACC) plays a far greater role in biomineralization than previously suspected.[2] ACC is the thermodynamically least stable among all $CaCO_3$ polymorphs. However, being amorphous, its formation is kinetically favored and thus it is frequently observed first in the course of precipitation from solution, to subsequently transform more or less rapidly towards phases of higher stability, eventually calcite under ambient conditions.[3-5] Living organisms can obviously thwart the spontaneous transformation of ACC in a deliberate manner, given that stable ACC has been identified as major structural element in some biominerals.[2,6] Mineral frameworks throughout which calcite and ACC coexist in separate domains have also been reported.[7,8] Apart from skeletal functions, the ACC material appears to serve mostly as depot for temporarily storing $CaCO_3$ units, which can later be released rather easily when needed due to the high solubility of ACC relative to the crystalline phases.[2] In addition to permanently stable forms, it was shown that living systems also use transiently stabilized ACC as solid precursor for calcification purposes, for instance during growth of sea urchin larval spicules[9] as well as mature spines[10] and teeth.[11] An apparent advantage in doing so is that amorphous matter, having no long-range crystalline order and preferred symmetry, can readily be molded in a predefined volume to adopt arbitrary shapes which are maintained upon re-crystallization and hence imprinted on the forming crystal. This strategy was successfully applied to synthesize calcite single crystals with complex curved shapes[12] and patterned thin films.[13]

Stabilization of ACC *in vivo* seems to be regulated in general by specialized proteins, often in combination with magnesium ions,[7,14-16] or by extended organic membranes enclosing the amorphous phase.[17] Though not fully understood to date, protection mechanisms likely involve, as a key concept, kinetic inhibition of ACC transformation by hindering dissolution, delimiting exchange with the surrounding solution, or selectively impeding crystal growth. Also, the degree of hydration and the particular short-range order of the amorphous phase are important factors in this context.[18,19] Stable forms of biogenic ACC were found to incorporate appreciable amounts of water, typically one mole per mole $CaCO_3$.[6,20] This structural water probably hampers reorganization into any of the anhydrous crystalline polymorphs.[2] In turn, when serving

as a transient intermediate, ACC contains little to no water or transforms to a dehydrated state prior to crystallization.[9,10,15]

In-vitro precipitation experiments conducted in the presence of macromolecules extracted from ACC-comprising biominerals confirmed their stabilizing effect on the amorphous precursors.[8] Likewise, emulations of membrane-controlled biological $CaCO_3$ crystallization using self-assembled monolayers revealed that such organic matrices can direct and modify the formation of crystalline polymorphs from intermediate ACC.[14]

Apart from that, there have been various approaches to protect ACC precursors against crystallization by means of non-biogenic additives. Rieger *et al.* demonstrated that soluble polycarboxylates adsorb on initially formed ACC particles and, at sufficiently high additive concentrations, cover their surface preventing dissolution and thus mineral scale formation.[5] Previous work had already shown that the lifetime of ACC in solution can be prolonged by addition of magnesium ions,[22] triphosphate[23] or polyphosphonate species.[24] Remarkably stable micron-sized ACC particles, coexisting with calcite for up to two weeks, were furthermore observed by Donners *et al.* in the presence of certain dendrimer-surfactant mixtures.[25] With the aid of phytic acid as inhibitor, Xu *et al.* prepared hollow ACC spheroids which developed due to the relative stability of hydrated ACC as compared to the anhydrous phase and persisted in solution for months without any onset of crystallization discernible.[26]

Additive-stabilized ACC intermediates have moreover proven to be versatile tools for $CaCO_3$ morphosynthesis and biomimetic mineralization.[27] For example, polymer-associated ACC particles can act as precursors for nanoscale crystalline building blocks used to construct higher-order architectures.[28] By precipitating initially an amorphous phase which is conserved by the polymers, transformation to crystalline polymorphs is decelerated and the design of complex ultrastructures through delicate crystal-polymer interactions becomes possible even at elevated supersaturation.[29]

Interestingly, most attempts reported so far to stabilize ACC and use it as source for directed crystallization rely on the action of an *organic* additive or template, often following Nature's strategies in biomineralization. In this chapter, it is shown that the progress of calcium carbonate crystallization can be modified and controlled in a similar way also in simple *inorganic* precipitation systems. The presence of sodium silicate during precipitation of $CaCO_3$ from supersaturated solutions at elevated pH produced many of the effects discussed above for biological and biomimetic crystallization, that

is, temporary or permanent storage of metastable ACC, delayed gradual transformation to crystalline polymorphs, and long-lasting coexistence of amorphous and crystalline phases, all based on the spontaneous deposition of siliceous skins around growing ACC particles.

2.3 Experimental Section

2.3.1 Materials

Calcium chloride dihydrate (ACS reagent, $\geq$ 99%) and sodium carbonate (anhydrous, $\geq$ 99%) were purchased from Riedel-de Haën and Roth, respectively, and used without further purification. The silica source was commercial water glass obtained from Sigma-Aldrich (reagent grade, sodium metasilicate solution with 26.8 wt% as SiO_2). All solutions and dilutions were prepared with water of Milli-Q quality, which was bubbled with N_2 overnight prior to use so as to remove dissolved CO_2, then filtered and stored in tightly stoppered plastic bottles.

2.3.2 Sample Preparation

All experiments and manipulations were done at a temperature of 20 ± 1°C. Precipitation of calcium carbonate was conducted in closed polypropylene vials, in order to avoid silica contamination from glass containers and the uptake of atmospheric CO_2 in the course of crystallization. Silica was introduced to the systems by dissolving sodium carbonate in fresh dilutions of the water glass stock with desired concentrations (0-4000 ppm as SiO_2, cf. Table 2-1). Crystallization was initiated by rapidly adding 5 mL $CaCl_2$ solution to 5 mL of the respective silicate-carbonate mixture. Afterwards, samples were left to evolve under quiescent conditions at ambient temperature. Parameters like the volume of the reagents or the speed, and particularly, the order of mixing were found to affect the behavior of the samples. Therefore, special care was taken to maintain the mixing procedure throughout this work, and experiments were repeated several times to ensure reproducibility.

Upon combining reagents, all samples turned turbid instantaneously as amorphous nanoparticles were nucleated homogeneously in the solutions. Turbidity persisted in the systems for different periods of time depending on the silica concentration, indicating that nanoparticles stayed suspended in the mixtures. As transformation of ACC proceeded, the solutions gradually became clearer until finally only crystals grown on the bottom and the walls of the vials remained. The presence of silica induced the

formation of an optically isotropic fluffy precipitate, which settled to the bottom leaving a still turbid solution on top. The time after which flocculation occurred, usually ranging from about 60 to 90 min, and the amount of the precipitated material varied with the additive concentration.

Suspended particles and flocculated precipitate were isolated together at distinct times after mixing by filtering solutions through mixed-ester cellulose membranes (Whatman, 200 nm) and brief washing with water. Instantly, filters were submerged in liquid nitrogen and freeze-dried for at least 2 hours (Edwards FreezeDryer Modulyo), in order to prevent uncontrolled transformation of ACC material. Crystalline products, observed primarily on the walls of the vials or associated to the floccules at higher silica concentrations, were loosened gently with a fine brush, washed repeatedly with water and ethanol, and dried at room temperature. Selective dissolution of the carbonate component from the generated particles was achieved by leaching freeze-dried samples in 0.01 M hydrochloric acid (Merck, p.a.) for several days. The remaining transparent precipitate was washed with water and dried in air.

2.3.3 Analytical Methods

The macroscopic behavior of the samples was monitored by recording time-lapsed photograph series of the vials, with an interval ranging from 5 s to 1 h between the pictures, using a remote-controlled digital camera from Canon (Powershot A640). pH measurements were carried out with the aid of a glass microelectrode (Mettler-Toledo, model InLab Micro) connected to a Schott CG-843 laboratory pH meter. The evolution of the pH in the mixtures was followed with time by leaving the microprobe immersed in the solutions and reading the pH automatically every 5 s. Formed crystals were inspected routinely by light microscopy using a Nikon Eclipse E400 microscope onto which a Canon EOS 350D camera was mounted for imaging.

2.3.3.1 Transmission Electron Microscopy

To investigate the amorphous precipitates observed at higher concentrations, floccules were transferred to an object slide with a pipette and examined while still in contact with the mother liquor. Suspended nanoparticles and precipitated floccules were investigated in detail by transmission electron microscopy (TEM). Samples were prepared by blotting small volumes of the suspensions on hydrophilized carbon-filmed copper mesh grids, followed by washing with water and drying in air. Images were taken on a Philips CM 12 microscope equipped with a Gatan TV 673 wide-angle

camera and a TVIPS slow-scan camera with external control using the EM-MENU 4 software. The TEM was operated at 120 kV under low-dose conditions to minimize radiation damage of the sensitive $CaCO_3$ particles. The elementary composition of the particles was characterized by means of energy-dispersive X-ray (EDX) spectroscopy, using an EDAX Genesis microanalyzer mounted on a Philips CM 20 electron microscope (200 kV, Olympus SIS Megaview CCD camera). For cryogenic transmission electron microscopy (cryo-TEM) and electron diffraction (ED), a small drop of the samples was placed on a lacey carbon grid, and excess liquid was removed with the aid of a filter paper. The resulting thin film was vitrified immediately by plunging the grid into liquid ethane. Studies were performed at temperatures around 90 K on a Zeiss EM922 EF microscope working at an acceleration voltage of 200 kV. Images were recorded with a Gatan Ultrascan 1000 CCD camera and processed using the Digital Micrograph 3.10 software package.

2.3.3.2 Scanning Electron Microscopy

Field-emission scanning electron microscopy (FESEM) was carried out on a Zeiss LEO Gemini 1530 microscope operated at 3 kV. Freeze-dried powders or isolated crystalline products were transferred onto aluminium SEM stubs covered with adhesive carbon tapes, and subsequently carbon- or platinum-coated. EDX analyses were performed at a working voltage of 10 kV using an INCA detector from Oxford. To gain representative results, at least three measurements were performed at different positions of the sample. In the case of the freeze-dried powders, signal was collected from large areas so as to obtain averaged data. Mean particle sizes and corresponding standard deviations were determined from both TEM and FESEM micrographs by manually measuring at least 100 individuals.

2.3.3.3 Dynamic Light Scattering

The aggregation of suspended nanoparticles in the mixtures was traced by means of in-situ dynamic light scattering (DLS). Experiments were performed at 25°C and a scattering angle of 90° using a CGS-2 goniometer system from ALV equipped with an ALV-5000/E Multiple Tau digital correlator and a He-Ne laser operating at a wavelength of 632.8 nm. The two reagent solutions were equilibrated at 25°C, then passed through syringe filters (VWR, 200 nm) and combined directly in the DLS cuvette. Measurements were initiated 2 min after mixing, and data were collected continuously for about 12 min with an acquisition time per run and hence a time

resolution of 30 s. All experiments were conducted in triplicate. Cuvettes were cleaned minutely prior to measurements in a custom-designed acetone reflux apparatus. Apparent particle sizes were calculated by fitting monomodal equations to the experimental correlation functions.

2.3.3.4 Turbidity Measurements

The duration of crystallization was estimated by monitoring the turbidity of the solutions as a function of time. Experiments were performed using an automated setup built in-house.[30] For measurement, reagents were mixed directly in corresponding cuvettes and inserted quickly into the apparatus. Data were acquired while stirring samples, reading values approximately every 17 s. Clearing times were determined from the inflection point of the sharp decrease in the turbidity-time profiles seen upon completion of crystallization.

2.3.3.5 X-Ray Diffraction and IR Spectroscopy

Powder X-ray diffraction (XRD) patterns of the freeze-dried samples were recorded on a STOE STADI P diffractometer using Cu-K_α radiation within a 2θ range of 8-90° at a scan rate of 0.8°/min. To gain comparable results, intensities were normalized for the mass of the sample put on the holder. The presence of amorphous calcium carbonate was verified by Fourier transform infrared spectroscopy (FTIR). For this purpose, powdered samples were mixed in appropriate ratios with anhydrous KBr (Merck, Uvasol) and pressed to a pellet. Data were recorded on a Varian Digilab FTS800 spectrometer at a resolution of 4 cm^{-1}.

2.4 Results

2.4.1 Effect of Silica on Growing ACC Particles

In a first set of experiments, particles precipitated from solutions containing 5 mM each of $CaCl_2$ and Na_2CO_3 and varying amounts of dissolved silica were investigated shortly after mixing by means of cryo-TEM (see Fig. 2-1 and Fig. 2-2). In the absence of the additive, almost perfectly spherical particles with a mean diameter of 152 ± 36 nm are observed, in good agreement with earlier work conducted under similar conditions.[5] Addition of silica changes the situation dramatically. On the one hand, the size of primary grains decreases exponentially as more and more silica is added, from 126 ± 37 nm at 135 ppm over 55 ± 8 nm at 750 ppm down to eventually 34 ± 7 nm at 1870 ppm

(Fig. 2-1c). Concomitantly, the size distribution of the particles becomes narrower, and the initially spherical contour is progressively distorted (Fig. 2-2). On the other hand, particle agglomeration is distinctly more pronounced at higher silica concentrations. While spherules seem to maintain only loose contact and widely exist isolated from one another at low silica content, networks of densely aggregated particles extending over lengths of several hundreds of nanometers predominate in silica-rich environments.

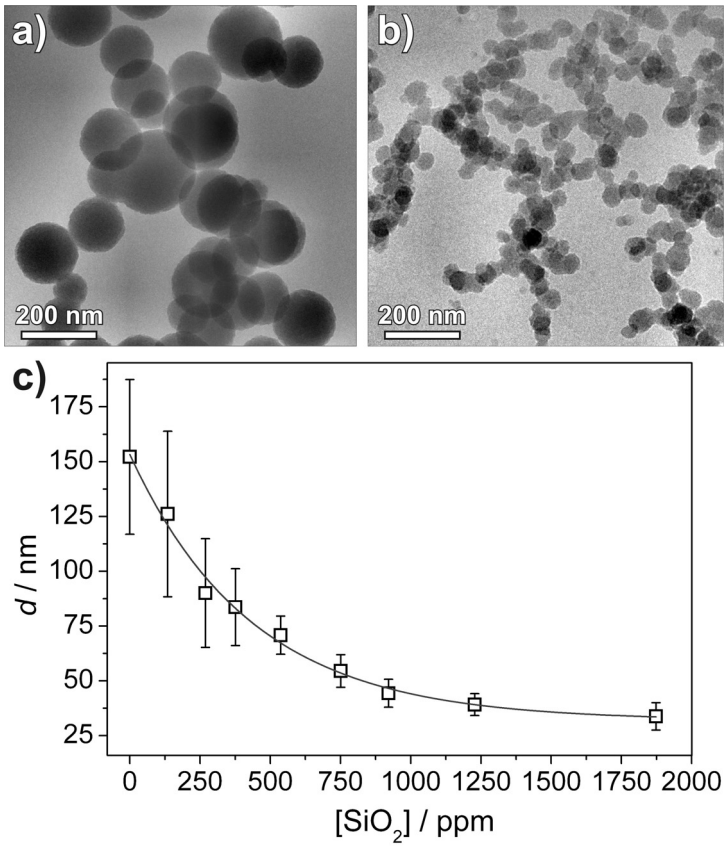

Fig. 2-1: The effect of silica on the size, shape and aggregation behavior of ACC nanoparticles. (a, b) Cryo-TEM micrographs of samples vitrified after 1 min in the absence and presence (750 ppm) of silica, respectively. (c) Average particle diameter d and corresponding standard deviation as a function of the amount of added silica. Values were obtained by measuring at least 100 individual particles in the micrographs. The full line is a tentative first-order exponential decay fit to the experimental data, of the form $d = a_0 + a_1 \cdot \exp(-a_2 \cdot [SiO_2])$ (fit parameters: $a_0 = (31 \pm 7)$ nm, $a_1 = (123 \pm 26)$ nm, $a_2 = (443 \pm 125)$ ppm^{-1}, $R^2 = 0.989$).

Corresponding powder samples obtained by filtration and subsequent freeze-drying were analyzed complementarily with the aid of scanning electron microscopy, yielding consistent results (Fig. 2-3). The nature of the as-formed particles was characterized by electron diffraction, energy-dispersive X-ray analysis and infrared spectroscopy. ED patterns in frozen state suggest that all particles are amorphous, regardless of the amount of added silica (see Fig. 2-2). Both EDX and IR data recorded using freeze-

dried powders show that the silica content of the precipitates increases with the analytical solution concentration (see Fig. 2-4, Fig. 2-5 and Table 2-1).

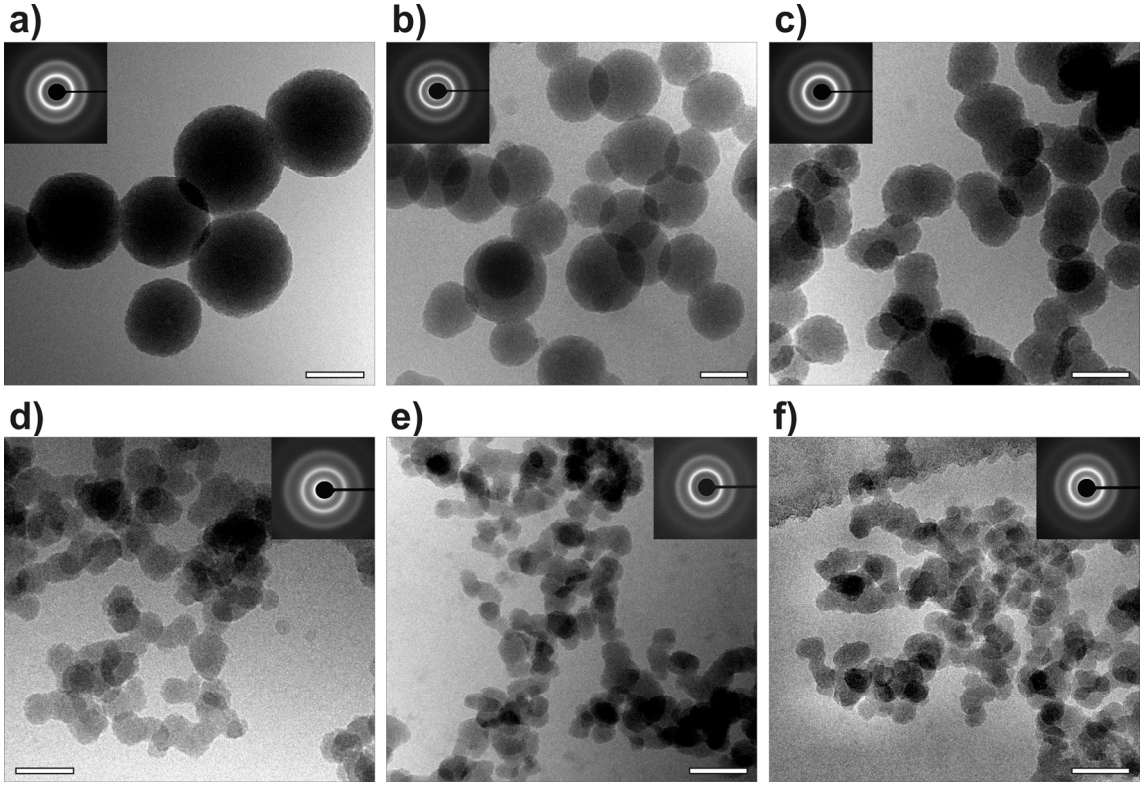

Fig. 2-2: Cryo-TEM images of nanoparticles formed 1 min after mixing equal volumes of 10 mM $CaCl_2$ and Na_2CO_3 solutions in the presence of (a) 0, (b) 135, (c) 375, (d) 750, (e) 1230, and (f) 1870 ppm SiO_2. Inserted electron diffraction patterns confirm that all particles are amorphous. From (a-c), it is evident that the contour of individual grains becomes less spherical as the concentration of silica is increased. The same trend can also be observed in (d-f), although pronounced cross-linking and the formation of dense networks render the identification of single particles difficult. In addition, the small size of the grains at higher silica content and their partial overlapping complicate the interpretation of contrast in the micrographs. Scale bars are 100 nm.

Below 400 ppm, the fraction of silica in the particles is generally rather small (Si/Ca atomic ratio < 0.2), while it rises steeply above that threshold to reach values of up to Si/Ca $\approx$ 3 at the highest studied concentrations. Concurrently, IR bands at 1490, 1425, 1075 and 865 cm^{-1}, together with the lack of a defined peak around 710 cm^{-1}, identify amorphous calcium carbonate in all samples and prove the absence of crystalline polymorphs.[2,31] Further bands at 1643, 1036, 782 and 467 cm^{-1} can be assigned to amorphous silica and non-free water.[32] We thus conclude that particles formed incipiently upon precipitation of $CaCO_3$ in silica-containing solutions are composites consisting of ACC and hydrated amorphous silica.

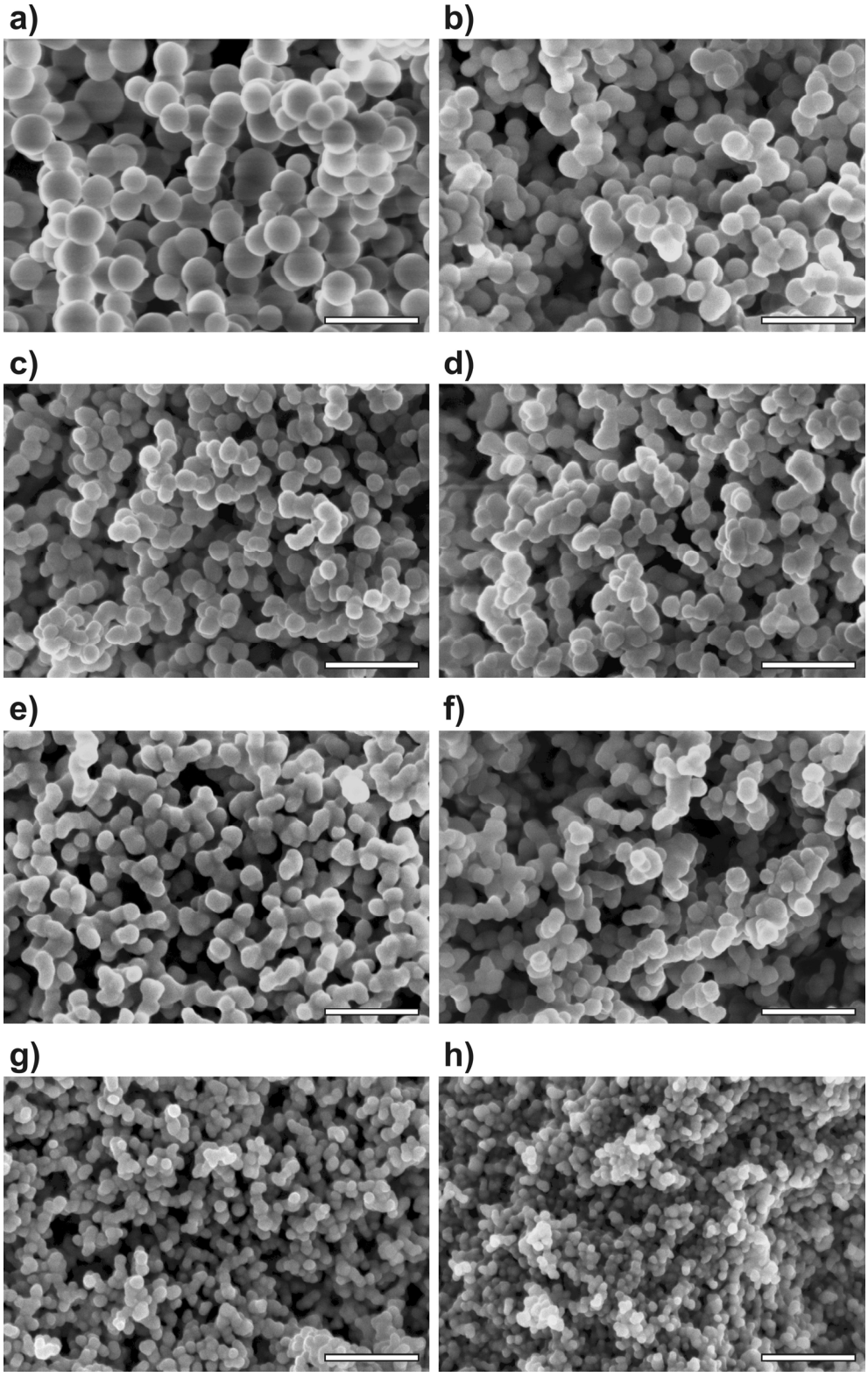

Fig. 2-3: FESEM images of nanoparticles isolated 5 min after mixing by filtration and subsequent freeze-drying from samples containing (a) 0, (b) 135, (c) 270, (d) 375, (e) 540, (f) 750, (g) 1230, and (h) 1870 ppm SiO_2. Increasing the silica concentration results in a distinct downsizing of primary ACC grains (cf. Fig. 2-1c), and promotes their agglomeration (cf. Fig. 2-7). Note that particles at a given concentration and reaction time are slightly larger than those imaged with cryo-TEM (± 20 nm), which is presumably due to drying artifacts. Scale bars are 500 nm.

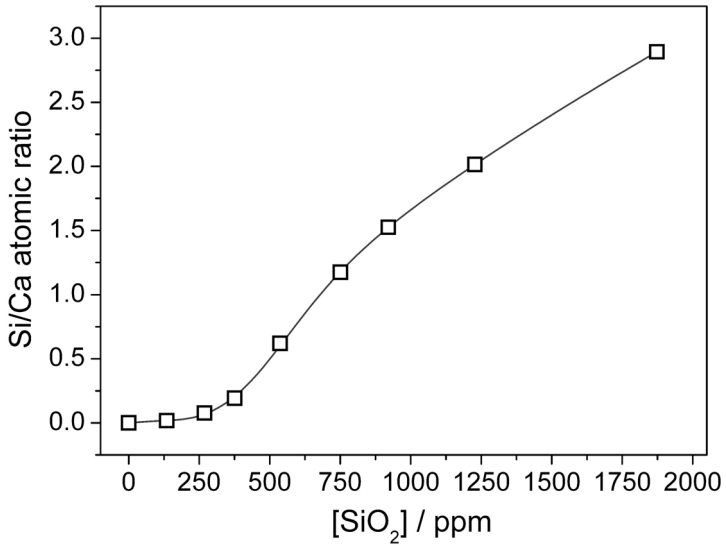

Fig. 2-4: The composition of the amorphous nanoparticles collected after 5 min as a function of the analytical silica concentration, expressed in terms of the Si/Ca atomic ratio as determined by EDX spectroscopy. The Ca/C ratio was found to be close to 1 in all cases when analyses were conducted on thick parts of the samples, where background contributions in particular from the carbon tape underneath are expected to be small. This confirms that all Ca exists as $CaCO_3$ and that no calcium silicate species are formed.

ppm SiO_2	mM SiO_2	Analytical Si/Ca	Measured Si/Ca	% Si in particles
135	2.25	0.45	0.02	3.9
270	4.50	0.90	0.08	8.5
375	6.24	1.25	0.19	15.4
540	8.99	1.80	0.62	34.5
750	12.48	2.50	1.17	47.0
1230	20.47	4.09	2.02	49.2
1870	31.13	6.23	2.89	46.5

Table 2-1: Comparison of the analytical Si/Ca molar ratio (at a constant Ca^{2+} concentration of 5 mM) to the measured values for the composite nanoparticles (cf. Fig. 2-4). Under the assumption that Ca^{2+} precipitates quantitatively as ACC, the percentage of silica associated to the formed particles out of the total molar amount of SiO_2 present can be calculated. Data show that this fraction grows drastically as the analytical additive concentration is increased from 135 to 750 ppm, and then levels off in the range of 45-50% up to 1870 ppm. Apparently, ample silica polymerization can only take place when a certain concentration of species is provided.

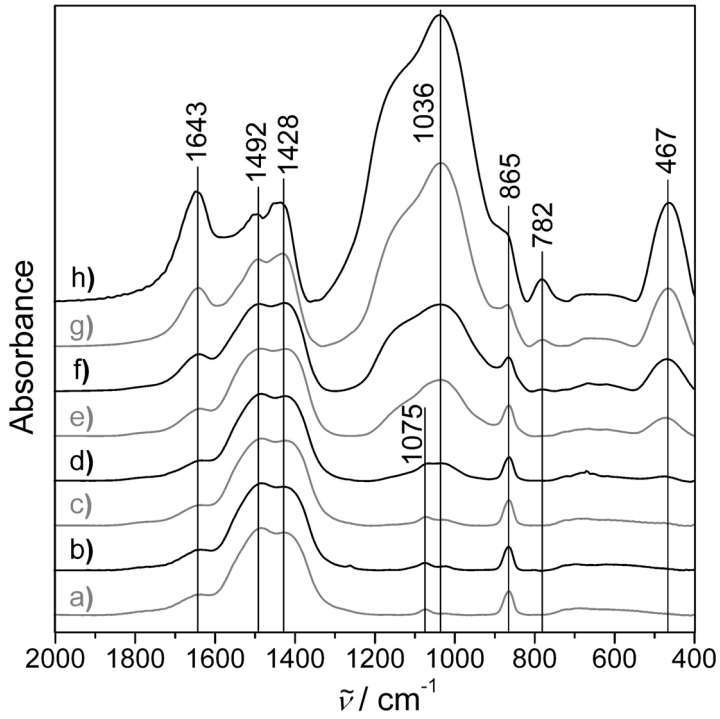

Fig. 2-5: Infrared spectra of precursor particles isolated after 5 min at (a) 0, (b) 135, (c) 270, (d) 375, (e) 540, (f) 750, (g) 1230, and (h) 1870 ppm SiO_2. The split peak at 1425/1490 cm^{-1} and the bands at 1075 and 865 cm^{-1} can be assigned to the υ_3, υ_1 and υ_2 vibrations of amorphous calcium carbonate. In addition, the absence of a distinct peak at about 710 cm^{-1} or rather the occurrence of a very broad band in this region is also typical for ACC.[2,31] In turn, peaks located at 467, 782 and 1036 cm^{-1} originate from bond-rocking, bond-bending and bond-stretching vibrations of silica, while the absorption at 1643 cm^{-1} can be attributed to water molecules associated to the precipitates.[32] Finally, the appearance of a pronounced shoulder around 1150 cm^{-1} at higher silica concentrations indicates the presence of increasingly polymerized siliceous species.[33] (i) Reference spectrum of synthetic calcite, obtained by allowing a sample without added silica to equilibrate for several hours. Optical and electron micrographs prove that all ACC had transformed quantitatively at the end of the experiment into uniform rhombohedral crystals (cf. Fig. 2-10), which were confirmed to be pure calcite by XRD. The recorded IR pattern complies well with data reported for calcite in literature.[31] The presence of a sharp υ_4 band at 710 cm^{-1}, a shift of the υ_2 peak to higher wavenumbers, as well as the occurrence of a single absorption at 1419 cm^{-1} instead of a split band distinguish the spectrum from those shown in (a-h), and thus substantiate the existence of ACC in the $CaCO_3$-silica composite particles.

A closer look at samples prepared by blotting solutions on TEM grids reveals further structural details of the nanoparticles (Fig. 2-6). Indeed, images resolve a thin layer of comparably low contrast sheathing a denser inner core. The thickness of these shells is in the range of 2 nm at 270 ppm SiO_2 and increases at higher additive concentrations, strongly suggesting that the skins are composed of silica and cover amorphous $CaCO_3$ particles. This notion is also supported by the observation that the core material tends to blister when irradiated, which is typical for calcium carbonate. Reference samples of pure silica were found to be stable under the same operating conditions. Apart from wrapping single ACC nanoparticles, the presumed silica skins seem to favor aggregation and interconnect grains by spanning a continuous envelope over multiple individuals.

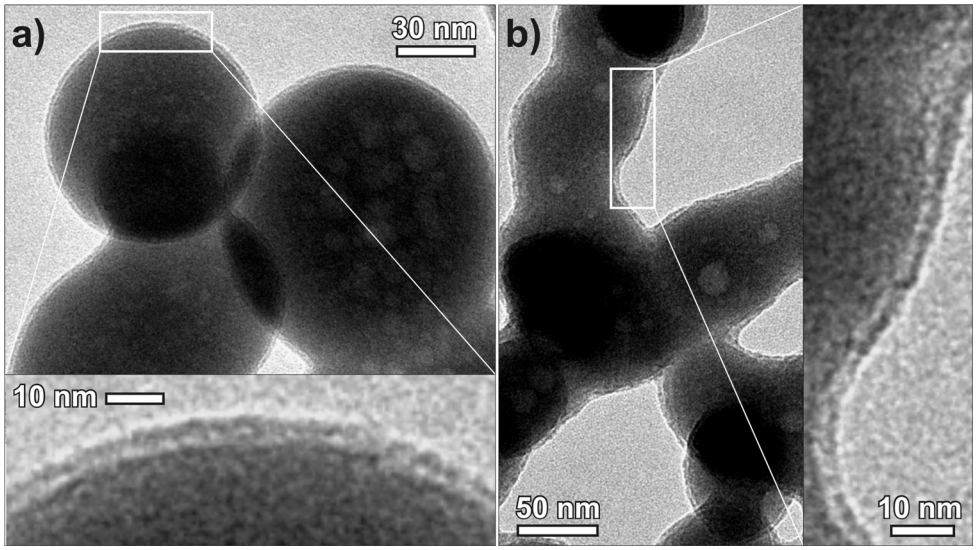

Fig. 2-6: Electron micrographs evidencing the core-shell structure of the composite particles isolated 1 min after mixing at silica concentrations of (a) 270 and (b) 540 ppm. The average thickness of the shells was determined to be 2.1 ± 0.2 and 3.3 ± 0.8 nm in (a) and (b), respectively.

2.4.2 Aggregation Behavior of Silica-Coated ACC Nanoparticles

At the rather high supersaturation chosen in this work, the ACC particles are nucleated homogeneously throughout the system imparting instantaneously an evenly turbid appearance to the mixtures. Visual observations suggest that, at low silica concentrations, the as-formed particles remain suspended in the solutions for prolonged frames of time. This allows for monitoring aggregation effects *in situ* by means of dynamic light scattering. Results show that the average diameter of scattering species increases linearly with time both in the absence and the presence of moderate amounts

of the additive (0-270 ppm), and that this increase is faster the more silica is added (Fig. 2-7).

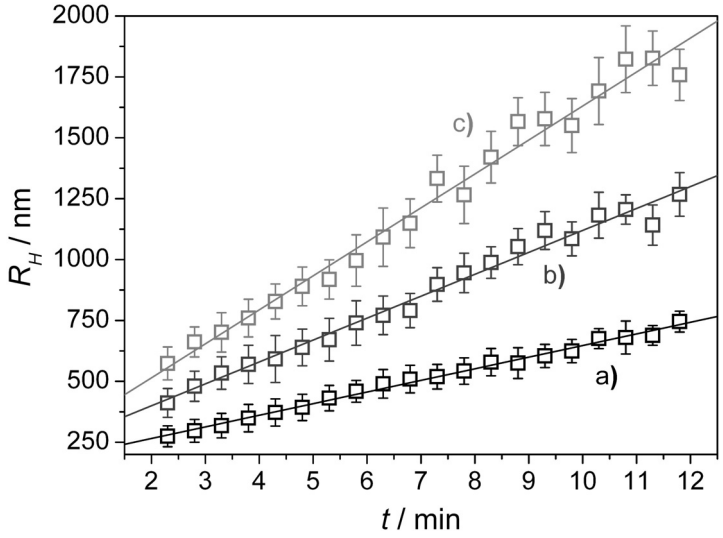

Fig. 2-7: Particle agglomeration as traced by dynamic light scattering. Open symbols represent the mean hydrodynamic radius R_H measured at different times after mixing in samples containing (a) 0, (b) 135, and (c) 270 ppm SiO_2. Obviously, the apparent size of the scattering species increases continuously with time and the faster the more silica is present. Full lines are linear fits of the data, having slopes of 47.7, 90.0 and 139.5 nm/min at 0, 135 and 270 ppm of the additive, with correlation coefficients greater than 0.991 in all cases. Extrapolation to $t = 0$ furnishes intercepts with the y-axis at radii of 170.0, 219.7 and 235.8 nm, respectively. These values are significantly larger than those obtained for the size of individual grains by measuring in electron micrographs (see Fig. 2-2), indicating that aggregation of particles occurs from the very beginning on. Note that agglomeration is enhanced in the presence of silica to such an extent that it overbalances the parallel decrease in primary grain size, resulting in bigger hydrodynamic radii at higher additive concentrations.

Apart from that, the measured size straight after mixing considerably exceeds that of discrete particles seen in TEM and SEM micrographs. Furthermore, precipitation runs quenched at later stages prove that individual particles do not grow further with time, also in silica-free systems. In light of these findings, the formation of ACC in the present experiments seems to be completed, more or less quantitatively, soon after mixing ($\leq$ 1 min). Consequently, the DLS data directly reflect aggregation processes and thus demonstrate that silica promotes agglomeration of primary grains. Ample conjunction of particles is probably driven by condensation reactions of free silanol groups between coating siliceous layers (2 –Si-OH → –Si-O-Si– + H_2O), which cause the silica to act like a glue sticking individuals together. Aggregation of additive-decorated amorphous precursors has previously been observed by DLS measurements during $CaCO_3$ crystallization under the influence of block copolymers.[29] Evidence that

ACC nanoparticles also tend to aggregate in solutions without any additives has as well been reported,[5,34] although other work has explicitly stated that particles grow under such conditions up to a certain, often well-defined size without being prone to noticeable agglomeration.[35] In the present experiments, both pure and silica-sheathed ACC particles are subject to substantial and progressive aggregation immediately after precipitation has been initiated

At higher silica concentrations (375-750 ppm), particle agglomeration becomes more and more enhanced and fairly large assemblies are formed within a few minutes, which coalesce macroscopically leading to sedimentation of a fluffy precipitate. To shed light on their composition, floccules at 750 ppm SiO_2 were isolated after 90 min and analyzed in detail (Fig. 2-8). Samples were found to be fully amorphous, showing IR characteristics typical for ACC and silica. Notably, there were also no crystals discernible on the walls or the surface of the solution. Hence, $CaCO_3$ exists still entirely as ACC. The flocs are composed of densely aggregated distorted nanoparticles which obviously exhibit core-shell morphology. In this concentration regime, the outer layer is very distinct and reaches a thickness of more than 10 nm, permitting EDX microanalysis of the shell region. Comparison of the data to those collected from the core indicates that the Ca signal drops when approaching the border of the particles while the Si count remains high. The Si/Ca ratio detected for the floccules (1.46) is significantly higher than in early particles isolated after 5 min at the same silica concentration (1.17), indicating that silica precipitation proceeds over extended frames of time.

2.4.3 Leaching Experiments

A final proof for the outer skins being silica can be given by treating the precipitates with acid. For this purpose, freeze-dried powders from a sample at 750 ppm silica were immersed in dilute HCl for several days, after which the gross part of the material had vanished. The remaining limpid floccules were studied with TEM, revealing hollow particles and networks thereof (Fig. 2-9). Acidifying the samples obviously leads to selective dissolution of the labile carbonate component from the particles, whereas the siliceous fraction is sparsely soluble and persists at low pH. This implies that the silica layers coating the ACC precursors must be porous and allow for exchange with the surrounding medium.

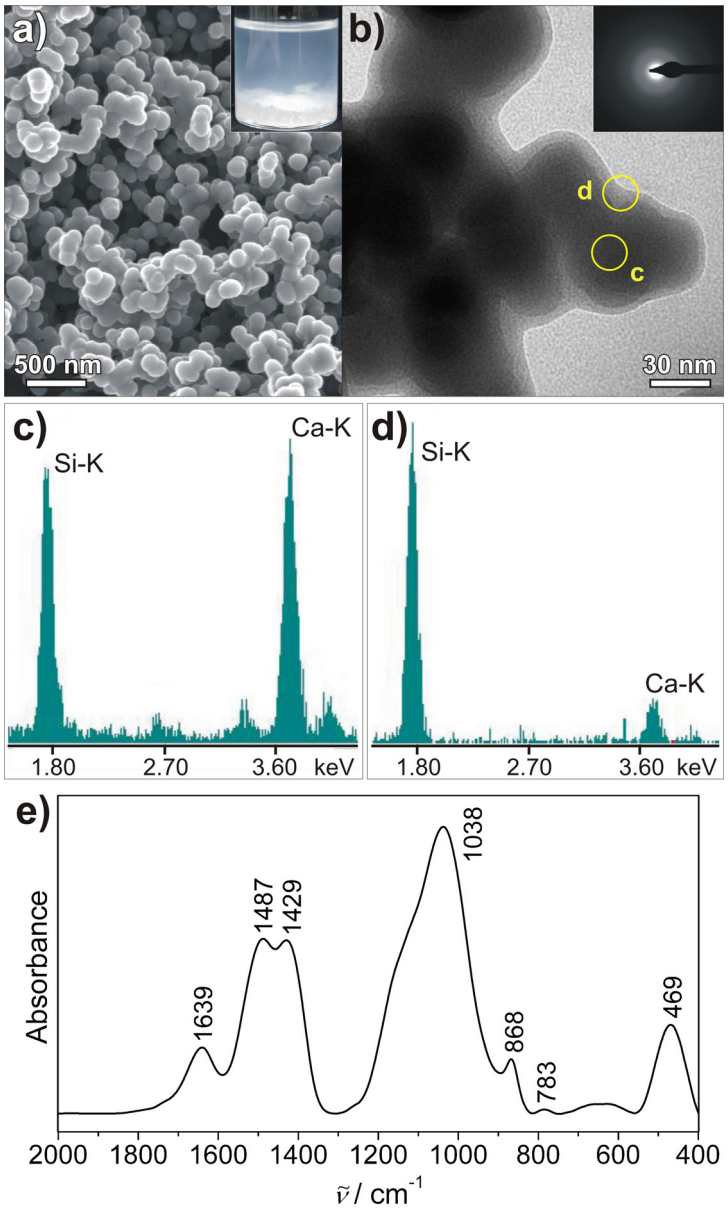

Fig. 2-8: Flocculation of ACC-silica composites in mixtures at 750 ppm SiO2 after 90 min. (a) FESEM image of the isolated solid showing networks of conflated nanoparticles, and a corresponding photograph illustrating sedimentation in the vials (inset). (b) TEM micrograph disclosing the structure of the floccules, and an electron diffraction pattern proving that the material is completely amorphous. Microanalyses of the dark inner region (c) and the lighter border area (d) strongly suggest that the core of the particles is rich in CaCO3 while the outer layer consists of silica. The mean thickness of the shells is 9.4 ± 3.3 nm. (e) Infrared spectrum of the precipitate with bands characteristic of ACC and silica.

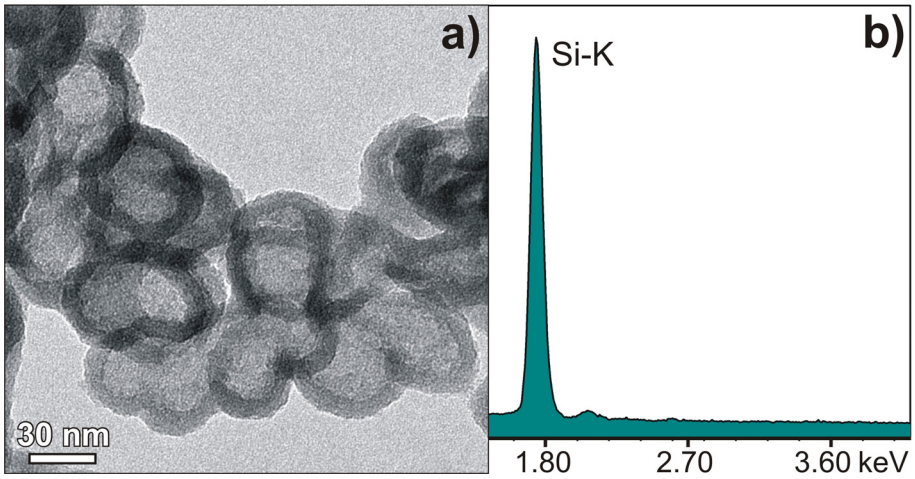

Fig. 2-9: Selective carbonate dissolution. (a) Hollow silica particle networks obtained by leaching samples prepared at 750 ppm SiO_2 in dilute acid. The average wall thickness is 9.0 ± 1.1 nm. (b) EDX profile demonstrating the absence of Ca.

Remarkably, the silica shells do not collapse during dissolution and the original morphology of the ACC particles is reflected in the shape of the silica remnants. Moreover, the thickness of the walls decreases a little upon leaching, due to either contraction caused by protonation or slight etching. To ensure that the formation of siliceous coatings around the ACC precursors is not an effect of filtering and drying, a second experiment was performed in which floccules were not directly isolated from solution. Instead, the supernatant was replaced repeatedly with water and eventually with acid. Results obtained by this procedure were identical to those reported for the freeze-dried powders. It can therefore be concluded that silica precipitation on the surface of ACC particles is a process intrinsic to the system which occurs spontaneously straight after mixing.

It shall be noted that Chen *et al.* prepared hollow silica particles with comparable sizes and morphologies following a similar procedure.[36] However, these authors used prefabricated calcite nanoparticles as templates onto which silica was deposited in a second step by controlled polymerization. This is in sharp contrast to the present experiments where direct co-precipitation of $CaCO_3$ and silica produced the core-shell particles at once.

2.4.4 Effect of Silica on the Transformation of ACC to Stable Calcite

Based on the above findings, the progress of ACC transformation to crystalline polymorphs was followed with time by repeatedly quenching and characterizing samples until its completion, when only crystals and a clear solution remained. Without

added silica, ACC was found to be the only phase present still after 10 min, while first crystalline products were detected after 30 min (Fig. 2-10).

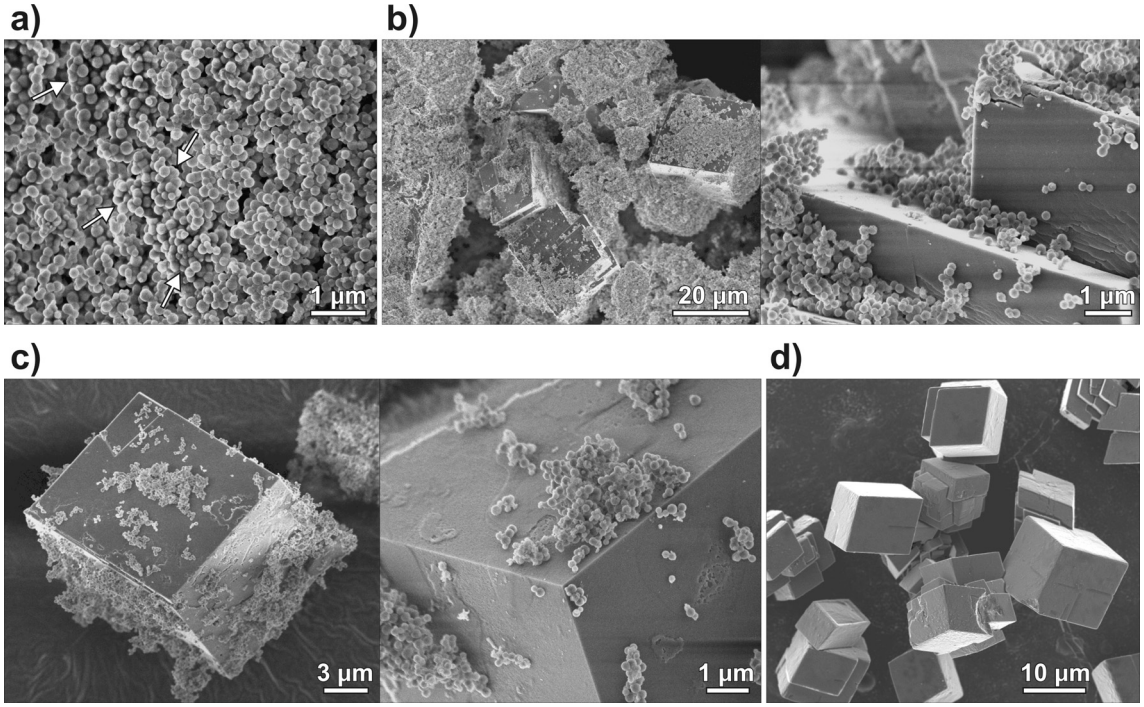

Fig. 2-10: $CaCO_3$ crystallization in the absence of silica. (a) Samples still consist entirely of amorphous nanoparticles after 10 min. Arrows indicate sites where particle agglomeration is noticeable. (b) 30 min: crystals with euhedral shapes are observed next to a preponderating fraction of amorphous material. (c) 60 min: crystals grow at the expense of the nanoparticles. The size of individual ACC grains does not change significantly with time, averaging 180 ± 40 nm in all samples. (d) 90 min: all ACC particles have vanished, leaving mainly classical rhombohedral crystals. Products were found to be calcite, with traces of vaterite seen in some cases (detected by XRD).

With proceeding crystal growth, the ACC fraction decreases, although significant amounts of amorphous particles could still be discerned even after 60 min. ACC hence persisted substantially longer in the experiments than in earlier studies at the same supersaturation.[5] Most probably, discrepancies arise as a consequence of different mixing conditions. Eventually, after 90 min, only characteristic calcite rhombohedra and very rarely also vaterite spheres were observed. Crystals thereby formed essentially on the walls of the vials or the surface of the solutions, thus strongly suggesting heterogeneous nucleation. Results hint at a dissolution-recrystallization pathway accounting for the transformation of ACC to stable calcite, as reported previously.[37] Moreover, a distinct vateritic phase acting as an intermediate stage during ACC conversion could not be detected, in contrast to other work where, in agreement with

Ostwald's rule of stages, vaterite formed first and subsequently re-dissolved to give calcite.[3,5]

The effect of silica on the crystallization process was first characterized by turbidity measurements. Since the presence of suspended ACC particles beclouds the mixtures, the time elapsed before the system clears off is a direct measure for the effective duration of crystallization. To gain reliable data, experiments had to be performed under stirred conditions. Therefore, the absolute values for the period after which crystallization is completed cannot be compared to those inferred from visual observation of the samples and SEM images (see below). The detected clearing times increase with growing concentration of the additive, implying that silica decelerates the crystallization process (Fig. 2-11).

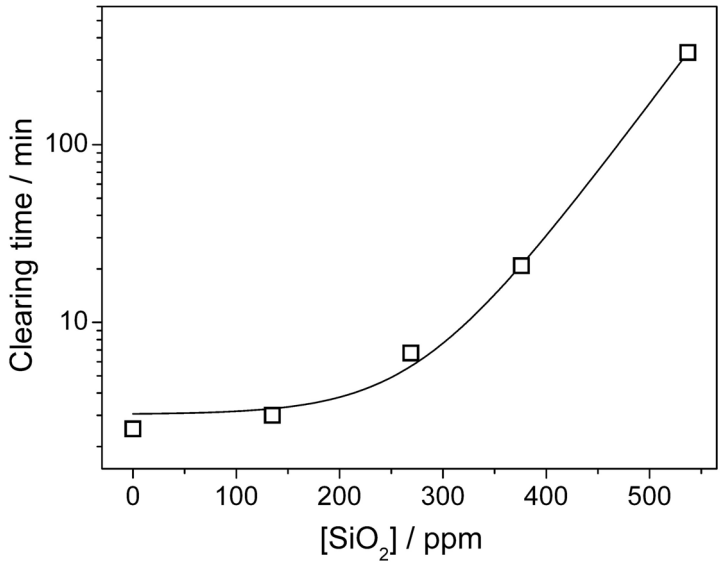

Fig. 2-11: Semi-logarithmic plot of the clearing time determined by turbidity measurements versus the amount of added silica, with a tentative exponential fit (full line) of the experimental data (open squares) ($t_C = a_0 + a_1 \cdot \exp([SiO_2] / a_2)$ with a_0 = (3.0 ± 0.6) min, a_1 = (0.021 ± 0.004) min, a_2 = (55 ± 2) ppm, R^2 = 0.99998) Data were acquired while stirring samples. Crystallization is consequently completed distinctly earlier than under the quiescent conditions chosen otherwise in this work.

Total conversion of ACC requires more than 5 hours in the presence of 540 ppm SiO_2, while clearing of the solution is already observed after 2.5 min when no silica is added. Inspecting non-stirred samples visually confirms the results from the turbidity measurements. Completion of crystallization can in this case be equalized not only to a clearing of the solutions, but also and in particular at higher silica concentrations to the disappearance of precipitated amorphous floccules. The latter gradually dissolve until finally only discrete crystalline objects remain adhered to the vial walls. Durations thus

determined are considerably longer than under stirred conditions, and range from about 70 min in the absence of silica over roughly 1 day at 375 ppm up to several months at 540 ppm. From these data, we deduce that addition of silica markedly inhibits the formation of crystalline $CaCO_3$ polymorphs from amorphous precursors. Inhibition can be ascribed to the siliceous skins precipitated *in situ* around the ACC particles, which impede both dissolution as well as direct contact of particles necessary for potential Ostwald ripening, and consequently stabilize particles against transformation.

Following the crystallization process by quenching and characterizing samples at different times in the presence of 270 ppm silica corroborates the notion that ACC is stabilized by the additive, given that precursor particles were observed still after 90 min (Fig. 2-12), while samples with 375 ppm were entirely amorphous at the same time (confirmed by XRD data). Powder diffraction patterns as well as SEM and TEM images disclose that at 540 ppm no crystalline polymorphs are formed before 3 hours.

After the respective delay, calcite crystals are nucleated the precipitated floccules (see Fig. 2-13a-b) and grow in direct contact with, or respectively from silica-coated ACC particle floccules (Fig. 2-12a-b). This suggests in principle that transformation of ACC to stable calcite occurs in this case through solid-state conversions. However, a closer look at precursor particles associated to a growing crystal reveals that some of them now have holes on their surface and indeed seem to be hollow (cf. Fig. 2-13a and the inset in Fig. 2-12b). Apparently, the inner ACC core was dissolved in order to supply $CaCO_3$ for crystal growth, which is supported by the finding that the Ca/Si atomic ratio of the amorphous fraction decreases successively with time (Fig. 2-12d). This indicates that the transformation of ACC to stable calcite occurs also *via* a dissolution-reprecipitation pathway in the presence of silica. Sheathing by silica prevents possible solid-state conversions as the ACC particles lack mutual contact and can therefore not merge. The fact that crystals grow directly on the amorphous floccules likely derives from the elevated supersaturation in the vicinity of particle aggregates which gradually release $CaCO_3$ units and, in addition, provide a surface facilitating nucleation. After equilibration, calcite crystals were the only solid product remaining in the vials while all nanoparticles, including the hollow ones, had vanished. This implies that, at silica concentrations of up to 540 ppm, conversion of ACC to calcite is quantitative and that the silica skin re-dissolves in the mother liquor once the inner ACC core had been detached. Thus, precipitation of silica seems to be favored only under the conditions prevailing locally around the ACC particles, but not under those existing in the bulk

solution. Re-dissolution of silica is likely to be supported by ongoing disintegration of the ACC core, which raises the pH and thus the solubility of silica in the vicinity of the particles.

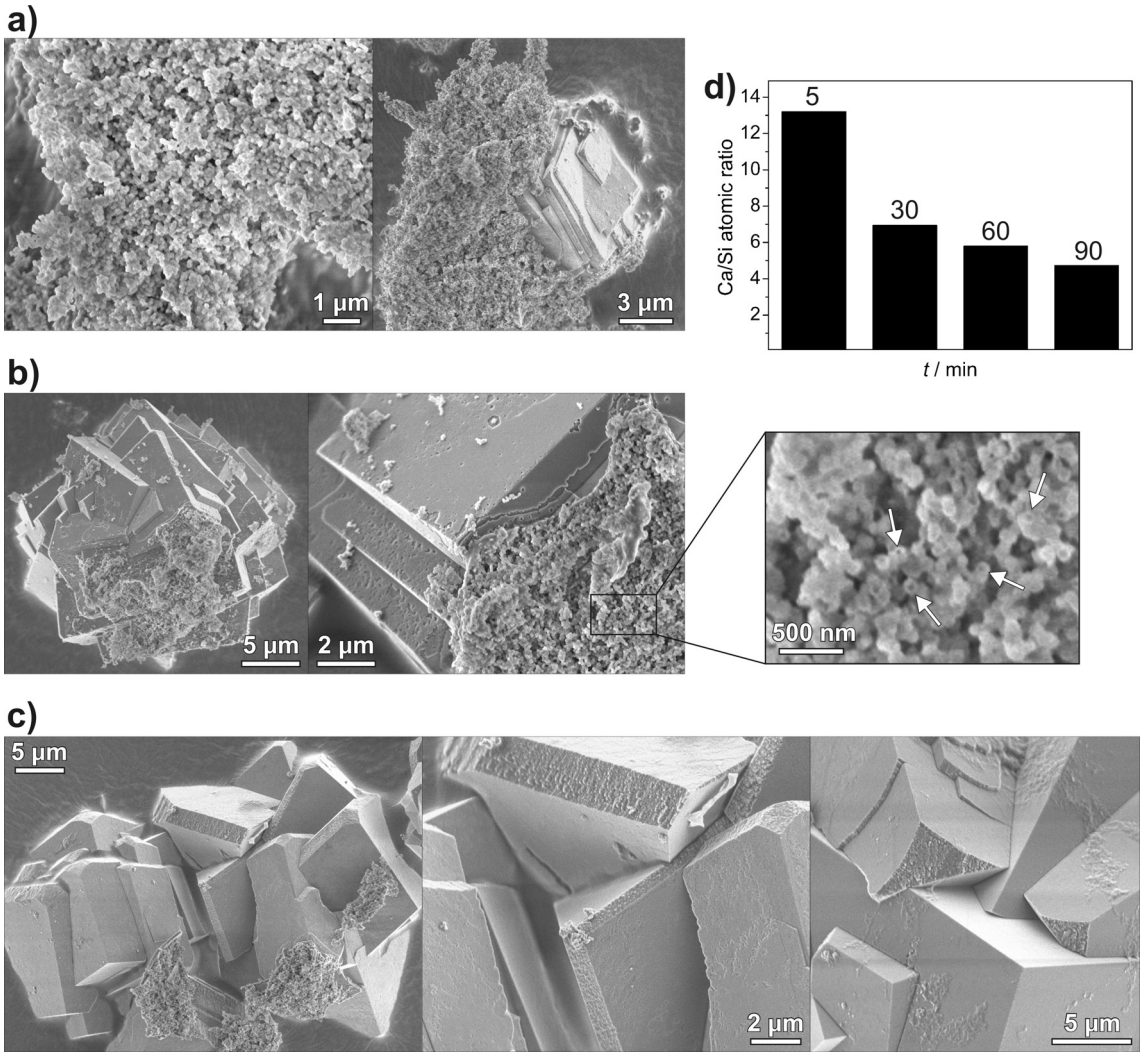

Fig. 2-12: $CaCO_3$ crystallization at 270 ppm SiO_2. (a) 30 min: Precipitates are mainly amorphous (left). Occasionally, crystalline objects are observed which have started to outgrow from flocs of nanoparticles (right). (b) 60 min: Micron-sized architectures of intergrown calcite individuals have formed (left). Crystals are often seen to maintain direct contact to ACC particle agglomerates (right). Higher magnifications of the latter reveal that some of the particles display holes and seem to be hollow (inset, holes indicated by the arrows). (c) 90 min: Crystal conglomerates have grown further at the expense of amorphous precursors. Nevertheless, there is still a considerable fraction of ACC material present. Edges of rhombohedral individuals appear to be truncated and rough oblique faces are expressed instead. The diameter of discrete ACC grains does not change with time and was found to be 115 ± 15 nm. X-ray diffraction identified all crystalline products as regular calcite. (d) The Ca/Si atomic ratio of amorphous particle networks measured by EDX spectroscopy at different times. The continuous depletion of Ca relative to Si in the floccules is likely due to dissolution of ACC from the composite particles and concomitant crystallization of calcite.

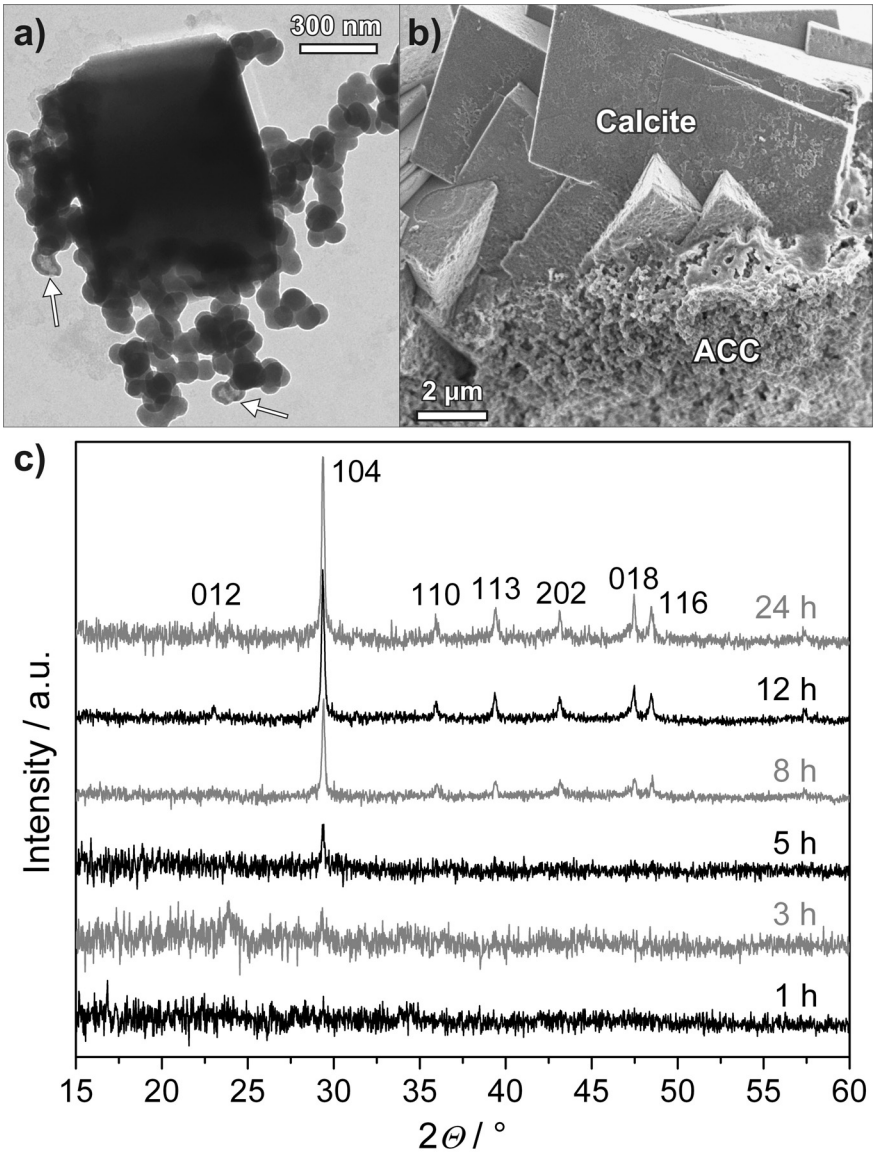

Fig. 2-13: Recrystallization of calcite from temporarily silica-stabilized ACC particle networks. (a) TEM image of a rhombohedral calcite crystallite nucleated on top of the precursor particles. Arrows indicate nanoparticles that appear to be hollow (375 ppm SiO_2, 90 min). (b) FESEM micrograph showing the boundary between amorphous particle floccules and calcite crystals which grow nourished by the inner ACC fraction of the core-shell particles (270 ppm SiO_2, 60 min). (c) Powder diffraction patterns of precipitates (both amorphous floccules and, if present, crystals) isolated from mixtures at 750 ppm SiO_2 after different times. The emergence of a weak calcite (104) peak after 5 h indicates the onset of crystallization. With time, further calcite reflections appear and the intensity of the signal increases.

When further increasing the silica content, a growing percentage of the precursor particles become sheathed by skins dense enough to permanently prevent dissolution and re-crystallization. For example, at 750 ppm SiO_2, powder diffraction data show that calcite formation commences after a delay of roughly 4-5 h and proceeds for up to about

1 day (Fig. 2-13c). Subsequently, no further change in the fraction of crystalline material (assessed by integration of the calcite (104) reflex) could be discerned even when the system was left to evolve for periods as long as 1 year (Fig. 2-14).

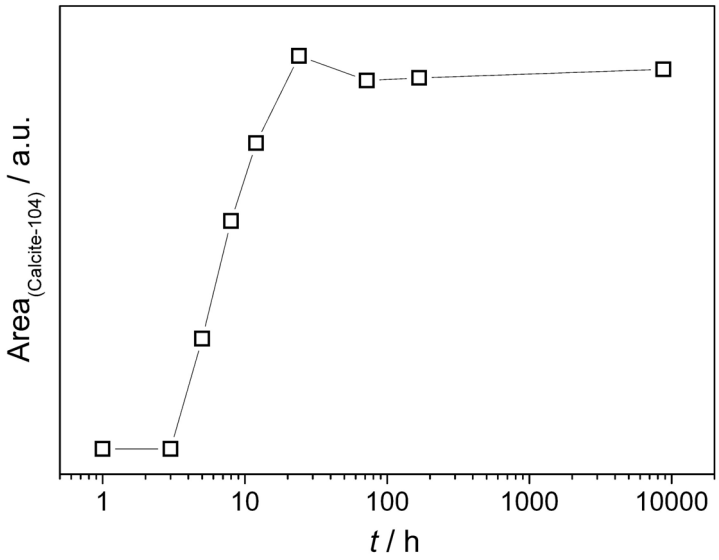

Fig. 2-14: Plot of the integrated area under the calcite (104) peak in XRD patterns (cf. Fig. 2-13c) of precipitates isolated at different times after mixing from samples at 750 ppm SiO_2. Crystallization of calcite occurs after a delay of 4-5 hours and is essentially terminated after about 1 day.

Optical micrographs and FESEM images yet clearly illustrate that a major part of the samples is still constituted by amorphous floccules after such extended frames of time. Separate analyses of the floccules by EDX spectroscopy reveal that upon apparent completion of crystallization, around 58 % of the total molar amount of Ca present is still enclosed in the nanoparticle networks (Fig. 2-15). Infrared spectra of powder samples isolated after 1 year verify the presence of both ACC and calcite (Fig. 2-16a). Furthermore, the calculated intensity ratio of the υ_2 (~870 cm^{-1}) and the υ_4 (~700 cm^{-1}) mode was used to estimate, according to previous work,[15] the overall ACC fraction in the sample to be about 50 %. Hence, after conversion of insufficiently protected ACC within the first 24 h after mixing, compositionally stable systems are obtained in which amorphous calcium carbonate and calcite co-exist without notable changes over timescales of years. To our knowledge, stabilization of ACC in contact with its mother solution for such extended periods of time has not been reported to date.

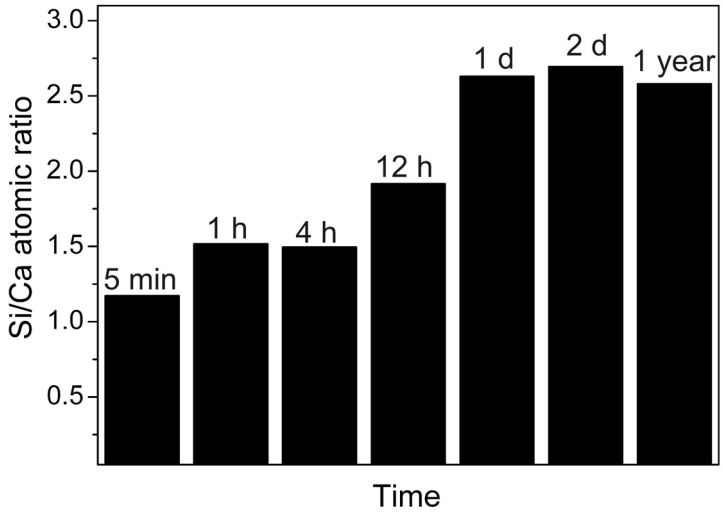

Fig. 2-15: Temporal evolution of the Si/Ca atomic ratio determined by EDX spectroscopy selectively for the amorphous floccules formed at 750 ppm silica. After an initial increase to about 1.5 within the first hour, which can be ascribed to continued precipitation of silica around the ACC precursors (densification of the shells), values remain approximately constant for several hours. At this stage, compositionally stable particles have been formed and silica polymerization is no longer active. As crystallization sets in, a second increase of the ratio to about 2.6 is observed, indicating that Ca is continuously removed from the floccules. After 1 day, no further significant changes were detected, even when samples were left to evolve for 1 year. This confirms on the one hand the results obtained by powder diffraction. On the other, the data imply that a significant fraction out of the total amount of $CaCO_3$ present in the system does still exist as ACC after a year. From a comparison of the final Si/Ca values to those characterizing the plateau between 1 and 4 h, it can be inferred that about 58 % of the $CaCO_3$ remain conserved in siliceous shells. Calcite and permanently stabilized ACC thus co-exist in samples at 750 ppm SiO_2.

Finally, at values well above 1000 ppm, all ACC material is effectively cemented in a siliceous matrix such that transformation to calcite is completely inhibited. Characterization of samples at 1870 ppm SiO_2 that were left to stand for more than one year confirms that protection of ACC precursors is an enduring effect under these conditions (Fig. 2-17). SEM and TEM images evidence that the isolated precipitates still consist entirely of rounded nanoparticles with no specific crystalline shapes distinguishable. Alongside, X-ray diffraction patterns identify the material as being fully amorphous, while IR spectra indicate the presence of calcium carbonate, most probably as ACC, next to an appreciable amount of amorphous silica (Fig. 2-16b). With the corresponding EDX data (Table 2-1) and the assumption that the stoichiometry of the components is properly described by $CaCO_3$ and SiO_2, the average mass fraction of ACC in the particles at 1870 ppm can be estimated to be about 36.5 %.

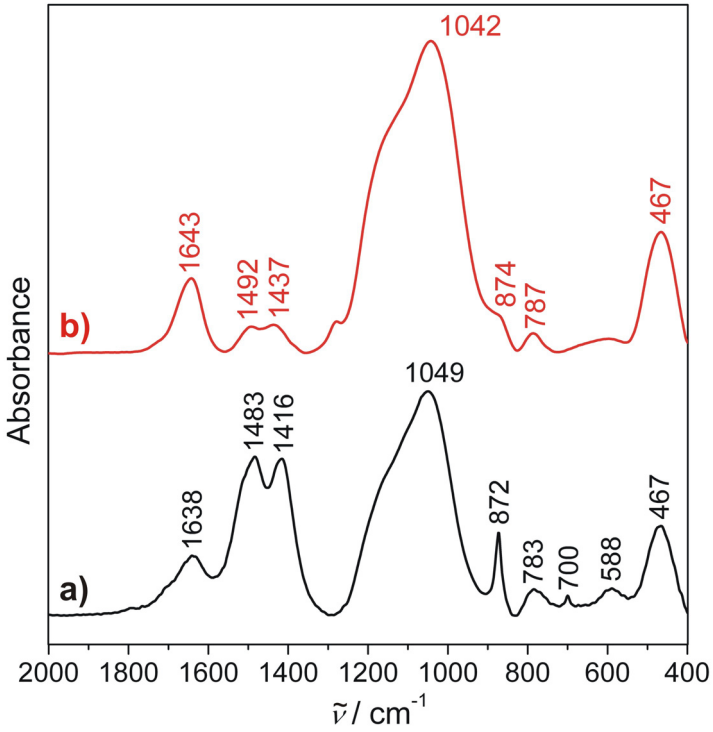

Fig. 2-16: (a) Infrared spectrum of the precipitates (both floccules and crystals) isolated from a sample at 750 ppm SiO_2 which was allowed to stand for 1 year. Absorptions at 467, 588, 783, 1049 and 1638 cm^{-1} can be assigned to amorphous silica.[32] The split band at 1416/1483 cm^{-1} verifies the presence of ACC.[2] In turn, the emergence of a distinct peak at 700 cm^{-1} (corresponding to the υ_4 mode of $CaCO_3$) indicates that crystalline polymorphs, in this case calcite (XRD data), have formed. The wavenumber observed for the band related to the υ_2 vibration of calcium carbonate (872 cm^{-1}) is exactly the average of the values reported in literature for ACC (865 cm^{-1}) and calcite (877 cm^{-1}).[31] According to Raz et al. the ratio of the maximum intensities measured for the υ_2 and the υ_4 band, $I_{max}\upsilon_2/I_{max}\upsilon_4$, is proportional to the ACC percentage in an ACC-calcite mixture.[15] By using their data as a "calibration" we calculated the fraction of ACC in the present sample to be around 50 % of the total $CaCO_3$ content, which is in fair agreement with the result obtained from the EDX measurements (Fig. 2-15). (b) IR spectrum of nanoparticles existing in samples at 1870 ppm SiO_2 after ageing for 1 year, showing intense bands of amorphous silica (467, 787, 1042 and 1643 cm^{-1}) as well as absorptions at frequencies typical for $CaCO_3$ (874, 1437 and 1492 cm^{-1}). The double band between 1400 and 1500 cm^{-1} and the absence of a peak near 710 cm^{-1} prove, together with the corresponding XRD pattern (Fig. 2-17c), that the core of the particles still consists entirely of ACC and that no noticeable transformation to calcite has occurred.

The diameter of primary ACC grains ranges typically between about 30 and 40 nm and does not change noticeably with time (Fig. 2-17b). Recently, Pouget *et al.* observed that particles with similar sizes were the first ACC species formed upon nucleation in the course of $CaCO_3$ crystallization.[38] This may hint at ACC becoming enveloped by the silica at 1870 ppm straight, or soon, after nucleation such that the smallest possible

particles are stabilized. The crystallization process is thus frozen at its utterly early stage.

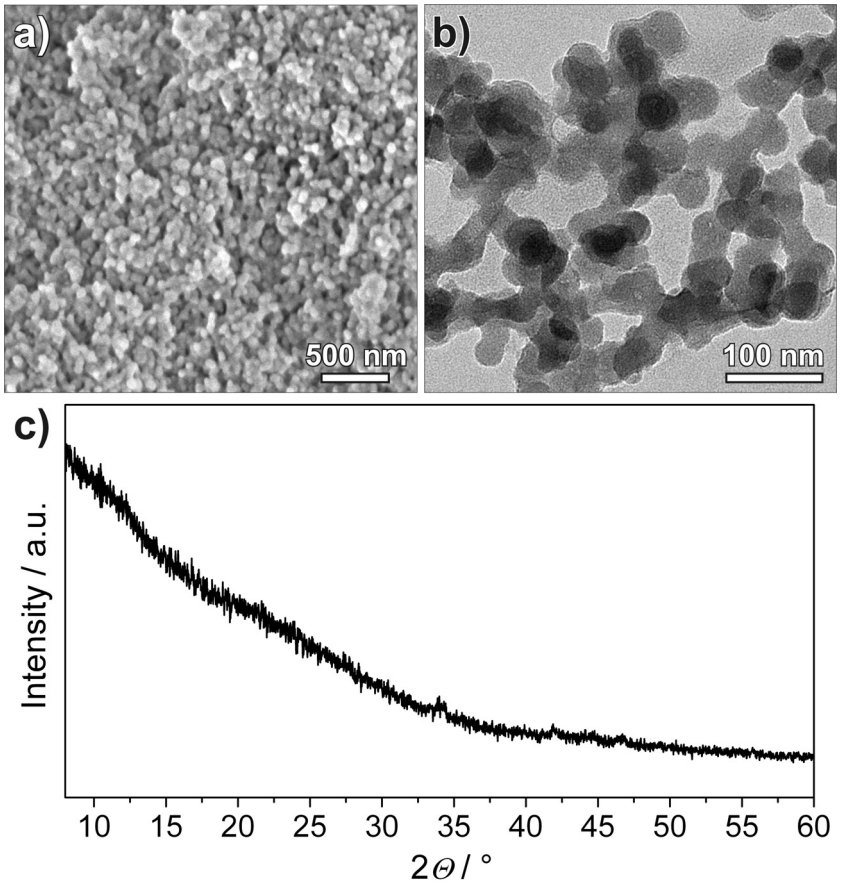

Fig. 2-17: Long-term stabilization of amorphous calcium carbonate at 1870 ppm SiO_2. (a) FESEM image of particles isolated from a sample after 1 year. (b) TEM micrograph of a dried sample displaying multiple spherical nanoparticles embedded in a translucent matrix. (c) XRD pattern of the particles verifying the absence of any crystalline matter.

2.4.5 pH Measurements

The pH of the samples was monitored by immersing a probe into the solutions straight after mixing reagents. Values were read constantly over a period of about 20 min, during which the formation of ACC nanoparticles and initial precipitation of silica on their surface are completed. The resulting progressions are shown in Fig. 2-18. The starting pH was found to be similar at all studied silica concentrations, ranging from about 10.5 to 10.75. Obviously, there is no clear correlation between the initial pH of the mixtures and the amount of added silica, and differences between the samples do partly not exceed common limits of error associated to pH measurements with glass electrodes in alkaline silica-containing media (± 0.1 units). In the absence or the presence of a small quantity of silica (135 ppm), the starting pH seems to be dominated

essentially by the carbonate ions which are in equilibrium with the ACC particles in the solutions. From 270 to 1230 ppm, the silica reduces the pH actually given by the carbonate to a quite narrow interval of 10.5-10.6. Finally, at the highest investigated concentration (1870 ppm), a significant re-increase in pH to about 10.7 is observed due to the alkaline character of the silica.

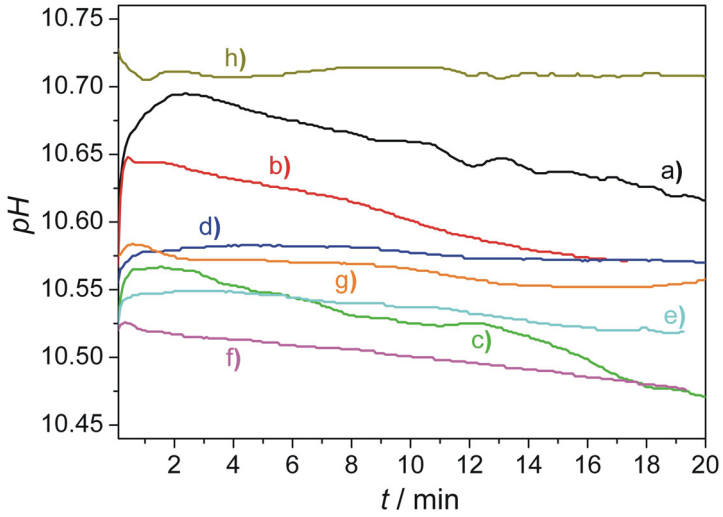

Fig. 2-18: Temporal evolution of the pH in samples containing (a) 0, (b) 135, (c) 270, (d) 375, (e) 540, (f) 750, (g) 1230, and (h) 1870 ppm SiO_2 during the first 20 min after mixing reagents.

Variations of the pH with time are overall sparsely pronounced. However, there is a slight but continuous decrease in pH discernible at low silica content, probably reflecting carbonate precipitation. This effect becomes buffered by the silica at higher concentrations, such that the pH remains more or less constant over the examined interval, and does also not change significantly in the long term.

2.5 Discussion

Our findings can be rationalized in a mechanism as depicted in Fig. 2-19. Right after mixing $CaCl_2$ and Na_2CO_3, amorphous calcium carbonate is nucleated throughout the solution in the form of spherical nanoparticles (Stage 1). At the given high pH of the mixtures (cf. Fig. 2-18), carbonate ions are expected to co-exist to a considerable extent with bicarbonate (see Appendix A, Section A.2). For instance, the fraction of HCO_3^- ions in equilibrium 2 min after mixing amounts to about 30-40 % depending on the silica concentration (see Table A-1 in Appendix A). Growth of ACC induces dissociation of bicarbonate and the release of protons according to

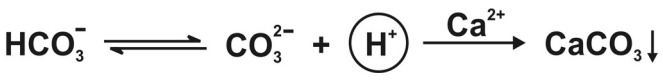

This should result in a decrease of pH around the surface of growing particles relative to the outer alkaline bulk (Stage 2).[39] Within the presumed local pH gradient, the solubility of silica will be markedly reduced (see Section A.1 in Appendix A) as protonation of silicate species becomes enhanced and free silanol groups liable to condensation reactions are formed:

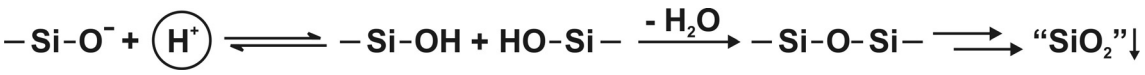

The nascent protons thus create $Si(OH)_4$ species that condense in rapid succession to higher oligomers, polymeric fragments and small colloidal particles,[40,41] which finally precipitate on the ACC grains (Stage 3). Deposition of silica nanoparticles on the carbonate surface will initially generate an inhomogeneous and porous layer with uneven topology, causing an apparent distortion of the original spherical shape especially at higher silica concentrations (cf. Fig. 2-1 and Fig. 2-2). According to Iler, the solubility equilibrium of a silica surface depends on the local curvature, with concave regions being essentially less soluble than convex ones.[41] Therefore, after initial pH-induced coagulation further dissolved silicate will be incorporated to the layers in order to fill concave crevices between the colloids, which progressively flattens the surface. This explains the detected increase in the Si/Ca ratio of the particles with time and suggests that the shells densify rather than continually growing in thickness. Eventually, these precipitation processes produce a smooth and homogeneous skin of amorphous silica all over the ACC particles (Stage 4), the final thickness and density of which is determined by the overall degree of polymerization and hence, amongst others, the concentration of silica. Coating of ACC by consolidated siliceous shells arrests growth and consequently defines the size of the particles, which become smaller when the amount of added silica is increased. The presence of external skins constrains dissolution and avoids potential Ostwald ripening. Therefore, energetically favored transformation to crystalline polymorphs is inhibited and usually transient ACC species are stabilized. Moreover, condensation reactions in-between the superficial silica layers promote aggregation of the core-shell particles yielding extended networks of tightly conjoint and necked individuals (Stage 5).

Depending on the specific silica concentration we found two limiting cases. Below 1000 ppm, calcite crystallizes after a certain delay at the expense of the ACC precursors since the skins around the particles are not sufficiently dense to prevent dissolution and subsequent nucleation of the stable phase in the long term (Stage 6a). Above 1000 ppm,

extensive silica polymerization leads to the formation of "leak-proof" coatings which allow for a permanent conservation of ACC on timescales of years (Stage 6b).

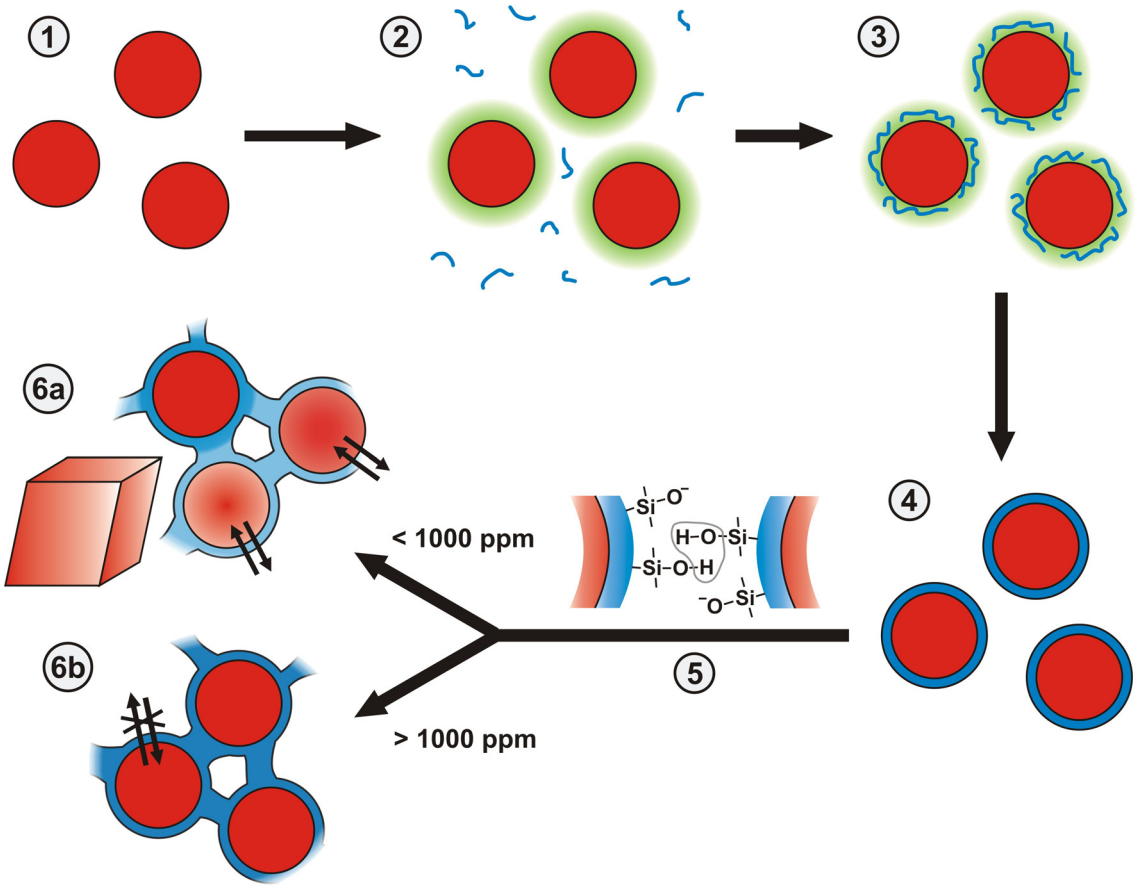

Fig. 2-19: Mechanism for silica-mediated stabilization of amorphous calcium carbonate and control over calcite crystallization. In alkaline solutions, growing ACC nanoparticles (red circles) generate pH gradients (green) over their surfaces due to dissociation of bicarbonate ions. Silicate species (blue) respond to these local changes by polymerization reactions which prompt in-situ precipitation of expanded silica skins around the particles (Stages 1-4). Condensation of superficial silanol groups favors particle aggregation and provokes flocculation of an amorphous ACC-silica composite material (Stage 5). Ultimately, calcite crystals are formed by transformation of ACC via dissolution-renucleation processes at silica concentrations of up to 1000 ppm (Stage 6a). Above that threshold, ACC precursors become cemented in siliceous matrices to such an extent that exchange with the solution is no longer possible and crystallization is completely and permanently prevented (Stage 6b). Note that structures are not drawn to relative scale.

At concentrations ranging from 750 to about 1000 ppm, effective stabilization is sustained only for a distinct fraction of the particles such that ACC and calcite co-exist side by side in equilibrium. This implies that the degree of silica condensation may vary between individual particles under these conditions, thus leading to shells of potentially different porosity and/or thickness. In fact, the porosity of precipitated nanoscale silica

coatings and their permeability for small molecules and ions has been demonstrated in earlier work dealing with metal nanoparticles.[42] In line with the present results, it was reported that both the thickness and the density of the silica layers determine the rate of exchange between the core material and the surrounding solution, and whether the particles are pervious for reagents or not.

Previous analyses on the composition of synthetically produced ACC have shown that the phase generated on precipitation usually contains water in variable amounts.[3,19,43] Therefore, it may be suspected that the ACC formed in the present experiments is also hydrated to a certain, yet unknown degree. In this regard, the role of the silica shells in stabilizing the amorphous particles may not be confined to acting as a barrier which delimits the release of ions into the solution and hence restrains dissolution of ACC. In addition, they might prohibit the expulsion of water molecules from the core and, thereby, prevent possible transformations of hydrated ACC to anhydrous crystalline polymorphs inside the compartments.[2]

The collected data demonstrate that the pH-based interplay of growing barium carbonate crystallites and dissolved silicate species recently proposed for the morphogenesis of silica biomorphs[39] can be employed to endow ACC particles *in situ* during $CaCO_3$ precipitation with distinct siliceous skins. In turn, since these skins could be, for the first time, explicitly imaged and experimentally verified as shown by the analyses presented herein, results provide a direct proof for the validity of the postulated model. Moreover, the concepts devised in this study might, in all likelihood, be readily transferable to compounds other than calcium carbonate, which are likewise capable of generating local pH gradients during growth in alkaline media. Promising candidates in this context are in principle all sparingly soluble carbonates ($BaCO_3$, $SrCO_3$, $FeCO_3$, $PbCO_3$, etc.) as well as other salts with multivalent anions, among which phosphates and sulfates may be of greatest interest

Beyond that and according to the introductory idea of this chapter, the described experiments have illustrated that addition of silica is a powerful means to concertedly modify the progress of $CaCO_3$ crystallization. Simply by adjusting the silica concentration, ACC can either be stabilized temporarily or permanently, or allowed to co-exist with tunable fractions of calcite. Living organisms retain similar, yet surely by far more sophisticated control over the stability of ACC in- and outside their tissues.[2,9-11,14-18,20] Nevertheless, it is surprising to which extent the delicate processes occurring in biological and bio-inspired synthetic environments can be emulated in purely *inorganic*

systems. This analogy is additionally fuelled by the ability of silica to produce exceptional crystal architectures of alkaline-earth carbonates reminiscent of biogenic forms, as already recognized in previous studies.[44] Calcite crystals isolated at elevated silica concentrations in this work exhibited as well morphologies and structures of remarkable complexity, a detailed description of which will be provided in Chapter 3. The key to structured crystallization under the given conditions lies in the temporary storage of $CaCO_3$ as silica-sheathed ACC and the concurrent relief of actual supersaturation. This is another strategy also applied in biomineralization.[2]

Furthermore, it is well-known that geological sediments of carbonate minerals often contain significant portions of silica, especially in marine environments.[45] Indeed, there are many instances in which quartz or other silica polymorphs were found to selectively incrust alkaline-earth carbonates,[46] or replace sediments thereof on geological timescales via dissolution.[47] Walker reported that in chert-bearing carbonate rocks multiple replacement reversals between silica and carbonate can occur, possibly induced by alkaline variations of the pH in interstitial waters.[48] Laboratory experiments meant to elucidate the apparent mutual affinity of silica and carbonate minerals in geological scales have revealed that dissolved silica is prone to adsorption on the surface of $CaCO_3$ crystals, the degree of which depends on diverse factors such as the silica solution concentration, $CaCO_3$ polymorphism, pH, ionic strength, specific surface area, as well as the presence of Mg species.[45,49,50] Localization of silica deposits on carbonate surfaces is thought to be governed either by irreversible physical adsorption[50] or a chemical reaction (chemosorption) potentially involving partial dissolution and re-precipitation of the carbonate material.[46] Studies on the crystallization of calcium carbonate from solution under seawater conditions (i.e. at near-neutral pH) showed that although silica distinctly influenced phase selection, it was incorporated to the crystals only in modest amounts during precipitation.[45,50] Based on that and the observation that precipitation rates were unaltered in the presence of silica, Klein *et al.* concluded that the silica content in marine carbonates originates from independent deposition after completed carbonate mineralization rather than direct co-precipitation.[50] By contrast, our data clearly evidence that direct co-precipitation of calcium carbonate and silica can readily result in a massive uptake of silica by the forming carbonate particles, and hence propose an alternative scenario for the frequent joint occurrence of the two minerals. Obviously, the effects described herein require at least a moderately alkaline pH and were most probably therefore not traced in the cited studies. Although natural waters

with elevated pH and high silica concentration are scarce today, they likely were common in former ages[51] and thus possibly hosted pH-coupled co-mineralization of carbonates and silica. Coating of carbonate surfaces by siliceous layers is thereby not necessarily restricted to freshly nucleated ACC particles or crystallites, but may also take place at previously grown mature crystals which partially dissolve and later recrystallize due to varying conditions. This might explain the formation of a "coagulated layer of silica gel" on calcite crystals which were immersed in an alkaline silica sol.[46] As noted already by Pina *et al.*,[52] the silica could in this sense have a dual function both in biomineralization and geology, acting as a dynamic additive which modifies and controls the crystallization process and at the same time being a true constituent of the developing mineral framework.

Finally, the presented results might have implications also for technical applications. For example, the finding that crystallization of calcium carbonate is completely avoided at high silica concentrations has obvious potential for the field of scale inhibition. In fact, samples at 1870 ppm SiO_2 are fairly stable colloidal suspensions which neither precipitate hard mineral deposits nor flocculate amorphous matter with time, and can thus easily be washed away. Silica, paradoxically being a substance which itself often contributes to industrial fouling, could consequently be used as cheap and environmentally harmless antiscalant agent, practicably replacing conventional polymeric additives which require laborious synthesis. Though being based on a different mechanism, the action of the silica during $CaCO_3$ crystallization is comparable to that of typical polycarboxylates (except for the sequestering effect of the latter), in that amorphous precursors become fully covered and colloidally stabilized against transformation if sufficient amounts are present.[5,53] This threshold in concentration is usually lower for the polymers, but at least in a similar order of magnitude for both additives (e.g. 150 ppm at 5 mM $CaCO_3$ for an acrylate-maleate copolymer[5] versus around 1000 ppm for silica). An evident disadvantage of silica in this respect rests upon the restriction of its efficiency to alkaline solutions. However, recent considerations to operate desalination facilities at elevated feed water pH in order to reduce the levels of hazardous boron compounds might render silica an interesting option for scale prevention.[54]

Apart from that, silica-coated calcium carbonate particles have attracted increasing attention in the past years due to their potential application as paper fillers, pigments, or in formulations of rubber or plastics.[55-61] Grafting of siliceous layers onto the particles is

thereby sought to alter their surface properties, enhance their stability and thus to overall improve the performance of the material. The preparation of such composites is often accomplished by a more or less complicated multi-step process, in which $CaCO_3$ particles with desired size are fabricated first. Coating can then be achieved for instance by addition of sodium silicate and subsequent acidification provoking silica precipitation,[56,57,60] or via polymerization of alkoxysilane precursors.[62] Other recipes for the synthesis of nanosized silica-calcium carbonate particles reported in literature recommend mixing of soluble calcium salts with the silicate component prior to carbonation of the system.[59,61] Under these conditions, $CaCO_3$ precipitation occurs by contrast clearly in the presence of silicate and effects as those observed in this study are likely at work, though not explicitly recognized by the authors. The results of the present work provide a mechanistic basis for spontaneous silica coating of calcium carbonate particles *in situ* during their formation. Further, the experiments demonstrate that directly mixing solutions of $CaCl_2$ and Na_2CO_3 with added sodium silicate is a straightforward one-step route – when reactions are quenched at proper times – for the manufacture of uniform silica-enveloped $CaCO_3$ nanoparticles. Moreover, the size of primary grains and the composition of the material can easily be tuned by varying the concentration of the additive.

2.6 Conclusion

In summary, the work described in this chapter has shown that the coupling between the speciations of carbonate and silicate in alkaline solutions imparts remarkable changes to the progress of $CaCO_3$ crystallization in silica-rich environments and can be exploited to coat ACC nanoparticles *in situ* with skins of amorphous silica. This results in suppression of chemical exchange with the surrounding medium and substantial inhibition of ACC transformation to calcite. The porosity of the silica layer around the precursor particles and hence the degree of stabilization were found to be a function of the silica concentration, ranging from slightly prolonged lifetimes of ACC to permanent conservation over years. Overall, the dynamic interplay between components maintains discrete control over ACC stability and the rate of calcite crystallization, and thus imitates in the absence of organic matter strategies recently identified to be used by various living organisms for concerted $CaCO_3$ mineralization. The concepts learned from this model precipitation system may further be of interest for fields like geology as

well as for distinct industrial applications, and should moreover be readily transferable to other minerals.

2.7 References

(1) Addadi, L.; Weiner, S. *Angew. Chem. Int. Ed.* **1992**, *31*, 153.

(2) Addadi, L.; Raz, S.; Weiner, S. *Adv. Mater.* **2003**, *15*, 959.

(3) (a) Ogino, T.; Suzuki, T.; Sawada, K. *Geochim. Cosmochim. Acta* **1987**, *51*, 2757. b) Brecevic, L.; Nielsen, A. E. *J. Cryst. Growth* **1989**, *89*, 504.

(4) Faatz, M.; Gröhn, F.; Wegner, G. *Adv. Mater.* 2004, 16, 996.

(5) Rieger, J.; Frechen, T.; Cox, G.; Heckmann, W.; Schmidt, C.; Thieme, J. *Faraday Discuss.* **2007**, *136*, 265.

(6) Taylor, M. G.; Simkiss, K.; Greaves, G. N.; Okazaki, M.; Mann, S. *Proc. R. Soc. Lond. B* **1993**, *252*, 75.

(7) Aizenberg, J.; Lambert, G.; Addadi, L.; Weiner, S. *J. Am. Chem. Soc.* **2002**, *124*, 32.

(8) Aizenberg, J.; Lambert, G.; Addadi, L.; Weiner, S. *Adv. Mater.* **1996**, *8*, 222.

(9) (a) Beniash, E.; Aizenberg, J.; Addadi, L.; Weiner, S. *Proc. R. Soc. Lond. B* **1997**, *264*, 461. (b) Politi, Y.; Levi-Kalisman, Y.; Raz, S.; Wilt, F.; Addadi, L.; Weiner, S.; Sagi, I. *Adv. Funct. Mater.* **2006**, *16*, 1289. (c) Politi, Y.; Metzler, R. A.; Abrecht, M.; Gilbert, B.; Wilt, F. H.; Sagi, I.; Addadi, L.; Weiner, S.; Gilbert, P. U. P. A. *Proc. Natl. Acad. Sci. USA* **2008**, *105*, 17362.

(10) Politi, Y.; Arad, T.; Klein, E.; Weiner, S.; Addadi, L. *Science* **2004**, *306*, 1161.

(11) (a) Ma, Y.; Weiner, S.; Addadi, L. *Adv. Funct. Mater.* **2007**, *17*, 2693. (b) Killian, C. E.; Metzler, R. A.; Gong, Y. U. T.; Olson, I. C.; Aizenberg, J.; Politi, Y.; Wilt, F. H.; Scholl, A.; Young, A.; Doran, A.; Kunz, M.; Tamura, N.; Coppersmith, S. N.; Gilbert, P. U. P. A. *J. Am. Chem. Soc.* **2009**, *131*, 18404.

(12) (a) Loste, E.; Meldrum, F. C. *Chem. Commun.* **2001**, 901. (b) Li, C.; Qi, L. *Angew. Chem. Int. Ed.* **2008**, *47*, 2388.

(13) (a) Xu, G.; Yao, N.; Aksay, I. A.; Groves, J. T. *J. Am. Chem. Soc*. **1998**, *120*, 11977. (b) (c) Aizenberg, J.; Muller, D. A.; Grazul, J. L.; Hamann, D. R. *Science* **2003**, *299*, 1205.

(14) Raz, S.; Weiner, S.; Addadi, L. *Adv. Mater.* **2000**, *12*, 38.

(15) Raz, S.; Hamilton, P. C.; Wilt, F. H.; Weiner, S.; Addadi, L. *Adv. Funct. Mater.* **2003**, *13*, 480.

(16) Tao, J.; Zhou, D.; Zhang, Z.; Xu, X.; Tang, R. *Proc. Natl. Acad. Sci. USA* **2009**, *106*, 22096

(17) Beniash, E.; Addadi, L.; Weiner, S. *J. Struct. Biol.* **1999**, *125*, 50.

(18) Levi-Kalisman, Y.; Raz, S.; Weiner, S.; Addadi, L.; Sagi, I. *Adv. Funct. Mater.* **2002**, *12*, 43.

(19) Radha, A. V.; Forbes, T. Z.; Killian, C. E.; Gilbert, P. U. P. A.; Navrotsky, A. *Proc. Natl. Acad. Sci. USA* **2010**, *107*, 16438.

(20) Levi-Kalisman, Y.; Raz, S.; Weiner, S.; Addadi, L.; Sagi, I. *J. Chem. Soc. Dalton Trans.* **2000**, 3977.

(21) (a) Lee, J. R. I.; Han, T. Y.; Willey, T. M.; Wang, D.; Meulenberg, R. W.; Nilsson, J.; Dove, P. M.; Terminello, L. J.; Van Buuren, T.; De Yoreo, J. J. *J. Am. Chem. Soc.* **2007**, *129*, 10370. (b) Pichon, B. P.; Bomans, P. H. H.; Frederik, P. M.; Sommerdijk, N. A. J. M. *J. Am. Chem. Soc.* **2008**, *130*, 4034.

(22) Loste, E.; Wilson, R. M.; Seshadri, R.; Meldrum, F. C. *J. Cryst. Growth* **2003**, *254*, 206.

(23) Clarkson, J. R.; Price, T. J.; Adams, C. A. *J. Chem. Soc. Faraday Trans.* **1992**, *88*, 243.

(24) Sawada, K. *Pure Appl. Chem.* **1997**, *69*, 921.

(25) Donners, J. J. J. M.; Heywood, B. R.; Meijer, E. W.; Nolte, R. J. M.; Roman, C.; Schenning, A. P. H. J.; Sommerdijk, N. A. J. M. *Chem. Commun.* **2000**, 1937.

(26) Xu, A. W.; Yu, Q.; Dong, W. F.; Antonietti, M.; Cölfen, H. *Adv. Mater.* **2005**, *17*, 2217.

(27) (a) Meldrum, F. C.; Cölfen, H. *Chem. Rev.* **2008**, *108*, 4332. (b) Gower, L. B. *Chem. Rev.* **2008,** *108*, 4551.

(28) (a) Wang, T.; Cölfen, H.; Antonietti, M. *J. Am. Chem. Soc.* **2005**, *127*, 3246. (b) Cölfen, H.; Antonietti, M. *Angew. Chem. Int. Ed.* **2005**, *44*, 5576.

(29) Cölfen, H.; Qi, L. *Chem. Eur. J.* **2001**, *7*, 106.

(30) Schrödle, S.; Buchner, R.; Kunz, W. *Fluid Phase Equilib.* **2004**, *216*, 175.

(31) Andersen, F. A.; Brecevic, L. *Acta Chem. Scand.* **1991**, *45*, 1018.

(32) Martínez, J. R.; Ruiz, F.; Vorobiev, Y. V.; Pérez-Robles, F.; González-Hernández, J. *J. Chem. Phys.* **1998**, *109*, 7511.

(33) Yang, X.; Roonasi, P.; Holmgren, A. *J. Colloid Interface Sci.* **2008**, *328*, 41.

(34) Bolze, J.; Pontoni, D.; Ballauff, M.; Narayanan, T.; Cölfen, H. *J. Colloid Interface Sci.* **2004**, *277*, 84.

(35) (a) Bolze, J.; Peng, B.; Dingenouts, N.; Panine, B.; Narayanan, T.; Ballauff, M. *Langmuir* **2002**, *18*, 8364. (b) Liu, J.; Rieger, J.; Huber, K. *Langmuir* **2008**, *24*, 8262.

(36) Chen, J. F.; Wang, J. X.; Liu, R. J.; Shao, L.; Wen, L. X. *Inorg. Chem. Commun.* **2004**, *7*, 447.

(37) (a) Rieger, J.; Thieme, J.; Schmidt, C. *Langmuir* **2000**, *16*, 8300. (b) Pontoni, D.; Bolze, J.; Dingenouts, N.; Narayanan, T.; Ballauff, M. *J. Phys. Chem. B* **2003**, *107*, 5123. (c) Wolf, S. E.; Leiterer, S.; Kappl, M.; Emmerling, F.; Tremel, W. *J. Am. Chem. Soc.* **2008**, *130*, 12342.

(38) Pouget, E. M.; Bomans, P. H. H.; Goos, J. A. C. M.; Frederik, P. M.; De With, G.; Sommerdijk, N. A. J. M. *Science* **2009**, *323*, 1455.

(39) (a) García-Ruiz, J. M.; Melero-García, E.; Hyde, S. T. *Science* **2009**, *323*, 362. (b) Kunz, W.; Kellermeier, M. *Science* **2009**, *323*, 344.

(40) Iler, R. K. *The chemistry of silica*, Wiley: New York, 1979.

(41) (a) Conrad, C. F.; Icopini, G. A.; Yasuhara, H.; Bandstra, J. Z.; Brantley, S. L.; Heaney, P. J. *Geochim. Cosmochim. Acta* **2007**, *71*, 531. (b) Navrotsky, A. *Proc. Natl. Acad. Sci. USA* **2004**, *101*, 12096.

(42) Giersig, M.; Ung, T.; Liz-Marzán, L. M.; Mulvaney, P. *Adv. Mater.* **1997**, *9*, 570.

(43) (a) Koga, N.; Nakagoe, Y.; Tanaka, H. *Thermochim. Acta* **1998**, *318*, 239. (b) Koga, N.; Yamane, Y. *J. Therm. Anal. Calorim.* **2008**, *94*, 379.

(44) (a) García-Ruiz, J. M.; Hyde, S. T.; Carnerup, A. M.; Christy, A. G.; Van Kranendonk, M. J.; Welham, N. J. *Science* **2003**, *302*, 1194. (b) Imai, H.; Terada, T.; Yamabi, S. *Chem. Commun.* **2003**, 484. (c) Voinescu, A. E.; Kellermeier, M.; Bartel, B.; Carnerup, A. M.; Larsson, A. K.; Touraud, D.; Kunz, W.; Kienle, L.; Pfitzner, A.; Hyde, S. T. *Cryst. Growth Des.* **2008**, *8*, 1515.

(45) Kitano, Y.; Okumura, M.; Idogaki, M. *Geochem. J.* **1979**, *13*, 253.

(46) Frondel, C. *Am. Mineral.* **1937**, *22*, 1104.

(47) (a) Jacka, A. D. *J. Sediment. Petrol.* **1974**, *44*, 421. (b) Meyers, W. J. *Sedimentology* **1977**, *24*, 75. (c) McBride, E. F. *J. Sediment. Res.* **1988**, *58*, 862.

(48) Walker, T. R. *Geol. Soc. Am. Bull.* **1962**, *73*, 237.

(49) Kastner, M.; Keene, J. B.; Gieskes, J. M. *Geochim. Cosmochim. Acta* **1977**, *41*, 1041.

(50) Klein, R. T.; Walter, L. M. *Chem. Geol.* **1995**, *125*, 29.

(51) García-Ruiz, J. M. *Geology* **1998**, *26*, 843.

(52) Pina, C. M.; Merkel, C.; Jordan, G. *Cryst. Growth Des.* **2009**, *9*, 4084.

(53) Rieger, J. *Tenside, Surfactants, Deterg.* **2002**, *39*, 221.

(54) (a) Gorenflo, A.; Brusilovsky, M.; Faigon, M.; Liberman, B. *Desalination* **2007**, *203*, 82. (b) Andrews, B.; Davé, B.; López-Serrano, P.; Tsai, S. P.; Frank, R.; Wilf, M.; Koutsakos, E. *Desalination* **2008**, *220*, 295.

(55) Shui, M.; Reng, Y.; Pu, B.; Li, J. *J. Colloid Interface Sci.* **2004**, *273*, 205.

(56) Bala, H.; Zhang, Y.; Ynag, H.; Wang, C.; Li, M.; Lv, X.; Wang, Z. *Colloids Surf. A* **2007**, *294*, 8.

(57) Chatani, A.; Okago, K.; Akaishi, S.; Morii, H. Patent No. JP 2006097138 (2006).

(58) Fukuda, Y.; Nagahara, D.; Tanaka, N.; Takagi, A.; Yanai, K.; Yoshida, Y.; Kurimoto, K.; Kawashima, M. Patent No. WO 2006035661 (2006).

(59) Ota, K.; Koga, Y. Patent No. JP 2009040612 (2009).

(60) Gu, D.; Ling, G.; Yao, C.; Deng, L.; Zhu, S.; Wang, X. Patent No. CN 101412818 (2009).

(61) Zhang, X.; Zhao, L.; Bao, M.; Ma, S.; Deng, M. Patent No. CN 101565564 (2009).

(62) Jiang, L.; Pan, K.; Dan, Y. *Colloid Polym. Sci.* **2006**, *285*, 65.

Chapter 3 Biomimetic Crystallization in Purely Inorganic Precipitation Systems

3.1 Abstract

The crystallization of alkaline-earth carbonates in silica-containing environments at elevated pH has for long been a fascinating example for the formation of crystal architectures with bio-like appearance in the absence of organic matter. Recent insight to the interactions between precipitating calcium carbonate and dissolved silica has revealed that early-formed amorphous $CaCO_3$ (ACC) precursors become stabilized in solution due to their spontaneous encapsulation in extended silica skins (Chapter 2). The lifetime of the ACC phase in the resulting core-shell particles and the duration of its transformation to more stable polymorphs could thereby be tuned by adjusting the silica concentration. In this chapter, it is demonstrated that the intermediate storage of ACC thus achieved allows for the synthesis of elaborate crystal morphologies even under conditions of high supersaturation. Continuous release of $CaCO_3$ units from the ACC depots was found to enable gradual crystallization under the progressive influence of silica. Owing to adsorption and precipitation phenomena, the obtained calcite crystals exhibit a growing degree of complexity when increasing the total silica content, ranging from rounded rhombohedra over fibers with threefold symmetry to unique aggregates of miniaturized needle-shaped individuals. The crystallization pathways observed in these simple inorganic systems mimic strategies apparently applied in biomineralization and may devise novel routes for the design of advanced materials.

3.2 Introduction

The role of amorphous precursors in crystallization processes is a rapidly growing area of research and has attracted a considerable deal of attention in the past years. Recently, particular interest stems from the field of biomineralization, where amorphous mineral phases were identified both as temporary intermediates and in a permanently stable state as structural elements.[1-4] Striking examples for the latter case are the porous silica skeletons produced by various freshwater and marine algae, such as diatoms or radiolarians,[5] which are formed via a template-patterning route occurring in specialized intracellular compartments under the influence of certain peptides and polyamines that direct structured silicification.[6,7] Their abundance in nature can readily be understood

when considering the relatively high stability of amorphous silica against transformation to crystalline polymorphs.[8] By contrast, the amorphous phases of other widespread biominerals, like calcium carbonate and calcium phosphate, are usually transient species which crystallize quickly in aqueous media unless kinetically stabilized.[9] Nevertheless, frameworks comprising stable amorphous domains of both minerals were found in the tissues of diverse living organisms, including plant cystoliths,[10] ascidians,[11] calcareous sponges,[12] or the cuticles of some crustaceans.[13] The advantage of using amorphous instead of crystalline material may lie in beneficial mechanical properties like flexibility, or in the commonly higher solubility of amorphous phases which allows for intermittent storage and fast mobilization of calcium ions when needed (e.g. during moulting processes).[1-3,14] Beyond that, investigations of the formation mechanisms leading to the complex structures of selected biominerals have revealed that at least in some cases the inorganic component is precipitated first in an amorphous form to later crystallize in the particular polymorph which is most suitable for the given demands.[15] This was described in detail for the spicules, spines and teeth of sea urchins[16] and observed also during the development of the shells of certain mollusks,[17] the calciferous glands of earthworms,[18] and the teeth of chitons,[19] as well as in the mineralization of vertebrate bone[20] and dental enamel.[21] Evidence for amorphous precursors participating in crystallization scenarios and stabilized amorphous coatings sheathing crystal building units in the final mineral was furthermore reported for the morphogenesis of natural nacre.[22] Though not clarified to date, the choice of a multistep mineralization pathway involving amorphous intermediates might originate from the benefit that crystallization becomes in this way independent from solution parameters like solubility products or pH.[3,22a] In addition, for lack of crystallographic symmetry restraints, amorphous phases can easily be shaped into any desired form before they crystallize, thus enabling the generation of complex crystal morphologies as confirmed in laboratory syntheses utilizing distinct artificial molds.[23]

These findings have stimulated a broad panoply of bio-inspired crystallization assays meant to mimic strategies recognized in biomineralization in order to design novel materials with advanced structure and properties.[24] Calcium carbonate is an often chosen model system in this context not only due to its importance as abundant biomineral, but also in view of its rich polymorphism, ample occurrence in geological sediments and relevance for a wide range of industrial applications.[25] Early studies have

shown that precipitation of $CaCO_3$ at high supersaturation initially yields nanoparticles of amorphous calcium carbonate (ACC) which, when left in contact with a solution at ambient conditions, subsequently undergo transition to thermodynamically stable calcite either directly or via an intermediate vaterite phase.[26] In some experiments, an even earlier precursor was traced in the course of the crystallization process, which appeared to exhibit liquid-like character and was proposed to result as a consequence of binodal or spinodal decomposition.[27] Recent work has moreover illustrated that nucleation and growth of ACC particles are preceded by the formation of neutral nanoclusters which are stable in equilibrium with the dissolved ions, as opposed to classical nucleation theories.[28]

There have been numerous attempts to prevent ACC from transforming to crystalline polymorphs in vitro, partly for the sake of scale inhibition.[29] For instance, added magnesium ions were found to be capable of increasing the lifetime of ACC from few minutes up to days,[30] which is in line with the supposition that the stability of amorphous $CaCO_3$ minerals in vivo is intimately regulated by the cooperative effect of biological macromolecules and Mg^{2+} cations.[31] Successful stabilization of ACC particles in synthetic systems over periods sometimes as long as several months was further achieved by introducing additives like phosphate or phosphonate species,[32] alkylbenzenesulfonate surfactants,[33] polycarboxylates,[27b,29] double-hydrophilic block copolymers (DHBC),[34] poly(propylene imine) dendrimers in combination with octadecylamine,[35] and phytic acid,[36] or by confining the reaction volume.[37] Apart from that, Gower *et al.* discovered that by means of polyelectrolytes such as polyacrylate or polyaspartate, liquid-liquid phase separation can be deliberately promoted.[24b,38] During this so-called polymer-induced liquid-precursor (PILP) process, fluid-like droplets enriched in $CaCO_3$ and the polymeric additive and containing high amounts of water are segregated, which may coalesce in the following but remain protected against crystallization over prolonged timeframes.

In analogy to biomineralization, temporarily stabilized amorphous phases serving as precursors for elaborate crystalline architectures have been detected frequently and for a variety of different materials also in biomimetic approaches of morphosynthesis.[24,39] For example, adsorption of hydrophilic polymers on precipitated amorphous nanoparticles increases their stability such that, upon aggregation, particle networks may act as depots which supply mineral units only gradually, hence uncoupling morphogenesis from particular solution conditions. Potentially, this leads to the self-organization of small

crystal building blocks into manifold superstructures,[40] often through mesoscale transformations via a non-classical crystallization pathway.[41] On a similar basis, ordered arrays of $CaCO_3$ nanocrystals and peculiar aragonite microparticles were obtained when surfactant-coated ACC was destabilized by dispersion in water-in-oil microemulsions.[42] Likewise, due to their liquid-like behavior, PILP phases proved to be valuable tools for the fabrication of crystals with extraordinary morphologies and occasionally molten appearance, as the precursors can be given distinct shapes prior to crystallization. Applying this strategy, extended single- or polycrystalline thin films[43] and other non-equilibrium forms like tablets, spheroids or helices[44] were prepared, and collagen fibrils as well as polymeric replica were effectively infiltrated and mineralized in attempts to imitate the formation of bone and sea urchin spine, respectively.[45]

In the preceding chapter, it was demonstrated that – as an inorganic alternative to the typically employed, more or less complicated organic additives – dissolved silicate can be used to stabilize ACC in highly supersaturated alkaline solutions.[46] Thereby, local changes in conditions nearby the surface of growing ACC particles, induced by the release of protons upon dissociation of bicarbonate ions, were proposed to provoke polymerization of silicate species and a coating of the particles in continuous skins of amorphous silica. These shells were found to be porous and permeable to reagents at low silica concentrations, such that crystallization occurred after considerable periods of delay and at markedly depressed rates. By contrast, high concentrations caused dense cementation of ACC grains in a silica matrix and thus permanent conservation of the amorphous phase on timescales of years. Interestingly, a stabilizing effect of silicate ions on ACC was observed independently by Gal *et al.* who examined the transition of dried samples to calcite upon heating.[47] Their investigations comprised both synthetic particles and biogenic ACC minerals, namely cystoliths extracted from the leaves of certain trees. Results evidenced that the thermal stability of ACC increases with the amount of silicate present during precipitation and that cystoliths with greater silica content crystallize at higher temperatures than their silicate-poor counterparts. Based thereon and in light of the abundance of silica in many plants,[7] it was suggested that in addition to forming mineral deposits in tissues by themselves, silicate species could perform the secondary function of a stabilizing agent for ACC in biomineralization processes.

Previous work has pointed out that precipitation of alkaline-earth carbonates in silica-rich media at elevated pH can afford crystal architectures with unusual shapes and

structure.[48] For $CaCO_3$, hierarchical "sheaf-of-wheat" patterns consisting of fibrous stacks of cleaved calcite rhombohedra were reported.[49,50] With the higher homologues $SrCO_3$ and $BaCO_3$, self-assembled aggregates of uniform elongated nanocrystals were obtained, which display stunning non-crystallographic morphologies such as sinuous sheets and twisted filaments.[51-54] Coral-like polycrystalline $CaCO_3$ particles exhibiting a similar mode of construction were grown under conditions favoring aragonite formation.[55] The striking resemblance of these materials to biotic minerals led to the conclusion that morphology alone is not sufficient for the identification of biogenicity, and that curved shapes and higher-order textures – intuitively associated with the animate nature – may very well be produced also by the interplay of purely abiotic components.[56]

In the following, it is described how silica-mediated stabilization of amorphous precursors can contribute to the morphogenesis of complex crystal forms in such environments and facilitate structured crystallization even at nominally high supersaturation. To that end, calcium carbonate was precipitated from solution by adding calcium chloride to mixtures of sodium carbonate and sodium silicate. The evolution of samples with varying silica content was followed with time and initially generated amorphous particles, their gradual transformation to calcite and in particular the morphology and structure of the final crystalline products were characterized by different techniques. The observed growth behavior, involving intermittently stabilized ACC, bears fundamental analogy to concepts in biomineralization and modern morphosynthesis, and thus underlines the biomimetic character of these plain inorganic precipitation systems.

3.3 Experimental Section

3.3.1 Crystallization Experiments

First, suitable sodium silicate solutions were prepared by diluting commercial water glass stock (Sigma-Aldrich, reagent grade, containing 26.7 wt% SiO_2 and 13.8 wt% NaOH) in ratios ranging from 1-250 to 1-1400 (v/v) with water of Milli-Q quality. These sols were purged with H_2O-saturated nitrogen for about 1 h in order to dispel previously absorbed carbon dioxide, and then used to dissolve 10 mM Na_2CO_3 (Roth, anhydrous, $\geq$ 99%). The resulting solutions were filtered (450 nm), stored in tightly stoppered plastic bottles and replaced by fresh ones at least weekly. Samples were prepared by combining 5 mL silica-carbonate mixture with the same volume of a CO_2-

free 10 mM solution of $CaCl_2 \cdot 2H_2O$ (Riedel-de Haën, ACS reagent, ≥ 99%), as described in Section 2.3.2. The vials were closed and samples were allowed to age under quiescent conditions at 20 ± 1°C. Silica concentrations investigated in this part of the work ranged from 0 to 750 ppm SiO_2. Crystalline structures developed in all samples and were observed both adhering firmly to the vessel walls and growing directly on or within the amorphous floccules, in particular at higher silica contents. The time after mixing at which first crystals were sighted was found to be the longer the more silica was added. Quenching of the reaction at distinct stages and isolation of the formed precipitates was accomplished in two different ways. Either, the suspensions were passed through membrane filters (Whatman, 200 nm) and freeze-dried (see Section 2.3.2) together with the sedimented floccules and potentially occurring crystals, which were detached from the walls by careful manipulation with a fine brush and transferred onto the filter by rinsing with a small quantity of water. Alternatively, to separate crystalline products from amorphous particles, the mother liquor was withdrawn and replaced by water. The flocculated material was then dispersed vigorously such that the crystals were released from the particle networks and settled to the ground. Suspended floccules could thus be selectively removed along with the supernatant by sucking with a pipette. This procedure was repeated until no more amorphous precipitates could be distinguished. Finally, the residual crystals were washed twice with water and ethanol and left to dry in air.

3.3.2 Analytical Methods

3.3.2.1 Visual Observations

The evolution of the samples with time was followed visually by inspecting the vials in regular intervals until ongoing crystallization processes were apparently terminated, that is, when either all amorphous particles had vanished and a clear solution with crystals on the walls was achieved or, at higher silica concentrations, when the amount of precipitated floccules did no longer change noticeably. Complementarily, series of photographs were acquired from the solutions over periods up to months. For this purpose, experiments were carried out in plain glass tubes. Pictures were taken with a Canon Powershot A640 digital camera connected to a PC.

3.3.2.2 Light Microscopy

Crystalline architectures obtained from the syntheses were investigated first with an optical microscope (Nikon Eclipse E400). An attached Canon EOS 350D camera was used for imaging. Coagulated particle networks as well as crystals associated to or embedded in them were studied by decanting the bulk volume of the supernatant solution at defined times after mixing, and loading parts of the floccules together with the remaining mother liquid on glass slides. Comparative analyses showed that this treatment did not affect the state of the samples and there was no induced additional conversion of ACC species to crystalline polymorphs upon manipulation. The observed structures can thus be considered representative of the situation in solution at the corresponding time.

3.3.2.3 Electron Microscopy

Samples of the suspended nanoparticles and those in the precipitated floccules were prepared for transmission electron microscopy (TEM) as described in Section 2.3.3.1. The crystal aggregates formed at higher silica concentrations were examined by gathering a practicable amount of sample, crushing the specimens and grinding them intensively in ethanol to yield a fine suspension, a small volume of which was subsequently evaporated on a grid. TEM analyses were performed on a Philips CM 12 microscope at 120 kV under low-dose conditions, using CCD cameras from Gatan (model TV 673) and TVIPS (model TEM1000). Images were acquired and processed with the EM-MENU 4 software package.

For field-emission scanning electron microscopy (FESEM), both the freeze-dried powders and separated crystals were transferred onto conducting double-sided adhesive carbon tabs, which were fixed on standard aluminum SEM pin stubs. Samples were coated with carbon prior to analysis, using a Balzers MED 010 sputter coater. FESEM studies were carried out on a Zeiss LEO Gemini 1530 microscope at an acceleration voltage of 2 or 3 kV and working distances in the range of 3-5 mm. Most images were recorded by mixing signal from the in-lens and secondary electron detectors. EDX measurements were conducted at 10 kV with the aid of an installed Oxford INCA microanalysis system. Thereby, in case of the crystalline products, several typical specimens were probed independently at each silica concentration, sampling a series of different positions per particle and averaging results for a given sample.

3.3.2.4 X-Ray Diffraction

The polymorphism of the isolated crystalline objects was investigated by picking up individuals using a micro-loop wetted with a drop of oil. Diffraction of the specimens was measured with a Bruker X8 Proteum setup (Kappa configuration) comprising a Microstar high-brilliance rotating anode source (Cu-K_α radiation) and a Smart 6000 two-dimensional CCD detector having 512x512 pixels. During data collection, samples were rotated around the φ-axis by 180° in steps of 5°, the integration time per image being 20 s.

3.4 Results

3.4.1 Crystallization of $CaCO_3$ from Silica-Coated ACC

The development of crystalline structures in the systems can readily be monitored by stopping the reaction at different times and analyzing the existing precipitates by means of SEM and TEM. In general, data show that the onset of crystallization becomes increasingly delayed as more silica is added. Coherently, the period up to which amorphous particles were discerned in the samples was longer at higher silica concentrations, in line with the conclusions drawn from turbidity measurements (see Fig. 2-11 in Section 2.4.4). At 270 ppm SiO_2, first crystals were sighted around 30 min after mixing which then grew at the expense of the nanoparticles until after about 3 h all amorphous material had vanished and only micron-sized crystalline architectures were left. In most cases, crystallization took place in the immediate vicinity of coagulated floccules, and crystals were often found to evolve directly on top of the networks with a multitude of precursor particles decorating or tightly adhering to crystal faces (Fig. 3-1a-c). Since the carbonate nanoparticles are shielded against each other and the growing crystal surface by their silica skins, the only feasible way of ACC conversion to crystalline phases is dissolution of the $CaCO_3$ core through the outer shell and subsequent re-precipitation. This is supported by high-magnification SEM images of the amorphous particles during crystallization which, in some instances, disclose that the surface of single grains is perforated and their interior is hollow (Fig. 3-1d).

In this manner, the silica-coated ACC particles act as depots which constantly supply the surrounding solution with growth units. Consequently, the supersaturation is expected to be highest nearby the precipitated floccules, thus explaining why crystals are preferentially nucleated upon or inside the networks. The rate of $CaCO_3$ release

from the core of the composite particles is essentially determined by the amount of silica added.

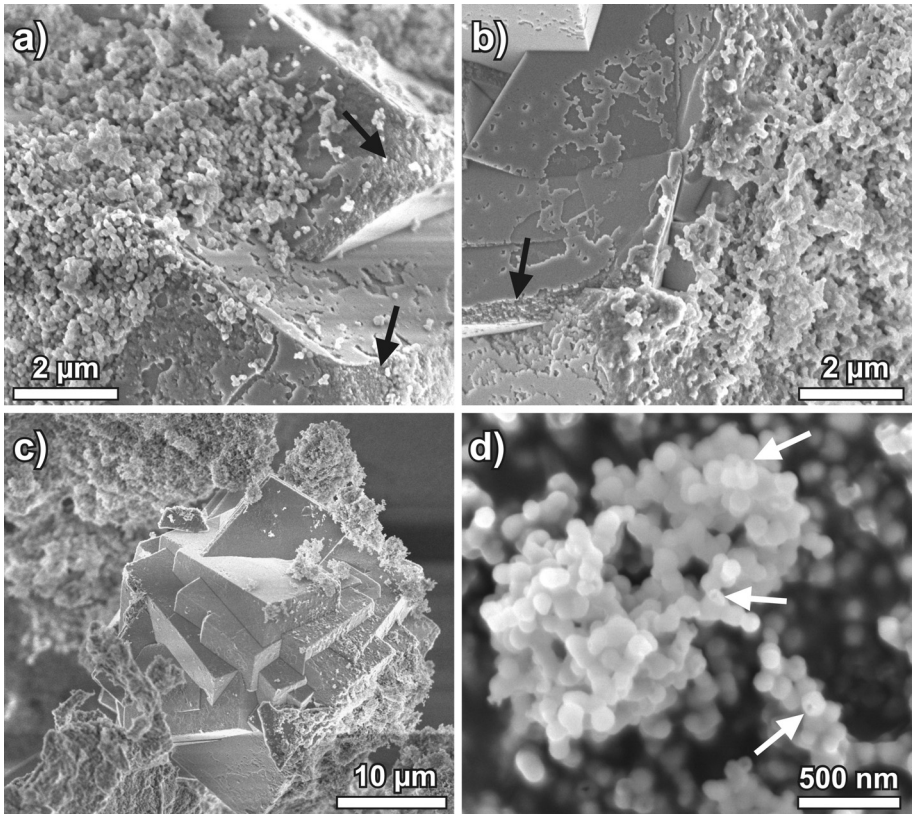

Fig. 3-1: Transformation of silica-stabilized ACC to calcite at 270 ppm SiO_2. (a-c) FESEM images of samples quenched 1 h after mixing, revealing that crystals emerge from networks of amorphous nanoparticles and grow attached to the floccules in the following. Black arrows indicate sites where truncation of corners or edges of the rhombohedral calcite habit is obvious. (d) Close-up view of particle agglomerates isolated after 30 min. White arrows point to individuals which appear to have holes or cracks as a consequence of ongoing disintegration.

Higher concentrations lead to the formation of less porous skins,[46] which slow down the transport of reagents and hence accretively enlarge the window of time throughout which crystallization is active (see Chapter 2). At silica contents of up to 540 ppm, all amorphous particles are eventually consumed and, remarkably, the silica shells also dissolve after having released their ACC core. Therefore, the concentration of silica in solution should increase continuously as crystallization proceeds.

Similar observations were made as well for samples drawn from mixtures containing 750 ppm SiO_2. Fig. 3-2 gives a gallery of typical images visualizing the evolution of crystalline matter in the system. In this concentration regime, the amount of flocculated material is fairly large such that spacious three-dimensional networks extending over the entire bottom of the vials are generated (Fig. 3-2a and e). Transformation of ACC

sets in after around 5 h to produce rounded and dumbbell-shaped structures with diameters of 10-20 µm in the following 7 h (Fig. 3-2a-b).

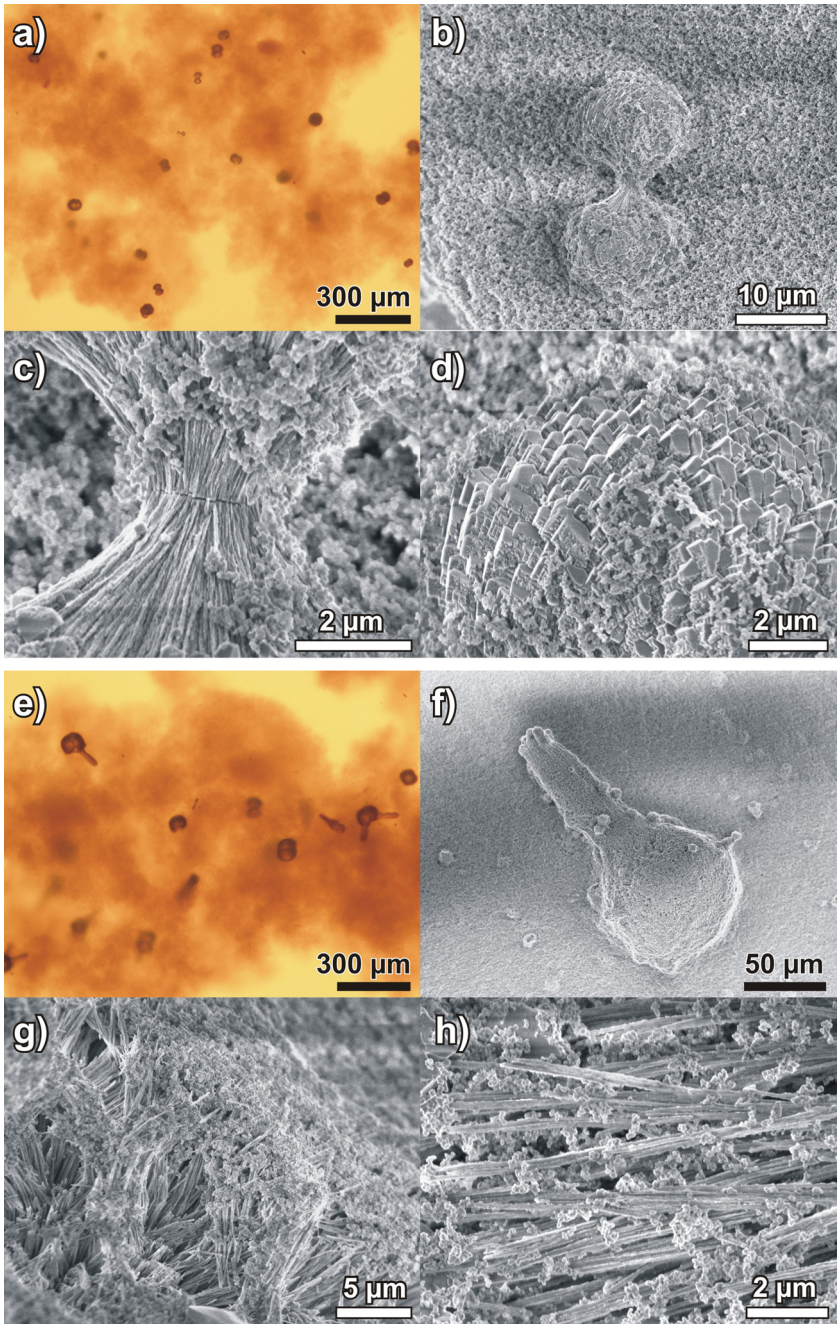

Fig. 3-2: Optical and FESEM micrographs illustrating the growth of peculiar crystal aggregates from heavily condensed meshes of silica-coated ACC particles in samples at 750 ppm SiO_2. Precipitates were isolated after (a-d) 12 h and (e-h) 1 week.

Growth of these forms continues up to about 1 day after mixing, while subsequently no further changes neither in the size and morphology of particles nor in the overall composition and crystallinity of the samples could be distinguished. Micrographs taken from precipitates isolated after standing for 1 week confirm that a bulk part of the

originally deposited amorphous floccules still persists at this stage, along with numerous bigger spherical objects (or notched spheres) from which frequently thick linear strands sprout outwards (Fig. 3-2e-f). These uncommon morphologies usually develop using beds of aggregated amorphous nanoparticles as substrates, in which they appear to be partially buried (Fig. 3-2b and f).

Zooming into the as-grown dumbbell-like and spheroidal architectures reveals that both are constituted by fibrous crystallites (Fig. 3-2c, g and h). Often, clusters of ACC-silica precursor particles are seen to be firmly associated to needle-shaped individuals (Fig. **3-2**c), decorate the crystal aggregates in the form of extended superficial layers (Fig. 3-2g), and sometimes even interpenetrate the assembly (Fig. 3-2h). TEM analyses of mature samples prove the presence of condensed spherical nanoparticles next to a multitude of uniform elongate crystals. Furthermore, frameworks of hollow particles were repeatedly observed adjacent to aggregates of crystallites (Fig. 3-3), in particular during the earlier stages of crystallization.

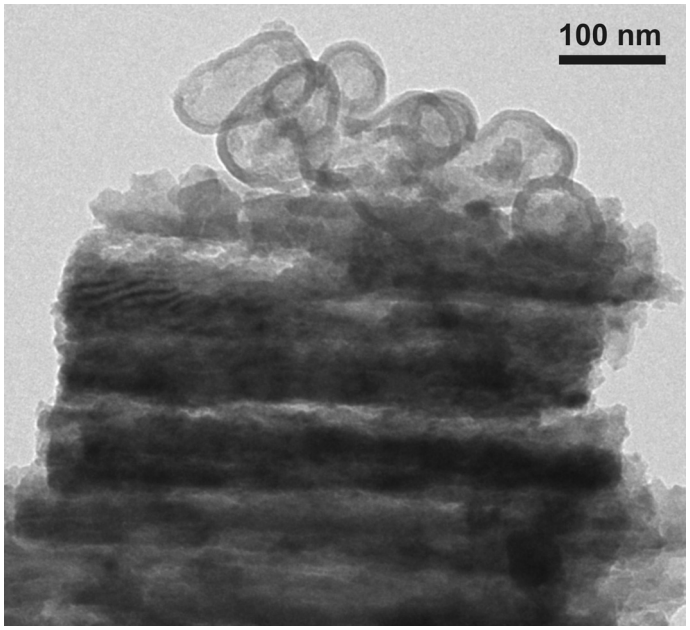

Fig. 3-3: TEM image of structures formed in solutions containing 750 ppm SiO_2 after ageing for 1 week, with hollow silica particles lying on top of a stack of piled rod-shaped crystallites.

EDX data demonstrate that these remnants consist of silica only and hence suggest that the ACC core but not as yet the silica skin was dissolved. Again, this is clear evidence that silica-coated ACC transforms into crystalline polymorphs through dissolution-renucleation processes. Those particles which endure in solutions at 750 ppm SiO_2 upon prolonged ageing in turn seem to be sheathed by layers of somewhat lower porosity,

which efficiently prevent exchange between the enclosed volume and the surrounding medium.

3.4.2 Morphology and Texture of the Final Crystalline Products

The vast majority of crystals isolated at the end of experiments performed without added silica were regular rhombohedra characteristic of calcite (see Fig. 2-10 in Section 2.4.4). The perfection of the rhombohedral shape recognized in most cases indicates that the crystalline phase grows via a dissolution-assisted route also in the silica-free reference.[58] Sporadically, spherical morphologies were sighted next to the euhedral forms, indicating that the samples contain traces of vaterite. The presence of 135 ppm silica was found to have no noticeable effect on the appearance of the final crystals (Fig. 3-4a).

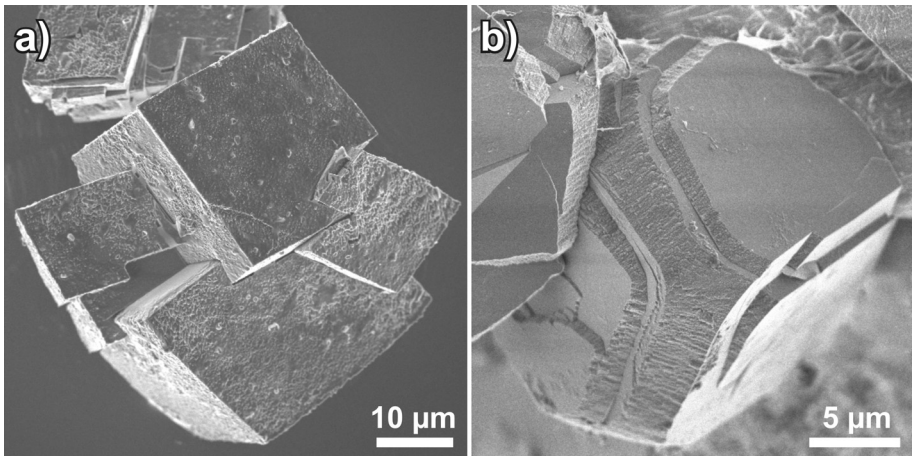

Fig. 3-4: Final products of $CaCO_3$ crystallization conducted in the presence of (a) 135 and (b) 270 ppm SiO_2. Crystals were isolated after a period of 24 h, that is, well after all amorphous precursor particles had vanished. Classical rhombohedra with colloidal silica adsorbed unspecifically on their surfaces are observed at 135 ppm SiO_2, while characteristic rounding of corners and edges occurs at 270 ppm.

Indeed, the surface of the rhombohedra happens to be covered by a film of silica made up of densely agglomerated colloidal spheres. This feature may however originate from secondary deposition of silica on the crystals upon isolation and drying. On raising its concentration, the silica does not only stabilize ACC precursors and thereby delay crystallization, but also starts to distinctly affect crystal growth and the emerging morphologies. At 270 ppm SiO_2, edges and corners of the classical rhombohedral habit become truncated especially in the later course of the crystallization process and are thus replaced by oblique, often rough faces (Fig. 3-4b and Fig. 3-1a-b).

Moreover, at silica contents of 135 and 270 ppm the formation of conglomerates of intergrown crystals seems to be favored (cf. Fig. 3-1c and Fig. 3-4a), whereas in the control experiment at 0 ppm predominantly individual rhombohedra were obtained. This is reasonable when considering that the ACC-silica particle networks are preferential sites for nucleation. Therefore, it is likely that multiple events of nucleation will take place close to one another. Continued crystal growth then inevitably leads to merging and the pronounced occurrence of intergrown architectures.

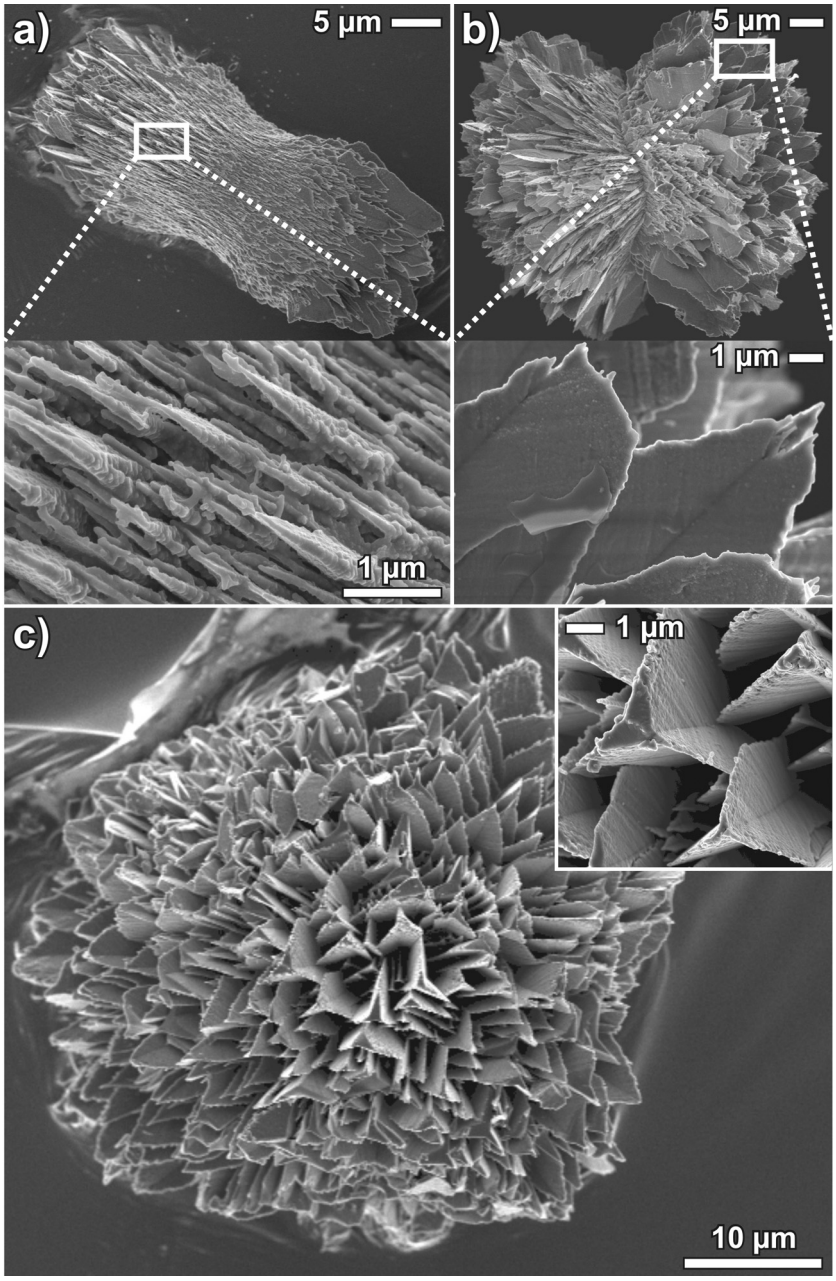

Fig. 3-5: FESEM micrographs of crystal architectures produced at 375 ppm SiO_2 after 24 hours.

Increasing the amount of silica to 375 ppm brings about further profound morphological and structural changes. After equilibration and quantitative consumption of all ACC

material, a relatively small number of quite large, isolated crystalline objects were recovered from the bottom and the walls of the vials, which had adopted exceptional forms as those depicted in Fig. 3-5. From a phenomenological point of view, the observed morphologies evolve at first by dilation of an initial regular rhombohedron through extrusion of multiple fibrous projections with diameters in the range of 150-300 nm along the crystallographic c-axis (Fig. 3-5a). The resulting elongated crystal then grows preferentially at its two outer tip regions, where the projections develop platy wing-like domains and hence impart a dumbbell-shaped aspect to the specimen (Fig. 3-5b). Remarkably, each strand consists of three wings which are arranged at angles of ~120° between one another, such that the cross-section of the strand takes the form of a three-pointed star (see inset in Fig. 3-5c). Individual wings reach widths of up to while being as thin as 100-200 nm, and often exhibit a somewhat ribbed surface texture. Upon continued growth, these characteristic projections eventually sprout in all directions from the central crystal, leading to spherulitic entities decorated uniformly by three-pointed stars (Fig. 3-5c).

Apart from such delicate ultrastructures, another type of elongated morphology was repeatedly, though in general less frequently encountered in experiments at 375 ppm SiO_2 (see Fig. 3-6). Most evidently, these crystals are distinguished by the presence of a spacious, dome-like outgrowth at one of their ends (Fig. 3-6a). Further, as in the case of the architectures shown in Fig. 3-5, they appear to be constituted by micron-sized subunits, namely tabular bricks which are typically 0.5-1 μm wide and about 100 nm thick (Fig. 3-6b-c).

Crystallization of calcium carbonate in solutions with higher silica content yields in the formation of further intricate morphologies which are, especially in terms of their mode of construction, substantially different from those produced at 375 ppm (Fig. 3-7). Though forming on distinct timescales and consuming to varying degrees the available ACC precursors, the growth behavior and final structure of the crystalline products obtained at 540 and 750 ppm SiO_2 are widely identical. Once initiated, the morphological evolution in these systems can be summarized as follows. First, elongated seeds are discerned within the precipitated amorphous floccules, which transform consecutively into dumbbell shapes (Fig. 3-7a and Fig. 3-2b-c) and, later, closed spherulites with diameters of around 100 μm (Fig. 3-7b). The latter are porous, with manifold voids characterizing their surface that lend a flowery appearance to the architectures.

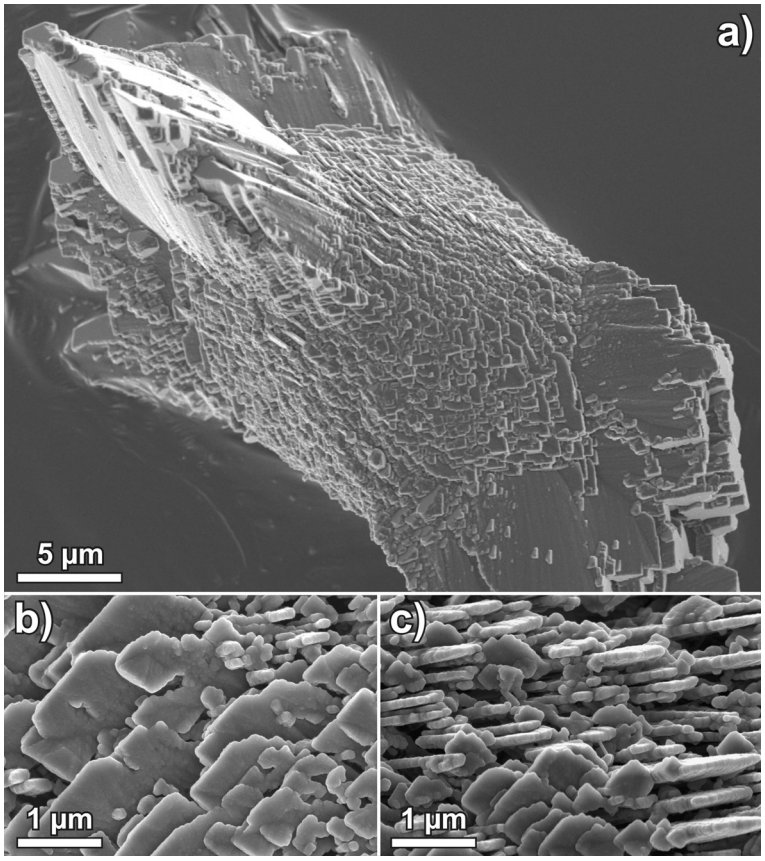

Fig. 3-6: (a) Unusual $CaCO_3$ crystal isolated from samples at 375 ppm as a common by-product of three-pointed star-like forms. (b-c) Zooms into (a) revealing textural details of the specimen.

In a final step, usually after some days, rather thick trunk-like outgrowths develop from the spherulites (Fig. 3-7c and Fig. 3-2f), such that the resulting morphologies to some extent resemble those of natural radiolarians.[5] Mostly, either one or two of these extrusions sprout from a given spherulite and grow in a quasi-linear fashion over lengths of up to 100 µm. In line with the observations made for crystals isolated while still embedded in networks of amorphous nanoparticles (Fig. 3-7c, g and h), the precipitates were at all growth stages confirmed to be aggregates of myriad acicular crystallites exhibiting a fairly narrow size distribution (Fig. 3-7d-f). The diameter of the needles was found to be more or less constant throughout the entire assembly, usually measuring between 70 and 120 nm. By contrast, their length seems to vary depending on the position within the aggregate, that is, individuals become shorter as growth proceeds. Typical values thus range in a quite broad interval of about 500 nm to 5 µm. Generally, the needles tend to be oriented with their long axis pointing along the respective current growth direction. Therefore, neighboring crystallites are aligned preferentially parallel to each other (cf. Fig. 3-7f).

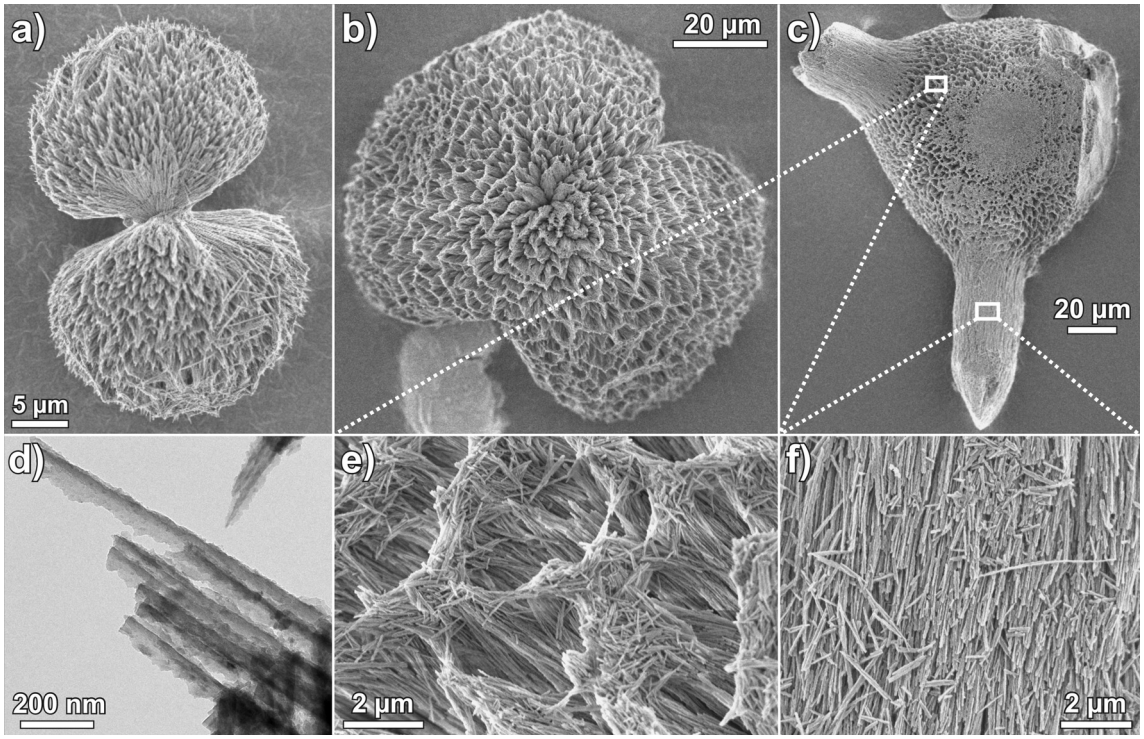

Fig. 3-7: Crystal aggregates obtained at a silica concentration of 750 ppm. (a) A dumbbell-shaped particle isolated after 12 h. (b) Porous spherulitic architecture collected after 1 day. (c) After 1 week, trunk-like outgrowths have emerged from the spherulites. (d) TEM micrograph of a crushed sample grown for 1 week, displaying aligned needle-like microcrystallites. (e-f) Zooms into the aggregate shown in (c), spotting the voids in the central spheroidal part and the co-orientation of the crystallites within a trunk. Note that the specimens were cleaned from amorphous material prior to isolation (in contrast to the samples depicted in Fig. 3-2).

In sinuous parts of the aggregates, the needles however have to be arranged with a slight twist to one another, so as to describe the given curvature. Finally, we note that on occasion the surface of the aggregates becomes overcast by an array of blocky rhombohedra (see Fig. 3-2d), most probably as a consequence of secondary crystallization.

To understand the role of the silica during the crystallization process, it is crucial to realize that not the whole amount of silica added is co-precipitated with the ACC particles at the beginning of the experiments. From the Si/Ca atomic ratio determined by EDX for the amorphous material isolated 5 min after mixing (see Fig. 2-4 and Table 2-1 in Section 2.4.1), the concentration of silica remaining dissolved in solution at that time can be calculated when assuming, in an approximation, that Ca^{2+} reacts quantitatively to ACC. Results are shown in Fig. 3-8. At 135 and 270 ppm SiO_2, less than 10% of the available silicate species have in fact been deposited on the ACC nanoparticles, while around 15% have precipitated at 375 ppm. The fraction of silica

removed from solution increases considerably when further raising the overall content, to about 35 and 47% at 540 and 750 ppm, respectively. In turn, this means that at least more than half of the introduced molar amount of silica exists as soluble mono- and/or oligomers in the systems after initial ACC particle formation.

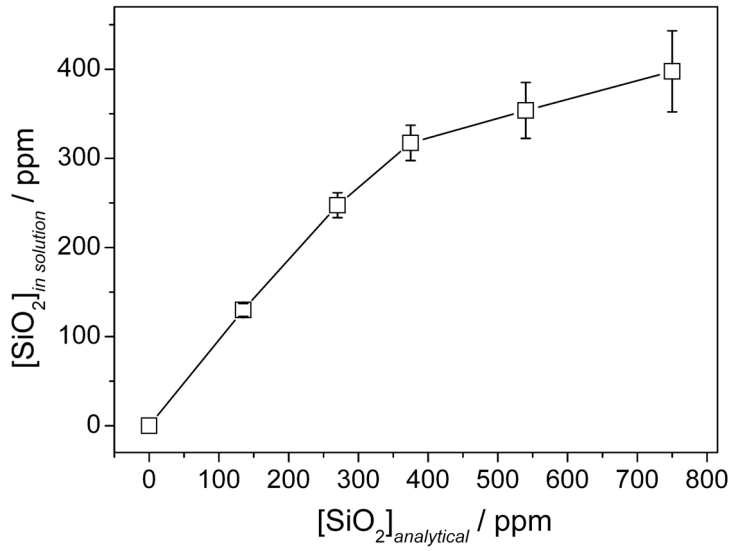

Fig. 3-8: Estimated concentrations of dissolved silica in the mixtures after 5 min and corresponding standard deviations, outlined as a function of the respective total SiO_2 content. Values were obtained by calculating the amount of precipitated silica on the basis of the Si/Ca ratio measured by EDX spectroscopy (see Fig. 2-4 in Section 2.4.1), premising that the present 5 mM $CaCO_3$ were completely converted to ACC.

Thus, data evidence that addition of more silica does not only entail longer-term stabilization of ACC precursors, but also implicates that crystallization of $CaCO_3$ occurs under the influence of a higher concentration of dissolved silicate ions in solution. On the other hand, once crystallization has commenced, ongoing re-dissolution of empty silica skins should cause a steady increase of the concentration in solution with time and as growth proceeds.

3.4.3 Crystal Polymorphism and Composition

Powder diffraction patterns of crystals recovered from samples at 135 and 270 ppm SiO_2 demonstrate that the only polymorph formed in the experiments was calcite, as expected in view of the observed rhombohedral habit (cf. Fig. 3-4). SEM analyses further prove that the small fraction of vaterite particles traced in the silica-free reference was consistently absent in the presence of silica. This may indicate that added silica promotes the formation of calcite relative to vaterite under the given conditions, and would hence support the results of a recent study on the effect of dissolved silica on

$CaCO_3$ crystallization.[59] The polymorphism of structures generated at higher silica concentrations was investigated by monitoring the diffraction of selected individual particles. Diffraction images of the morphologies obtained at 375 ppm SiO_2 typically display multiple pairs of isolated spots along various virtual rings (Fig. 3-9a).

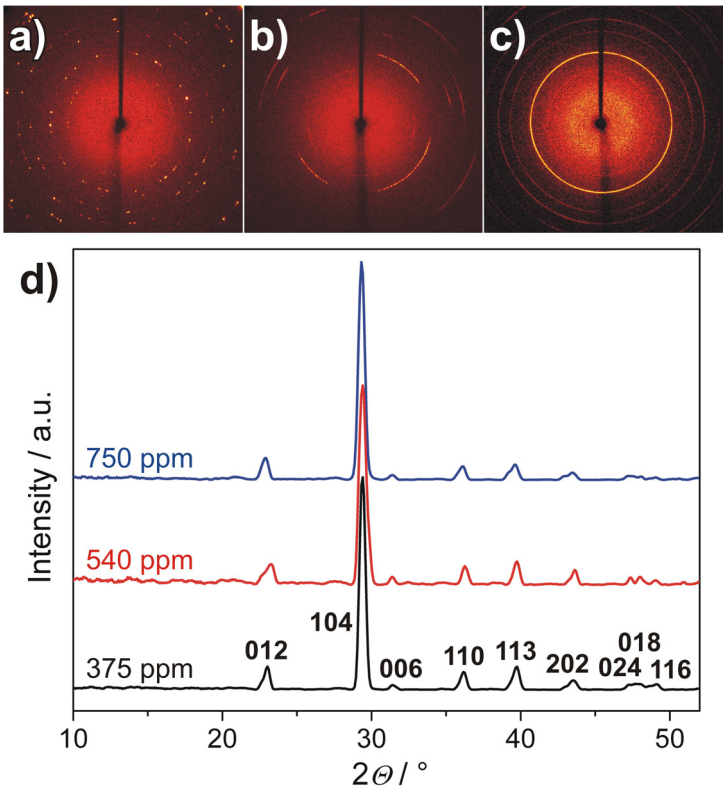

Fig. 3-9: Single X-ray diffraction images acquired from (a) a three-pointed star-decorated spherulite formed at 375 ppm (Fig. 3-5c), (b) a dumbbell consisting of fibrous microneedles at 540 ppm (Fig. 3-7a), and (c) an open porous spheroidal structure at 750 ppm SiO_2 (Fig. 3-7b). (d) Diffractograms derived by summing up all diffraction images collected for a given specimen (after background subtraction) and integrating the intensity radially over all angles. The occurring reflections can exclusively be assigned to the calcite lattice.

Such behavior argues for the existence of several larger, crystallographically coherent domains maintaining different orientations. This suggests that each of the projections eventually developing threefold symmetry is of single-crystalline nature (cf. Fig. 3-5c). As opposed to that, patterns obtained for the architectures grown at 540 and 750 ppm SiO_2 show arc-like reflections (Fig. 3-9b) or full rings (Fig. 3-9c) and thus confirm that these samples are polycrystalline aggregates. Streaking of spots was thereby observed only for dumbbell-like specimens and can hence likely be ascribed to the shape anisotropy of this kind of morphology – in contrast to the quasi-isotropic geometry of spherulitic aggregates which gives continuous rings.

These differences hint at distinct morphogenetic pathways being responsible for the formation of the extraordinary structures retrieved at 375 and 540/750 ppm silica, respectively, although both share a phenomenological growth sequence involving elongated precursors, dumbbell-shaped intermediates and spherulitic terminal morphologies. Despite the fact that the rod-like habit of the crystallites constituting the aggregates isolated at higher silica concentrations is commonly associated with the aragonite modification, analyses of the diffraction data evidence that all products were pure calcite and no other phase was present (Fig. 3-9d).

The degree of silica incorporation to the emerging crystal architectures was studied by measuring the content of Si relative to Ca for a series of representative structures at each concentration by means of EDX spectroscopy. For this purpose, specimens were washed carefully prior to measurement in order to remove potentially adhering silica-containing amorphous floccules. Results were found to be well reproducible. Averaged values for the Si/Ca atomic ratio are plotted in Fig. 3-10.

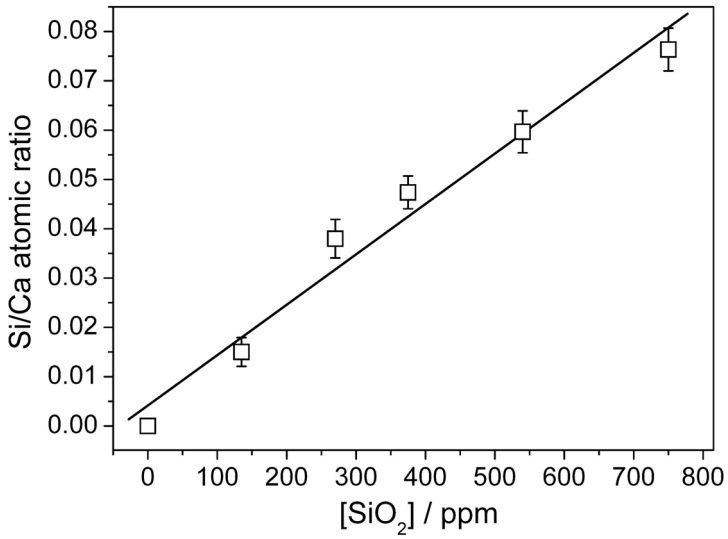

Fig. 3-10: Mean silicon content of characteristic crystalline morphologies obtained from samples at different silica concentrations, given by the Si/Ca atomic ratio determined by EDX and its standard deviation. The full line is a linear fit to the data (Si/Ca = $(4 \pm 4)\cdot10^{-3}$ + $(1.02 \pm 0.09)\cdot10^{-4}\cdot[SiO_2]$ / ppm).

The fraction of silica included in the final crystals is generally rather small (< 0.01) as compared to the ACC precursor particles (see Fig. 2-4 and Table 2-1 in Section 2.4.1), but apparently scales in more or less linear manner with the analytical amount added, though a slight trend toward saturation can be discerned at higher concentrations. This implies that reinforced interactions between the growing carbonate crystals and

dissolved silicate species are to be expected when increasing the total content of silica in the samples.

3.5 Discussion

The collected data suggest a scenario as illustrated in Fig. 3-11. Upon combining 10 mM solutions of calcium chloride and sodium carbonate, the created high supersaturation leads to rapid nucleation of calcium carbonate and the formation of spherical ACC nanoparticles throughout the entire mixture.

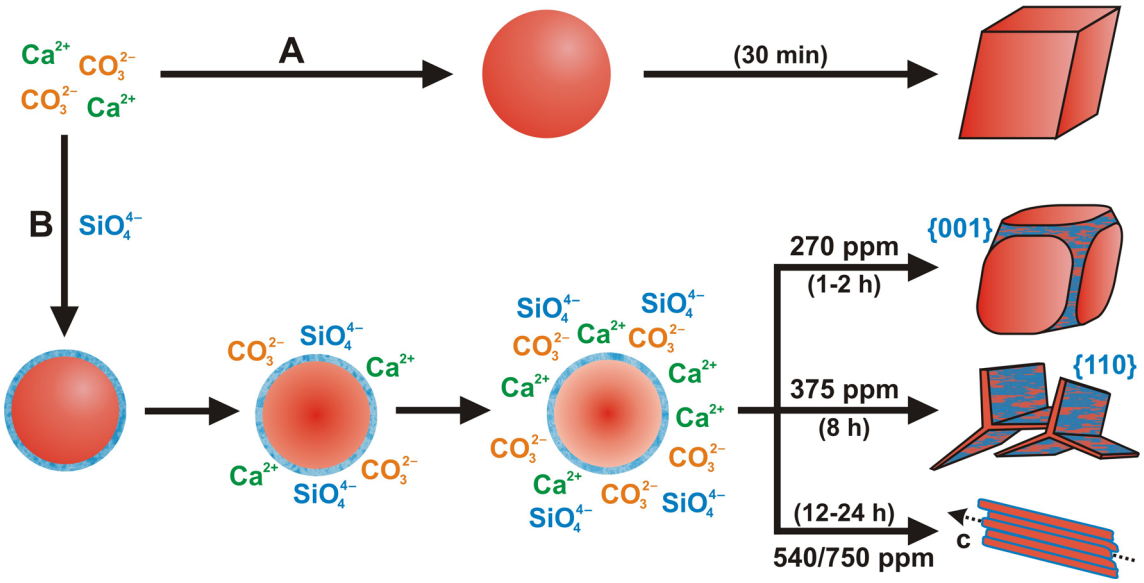

Fig. 3-11: Crystallization of calcite under precipitation conditions in the absence (path A) and presence of different amounts of sodium silicate (path B). Added silicate precipitates spontaneously on growing ACC particles (red spheres) forming continuous layers of amorphous silica all over their surface (indicated in hachured blue). These shells impede exchange with the surrounding medium, thus decelerating ACC re-dissolution and transformation to calcite. Crystallization is protracted the longer the higher the silica concentration, such that more time is granted for structure evolution. By this means, dissolved silicate interferes in distinct ways and to varying degrees with crystal growth, resulting in morphologies of increasing complexity (end of path B, blue parts mark preferential sites for silica adsorption and/or precipitation). Times in brackets specify the approximate period after which first mature crystals or crystal aggregates were observed in the respective sample. For the sake of simplicity, the term "SiO_4^{4-}" is meant to represent all soluble silicate species present in the systems and bicarbonate ions existing in equilibrium with carbonate are not depicted in the sketch. Note further that structures are not drawn to relative scale.

When no silica is present, the lifetime of these precursor species is quite short and stable calcite crystals exhibiting classical rhombohedral equilibrium morphologies develop at their expense after a delay on the order of minutes (path A in Fig. 3-11). On addition of

silica, protons generated at the surface of growing ACC particles due to dissociation of bicarbonate ions virtually decrease the local pH relative to the alkaline bulk medium ($pH_{bulk} \approx 10.6$) and thus trigger polymerization of silica in the close vicinity (see Chapter 2).[46] This results in the deposition of extended skins of amorphous silica around the nanoparticles (path B in Fig. 3-11), the thickness of which increase with the amount of silica present. In the studied range of silica concentrations, these outer layers are porous and hence pervious to reagents (except for the fraction of long-term stable core-shell particles at 750 ppm SiO_2). Nevertheless, coating of the ACC precursors in silica clearly restricts the accessibility to the solvent such that dissolution of ACC and concurrent growth of crystalline phases are slowed down. Therefore, $CaCO_3$ units are released only gradually from the core volume. Since the overall porosity of the skins tends to be lower at higher silica content (see Chapter 2),[46] the rate of crystallization becomes reduced incrementally as more silica is added and its onset is consistently retarded.

Based thereon, excess silica in solution is able to influence the growth behavior of calcite crystals forming in the samples and induce extraordinary morphologies and textures, which are discussed in the following. Generally speaking, the precipitation conditions chosen in this study are not favorable for the design of complex crystal architectures, since additives have barely time to intervene with the growth process. However, with the embedding of ACC particles in siliceous shells, the supersaturation of the system with respect to calcite becomes relieved. This temporary storage of $CaCO_3$ as protected solid ACC establishes a situation in which structured mineralization over timeframes of hours or days is possible.

At 135 ppm SiO_2, there were no significant morphological changes discernible on the final crystals in comparison to the control experiment at 0 ppm, apart from irregular silica deposits on the surface of as-grown rhombohedra (Fig. 3-4a). This can presumably be ascribed to the relatively low concentration of dissolved silicate species in the system (cf. Fig. 3-8) or insufficient deceleration of crystallization, both preventing pronounced interactions between the developing crystals and the additive. Marked effects can in turn be distinguished starting from 270 ppm SiO_2. First, truncation of the sharp edges and corners usually delimiting the rhombohedral shape is observed, causing a rounded appearance and indicating the expression of uncommon {001} faces (Fig. 3-4b). Similar structures have been reported previously for calcite crystals grown in the presence of polystyrenesulfonate[60] or double-hydrophilic

copolymers comprising an anionic block of aromatic sulfonate groups.[61] The exposure of highly charged {001} planes was thereby attributed to stabilization via selective adsorption of the polyelectrolyte additives. Higher silicate oligomers, generated during local polymerization and later in the course of shell re-dissolution, could act as polyanionic impurities modulating crystal growth in an analogical manner and hence effectuating the found distortion of the rhombohedral habit.

By contrast, crystals forming in samples at 375 ppm SiO_2 experience elongation along their c-axes which occurs through successive splitting of an initial rhomb and the emergence of fibrous projections that later develop into single-crystalline strands having three wings at mutual angles of 120° (Fig. 3-5). Calcite morphologies with such 3m rotational symmetry as well as those featured by dome-like outgrowths (Fig. 3-6) were first observed and described by García-Ruiz *et al.* for $CaCO_3$ crystallization in silica-rich media.[49] Recently, Imai and co-workers prepared hierarchical self-similar calcite superstructures consisting of multiple, progressively miniaturized three-pointed stars in alkaline silica gels.[62] Both elongation and the subsequent formation of projections with threefold symmetry were explained on the basis of preferential adsorption and condensation of silicate ions on the {110} planes parallel to the c-axis (cf. Fig. 3-11). Thereby, a gradually growing influence of the silica was proposed to induce the transition from fibers to three-pointed stars. Most likely, a similar mechanism accounts for morphogenesis in the present case, especially in light of the finding that calcite crystallization from ACC precursors is accompanied by re-dissolution of silica skins and hence a continuous increase in the concentration of soluble silicate ions during growth. It is worth stressing at this point that previous syntheses yielding such delicate calcite architectures were carried out exclusively under conditions of slow and controlled crystallization, that is, reagents were allowed to diffuse into a silica gel matrix where precipitation took place.[49,62] Here, structures of comparable complexity were obtained simply by mixing $CaCl_2$ and Na_2CO_3 in the presence of dissolved sodium silicate, taking advantage of transitory stabilization of ACC particles due to sheathing by silica. In this regard, results strongly suggest that intimate interactions between amorphous carbonate precursors and silicate species play an important role during the evolution of unusual crystal forms also and in particular at the lower $CaCO_3$ supersaturation prevailing in typical gel experiments.

As opposed to these elaborately shaped single crystals, growth of calcite in the presence of 540 and 750 ppm SiO_2 affords polycrystalline aggregates comprising a multitude of

co-oriented microneedles (Fig. 3-7). Though not common, needle-like calcite crystals have been reported in literature. For instance, acicular morphologies are well-known in pedology, given that so-called "needle-fiber calcite" (NFC) represents one of the major fractions of calcium carbonate found in vadose soil environments.[63] The formation of elongated crystals is thereby thought to either be caused by drastic physicochemical conditions during crystallization (such as fast evaporation), or to originate from the influence of biogenic matter (e.g. mineralization in plant tissues or bacterial activity). Another example for naturally occurring needle-shaped calcite is the teeth of sea urchins where micron-sized rods grow from a base plate along the unusual [102] direction.[64] Synthetically, spicular calcite crystals have been prepared via a mild solution-precursor-solid (SPS) pathway using PILP droplets,[65] through spherulitic growth from a central core of polysaccharide-stabilized ACC,[66] or by addition of certain acrylate/styrene copolymers.[67] In the latter case, morphological control was proposed to be achieved by specific adsorption of the polymeric additives on a subset of planes parallel to the c-axis, onto which the carboxylate chains match stereochemically. Consistent effects were verified also for macromolecules extracted from sea urchin tests.[68] Condensed silicate oligomers probably perform related functions and block crystal faces parallel to c, thus causing the observed elongation of the crystallites.

Apparently, there is a change in the mode of interaction between growing calcite crystals and added silica when increasing the SiO_2 concentration. At lower silica content (270 ppm), it is the highly charged {001} faces perpendicular to the c-axis that become subject to pronounced adsorption, whereas at higher concentrations (375-750 ppm) planes parallel to c such as {110} are stabilized. Adsorption on {001} is generally considered to be dominated by non-specific electrostatic binding, while deposition of additive molecules on {110} faces typically requires a geometrical conformance of the molecular structure and the arrangement of ions in the respective crystal plane (i.e. the position and orientation of carbonate groups). This indicates that the silica exists in different speciations in the samples despite their virtually identical bulk pH, possibly as a consequence of distinct degrees of condensation resulting from local polymerization and dissolution processes or due to the varying concentration itself.

When comparing the structures formed at 375 and 540/750 ppm, there are further peculiarities worth noting. At the lower concentration, the silica initially provokes splitting of a rhombohedral crystal which is, most probably, induced by insular blocking of the {001} faces. In the following, fibrous projections grow from the parent crystal

maintaining its crystallographic orientation, with silicate species adsorbing strongly on multiple planes parallel to c. Eventually, adsorption on {110} becomes particularly favored and three-pointed stars are generated. Thus, by stabilizing distinct faces to a different extent depending on the stage of growth, the silica accretively deforms the regular calcite habit producing fractal architectures of predominantly single-crystalline nature. At higher silica concentrations, elongation along the c-axis occurs straight after nucleation as the effects discussed above are significantly more pronounced. In addition, crystal growth is effectively abandoned once the needles have reached lengths in the range of some microns, yielding fairly monodisperse crystallites which assemble under the conditions of the experiments to build up intriguing shapes as those displayed in Fig. 3-7. It has been shown previously that precipitation of aragonite-type alkaline-earth carbonates in silica-containing media at elevated pH can lead to crystal aggregates with exceptional morphologies, which are constituted by uniform rod-like nanocrystals.[48,51-56] The stability of the crystallites against ripening is in this case thought to be facilitated by local silica polymerization and consequent coating of the particles.[54] Probably, such a scenario also accounts for the stabilization of calcite microneedles in the present systems, that is, specific adsorption of silicate oligomers on certain crystal faces passes into extensive silica precipitation over the entire surface at some point. This notion is supported by the measured relative content of Si in the aggregates (cf. Fig. 3-10), which complies with values reported for silica biomorphs.[69] The resulting silica deposits prevent crystallites from growing larger – which is in full analogy to the stabilization of ACC particles traced immediately after the onset of $CaCO_3$ precipitation, where the presumed silica skins could be experimentally verified (cf. Chapter 2 and Fig. 3-3).

The origin of the morphologies found at 540 and 750 ppm SiO_2 remains uncertain. The observed "rod-to-dumbbell-to-sphere" transition has been described in literature for biomimetic fluorapatite-gelatine composites, where morphogenesis was discussed in the framework of potential intrinsic electric fields.[70] A similar morphological evolution was recently identified to characterize the early stages of the formation of silica biomorphs.[54] Thereby, a single crystal core undergoes continuous branching at non-crystallographic angles due to poisoning by oligomeric silicate impurities, which ultimately gives fractal spherulitic clusters. The aggregates prepared in this study indeed exhibit related shapes, but are evidently composed of fibrous subunits from the very beginning on (see Fig. 3-2c). Interestingly, there are further analogies between the

present polycrystalline architectures and silica biomorphs. First, the open porous structure of the spherulite shown in Fig. 3-7b is reminiscent of distinct flower- and coral-like morphologies occasionally displayed by $BaCO_3$ and $CaCO_3$ biomorphs.[52,55] Second, the eventual reduction of global growth dimensionality to one (i.e. the formation of linear outgrowths) is a common feature of the two systems (see Fig. 3-7c),[56] although the striking filaments of silica biomorphs are clearly distinguished by their regular winding and helicity.[48,51-54] Finally, the arrangement of the crystallites within the aggregates deserves attention. In biomorphs, the nanorods are largely co-oriented with respect to their long axis, but maintain a coherent mutual misalignment particularly in curved segments. This leads to specific orientational ordering of the building units over extended scales.[52] Fairly akin structural principles are encountered in the $CaCO_3$ precipitates isolated at high silica concentrations in the present experiments (cf. Fig. 3-7d-f). This suggests that particle co-orientation is governed by similar interaction forces, which is reasonable when assuming that the crystallites are in both cases covered by silica. Thus, for lack of an adequate model explaining morphogenesis, it shall be noted that the crystal aggregates obtained at 540/750 ppm SiO_2 resemble silica biomorphs to a certain extent in terms of morphology and texture, with the marked distinction that the former consist of calcite microneedles while the latter are constructed from nanorods of aragonite-type carbonates.

3.6 Conclusion

Taken together, the experiments have demonstrated that adjusting the concentration of added silica during precipitation of calcium carbonate from solution is a simple but effective way to tune the stability of the initially formed ACC phase and, at the same time, create a variety of unusual calcite morphologies. During the early stages of precipitation, dissolved silicate species respond to pH changes occurring in the vicinity of growing ACC particles due to re-equilibration of the carbonate speciation by local polymerization and the deposition of silica skins all over the surface of the particles, which impedes energetically favored transformation to crystalline polymorphs. As crystallization sets in after increasing periods of delay, excess silica in solution as well as oligomers re-dissolved upon disintegration of the core-shell particles progressively affect calcite crystal growth as a result of combined adsorption and precipitation phenomena. Thereby, preceding stabilization of ACC precursors and the associated gradual supply of the medium with $CaCO_3$ units are essential prerequisites for concerted

structure evolution, as fast precipitation at the given high supersaturation would otherwise prevent any significant influence of the silica. The use of stabilized ACC as temporary storage depot for $CaCO_3$ in order to lower the concentration of ions in solution (and corresponding osmotic stresses) and their subsequent release on demand are well-established concepts suggested to be applied *in vivo* during biomineralization.[1-3,14] In this regard, though being purely inorganic, the present systems mimic to some degree the intricate processes underlying the formation of unique calcified tissues in living organisms.

On that basis, direct mixing of the components afforded crystalline structures exhibiting a complexity previously observed only for products obtained from syntheses under controlled conditions. Specific adsorption and condensation of silicate species on distinct planes of the calcite lattice and the concurrent alteration of relative growth rates led to an accretive deformation of the regular rhombohedral habit towards single crystals with threefold symmetry when increasing the amount of silica added. At high silica concentrations, enhanced adsorption caused rapid elongation of nuclei which became stabilized at micronscale dimensions probably through cementation in silica. The resulting needle-like crystallites were found to self-assemble into polycrystalline aggregates exhibiting intriguing non-crystallographic morphologies. Hence, a most prominent effect of the silica on calcite crystal growth is to stepwise miniaturize structural building units and thus enable hierarchical design – which again imitates strategies apparently employed by biomineralization to create materials with higher-order textures.[71]

These findings highlight the singularity of the interplay between crystallizing carbonates and added silica which, despite the simplicity of the reagents involved, is capable of inducing elaborate mineralization processes traditionally thought to rely on the presence of more complex organic additives, and show that (stabilized) amorphous precursors are important intermediate species also in these valuable laboratory model systems.

3.7 References

(1) Lowenstam, H. A.; Weiner, S. *On biomineralization*; Oxford University Press: New York, 1989.

(2) Addadi, L.; Weiner, S. *Angew. Chem. Int. Ed.* **1992**, *31*, 153.

(3) Addadi, L.; Raz, S.; Weiner, S. *Adv. Mater.* **2003**, *15*, 959.

(4) Mann, S. *Biomineralization: principles and concepts in bioinorganic materials chemistry*; Oxford University Press: New York, 2001.

(5) (a) Haeckel, E. *Art Forms from the Ocean: The Radiolarian Atlas of 1862*; Prestel Publishing: Munich/London, 2005. (b) Ozin, G. A. *Acc. Chem. Res.* **1997**, *30*, 17. (c) Sanchez, C.; Arribart, H.; Guille, M. M. G. *Nat. Mater.* **2005**, *4*, 277.

(6) (a) Kröger, N.; Lorenz, S.; Brunner, E.; Sumper, M. *Science* **2002**, *298*, 584. (b) Poulsen, N.; Sumper, M.; Kröger, N. *Proc. Natl. Acad. Sci. U.S.A.* **2003**, *100*, 12075. (c) Sumper, M.; Brunner, E. *Adv. Funct. Mater.* **2006**, *16*, 17.

(7) (a) Perry, C. C.; Keeling-Tucker, T. *J. Biol. Inorg. Chem.* **2000**, *5*, 537. (b) Perry, C. C. *Rev. Mineral. Geochem.* **2003**, *54*, 291.

(8) (a) Bettermann, P.; Liebau, F. *Contrib. Mineral. Petrol.* **1975**, *53*, 25. (b) Yamaguchi, O.; Kanazawa, T.; Shimizu, K. *J. Chem. Soc., Dalton Trans.* **1982**, *5*, 1005.

(9) (a) Pontoni, D.; Bolze, J.; Dingenouts, N.; Narayanan, T.; Ballauff, M. *J. Phys. Chem. B* **2003**, *107*, 5123. (b) Pan, H.; Liu, X. Y.; Tang, R.; Xu, H. Y. *Chem. Commun.* **2010**, *46*, 7415.

(10) Taylor, M. G.; Simkiss, K.; Greaves, G. N.; Okazaki, M.; Mann, S. *Proc. R. Soc. London, Ser. B* **1993**, *252*, 75.

(11) (a) Lowenstam, H. A. *Bull. Mar. Sci.* **1989**, *45*, 243. (b) Levi-Kalisman, Y.; Raz, S.; Weiner, S.; Addadi, L.; Sagi, I. *J. Chem. Soc., Dalton Trans.* **2000**, 3977. (c) Aizenberg, J.; Lambert, G.; Addadi, L.; Weiner, S. *J. Am. Chem. Soc.* **2002**, *124*, 32.

(12) Aizenberg, J.; Lambert, G.; Addadi, L.; Weiner, S. *Adv. Mater.* **1996**, *8*, 222.

(13) (a) Becker, A.; Ziegler, A.; Epple, M. *Dalton Trans.* **2005**, 1814. (b) Al-Sawalmih, A.; Li, C.; Siegel, S.; Fratzl, P.; Paris, O. *Adv. Mater.* **2009**, *21*, 4011.

(14) (a) Ziegler, A. *J. Struct. Biol.* **1994**, *112*, 110. (b) Becker, A.; Bismayer, U.; Epple, M.; Fabritius, H.; Hasse, B.; Shi, J.; Ziegler, A. *Dalton Trans.* **2003**, 551.

(15) Weiner, S.; Mahamid, J.; Politi, Y.; Ma, Y.; Addadi, L. *Front. Mater. Sci. China* **2009**, *3*, 104.

(16) (a) Beniash, E.; Aizenberg, J.; Addadi, L.; Weiner, S. *Proc. R. Soc. Lond. B* **1997**, *264*, 461. (b) Politi, Y.; Metzler, R. A.; Abrecht, M.; Gilbert, B.; Wilt, F. H.; Sagi, I.; Addadi, L.; Weiner, S.; Gilbert, P. U. P. A. *Proc. Natl. Acad. Sci. USA* **2008**, *105*, 17362. (c) Politi, Y.; Arad, T.; Klein, E.; Weiner, S.; Addadi, L. *Science* **2004**, *306*, 1161. (d) Ma, Y.; Weiner, S.; Addadi, L. *Adv. Funct. Mater.* **2007**, *17*, 2693. (e) Killian, C. E.; Metzler, R. A.; Gong, Y. U. T.; Olson, I. C.; Aizenberg, J.; Politi, Y.; Wilt, F. H.; Scholl, A.; Young, A.; Doran, A.; Kunz, M.; Tamura, N.; Coppersmith, S. N.; Gilbert, P. U. P. A. *J. Am. Chem. Soc.* **2009**, *131*, 18404.

(17) (a) Hasse, B.; Ehrenberg, H.; Marxen, J. C.; Becker, W.; Epple, M. *Chem. Eur. J.* **2000**, *6*, 3679. (b) Weiss, I. M.; Tuross, N.; Addadi, L.; Weiner, S. *J. Exp. Zool.* **2002**, *293*, 478.

(18) Gago-Duport, L.; Briones, M. J. I.; Rodríguez, J. B.; Covelo, B. *J. Struct. Biol.* **2008**, *162*, 422.

(19) Lowenstam, H. A. *Science* **1985**, *227*, 51.

(20) (a) Mahamid, J.; Sharir, A.; Addadi, L.; Weiner, S. *Proc. Natl. Acad. Sci. USA* **2008**, *105*, 12748. (b) Mahamid, J.; Aichmayer, B.; Shimoni, E.; Ziblat, R.; Li, C.; Siegel, S.; Paris, O.; Fratzl, P.; Weiner, S.; Addadi, L. *Proc. Natl. Acad. Sci. USA* **2010**, *107*, 6316. (c) Nudelman, F.; Pieterse, K.; George, A.; Bomans, P. H. H.; Friedrich, H.; Brylka, L. J.; Hilbers, P. A. J.; de With, G.; Sommerdijk, N. A. J. M. *Nat. Mater.* **2010**, DOI: 10.1038/NMAT2875.

(21) Beniash, A.; Metzler, R. A.; Lam, R. S. K.; Gilbert, P. U. P. A. *J. Struct. Biol.* **2009**, *166*, 133.

(22) (a) Gehrke, N.; Nassif, N.; Pinna, N.; Antonietti, M.; Gupta, H. S.; Cölfen, H. *Chem. Mater.* **2005**, *17*, 6514. (b) Nassif, N.; Pinna, N.; Gehrke, N.; Antonietti, M.; Jäger, C.; Cölfen, H. *Proc. Natl. Acad. Sci. USA* **2005**, *102*, 12653.

(23) (a) Aizenberg, J.; Muller, D. A.; Grazul, J. L.; Hamann, D. R. *Science* **2003**, *299*, 1205. (b) Loste, E.; Park, R. J.; Warren, J.; Meldrum, F. C. *Adv. Funct. Mater.* **2004**, *14*, 1211. (c) Li, C.; Qi, L. *Angew. Chem. Int. Ed.* **2008**, *47*, 2388.

(24) (a) Meldrum, F. C.; Cölfen, H. *Chem. Rev.* **2008**, *108*, 4332. (b) Gower, L. B. *Chem. Rev.* **2008,** *108*, 4551.

(25) (a) Meldrum, F. C. *Int. Mater. Rev.* **2003**, *48*, 187. (b) Tegethoff, W.; Rohleder, J.; Kroker, E. *Calcium carbonate: from the cretaceous period to the 21st century*; Birkhäuser Verlag: Basel, 2001.

(26) (a) Ogino, T.; Suzuki, T.; Sawada, K. *Geochim. Cosmochim. Acta* **1987**, *51*, 2757. b) Brecevic, L.; Nielsen, A. E. *J. Cryst. Growth* **1989**, *89*, 504.

(27) (a) Faatz, M.; Gröhn, F.; Wegner, G. *Adv. Mater.* **2004**, *16*, 996. (b) Rieger, J.; Frechen, T.; Cox, G.; Heckmann, W.; Schmidt, C.; Thieme, J. *Faraday Discuss.* **2007**, *136*, 265.

(28) (a) Gebauer, D.; Völkel, A.; Cölfen, H. *Science* **2008**, *322*, 1819. (b) Pouget, E. M.; Bomans, P. H. H.; Goos, J. A. C. M.; Frederik, P. M.; De With, G.; Sommerdijk, N. A. J. M. *Science* **2009**, *323*, 1455.

(29) (a) Rieger, J.; Hädicke, E.; Rau, I. U.; Boeckh, D. *Tenside Surf. Det.* **1997**, *34*, 430. (b) Rieger, J. *Tenside Surf. Det.* **2002**, *39*, 6.

(30) (a) Reddy, M. M.; Nancollas, G. H. *J. Cryst. Growth* **1976**, *35*, 33. (b) Loste, E.; Wilson, R. M.; Seshadri, R.; Meldrum, F. C. *J. Cryst. Growth* **2003**, *254*, 206.

(31) (a) Raz, S.; Hamilton, P. C.; Wilt, F. H.; Weiner, S.; Addadi, L. *Adv. Funct. Mater.* **2003**, *13*, 480. (b) Tao, J.; Zhou, D.; Zhang, Z.; Xu, X.; Tang, R. *Proc. Natl. Acad. Sci. USA* **2009**, *106*, 22096. (c) Politi, Y.; Batchelor, D. R.; Zaslansky, P.; Chmelka, B. F.; Weaver, J. C.; Sagi, I.; Weiner, S.; Addadi, L. *Chem. Mater.* **2010**, *22*, 161.

(32) (a) Clarkson, J. R.; Price, T. J.; Adams, C. A. *J. Chem. Soc., Faraday Trans.* **1992**, *88*, 243. (b) Sawada, K. *Pure Appl. Chem.* **1997**, *69*, 921.

(33) (a) Markovic, I.; Ottewill, R. H. *Colloid Polym. Sci.* **1986**, *264*, 454. (b) Steytler, D. C.; Robinson, B. H.; Eastoe, J.; Ibel, K.; Dore, J. C.; MacDonald, I. *Langmuir* **1993**, *9*, 903.

(34) Guillemet, B.; Faatz, M.; Gröhn, F.; Wegner, G.; Gnanou, Y. *Langmuir* **2006**, *22*, 1875.

(35) Donners, J. J. J. M.; Heywood, B. R.; Meijer, E. W.; Nolte, R. J. M.; Sommerdijk, N. A. J. M. *Chem. Eur. J.* **2002**, *8*, 2561.

(36) Xu, A. W.; Yu, Q.; Dong, W. F.; Antonietti, M.; Cölfen, H. *Adv. Mater.* **2005**, *17*, 2217.

(37) Stephens, C. J.; Ladden, S. F.; Meldrum, F. C.; Christenson, H. K. *Adv. Funct. Mater.* **2010**, *20*, 2108.

(38) (a) Gower, L. B.; Tirrell, D. A. *J. Cryst. Growth* **1998**, *191*, 153. (b) Gower, L. B.; Odom, D. J. *J. Cryst. Growth* **2000**, *210*, 719. (b) Dai, L.; Douglas, E. P.; Gower, L. B. *J. Non-Cryst. Solids* **2008**, *354*, 1845.

(39) (a) Yu, S. H.; Cölfen, H. *J. Mater. Chem.* **2004**, *14*, 2124. (b) Cölfen, H. *Top. Curr. Chem.* **2007**, *271*, 1.

(40) (a) Antonietti, M.; Breulmann, M.; Göltner, C. G.; Cölfen, H.; Wong, K. K. W.; Walsh, D.; Mann, S. *Chem. Eur. J.* **1998**, *4*, 2493. (b) Cölfen, H.; Qi, L. *Chem. Eur. J.* **2001**, *7*, 106. (c) Qi, L.; Cölfen, H.; Antionietti, M.; Li, M.; Hopwood, J. D.; Ashley, A. J.; Mann, S. *Chem. Eur. J.* **2001**, *7*, 3526. (d) Yu, S. H.; Cölfen, H.; Antonietti, M. *Chem. Eur. J.* **2002**, *8*, 2937. (e) Yu, S. H.; Cölfen, H.; Antonietti, M. *J. Phys. Chem. B* **2003**, *107*, 7396.

(41) Cölfen, H.; Mann, S. *Angew. Chem. Int. Ed.* **2003**, *42*, 2350.

(42) (a) Li, M.; Mann, S. *Adv. Funct. Mater*. **2002**, *12*, 773. (b) Li, M.; Lebeau, B.; Mann, S. *Adv. Mater.* **2003**, *15*, 2032.

(43) (a) Xu, G.; Yao, N.; Aksay, I. A.; Groves, J. T. *J. Am. Chem. Soc.* **1998**, *120*, 11977. (b) Sugawara, A.; Ishii, T.; Kato, T. *Angew. Chem. Int. Ed.* **2003**, *42*,

5299. (c) Volkmer, D.; Harms, M.; Gower, L.; Ziegler, A. *Angew. Chem. Int. Ed.* **2005**, *44*, 639. (d) Kim, Y. Y.; Douglas, E. P.; Gower, L. B. *Langmuir* **2007**, *23*, 4862.

(44) Amos, F. F.; Sharbaugh, D. M.; Talham, D. R.; Gower, L. B.; Fricke, M.; Volkmer, D. *Langmuir* **2007**, *23*, 1988.

(45) (a) Lee, S. S.; Culver, L.; Li, Y.; Douglas, E. P.; Gower, L. B. *J. Cryst. Growth* **2010**, *312*, 1249. (b) Cheng, X.; Gower, L. B. *Biotechnol. Progr.* **2006**, *22*, 141.

(46) Kellermeier, M.; Melero-García, E.; Glaab, F.; Klein, R.; Drechsler, M.; Rachel, R.; García-Ruiz, J. M.; Kunz, W. *J. Am. Chem. Soc.* **2010**, *132*, 17859.

(47) Gal, A.; Weiner, S.; Addadi, L. *J. Am. Chem. Soc.* **2010**, *132*, 13208.

(48) (a) García-Ruiz, J. M.; Amorós, J. L. *J. Cryst. Growth* **1981**, *55*, 379. (b) García-Ruiz, J. M. *J. Cryst. Growth* **1985**, *73*, 251.

(49) Domínguez-Bella, S.; García-Ruiz, J. M. *J. Cryst. Growth* **1986**, *79*, 236.

(50) Domínguez-Bella, S.; García-Ruiz, J. M. *J. Mater. Sci.* **1987**, *22*, 3095.

(51) Terada, T.; Yamabi, S.; Imai, H. *J. Cryst. Growth* **2003**, *253*, 435

(52) Hyde, S. T.; Carnerup, A. M.; Larsson, A. K.; Christy, A. G.; Garcia-Ruiz, J. M. *Physica A* **2004**, *339*, 24.

(53) Bittarello, E.; Aquilano, D. *Eur. J. Mineral.* **2007**, *19*, 345.

(54) (a) García-Ruiz, J. M.; Melero-García, E.; Hyde, S. T. *Science* **2009**, *323*, 362. (b) Kunz, W.; Kellermeier, M. *Science* **2009**, *323*, 344. (c) Melero-García, E.; Santisteban-Bailón, R.; García-Ruiz, J. M. *Cryst. Growth Des.* **2009**, *9*, 4730.

(55) (a) Imai, H.; Terada, T.; Miura, T.; Yamabi, S. *J. Cryst. Growth* **2002**, *244*, 200. (b) Voinescu, A. E.; Kellermeier, M.; Bartel, B.; Carnerup, A. M.; Larsson, A. K.; Touraud, D.; Kunz, W.; Kienle, L.; Pfitzner, A.; Hyde, S. T. *Cryst. Growth Des.* **2008**, *8*, 1515.

(56) (a) García-Ruiz, J. M. *Origins Life Evol. Biosphere* **1993**, *24*, 251. (b) García-Ruiz, J. M.; Carnerup, A. M.; Christy, A. G.; Welham, N. J.; Hyde, S. T.

Astrobiology **2002**, *2*, 353. (c) García-Ruiz, J. M.; Hyde, S. T.; Carnerup, A. M.; Christy, A. G.; Van Kranendonk, M. J.; Welham, N. J. *Science* **2003**, *302*, 1194.

(57) Schrödle, S.; Buchner, R.; Kunz, W. *Fluid Phase Equilib.* **2004**, *216*, 175.

(58) (a) Wolf, S. E.; Leiterer, J.; Kappl, M.; Emmerling, F.; Tremel, W. *J. Am. Chem. Soc.* **2008**, *130*, 12342. (b) Rieger, J.; Thieme, J.; Schmidt, C. *Langmuir* **2000**, *16*, 8300.

(59) Lakshtanov, L. Z.; Stipp, S. L. S. *Geochim. Cosmochim. Acta* **2010**, *74*, 2655.

(60) (a) Wang, T.; Cölfen, H.; Antonietti, M. *J. Am. Chem. Soc.* **2005**, *127*, 3246. (b) Wang, T.; Cölfen, H.; Antonietti, M. *Chem. Eur. J.* **2006**, *12*, 5722.

(61) Kulak, A. N.; Iddon, P.; Li, Y.; Armes, S. P.; Cölfen, H.; Paris, O.; Wilson, R. M.; Meldrum, F. C. *J. Am. Chem. Soc.* **2007**, *129*, 3729.

(62) Imai, H.; Terada, T.; Yamabi, S. *Chem. Commun.* **2003**, 484.

(63) (a) Verrecchia, E. P.; Verrecchia, K. E. *J. Sediment. Res.* **1994**, *64*, 650. (b) Borsato, A.; Frisia, S.; Jones, B.; Van Der Borg, K. *J. Sediment. Res.* **2000**, *70*, 1171. (c) Cailleau, G.; Verrecchia, E. P.; Braissant, O.; Emmanuel, L. *Sedimentology* **2009**, *56*, 1858. (d) Bajnoczi, B. *Chem. Erde* **2006**, *66*, 203.

(64) (a) Berman, A.; Hanson, J.; Leiserowitz, L.; Koetzle, T. F.; Weiner, S.; Addadi, L. *Science* **1993**, *259*, 776. (b) Ma, Y.; Weiner, S.; Addadi, L. *Adv. Funct. Mater.* **2007**, *17*, 2693.

(65) Olszta, M. J.; Gajjeraman, S.; Kaufman, M.; Gower, L. B. *Chem. Mater.* **2004**, *16*, 2355.

(66) Zhong, C.; Chu, C. C. *Cryst. Growth Des.* **2010**, DOI: 10.1021/cg1002644.

(67) Moore, L.; Hopwood, J. D.; Davey, R. J. *J. Cryst. Growth* **2004**, *261*, 93.

(68) (a) Berman, A.; Addadi, L.; Weiner, S. *Nature* **1988**, *331*, 546. (b) Berman, A.; Addadi, L.; Kvick, A.; Leiserowitz, L.; Nelson, M.; Weiner, S. *Science* **1990**, *250*, 664.

(69) (a) Voinescu, A. E.; Kellermeier, M.; Carnerup, A. M.; Larsson, A. K.; Touraud, D.; Hyde, S. T.; Kunz, W. *J. Cryst. Growth* **2007**, *306*, 152. (b) Kellermeier, M.;

Glaab, F.; Carnerup, A. M.; Drechsler, M.; Gossler, B.; Hyde, S. T.; Kunz, W. *J. Cryst. Growth* **2009**, *311*, 2530

(70) (a) Busch, S.; Dolhaine, H.; DuChesne, A.; Heinz, S.; Hochrein, O.; Laeri, F.; Podebrad, O.; Vietze, U.; Weiland, T.; Kniep, R. *Eur. J. Inorg. Chem.* **1999**, 1643. (b) Rosseeva, E.; Buder, J.; Simon, P.; Schwarz, U.; Frank-Kamenetskaya, O. V.; Kniep, R. *Chem. Mater.* **2008**, *20*, 6003.

(71) Oaki, Y.; Kotachi, A.; Miura, T.; Imai, H. *Adv. Funct. Mater.* **2006**, *16*, 1633.#

Chapter 4 Capturing Calcium Carbonate Pre-Nucleation Clusters in Alkaline Silica Sols

4.1 Abstract

Crystallization of calcium carbonate from solution typically proceeds *via* a complex sequential scenario involving amorphous precursors and several successive phase transitions before finally stable crystals are obtained. Recent insight into the very early stages of this process has shown that prior to the nucleation of a true solid phase, neutral ion clusters with dimensions of few nanometers are formed which exist in thermodynamic equilibrium with the dissolved ions and transform above a certain concentration to yield in nanoparticles of ACC. This picture challenges classical theories, which assume that the onset of precipitation relies on the stochastic formation of metastable nuclei that grow via attachment of ions, once having reached a critical size. In this chapter, it is demonstrated that these novel so-called "pre-nucleation clusters" can be captured when calcium carbonate is precipitated from silica-rich solutions at high pH. Due to binding of silicate species in the periphery of the clusters, their aggregation is impeded and crystallization remains prevented in the long term. Despite the chosen high supersaturation, stable solutions are obtained in which myriads of individual nanoclusters co-exist with a minor fraction of cluster aggregates. In turn, by a step-wise lowering of the pH, crystallization can be allowed to progress gradually and different transient structures on the way to amorphous nanoparticles are revealed. The as-formed silica-decorated clusters and their agglomerates were investigated by cryo-TEM and characterized concerning their size and temporal evolution by various *in-situ* techniques. The presented results show that addition of silica is an effective means to access pre-nucleation clusters experimentally and even isolate them in dry state without notable structural changes. Beyond that, the collected data shed light on the processes which underlie homogeneous nucleation of calcium carbonate and suggest that it is based on aggregation of pre-nucleation clusters. This model may apply also to other minerals.

4.2 Introduction

Nucleation and crystal growth are fundamental processes in the focus of scientific interest, even more than 70 years after the classical nucleation theory was introduced.[1]

The reason is that phenomena like non-classical crystallization, as observed in biological as well as biomimetic additive-controlled mineralization, can hardly be explained by classical models, and have recently been shown to proceed via particle-based pathways.[2,3] Calcium carbonate is an often chosen model system in this context, due to its rich polymorphism and its broad relevance for diverse fields of research. For example, during biomineralization, $CaCO_3$ is segregated under the influence of organic matter in a highly controlled manner, yielding in complex, hierarchically structured materials such as nacre.[4] On the other hand, undesired formation of solid $CaCO_3$ in pipes or heating devices leads to mineral incrustation in the household and especially in industrial settings. This may cause a loss in performance and unscheduled downtimes of facilities, necessitating costly repair, even when antiscalant agents are used.[5] Clearly, a fundamental understanding of the crystallization process on multiple time and length scales and means to influence it concertedly would be of benefit for a variety of purposes.

Under moderate conditions, calcium carbonate can exist in five different crystalline phases, among which the three anhydrous forms vaterite, aragonite and calcite are most common.[6] Another well-established, though generally metastable phase is amorphous calcium carbonate (ACC), which has attracted increasing attention in the past years due to its occurrence as biogenic mineral.[7]

Previous studies have pointed out that the crystallization of $CaCO_3$ does often and especially at high supersaturation not follow the classical route, i.e. proceed via nucleation and subsequent crystal growth, but may involve a series of intermediates before eventually a stable mineral precipitate is obtained.[8-10] In such a sequential process, less stable phases are kinetically favored and thus formed first, but undergo in the following stepwise transitions through intermediates of increasing stability towards the thermodynamic product (Ostwald rule of stages).[11,12] During $CaCO_3$ precipitation, the first solid phase observed was reported to consist of amorphous nanoparticles,[8-10,13-16] though in some cases evidence was provided for an earlier liquid-like precursor to these particles, induced by binodal or spinodal demixing.[10,14,17,18]

Conventional strategies to steer the course of $CaCO_3$ crystallization mostly rely on the action of additives that are capable of interacting specifically with one or several of the distinct precursor and crystalline phases. Such additives are typically of organic nature, and range from simple molecules over polymers to extended template matrices, frequently modeled upon the principles learned from natural biomineralization.[2] On that

basis, a vast amount of work has been devoted to finding ways to tune important material properties like polymorphism, texture and morphology.[19] Nowadays, focus is more and more placed on generating defined nanoscale particles, which may be employed for the design of novel materials with complex higher-order structures through additive-directed self-assembly,[12,20] or forthright used for a broad panoply of technical and industrial applications.[21]

Access to nanoparticles of amorphous calcium carbonate can readily be gained by arresting crystallization *in situ* at its early stages, usually through kinetic stabilization of the transient species against transformation to crystalline polymorphs. For instance, suitable polyelectrolytes can adsorb on as-formed ACC particles, delimit chemical exchange with the surrounding medium and thus drastically reduce transformation rates.[10,22] Temporary storage of $CaCO_3$ as stabilized ACC (and the concurrent relief of actual solution supersaturation) furthermore appears to be a key concept in the construction of at least some biominerals,[6,23] and has been utilized successfully also for laboratory morphosynthesis.[24]

Very recent work has elucidated that during $CaCO_3$ crystallization the nucleation of a continuous solid amorphous phase is preceded by the formation of neutral ion clusters consisting of about 35 $CaCO_3$ units and measuring only about 1-2 nm in size.[25,26] Unlike the sub-critical clusters envisaged in classical nucleation theories, these so-called pre-nucleation clusters were shown to exist in thermodynamic equilibrium with the dissolved ions both in the under- and supersaturated regime. Imaging of these tiny species was first accomplished by Pouget *et al.* who traced $CaCO_3$ clusters in solutions of calcium bicarbonate by means of cryo-transmission electron microscopy (cryo-TEM).[27] Nevertheless, a system containing such thermodynamically stable clusters may become metastable at a certain point (for instance upon concentration changes), leading to the nucleation of the solid phase. It was suggested that aggregation of the clusters is inherent to this step,[25] initially yielding nanoparticles of amorphous calcium carbonate (ACC) with diameters in the range of ~30 nm which subsequently grew and transformed to vaterite.[27] However, direct insight into the supposed aggregation processes could not yet be achieved. Essentially, the low concentrations of the precursors in under- or slightly supersaturated systems and the highly transient character of distinct solution states at practical supersaturations render experimental detection and investigations difficult. Still, for a detailed analysis of the various stages at the very

beginning of crystallization, the transformation of ion clusters into ACC nanoparticles must be significantly slowed down.

There is evidence that the as-nucleated ACC may exhibit different local atomic structures, which depend on synthesis conditions,[28,29] and are reflected in variable solubilities of the amorphous particles after nucleation.[25] The intrinsic short-range order in the ACC materials was sometimes found to predetermine the subsequently formed crystalline phase,[25,29-31] indicating that the final polymorph can be encoded already in the stage of pre-nucleation clusters. Moreover, the effect of certain additives on the cluster equilibrium was investigated, proving a partially remarkable influence on the relative stability of the clusters and the nucleation behavior.[32,33]

The existence of stable nanoclusters in solution prior to and after nucleation is however not a phenomenon unique to calcium carbonate, but has been postulated and verified also for a series of other materials. These include polymerizing and hence covalently bound substances like silica or aluminium oxyhydroxide,[34,35] simple ionic salts such as sodium nitrate,[36] as well as "intermediate" compounds like calcium phosphate.[37-39] Ion clusters and corresponding small polymeric particles obviously play an essential role in biomineralization, acting as building blocks which nourish growing inorganic frameworks via (oriented) incorporation.[38-41]

In Chapter 2, it was demonstrated that precipitating calcium carbonate under alkaline conditions leads to local pH gradients around forming ACC nanoparticles which trigger in-situ deposition of expanded siliceous skins all over their surface.[42] In the following, it is shown that this concept can be extended to interfere with the crystallization of $CaCO_3$ at an even earlier stage – that of pre-nucleation clusters. To this end, calcium carbonate was precipitated by directly mixing solutions of calcium chloride and sodium carbonate in the presence of substantially higher amounts of dissolved silica. Results illustrate that isolated cluster species abound in the system and co-exist with a rather small, temporally changing fraction of cluster agglomerates. Strikingly, despite the fairly huge supersaturation chosen, clusters remain widely isolated in solution and no nucleation is observed in the long term, indicating that added silica shields individual clusters against each other and thus renders this very first stage of $CaCO_3$ crystallization accessible. By varying the pH, crystallization can in turn be allowed to proceed gradually, such that the different transient solution states occurring during nucleation – essentially distinct aggregates of clusters – are progressively stabilized and hence can be monitored

experimentally. Based on the collected data, a model for the species and processes that underlie homogeneous nucleation of calcium carbonate is proposed.

4.3 Experimental Section

4.3.1 Materials and Sample Preparation

4.3.1.1 Preparation of Solutions

Calcium chloride dihydrate (Riedel-de Haën, ACS reagent, ≥ 99%), sodium carbonate (Roth, anhydrous, ≥ 99%) and sodium metasilicate solution (Aldrich, reagent grade) were used as received without further purification. For all experiments, the same lot of water glass (89597PJ) served as silica source, specified to contain 13.8 wt% NaOH and 26.7 wt% SiO_2. Water was taken from a Millipore system and bubbled overnight with N_2 to displace dissolved CO_2 prior to use. CO_2-free silica sols were obtained by adding water in appropriate volumetric ratios to the silica stock and purging the resulting dilutions with H_2O-saturated nitrogen for several hours. These sols were then used to dissolve Na_2CO_3 and thus gain solutions with defined carbonate concentration. To preclude ageing effects, silica dilutions and silica-carbonate mixtures were replaced by fresh ones at least every week. All solutions were filtered straight after preparation (450 nm cut-off) and subsequently stored in firmly closed plastic bottles under inert gas atmosphere.

4.3.1.2 Precipitation Experiments

Crystallization of calcium carbonate was initiated by rapidly combining aqueous solutions of calcium chloride and sodium carbonate (5 mL each) with the aid of a graded pipette. Studies were focused primarily on equimolar mixtures at concentrations ranging from 2.5 to 20 mM. The amount of added silica was adjusted such that the effective molar ratio of $SiO_2/CaCO_3$ was about 12.5 and hence substantially higher than in the experiments described in Chapter 2. Precipitation was carried out at 25°C in polypropylene vials, unless required otherwise by the respective technique applied. Generally, special care was taken to prevent uptake of atmospheric carbon dioxide by the alkaline mixtures, which proved to be significant when vessels with leaky stoppers were employed. Therefore, especially when investigating temporal evolutions in the long term, vials were sealed with Parafilm and placed, until sampling, in a chamber gently flooded with nitrogen. As references, series of samples with identical species concentrations but lacking one of the components were prepared by adding water

instead of $CaCl_2$ to the particular Na_2CO_3-SiO_2 mixture (no Ca^{2+}), or by converting silica dilutions directly with $CaCl_2$ without preceding dissolution of Na_2CO_3 (no CO_3^{2-}). Starting pH values of typical samples and corresponding references are listed in Table 4-1. Hereinafter, dilution factors quoted for silica in the distinct experiments refer to the sols obtained initially after dilution of the water glass stock. Note that mixing of the reagents brings about an additional dilution factor of 2.

$[CaCl_2]$ / mM	$[Na_2CO_3]$ / mM	Used silica dilution (v/v)	$[SiO_2]$ / mM	$[SiO_2]$ / ppm	pH
5	5	1-50	61.9	3720	11.00
5	0	1-50	61.9	3720	10.97
0	5	1-50	61.9	3720	11.11
5	5	1-25	123.8	3720	11.29
10	10	1-25	123.8	7440	11.20
10	0	1-25	123.8	7440	11.20
0	10	1-25	123.8	7440	11.36
20	20	1-12.5	247.5	14870	11.38

Table 4-1: Composition and initial pH of the most intensively studied samples. Molar concentrations and ppm values apply for the final mixture after combining reagents, whereas the given silica dilution factors correspond to the sols used for dissolution of sodium carbonate before mixing with calcium chloride.

The pH of the "standard" sample, i.e. a solution containing 5 mM each of $CaCl_2$ and Na_2CO_3 and 3720 ppm SiO_2, was varied within a range of 7-11. For this purpose, 10 mM solutions of $CaCl_2$ were prepared using dilute HCl (Merck, p.a.) with different concentrations (0-100 mM) as solvent, and combined with a mixture of 10 mM Na_2CO_3 and 1-50 silica. The initial pH values thus achieved were 11.00, 10.63, 10.29, 9.96, 9.32, 8.55 and 7.25 for final HCl contents of 0, 10, 20, 30, 40, 45 and 50 mM, respectively. Variations of the ionic strength of the system were done by adding proper amounts of sodium chloride (Merck, p.a.) to the $CaCl_2$ solution prior to mixing.

4.3.2 Cryo-TEM

For cryo-TEM, aliquots were drawn from the solutions at different times after mixing, and spread on lacey carbon grids by blotting with a filter paper to give a thin film, which was vitrified by quickly plunging the grids into liquid ethane at its freezing point utilizing a Zeiss cryobox. TEM studies were performed at temperatures around 90 K. Clusters formed in mixtures of $CaCl_2$, Na_2CO_3 and silica at pH 11 and their evolution

with time were primarily investigated with a Zeiss EM922 EF microscope, operated at 200 kV, and equipped with a Gatan CT3500 cryo transfer holder (experiments at the University of Bayreuth). Images were acquired with a Gatan Ultrascan US 1000 high-resolution cooled CCD camera and processed using the Digital Micrograph Suite 1.8 software package. First, the background of the images was subtracted by means of a routine which calculates a slowly-varying background, and removes it by successive reduction and bilinear interpolation scaling. In a second step, a third-order low-pass Butterworth filter with a cut-off radius of $R_0 = 1.0\ nm^{-1}$ was applied so as to reduce noise and smoothen the images.[43] The micrographs shown in Fig. 4-3, Fig. 4-5, Fig. 4-7, and Fig. 4-9 were obtained on the basis of this procedure.

The size of the clusters was determined automatically with the help of the particle-analysis function in Digital Micrograph, using images that displayed predominantly separate clusters and lacked cluster aggregates. Satisfactory particle recognition was thereby usually achieved when the threshold was set to about 20% of the maximum in the histogram. Obvious mistakes of the particle-finding routine were corrected for by manually deselecting corresponding structures. The chosen output parameter characterizing the size of the clusters was the virtual circular particle diameter measured by the software. Values less than 0.5 nm were regarded as noise, and were therefore not considered for the calculation of cluster size distributions.

Analyses of reference samples (see Section 4.4.5) and systems with varying starting pH (see Section 4.4.11) were carried out at 120 kV on a FEI T12 G^2 transmission electron microscope equipped with a Gatan 626 cryo-holder system and a Gatan US1000 high-resolution cooled-CCD camera (experiments at Technion Haifa). During these experiment series, specimens were prepared in a controlled environment vitrification system (CEVS) at a constant temperature of 25°C and fixed relative humidity of 100%, as described elsewhere.[44] Images collected with this cryo-TEM setup were processed only with a background-subtraction routine (and no smoothing filter), as it proved to be sufficient to clearly visualize the clusters and their aggregated states.

4.3.3 Dynamic Light Scattering

4.3.3.1 Experimental and Data Evaluation

Colloids present in the samples were investigated concerning their size and its evolution with time by means of dynamic light scattering (DLS). Experiments were conducted at 25°C and a scattering angle of 90°, using an ALV CGS-2 goniometer setup equipped

with an ALV-5000/E Multiple Tau digital correlator and a He-Ne laser (λ = 632.8 nm). For measurement, equilibrated reagent solutions were filtered (200 nm cut-off, VWR syringe filters) and combined directly in suitable glass cuvettes (t = 0), previously cleaned from dust by refluxing acetone. First, samples were studied with respect to temporal changes by monitoring scattering continuously after an initial delay of 2 min for up to around 24 h, with an acquisition time per run of 45 s. The waiting period between individual runs was chosen to be 15 s at the beginning and set to increase exponentially in the course of the experiment with a multiplier of 1.04. Overall, a maximum of 140 runs were thus performed with eventual delay times of about 50 min. The obtained autocorrelation functions ($g_2(\tau)$-1) versus the lag time τ were found to be described adequately well in most cases by a monomodal decay and were hence fitted with a single-exponential equation, according to:

$$\left(g_2(t)-1\right) = a_0 + \left[a_1 \cdot \exp\left(-a_2 \cdot t\right)\right]^2 \qquad \text{(Eqn. 4-3)}$$

where $a_2 = q^2 D$ and $q = 4\pi n_0 \cdot \sin(\theta/2) / \lambda$ (a_0, a_1: constants, q: wave vector, n_0: solvent refractive index, λ: laser wavelength, θ: scattering angle). On that basis, a mean diffusion coefficient D of the major scattering species was calculated for each run and, assuming sphericity, converted to the corresponding hydrodynamic radius using the Stokes-Einstein relation (Eqn. 4-2). In addition to correlation data, the count rate of the detector was recorded during each run, averaged and related to the intensity of the incident laser beam.

Alternatively, longer measurements (averaging 10 subsequent runs of 60 or 120 s duration) were conducted in order to derive size distribution profiles at discrete times based on data with good statistics. Size distributions were computed with the ALV-5000/E software package (v.1.4.7), which fits an integral-type model function to the experimental correlation function utilizing a constrained regularization method introduced by Provencher with the CONTIN program.[45]

4.3.3.2 Separation of Cluster Aggregates by Centrifugation

To enrich samples in single clusters relative to cluster aggregates and thus to improve their detectability by means of DLS, larger agglomerated structures were selectively removed by centrifugation. A corresponding experiment was performed with a mixture of 5 mM $CaCl_2$ and Na_2CO_3 in a 1-50 silica dilution. First, the sample was left to evolve for about 2 hours after mixing and characterized during that time by *in-situ* DLS

analysis. Subsequently, a part of the solution was withdrawn and centrifuged (Heraeus Biofuge Pico) for 90 min at a speed of 13000 rpm (16060 *g*). After centrifugation, a gel-like sediment covered the bottom of the vial, which probably formed due to an increase in the local silica concentration. The clear supernatant was transferred back into the DLS cuvette and continuous measurements were resumed for another 24 h.

4.3.4 Small-Angle X-Ray Scattering

4.3.4.1 Experimental

SAXS measurements were performed on a "SAXSess mc^2" instrument (Anton Paar GmbH, Graz, Austria) attached to an ID3003 sealed-tube anode X-ray generator (GE Sensing and Inspection Technologies, Germany), which was operated at 40 kV and 50 mA. A focused monochromatic beam of Cu-Kα radiation (wavelength λ = 1.54 Å) was obtained using a Göbel mirror and a slit collimation system. Reagents were mixed externally in vials and, after a delay of 30 min, injected via a flow-cell setup to a thin quartz capillary (1 mm inner diameter, 10 µm wall thickness) mounted in a holder (TCS 120) held at a constant temperature of 25°C. Mixtures of 5 mM $CaCl_2$ and 5 mM Na_2CO_3 in 1-50 silica showed good scattering contrast, such that an acquisition time of only 5 min was sufficient to produce data of satisfactory quality. As background, the Na_2CO_3-SiO_2 solution was combined 1-1 with water and measured under the same conditions.

Scattered X-rays were recorded with a CCD detector (Princeton Instruments PI.SCX:4300, having a 2048x2048 imaging array and a pixel size of 24x24 µm). Data were integrated into one-dimensional scattering patterns $I(q)$ as a function of the scattering vector q, which is defined as:

$$q = \frac{4\pi}{\lambda}\sin\left(\frac{\theta}{2}\right) \qquad \text{(Eqn. 4-4)}$$

with θ being the total scattering angle. The accessible q-range in the experiments was about 0.05-4 nm^{-1}. Primary data were processed with the SAXSquant software. Measured intensities were corrected for transmission as well as the empty-capillary and background scattering. Smearing effects caused by the chosen geometry were evaluated and accounted for by measuring the slit profiles. The resulting raw spectrum is displayed in Fig. 4-1.

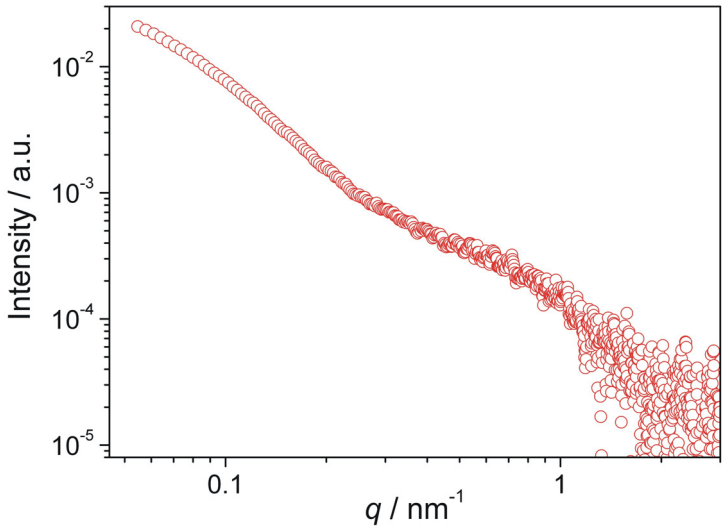

Fig. 4-1: Small-angle X-ray scattering pattern collected from a sample 30 min after mixing. $[Ca^{2+}] = [CO_3^{2-}] = 5$ mM, 3720 ppm silica.

4.3.4.2 Data Analysis by the IFT Method

Size and polydispersity analyses were performed based on the indirect Fourier transformation (IFT) method.[46] Thereby, clusters and their aggregates were in an approximation assumed to be homogeneous spheres with negligible inter-particle interaction. Under these conditions, the intensity-weighted size distribution $D_I(R)$ can be calculated by inverting

$$I(q) = \int_0^{R_{max}} D_I(R) \cdot \left[3 \frac{\sin(qR) - qR\cos(qR)}{(qR)^3} \right]^2 dR \qquad \text{(Eqn. 4-5)}$$

where R is a linear size parameter equal to the radius of the spheres and R_{max} the upper limit of a finite range of radii for which $D_I(R)$ shall be computed, herein chosen to be 40 nm. The distribution function thus obtained from the processed data is reproduced in Fig. 4-2. Finally, $D_I(R)$ was converted to the volume-weighted size distribution function $D_V(R)$ (cf. Fig. 4-18) via the following relation:

$$D_I(R) = R^3 \cdot D_V(R) \qquad \text{(Eqn. 4-6)}$$

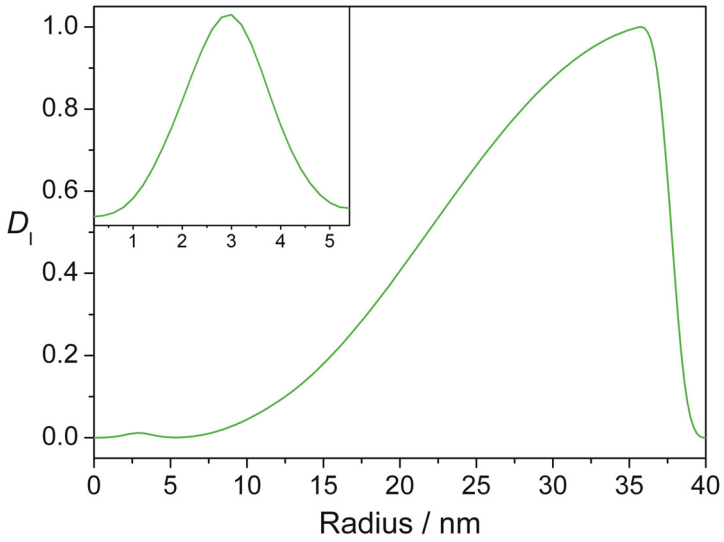

Fig. 4-2: Intensity-weighted size distribution profile calculated using Eqn. 4-5. The peak at radii < 5 nm is enlarged in the inset. Its resolution next to species with significantly larger dimensions demonstrates that the concentration of single clusters must be considerably higher than that of aggregates. Note that the steep decline in D_I between 35 and 40 nm is not a true feature of the sample, but originates from the fact that R_{max} was set to 40 nm in the calculations.

4.3.4.3 Determination of Particle Sizes by Guinier-Type Plots

In a second approach, particle sizes were derived on the basis of the Guinier approximation.[47] In the framework of this model, the intensity scattered by particles of arbitrary shape is supposed to decay in the regime of low q according to:

$$I(q) = I(0) \cdot \exp\left[-\frac{R_g^2}{3} \cdot q^2 \right] \qquad \text{(Eqn. 4-7)}$$

In general, Guinier's law can be applied for dilute isotropic systems after subtraction of the solvent or matrix background. The range of q in which Eqn. 4-7 holds is given by the condition $q_{max} \cdot R_g < 1$. In the present case, the upper limit of q was estimated assuming the average radius of single clusters to be 1.5 nm, as determined from the volume-weighted distribution function calculated with the IFT method (cf. Fig. 4-18). With a corresponding radius of gyration of 1.16 nm, q_{max} is found to be 0.86 nm^{-1} or, in terms of q^2, 0.74 nm^{-2}. To ensure validity, only data up to $q^2 = 0.7$ nm^{-2} were considered for evaluation.

4.3.5 Analytical Ultracentrifugation

4.3.5.1 Background

Analytical ultracentrifugation (AUC) is a powerful method for the characterization of small colloids, especially species with dimensions < 10 nm.[48] In a strong centrifugal field, particles sediment with a certain speed which is essentially determined by their size, density and shape. Different populations co-existing in a sample thus become fractionated in the course of the experiment and can therefore be detected in parallel and analyzed separately. Since under stationary conditions sedimentation is in equilibrium with back-diffusion, evaluation of measured radial concentration profiles allows for a direct calculation of both the sedimentation and diffusion coefficient, which can in turn be used to estimate particle sizes. As opposed to scattering techniques, multiple species present in a polydisperse system can readily be resolved by AUC without the disadvantage of size-dependent sensitivity.

4.3.5.2 Experimental

AUC measurements were performed on a Beckman-Coulter XL-I ultracentrifuge equipped with Rayleigh interference optics and operated at a constant speed of 60000 rpm. First test runs showed that at concentrations of 5 mM for $CaCl_2$ and Na_2CO_3 at 3720 ppm silica, the large number of clusters leads to strong disturbance of the signal and bad-quality data owing to convection. Therefore, all solutions were diluted 1-1 (v/v) with water prior to mixing. Experiments were conducted at 25°C and initiated immediately after reagents had been combined in a vial and subsequently injected into custom-designed titanium centerpieces with sapphire windows. Data were acquired overnight for at least 8 h. As references, pure $CaCl_2$ and silica solutions as well as mixtures of $CaCl_2$ and silica and Na_2CO_3 and silica were investigated under identical conditions. All samples were measured twice to ensure reproducibility.

4.3.5.3 Data Evaluation

Distinct sedimentation and diffusion coefficients were obtained by fitting experimental data with the Sedfit software package.[49] Previous efforts to detect $CaCO_3$ pre-nucleation clusters in supersaturated systems by means of AUC have shown that with the procedures also applied in this work, sedimentation coefficients of small clusters can be determined in a reliable manner even in the presence of a tremendous excess of likewise sedimenting ions.[25] For a situation in which different species migrate simultaneously in a centrifugal field, the Sedfit software provides a fitting routine yielding discrete values

of *s* and *D* for a predefined number of components, within the framework of a model assuming monodisperse individual populations and non-interacting species. Based thereupon, sedimentation and diffusion coefficients were calculated for all studied samples. The number of components n was varied and finally chosen for each system according to the quality of resulting fits. Generally, neat solutions of $CaCl_2$ and silica were found to be adequately described by a model involving 1-2 distinct species, whereas mixtures containing silica and either $CaCl_2$, Na_2CO_3 or both of them required prescription of 3-4 components to give satisfactory fits. Values thus obtained for *s* and *D* are listed in Table 4-5 and Table 4-6, respectively. Although Sedfit evaluations do in principle also permit conclusions about the relative concentrations of the different components, this parameter was not considered to be significant throughout the analyses, in compliance with literature.[25]

Particle sizes, i.e. their hydrodynamic diameter d_H, can be directly calculated from measured sedimentation coefficients using Eqn. 4-1, where η and ρ_S are the viscosity and density of the medium and ρ_P is the density of the particles).[48]

$$d_H = \sqrt{\frac{18\,\eta\,s}{\rho_P - \rho_S}} \qquad \text{(Eqn. 4-1)}$$

However, since the density is known neither for hydrated ions, nor for the clusters and their aggregates, the above equation can as such not be applied in the present case. An alternative way to derive particle sizes from the collected data is to convert the determined diffusion coefficients to hydrodynamic diameters, assuming spherical geometry for all species, via the Stokes-Einstein equation:

$$d_H = \frac{k\,T}{3\,\pi\,\eta\,D} \qquad \text{(Eqn. 4-2)}$$

where *k* is the Boltzmann constant and *T* the temperature.

4.3.6 Solution NMR spectroscopy

All NMR measurements were performed on a Bruker Avance III 600 instrument operating at 600.25 MHz. Samples were prepared using ^{13}C-enriched sodium carbonate (Aldrich, 99%) to be able to work in dilute solutions (5 mM). The pH was adjusted to desired values by adding small volumes of 1 M HCl or NaOH (Merck), and measured immediately before and after each NMR experiment with the aid of a microelectrode (Mettler-Toledo InLab Micro) connected to a Schott laboratory pH meter (model CG-

843). The chosen setup allowed for a determination of the pH with an accuracy better than ± 0.02 units. Furthermore, all manipulations during sample preparation and pH measurements were carried out in a glove box supplied with water-saturated nitrogen, in order to avoid any interfering influence of atmospheric CO_2. For NMR studies, solutions were filled in sample tubes under N_2, sealed with Parafilm and measured forthwith. Independent analyses on the evolution of pH with time in a typical sample (5 mM each of $CaCl_2$ and Na_2CO_3 in 1-50 silica) showed that, owing to silica condensation, the pH increases during the first 20 h after mixing from initially 11.00 to 11.08 and remains constant afterwards. Hence, this final value was taken as a benchmark to which the pH of the carbonate standards and the Ca-free reference was adapted relatively. Likewise, NMR measurements of the actual sample were started not before an ageing period of about 1 day.

For the determination of carbon-13 chemical shifts, NMR spectra were acquired at 298.0 K with a routine comprising 128 scans with a pulse width of 30% of 90° and a pulse delay of 2.0 s. Since working in purely aqueous media was preferred, acetonitrile-D_3 (Deutero GmbH, 99.96%) was added in thin, flame-sealed glass capillaries to the NMR tubes containing the samples. The observed δ values for carbonate species were normalized to the signal of the methyl group in CD_3CN (usually centered at 1.27 ppm) in each spectrum and are given relative to external tetramethylsilane standard.

Data for the experiments with pH-adjusted sodium carbonate solutions as internal standard were recorded in 256 scans with a pulse delay of 20 s, either in pure water as solvent without field lock or using mixtures prepared with D_2O (Deutero GmbH, 99.95%).

4.3.7 Solution IR Spectroscopy

In order to acquire IR spectra directly from the as-prepared solutions, reagents were mixed and injected after equilibration to a liquid cell consisting of two IR-transparent ZnSe plates with a lead spacer of 25 μm thickness in-between. Data were collected in transmission mode on a FT-IR instrument from Jasco (model 610) in 100 scans at a resolution of 2 cm^{-1}, with water as background.

4.3.8 Preparation of Dry Cluster Samples

In the following, procedures are described which were tested for transferring the cluster species traced in solution into a dry state without previous nucleation or structural rearrangements in general.

4.3.8.1 Direct Freeze-Drying

In a first approach, samples containing 5 mM of $CaCl_2$ and Na_2CO_3 in 1-50 silica and references without added $CaCl_2$ or Na_2CO_3 were quenched 1 hour after mixing by plunging 10 mL portions in glass vials into a reservoir of liquid nitrogen. Frozen solutions were dried in a lyophilizer (Edwards FreezeDryer Modulyo) for at least 3 days.

4.3.8.2 Dialysis

For dialysis, portions of 2.5 mL sample (5 mM $CaCl_2$ and Na_2CO_3, 1-50 silica) were pipetted in plastic tubes onto which a special cap securing a horizontal dialysis membrane was screwed (G-Biosciences Tube-O-Dialyzer Medi). The molecular weight cut-off (MWCO) of the membrane was chosen to be 1 kDa. Assuming that the clusters are composed of about 35 $CaCO_3$ units,[25] the membrane should hence easily prevent them from penetrating and let pass selectively simple salts and silicates. After fitting a float device to the filled tube, the whole assembly was inverted and placed on a stirred reservoir of pure water (~650 mL). The conductivity of the reservoir was monitored continuously so as to follow the progression of dialysis. Water was replaced every 24 h, until after 8 days no more changes in conductivity were observed. The resulting solution was a clear and colorless liquid, which was dried by freezing and subsequent lyophilization, yielding a fluffy white material.

4.3.8.3 Centrifugation

10 mL sample (5 mM $CaCl_2$ and Na_2CO_3, 1-50 silica) were mixed in a large plastic vial and subsequently ultracentrifuged (Beckman-Coulter XL-I) at 80000 rpm for 6 h. This led to the deposition of a gel body on the bottom of the vial which was removed with a spatula after decanting the supernatanty and rinsed briefly with water. Freeze-drying left about 0.05 g of a white solid.

4.3.8.4 Induced Precipitation

Partial coagulation of silica was induced by dissolving 0.4 M NaCl in 10 mM $CaCl_2$ and mixing the solution with 10 mM Na_2CO_3 in 1-50 silica. Samples turned noticeably

turbid already straight after mixing, and flocculation set in after some hours. Precipitates were isolated after equilibration for 1 day by filtration. The formed floccules were relatively coarse and could be rapidly separated with a filter of 5 μm pore size. Eventually, the filter papers carrying the residue were submerged in liquid nitrogen and immediately lyophilized, in order to preclude potential transformations during drying in air.

4.3.8.5 X-Ray Diffraction and IR Spectroscopy

Powders obtained by the different isolation procedures were studied by infrared spectroscopy, using pellets pressed from appropriate mixtures of sample and anhydrous potassium bromide (Merck, Uvasol). Data were acquired on a Varian Digilab FTS 800 spectrometer in 128 scans at a resolution of 2 cm^{-1}. Complementarily, powder X-ray diffraction (XRD) patterns were recorded on a STOE STADI P instrument operating with Cu-Kα radiation. Scans were performed over a 2θ range of 8-90° at a rate of 0.8°/min.

4.3.8.6 TEM Studies

For transmission electron microscopy, small drops of dialyzed solution were placed on hydrophilized carbon-filmed copper grids and left to evaporate in a flow of nitrogen. TEM studies were carried out on a Tecnai F30 ST microscope (University of Kiel), operated at 200 kV and equipped with a Gatan multiscan CCD camera. Images were processed and evaluated with the Digital Micrograph software as described in Section 4.3.2, except for that the cut-off radius chosen in the Butterworth filtering routine was set to 0.75 nm^{-1}. Elemental analyses were performed by energy-dispersive X-ray (EDX) spectroscopy.

4.3.9 Zeta Potential Measurements

4.3.9.1 Experimental

The Zeta potential of samples at different initial pH was determined using a Zetasizer Nano ZS from Malvern Instruments. It measures the velocity of colloids migrating in an applied electrical field by means of laser Doppler anemometry. The obtained electrophoretic mobility U_e is related to the Zeta potential ζ according to:

$$U_e = \frac{2\,\varepsilon\,\zeta\,f(\kappa a)}{3\eta} \qquad \text{(Eqn. 4-8)}$$

where ε is the dielectric constant of the dispersant, η its viscosity and $f(\kappa a)$ the Henry function (with κ and a being the Debye screening length and the particle radius, respectively). For measurement, samples were prepared and filled into clear disposable cells (total volume: 0.9 mL) immediately after combining reagents. Once the cell had been inserted into the instrument (~2 min after mixing), samples were equilibrated at 25°C for 5 min before data acquisition was started. The routine chosen to determine the Zeta potential comprised 10 subsequent measurements, each consisting of a minimum of 10 and a maximum of 100 individual runs. The particular number of performed runs and their duration were controlled by the auto-sampling mode of the instrument, which automatically rates the quality of the accumulated data. Usually, between 15 and 50 runs were sufficient to achieve "good" results. The period over which the Zeta potential was monitored thus varied from sample to sample, but typically covered an interval of 7-20 min after mixing. In general, there were no distinct temporal changes in the electrophoretic mobility discernible and results were therefore averaged. Electrophoretic mobilities were converted to Zeta potentials using the viscosity and dielectric constant of water at 25°C (η = 0.8872 cP, ε = 78.5) and the Smoluchowski approach for the Henry function (i.e. $f(\kappa a) = 1.5$).[50]

4.3.9.2 DLVO Calculations

The collected data were used to evaluate inter-particle potential energies in the framework of the Derjaguin-Landau-Verwey-Overbeek (DLVO) theory. This model has been developed based on the assumption that the total potential energy V_T of a particle in solution results from the balance of attractive van-der-Waals interactions (potential V_A) and repulsive electrostatic forces (potential V_R), and can be written as the sum of both contributions ($V_T = V_A + V_R$).[51] In a simplified manner and for uniform spherical

particles, the two terms can be expressed as defined in Eqns. 4-9 and 4-10, where A is the Hamaker constant and D the distance from the particle surface.

$$V_{\mathrm{A}} = -\frac{A}{12\pi D^2} \qquad \text{(Eqn. 4-9)}$$

$$V_{\mathrm{R}} = 2\pi\varepsilon a\zeta^2 \exp(-\kappa D) \qquad \text{(Eqn. 4-10)}$$

Calculations of V_{T} as a function of the distance D were carried out with the aid of the Hamaker 2.1.0 software.[53] It requires, as input parameters, the concentrations of all dissolved ionic species, the Zeta potential, and the Hamaker constant of the particles. Since the latter quantity is not known for $CaCO_3$ clusters to which silica is bound, the respective value of amorphous silica was used (A = 0.71 at 25°C).[53] This was considered to be the most reasonable approach, given that the periphery of the clusters is thought to be rich in silica and van-der-Waals forces are short-range interactions. In addition, rough estimations had to be made concerning the concentrations of carbonate and silicate ions in the system. While the absolute amount of the different carbonate species is known, the percentage of carbonate ions bound in the clusters remains uncertain. Therefore, calculations were conducted for a hypothetical case in which all carbonate exists free in solution. For each sample, the actual concentrations of carbonate and bicarbonate ions present in equilibrium were determined as described in Appendix A.1, using the respective initial pH. Moreover, the contributions of dissolved silicate oligomers to the ionic strength and charge-screening effects were completely neglected in the evaluations since, on the one hand, the amount of silica bound to the clusters is unknown. On the other hand, the fractional distribution of the various oligomers possibly present under the prevailing conditions (essentially monomers up to octamers, either cyclic or linear, but also polymers, and all potentially carrying distinct numbers of charges) is a complex function of the detailed composition and will vary sensibly with the pH (see Appendix A.1).[54] Consequently, determining the concentrations of the different species is a highly non-trivial issue which was not addressed in this work as other parameters turned out to affect the results much more substantially (see Section 4.4.12).

4.4 Results and Discussion

4.4.1 Nanoclusters in Silica-Rich Solutions of Calcium Carbonate

When $CaCl_2$ and Na_2CO_3 are mixed in the absence or the presence of modest amounts of silica, instant formation and aggregation of (silica-coated) ACC nanoparticles, with dimensions in the range of at least several tens of nanometers, impart a cloudy appearance to the sample and finally lead to the flocculation of an amorphous precipitate (see Chapter 2).[42] By contrast, when increasing the silica concentrations beyond a certain threshold (e.g. > 3000 ppm at 5 mM $CaCO_3$), the resulting mixture is a clear and transparent solution with no noticeable indication for visual precipitation. Particles present in such solutions were investigated by freezing aliquots at different times and studying a vitrified thin film by cryo-TEM. For a typical sample with an initial pH of 11, micrographs recorded shortly after mixing display a huge number of fairly small objects (Fig. 4-3).

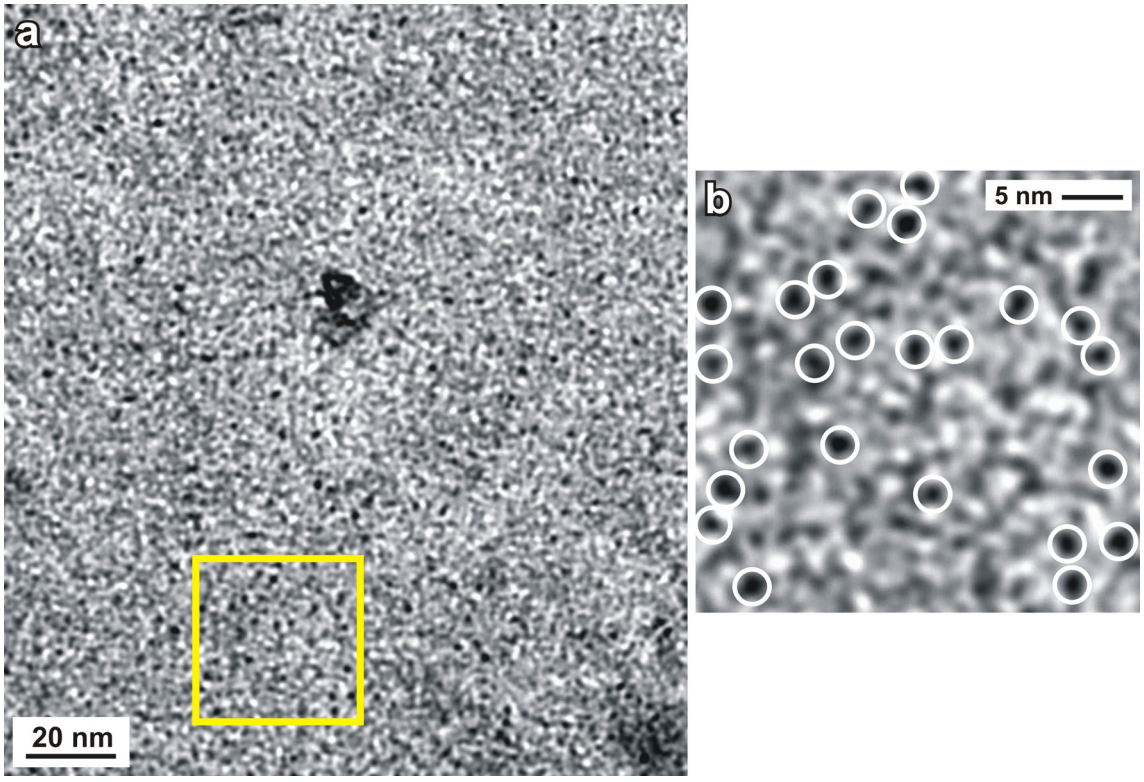

Fig. 4-3: Nanoclusters in silica-rich supersaturated solutions of calcium carbonate, quenched in liquid ethane 3 min after mixing reagents. (a) Cryo-TEM micrograph of a sample containing 5 mM $CaCO_3$ and 3720 ppm SiO_2 at pH 11. (b) Enlargement of the area delimited by the yellow rectangle in (a), illustrating the presence of myriad individual nanoclusters (highlighted by white circles).

Apparently, the high excess of silica used in the experiments effectively prevents rapid nucleation of calcium carbonate and the occurrence of larger ACC particles straight after mixing, as usually expected at the given supersaturation. Instead, $CaCO_3$ seems to exist exclusively in the form of nanoclusters. The diameter of these clusters, determined with the aid of a software routine (cf. Section 4.3.2), varies roughly between 0.5 and 3 nm (Fig. 4-4) and averages 1.1 ± 0.6 nm. Clusters observed in silica-rich media are thus slightly bigger than those found in pure solutions of calcium bicarbonate,[27] indicating that silica is bound in their periphery.

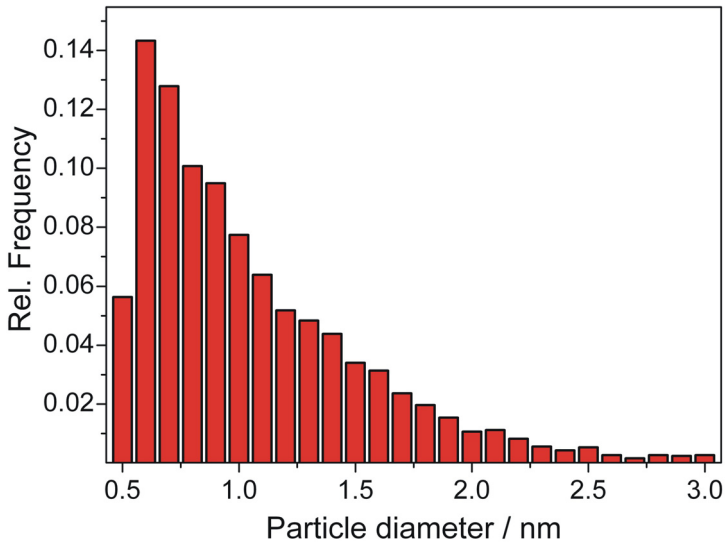

Fig. 4-4: Size distribution diagram obtained by measuring the clusters in the cryo-TEM images. The average cluster diameter is 1.1 ± 0.6 nm.

4.4.2 Aggregation behavior

Along with individual cluster species, cryo-TEM images frequently show larger diffuse entities with typical dimensions of 20-50 nm which, at a closer look, are identified as aggregates of more or less densely agglomerated single nanoclusters (Fig. 4-5). Continuous DLS monitoring of as-prepared solutions confirm that these aggregates exist in the samples virtually from the very beginning on. Most light scattering experiments were done at a concentration of 5 mM for $CaCl_2$ and Na_2CO_3 with a 1-50 silica dilution, and repeated multiple times to test reproducibility. Typical time-dependent progressions of the hydrodynamic radius R_H and the corresponding correlation coefficients R^2 of the monomodal fits for each run are shown in Fig. 4-6. It is evident that, subsequent to an initial period of induction, the apparent mean size of scattering species remains more or less constant with diameters in the range of 70 nm

(Fig. 4-6a). Likewise, the correlation coefficients of the fits exhibit consistently high values (around 0.9998) after some delay, indicating that a single population dominates the signal (Fig. 4-6b). In view of the cryo-TEM images, these species are identified as cluster aggregates. Although their frequency is low as compared to isolated clusters, it is reasonable to expect that the larger particles contribute by far strongest to the overall scattering, considering the R^6-dependency of sensitivity in light scattering techniques.

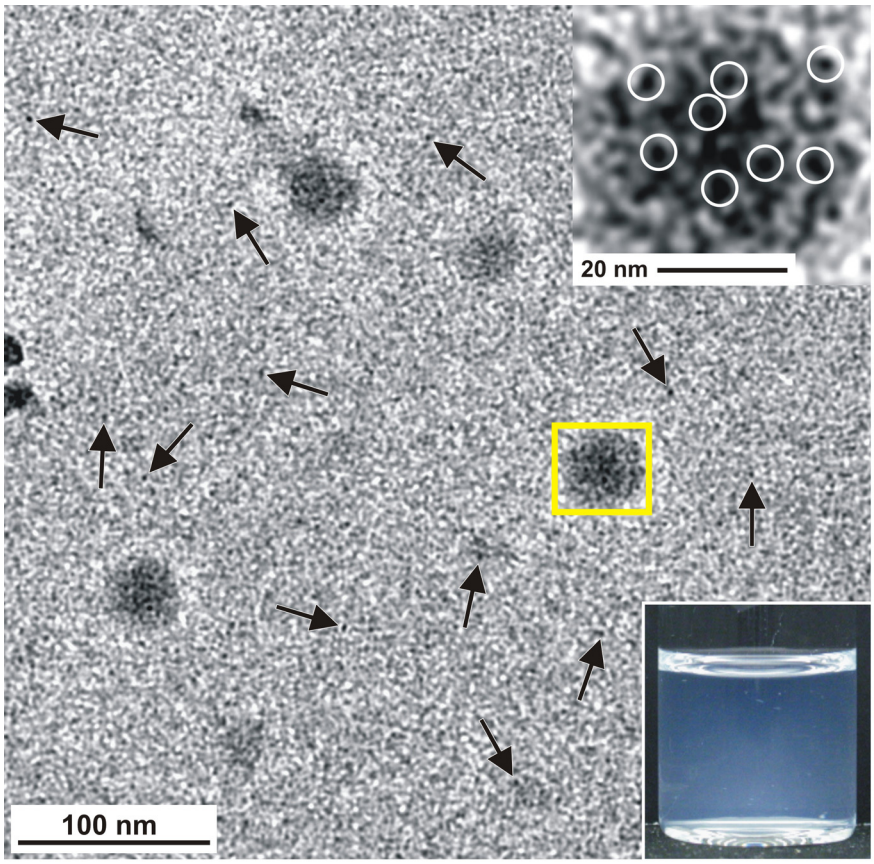

Fig. 4-5: Cluster agglomeration. Lower-magnification cryo-TEM image of a sample after 3 min, showing larger objects next to single cluster species (indicated by the arrows). A close-up view (top right) of the area marked in yellow suggests that the dark domains are aggregates of multiple clusters. The presence of these aggregates becomes manifest in a slightly turbid macroscopic appearance of the sample (see inserted photograph, bottom right).

To substantiate the existence of individual clusters next to larger agglomerates in the mixtures, size distributions were calculated based on the collected data. Typical distribution functions exhibit, as expected, a strong peak whose maximum is located at R_H values between 30 and 40 nm. This peak is usually quite broad, extending over several tens of nanometers and covering almost 100 nm in most cases. This suggests that the size of agglomerates varies in a wider range (commonly between 10 and 100 nm in terms of R_H) than suspected in view of the good correlation of monomodal fits to

the experimental data. Alongside, a discrete second population with hydrodynamic radii of about 3-6 nm can be discerned, though showing relatively weak intensity (Fig. 4-7). This signal verifies the presence of isolated cluster species. Again, the sheer detection of small clusters next to considerably larger aggregates by DLS corroborates that the concentration of the former must be substantially higher than that of the latter.

The detector count rate increases steeply during the first hours and asymptotically levels off towards the end of the measurement (Fig. 4-8). Given that the recorded correlation data all describe a quasi-monomodal decay, the intensity is a direct measure for the actual concentration of cluster aggregates.

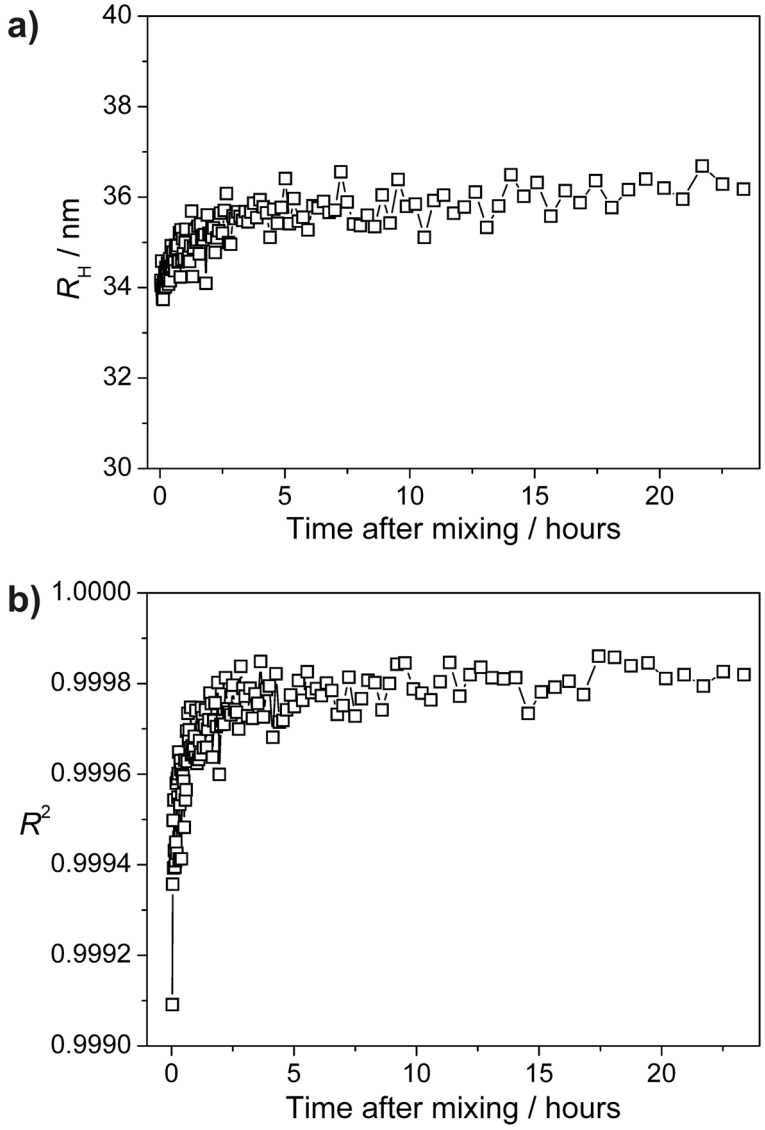

Fig. 4-6: (a) Apparent hydrodynamic radii R_H and (b) correlation coefficients R^2 obtained from monomodal fits to the experimental autocorrelation functions collected at distinct times after mixing reagents. $[Ca^{2+}] = [CO_3^{2-}] = 5$ mM, 3720 ppm silica.

Obviously, this implies that individual nanoclusters aggregate steadily over periods of hours to form assemblies of approximately similar dimensions. The rather narrow size distribution of the aggregates may be related to the generation of charge that limits further aggregation beyond a critical size.[55] The traced increase in the concentration of aggregates with time is visible to the naked eye, as the mixtures adopt a slight cast of blue after some hours (cf. inset in Fig. 4-5).

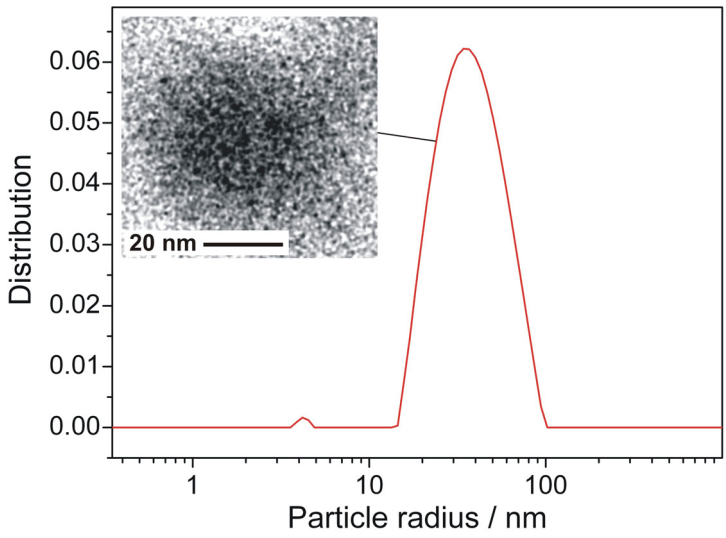

Fig. 4-7: Particle size distribution profile derived from DLS data collected within the first 5 min after mixing, with an inserted cryo-TEM image of a cluster aggregate.

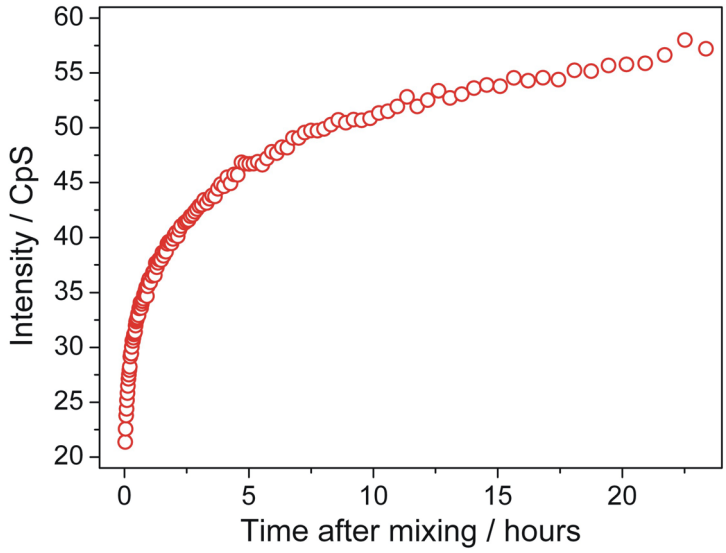

Fig. 4-8: Plot of the scattering intensity as a function of time in DLS experiments performed continuously over a period of 24 h after mixing.

Cryo-TEM analyses of equilibrated samples verify that although aggregated structures occur by trend more frequently, the number of single clusters is still overwhelming. Fig.

4-9 shows a compilation of images recorded from a sample which was allowed to age for about a day before quenching. Along with myriads of individual clusters, aggregates of various size and shape are observed. Primary agglomerates are thereby frequently seen to interconnect, reversibly forming structures with dimensions up to 200 nm (see inset in Fig. 4-9a). In turn, the size of individual clusters is comparable to that found immediately after reagents were mixed. The temporal increase in the fraction of cluster aggregates suggested by the scattering intensity (cf. Fig. 4-8) is not noticeably reflected in the micrographs. Likely, this is due to the fact that such large particles tend to be removed when blotting solutions during sample preparation for cryo-TEM. It should furthermore be noted that the diameters obtained for the two populations from DLS measurements significantly exceed those estimated from the cryo-TEM micrographs. This indicates marked hydration of the clusters and their aggregates although, in case of the latter, merging of primary cluster assemblies as seen in Fig. 4-9a is expected to significantly broaden the size distribution function towards radii larger than 50 nm.

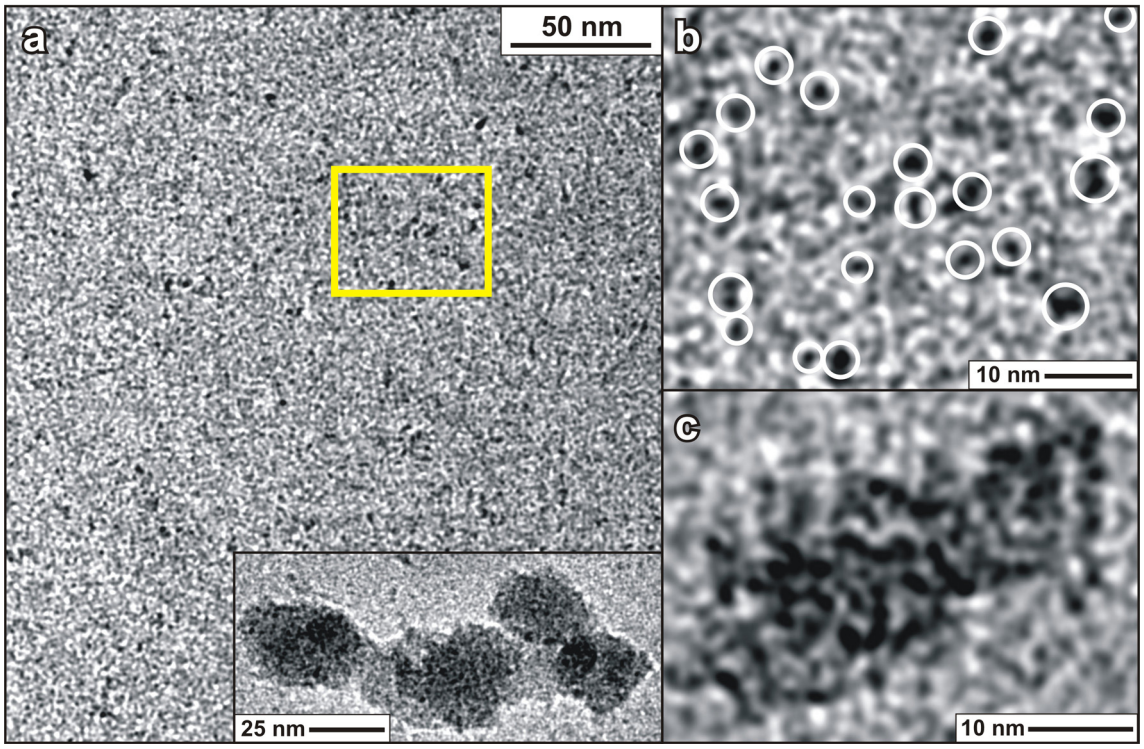

Fig. 4-9: Cryo-TEM micrographs of a sample left to evolve under quiescent conditions for 24 h at $[Ca^{2+}] = [CO_3^{2-}] = 5$ mM, 3720 ppm silica, and pH 11. (a) Overview of a region where only single nanoclusters are present. Inset: several cluster aggregates, all with diameters in the range of 30 nm, which have merged to form a larger structure, as detected by DLS. (b) Zoom into the yellow rectangle in (a), clearly confirming the existence of individual nanoclusters (white circles) in the system also after prolonged equilibration. The size of the clusters does not change significantly with time. (c) High-magnification image of a cluster aggregate.

The data reproduced in Fig. 4-9 and also images taken at later times demonstrate that homogeneous nucleation of calcium carbonate remains prevented in the system at pH 11. Likewise, visual inspections and optical microscopy verify that, apart from adopting a slight turbidity, the solutions do not change macroscopically over months, and neither flocculation nor crystallization on the walls occur. In fact, no further changes could be discerned with neither of the used methods even when the system was aged for more than a year. Therefore, it can be concluded that single nanoclusters and cluster aggregates co-exist permanently once the underlying aggregation processes have established a state of dynamic equilibrium.

4.4.3 Means to Enrich Samples in Single Clusters

Further efforts were made to increase the fraction of single clusters in the samples by decreasing the amount of cluster aggregates present, so as to gain better signal in DLS measurements for individuals. This was achieved on the one hand by raising the silica concentration and, with it, simultaneously also the pH and electrostatic repulsions. On the other, it was found that centrifugation of as-prepared samples at moderate speed permits selective separation of larger aggregates while single clusters remain suspended in solution.

4.4.3.1 Effect of the Silica Concentration

Samples with different contents of silica were investigated at a constant concentration of 5 mM for Ca^{2+} and CO_3^{2-}. For example, when a 1-25 dilution of water glass (instead of 1-50) is used for preparation, the resulting size distribution profile exhibits a quite intense peak centered at 1.65 nm and ranging from about 0.7 to 4 nm, together with a less distinct signal around 7.5 nm and a strong peak at $R_H \approx 60$ nm (Fig. 4-10). Though causing an increase in the mean size of the larger agglomerates, the higher $SiO_2/CaCO_3$ ratio primarily enables a considerable quantity of cluster species to remain isolated from one another. Possible reasons for this finding might be the elevated pH (~11.4) at higher silica concentration, which raises the amount of charges at siliceous species and thus reinforces mutual repulsion of silica-decorated clusters, or simply an increment in the absolute number of clusters existing in equilibrium with the free ions due to the enhanced availability of protecting silica. Smaller aggregates with hydrodynamic radii in the range of 10 nm were moreover repeatedly found in the analyses, and seem to represent a second preferred state of agglomeration for the clusters.

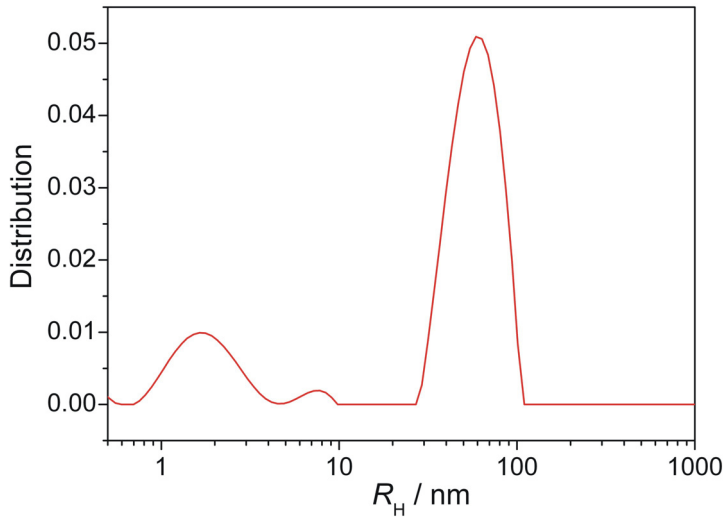

Fig. 4-10: Size distribution profile for a sample with increased silica content relative to $CaCO_3$. The curve was derived from a measurement started after 5 min with 20 min total duration. $[Ca^{2+}] = [CO_3^{2-}] = 5$ mM, 7440 ppm silica.

4.4.3.2 Centrifugation

Results of the centrifugation experiment described in Section 4.3.3.2 are shown in Fig. 4-11. It is evident that the larger aggregates were separated in the course of centrifugation, presumably due to accumulation at the bottom and incorporation to the forming silica gel body.

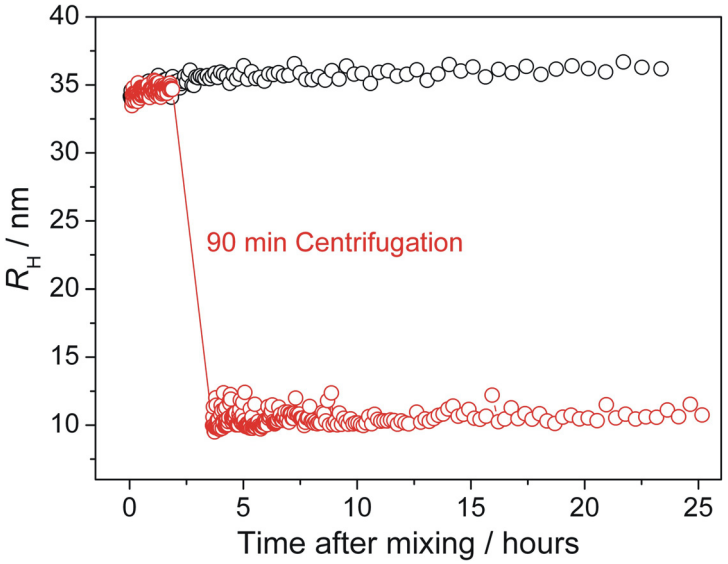

Fig. 4-11: Time-dependent progression of the apparent hydrodynamic radius in a sample which was centrifuged for 90 min about 2 h after mixing (red). Prior to centrifugation, values of R_H match in good agreement those of a reference with equal composition (black) measured continuously for 24 h without manipulation. Upon centrifugation, the average radius of scattering species drops by about 25 nm relative to the reference. $[Ca^{2+}] = [CO_3^{2-}] = 5$ mM, 3720 ppm silica.

Species remaining suspended in the solution now have average hydrodynamic radii of roughly 10 nm and exhibit a congruently decreased scattering intensity. Calculation of size distribution functions from correlation data acquired immediately after completed centrifugation proves the occurrence of an increased fraction of isolated clusters with R_H ≈ 1.3 nm along with aggregates around 9 nm in radius (Fig. 4-12). Both peaks are initially quite narrow, but experience marked broadening when the sample is allowed to stand for a day. Afterwards, no further changes were observed.

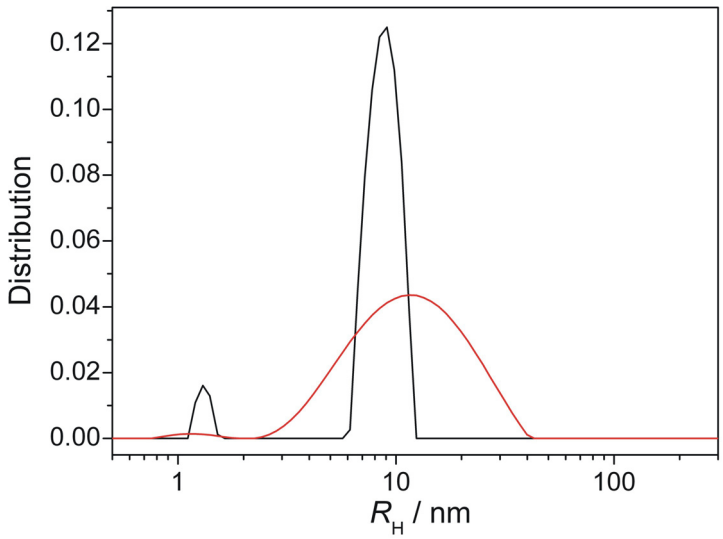

Fig. 4-12: Size distribution diagrams of a sample straight after 90 min centrifugation (black), and after subsequent equilibration for 1 day (red). Measurement duration: 10 min. $[Ca^{2+}]$ = $[CO_3^{2-}]$ = 5 mM, 3720 ppm silica.

Obviously, centrifugation leaves two at first discrete populations, namely single clusters and assemblies with reduced mean aggregation number. Based on equilibrium thermodynamics, it seems likely that upon effective elimination of a considerable quantity of clusters, new ones will be generated at the expense of previously free ions. With time, novel dynamic agglomeration processes under meanwhile modified conditions (overall less clusters and silica available) result in the formation of various aggregated species with different sizes, yet consistently smaller than the agglomerates traced prior to centrifugation. The latter can probably no longer be formed due to the lowered content of $CaCO_3$ after centrifugation.

Thus, with both methods the intensity of the peak at radii smaller than 5 nm could be markedly increased. Beyond that, the diameters obtained by DLS for individual clusters from the experiments at increased $SiO_2/CaCO_3$ ratio (3.3 nm) and after preceding centrifugation (2.6 nm) coincide well with the mean size determined independently by SAXS measurements (~3 nm, see below), and appear to be realistic values for the

species imaged by cryo-TEM (cf. Fig. 4-3) when considering a hydration shell around the silica-bearing clusters. By contrast, diameters detected for a regular sample (> 5 nm for 5 mM $CaCO_3$ / 3720 ppm silica, Fig. 4-7) differ notably in this respect. This might be due to shortcomings of data evaluation routines in a situation where scattering is dominated vastly by larger agglomerates and the signal of individual clusters is comparatively low. Alternatively, the small peak seen in size distribution functions could include contributions not only from single clusters, but also from smaller aggregates.

4.4.4 Variation of Distinct Experimental Parameters

In order to shed light on the interactions between individual cluster units that drive partial aggregation, additional DLS experiments were carried out in which the influence of factors like the age of the silica sol, the concentration of the reagents, the ionic strength, and the molar ratio of Ca^{2+} and CO_3^{2-} on particle sizes and agglomeration behavior was examined. Relevant parameters representing the results for selected samples are compiled in Table 4-2.

Sample	$R_{H,av}$ / nm	$t_{ind}(R_H)$ / h	R^2_{av}	$t_{ind}(R^2)$ / h
5 mM Ca^{2+}, 5 mM CO_3^{2-} 3720 ppm SiO_2	35.8 ± 0.4	5.1	0.9997	2.0
5 mM Ca^{2+}, 5 mM CO_3^{2-} 3720 ppm SiO_2 (aged)	55.0 ± 0.5	1.1	0.9998	0.5
10 mM Ca^{2+}, 10 mM CO_3^{2-} 7440 ppm SiO_2	55.0 ± 0.9	> 20	0.9997	0.5
5 mM Ca^{2+}, 25 mM CO_3^{2-} 3720 ppm SiO_2	46.9 ± 0.6	8.4	0.9998	0.7

Table 4-2: Results of continuous DLS measurements for selected samples. $R_{H,av}$: arithmetic mean of the hydrodynamic radius after initial induction period. R^2_{av}: average correlation coefficient of monomodal fits. $t_{ind}(R_H)$, $t_{ind}(R^2)$: approximate induction time before roughly constant values of R_H and R^2 are obtained.

Generally, dynamic aggregation processes were traced in all systems and fitting monomodal equations to the data of individual runs showed good correlation. Using an aged dilution of water glass (several months) for preparation leads to an increase in the final average agglomerate size and propagates the rate of aggregation. In turn, gradual aggregation to eventually larger entities is observed when the concentrations of all

species involved are doubled. Raising stepwise the amount of added carbonate at a constant concentration of Ca^{2+} also provokes an increment in the hydrodynamic radius of the presumed cluster agglomerates.

These results provide clear evidence that the rate and final degree of aggregation can be correlated with the speciation of silica in solution expected under the respective conditions. In all cases, aggregation starts straight after mixing and produces, within a certain frame of time (the induction period), agglomerates of well-defined size which do not grow further. The latter might be the consequence of a compromise between attractive (covalent linking, H-bonds) and repulsive (negative charges) forces. In that sense, the mean size of aggregates will essentially be determined by the propensity of silica to undergo condensation processes. Coherently, the age of the used sol plays a crucial role in this context, that is, aggregation is the faster and final aggregates the larger the older the silica sol (and hence the higher the fraction of oligomerized species). Similar changes occur when the overall concentrations of the reagents are incremented, since more clusters to be connected and a higher amount of screening Ca^{2+} cations are available. The notion that silica oligomerization processes account for the cross-linking of single clusters is moreover supported by the observation that the pH of a standard sample (5 mM $CaCO_3$, 3720 ppm silica) increases by about 0.1 units during the first 24 hours. Polycondensation of silica has been reported to provoke an increase in pH as acidic silanol groups are consumed.[56] More subtle effects appear to operate when the Ca^{2+}/CO_3^{2-} ratio is varied. Importantly, it must be stressed that even at an enormous excess of carbonate ions relative to Ca^{2+} (e.g. 100 mM CO_3^{2-} vs. 5 mM Ca^{2+} at 62 mM SiO_2), no crystallization of $CaCO_3$ or nucleation of ACC is observed. Rather, the measured size of cluster agglomerates grows continuously until large assemblies are formed and flocculation of an amorphous precipitate occurs. Therefore, it can be excluded that prevention of crystallization relies on direct binding of Ca^{2+} to silicate species in competition with carbonate ions. In light of these findings, the enhanced degree of agglomeration traced at increased carbonate concentrations likely originates from the higher ionic strength of the system, in particular when noting that reference experiments with added NaCl instead of excess Na_2CO_3 showed comparable trends.

Size distribution profiles of samples with elevated carbonate concentration (red curve in Fig. 4-13) display a broad peak for cluster agglomerates which is shifted slightly towards higher R_H compared to the mixture equimolar in Ca^{2+} and CO_3^{2-} (cf. Fig. 4-7), in agreement with the average hydrodynamic radii calculated from the continuous

measurements (cf. Table 4-2). By contrast, the position of the peak for single clusters does not change appreciably, again indicating that excess carbonate ions do not affect the size (and structure) of individual clusters, but barely their aggregation behavior by raising the salinity. Increasing the total concentration of the system by a factor of 2 significantly alters the corresponding size distribution function (black curve in Fig. 4-13). Aside from a major peak around 50-55 nm, additional weaker features arise at both higher (300-400 nm) and lower (~10 nm) R_H values, whereas a signal for isolated clusters is no longer resolved. Apparently, the high abundance of silica-decorated clusters promotes aggregation to an extent that at least several individuals are connected on average.

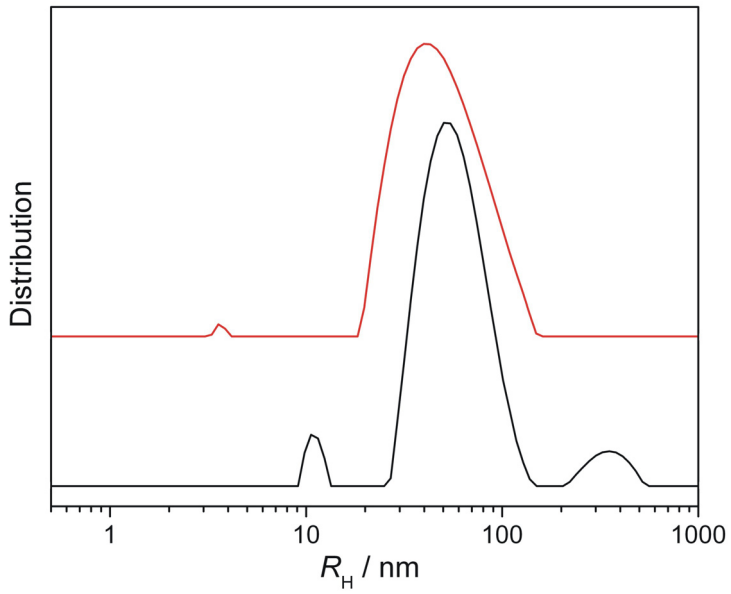

Fig. 4-13: Size distribution functions obtained for samples at increased total species concentrations (black, $[Ca^{2+}] = [CO_3^{2-}] = 10$ mM, 7440 ppm silica) and a higher CO_3^{2-}/Ca^{2+} ratio (red, $[Ca^{2+}] = 5$ mM, $[CO_3^{2-}] = 25$ mM, 3720 ppm silica).

4.4.5 Reference Systems

To ascertain that the traced cluster species are in fact precursors of calcium carbonate and do not originate from the precipitation of any other compound (e.g. pure silica or calcium silicate), reference samples were investigated in which one of the reagents was omitted (either $CaCl_2$ or Na_2CO_3) such that $CaCO_3$ formation cannot occur. In the reference without added carbonate (i.e. a sample containing 5 mM $CaCl_2$ and 3720 ppm SiO_2, but no Na_2CO_3), similar aggregation phenomena as in the standard system are observed, with minor differences regarding absolute values of R_H and the count rate (Fig. 4-14). By contrast, DLS data collected in the absence of Ca^{2+} (5 mM Na_2CO_3 in 1-

50 silica) differ drastically from those reported above. Monomodal evaluation yields a dominant population with high polydispersity (estimated by the relatively poor quality of the fits) and hydrodynamic radii around 50 nm (Fig. S7). Neither R_H nor the scattering intensity display noticeable changes with time. Moreover, as the count rate is very small, the concentration of aggregates in the system should be markedly lower than in the presence of Ca^{2+}. This becomes also manifest in the macroscopic appearance of the sample, which is a clear and colorless solution lacking the faint turbidity distinguishing mixtures to which Ca^{2+} ions were added.

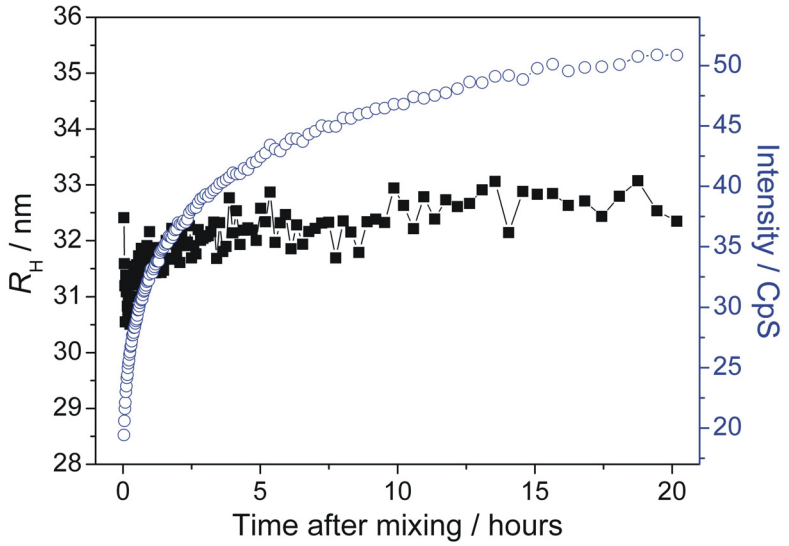

Fig. 4-14: Temporal evolution of the apparent hydrodynamic radius of scattering species (black) and the scattering intensity (blue, in counts per second) in a sample containing no carbonate. $[Ca^{2+}]$ = 5 mM, 3720 ppm silica.

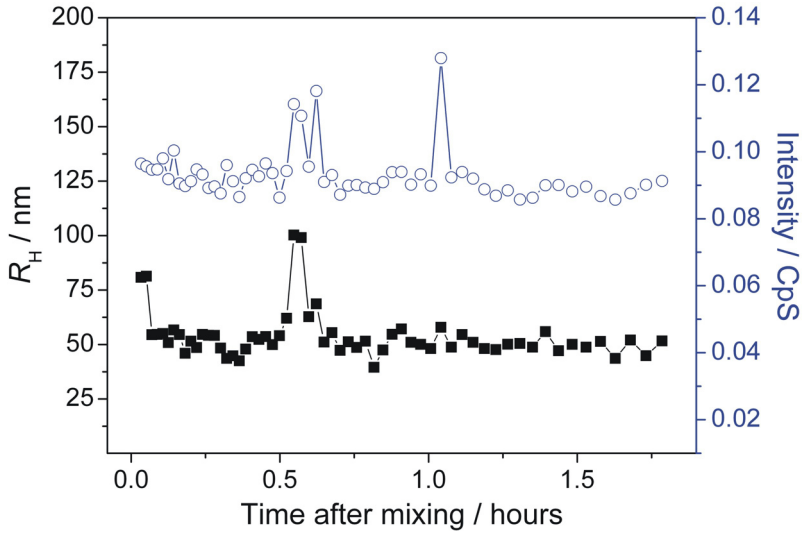

Fig. 4-15: R_H (black) and the scattering intensity (blue) outlined as a function of time for the Ca^{2+}-free reference. $[CO_3^{2-}]$ = 5 mM, 3720 ppm silica.

Parameters characterizing the traced evolution of particle size and intensity in the two references are listed in Table 4-3, together with the data of the standard system for comparison. It is obvious that although there are bigger entities in all three samples, their abundance is dramatically enhanced as soon as Ca^{2+} ions are introduced.

Sample	$R_{H,av}$ / nm	$t_{ind}(R_H)$ / h	R^2_{av}	$t_{ind}(R^2)$ / h
5 mM Ca^{2+}, 5 mM CO_3^{2-} 3720 ppm SiO_2	35.8 ± 0.4	5.1	0.9997	2.0
5 mM Ca^{2+}, No CO_3^{2-} 3720 ppm SiO_2	32.4 ± 0.4	2.0	0.9997	3.2
No Ca^{2+}, 5 mM CO_3^{2-} 3720 ppm SiO_2	51 ± 5	0	0.9702	0

Table 4-3: Parameters obtained from in-situ DLS analyses of reference samples lacking either Ca^{2+} or CO_3^{2-}, as compared to the system in which both are present.

Reasonably, the presence of Ca^{2+} promotes cross-linking of siliceous species and clusters associated to them by screening negative charges.[57] However, this implies as well that binding of Ca^{2+} (and CO_3^{2-}) ions in clusters cannot be quantitative in the system $CaCl_2$-Na_2CO_3-SiO_2 but that a significant fraction of the ions must remain more or less free in solution, probably in equilibrium with those bound in clusters. Size distribution functions calculated for the two references based on DLS data acquired during the first 5 min after mixing are shown in Fig. 4-16.

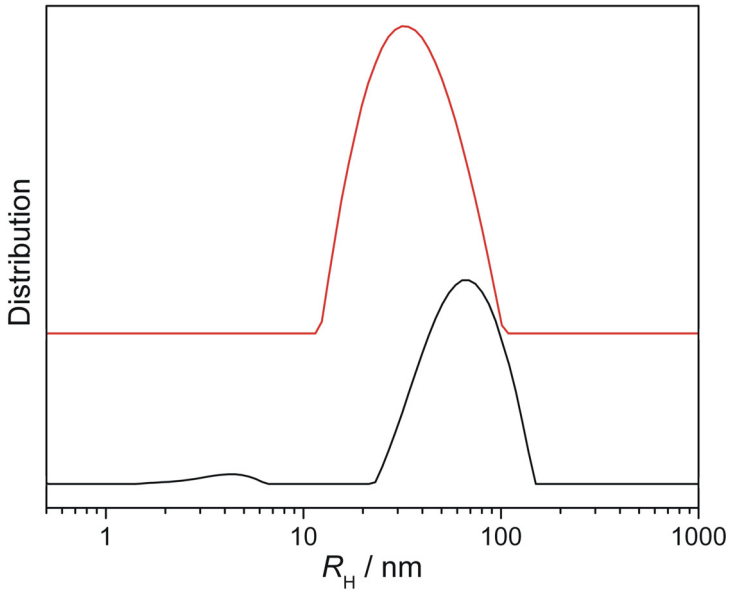

Fig. 4-16: Size distribution profiles derived for samples containing no Ca^{2+} (black) and no CO_3^{2-} (red).

The intense peak representing larger aggregates is located at a similar position in the CO_3^{2-}-free reference as found for the standard sample and has a comparable width (cf. Fig. 4-7), whereas it is shifted to larger R_H values in case of the system devoid of Ca^{2+}. Further, there is broad feature at hydrodynamic radii between 2 and 7 nm in the distribution function of the latter sample, while no such signal occurs for the mixture without added carbonate. The absence of a peak in this region does however not necessarily imply that the respective sample does not contain individual clusters. Rather, since the integral intensity of the cluster peak is small compared to that of cluster agglomerates due to size-dependent sensitivity, it cannot be resolved when the concentration of clusters is too low relative to the amount of aggregates. Therefore, it can be concluded that although stable cluster species appear to be formed likewise when either $CaCl_2$ or Na_2CO_3 are dissolved in the silica sol (see Section 4.4.8), their concentration is highest when both salts are mixed. Another important observation is that pure silica solutions without added salts do not show interpretable correlation in DLS measurements. This demonstrates that the occurrence of clusters and aggregates in the Ca^{2+}-free reference is intimately associated to the presence of sodium carbonate, and that cluster-like silica colloids occasionally found in neat silica sols[35] do not contribute noticeably to the DLS signal.

Cryo-TEM images of the system without added carbonate display quite polydisperse spherical particles with diameters roughly ranging from 20 to 40 nm (Fig. 4-17a), which become subject to noticeable agglomeration building variously shaped network and chain structures (Fig. 4-17b).

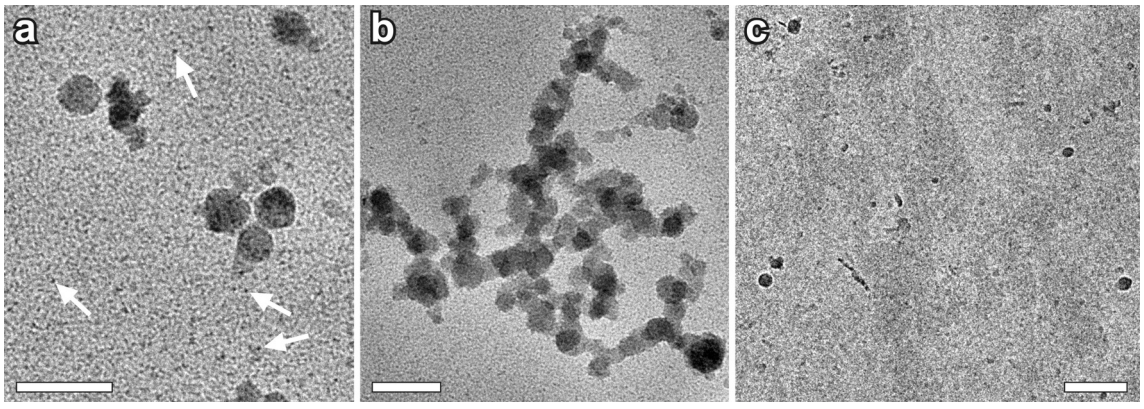

Fig. 4-17: Cryo-TEM micrographs of reference samples containing (a-b) no carbonate (5 mM $CaCl_2$ in 1-50 silica), and (c) no calcium (5 mM Na_2CO_3 in 1-50 silica). Images were taken 30 min after sample preparation.

Next to these, small objects measuring less than 5 nm can also be discerned (see arrows in Fig. 4-17a). Apparently, cluster-like species are also inherent in the carbonate-free reference, as suggested also by the AUC data (see below).

In the system without added $CaCl_2$, by far less characteristic features could be distinguished in the micrographs. Generally, there are compact particles exhibiting a size distribution centered around 20 nm, as well as some smaller objects with diameters below 10 nm (Fig. 4-17c). Due to their low concentration, it cannot be ascertained unambiguously whether the observed particles are single clusters and aggregates thereof, possibly based on Na_2CO_3 and interconnected by bound silica, or purely siliceous colloids. Similar particle populations (i.e. fragments of only few nanometers in diameter as well as larger spherical and partially agglomerated colloids) were indeed also found in sodium silicate solutions devoid of both $CaCl_2$ and Na_2CO_3, although their occurrence is in this case by trend rarer. However, a sheer comparison of corresponding cryo-TEM images to those acquired for samples containing Na_2CO_3 does not allow for a reliable estimation of relative frequencies, which can rather be achieved on the basis of the DLS data. Finally, it should be noted that micrographs taken from vitrified water as a blank do not display any noticeable features, hence verifying its purity and precluding feasible artifacts due to contaminations.

4.4.6 Determination of Cluster Size by SAXS

The existence of nanoclusters in the standard samples was furthermore substantiated by small-angle X-ray scattering (SAXS). Since, relative to the under- or slightly supersaturated solutions in which $CaCO_3$ prenucleation clusters were previously detected,[25,27] the concentration of clusters in the present systems is high, the contrast of the samples was excellent, thus facilitating good-quality data even at short acquisition times. Recorded spectra were processed (Fig. 4-1) and used to derive, by means of the indirect Fourier transformation (IFT) method (see Section 4.3.4.2), intensity-weighted particle size distribution functions (Fig. 4-2). As in the DLS experiments, larger aggregated structures contribute disproportionately to the overall scattering. To account for the polydispersity of the system and retrieve a representative picture of the numerical frequency of species with distinct sizes in the sample, the intensity distribution function was weighted with the volume expected under the assumption of a spherical geometry for all particles (cf. Eqn. 4-6). The resulting volume distribution of particle radii is shown in Fig. 4-18.

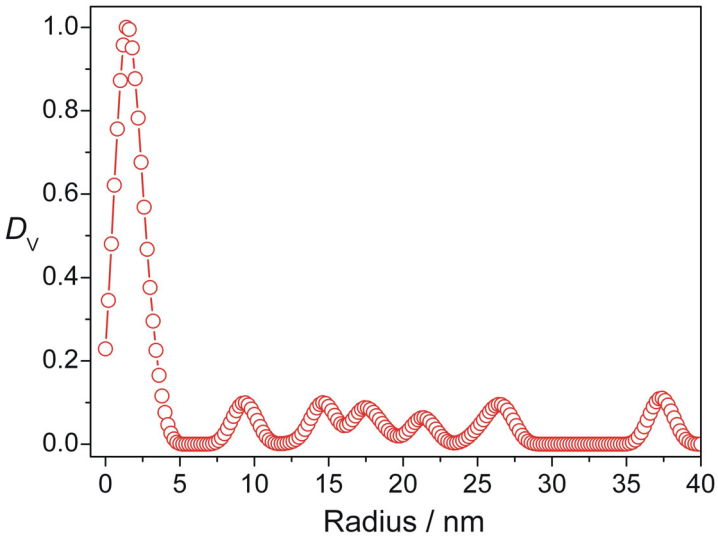

Fig. 4-18: Volume-weighted size distribution function $D_V(R)$ calculated on the basis of the SAXS data for non-interacting spherical particles.

In accordance with observations made by cryo-TEM, a strong and rather narrow peak at radii < 5 nm suggests that a major fraction of the clusters exists in an isolated state in the solution. The maximum of the peak is located at about 1.45 nm and hence confirms the mean size estimated from DLS measurements for hydrated clusters (see Section 4.4.3). Alongside, the distribution function exhibits several smaller peaks at radii between 10 and 40 nm, presumably all belonging to cluster assemblies with different aggregation numbers.

Similar results were obtained when evaluating the data separately via a Guinier analysis (see Section 4.3.4.3). From Fig. 4-19, it is evident that the resulting Guinier plot is not linear over the entire range inspected, but can rather be described by fitting multiple straight lines to distinct sections of the curve. Such behavior is comprehensible with regard to the polydispersity of the sample. A fairly long and flat quasi-linear branch in the plot over a q^2-range of 0.2-0.7 nm^{-2} indicates small particles. The presence of larger aggregates becomes noticeable towards lower q-values, where marked deviation from linearity is observed. As the slope of the curve increases more or less continuously in this region, it can be inferred that agglomerates with various sizes (i.e. aggregation numbers) co-exist in the system. To account for this, the curve was exemplarily segmented by choosing six intervals in which data points show satisfactorily linear trends. The regions selected for the fits and the resulting parameters are summarized in Table 4-4. Values thus obtained for the average size of the discrete populations agree reasonably well with those from the IFT evaluation. In particular, the radii estimated for

the larger aggregates (R ≥ 10 nm) approximately coincide with the position of the respective maxima in the volume distribution function (cf. Fig. 4-18 and Table 4-4).

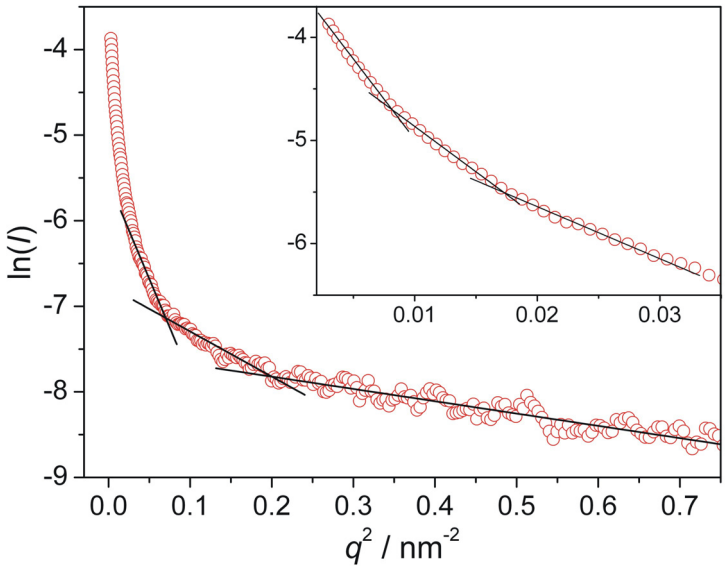

Fig. 4-19: Guinier representation of the processed SAXS spectrum displayed in Fig. 4-1. The region of very low q is enlarged in the inset. Black lines are linear fits to the data in predefined intervals.

q^2-range for fit / nm^{-2}	R^2	Slope / nm^2	R_g / nm	R / nm	$R_{max}(D_V)$ / nm
0.003..0.008	0.9980	-156 ± 3	21.6 ± 0.4	27.9 ± 0.6	26.5
0.008..0.017	0.9975	-88 ± 2	16.2 ± 0.4	21.0 ± 0.5	21.3
0.017..0.030	0.9965	-50 ± 1	12.3 ± 0.3	15.9 ± 0.4	14.6 / 17.5
0.030..0.070	0.9868	-22.7 ± 0.7	8.3 ± 0.3	10.7 ± 0.3	9.3
0.070..0.200	0.9662	-5.3 ± 0.2	4.0 ± 0.1	5.1 ± 0.2	---
0.200..0.700	0.9301	-1.44 ± 0.05	2.08 ± 0.07	2.7 ± 0.1	1.5

Table 4-4: Fit parameters and apparent particle radii for a multiple-species Guinier-type analysis of the SAXS data. Radii (R) were calculated under the assumption of spherical geometry. R^2: correlation coefficient of the fit. R_g: radius of gyration. $R_{max}(D_V)$: maxima in the volume distribution function corresponding to the different particle populations distinguished in the Guinier plot.

More significant discrepancies are in turn noted concerning the size of single clusters and small agglomerates. The lowest radius received from Guinier plots when varying the fitted interval amounts to around 2.5-2.7 nm, and hence exceeds those predicted by the IFT method and measured in electron micrographs for individual particles. Probably, the Guinier procedure does under the given conditions not permit a

differentiation of single species and aggregates of only a few clusters, consequently yielding intermediate values for the radius.

Essentially, both the IFT and Guinier evaluation of the SAXS data confirm that there is not a single preferential size for the cluster aggregates as indicated to some degree by the DLS measurements (cf. Fig. 4-6). Rather, multiple populations with distinct apparent diameters in the range of 10-100 nm could be detected. The contributions of all these species merge and overlap in the DLS signal, giving a single broad peak in the size distribution function (Fig. 4-7), which in addition tends to be shifted to larger R_H values due to the higher weight of bigger particles in the distribution.

4.4.7 Cluster Detection by Analytical Ultracentrifugation

In another set of experiments, nanoclusters present in the systems were characterized by analytical ultracentrifugation (AUC). Sedimentation and diffusion coefficients yielding from multiple-component analyses of the data are listed for various samples in Table 4-5 and Table 4-6.

Sample	***n***	**Sedimentation coefficient / S**			
		Species 1	Species 2	Species 3	Species 4
$CaCl_2$	1 / 2	0.15 / 0.49	--- / 0.98	---	---
SiO_2	2	0.03 / 0.34	0.76 / 0.96	---	---
Na_2CO_3-SiO_2	4 / 3	0.12 / 0.09	0.52 / 0.57	1.32 / 1.42	2.91 / ---
$CaCl_2$-SiO_2	3 / 4	0.26 / 0.26	0.50 / 0.32	2.76 / 5.49	--- / 9.05
$CaCl_2$-Na_2CO_3-SiO_2	4 / 3	0.26 / 0.08	0.41 / 0.55	3.37 / 3.22	13.08 / ---

Table 4-5: Sedimentation coefficients obtained from AUC experiments with various samples ([$CaCl_2$] = [Na_2CO_3] = 2.5 mM, 1860 ppm silica). Measurements were conducted twice and the results for each run are listed. Proper description of the data required a differing number of components *n* to be assumed for fitting.

The observed sedimentation coefficients can roughly be subdivided into four relevant intervals (Fig. 4-20), partly following a classification suggested by Pouget *et al.*.[27] Values in the range of 0-0.5 S are assigned to ions which were, as expected, traced in all experiments. Species with $0.5 < s < 2$ were consistently found in samples containing silica, regardless of the presence of $CaCl_2$ and/or Na_2CO_3, and are therefore interpreted as low-molecular silicate oligomers (dimers, trimers, cyclic structures etc.) commonly present in alkaline silica sols. Distinct from these, mixtures of $CaCl_2$, Na_2CO_3 and silica (system (4) in Fig. 4-20) contain a further population with $2 < s < 3.5$, most likely

corresponding to the multitude of individual nanoclusters recognized in cryo-TEM images. Finally, a fourth component was repeatedly identified exhibiting quite large *s* values (> 5 S) and hence sedimenting rapidly at the given high angular velocity, which is allocated to cluster aggregates in agreement with the DLS and SAXS data (see Sections 4.4.2 and 4.4.6).

Sample	***n***	**Diffusion coefficient / 10^{-6} cm^2s^{-1}**			
		Species 1	Species 2	Species 3	Species 4
$CaCl_2$	1 / 2	12.69 / 15.26	--- / 6.28	---	---
SiO_2	2	8.22 / 9.12	2.91 / 5.67	---	---
Na_2CO_3-SiO_2	4 / 3	9.61 / 9.32	5.26 / 5.35	2.40 / 1.95	0.11 / ---
$CaCl_2$-SiO_2	3 / 4	9.58 / 8.98	3.97 / 1.91	0.96 / 0.11	--- / 0.10
$CaCl_2$-Na_2CO_3-SiO_2	4 / 3	10.57 / 9.86	4.45 / 6.26	1.06 / 1.94	0.11 / ---

Table 4-6: Diffusion coefficients of the distinct species traced by AUC measurements.

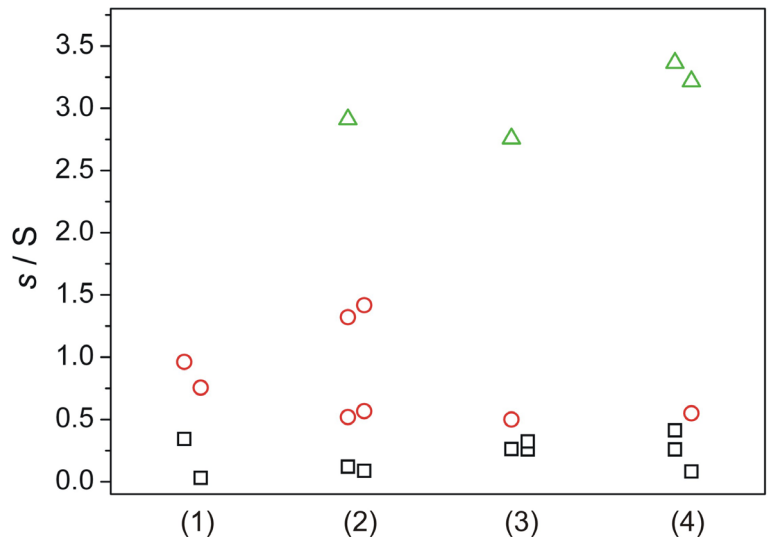

Fig. 4-20: Sedimentation coefficients measured for samples containing (1) only silica, (2) Na_2CO_3 and silica, (3) $CaCl_2$ and silica, and (4) $CaCl_2$, Na_2CO_3 and silica. According to the classification mentioned in the text, *s* values expected for free ions, low-molecular silica oligomers and nanoclusters are drawn in black, red and green, respectively.

The sedimentation coefficients found for single clusters are somewhat higher than those reported previously (1.5-3 S).[25,27] This difference may be ascribed to binding of silica on the clusters, which increases their effective size. Further, species with *s* values in the ranges typical for nanoclusters and cluster aggregates do also occur in the reference samples Na_2CO_3-silica and $CaCl_2$-silica (systems (2) and (3) in Fig. 4-20), as suggested

likewise by DLS measurements and cryo-TEM images. The origin of these species will be discussed in detail in Section 4.4.8.

The notion of silica binding onto the clusters is confirmed by the apparent hydrodynamic diameters calculated on the basis of the measured diffusion coefficients for the clusters (Table 4-7).

Sample	*n*	Diameter from diffusion coefficient / nm			
		Species 1	Species 2	Species 3	Species 4
$CaCl_2$	1 / 2	0.39 / 0.32	--- / 0.78	---	---
SiO_2	2	0.60 / 0.54	1.68 / 0.87	---	---
Na_2CO_3-SiO_2	4 / 3	0.51 / 0.53	0.92 / 1.24	2.04 / 2.52	44.36 / ---
$CaCl_2$-SiO_2	3 / 4	0.51 / 0.55	1.24 / 2.56	5.13 / 46.36	--- / 49.70
$CaCl_2$-Na_2CO_3-SiO_2	4 / 3	0.46 / 0.50	1.10 / 0.78	4.61 / 2.53	42.94 / ---

Table 4-7: Apparent hydrodynamic diameters of sedimenting species calculated from the measured diffusion coefficients via the Stokes-Einstein equation (Eqn. 4-2). Note that in view of due polydispersity of individual populations, results should be considered lower limits for the true values of d_H.[25]

Previous calculations of d_H in systems containing $CaCO_3$ clusters without any additive gave averaged values of about 0.4 and 2 nm for free hydrated ions and single clusters, respectively.[25] The presence of silica complicates the situation and does no longer allow for such a discrete separation of components. For instance, free ions (Species 1 in Table 4-7) display in this case mean diameters slightly larger than actually expected for simple ions (cf. values for pure $CaCl_2$ solution). This might be ascribed to a superposition of signals belonging to e.g. Na^+ and abundant silicate monomers. Oligomers exhibit apparent sizes between 0.7 and 1.7 nm, while the diameters of presumed clusters roughly range from 2 to 6 nm. However, it is proximate that these two populations overlap to some extent and that there is no sharp boundary between them during sedimentation. In any case, the size of individual clusters determined by AUC notably exceeds that measured in cryo-TEM images (predominantly 1-2 nm, see Fig. 4-4). Differences can on the one hand clearly be attributed to the hydration shell around the clusters, which is enhanced when they are coated by charged silicate species and reflected as well by the DLS and SAXS data. On the other hand, we cannot exclude the possibility that the 2-6 nm population discerned in AUC experiments also comprises a certain fraction of smaller cluster agglomerates. Exemplarily, hydrodynamic diameters were calculated for the system $CaCl_2/Na_2CO_3/SiO_2$ with Eqn. 4-3 utilizing the density

of ACC (ρ_{ACC} = 1.48 g/mL)[25] as an approximation for the clusters and thus neglecting the contribution of bound silica. The resulting sizes for Species 3 in Table 4-7 are 3.34 and 3.21 nm and do hence comply fairly well with the average of the values received when using the Stokes-Einstein equation (4.61 and 2.53 nm). Eventually, the diffusion coefficients and corresponding hydrodynamic diameters estimated for Species 4 in Table 4-6 and Table 4-7 suggest the occurrence of larger cluster aggregates (40-50 nm) in mixtures of silica and one or both of the salts, in good agreement with the DLS data (see Section 4.4.5).

Additional experiments were carried out during which, at a given concentration of $CaCl_2$ and Na_2CO_3, the content of silica in the mixtures and the period of ageing before measurement start were varied. Replacing the otherwise used 1-100 dilution of water glass by a 1-125 (effectively 25 mM instead of 31 mM silica) led to a reduction of the observed sedimentation coefficient of cluster species by about 0.3-0.5 and 1 S in samples of both 2.5 mM Na_2CO_3 and $CaCl_2/Na_2CO_3$, respectively (Fig. 4-21).

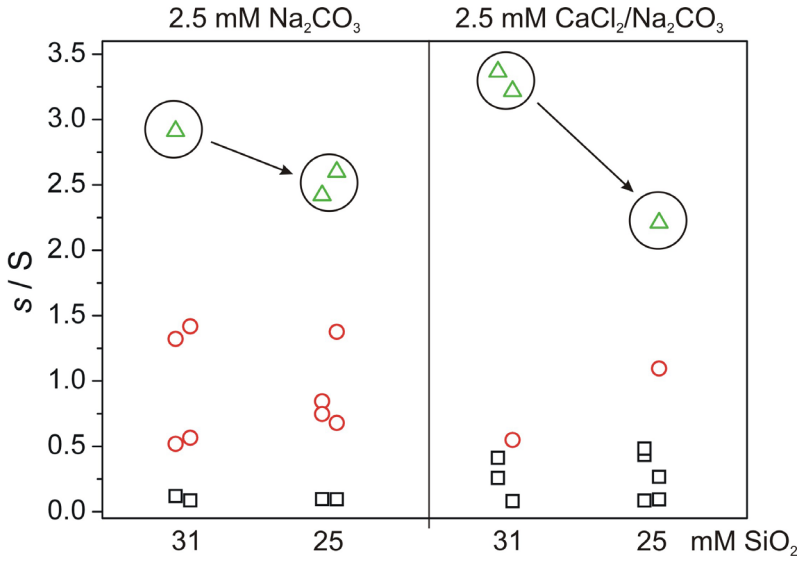

Fig. 4-21: The effect of the silica concentration on the sedimentation coefficients determined for samples containing a fixed amount of Na_2CO_3 (left) or $CaCl_2$ and Na_2CO_3 (right).

This suggests that less silica is bound to the clusters at the lower concentration. Further, cluster aggregation appears to be pronounced to a minor degree under these conditions, since fits of the data did not yield corresponding components with higher *s*. However, the presence of at least some agglomerates is supported by the obtained diffusion coefficients, with values around $1 \cdot 10^{-7}$ cm^2 s^{-1} signifying entities having diameters in the range of 50 nm as in the case of the higher silica concentration (cf. Table 4-7).

The effect of ageing time on the results of AUC measurements is visualized for the system $CaCl_2/Na_2CO_3/SiO_2$ in Fig. 4-22, where the sedimentation coefficients calculated from an experiment initiated straight after mixing are compared to those obtained when the sample was previously allowed to stand for about 1 day.

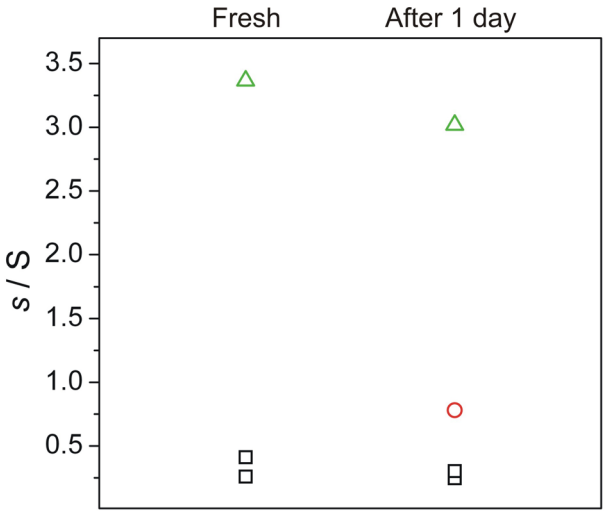

Fig. 4-22: The influence of ageing time on the sedimentation coefficients measured for a solution of $CaCl_2$ and Na_2CO_3 (both 2.5 mM) at 1860 ppm silica.

It is evident that there are no fundamental changes occurring with time, thus showing that solutions are stable and $CaCO_3$ crystallization is prevented by the silica. Ongoing agglomeration processes, as detected by DLS, cannot be resolved directly by AUC analysis. A slight decrease in the sedimentation coefficient assigned to individual clusters (from around 3.35 to 3.0 S) as well as in the hydrodynamic diameter derived from the diffusion coefficients (from 4.6 to 4.3 nm) might hint at a certain contraction of the silica-coated clusters, possibly owing to densification via proceeding silica condensation, although differences do hardly surpass the expected margins of error in *s* (typically ~0.3 S).[25] Likewise, the appearance of a species with putatively larger *s* (~0.75 S) after 1 day may be ascribed to limited experimental accuracy, but could also arise from common ageing of the silica sol producing an increased fraction of higher oligomers.

4.4.8 Origin of Cluster-like Species in the Reference Samples

In view of the results obtained from DLS and AUC measurements (Sections 4.4.5 and 4.4.7), the origin of nanoclusters in the two reference samples deserves special attention. First of all, it must be emphasized that neat silica sols do not show noticeable correlation in light scattering experiments (see Section 4.4.5), thus ensuring that the

existence of the traced particles is directly related to the presence of $CaCl_2$ and Na_2CO_3, respectively. Further, though not clearly reflected in the cryo-TEM images, the DLS data support the occurrence of clusters with radii of 2-7 nm also in the sample without Ca^{2+}, next to a larger fraction with $R_{H,av} \approx 50$ nm (see Fig. 4-16). By contrast, for solutions containing only $CaCl_2$ and silica, cryo-TEM micrographs reveal a considerable number of nanoclusters which, however, are not resolved in DLS size distribution profiles. This indicates that the concentration of clusters relative to larger particles is lower here than in the sample $CaCl_2$-Na_2CO_3-silica. Finally, in the system Na_2CO_3-silica, cluster-like species are comparatively rare as judged by cryo-TEM, but can nevertheless be detected by DLS because the amount of nanoparticles is in this case likewise rather small, in accordance to the detected count rate (Fig. 4-15).

A possible explanation for the formation of clusters in the absence of carbonate ions might be Ca^{2+}-induced silica polymerization. It has been reported that the solubility of amorphous silica is reduced in $CaCl_2$ solutions as compared to water owing to the strong "salting-out" effect of hard divalent cations,[58] which triggers silica condensation by screening otherwise repulsive charges.[57] Furthermore, small polymeric particles with sizes of only few nanometers and spherical colloids measuring several tens of nanometers are common in the course of silica precipitation from solution.[59]

These considerations inevitably raise the question of whether the clusters found in the actual samples could also consist of silica or calcium silicates, rather than directly involving calcium carbonate. A crucial point in this context is to clarify if the calcium ions do merely assist in the polymerization process or are in fact co-precipitated with the silica. The latter would imply that the cations are removed and no longer available for $CaCO_3$ formation. Contrarily, sheer colloidal interactions with the Ca^{2+} screening and bridging oligomers should, at least partially, allow $CaCO_3$ crystallization to be initiated, especially with regard to the high supersaturation of the systems (and the low solubility of $CaCO_3$). To check this, independent experiments were conducted in which silica sols were deliberately coagulated by adding Ca^{2+}. This was for example achieved by mixing 10 mM $CaCl_2$ with an alkaline solution of 16 mM SiO_2. The flocculated material was isolated and investigated by IR spectroscopy and elemental analysis. Results show that the precipitates essentially consist of amorphous silica (no calcium silicate), with minor amounts of Ca entrapped between the coagulated particles. Precipitation of calcium-rich silica particles in the samples can therefore be ruled out. Further, if prevention of $CaCO_3$ nucleation and crystallization would rest upon an

effective binding of Ca^{2+} ions by silica in competition with carbonate ions rather than inhibition of cluster agglomeration and fusion, increasing the CO_3^{2-}/Ca^{2+} ratio should eventually lead to the formation of calcium carbonate, which is not observed (see Section 4.4.4).

In turn, enhanced silica condensation can hardly account for the clusters and nanoparticles traced in mixtures of sodium carbonate and silica, since no such species were found in pure sodium silicate solutions and the increase in the ionic strength brought about by addition of Na_2CO_3 appears to be insignificant (5 mM Na_2CO_3 introduced to a silica sol already containing about 62 mM silica and 48 mM Na^+). Rather, one may speculate that the origin of these particles is related to the formation of sodium carbonate clusters. Clustering of actually well-soluble salts has been demonstrated in earlier work, though mainly in supersaturated solutions.[36] However, since cluster formation relies on equilibrium thermodynamics (at least in the case of $CaCO_3$),[25] coating by silica may cause a shift in the equilibrium with the free ions in favor of the bound state, hence potentially increasing the number of clusters to a measurable amount also in dilute systems. The still rare occurrence of sodium carbonate clusters as compared to $CaCO_3$ appears reasonable when presuming that the degree of binding correlates at least qualitatively with the solubility. In addition, the existence of Na_2CO_3 clusters and their capture by silica is supported by the IR and XRD data recorded from freeze-dried samples (see Section 4.4.10.2), which prove the presence of a seemingly amorphous sodium carbonate phase, and the NMR spectra recorded from corresponding solutions (see Section 4.4.9.1).

Similar scenarios may apply as well for calcium chloride. Indeed, AUC measurements with pure $CaCl_2$ solutions occasionally gave sedimentation coefficients noticeably exceeding those of simple ions (cf. Species 2 in Table 4-5), and therefore confirm that cluster-like structures are formed also by soluble compounds. $CaCl_2$ clusters might hence make up a certain fraction of the small particles observed in the reference without added carbonate. Nevertheless, in view of their abundance (Fig. 4-17a), it is likely that most of the clusters, if not all, consist of a more or less purely siliceous phase in this case.

In light of these findings, the possibility that polymeric silica particles and silica-associated clusters of other salts, both with similar sizes, co-exist with clusters of calcium carbonate in the actual samples cannot be fundamentally excluded. However, with respect to the above argumentation, results from *in-situ* IR studies (see Section

4.4.9.2), the temporal evolution of the system traced at different initial pH values (see Section 4.4.11) and, above all, the analyses performed on dried clusters (see Section 4.4.10.2), it is concluded that the vast majority of cluster species observed in the solutions are composed of $CaCO_3$.

4.4.9 Spectroscopic Analysis of Cluster-Containing Solutions

In an attempt to shed light on the nature of carbonate species in solution and thereby possibly trace the formation of $CaCO_3$ clusters in the systems, ^{13}C-NMR and infrared spectra were acquired directly from the standard sample (5 or 10 mM each of $CaCl_2$ and Na_2CO_3 in 1-50 silica) and the reference without added Ca^{2+} (5 or 10 mM Na_2CO_3 in 1-50 silica) after sufficient equilibration (at least 24 h).

4.4.9.1 NMR Spectroscopy

An essential prerequisite for the study of changes in the chemical environment of carbonate species in solution via ^{13}C-NMR spectroscopy is to carefully control the pH of the system. Earlier work has pointed out that the rapid exchange between HCO_3^- and CO_3^{2-} causes a single signal in the carbonyl region whose chemical shift depends on the relative fractions of the two ions present in equilibrium and thus on the actual pH.[60] Therefore, a series of neat carbonate solutions with different pH values was first investigated to check for the magnitude of this effect under the given experimental conditions. Afterwards, solutions of enriched sodium carbonate in dilute water glass and mixtures additionally containing calcium chloride were prepared and analyzed identically. Results thus obtained are reproduced in Fig. 4-23. As expected, the chemical shift of neat sodium carbonate solutions (black squares in Fig. 4-23) increases with the bulk pH and hence the fraction of CO_3^{2-} ions in equilibrium. In the examined interval, data can be approximated by a linear fit, although a slightly asymptotic trend according to the progress of carbonate species distribution with pH is obvious (see Appendix A.1). From the slope of the fitted straight line, it can be inferred that an increment of 0.1 in pH results in a shift of δ by 0.278 ppm towards higher values. Based on these data, solutions of enriched sodium carbonate in dilute water glass and mixtures additionally containing calcium chloride were prepared and analyzed identically. The detected chemical shifts of the two samples are similar, but differ noticeably – namely by about 0.28 ppm to high frequency – from the neat sodium carbonate reference at equal pH (colored symbols in Fig. 4-23). Though rather small, this difference in δ caused by the presence of silica was reproduced in a number of independent

experiments and is consequently, with respect to the limits of error, judged to be significant. For comparison, the traced changes would correspond to an increase of around 0.11 in pH, which is clearly covered by the precision of the used pH meter.

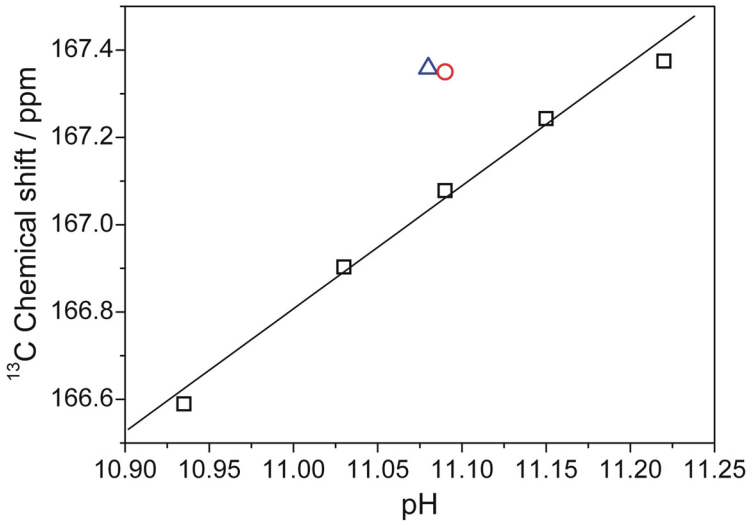

Fig. 4-23: Carbon-13 chemical shifts measured for aqueous solutions of ^{13}C-enriched sodium carbonate at different pH (black squares), as compared to the values obtained for solutions of $Na_2{}^{13}CO_3$ (red circle) and $CaCl_2/Na_2{}^{13}CO_3$ (blue triangle) in a 1-50 dilution of water glass ($[CO_3^{2-}]$ = 5 mM, $[Ca^{2+}]$ = 5 mM).

^{13}C NMR: δ 166.59 ($Na_2{}^{13}CO_3$, pH 10.94), 166.90 ($Na_2{}^{13}CO_3$, pH 11.03), 167.08 ($Na_2{}^{13}CO_3$, pH 11.09), 167.24 ($Na_2{}^{13}CO_3$, pH 11.15), 167.37 ($Na_2{}^{13}CO_3$, pH 11.22), 167.35 ($Na_2{}^{13}CO_3$ in 1-50 silica, pH 11.09), 167.36 ($CaCl_2/Na_2{}^{13}CO_3$ in 1-50 silica, pH 11.08).

It can therefore be concluded that addition of silica, both in the presence and absence of Ca^{2+} ions, leads to modifications in the speciation of carbonate in solution. The measured displacement of the carbon signal to higher δ values is coherent with a scenario in which a certain fraction of carbonate ions are bound in clusters with either sodium or calcium, as this would as such cause a downfield shift of the signal[61] or move the equilibrium in solution towards more CO_3^{2-} ions. When assigning an "apparent" pH of 11.19 to the silica-containing samples, the net extra-amount of carbonate existing in equilibrium with bicarbonate due to the presence of the additive can be estimated to about 4% in molar terms.

In view of the fairly large number of cluster species seen in cryo-TEM micrographs and detected by the SAXS measurements, it seems implausible that such a small fraction represents the average quantity of carbonate ions bound in clusters. To explore whether binding substantially prolongs the relaxation time such that saturation occurs and a possibly separated signal for bound carbonate is not resolved, the pulse delay was

increased to 20 s for selected samples. This, however, did not affect the appearance of the spectra. Another observation suggesting that all carbonate species present in the system produce a single, average signal is that the integral intensity of the peak in every spectrum, when normalized to the internal standard, coincides with that of the neat sodium carbonate reference. The only reasonable explanation for these findings is that although silica hinders transformation of pre-nucleation clusters into a true solid phase (i.e. prevents nucleation) by decorating their periphery, it still permits dynamic exchange of bound and free carbonate ions. As a consequence, the NMR signal experiences a shift to higher δ values instead of splitting into two peaks, which would be expected for two distinct, non- or slowly exchanging populations.

Finally, to ascertain that the traced changes in the chemical shift are reliable and well above the resolution limit of the used spectrometer, further experiments were conducted in which solutions of $Na_2{}^{13}CO_3$ and $CaCl_2/Na_2{}^{13}CO_3$ in 1-50 silica were measured simultaneously with a silica-free reference of the same pH. This was accomplished by replacing the acetonitrile standard in the inserted capillary with neat carbonate solution. Essentially, all spectra exhibited two discrete, well-separated peaks at ppm values close to those found for the respective samples in individual measurements. This is again clear evidence that the chemical environment of carbonate species in solution is, in average, affected by the presence of silica.

4.4.9.2 IR Spectroscopy

Typical infrared spectra recorded from the solutions are shown in Fig. 4-24. Comparative analyses using different reference samples (neat Na_2CO_3 and silica solutions, and mixtures of $CaCl_2$ and silica) suggest an assignment of the prominent band at ~1020 cm^{-1} with its shoulder at ~1080 cm^{-1} as well as the weaker features at ~890 cm^{-1} and ~1260 cm^{-1} to dissolved silica, while the broad absorption centered at about 1400 cm^{-1} clearly originates from carbonate.

Previous IR studies on the constitution of silica in aqueous solution as a function of pH led to the conclusion that the bands at ~1020 cm^{-1} and ~890 cm^{-1} are caused by Si-O stretching vibrations of monomeric silicate species, likely $SiO(OH)_3^-$.[62,63] The shoulder at ~1080 cm^{-1} in turn stems from Si-O-Si entities generated in condensation processes. Eventually, the small hump at ~1260 cm^{-1}, which also occurred in pure silica solutions, may be attributed to traces of nanoscale crystalline silicates.[62] Concerning the carbonate band ~1400 cm^{-1}, there were no notable changes discernible when Ca^{2+} was added to the system. In terms of position and shape, the peak was further not distinguishable from

that observed for neat sodium carbonate solutions. According to literature, the υ_3-mode of carbonate ions in an aqueous environment results in two infrared absorptions located at about 1375 and 1430 cm^{-1} which overlap to produce one broad signal,[64] as detected in the present work. However, for a situation in which a major part of the carbonate ions present is bound in $CaCO_3$ clusters, IR characteristics more resembling those of ACC may be expected, that is, a split band at somewhat higher wavenumbers (1425/1490 cm^{-1}) should be monitored.[65] However, the fact that the clusters are solutes[25] and probably represent a dynamic structure in equilibrium with dissolved ions, significant participation of sodium ions in cluster formation or simply insufficient resolution of the used instrument at the given low total transmission might account for the observed signal and the lack of a band shift or splitting.

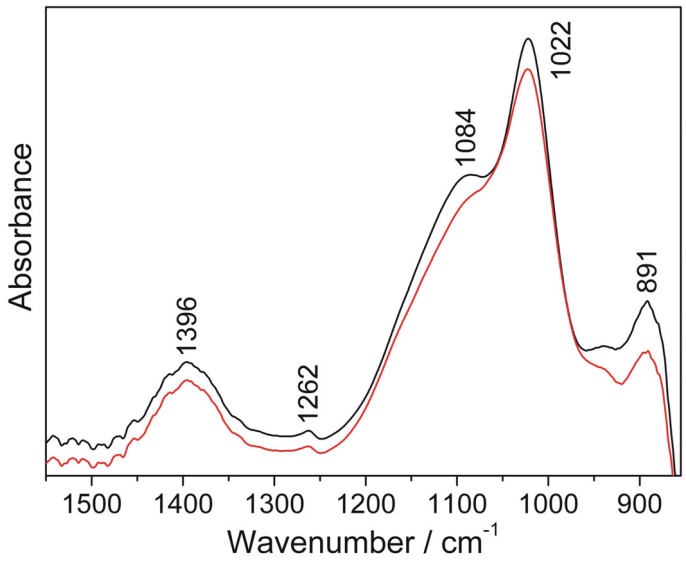

Fig. 4-24: Vibrational spectra acquired from solutions of Na_2CO_3 (black) and $CaCl_2/Na_2CO_3$ (red) in dilute water glass ($[CO_3^{2-}]$ = 10 mM, $[Ca^{2+}]$ = 10 mM, 1-25 silica). The spectral range is limited to the shown interval due to the restricted transmittance of the used ZnSe windows and strong absorption of water.

The only considerable and reproducibly found difference in the collected spectra refers to the detailed form of the shoulder at ~1080 cm^{-1}. Generally, this band reflects the degree of silica polymerization and should gain intensity when the amount of polymeric species increases.[63] In the present experiments, the shoulder was less pronounced in samples containing Ca^{2+}, regardless of the presence of carbonate. It is well-known that multivalent cations can promote silica condensation and trigger coagulation of sols without being incorporated into the precipitating phase to a large extent.[57] Based thereon and the finding that the pH of the samples increases slightly with time, the

discerned changes are ascribed to fractional silica condensation reactions initiated upon addition of Ca^{2+} ions, even though such processes should in principle amplify the signal at ~1080 cm^{-1}. This is in line with the DLS measurements and cryo-TEM images when assuming that cluster aggregation is mainly driven by silica oligomerization.

On the other hand, since there are only minor alterations in the vibrational characteristics of silica in the samples as compared to the pure silica reference solution, these in-situ IR spectra suggest that the speciation of silica is not drastically affected by the presence of Ca^{2+} ions. Ample nucleation of a siliceous phase or the precipitation of hydrated calcium silicates would be associated with more distinct shifts of bands and changes in relative intensities, or the emergence of other peaks.[66] Thus, in line with the argumentation put forward in Section 4.4.8, the possibility that the cluster species imaged by cryo-TEM are related to silica polymerization alone or derive from calcium silicate formation can likely be ruled out.

4.4.10 Cluster Isolation

4.4.10.1 Rationale of the Experiments

As chemical analysis of the cluster species in the cryo-TEM experiments was not possible and IR data acquired directly from the solutions did not allow for an unambiguous identification of the phases present, efforts were made to dry the samples while conserving the existing structures, so as to enable conventional techniques to be used for characterizing the composition of the clusters. On the one hand, this was achieved by freezing as-prepared solutions in liquid nitrogen and removing water by lyophilization. As an advantage of this method, quenching is quick and structural rearrangements are therefore unlikely to occur. In turn, it brings about the disadvantage that all salt previously dissolved in the mixtures (NaCl and in particular excess silica) is also solidified and may conceal features of silica-decorated carbonate clusters. Therefore, on the other hand, isolation procedures were sought with which cluster species could be enriched relative to excess salt prior to drying. A suitable means to accomplish this was to dialyze the samples using membranes permeable for simple ions and smaller silica oligomers, but withholding larger clusters and agglomerates. Further, the gel sediment formed when centrifuging the mixtures at high speed (cf. Section 4.3.3.2) was considered an interesting specimen, assuming that carbonate clusters are accumulated along with silica on the bottom of the vial and incorporated to the gel body during silica condensation. In a third approach, fractional precipitation of the dissolved

silica was induced by increasing the ionic strength of the system via addition of NaCl. Enhanced polymerization under these conditions led to flocculation of an optically isotropic phase which, if silica associated with clusters participates in cross-linking, is expected to contain a certain amount of protected clusters next to a preponderating fraction of silica. Precipitates could then be isolated by filtration, while the gel sediment and the dialyzed solutions were dried by freezing and subsequent lyophilization. A crucial working hypothesis for all three methods is that changes in the actual composition of the samples in the course of dialysis and precipitation as well as imposed forces and concentration gradients during centrifugation do not essentially affect the clusters and consequently will not provoke any transformation and/or crystallization.

4.4.10.2 Characterization of Dried Samples

Direct Freeze-Drying

IR spectra of the powders obtained by the method of direct freeze-drying and, for comparison, pure sodium carbonate are shown in Fig. 4-25.

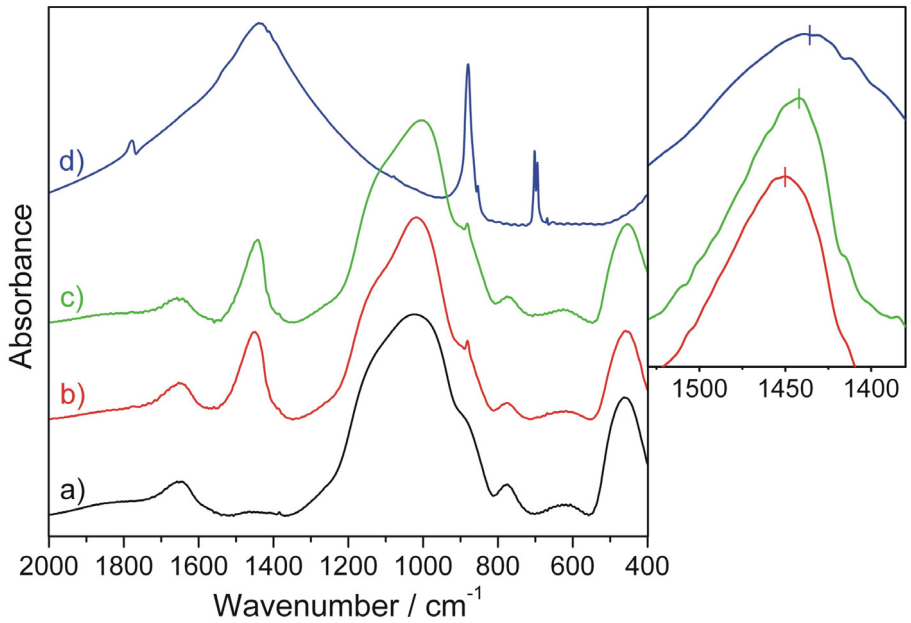

Fig. 4-25: Infrared spectra of (a-c) samples prepared by direct freeze-drying and (d) anhydrous sodium carbonate as reference. Inset: zoom into the region of the υ_3-mode of carbonate, revealing slight but distinct shifts of the peak position. The initial compositions of the solutions were: (a) $[Ca^{2+}]$ = 5 mM, $[CO_3^{2-}]$ = 0, 3720 ppm silica. (b) $[Ca^{2+}] = [CO_3^{2-}]$ = 5 mM, 3720 ppm silica. (c) $[Ca^{2+}]$ = 0, $[CO_3^{2-}]$ = 5 mM, 3720 ppm silica.

In general, infrared spectra of amorphous silica are characterized by strong absorption in the range of 900-1300 cm^{-1} owing to Si-O-Si bond-stretching vibrations in the SiO_2 lattice.[67] The position of the global maximum in this region as well as the occurrence of shoulders varies with the detailed constitution and the dimensionality of the formed structure. Shifts towards higher wavenumbers usually indicate an increased degree of condensation.[63] Further peaks at around 450, 800 and 1630 cm^{-1} are attributed to bond-rocking and bond-bending vibrations and to deformation modes of entrapped water molecules, respectively.[67] Prominent bands of $CaCO_3$ are located at 690-750 cm^{-1} (υ_4 mode), 850-880 cm^{-1} (υ_2 mode) and 1420-1490 cm^{-1} (υ_3 mode), depending on polymorphism.[65] As opposed to crystalline phases, ACC can be distinguished by a specific splitting of the υ_3 peak and a marked broadening or disappearance of the υ_4 absorption.[6b] Sodium carbonate exhibits major IR features quite similar to $CaCO_3$, except for that the υ_4 band is often split in this case. Absorption frequencies reported in literature are 1451, 881 and 702/694 cm^{-1} for the υ_3, υ_2 and υ_4 modes.[68] Based thereupon, peaks observed for the freeze-dried samples and the Na_2CO_3 reference are listed in Table 4-8 and assigned to distinct vibrational modes.

Sample	**υ (CO_3) / cm^{-1}**			**υ (SiO_2) / cm^{-1}**			
	υ_2	υ_3	υ_4	stretching	bending	rocking	Water
$CaCl_2$-SiO_2	---	---	---	1023	775	460	1649
$CaCl_2$-Na_2CO_3-SiO_2	881	1451	---	1017	775	458	1650
Na_2CO_3-SiO_2	881	1442	---	1004	772	454	1652
Na_2CO_3	879	1439	694/702	---	---	---	---

Table 4-8: IR peak positions and band assignment for the freeze-dried powders. Note the absence of a υ_4 vibration in the systems $CaCl_2$-Na_2CO_3-SiO_2 and Na_2CO_3-SiO_2 as well as the shifts of the bands corresponding to the υ_3 mode of carbonate and the bond-stretching vibration of silica.

Neither in the system $CaCl_2$-Na_2CO_3-SiO_2 nor in the reference without Ca^{2+}, a discrete band around 700 cm^{-1} can be discerned, suggesting that no crystalline carbonates were formed during lyophilization. This is supported also by diffraction data. Patterns of all freeze-dried powders exhibit predominantly contributions from amorphous background scattering along with some sharp reflexes of fairly low intensity (Fig. 4-26). The latter originate from traces of sodium chloride which crystallized upon drying. In both carbonate-containing samples, the IR band corresponding to the υ_3 mode is not noticeably split and occurs at frequencies roughly similar to those of pure Na_2CO_3. A

closer look yet illustrates that the maximum of this peak is shifted by about 10-15 cm^{-1} to higher wavenumbers when Ca^{2+} is present (cf. Fig. 4-25). This shift was reproduced in a number of independent experiments and is thus appreciated to be significant.

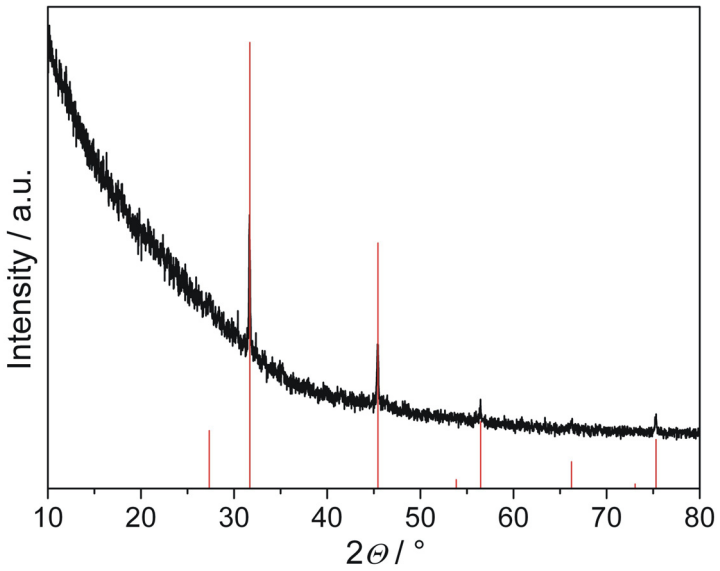

Fig. 4-26: XRD pattern of a powder isolated by freeze-drying a mixture of $CaCl_2$, Na_2CO_3 and silica. The sample is mainly amorphous. Weaker discrete signals arise due to partial crystallization of sodium chloride during lyophilization (red: database reflections for NaCl).

For a situation in which $CaCO_3$ clusters are embedded in a silica matrix, a twin peak with maxima at about 1425 and 1490 cm^{-1} would be expected, given that the clusters are considered to be precursors of ACC. However, if only a certain percentage of the total amount of carbonate ions present is bound in clusters with calcium and the residual fraction is associated with sodium ions in the powder, the resulting absorption band could readily be a superposition of the two individual signals, which overlap to an extent that discrete peaks are no longer resolved. Overall, with respect to the detected wavenumber of the υ_3 mode in the absence of Ca^{2+} (~1440 cm^{-1}), the averaged signal should then be shifted slightly to higher frequency, as observed. The notion that Ca^{2+} and CO_3^{2-} ions are only fractionally bound in clusters, both in the solutions before drying and the final powders, is also reflected by the position of the silica bond-stretching vibration band. Addition of Ca^{2+} leads to an increment in the wavenumber of the peak maximum, as species with an increased degree of polymerization are generated during solidification as a consequence of beneficial charge screening. This shift in υ is yet somewhat more pronounced when no carbonate is present (cf. Table 4-8), since a higher amount of free divalent cations are available for cross-linking in this case.

These results suggest that mutual shielding of clusters against direct aggregation by dissolved silica is effective to avoid crystallization of $CaCO_3$ even when samples undergo a freeze-drying process. Moreover, as there were likewise no crystalline sodium carbonate-based phases traced in the Ca^{2+}-free reference, it seems as if similar scenarios apply for clusters of Na_2CO_3 too, as indicated also by other techniques (see Sections 4.4.5, 4.4.8, and 4.4.9).

Dialysis, Centrifugation and Induced Precipitation

Infrared spectra recorded from the powders prepared by dialysis, centrifugation and induced precipitation are shown in Fig. 4-27, while Table 4-9 summarizes the detected peaks and provides an allocation of the bands to vibrations of carbonate and silicate entities.

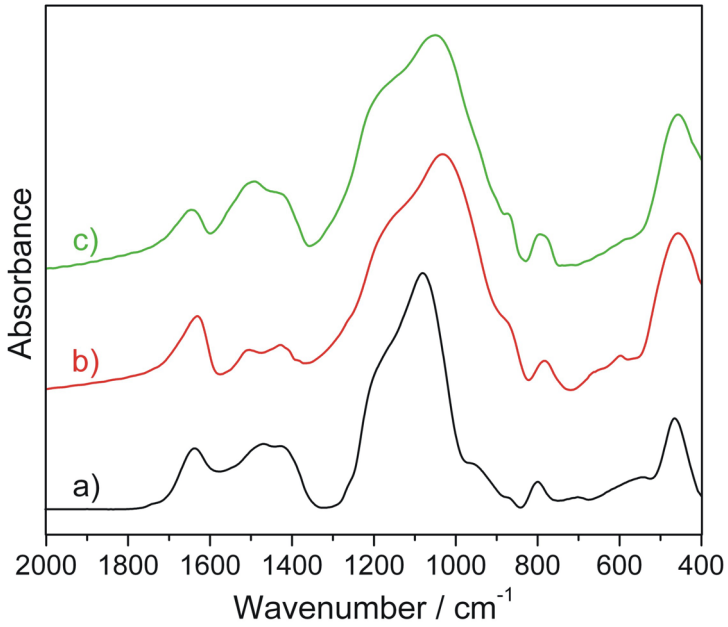

Fig. 4-27: Vibrational spectra of powders obtained by (a) lyophilization of dialyzed solutions, (b) ultracentrifugation and subsequent freeze-drying of the gel body deposited on the bottom of the vial, and (c) filtration of the precipitate formed upon adding NaCl. The initial compositions of the solutions were: (a-b) $[Ca^{2+}] = [CO_3^{2-}] = 5$ mM, 3720 ppm silica. (c) $[Ca^{2+}] = [CO_3^{2-}] = 5$ mM, [NaCl] = 0.2 M, 3720 ppm silica.

Absorption in the range of 1400-1500 cm^{-1} is observed in all three samples, confirming that carbonate species are still present and that the powders do not consist merely of silica. Further, the υ_3 band is clearly split and there is no distinct peak or broad feature at ~700 cm^{-1}. Therefore, we conclude that the major carbonate phase in the solids is ACC. This is also supported by the frequencies detected for the υ_2 band, which approximate values reported for ACC in literature (866 cm^{-1})[6b] closer than those found for powders

isolated by direct freeze-drying. Apparently, the applied procedures successfully enriched the resulting samples in clusters of $CaCO_3$ relative to non-bound carbonate and/or Na_2CO_3 clusters.

Sample	υ (CO_3) / cm^{-1}			υ (SiO_2) / cm^{-1}			
	υ_2	υ_3	υ_4	stretching	bending	rocking	Water
Dialysis	1470	1426	869	1080	800	465	1638
Centrifugation	1504	1428	869	1033	783	457	1631
Precipitation	1493	1427	874	1051	795	457	1646

Table 4-9: Vibration frequencies traced in powders resulting from the different experimental procedures and their assignment to normal modes of carbonate and silica.

Differences in the absorption maxima of the siliceous component in the powders indicate varying degrees of condensation, probably caused by unlike conditions during polymerization. In particular, the bond-stretching vibration in the dialyzed sample is located at rather high wavenumbers, arguing for a heavily cross-linked structure. In this case, a separate band at about 950 cm^{-1} can be distinguished, likely stemming from stretching vibrations of free silanol (Si-OH) groups.[67]

XRD data identify all investigated samples as being fully amorphous and thus corroborate that the solids contain $CaCO_3$ clusters, or at least an ACC-like phase. Exemplarily, a background-subtracted pattern of the dried sediment from the centrifugation experiment is reproduced in Fig. 4-28.

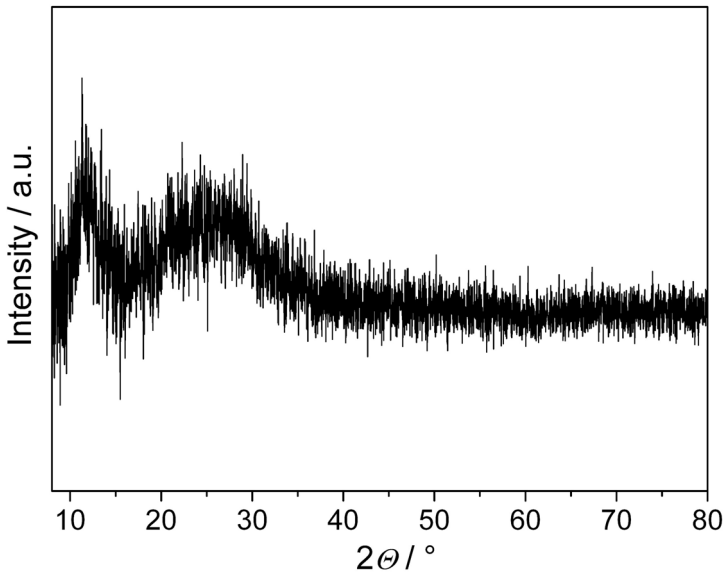

Fig. 4-28: Background-subtracted X-ray diffractogram of the gel sediment segregated during centrifugation after freeze-drying, verifying that the sample is entirely amorphous.

Broad and undefined peaks in the ranges of 10-15° and 15-35° suggest the presence of amorphous structures with some ordering, in agreement with previous studies on amorphous silica,[69] calcium silicates,[70] and ACC.[14,71]

TEM Analyses

To ensure that the procedures used for isolation did not alter fundamentally the properties of the system or cause undesired transformations of the cluster species (e.g. nucleation of an ACC phase), particles present in dried state were examined by TEM. As illustrated in Fig. 4-29, micrographs recorded for samples prepared by dialysis are characterized by a multitude of discrete nanoclusters, which predominantly lie isolated from one another. Measuring more than 200 individuals yields an average particle diameter of 1.2 ± 0.8 nm, which nearly coincides with the value determined for the clusters in cryo-TEM images (1.1 ± 0.6 nm, cf. Fig. 4-4). Thus, the clusters appear to be widely unaffected by the removal of excess salt during dialysis and are conserved through protection by the silica. In combination with the corresponding IR data, this is clear evidence that the clusters consist of $CaCO_3$. Moreover, we note that the number of cluster agglomerates found on the grids is lower than in samples investigated by cryo-TEM, suggesting that aggregates dissociated as the bulk concentration of silica was reduced while dialyzing.

Aside from $CaCO_3$ clusters, larger particles with typical sizes of 50-100 nm were frequently observed (Fig. 4-29c), which turned out to be highly sensitive to the electron beam. Diffraction patterns acquired from these objects show crystalline reflections that can be assigned to the calcite lattice (Fig. 4-29d). Upon prolonged irradiation (~ 3 s), the crystals continuously disintegrated such that in the end only material accumulated on the former borders of the particles remained (Fig. 4-29e). Elemental analyses on intact crystals were therefore not possible. Their remnants, however, proved to be rich in Ca. Thermal decomposition of $CaCO_3$ via decarboxylation to calcium oxide under the applied high-vacuum is a well-known phenomenon in electron microscopy.[72]

The occurrence of calcite crystals in the micrographs demonstrates that inhibition of nucleation is yet not perfectly efficient under the circumstances during sample preparation. Obviously, a certain fraction of the clusters is insufficiently protected and becomes subject to aggregation and subsequent crystallization. Since neither the IR spectrum nor the XRD pattern of the freeze-dried powder displayed signals of calcite, the formation of crystals must be due to the relatively slow drying process on the TEM grid. Probably, the concurrent gradual increase in the concentration of clusters and the

comparatively low amount of silica present after dialysis allow for nucleation at some point.

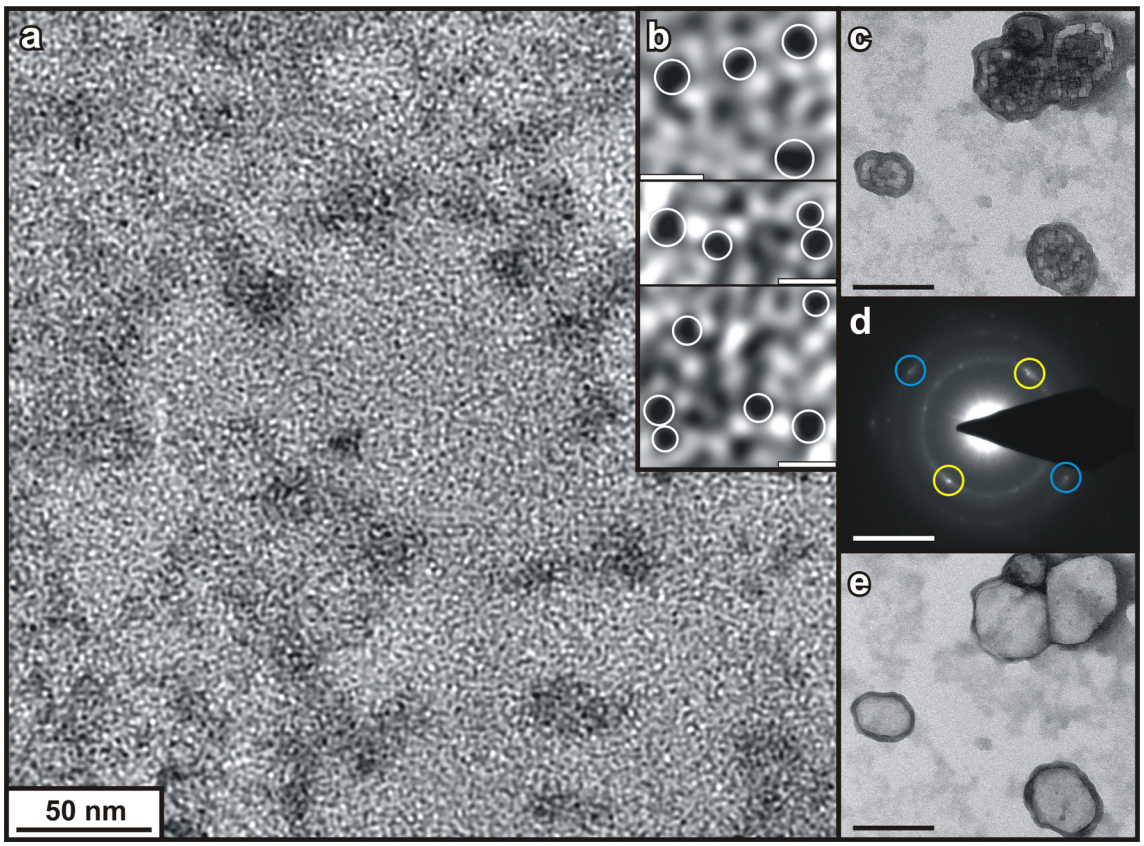

Fig. 4-29: Silica-stabilized $CaCO_3$ nanoclusters in dry state. (a) TEM micrograph of the residue obtained upon drying aliquots of dialysed solution, showing myriads of isolated tiny particles dispersed over the whole image area. (b) Zooms into selected regions of (a), revealing single cluster species (white circles) with dimensions in the range of 1-2 nm. Scale bars: 5 nm. (c) Nanocrystals found at a different site on the grid. Fragmentation of the crystals indicates ongoing decomposition. Scale bar: 100 nm. (d) Electron diffraction pattern of the crystals, displaying faint spots along two discrete rings. Measured distances in-between pairs of reflections correspond to lattice spacings of 3.02 Å (yellow circles) and 2.16 Å (blue circles). With respect to the common limits of error in electron diffraction, reflections can be indexed to the (104) and (202) planes of calcite (database spacings: C-104: 3.035 Å, C-202: 2.095 Å). Scale bar: 4 nm^{-1}. (e) Crystals after exposure to the electron beam during diffraction analysis. Exhaustive decomposition of the beam-sensitive carbonate material left heavily eroded hollow particles with margins rich in Ca (verified by EDX elemental mapping). Scale bar: 100 nm.

Unfortunately, probing the chemical composition of the tiny cluster species by means of EDX spectroscopy and elemental mapping failed because of their beam sensitivity. Upon longer exposures necessary for the measurements, the clusters had quantitatively vanished. Marked degradation was discernible already after acquisition of a single image. In elemental maps collected from regions comprising cluster aggregates, increased counts of Si were detected on areas formerly covered by the aggregates,

whereas Ca intensities were evenly distributed and low. This means that the $CaCO_3$ clusters in the agglomerates were destroyed by the electron beam while the silica matrix hosting them persisted. Hence, it can be concluded that silica is stable under the given operating conditions. This, in turn, serves as a further indirect but substantial proof for the claim that the clusters do not consist of a siliceous phase, but calcium carbonate.

4.4.11 Variation of pH

In order to investigate in more detail the mode of interaction between silica and $CaCO_3$ pre-nucleation clusters and in particular to shed light on the role of silica during cluster aggregation, the starting pH of samples at 5 mM $CaCl_2$/Na_2CO_3 and 3720 ppm silica was varied within a range of 7-11 by addition of HCl. In Fig. 4-30, the time-dependent evolution of species present in the systems is visualized by cryo-TEM images exemplarily for initial pH values of 10.29 and 9.32.

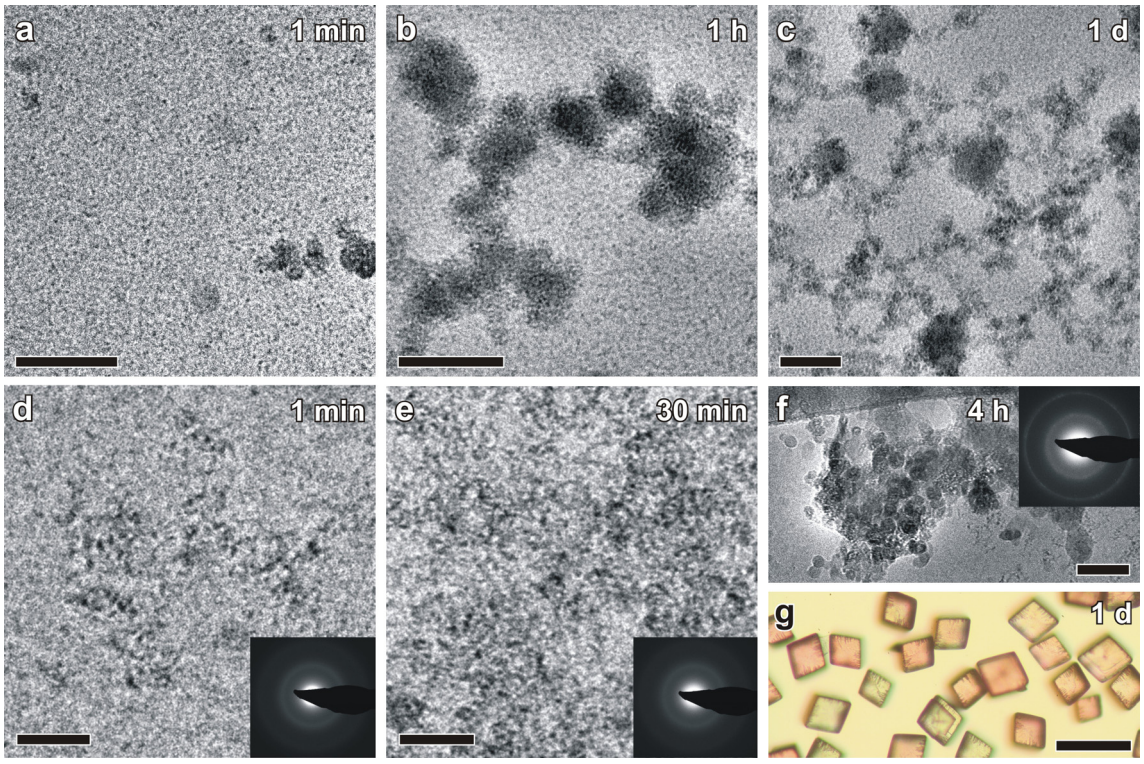

Fig. 4-30: Sequences of cryo-TEM images taken at different times after mixing from samples with an initial pH of (a-c) 10.29 and (d-g) 9.32. ED patterns acquired from the low-pH series (see insets) indicate that the open cluster networks formed within 30 min are still amorphous. After 4 h, agglomerates of more compact particles are observed in which some crystallinity is already inherent. The optical micrograph of the sample after 1 day shows rhombohedral crystals which were confirmed to be calcite by X-ray diffraction (see Fig. 4-31). Scale bars: (a-e) 50 nm, (f) 100 nm, (g) 100 µm.

Although the applied blotting procedure implicates a not necessarily representative picture in terms of the relative frequency of smaller and larger objects, results show a clear and coherent trend with decreasing pH. At pH 10.29, the situation encountered 1 min after mixing resembles that in samples without added HCl (pH 11, cf. Fig. 4-3a), with individual clusters abounding and co-existing with a minor fraction of diffuse aggregates (Fig. 4-30a). After 1 h, a considerable amount of larger agglomerates has developed which (Fig. 4-30b), with time, become more and more interconnected by less dense domains to form extended network structures (Fig. 4-30c). A closer look at the texture of the compact objects and the interjacent mesh reveals that both are constituted by smaller primary units (2-3 nm) with high electron contrast which seem to be embedded in a lighter matrix.

At pH 9.32, the sample after 1 min contains predominantly isolated clusters which have yet already aggregated to loose networks in some instances (Fig. 4-30d). After 30 min, spacious conglomerates spanning across micron-scale dimensions can be discerned in the micrographs, which again are obviously inhomogeneous (Fig. 4-30e). The darker particles within these networks are somewhat larger (up to 10 nm) than those found at higher pH. After about 4 h, a novel population of fairly consolidated spherical particles with diameters of around 30 nm is identified next to porous cluster networks. These particles are also prone to aggregation and electron diffraction (ED) patterns taken from a corresponding assembly suggest the presence of partially crystalline material (Fig. 4-30f); however, purely amorphous nanoparticles were also observed. These findings evidence that primary ACC grains form *via* aggregation of pre-nucleation clusters. Upon continued equilibration, metastable ACC finally transforms to yield numerous micron-sized crystals (Fig. 4-30g).

In general, lowering the pH causes enhanced protonation of silicate species in solution, which in turn favors condensation reactions and hence reduces the overall solubility.[57] At the chosen concentrations, this is expected to result in the formation of a hydrogel, which in fact occurred after a certain delay for all samples to which HCl was added. At initial pH values above 10, gradual silica polymerization over periods of weeks eventually led to the deposition of a homogeneous layer of an optically isotropic gel on the bottom of the vial, leaving a clear solution on top. Exemplarily, the gel body formed at pH 10.29 was separated from its mother liquor, washed with water and dried by lyophilization. X-ray diffractograms of the resulting powder prove the absence of crystalline material. This suggests that inhibition of nucleation can be maintained during

gel formation and isolation, such that a composite of nanoscale $CaCO_3$ clusters embedded in a silica matrix is obtained.

In solutions with a starting pH of 9.32, marked gel formation was discerned already after about 1 day, as gelled clumps were dispersed throughout the whole volume. Accordingly, the pH had increased to 9.93. Within and in-between the gel bodies, a multitude of crystals with rhombohedral shape and sizes of several tens of microns were found (Fig. 4-30g), which could be extracted by selective dissolution of the silica gel in 1 M NaOH and subsequent repeated washing with water. X-ray diffraction patterns of crystals harvested after standing for 1 week verify the presence of calcite (Fig. 4-31). Crystallization of calcitic products essentially occurred in all samples with starting pH values lower than 10 and higher than 8.

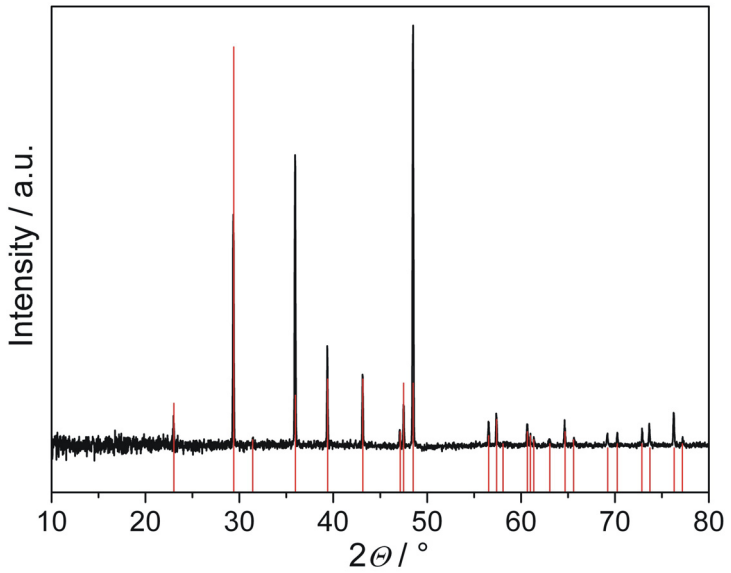

Fig. 4-31: XRD pattern of crystals retrieved from a sample with an initial pH of 9.32 after ageing for 1 week. Red columns indicate database reflections expected for calcite.

Apart from strongly influencing the chemistry of silica, the pH is a crucial parameter also for the speciation of carbonate in solution and therefore intimately affects the precipitation of calcium carbonate. Generally, the fraction of carbonate ions in equilibrium with bicarbonate ions decreases with the pH (see Appendix A.1); calculated molar percentages of CO_3^{2-} ions in solution amount to 82.4% at pH 11, 48.3% at pH 10.3, and 8.5% at pH 9.3. This explains why crystallization of calcite is not observed beneath pH 8, where the concentration of available CO_3^{2-} is apparently too low to facilitate $CaCO_3$ precipitation. On the other hand, the pH-dependent distribution of carbonate species implies that the number of clusters present in the samples should be highest at pH 11 and gradually diminish as the pH is decreased, given that their

formation is based on equilibrium thermodynamics.[25] In turn, at low pH, polymerization of silica is much more enhanced and the concurrent increment of pH in the vicinity of the growing silica matrix may cause a local increase in the carbonate concentration and hence the number of clusters. This would rationalize the observation that numerous clusters occur also at lower pH levels and are directly incorporated into the forming siliceous networks.

Nevertheless, it may be suspected that higher pH values lead to a faster formation of the different $CaCO_3$ species and a still higher net frequency of clusters in the samples. However, a more efficient stabilization of the distinct aggregated states against nucleation is found at elevated pH. Therefore, it can be inferred that the chemistry of silica is responsible for the observed effects. At pH 11, the number of charges at siliceous species is high and the amount of free silanol groups rather low, thus rendering the net forces between silica-bearing clusters predominantly repulsive. Cluster aggregation is consequently unfavorable under these conditions, and only few agglomerates exist in equilibrium with a preponderant fraction of isolated clusters. Screening of clusters by the silica hinders direct mutual contact and consequently prevents nucleation and crystallization from being initiated. At lower pH, enhanced protonation of silicate species diminishes repulsive forces and triggers condensation processes, which also involve the silica associated with the clusters. This leads to cross-linking of silica-decorated clusters and the development of a siliceous network inclosing carbonate clusters, as shown by the electron micrographs in Fig. 4-30. At pH 10.29, the clusters incorporated into the silica matrix of the forming gel remain permanently conserved. By contrast, during polymerization in less alkaline environments, the silica must release clusters to account for the observed crystallization of calcite. Deficient stabilization against nucleation at low pH likely originates from reduced charges on silica-decorated clusters and hence lacking mutual repulsion. Alternatively, fast condensation rates might obviate tight integration of clusters into the network and withdraw oligomeric silicate from their periphery. A third option is that the mode of silica binding to the clusters necessitates a high pH, for example because charges are crucial for interaction. At a certain point, liberation of pre-nucleation clusters increases their factual free concentration until locally a critical threshold is exceeded and nucleation of an ACC phase, in the form of spherical nanoparticles occurs (Fig. 4-30f), since direct aggregation is now possible. Both the size of primary ACC grains and the fact that randomly oriented crystalline domains are detected inside or nearby the

agglomerates after some time agree well with the results of a previous study.[27] Essentially, the traced temporal evolution of the samples (single clusters – cluster aggregates – ACC nanoparticles – calcite crystals) confirms that the observed clusters and aggregated states are indeed precursors of crystalline calcium carbonate.

The varying fractions of carbonate ions in the samples at different pH may moreover have an impact on the particular structure and typical size of the clusters. However, the mean diameter determined for individual clusters at pH 11 (or respectively its distribution, cf. Fig. 4-4) does not differ significantly from values reported by Pouget *et al.* for clusters formed at pH < 8.[27] This suggests that the size of single pre-nucleation clusters – unlike their local atomic structure[29] – is fairly independent of the pH and other conditions (such as ionic strength). However, possible changes of the cluster diameter with the pH would anyway be hard to interpret in the presence of silica, as binding of silicate species onto the clusters might increase their size and consequently conceal effects of the pH. Therefore, and for lack of information on the short-range order within the clusters, no definite conclusions about variations of both the size and structure of the clusters in the samples can be drawn based on the existing data.

4.4.12 Evaluation of Colloidal Stabilities by Means of the DLVO Theory

To verify the influence of the pH on cluster aggregation and coalescence, and hence the degree of stabilization of the system against nucleation, the Zeta potential of samples with varying starting pH was measured and used to assess the colloidal stability of the solutions based on DLVO theory. Experimentally determined mean values of the electrophoretic mobility U_e and calculated magnitudes of the Zeta potential ζ are listed in Table 4-10.

pH	U_e / µm·cm·V^{-1}·s^{-1}	ζ / mV	Stabilization / kT
11.00	– 2.67 ± 0.12	– 34.0 ± 1.5	1.05
10.29	– 2.74 ± 0.20	– 34.9 ± 2.5	1.16
9.32	– 1.63 ± 0.19	– 20.8 ± 2.4	0.32

Table 4-10: Measured electrophoretic mobilities U_e, calculated values for the Zeta potential ζ, and the apparent degree of colloidal stability estimated using the DLVO theory for samples of different initial pH. The given barrier heights in kT apply for a cluster size of 1.1 nm.

The obtained values for the Zeta potential comply well with those reported previously for silica surfaces in contact with a solution at corresponding pH levels and a

comparable ionic strength ($I \approx 80$ mM in the present experiments).[73] This appears reasonable when assuming that the $CaCO_3$ clusters are covered by silicate species. In turn, the agreement of the calculated values with the literature suggests that the applied Smoluchowski approximation yields fairly reliable data for the Zeta potential under the given conditions, although the silica-bearing clusters are very small and, hence, principally do not meet the common criteria of the approach (high salinities and large particles, that is, $\kappa \cdot a >> 1$, see Section 4.3.9.1).[50] Further, it is evident that the Zeta potentials of the samples at pH 11.00 and 10.29 are roughly equal with respect to the limits of error, whereas the magnitude of the value obtained for pH 9.32 is significantly lower.

Potential energy-distance profiles derived by DLVO theory based on the assumptions mentioned in Section 4.3.9.2 are shown in Fig. 4-32. Generally, application of the DLVO theory to colloidal systems yields an energy barrier caused by double-layer repulsions which must be overcome in order to allow particles to approach and adhere. In turn, the height of this barrier provides a measure for the colloidal stability of the system.

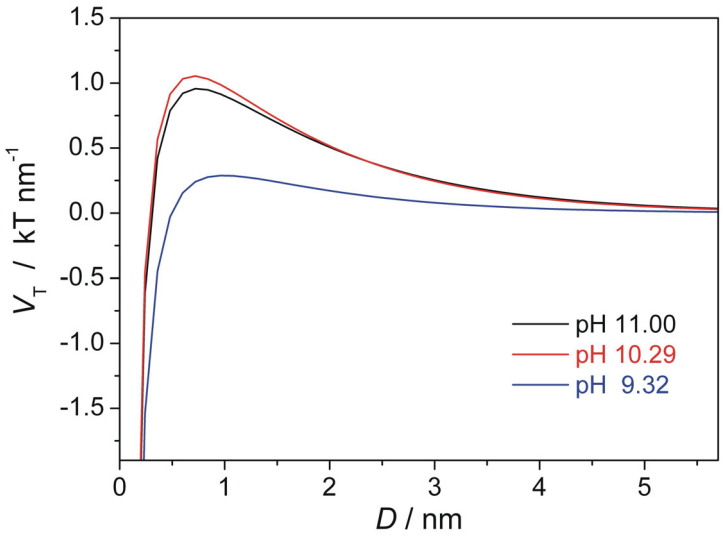

Fig. 4-32: Size-normalized total inter-particle potential energy V_T outlined as a function of the distance from the surface D for samples at different initial pH ($[Ca^{2+}] = [CO_3^{2-}] = 5$ mM and 3720 ppm silica). Curves were derived from the measured ζ potentials by applying simple DLVO theory.

It is obvious from Fig. 4-32 that a distinct barrier exists in case of the samples at pH 11.00 and 10.29, as evidenced by the pronounced maximum of V_T at about 0.7 nm (which agrees qualitatively with the observed spatial separation of nanoclusters within aggregates, cf. Fig. 4-5 and Fig. 4-9c). By contrast, the progression of the curve

calculated for pH 9.32 is much flatter. Taking the mean cluster diameter to be 1.1 nm (which corresponds to the average of the size values displayed in Fig. 4-4), barrier heights amount to approximately 1.1 kT for pH 11.00 and 10.29, and only to about 0.3 kT at pH 9.32 (cf. Table 4-10). This finding is well in line with the behavior of the samples observed by cryo-TEM (cf. Fig. 4-30) as well as visual inspection and XRD (see Section 4.4.11). The poor colloidal stability of the system at pH 9.32 becomes manifest in reinforced cluster aggregation and their embedding in an emerging silica gel matrix, which is possible due to weaker repulsions in-between silicate oligomers bound to clusters and forming purely siliceous colloids or polymeric fragments. In addition, reduced repulsion permits direct contact of silica-decorated clusters, which facilitates cluster aggregation and eventually leads to nucleation. As opposed to that, solutions at higher pH contain mutually repulsive single clusters or different aggregated states which are yet still stabilized against cluster coalescence and nucleation.

It is worth mentioning at this point that the calculated energy barriers are relatively small. As a rule of thumb, colloidal dispersions are assumed to be stable against flocculation for a barrier height of $\geq$ 10 kT.[74] In principle, the fact that the carbonate concentration used in the evaluations exceeds the expected value in the solutions would implicate a higher actual barrier, whereas neglecting the presence of charged silicate species should have an opposite effect. However, doubling the ion concentrations in the calculations showed that both parameters influence the barrier height to a minor extent as compared to shortcomings introduced to the model when using the Hamaker constant of amorphous silica. The latter applies for a bulk silica phase and will therefore drastically overestimate the attractive potential between hydrated layers of silicate oligomers bound in the periphery of the clusters. This implies that the true magnitude of V_A should be markedly lower, thus increasing the energy barrier. This context is addressed in recent reviews of the capability of the DLVO theory to predict the stability of colloidal dispersions, concluding that simple considerations of van-der-Waals attraction and double-layer repulsion result in energy barriers which are too low to validate experimental observations.[75] These discrepancies were ascribed to the lack of input data on both compositional variations throughout the volume of the particles (e.g. core-shell character) and structural details of their surface. One such effect refers to the role of adsorbed layers of organic polymers, for which it was suggested that steric hindrance of protruding polymeric chains may substantially contribute to a prevention of particle aggregation.[76] In fact, a similar mechanism was proposed to explain the

partially anomalous coagulation behavior of dispersed silica colloids, and there is evidence that oligomeric and polymeric silicate species occur at the silica-water interface.[77] It may readily be envisaged that such an "electrosteric" scenario also accounts for the stability of silica-bearing clusters in the present systems and further rationalizes the low energy barriers obtained on the basis of the DLVO theory.

4.5 Summary and Conclusions

In consistency with earlier studies, the performed experiments have shown that nanoclusters of calcium carbonate are formed in solution prior to nucleation[25] and that these earliest precursors can be imaged by means of cryo-TEM.[27] In supersaturated systems without any additives, the first post-nucleation species detected are ACC particles with a typical size of ~30 nm (Fig. 4-33, path a),[27] which grow in the following through Ostwald ripening or nourished either by simple monomer addition or continuous attachment of cluster units. Ultimately, the ACC phase is transformed directly to stable calcite or first to one of the kinetically favored metastable crystalline polymorphs,[8-10] based on either a dissolution-reprecipitation mechanism or solid-state conversions.[15,18a]

When precipitating $CaCO_3$ in the presence of silica, the crystallization process can be arrested at distinct stages, depending on the specific conditions chosen. In rather dilute sols, as-formed ACC nanoparticles become enveloped by a skin of silica and hence protected against the amorphous-to-crystalline phase transformation (see Chapter 2).[42] At higher concentrations as in the present experiments, the silica interferes already in the pre-nucleation stage by interacting with ion clusters, presumably replacing water and/or hydroxide ions[18b] in the hydration shell around them. In strongly alkaline media, sheathing of the clusters by silica efficiently impedes cluster-cluster aggregation and coalescence, such that merely loose agglomerates exist in equilibrium and nucleation remains prevented in the long term (Fig. 4-33, path d). Binding of oligomeric silicate species in the periphery of the clusters thus permits partial aggregation, but not fusion. Consequently, though heavily supersaturated with respect to both ACC and calcite, the solutions precipitate neither colloidal amorphous particles nor crystallites. Instead, cryo-TEM images prove the presence of numerous nanoclusters even after prolonged ageing. To our knowledge, this is for the first time that these early $CaCO_3$ precursors were stabilized against nucleation at high concentrations in solution over long terms.

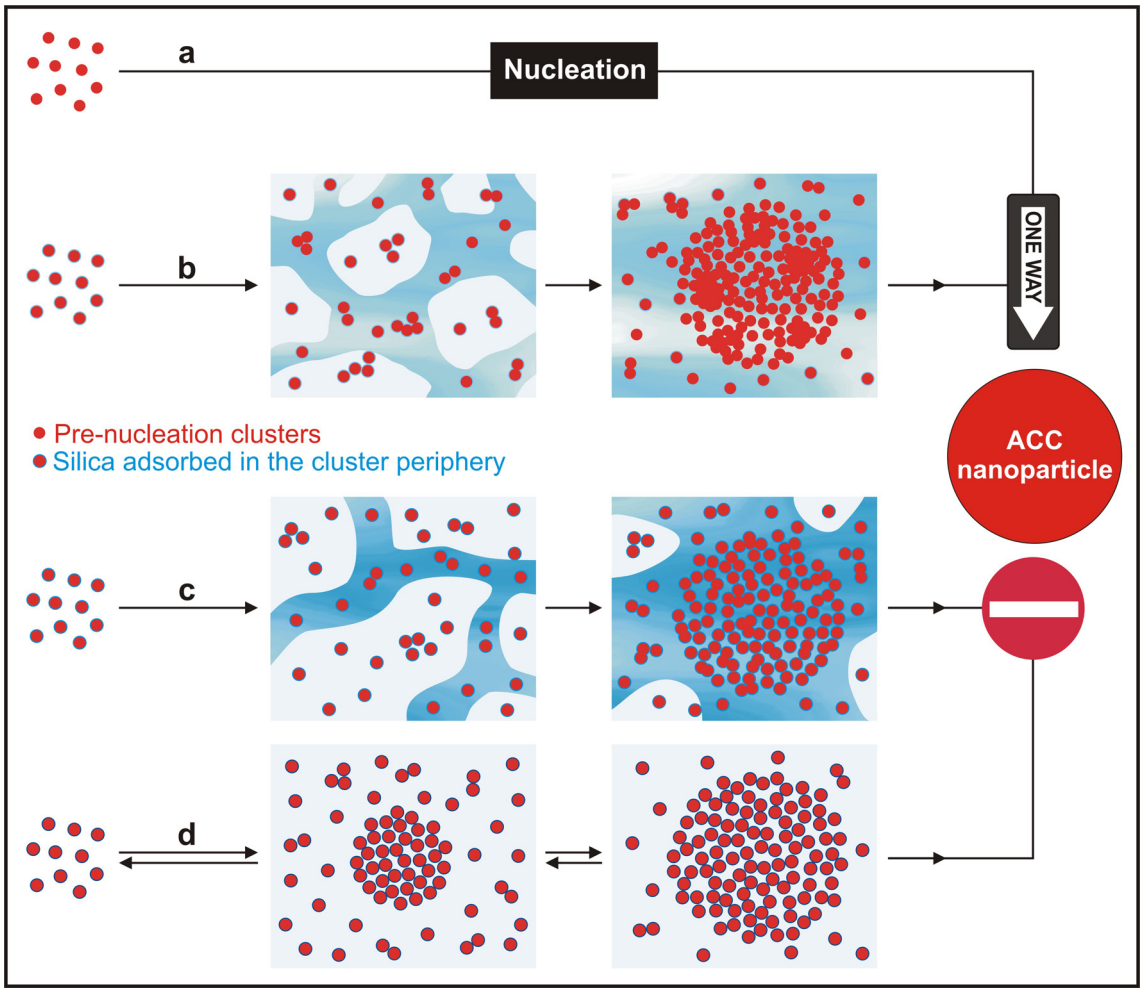

Fig. 4-33: Early stages of $CaCO_3$ crystallization (a) and the effect of added silica on the aggregation behavior and coalescence of pre-nucleation clusters at pH 9.32 (b), 10.29 (c), and 11.00 (d). Blue domains in (b) and (c) signify the silica gel matrix forming at lower pH. Note that structures are not drawn to scale

Indeed, Oaki *et al.* obtained a hybrid material consisting of ACC grains with sizes of 2-3 nm embedded in an organic matrix by co-precipitating $CaCO_3$ with a considerable amount of polyacrylic acid,[78] suggesting that pre-nucleation clusters were cemented by the polymer into solid state before potential nucleation. By contrast, the effect of dissolved silica appears to rely on a virtual encapsulation of individual carbonate clusters, such that they exist primarily isolated from each other and remain dispersed in solution.

Due to their abundance and temporal stability in the system, the clusters can readily be characterized *in situ* by common techniques like DLS or SAXS, as exemplified by the analyses conducted in this work. Under the given conditions, protection by the silica is furthermore efficient to enable drying of the clusters without affecting their structural integrity. Thereby, straight isolation procedures such as freeze-drying the solutions or induced precipitation gave a bulk composite material of $CaCO_3$ clusters accommodated

in a matrix of amorphous silica, while preceding careful dialysis allowed for the deposition of discrete clusters on TEM grids. The developed isolation protocols appear highly promising in view of an experimental route to provide pre-nucleation clusters in large amounts and thus facilitate concerted in-depth analyses of these elusive species. IR and TEM studies performed on dry samples further corroborate that the traced clusters consist of $CaCO_3$ and that the major phase present is ACC.

The most important observation made in this work is that the capability of silica to stabilize the system against nucleation of calcium carbonate can be reduced by lowering the initial pH of the samples. Thereby, the degree of the inhibition of cluster fusion inside the aggregates could be tuned and, in doing so, insight was gained into the fundamentals of homogeneous nucleation. With decreasing pH, the enhanced tendency of silica to undergo condensation reactions results in a growing fraction of aggregated structures, which interconnect progressively to constitute a gel accommodating the carbonate clusters (Fig. 4-33, path c). Shielding of the clusters fails at lower pH, and individual clusters become subject to local fusion and coalescence. Below a certain threshold in pH (Fig. 4-33, path d), deficient cluster stabilization allows for the formation of larger and denser aggregates with direct cluster-cluster contact, which eventually merge to build nanoparticles of ACC. Extrapolating these findings to the situation in the absence of silica (black box in path a of Fig. 4-33) strongly suggests that nucleation is induced by aggregation of pre-nucleation clusters. The generation of a true interface, i.e. phase separation, appears to rest upon the coalescence of clusters within the aggregates, at a yet unknown stage. Fusion of the clusters might be triggered by the release of (structural) water from the inside of the aggregates, driven by osmotic pressures. Continued cluster fusion ultimately leads to the precipitation of ACC nanoparticles, the initial diameter of which is determined by the size of the preceding cluster aggregates, which in turn is limited to ~30 nm probably due to surface charge effects during aggregation. The role of the silica is thus to decelerate the processes that underlie nucleation, and enable their experimental observation.

The detailed mode of silica binding on $CaCO_3$ clusters remains uncertain. A mechanism based on local acidification around forming clusters due to dissociation of bicarbonate ions and consequent silica polymerization, as found for ACC nanoparticles growing in alkaline silica solutions (see Chapter 2 and Fig. 4-34),[42] is in principle feasible but at least worth discussing when considering the dimensions of the clusters. Since the clusters were shown to consist of approximately 35 $CaCO_3$ units only,[25] it must be

doubted if the dissociation of on average about 6 bicarbonate ions during formation of a single cluster at pH 11 is enough to provoke a sensible decrease in the local pH and trigger condensation of silica. On the other hand, the bulk pH is relatively high in the present experiments and therefore the amount of bicarbonate ions producing local pH gradients in general fairly low.

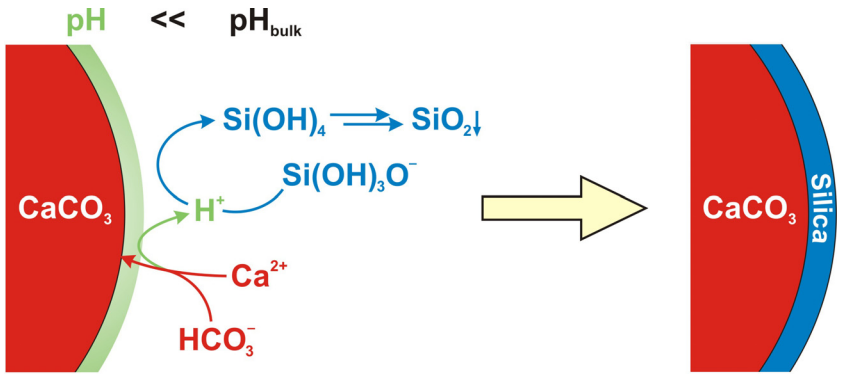

Fig. 4-34: Scheme depicting the surface of a $CaCO_3$ particle growing at moderately high pH in the presence of dissolved silica. Dissociating bicarbonate ions release protons nearby the surface of the particle, thus causing a decrease in the local pH (zone of lower pH indicated in green) and the deposition of a layer of amorphous silica all over the particle.

An alternative plausible scenario is that silicate species bind to the clusters owing to electrostatic interactions with Ca^{2+} ions in the cluster periphery assisted by water molecules, in analogy to the effect of polyacrylate.[78] The latter may be driven by a gain in entropy,[79] and would explain the poor stabilization found at lower pH.

The described experiments have further pointed out that nano-sized clusters apparently not consisting of a purely siliceous phase also occur in the studied reference samples, especially in mixtures of sodium carbonate and silica. Although more profound investigations are necessarily required, it seems reasonable to infer that the silica is capable of binding more or less non-specifically on clusters of different, even actually well-soluble salts and, in doing so, increasing the frequency of such species in solution relative to the free ions in equilibrium. This may render the addition of silica an interesting analytical tool for the identification, capture and characterization of pre-nucleation clusters in general, as described exemplarily for the model system $CaCO_3$ in this work.

It is furthermore obvious that the model of aggregation-based nucleation bears general relevance for crystallization processes, especially when considering that cluster-like species were reported also for a series of other minerals.[34-41] Finally, the presented results illustrate that the crystallization of calcium carbonate can be influenced already

in the pre-nucleation stage by means of suitable additives. In a similar manner as reported for polyacrylate and triphosphate[32] as well as certain peptides,[33] the interaction between dissolved silica and neutral ion clusters was found to hinder effectively their aggregation and thus impede nucleation Clearly, colloidal stabilization of solutions containing pre-nucleation clusters is a powerful concept for the deliberate prevention of crystallization and hence depicts a promising approach towards novel strategies for scale inhibition.

4.6 References

(1) Becker, R.; Döring, W. *Ann. Phys.* **1935**, *24*, 719.

(2) Meldrum, F. C.; Cölfen, H. *Chem. Rev.* **2008**, *108*, 4332.

(3) Cölfen, H.; Antonietti, M. *Mesocrystals and non-classical crystallization*; Wiley: Chichester, 2008.

(4) Cusack, M.; Freer, A. *Chem. Rev.* **2008**, *108*, 4433.

(5) MacAdam, J.; Parsons, S. A. *Reviews Environ. Sci. Biotechnol.* **2005**, *3*, 159.

(6) (a) Aizenberg, J.; Lambert, G.; Weiner, S.; Addadi, L. *J. Am. Chem. Soc.* **2002**, *124*, 32. (b) Addadi, L.; Raz, S.; Weiner, S. *Adv. Mater.* **2003**, *15*, 959.

(7) Meldrum, F. C. *Int. Mater. Rev.* **2003**, *48*, 187.

(8) (a) Reddy, M. M.; Nancollas, G. H. *J. Cryst. Growth* **1976**, *35*, 33. (b) Tracy, S. L.; Williams, D. A.; Jennings, H. M. *J. Cryst. Growth* **1998**, *193*, 382.

(9) Ogino, T.; Suzuki, T.; Sawada, K. *Geochim. Cosmochim. Acta* **1987**, *51*, 2757.

(10) Rieger, J.; Frechen, T.; Cox, G.; Heckmann, W.; Schmidt, C.; Thieme, J. *Faraday Discuss.* **2007**, *136*, 265.

(11) Nyvlt, J. *Cryst. Res. Technol.* **1995**, *30*, 443.

(12) Mann, S.; Cölfen, H. *Angew. Chem. Int. Ed.* **2003**, *42*, 2350.

(13) Brecevic, L.; Nielsen, A. E. *J. Cryst. Growth* **1989**, *98*, 504.

(14) Faatz, M.; Gröhn, F.; Wegner, G. *Adv. Mater.* **2004**, *16*, 996.

(15) Bolze, J.; Peng, B.; Dingenouts, N.; Panine, B.; Narayanan, T.; Ballauff, M. *Langmuir* **2002**, *18*, 8364.

(16) Weiner, S.; Sagi, I.; Addadi, L. *Science* **2005**, *309*, 1027.

(17) (a) Gower, L. B.; Odom, D. J. *J. Cryst. Growth* **2000**, *210*, 719. (b) Gower, L. B. *Chem. Rev.* **2008**, *108*, 4551.

(18) (a) Wolf, S. E.; Leiterer, J.; Kappl, M.; Emmerling, F.; Tremel, W. *J. Am. Chem. Soc.* **2008**, *130*, 12342. (b) Wolf, S. E.; Müller, L.; Barrea, R.; Kampf, C. J.; Leiterer, J.; Panne, U.; Hoffmann, T.; Emmerling, F.; Tremel, W. *Nanoscale* **2011**, DOI: 10.1039/c0nr00761g.

(19) Cölfen, H. *Curr. Opin. Colloid Interface Sci.* **2003**, *8*, 23.

(20) Mann, S. *Nature Mater.* **2009**, *8*, 781.

(21) Horn, D.; Rieger, J. *Angew. Chem. Int. Ed.* **2001**, *40*, 4330.

(22) Guillemet, B.; Faatz, M.; Gröhn, F.; Wegner, G.; Gnanou, Y. *Langmuir* **2006**, *22*, 1875.

(23) Beniash, E.; Aizenberg, J.; Addadi, L.; Weiner, S. *Proc. R. Soc. Lond. B* **1997**, *264*, 461.

(24) Cölfen, H.; Qi, L. *Chem. Eur. J.* **2001**, *7*, 106.

(25) Gebauer, D.; Völkel, A.; Cölfen, H. *Science* **2008**, *322*, 1819.

(26) Meldrum, F. C.; Sear, R. P. *Science* **2008**, *322*, 1802.

(27) Pouget, E. M.; Bomans, P. H. H.; Goos, J. A. C. M.; Frederik, P. M.; de With, G.; Sommerdijk, N. A. J. M. *Science* **2009**, *323*, 1455.

(28) Lam, R. S. K.; Charnock, J. M.; Lennie, A.; Meldrum, F. C. *Cryst. Eng. Comm.* **2007**, *9*, 1226.

(29) Gebauer, D.; Gunawidjaja, P. N.; Ko, J. Y. P.; Bacsik, Z.; Aziz, B.; Liu, L.; Hu, Y.; Bergström, L.; Tai, C. W.; Sham, T. K.; Eden, M.; Hedin, N. *Angew. Chem. Int. Ed.* **2010**, *49*, 1.

(30) Politi, Y.; Levi-Kalisman, Y.; Raz, S.; Wilt, F.; Addadi, L.; Weiner, S.; Sagi, I. *Adv. Funct. Mater.* **2006**, *16*, 1289.

(31) Hasse, B.; Ehrenberg, H.; Marxen, J. C.; Becker, W.; Epple, M. *Chem. Eur. J.* **2000**, *6*, 3679.

(32) Gebauer, D.; Cölfen, H.; Verch, A.; Antonietti, M. *Adv. Mater.* **2009**, *21*, 435.

(33) Gebauer, D.; Verch, A.; Börner, H. G.; Cölfen, H. *Cryst. Growth Des.* **2009**, *9*, 2398.

(34) Furrer, G.; Phillips, B. L.; Ulrich, K. U.; Pöthig, R.; Casey, W. H. *Science* **2002**, *297*, 2245.

(35) Navrotsky, A. *Proc. Natl. Acad. Sci. U.S.A.* **2004**, *101*, 12096.

(36) Larson, M. A.; Garside, J. *Chem. Eng. Sci.* **1986**, *41*, 1285.

(37) Posner, S.; Betts, F. *Acc. Chem. Res.* **1975**, *8*, 273.

(38) Yang, X.; Wang, L.; Qin, Y.; Sun, Z.; Henneman, Z. J.; Moradian-Oldak, J.; Nancollas, G. H. *J. Phys. Chem. B* **2010**, *114*, 2293.

(39) Dey, A.; Bomans, P. H. H.; Müller, F. A.; Will, J.; Frederik, P. M.; de With, G.; Sommerdijk, N. A. J. M. *Nature Mater.* **2010**, *9*, 1010.

(40) Perry, C. C. *Rev. Miner. Geochem.* **2003**, *54*, 291.

(41) Banfield, J. F.; Welch, S. A.; Zhang, H.; Ebert T. T.; Penn, R. L. *Science* **2000**, *289*, 751.

(42) Kellermeier, M.; Melero-García, E.; Glaab, F.; Klein, R.; Drechsler, M.; Rachel, R.; García-Ruiz, J. M.; Kunz, W. *J. Am. Chem. Soc.* **2010**, *132*, 17859.

(43) Russ, J. C. *The Image Processing Handbook*; CRC Press: Boca Raton, 2007.

(44) Talmon, Y. in *Modern Characterization Methods of Surfactant Systems*; Binks, B. P., Ed., Marcel Dekker Publishing Company: New York, 1999, p. 147.

(45) Provencher, S. W. *Comput. Phys. Commun.* **1982**, *27*, 213.

(46) (a) Glatter, O. *J. Appl. Crystallogr.* **1979**, *12*, 166. (b) Glatter, O. *J. Appl. Crystallogr.* **1980**, *13*, 7.

(47) Guinier, A.; Fournet, G. *Small Angle Scattering of X-rays*; Wiley: New York, 1955.

(48) Cölfen, H.; Völkel, A. *Prog. Colloid Polym. Sci.* **2004**, *127*, 31.

(49) Schuck, P. *Biophys. J.* **2000**, *78*, 1606.

(50) Hunter, R. J. *Zeta Potential in Colloid Science, Principles and Applications*; Elsevier: London/New York, 1981.

(51) Russel, W. B.; Saville, D. A.; Schowalter, W. R. *Colloidal Dispersions*; Cambridge University Press: Cambridge, 1989.

(52) Kindly provided by Dr. Uli Aschauer (Princeton University).

(53) Bergström, L. *Adv. Colloid Interface Sci.* **1997**, *70*, 125.

(54) Sjöberg, S. *J. Non-Cryst. Solids* **1996**, *196*, 51.

(55) Bogush, G. H.; Tracy, M. A.; Zukoski, C. F. *J. Non-Cryst. Solids* **1988**, *104*, 95.

(56) Voinescu, A. E.; Kellermeier, M.; Carnerup, A. M.; Larsson, A. K.; Touraud, D.; Hyde, S. T.; Kunz, W. *J. Cryst. Growth* **2007**, *306*, 152.

(57) Iler, R. K. *The chemistry of silica*; Wiley: New York, 1979.

(58) Marshall, W. L.; Warakomski, J. M. *Geochim. Cosmochim. Acta* **1980**, *44*, 915.

(59) Yang, S.; Navrotsky, A. *Chem. Mater.* **2002**, *14*, 2803.

(60) (a) Bar, R.; Sasson, Y. *Anal. Chim. Acta* **1982**, *142*, 345. (b) Kakiuchi, K.; Akutsu, H. *Biopolymers* **1983**, *22*, 1027. (c) Mani, F., Peruzzini, M.; Stoppioni, P. *Green Chem.* **2006**, *8*, 995.

(61) Nebel, H.; Neumann, M.; Mayer, C.; Epple, M *Inorg. Chem.* **2008**, *47*, 7874.

(62) Halasz, I.; Agarwal, M.; Li, R.; Miller, N. *Catal. Lett.* **2007**, *117*, 34.

(63) Yang, X.; Roonasi, P.; Holmgren, A. *J. Colloid Interface Sci.* **2008**, *328*, 41.

(64) Davis, A. R.; Oliver, B. G. *J. Sol. Chem.* **1972**, *1*, 329.

(65) Andersen, F. A.; Brecevic, L. *Acta Chem. Scand.* **1991**, *45*, 1018.

(66) Suzuki, S.; Sinn, E. *J. Mater. Sci. Lett.* **1994**, *13*, 1058.

(67) Martínez, J. R.; Ruiz, F.; Vorobiev, Y. V.; Pérez-Robles, F.; González-Hernández, J. *J. Chem. Phys.* **1998**, *109*, 7511.

(68) Buijs, K.; Schutte, C. J. H. *Spectrochim. Acta* **1961**, *17*, 927.

(69) Sobczynski, A. *Monatsh. Chem.* **1992**, *123*, 211.

(70) Li, X.; Shi, J.; Zhu, Y.; Shen, W.; Li, H.; Liang, J.; Gao, J. *J. Biomed. Mater. Res. Part B* **2007**, *83*, 431.

(71) Raz, S.; Testeniere, O.; Hecker, A.; Weiner, S.; Luquet, G. *Biol. Bull.* **2002**, *203*, 269.

(72) Singh, A.; Dash, S.; Kamruddin, M.; Ajikumar, P. K.; Tyagi, A. K.; Raghunathan, V. S.; Raj, B. *J. Am. Ceram. Soc.* **2002**, *85*, 927.

(73) Scales, P. J.; Grieser, F.; Healy, T. W.; White, L. R.; Chan, D. Y. C. *Langmuir* **1992**, *8*, 965.

(74) Buscall, R.; Ottewil, R. H. in *Polymer Colloids*; Buscall, R., Corner, T., Stageman, J. F., Eds., Elsevier: New York, 1985, Ch. 5, pp. 141-217.

(75) Croll, S. *Prog. Org. Coat.* **2002**, *44*, 131.

(76) Einarson, M. B.; Berg, J. C. *J. Colloid Interface Sci.* **1993**, *155*, 165.

(77) Healy, T. W. in *The colloid chemistry of silica*; Bergna, H. E., Ed., American Chemical Society: Washington, DC, 1994, Vol. 234, Ch. 7, pp. 147-159.

(78) Oaki, Y.; Kajiyama, S.; Nishimura, T.; Imai, H.; Kato, T. *Adv. Mater.* **2008**, *20*, 3633.

(79) Sinn, C. G.; Dimova, R.; Antonietti, M. *Macromolecules* **2004**, *37*, 3444.

(80)

Chapter 5 Monitoring Calcium Carbonate Crystallization by On-Line X-Ray Diffraction

5.1 Abstract

Calcium carbonate is the most abundant biomineral and a compound of great industrial importance. Its precipitation from solution has been studied extensively and was often shown to proceed via distinct intermediate phases which undergo sequential transformations before eventually yielding the stable crystalline polymorph, calcite. In this part of the work, the crystallization of calcium carbonate from heavily supersaturated brines was investigated in a time-resolved and non-invasive manner by means of energy-dispersive X-ray diffraction (EDXRD) using synchrotron radiation. Further, the role of silica as a soluble additive during the crystallization process was examined. Measurements were carried out at different temperatures (20, 50 and 80°C) and various silica concentrations. Experiments conducted in the absence of silica demonstrate that the technique allows for tracing the conversion of kinetically formed metastable polymorphs (vaterite and aragonite) to calcite and quantifying the progress of transformation. Addition of silica induced partially remarkable changes in the temporal evolution of polymorphic fractions existing in the system. Essentially, the formation of calcite was found to be accelerated at 20°C whereas a marked retardation or full inhibition of phase transitions was observed at higher temperatures. These findings are explained in terms of a competition between a promotional effect of silica on calcite growth rates and the kinetic stabilization of vaterite and aragonite due to adsorption or precipitation of silica on their surfaces, along with temperature-dependent variations of silica condensation rates. At high silica concentrations, the prolonged occurrence of an amorphous phase can be deduced from the data, suggesting that initially generated particles of amorphous calcium carbonate (ACC) are progressively stabilized by the silica. The results exemplify that profound insight into the mode of action and degree of influence exerted by an additive during $CaCO_3$ mineralization can be gained with the aid of on-line diffraction analysis.

5.2 Introduction

In-situ techniques which deliver data on-line from a sample in a time-dependent and non-invasive fashion are valuable tools for the investigation of crystallization scenarios

in solution, as they avoid the necessity of quenching the reaction and preclude possible artifacts or uncontrolled phase changes during workup. Rather, the traced signal reliably reflects the real situation in the system at a given time and hence potentially allows for resolving the key stages of the process and elucidating the role of additives. From the early works on, profound insight to the progress of $CaCO_3$ crystallization has in this manner been gained already by simple methods including pH, calcium activity, turbidity, or conductivity measurements.[1-9]

In combination with *ex-situ* characterizations of particles formed under certain conditions after a certain time – typically performed using techniques like light and electron microscopy, powder X-ray diffraction or infrared spectroscopy – such experimentation has contributed substantially to an understanding of the phenomena occurring during precipitation of calcium carbonate from solution. Essentially, it was confirmed that crystallization commonly involves a series of intermediates which transform into one another towards phases of higher stability.[10] At ambient temperature and pressure, amorphous calcium carbonate (ACC) was often found to be the initial solid phase nucleated, in particular under kinetic control (that is, for example, at high supersaturation).[11-13] With time, the ACC particles were converted first into the metastable crystalline polymorph vaterite and, subsequently, thermodynamically stable calcite.[1,2,5,7,14] The occurrence and lifetime of a particular phase was thereby recognized to depend strongly on the chosen experimental parameters like species concentrations, pH, agitation or the mixing procedure.[15] Temperature is another key factor in the determination of which polymorph is generated and for how long it persists in contact with a solution. Previous studies have demonstrated that heating favors the formation of aragonite.[16-18] Starting from about 40°C, noticeable amounts of aragonite were detected upon precipitation after initial conversion of ACC, at first in co-existence with either only vaterite or both calcite and vaterite.[2,16] On raising the temperature to 60-70°C, the fraction of aragonite increases at the expense of vaterite,[16] before ultimately, at ≥ 80°C, more or less pure aragonite is obtained straight after mixing.[16-18] When left in solution, the aragonite phase gradually transforms into calcite upon ageing,[2] and thus replaces vaterite as metastable intermediate in the crystallization of $CaCO_3$ at higher temperatures.

Nowadays, a number of novel techniques have been developed and applied to study calcium carbonate formation *in situ*. For instance, Rieger *et al.* recorded the crystallization of calcite from ACC and vaterite precursors in solution using X-ray

microscopy and examined the influence of added polycarboxylates on phase transitions.[7,19] Further, synchrotron small-angle X-ray scattering (SAXS) was used to monitor the initial nucleation of ACC nanoparticles in supersaturated solutions and their subsequent evolution with time in terms of size, mass and shape.[20] These experiments shed particular light on particle growth mechanisms and suggested an enlargement via addition of ions or small clusters rather than particle coalescence. This was confirmed also by static light scattering studies,[21] whereas dynamic measurements provided further information on nucleation kinetics and particle aggregation behavior under various conditions.[22,23] Combined small- and wide-angle X-ray scattering (SAXS/WAXS) setups extended the window of stages accessible by *in-situ* methodology during $CaCO_3$ crystallization, as amorphous precursors and forming crystalline particles can be detected simultaneously. By this means, Pontoni *et al.* observed growth of $CaCO_3$ microcrystals on the walls of their sample tube via gradual dissolution of ACC nanoparticles generated in mixtures of calcium chloride and sodium carbonate,[24] while Heeley *et al.* followed the amorphous-to-crystalline transformation in more concentrated suspensions with a time resolution on the order of seconds inside a circulatory cell mimicking the conditions prevailing in industrial reactors.[25] Wolf *et al.* triggered $CaCO_3$ precipitation in the contact-free environment of levitated droplets by the release of CO_2 from sodium bicarbonate solutions.[26] Cryogenic electron microscopy showed that ACC particles formed homogeneously throughout the droplets and were, as evidenced by *in-situ* WAXS, successively converted to calcite which grew heterogeneously starting from the droplet surface. In a further time-resolved WAXS study, Chen *et al.* investigated the crystallization of $CaCO_3$ upon combining calcium chloride and sodium bicarbonate at 25 and 80°C in a flow-through chamber designed to simulate practical scale formation.[27] They reported an "unstable" induction period during which signals of all three crystalline polymorphs occurred and disappeared again, as crystals nucleated in the bulk solution were pumped in and out the sampled volume. With time, particular crystalline reflections stabilized in the diffraction patterns and their intensity began to increase, which was ascribed to heterogeneous nucleation and subsequent growth on the cell walls. At the end of the experiments, only calcite was observed at 25°C whereas significant fractions of both vaterite and aragonite co-existed in equilibrium at 80°C after a reaction time of 18 min. Although distinct transformations in-between the different crystalline phases could not be directly traced in this work, it nevertheless clearly pointed out the potential of on-line diffraction analyses for

monitoring the progress of $CaCO_3$ crystallization. However, apart from the mentioned studies the amount of *in-situ* data characterizing the formation and interconversion of crystalline $CaCO_3$ polymorphs during precipitation from solution is still strongly limited, and there is no systematic investigation reported in literature particularly concerning the effect of additives on crystallization scenarios.

Energy-dispersive X-ray diffraction (EDXRD) is another method which allows for detecting *in situ* the occurrence of crystalline precursors and intermediates as a function of time on the way towards a stable mineral phase, thus permitting a characterization of crystallization mechanisms and kinetics. Previously, it has been applied for example to study solvothermal syntheses of inorganic compounds,[28] or to assess the performance and structural changes of catalysts in realistic reaction environments.[29] In the present work, this technique was used to follow the crystallization of calcium carbonate in water at temperatures ranging from 20 to 80°C. For this purpose, aqueous solutions of calcium chloride and sodium carbonate were mixed and the diffraction of the resulting suspensions was recorded over extended frames of time. In addition, the influence of added silica on transformation rates and polymorph selection was investigated. Experiments were carried out with brines of high supersaturation, in order to both ensure proper signal and imitate operating conditions in industrial settings.

5.3 Experimental Section

5.3.1 Sample Preparation and pH Measurements

Crystallization of calcium carbonate was induced by directly combining calcium chloride and sodium carbonate at high concentrations. Experiments were carried out in cylindrical quartz vials (Duran, culture tubes, outer dimensions: 12x100 mm), which had previously been cleaned by successive treatment with a solution of KOH in isopropanol, 3 M HCl, and boiling 30% HNO_3, followed by extensive rinsing with water and drying at 120°C.

The reaction was started by rapidly adding, with the aid of a graded pipette, 2.5 mL of a 0.5 M solution of $CaCl_2 \cdot 2H_2O$ (Riedel-de Haën, ACS reagent, ≥99%) to the same volume of a 0.5 M solution of sodium carbonate (Roth, anhydrous, ≥99%) (no silica) or respectively mixtures of Na_2CO_3 (0.5 M) and silica, placed in the vials together with a teflon-coated stirrer bar (15x4.5 mm). Reagent solutions were freed from CO_2 and equilibrated in tightly stoppered plastic bottles at the desired temperature for at least 2 h prior to the experiments. Notably, the order of mixing was strictly maintained in this

work as it proved to be, among other factors, essential for the reproducibility of the results. Final species concentrations in the samples were 250 mM each of $CaCl_2$ and Na_2CO_3, with silica contents of 0, 200, 600, 1200, 2000, 5000, 10000, and 20000 ppm (which corresponds to molar concentrations of 0, 3.3, 10.0, 20.0, 33.3, 83.2, 166.4, and 332.9 mM or Si/Ca molar ratios of 0.013, 0.040, 0.080, 0.133, 0.333, 0.666, and 1.332). Straight after combining reagents, vials were closed firmly with a screw cap and turned upside down once to facilitate the mixing process. This was found to be important at 20°C as the samples initially were gelous brines and developed within few minutes into less viscous and stirrable slurries, while at higher temperatures a homogeneous suspension was achieved more or less instantaneously.

The pH of the samples was determined at 20°C in an independent series of experiments. To that end, reagents were combined in small beakers and a glass electrode (Mettler-Toledo InLab Micro) was quickly immersed in the solution. The system was sealed against the atmosphere using Parafilm and the pH was measured under vigorous stirring with a Schott laboratory pH meter (model CG-843), which was connected to a computer. Values were read continuously in steps of 5 s over a total period of 60 min after mixing.

5.3.2 Energy-Dispersive X-Ray Diffraction (EDXRD) Experiments

EDXRD measurements were performed using beamline F3 of the storage ring DORIS III at HASYLAB (DESY, Hamburg, Germany). It receives white synchrotron radiation from a bending magnet with a critical energy E_C of 16 keV and positron beam energy of 4.45 GeV. X-rays diffracted by a sample are traced by a nitrogen-cooled solid-state germanium detector with 2048 channels, which has an energy resolution $\Delta E/E$ of about 0.01 above 26 keV and can be positioned at horizontal angles of $0 < 2\theta < 30°$ relative to the incident beam. Detector channels were calibrated for energies by measuring fluorescence lines of several different heavy metals (Mo, Sn, Gd, and Ba). The interval of energies observable with the settings chosen in this work was found to range roughly from 6 to 52 keV. For a given detector angle, E values of occurring peaks can be translated to d spacings of the corresponding crystal planes via Eqn. 5-1, where h is Planck's constant and c the speed of light.

$$d = \frac{hc}{2E\sin(\theta)} \qquad \text{(Eqn. 5-1)}$$

To cover all relevant Bragg reflections of the different $CaCO_3$ polymorphs, 2θ was adjusted to approximately 10° in the present study thus rendering d spacings from about 1.37 to 12.1 Å accessible. The as-calculated experimental d-scale was tested and confirmed by measuring standard crystalline calcite and witherite ($BaCO_3$) as references.

Immediately after mixing reagents, the quartz tubes containing the samples were inserted into a custom-designed glass jacket which was centered in the beam and had windows on both sides of the vial allowing the X-rays to pass the solutions without the need to travel also through the outer mantle. A sketch depicting the assembly used for the experiments is shown in Fig. 5-1.

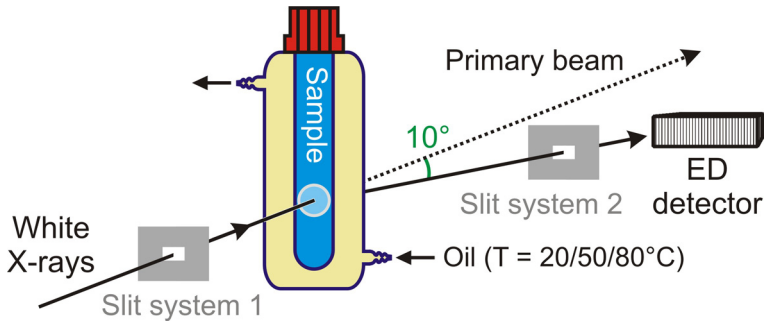

Fig. 5-1: Scheme of the experimental setup used for EDXRD measurements.

The glass jacket surrounding the tubes was circulated by oil supplied from a thermostat (Julabo FP50), which was regulated such that the temperature of the solution inside the tubes was kept constant at 20, 50 and 80°C, respectively. The temperature accuracy of the setup is estimated to ± 0.5°C. The incident beam was collimated to the sample with a tungsten double-slit system adjusted to 300x300 µm, while a second slit system located in-between sample and detector (set to 200x200 µm for best results) served to reduce Compton scattering.

As soon as the vial was mounted and X-rays were available, data acquisition was initiated. The delay between mixing and measurement start, usually being in the range of 1-2 min, was noted and accounted for in the evaluations. For all samples, diffraction was monitored in 20 subsequent runs, each averaging over a period of 450 s (which therefore is the time resolution of the present experiments). During data collection, solutions were stirred at a constant frequency of 1200 rpm by a magnetic plate placed underneath the thermostatted jacket, ensuring that precipitated material was evenly suspended and thus uniformly hit by the beam.

5.3.3 Data Evaluation

The obtained raw data were first normalized for the time-dependent intensity of the incident beam, that is, spectra were divided by the mean ring current operating during the respective run. Subsequently and before any further processing of the data, the integral area of the most important reflections was determined relative to the background for each of the polymorphs occurring in the respective sample, which were (104) ($E_{\text{C-104}} \approx 23.1$ keV, $d_{\text{Lit}} = 3.035$ Å) for calcite, (110) ($E_{\text{V-110}} \approx 19.7$ keV, $d_{\text{Lit}} = 3.573$ Å), (112) ($E_{\text{V-112}} \approx 21.3$ keV, $d_{\text{Lit}} = 3.294$ Å) and (114) ($E_{\text{V-114}} \approx 25.7$ keV, $d_{\text{Lit}} = 2.730$ Å) for vaterite, and (111) ($E_{\text{A-111}} \approx 21.4$ keV, $d_{\text{Lit}} = 4.341$ Å) as well as (012) ($E_{\text{A-012}} \approx 25.9$ keV, $d_{\text{Lit}} = 2.734$ Å) for aragonite.[30] Based on the results and since the only phase detected at the end of experiments conducted in the absence of silica was calcite, the reaction progress α as a function of time was defined and calculated as the ratio of the integral area of the (104) reflection at time t and the corresponding average value determined for the silica-free samples at each temperature after complete conversion to calcite, according to:

$$\alpha(t) = \frac{A_{\text{C-104}}(t)}{A_{\text{C-104, final}}} \qquad \text{(Eqn. 5-2)}$$

The relative fraction of calcite (f_{C}) present at a given time in binary mixtures with vaterite, typically encountered at 20 and 50°C, was derived using Rao's equation but employing integrated peak areas instead of maximum intensities:[31]

$$f_{\text{C}} = \frac{A_{\text{C-104}}}{A_{\text{C-104}} + A_{\text{V-110}} + A_{\text{V-112}} + A_{\text{V-114}}} \qquad \text{(Eqn. 5-3)}$$

For systems in which calcite coexisted with aragonite, as observed commonly at 80°C, f_{C} was obtained from the peak areas of the two nominally strongest reflections, i.e. calcite-(104) and aragonite-(111), utilizing an empirical relation suggested by Wada *et al.* (Eqn. 5-4).[32]

$$f_{\text{C}} = \frac{1}{1 + 3.9 \cdot A_{\text{A-111}} / A_{\text{C-104}}} \qquad \text{(Eqn. 5-4)}$$

Since none of the samples contained all three polymorphs, the fraction of the occurring metastable phase could readily be calculated via $f_{\text{V/A}} = 1 - f_{\text{C}}$. Note that values for α and f as well as diffraction patterns are referred to the time when half of the corresponding measurement run was completed.

After the above evaluations, data were further processed to facilitate graphical visualization of the temporal evolution in the diffraction patterns. First, background scattering originating mainly from the glass walls of the vials and water was subtracted by fitting 50-point baselines to the broad amorphous hillock extending over almost the entire raw spectra. Background-corrected patterns were subsequently smoothed using a moving-average routine with a box width of 10 points, in order to reduce noise. This procedure did not affect peak heights and areas to a noticeable extent. Finally, to enable a better comparison, intensity values of patterns acquired for samples with various silica concentrations at a given temperature were normalized with respect to the final peak maximum of the calcite (104) reflection in the corresponding reference without added silica, which was arbitrarily set to $I = 100$. With the processed data, two-dimensional (2D) intensity contour plots as well as three-dimensional (3D) representations of time-dependent pattern series were generated. Selected graphs are shown in the following, while the full dataset is reproduced in Appendix B.

5.4 Results and Discussion

5.4.1 pH Measurements

Since the pH is a crucial parameter for the chemistry of both carbonate and silicate in aqueous media and, in turn, provides information on the speciation of the components in solution as well as ongoing precipitation or polymerization processes, it was measured exemplarily at 20°C for samples at different silica concentrations. The resulting time-dependent progressions of the pH during the first hour after combining reagents are displayed in Fig. 5-2. When no silica is added (Fig. 5-2a), the pH – initially being about 9.8-9.9 – drops to values below 8.5 within the first 5 min after mixing, which reflects the precipitation of $CaCO_3$ from solution and has been described as “unstable stage” or induction period in the literature.[2-4] During this interval, ACC particles are likely to be generated. Their transformation to crystalline polymorphs is accompanied by a decrease in pH due to the higher solubility of ACC relative to the anhydrous phases,[11] which causes the concentration of carbonate ions in solution and hence the alkalinity to lower in the course of transformation. ACC conversion is essentially completed once the incipient steep decline in pH is terminated (i.e. after ~5 min). At this point, a plateau is reached and the pH decays only slightly in the following before, at around 25 min, a second step-like decrease from about 8.3 to 8.0 is observed. Eventually, a constant level of pH is achieved and there are no further significant changes with time, indicating that

a stable equilibrium between the solid phase and the dissolved ions has been established.

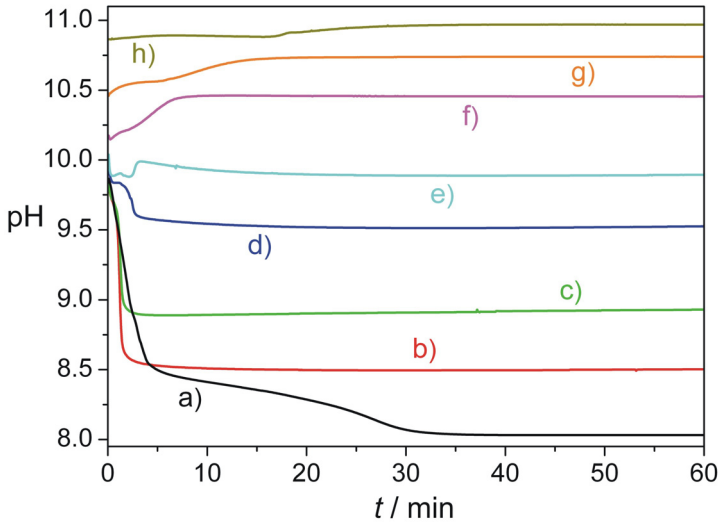

Fig. 5-2: Temporal evolution of the pH during crystallization of calcium carbonate from solutions at 20°C and $[Ca^{2+}] = [CO_3^{2-}] = 250$ mM in the presence of (a) 0, (b) 200, (c) 600, (d) 1200, (e) 2000, (f) 5000, (g) 10000, and (h) 20000 ppm SiO_2, monitored over a period of 60 min after mixing reagents.

The occurrence of a plateau in the pH-time curve and the found two-step relaxation suggest that a metastable crystalline polymorph, likely vaterite at the given temperature, was formed as an intermediate phase and fully converted to calcite after a certain delay, as reported previously.[4] This conclusion can be rationalized when considering that calcite is less soluble than vaterite[11] and that the concentration of dissolved carbonate ions is determined by the solubility product of the most soluble phase, that is, the pH will correspond to the value set by vaterite as long as noticeable amounts of it are present in equilibrium.

Thus, the pH data hint at a significant fraction of vaterite being generated during the early stages of precipitation in the absence of silica, which is coherent with the results of EDXRD measurements (see below, Fig. 5-3a and Fig. 5-4a). Moreover, the apparent period for which the metastable intermediate endures in solution before being completely transformed to calcite (25-30 min as judged from the pH curve) is in fair agreement with what is estimated for the lifetime of vaterite at 20°C on the basis of the diffraction patterns (30-40 min, cf. Fig. 5-4a).

On addition of silica, the initial pH of the mixtures does at first not change markedly, most probably because the alkalinity of the carbonate ions outrivals any influence of the silica (Fig. 5-2b-e). In turn, at concentrations equal to or higher than 5000 ppm SiO_2, the

basic character of the additive becomes noticeable and gradually increases the starting pH to values between 10 and 11 (Fig. 5-2f-h). Precipitation of $CaCO_3$ at silica contents of 200-1200 ppm leads to an instant decrease in pH as observed for the silica-free reference. However, the final pH of the samples is the higher the more silica was added and, importantly, the pH remains constant immediately after the induction period has expired. These findings can be explained by the buffering ability of silica, which maintains the pH at the level corresponding to the particular concentration once the major part of the carbonate ions has precipitated. This implies that conclusions on possibly occurring metastable intermediate phases and crystallization kinetics can no longer be drawn from the pH data when silica is present.

At 1200 ppm SiO_2, the alkaline nature of silicate is almost sufficient to compensate the removal of carbonate ions such that the pH is only slightly lowered before reaching a constant value. When further raising the silica concentration, the former decrease in pH turns into an increase with time, which is particularly pronounced at 5000 and 10000 ppm SiO_2 (Fig. 5-2f-g). Presumably, this feature originates from enhanced silica condensation reactions, which have been shown to provoke an increment in pH as acidic silanol groups are consumed.[33] In this regard, data indicate that samples at higher silica concentrations contain an appreciable amount of polymerized silicates, which may readily adsorb on or co-precipitate with $CaCO_3$ polymorphs.

Oligomerization of silica under the given conditions might be triggered by the presence of free Ca^{2+} ions which screen negative charges and thereby facilitate condensation.[34] Alternatively, the formation of $CaCO_3$ (both amorphous and crystalline) could by itself induce polymerization of siliceous species. It has been proposed that, in alkaline media, growing carbonate particles cause a reduction of the pH in their vicinity as bicarbonate ions dissociate to locally restore equilibrium speciation.[35] This is expected to sensibly decrease the solubility of silica nearby the surface of the particles, potentially resulting in local silica precipitation as observed for grains of ACC which were coated in situ by siliceous skins when growing in silica-rich solutions at high pH (see Chapter 2).[22]

The initial period over which condensation processes are active evidently increases with the amount of silica added, from ~3 min at 2000 ppm SiO_2 to around 15 min at 10000 ppm. This suggests either that condensation is slower at higher concentrations or, more probably, that a growing fraction of the silica polymerizes. At the highest studied silica concentration (20000 ppm), time-dependent changes of the pH are in turn much less distinct and there is only a slight increase during the first 30 min discernible (Fig. 5-2h).

Most likely, the excess of silica present under these conditions effectively buffers any variations due to carbonate precipitation and silica condensation, such that the pH remains virtually the same from the very beginning on. Similar effects seem to operate also to some extent at 10000 ppm SiO_2, given that in this case a smaller total rise in pH is found than at 5000 ppm.

In any case, measurements evidence that calcium carbonate formation takes place at a more or less constant pH in all silica-containing systems subsequent to an induction period of typically ≤ 20 min. However, the particular final pH value differs significantly between the various samples, which has to be taken into account when discussing the influence of the silica on phase transformations occurring during the later stages of crystallization.

5.4.2 Crystallization of Calcium Carbonate in the Absence of Silica

Following the crystallization of $CaCO_3$ by means of EDXRD in 250 mM suspensions without added silica results in sequential diffraction patterns as illustrated in Fig. 5-3. It is obvious that, at all studied temperatures, large amounts of crystalline material are formed already within 5 min after mixing, when the first spectrum was acquired. This is in line with the progression of the pH traced for the sample at 20°C (Fig. 5-2a), which indicates that transformation of possibly occurring amorphous intermediates to crystalline phases is completed during that interval. In turn, the present findings disagree with those of previous *in-situ* diffraction studies, where an incipient period was observed in which the precipitates were entirely amorphous, ranging from about 5 min to 1 h.[24-26] This discrepancy can most probably be ascribed to unlike synthesis conditions, given that the experiments described in literature were carried out either at drastically lower supersaturation and/or distinct pH values,[24,26] or using a different mixing procedure and circulating the suspensions through a flow cell instead of simply stirring them.[25]

At both 20 and 50°C, calcite and vaterite initially co-exist in noticeable fractions. Interestingly, the vaterite signals after ~5 min are clearly stronger at 50°C than at 20°C, whereas the intensity of calcite reflections is much lower at the higher temperature (Fig. 5-3a-b). At 80°C, the major phase present in the first pattern is aragonite, with relatively small amounts of calcite (small (104) peak) and no vaterite being discernible (Fig. 5-3c). This confirms that aragonite is the preferential kinetic product formed at elevated temperatures, as reported in earlier work.[2,16-18,36]

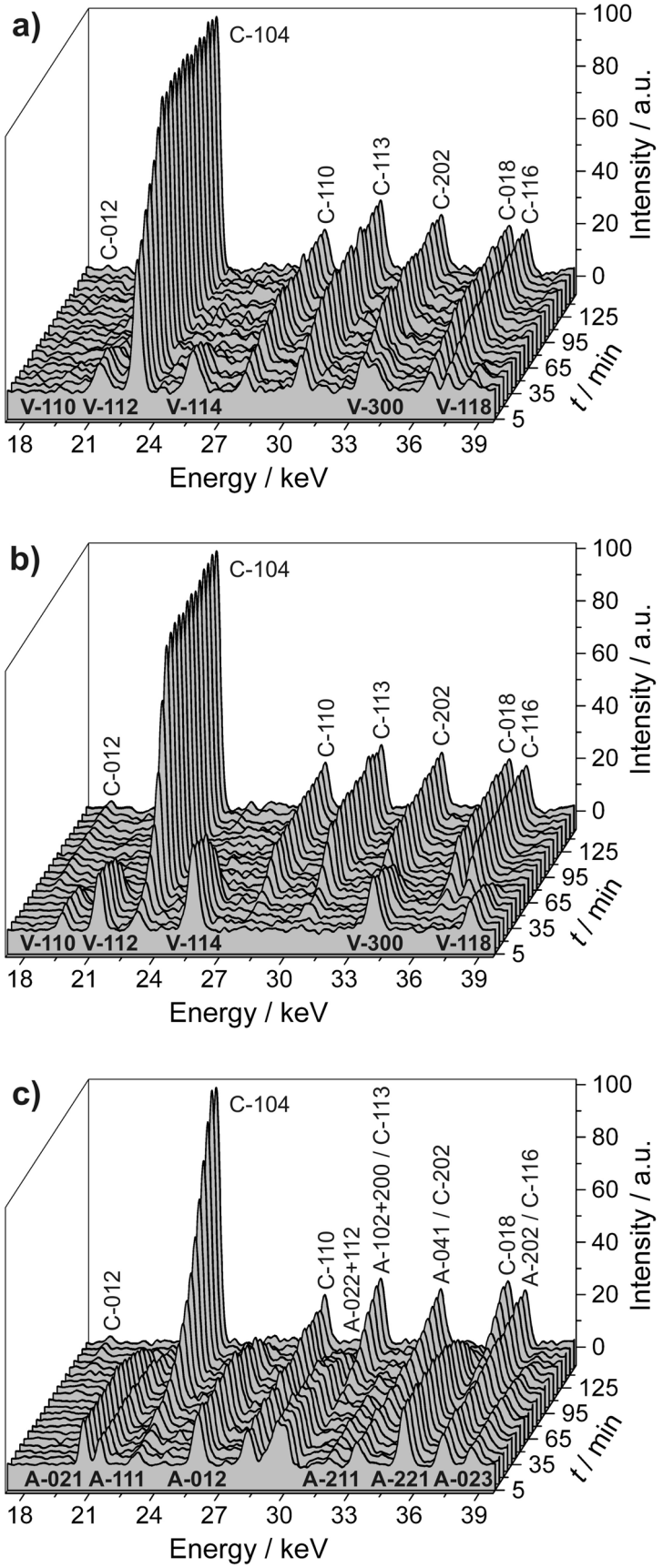

Fig. 5-3: 3D representations of time-resolved EDXRD patterns collected continuously after mixing 250 mM solutions of $CaCl_2$ and Na_2CO_3 at a temperature of (a) 20°C, (b) 50°C, and (c) 80°C. Each reflection is assigned to one or, in case of overlapping peaks, several crystal planes belonging to the distinct polymorphs and characterized by the respective Miller indices.

As time proceeds, the heights of peaks belonging to the respective metastable polymorph decrease gradually at all three temperatures. Concurrently, calcite reflections grow in intensity to reach a constant level once signals of vaterite/aragonite have vanished. As far as we are aware, this is the first time that a continuous transformation of metastable crystalline $CaCO_3$ polymorphs to calcite in solution could be directly monitored by on-line diffraction analysis. To quantify the progress of conversion, the fractions of calcite and vaterite/aragonite at a given time were calculated from the data according to Eqns. 5-3 and 5-4. Resulting values are outlined as a function of time in Fig. 5-4. Apparently, an approximately constant fraction of calcite is achieved after ~40 min at 20°C, while taking almost 60 min at 50°C and more than 130 min at 80°C. Thus, the period required for the transformation of the metastable polymorph to be completed is the longer the higher temperature.

In principle, this is in conflict with the reported increase in the rate of calcite growth with temperature which, being the overall rate-determining step during transformation in seeded solutions, implicated that conversion of both vaterite and aragonite became faster when raising the temperature.[3,4] However, Ogino *et al.* found an inverse trend when investigating precipitates formed upon direct mixing of $CaCl_2$ and Na_2CO_3 in the absence of calcite seed material.[2] They interpreted their results in terms of an increasing number of growing calcite crystals towards lower temperatures due to enhanced relative supersaturation values caused by the increase in the solubility of the metastable phases with decreasing temperature. Most likely, such effects operate also in the present experiments since the same tendency is observed for the rate of conversion and even similar ratios were found for the relative duration of quantitative transformation to calcite, which is ~3.25 times faster at 20°C than at 80°C as compared to a factor of 3-6 noted by Ogino *et al.*.[2] Decelerated conversion of vaterite and aragonite to calcite at higher temperatures was moreover distinguished in the *in-situ* WAXS study by Chen *et al.* where appreciable fractions of both polymorphs were detected only at 80°C.[27]

Inspection of the samples after the EDXRD measurements were terminated further showed that there were no $CaCO_3$ crystals stuck on the walls of the vials at all temperatures and silica concentrations examined. By contrast, solid deposits on the surface of the sample container were noted by Chen *et al.* and used to explain their diffraction data on the basis of delayed heterogeneous nucleation on the walls.[27] Such a scenario can likely be ruled out in this work.

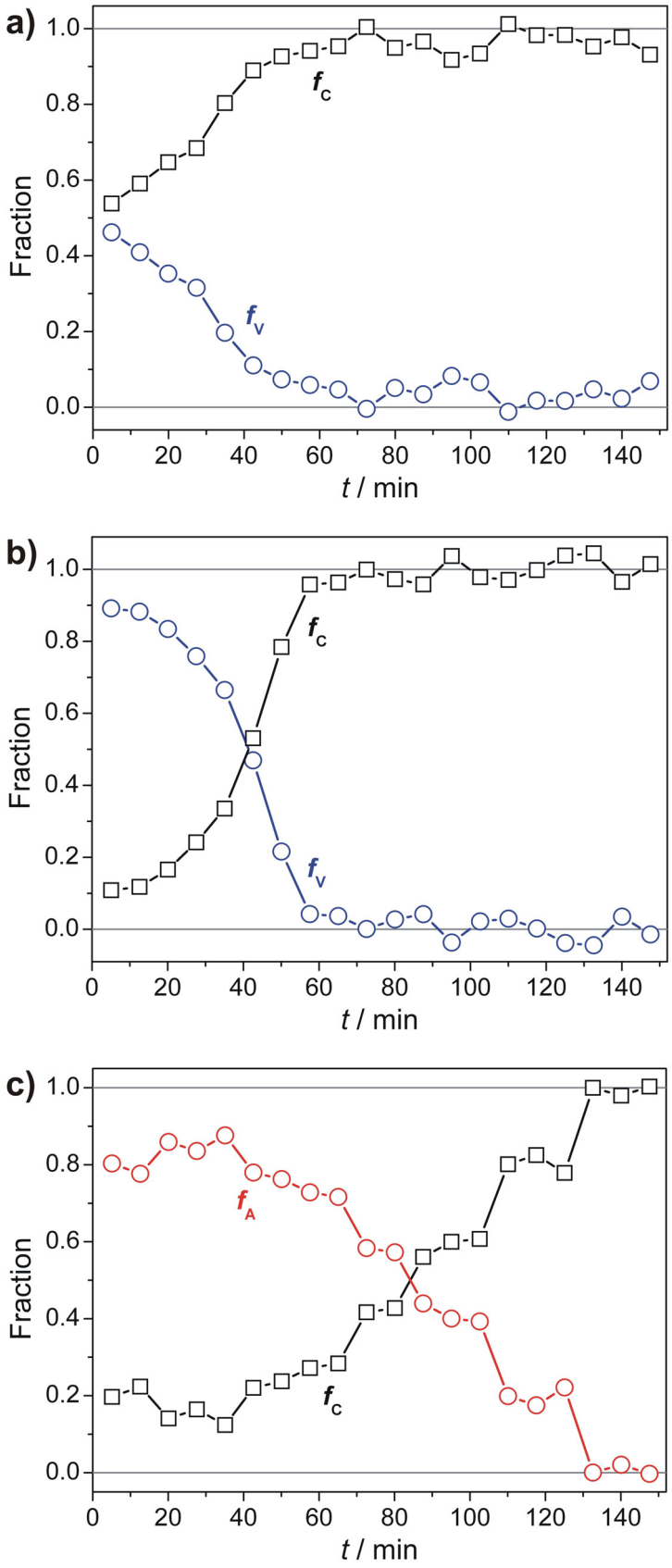

Fig. 5-4: Time-dependent progressions of the relative fractions of calcite (black squares) and vaterite (blue circles) in samples at (a) 20°C and (b) 50°C, and (c) of calcite and aragonite (red circles) at 80°C.

Upon combining reagents, precipitation of $CaCO_3$ instantly produced a "gelatinous" phase throughout the entire sample volume indicating, as suggested by Heeley *et al.*,[25] that ACC was nucleated homogeneously in solution. Subsequent transformation of the amorphous phase to the kinetic crystalline product is quick, yielding a less viscous suspension within few minutes. As no crystals of any of the polymorphs could be discerned adhering to the vial walls at any stage of the crystallization process and since the diffraction patterns display gradual variations with time from the very beginning on rather than abrupt changes,[27] it can be assumed that transformations in-between the different phases occur in the bulk solution, either through solid-state restructuring or via successive dissolution and homogeneous nucleation of the more stable polymorph.[2,7,21,26] These considerations apply likewise for samples containing silica although polymeric species, which are likely to be formed under the given conditions and in particular at higher silica concentrations,[34] may serve as nucleation sites for $CaCO_3$ crystals[9] and hence favor to some degree heterogeneous nucleation in the bulk, but still not on vial walls.

5.4.3 Effect of Added Silica on the Fractions of the Different Polymorphs

In order to facilitate a comparison of diffraction data recorded in the presence of silica to those acquired for neat $CaCO_3$ suspensions and thus to illustrate the effect of silica on $CaCO_3$ crystallization, a virtual reaction progress α was calculated in addition to the relative fractions of the different polymorphs. It is defined as the ratio of the integral determined for the calcite (104) reflection of the sample at time t and the mean area of (104) peaks found for the references without silica at each temperature after temporal changes were terminated and constant values were reached (cf. Eqn. 5-2). The latter situation is considered to be an equilibrium state in which all $CaCO_3$ present in the system has fully transformed to calcite ($\alpha = 1$). Values obtained for α and the fractions of the occurring metastable phase at distinct times are shown in Fig. 5-5 for samples at different silica concentrations and temperatures.

20°C

At 20°C (Fig. 5-5a), addition of both 200 and 600 ppm SiO_2 does apparently not affect the crystallization process to a significant extent. Except for minor differences in the progressions of f_V with time, the temporal evolution of the suspensions with respect to polymorph fractions and transformations is widely identical to what is observed in the absence of silica. In turn, when further increasing the silica concentration, marked

changes are identified. At 1200 and 2000 ppm SiO_2, the fraction of vaterite immediately after mixing is extremely low and the conversion to calcite appears to be largely completed already after the first or second EDXRD run.

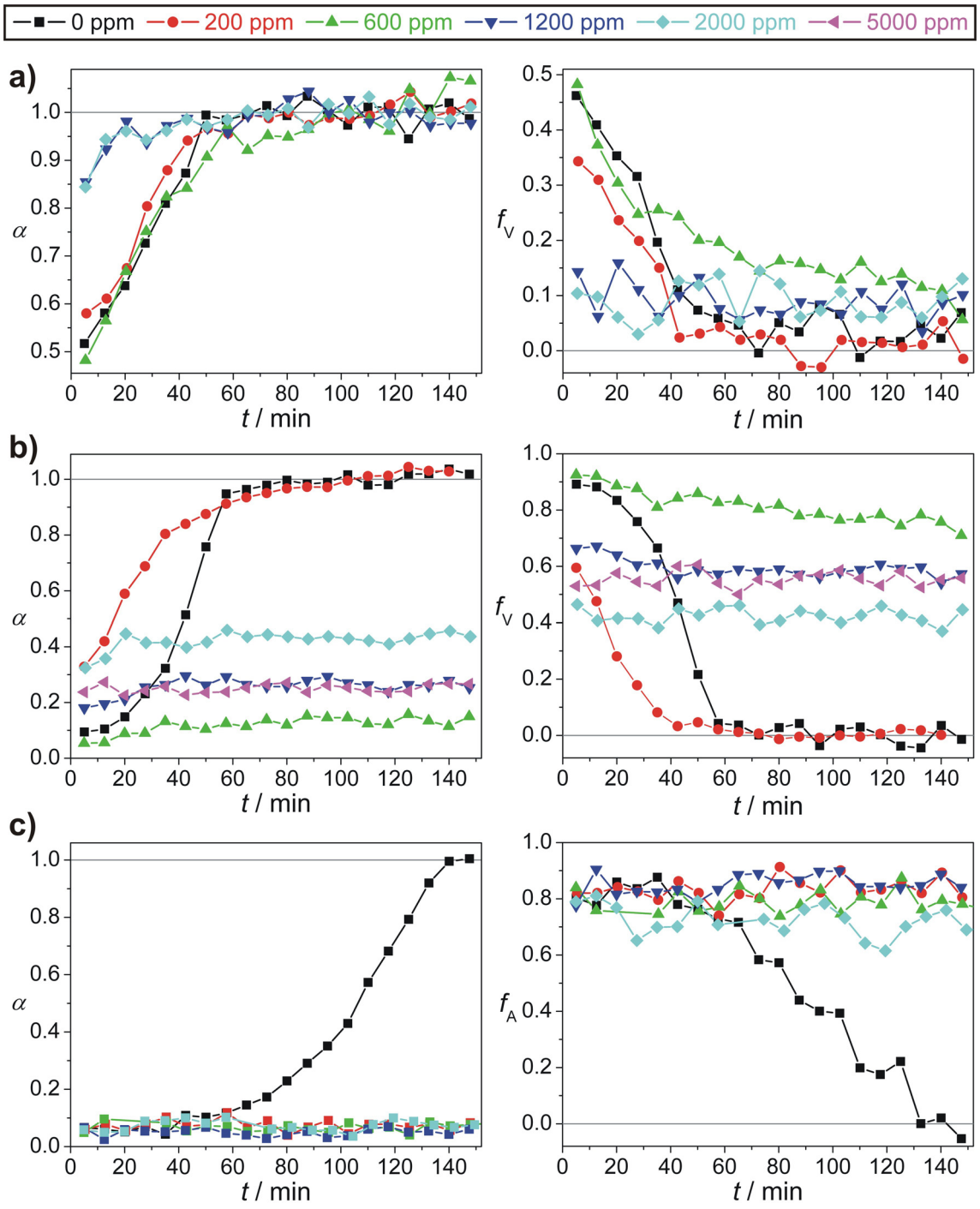

Fig. 5-5: Plots of the reaction progress α (left) and the fraction of the respective metastable polymorph f_V/f_A (right) as a function of time, as determined for samples at different silica concentrations and a temperature of (a) 20°C, (b) 50°C, and (c) 80°C.

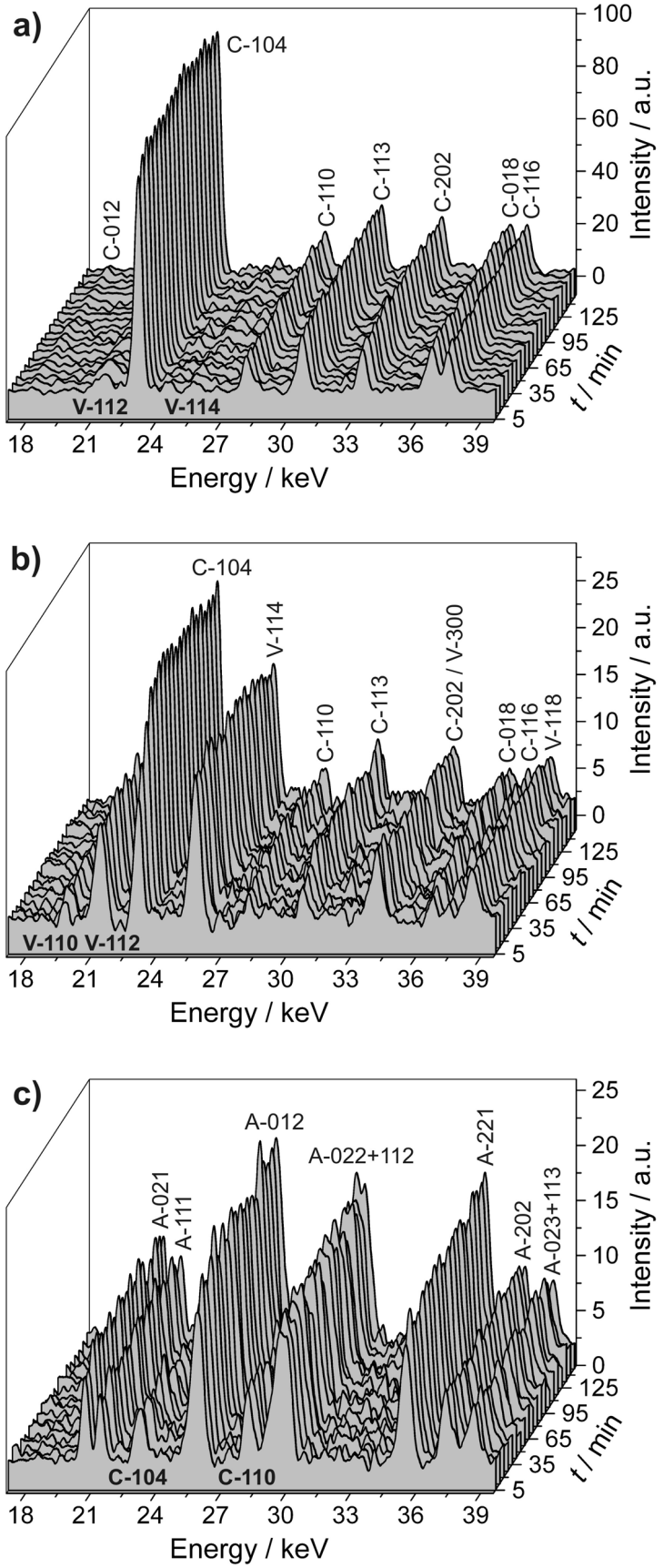

Fig. 5-6: Three-dimensional view of diffraction patterns acquired at different times from $CaCO_3$ suspensions containing 1200 ppm SiO_2 at (a) 20°C, (b) 50°C, and (c) 80°C.

Accordingly, diffraction patterns exhibit hardly any variations with time from the very beginning on, as exemplified for the sample at 1200 ppm in Fig. 5-6a (see Appendix B for EDXRD data on different silica contents). This suggests that, in the concerned concentration range, added silica promotes the formation of calcite while inhibiting or leaving unaffected growth rates of vaterite and aragonite.

A similar influence of dissolved silica on the polymorphism of calcium carbonate has been recognized in previous studies and was tentatively ascribed to reduced nucleation barriers for calcite.[9,37] Recent AFM studies revealed that promotion of calcite rests upon enhanced two-dimensional nucleation on the (104) face due to adsorbed negatively charged polymeric silica particles which attract Ca^{2+} ions and, on the other hand, reinforced kink generation and propagation caused by the attachment of small mono- and oligomers to step edges.[38] The latter phenomenon turned into an inhibitory effect at higher silica concentrations and hence provoked a net reduction of calcite growth rates, which was however not observed in the present work (higher silica contents are discussed below). These findings imply either that more calcite grows directly from the presumed amorphous precursors, or that the conversion of vaterite to calcite is accelerated under these conditions, or both.

50°C

At 50°C (Fig. 5-5b), the presence of only 200 ppm SiO_2 already seems to have a related impact on polymorph selection and transformation kinetics, as consistently lower fractions of vaterite are detected relative to the silica-free reference during the stage where calcite and vaterite co-exist. On the other hand, the period required for conversion to be virtually quantitative is in both cases about the same, indicating that generated vaterite is temporarily stabilized by dissolved silica. This effect becomes drastically more pronounced when increasing the silica concentration. At 600 ppm, the fraction of vaterite decreases only slightly with time and is as high as 80-90% over the entire period monitored. Apparently, stabilization of vaterite by silica is much more efficient than at 200 ppm, such that merely small amounts of calcite are formed. Starting from 1200 and up to 5000 ppm SiO_2, there are no longer significant temporal changes in f_V and α, apart from an initial period of about 40 and 20 min at 1200 and 2000 ppm, respectively, during which the intensity of the calcite (104) reflection gradually increases before approximately constant values are obtained (cf. Fig. 5-6b and data in Appendix B). The latter observation may originate from a retarded conversion of amorphous precursors (see below) to calcite, given that the area of vaterite peaks does

not change simultaneously. Thus, all vaterite generated in the samples is effectively prevented from transforming into stable calcite in this range of silica concentrations, at least over the studied period of around 150 min after mixing.

However, the amount of vaterite co-existing in a steady manner with calcite in the systems is reduced from > 80% to 40-60% when raising the silica content from 600 to 1200 ppm SiO_2 or higher, whereas there is no clear trend in f_V recognizable between 1200 and 5000 ppm. This behavior probably arises as a consequence of a competition between two opposing effects, namely the stabilization of vaterite by silicate species and their promotion of calcite growth rates. In analogy to what was found at 20°C, the latter phenomenon becomes enhanced starting from 1200 ppm, such that varying mean fractions of vaterite occur up to 5000 ppm depending on the degree of the influence of each factor in the particular experiment. Furthermore, since there was no distinct transformation of vaterite to calcite discernible in these samples and stabilization of formed vaterite seems to be more or less quantitative, we suggest that the traced fraction of calcite grew forthright from an initial ACC phase without involving vaterite as an intermediate. That is, silica favors the direct formation of calcite from ACC rather than accelerating the vaterite-to-calcite transition as discussed above.

Stabilization of vaterite by soluble additives has been achieved in a number of previous studies, for instance by introducing foreign ions like sulfate,[39] ammonium,[40] lanthanum,[41] or phosphate,[42] which may be incorporated to the vaterite lattice or electrostatically bound to certain faces and thus hinder its dissolution while at the same time impeding growth of calcite. Inhibition of the conversion of kinetically produced vaterite to calcite was accomplished also in solutions containing different alcohols.[43] Finally, the presence of certain surfactants[44] and polymers[45] was shown to be effective to prevent vaterite from energetically favored transformation to calcite. In this case, the additives are thought to adsorb on the surface of as-nucleated crystallites and thereby stabilize them against ripening and phase transition. Dissolved silica likely acts in a similar way, protecting vaterite particles via adsorption or precipitation on their surface. The fact that silica-mediated stabilization of vaterite occurs at 50°C but not at 20°C can readily be understood on the basis of the temperature-dependent solution chemistry of silica. Although the equilibrium solubility of silica increases with temperature,[34,46] condensation rates are higher and hence precipitation will proceed faster when solutions are heated, at least within the studied range of temperatures.[47] Under kinetic control, silica condensation – whether induced directly by growth of carbonate particles or not –

will therefore yield higher oligomers in a shorter frame of time at 50°C than at 20°C. The resulting polymeric species are expected to be much more suitable for adsorption on vaterite faces and an efficient hindrance of transformation than small mono- or dimers commonly existing in solution at the given pH values.[48] In an extreme case, reinforced condensation at higher temperatures may lead to the deposition of extended silica layers all over the carbonate crystallites, such that they become enveloped in true shells of silica as observed under different conditions previously for ACC particles (see Chapter 2).[22]

80°C

At 80°C (Fig. 5-5c), the effect of added silica is most prominent and clearly manifest already at the lowest investigated concentration. In fact, as soon as 200 ppm SiO_2 are present, diffraction patterns no longer display any marked temporal evolution. This applies likewise for all other silica contents studied (see Fig. 5-6c and Appendix B for additional data). Calculations of polymorphic ratios indicate that, for concentrations of up to 2000 ppm SiO_2, the fraction of aragonite is approximately constant over the examined period of time and amounts in all cases to about 80% (cf. Fig. 5-5c). This is in sharp contrast to the results obtained for the silica-free reference sample at 80°C, where gradual and eventually quantitative transformation of aragonite to calcite was observed. Thus, silica is obviously also capable of stabilizing aragonite as kinetic crystalline product at 80°C against conversion to calcite. The fraction of calcite in the silica-containing samples is about the same (~20%) as in the system without silica before transformation of aragonite sets in. This implies that the initially generated fractions of the two polymorphs are not noticeably affected by the presence of silica. In turn, all aragonite formed before the first EDXRD run is terminated becomes protected by the silica regardless of its concentration such that, overall, the crystallization process is virtually frozen soon after mixing.

Conservation of aragonite particles formed upon $CaCO_3$ precipitation at elevated temperature has previously been realized for example with the aid of cationic surfactants like CTAB.[49] On addition of silica, stable polycrystalline aggregates of nano-sized aragonite were obtained at 80°C from alkaline solutions under conditions of slow crystallization, yet only in relatively small amounts next to a predominant fraction of calcite.[36] Analyses showed that the aragonite crystallites were interwoven by a matrix of amorphous silica, while other work provided evidence that some of the particles were sheathed individually by a distinct siliceous skin.[50] This indicates that the nanocrystals

were stabilized by precipitation of silica around them. Such a scenario may well account for the present results. The high efficiency of silica in preventing aragonite transformation as compared to the earlier experiments[36] is thereby likely related to the increased supersaturation and corresponding changes in $CaCO_3$ precipitation and silica condensation kinetics. Apart from that, it is also evident that the conversion of the metastable crystalline phase to calcite is impeded in a substantially more effective manner at 80°C than at 50°C, as much lower concentrations are sufficient to fully suppress transformation. This finding can probably be attributed to the additional increment in the condensation rate of silica when raising the temperature from 50°C to 80°C. Another factor that might contribute to this behavior is the tendency of silicate species to adsorb on crystal faces of the two polymorphs in question. Possibly, the aragonite lattice or respectively certain of its planes are more suitable, in terms of stereochemical matching and charge distribution, for silica oligomers and polymers to be bound than the vaterite structure.

It is worth mentioning at this point that the measured differences in the pH as a function of the silica concentration (cf. Fig. 5-2) may to some degree also influence the crystallization process. In fact, Ogino *et al.* reported a significant decrease in the transformation rate of vaterite to calcite in solutions at 50°C when the pH was raised well above 10.[3] However, this effect is considered to be negligible or at least very weak given that there was no stabilization of vaterite discernible at higher silica content in the series at 20°C. Further, although the pH increases with the silica concentration, it does not reach values beyond 10 below 5000 ppm SiO_2. In turn, drastic inhibition of vaterite transformation at 50°C is observed already at 1200 ppm. Finally, qualitative reference experiments in which the pH was raised to 10-11 by addition of sodium hydroxide in the absence of silica likewise did not give evidence for any prolonged endurance of the metastable polymorph in solution.

5.4.4 Stabilization of Amorphous Precursors at High Silica Concentrations

20°C

When the concentration of silica is increased to levels above 2000 ppm in samples at 20°C, calcite is the only crystalline phase detected by EDXRD owing to impelled growth rates caused by small oligomers. Unlike the data recorded for suspensions at 1200 and 2000 ppm SiO_2, the diffraction patterns display noticeable temporal evolution

again starting from 5000 ppm in that the intensity of calcite peaks grows with time rather than remaining constant from the beginning on (see Fig. 5-7a and Appendix B). Thereby, the period elapsed before no further changes occur was found to be the longer the higher the silica concentration, ranging from about 20 min at 5000 ppm over 40-45 min at 10000 ppm to more than 120 min at 20000 ppm. Since no reflections of other polymorphs are present at any time in the spectra, it can be concluded that the observed progressions reflect the gradual transformation of amorphous precursors into calcite.

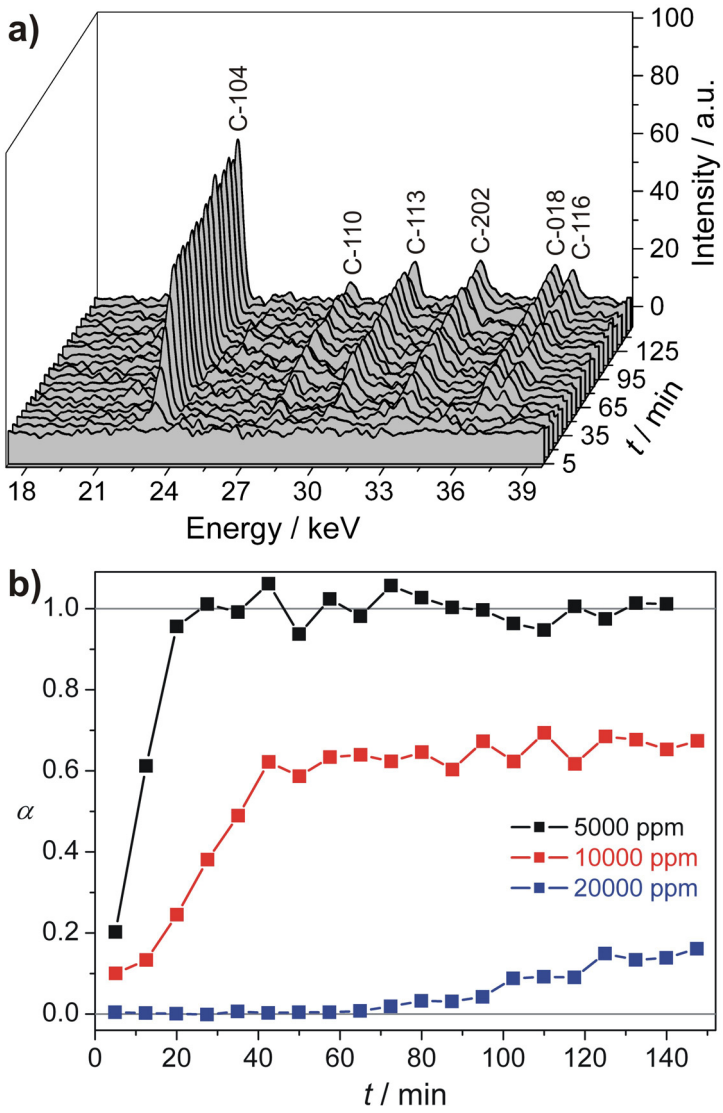

Fig. 5-7: (a) Time-dependent EDXRD profiles of a sample containing 10000 ppm SiO_2 at 20°C. (b) Degree of ACC transformation to calcite, expressed in terms of the reaction progress α, as a function of time for mixtures with different silica content (as indicated) at 20°C.

This suggests strongly that ACC particles generated during the early stages of precipitation are stabilized against rapid conversion by silica at high concentrations, in line with the results on the formation of ACC in silica-containing solutions at

comparatively low supersaturation described in Chapter 2.[22] It seems reasonable to assume that the effect observed here rests upon the same mechanism, that is, ACC particles become sheathed by a skin of silica which prevents, or retards, their dissolution.

Interestingly, incrementing the amount of silica added does not only lead to an increasing delay of stable conditions, but also affects the final yield of calcite. Calculations of the reaction progress α demonstrate that while conversion to calcite is eventually more or less quantitative at 5000 ppm SiO_2, only about 60% of the available $CaCO_3$ material crystallizes at 10000 ppm (Fig. 5-7b). In the presence of 20000 ppm, samples proved to be entirely amorphous for up to around 60 min and merely 14% of the ACC phase had transformed at the end of the experiment. This is consistent with light microscopy analyses of the precipitates after the measurements, which revealed numerous calcite crystals in samples with a silica content of up to 5000 ppm and, by contrast, an optically isotropic and almost translucent network with some embedded crystallites at both 10000 and 20000 ppm SiO_2. Thus, findings implicate that, at 20°C, a distinct fraction of the ACC particles is temporarily stabilized by the silica and converted to calcite with time at a concentration equal to or higher than 5000 ppm, whereas, beyond a certain threshold, a major part remains permanently conserved. Qualitatively, this is in good agreement with observations made in more dilute systems, where silica-stabilized ACC and calcite co-existed in solution in the long term when 750 ppm SiO_2 were added to a suspension containing 5 mM $CaCO_3$ (i.e. for a Si/Ca molar ratio of 2.5, see Chapter 2).[22] The relative amount of silica required to establish such a situation in the present samples is appreciably lower (Si/Ca $\geq$ 0.5). This discrepancy may derive from the drastically elevated absolute concentration of species used in this part of the work and associated changes in the polymerization behavior of silica under these circumstances.

50°C

At 50°C, distinct stabilization of amorphous precursors can be distinguished only at the highest silica concentration investigated at this temperature (10000 ppm). As at 20°C, EDXRD patterns are characterized by an initial increase in the height of calcite signals which is terminated after 20-30 min (Fig. 5-8a). The area determined for the (104) reflection at later times is roughly constant and indicates that the degree of transformation to calcite is about 45% (Fig. 5-8b). Notably, the diffraction data further show that calcite is the exclusive crystalline phase generated in the suspensions and that

vaterite no longer occurs as metastable intermediate under these conditions (Fig. **5-8**a) – in contrast to what was observed for lower silica concentrations at 50°C (cf. Fig. 5-5b and Fig. 5-6b). Presumably, growth of calcite fully prevails over vaterite formation at 10000 ppm SiO_2 due to drastic differences in the growth rates caused by the promotional effect of silicate oligomers on the kink density of calcite faces.[38]

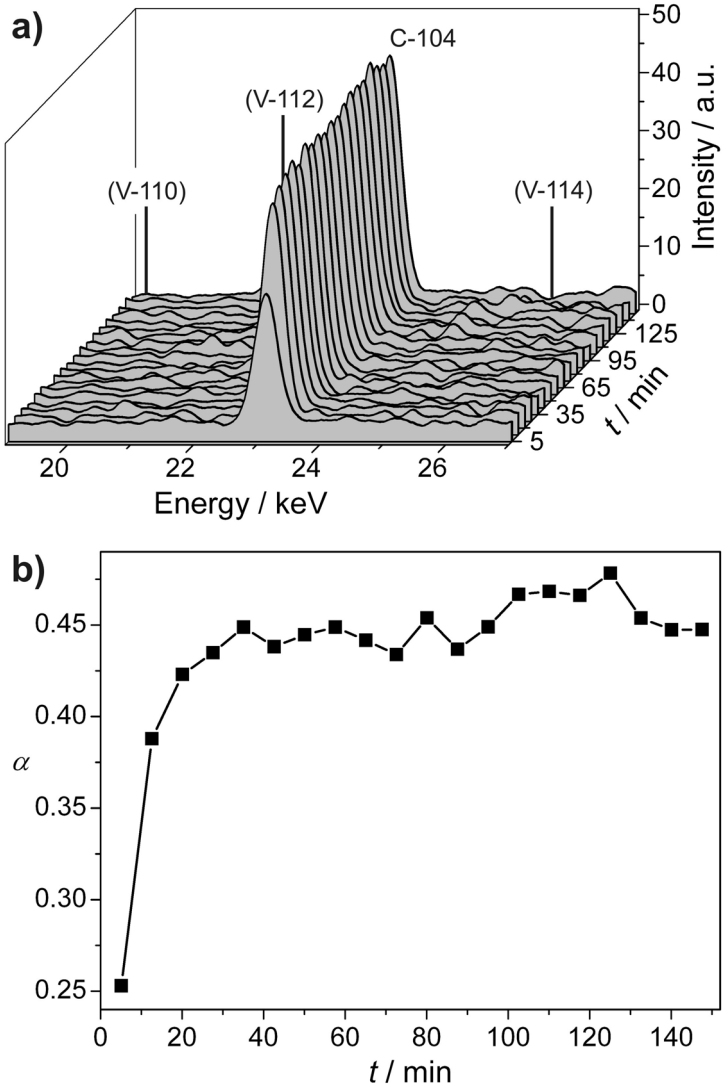

Fig. 5-8: Temporal evolution of (a) the calcite (104) reflection in diffraction patterns and (b) the calculated reaction progress α for a 250 mM suspension of $CaCO_3$ in the presence of 10000 ppm SiO_2 at 50°C. The interval of energies shown in (a) is chosen such that the region where the strongest vaterite peaks (indicated by vertical lines and their Miller indices) would be expected is also covered.

In other words, the fraction of ACC which is insufficiently protected by the silica will transform with strong preference directly to calcite, such that measurable quantities of vaterite do not exist at any stage of the crystallization process and silica-mediated stabilization of vaterite cannot take place.

80°C

At 80°C, a successive increase of the silica concentration to 5000 and 10000 ppm does not bring about reinforced temporal variations in the EDXRD profiles. Still, the system seems to be frozen rapidly upon precipitation in the presence of silica and crystalline reflections of both calcite and aragonite can be discerned in the diffraction patterns (see Appendix B). However, when comparing spectra of samples with rising silica content at a given time (Fig. 5-9a), it is evident that aragonite signals are noticeably weaker at 5000 ppm and in particular at 10000 ppm SiO_2 than at $\leq$ 2000 ppm. This is supported by integrations of the aragonite (021) reflection. Values obtained for the peak area at different silica concentrations are shown in Fig. 5-9b. Since the patterns do not change essentially during the experiments, calculated areas were averaged over all times. Results illustrate that the amount of aragonite present is clearly reduced at 5000 and 10000 ppm SiO_2. Between 200 and 2000 ppm, there is also a slight but not as obvious decrease in $A_{A\text{-}021}$ suggesting that, within the limits of error, less aragonite is formed when more silica is added. Overall, the data can be approximated by a linear fit as visualized by Fig. 5-9b. On the other hand, the fraction of calcite occurring in the suspensions, represented by the reaction progress α in Fig. 5-9b, does not vary significantly with the silica concentration. Indeed, α increases from ~0.06 at 2000 ppm SiO_2 to ~0.10 at 5000 and 10000 ppm (likely reflecting some degree of calcite promotion by silica), but still the total quantity of calcite in the samples is relatively low.

Thus, it can be inferred that a certain amount of ACC is stabilized by silica at 80°C starting from a concentration of 5000 ppm SiO_2 and essentially at the expense of formed aragonite. A corresponding percentage can be estimated on the basis of the known fraction of calcite out of the total quantity of $CaCO_3$ present ($\approx \alpha$) and considering the data of the reference without silica at 80°C (Fig. 5-4c). When assuming that there is no significant stabilization of ACC in the absence of silica, the latter allow for relating the integrated intensity of aragonite reflections to the fraction of all $CaCO_3$ existing as aragonite in the system ($\approx 1 - \alpha$ for the silica-free reference). The difference between the sum of these two fractions and unity should eventually represent the amount of stabilized ACC. In this way, values of 0.38 and 0.65 were obtained for samples at 5000 and 10000 ppm SiO_2, respectively. This means that for a silica concentration of 10000 ppm, the percentage of ACC which remains permanently protected in solution is approximately 40% at 20°C, 55% at 50°C, and 65% at 80°C. Hence, the capability of

silica to stabilize ACC increases with temperature, most probably as a consequence of enhanced silica condensation rates and the associated faster coating of transient amorphous particles.

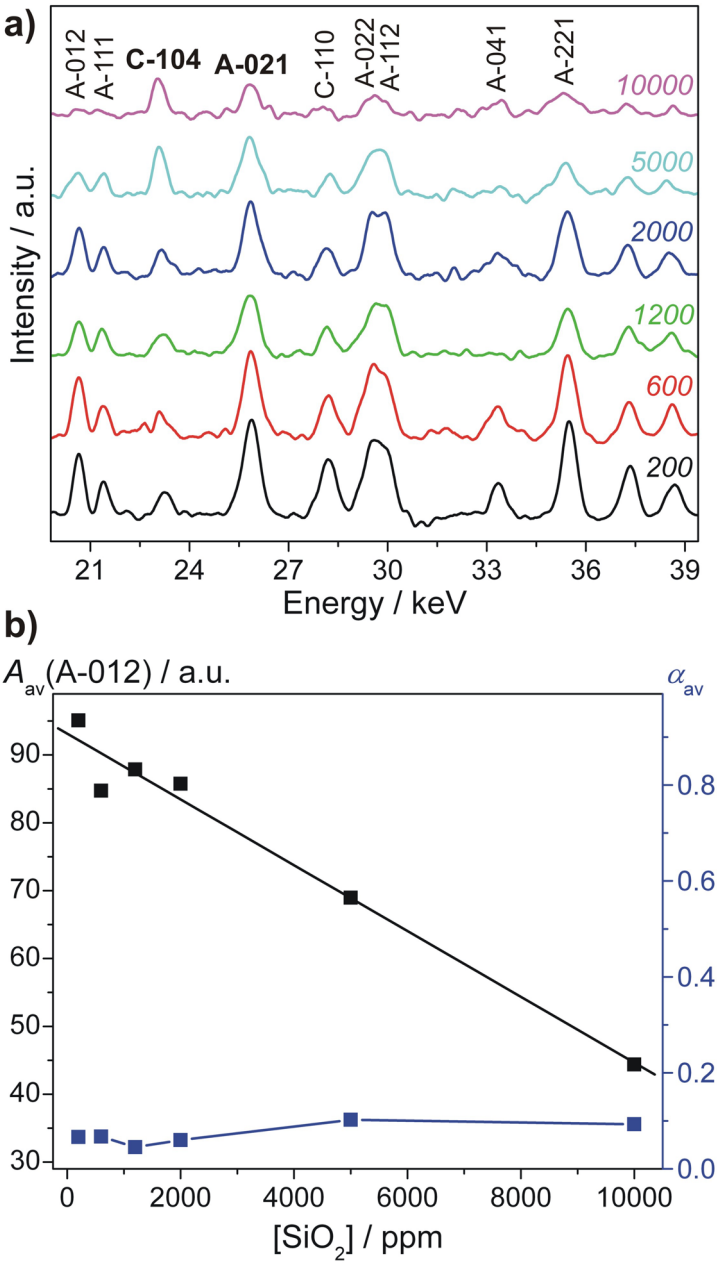

Fig. 5-9: (a) Sequence of diffraction profiles recorded from suspensions at 80°C and various silica contents (indicated as ppm values above each curve). Patterns represent the final run of the measurement series in all cases, that is, data were collected within a period of ~145-150 min after mixing. (b) Plots of the area under the aragonite (021) reflection, averaged over all 20 runs of each sample (black, full line is a linear fit of the data), and the corresponding mean value of the reaction progress α (blue) as a function of the silica content at 80°C.

A possible influence of the bulk pH on the stability of metastable $CaCO_3$ phases has also been reported for ACC in the literature. Koga *et al.* found that thermal

decomposition of ACC required higher temperatures when syntheses were conducted in solutions of growing alkalinity for a pH range of 11.2-13.[51] They ascribed the observed trend to a decreasing degree of atomic order in the ACC materials and thus a larger energetic effort for crystallization with increasing pH. Although a certain role of the pH in the stabilization of ACC cannot be fundamentally excluded in the present systems, it seems reasonable that the presence of silica is the pivotal factor because the pH is lower than 11 in all samples (cf. Fig. 5-2) and, furthermore, analyses of precipitates formed at elevated pH in silica-free solutions did not indicate noticeable changes in the lifetime of ACC.

5.5 Summary and Conclusions

The described experiments show that energy-dispersive X-ray diffraction is a powerful technique for tracing the crystallization of calcium carbonate from solution *in situ*. In particular, for samples to which no silica was added, the acquired time-resolved diffraction patterns verify that vaterite occurs as metastable crystalline intermediate at 20°C as well as 50°C, whereas aragonite is kinetically favored at 80°C. Both polymorphs transform with time into stable calcite. This process could be directly monitored with the used setup. From the acquired data, relative fractions of the different phases present at a given time were calculated and, thus, the temporal progress of transformation was quantified. Results demonstrate that completed conversion to calcite takes longer at higher temperature, which is in line with earlier work.[2]

Measurements performed with samples containing various amounts of sodium silicate proved a delicate influence of the additive on crystallization scenarios. The most essential findings are summarized in Fig. 5-10 in form of a concentration-temperature map visualizing the identified polymorphs and ongoing phase transformations under different conditions. Generally, the silica appears to affect $CaCO_3$ formation in two distinct ways. On the one hand, low molecular-weight silica oligomers attach onto calcite step edges and thereby impel growth rates relative to vaterite, assisted by a promotion of 2D nucleation due to adsorbed polymeric particles as described in detail by Pina *et al.*.[38] This effect is most obvious at 20°C where no more intermediate vaterite is observed at silica concentrations equal to or higher than 1200 ppm. It also accounts for the decrease in the fraction of vaterite between 600 and 1200 ppm SiO_2 at 50°C and the fact that calcite is the only crystalline phase at 10000 ppm, as well as for the slightly

increased amount of calcite present in samples with a silica content above 2000 ppm at 80°C.

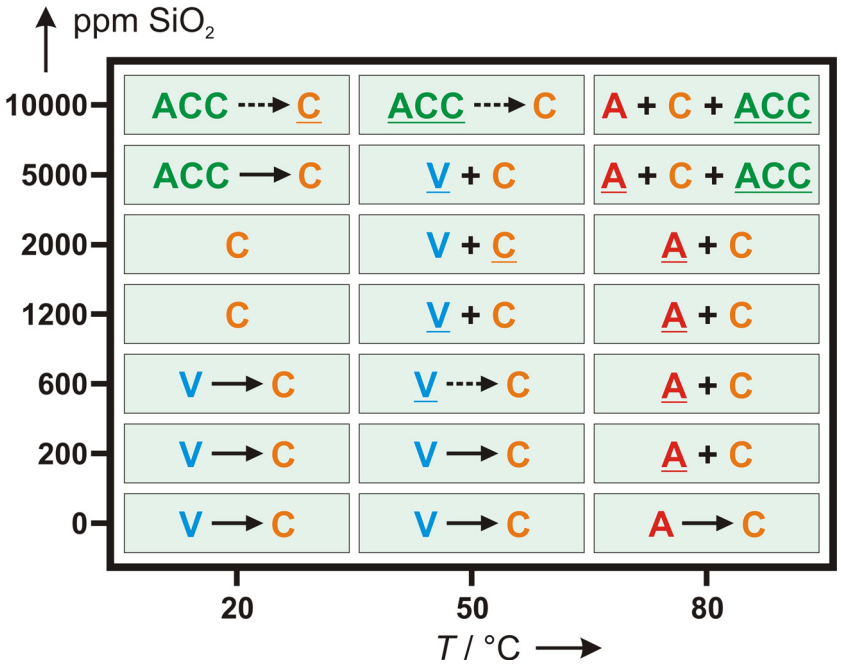

Fig. 5-10: Observed phases and phase transformations in the course of EDXRD experiments conducted at different silica concentrations and temperatures. Dashed arrows indicate that the corresponding transformation is not quantitative while, for samples in which distinct polymorphs co-exist, the phase with the highest estimated fraction after completed conversion is underlined.

On the other hand, dissolved silica was found to be capable of stabilizing all of the metastable $CaCO_3$ polymorphs formed in the solutions. This feature is ascribed to adsorption and/or precipitation of silica on the carbonate particles, which inhibits re-dissolution and transformation to calcite. Silica deposition on $CaCO_3$ surfaces may derive from a local decrease in pH induced by the growth of carbonates in alkaline media, as reported for the spontaneous coating of ACC particles by silica shells in systems of lower supersaturation in Chapter 2.[22] The extent of stabilization and the resulting polymorphic ratios intimately depend on both temperature and the silica concentration. Raising the temperature causes an increment in the rate of silica condensation processes, hence accelerating the occurrence of higher oligomers and precipitation. Consequently, protection of metastable intermediates under kinetic control is more efficient at higher temperatures. This tendency is particularly evident from the data acquired at 80°C, which confirm that already 200 ppm SiO_2 effectively suppress conversion of aragonite to calcite. By contrast, 600-1200 ppm are required for a long-lasting stabilization of an even smaller fraction of vaterite at 50°C, while no

distinct stabilizing influence of silica on the vaterite phase could be distinguished at 20°C, also at higher concentrations. When more silica is added, the degree of transformation inhibition is in principle expected to be enhanced and yield larger amounts of metastable polymorphs in co-existence with calcite. However, this effect is counterbalanced by the simultaneous increase of calcite growth rates, that is, overall less vaterite/aragonite is generated and can thus be stabilized, while more calcite is formed directly without involving a kinetic crystalline product as intermediate. Nevertheless, the ability of silica to trap transient $CaCO_3$ phases becomes reinforced above a certain threshold in its concentration, typically between 5000 and 10000 ppm under the chosen conditions, as a considerable deal of amorphous calcium carbonate persists in solution either permanently until the end of the experiments or temporarily for measurable periods before being converted to calcite. This suggests that ACC is the initial solid phase formed upon nucleation, in agreement with results of previous in-situ X-ray diffraction studies.[24-26] In the present systems, the lifetime of ACC is utterly short in the absence of silica and at low silica content, such that it cannot be traced at the given time resolution. In turn, at sufficiently high concentrations of silica, transformation of ACC becomes slowed down or partially prevented, thus prolonging the endurance of the precursors in solution and rendering them experimentally detectable.

These findings emphasize the versatility of silica as an additive in the crystallization of calcium carbonate and illustrate the various ways in which dissolved silicate species can interact with the different intermediates occurring in the course of precipitation from solution. This is clearly of interest for basic material science, but may have implications also for the field of practical applications. For example, an interplay between forming calcium carbonate and silica might occur in cements and concretes which, in contact with atmospheric carbon dioxide during hydration or CO_2-containing fluids afterwards, are known to undergo carbonation and precipitate different $CaCO_3$ polymorphs deteriorating their performance.[52] Beyond that, it is conceivable that EDXRD experiments will provide valuable information on the action of other commonly used additives in $CaCO_3$ mineralization as well.

5.6 References

(1) Söhnel, O.; Mullin, J. W. *J. Cryst. Growth* **1982**, *60*, 239.

(2) Ogino, T.; Suzuki, T.; Sawada, K. *Geochim. Cosmochim. Acta* **1987**, *51*, 2757.

(3) Ogino, T.; Suzuki, T.; Sawada, K. *J. Cryst. Growth* **1990**, *100*, 159.

(4) Kralj, D.; Brecevic, L.; Kontrec, J. *J. Cryst. Growth* **1997**, *177*, 248.

(5) Tracy, S. L.; Williams, D. A.; Jennings, H. M. *J. Cryst. Growth* **1998**, *193*, 382.

(6) Chien, W. C.; Tai, C. Y.; Hsu, J. P. *J. Chem. Phys.* **1999**, *111*, 2657.

(7) Rieger, J.; Frechen, T.; Cox, G.; Heckmann, W.; Schmidt, C.; Thieme, J. *Faraday Discuss.* **2007**, *136*, 265

(8) Gebauer, D.; Völkel, A.; Cölfen, H. *Science* **2008**, *322*, 1819.

(9) Lakshtanov, L. Z.; Stipp, S. L. S. *Geochim. Cosmochim. Acta* **2010**, *74*, 2655.

(10) Cölfen, H.; Mann, S. *Angew. Chem. Int. Ed.* **2003**, *42*, 2350.

(11) Brecevic, L.; Nielsen, A. E. *J. Cryst. Growth* **1989**, *89*, 504.

(12) Clarkson, J. R.; Price, T. J.; Adams, C. J. *J. Chem. Soc., Faraday Trans.* **1992**, *88*, 243.

(13) Faatz, M.; Gröhn, F.; Wegner, G. *Adv. Mater.* **2004**, *16*, 996.

(14) (a) Kim, W. S.; Hirasawa, I.; Kim, W. S. *Ind. Eng. Chem. Res.* **2004**, *43*, 2650. (b) Xiao, J.; Wang, Z.; Tang, Y.; Yang, S. *Langmuir* **2010**, *26*, 4977. (c) Kosanovic, C.; Falini, G.; Kralj, D. *Cryst. Growth Des.* **2011**, *11*, 269.

(15) (a) Richter, A.; Petzold, D.; Hoffmann, H.; Ullrich, B. *Chem. Tech.* **1995**, *48*, 271. (b) Kabasci, S.; Althaus, W.; Weinspach, P. M. *Chem. Eng. Res. Des.* **1996**, *74*, 765. (c) Spanos, N.; Koutsoukos, P. G. *J. Cryst. Growth* **1998**, *191*, 783. (d) Sondi, I.; Matijevic, E. *J. Colloid Interf. Sci.* **2001**, *238*, 208. (e) Kim, J. H.; Ahn, J. W.; Park, H. S.; Park, C. H. *Geosys. Eng.* **2004**, *7*, 95. (f) Kitamura, M. *Cryst. Eng. Comm.* **2009**, *11*, 949.

(16) (a) Wray, J. L.; Daniels, F. *J. Am. Chem. Soc.* **1957**, *79*, 2031. (b) Chen, J.; Xiang, L. *Powder Technol.* **2009**, 189, 64.

(17) Wang, L.; Sondi, I.; Matijevic, E. *J. Colloid Interf. Sci.* **1999**, *218*, 545.

(18) Zhao, D.; Zhu, Y.; Li, F.; Ruan, Q.; Zhang, S.; Zhang, L.; Xu, F. *Mater. Res. Bull.* **2010**, *45*, 80.

(19) Rieger, J.; Thieme, J.; Schmidt, C. *Langmuir* **2000**, *16*, 8300.

(20) (a) Bolze, J.; Peng, B.; Dingenouts, N.; Panine, P.; Narayanan, T.; Ballauff, M. *Langmuir* **2002**, *18*, 8364. (b) Bolze, J.; Pontoni, D.; Ballauff, M.; Nayaranan, T.; Cölfen, H. *J. Colloid Interf. Sci.* **2004**, *277*, 84. (c) Liu, J.; Pancera, S.; Boyko, V.; Shukla, A.; Nayaranan, T.; Huber, K. *Langmuir* **2010**, *26*, 17405.

(21) Liu, J.; Rieger, J.; Huber, K. *Langmuir* **2008**, *24*, 8262.

(22) Kellermeier, M.; Melero-García, E.; Glaab, F.; Klein, R.; Drechsler, M.; Rachel, R.; García-Ruiz, J. M.; Kunz, W. *J. Am. Chem. Soc.* **2010**, *132*, 17859.

(23) (a) Liu, X. Y.; Tsukamoto, K.; Sorai, M. *Langmuir* **2000**, *16*, 5499. (b) Cölfen, H.; Qi, L. *Chem. Eur. J.* **2001**, *7*, 106.

(24) Pontoni, D.; Bolze, J.; Dingenouts, N.; Narayanan, T.; Ballauff, M. *J. Phys. Chem. B* **2003**, *107*, 5123.

(25) Heeley, E. L.; Poh, C. K.; Li, W.; Maidens, A.; Bras, W.; Dolbnya, I. P.; Gleeson, A. J.; Terrill, N. J.; Fairclough, J. P. A.; Olmsted, P. D.; Ristic, R. I.; Hounslow, M. J.; Ryan, A. J. *Faraday Discuss.* **2002**, *122*, 343.

(26) Wolf, S. E.; Leiterer, J.; Kappl, M.; Emmerling, F.; Tremel, W. *J. Am. Chem. Soc.* **2008**, *130*, 12342.

(27) Chen, T.; Neville, A.; Sorbie, K.; Zhong, Z. *Faraday Discuss.* **2007**, *136*, 355.

(28) (a) Michailovski, A.; Grunwaldt, J. D.; Baiker, A.; Kiebach, R.; Bensch, W.; Patzke, G. R. *Angew. Chem. Int. Ed.* **2005**, *44*, 5643. (b) Kiebach, R.; Pienack, N.; Ordolff, M. E.; Studt, F.; Bensch, W. *Chem. Mater.* **2006**, *18*, 1196. (c) Zhou, Y.; Pienack, N.; Bensch, W.; Patzke, G. R. *Small* **2009**, *5*, 1978.

(29) (a) Sankar, G.; Thomas, J. M. *Top. Catal.* **1999**, *8*, 1. (b) Grunwaldt, J. D.; Clausen, B. S. *Top. Catal.* **2002**, *18*, 37.

(30) JCPDS Cards No. 5-586 (calcite), 33-268 (vaterite), and 71-2392 (aragonite).

(31) Rao, M. S. *Bull. Chem. Soc. Jpn.* **1973**, *46*, 1414.

(32) Wada, N.; Okazaki, M.; Tachikawa, S. *J. Cryst. Growth* **1993**, *132*, 115.

(33) Voinescu, A. E.; Kellermeier, M.; Carnerup, A. M.; Larsson, A. K.; Touraud, D.; Hyde, S. T.; Kunz, W. *J. Cryst. Growth* **2007**, *306*, 152.

(34) Iler, R. K. *The chemistry of silica*, Wiley: New York, 1979.

(35) (a) García-Ruiz, J. M.; Melero-García, E.; Hyde, S. T. *Science* **2009**, *323*, 362. (b) Kunz, W.; Kellermeier, M. *Science* **2009**, *323*, 344.

(36) Voinescu, A. E.; Kellermeier, M.; Bartel, B.; Carnerup, A. M.; Larsson, A. K.; Touraud, D.; Kunz, W.; Kienle, L.; Pfitzner, A.; Hyde, S. T. *Cryst. Growth Des.* **2008**, *8*, 1515.

(37) Kitano, Y.; Okumura, M.; Idogaki, M. *Geochem. J.* **1979**, *13*, 253.

(38) Pina, C. M.; Merkel, C.; Jordan, G. *Cryst. Growth Des.* **2009**, *9*, 4084.

(39) Fernández-Díaz, L.; Fernández-González, A.; Prieto, M. *Geochim. Cosmochim. Acta* **2010**, *74*, 6064.

(40) Gehrke, N.; Cölfen, H.; Pinna, N.; Antonietti, M.; Nassif, N. *Cryst. Growth Des.* **2005**, *5*, 1317.

(41) Tsuno, H.; Kagi, H.; Akagi, T. *Bull. Chem. Soc. Jpn.* **2001**, *74*, 479.

(42) Katsifaras, A.; Spanos, N. *J. Cryst. Growth* **1999**, *204*, 183.

(43) Manoli, F.; Dalas, E. *J. Cryst. Growth* **2000**, *218*, 359.

(44) (a) Dupont, L.; Portemer, F.; Figlarz, M *J. Mater. Chem.* **1997**, *7*, 797. (b) Shen, Q.; Wang, L.; Huang, Y.; Sun, J.; Wang, H.; Zhou, Y.; Wang, D. *J. Phys. Chem. B* **2006**, *110*, 23148. (c) Szczes, A.; Chibowski, E.; Holysz, L. *Colloids Surf., A* **2007**, *297*, 14.

(45) (a) Cölfen, H.; Antonietti, M. *Langmuir* **1998**, *14*, 582. (b) Wei, H.; Shen, Q.; Wang, H.; Gao, Y.; Zhao, Y.; Xu, D.; Wang, D. *J. Cryst. Growth* **2007**, *303*, 537. (c) Wang, Y.; Moo, Y. X.; Chen, C.; Gunawan, P.; Xu, R. *J. Colloid Interf. Sci.* **2010**, *352*, 393. (d) Su, Y.; Yang, H.; Shi, W.; Guo, H.; Zhao, Y.; Wang, D. *Colloids Surf., A* **2010**, *355*, 158.

(46) Alexander, G. B.; Heston, W. M.; Iler, R. K. *J. Am. Chem. Soc.* **1953**, *75*, 5655.

(47) (a) Alexander, G. B. *J. Am. Chem. Soc.* **1953**, *76*, 2094. (b) Greenberg, S. A.; Sinclair, D. *J. Phys. Chem.* **1955**, *59*, 435. (c) Belton, D. J.; Deschaume, O.; Patwardhan, S. V.; Perry, C. C. *J. Phys. Chem. B* **2010**, *114*, 9947.

(48) Sjöberg, S. *J. Non-Cryst. Solids* **1996**, *196*, 51.

(49) Yu, J.; Lei, M.; Cheng, B.; Zhao, X. *J. Cryst. Growth* **2004**, *261*, 566.

(50) Imai, H.; Terada, T.; Miura, T.; Yamabi, S. *J. Cryst. Growth* **2002**, *244*, 200.

(51) Koga, N.; Nakagoe, Y.; Tanaka, H. *Thermochim. Acta* **1998**, *318*, 239.

(52) (a) Stepkowska, E. T.; Pérez-Rodríguez, J. L.; Sayagués, M. J.; Martínez-Blanes, J. M. *J. Therm. Anal. Calorim.* **2003**, *73*, 247. (b) Shtepenko, O.; Hills, C.; Brough, A.; Thomas, M. *Chem. Eng. J.* **2006**, *118*, 107. (c) Palacios, M.; Puertas, F. *J. Am. Ceram. Soc.* **2006**, *89*, 3211. (d) Jacquemet, N.; Pironon, J.; Saint-Marc, J. *Environ. Sci. Technol.* **2008**, *42*, 282.

Chapter 6 Growth Behavior and Kinetics of Silica Biomorphs

6.1 Abstract

Upon slow crystallization from silica-containing solutions or gels at elevated pH, alkaline-earth carbonates spontaneously self-assemble into remarkable nanocrystalline ultrastructures, termed silica biomorphs, which exhibit curved morphologies beyond crystallographic symmetry and ordered textures reminiscent of the hierarchical design found in many biominerals. The formation of these fascinating materials is thought to be driven by a dynamic coupling of the components' speciations in solution which causes concerted autocatalytic mineralization of silica-stabilized nanocrystals over hours. In this chapter, the kinetics of the growth process are described based on in-situ data reflecting the concentrations of metal ions and carbonate species. Results are correlated with apparent growth rates determined by means of video microscopy. It is shown that crystallization proceeds linearly with time and is essentially reaction-controlled, which fits well in the proposed model and thus indirectly supports it. Measurements of the silica concentration in solution and analyses of crystal aggregates isolated at distinct stages of morphogenesis in turn demonstrate that the fraction of silica co-precipitated during active growth is rather small. These findings are discussed with respect to the role of silica in the formation of biomorphs and it is confirmed that the external silica skins occasionally sheathing the aggregates originate from secondary precipitation after growth is already terminated.

6.2 Introduction

Ordered polycrystalline arrays consisting of uniform small building blocks are a valuable structural motif for the production of mineral architectures with complex morphology and texture and, often, extraordinary properties. In nature, such materials are widespread and usually featured by outstanding functionality in view of the specific demands posed by the associated organism. For instance, the nacreous layers of mollusk shells are constructed from micron-sized tablets of calcium carbonate stacked in parallel laminae which are separated by organic sheets rich in proteins and polysaccharides.[1] The role of the organic matrix is to control nucleation, growth, polymorphism and the relative crystallographic orientation of individual units,[2] thus yielding a hybrid material

with unique toughness.[3] Other examples include bone, teeth, tendons, and dental enamel, where the formation and co-alignment of nanometric plate- or needle-shaped crystallites of carbonated apatite are intimately regulated by collagen fibrils and amelogenin, respectively.[4]

In this regard, applying strategies identified in biomineralization to laboratory syntheses appears a rational approach for the development of novel ideas in materials science, the experimental elaboration of which will likely enhance, at the same time, the understanding of the natural process. Accordingly, a vast amount of work has been devoted in the past years to extending the spectrum of structures accessible *via* such biomimetic routes.[5] Frequently, morphogenesis pathways rely on the beneficial effect of soluble organic additives on the crystallization of the inorganic mineral. Although directed growth of polycrystalline ultrastructures with special morphologies was in some cases accomplished merely using simple ions and/or small molecules,[6] more distinct influence can yet be exerted with the aid of polymeric additives. To date, numerous polymers have been employed for morphosynthesis, and crystal aggregates exhibiting diverse intricate forms were obtained with species ranging from polyacrylate[7] over double-hydrophilic block copolymers[8] to chiral phosphorylated polypeptides.[9] Thereby, a general mode by which polymers interfere with the crystallization process seems to rest upon (temporary) stabilization of nanoscale crystalline particles or amorphous precursors,[10] and subsequent additive-mediated particle aggregation. Oriented attachment of these building units to an emerging anisotropic assembly may ultimately be achieved by introducing face-specific crystal-polymer interactions which, ideally, would facilitate an *ab-initio* programmed, bottom-up self-organization of the components.[11] Polycrystalline solids with partially higher complexity and, in particular, reaching greater structural length scales can further be fabricated through templating procedures, for instance by molding readily shapeable amorphous phases into a predefined volume prior to crystallization,[12] or by coating existing frameworks *via* surface-selective sol-gel polymerization.[13] Templates suitable for this purpose may involve self-assembled structures in soft matter like microemulsions,[14] or biological scaffolds such as skeletal plates,[15] pollen grains,[16] or collagen,[17] potentially producing intriguing morphologies with dimensions up to the macroscopic level. Finally, nanocrystalline composite materials showing remarkable textures and ordering were also successfully synthesized *in vitro* using bio-inspired, gelatin-based hydrogels as crystallization media.[18]

The generation of crystal aggregates with elaborately curved forms is however not confined to the living world or, more generally speaking, the presence of organic species. There are some, but few examples where mineralization in purely inorganic environments can give rise to unusual non-crystallographic architectures, among which silica-carbonate biomorphs probably take the most exceptional position. These peculiar materials are composed of multiple elongated alkaline-earth metal carbonate nanocrystals, measuring several hundreds of nanometers in length and around 50 nm across, which are interwoven and sheathed by a matrix of amorphous silica.[19-26] Notably, the arrangement of the crystallites within an aggregate, though allowing for local defects, is well-defined on the mesoscale where the rods describe a smoothly varying orientational field with respect to their long axis.[23] Beyond that, on global scales, the crystal assemblies adopt striking curvilinear ultrastructures lacking any crystallographic symmetry – a feature traditionally thought to be exclusive to the animate nature.[27,28] Common morphologies include sinuous sheets, worm-like braids, spherulites reminiscent of corals or flowers, as well as twisted ribbons and helicoidal filaments, with some of these forms being able to grow up to the millimeter range. In the absence of a template, silica biomorphs thus display structural organization on length scales greater than in most other biomimetic materials, and emulate to some extent hierarchical construction principles observed in many biominerals.[29] On the other hand, their preparation is utmost simple, barely requiring a mildly alkaline, silica-containing medium (either a solution or a gel) in which the respective carbonate is crystallized gradually upon diffusion of one of the reagents (atmospheric CO_2 into solutions and metal ions into gels). This renders silica biomorphs interesting and easy-to-handle model systems for the study of higher-order self-organization processes based on actually plain components.

The detailed formation mechanism of these fascinating materials has been unraveled only recently.[30] Briefly summarized, it was found that growth starts from a micron-sized carbonate single crystal which, poisoned by silica oligomers, undergoes continued self-similar branching at its tips to eventually yield in a closed spherulitic, bifurcated architecture. At the end of this fractal route, a second stage is initiated during which uniform nanorods are steadily generated, at first through 3D nucleation, and self-assemble to build the various curved morphologies. The driving force underlying morphogenesis in this stage is a coupling incurred by the precipitations of carbonate and silica due to the reverse trends of their solubilities with pH: in alkaline solutions,

growing carbonate crystallites cause a decrease of the pH in their vicinity relative to the bulk as bicarbonate ions dissociate in order to locally restore equilibrium speciation. As a consequence, silica precipitates around the crystallites and prevents them from becoming larger than nanoscale dimensions. Ongoing silica polymerization yet in turn raises the pH and, with it, the local supersaturation of carbonate, thus facilitating a novel event of nucleation. In this manner, developing aggregates by themselves adjust the conditions prevailing nearby their active front to maintain growth by alternately increasing the supersaturation of the components to provoke their precipitation.[31] This dynamic, self-feeding mechanism bears fundamental similarity to autocatalytic phenomena such as Belousov-Zhabotinsky reactions,[32] but produces structured materials rather than only transitory patterns.

On a microscopic level, the morphological evolution of the crystal aggregates is characterized initially by the extrusion of quasi-2D laminar sections from the preceding fractal crystals. These sheets grow radially with equal velocities in all directions adopting circular shapes until they curl at some point around their rim. Curling arrests radial growth and its subsequent tangential propagation along the perimeter of the sheet alters the morphology and may induce, depending on relative growth rates and the directionality of individual curls, the formation of twisted structures.[30]

In this chapter, further insight to the chemistry involved in the morphogenesis of barium carbonate (witherite) biomorphs is provided. In particular, the kinetics of this unique self-assembling system are elucidated. To that end, the concentrations of reagents were monitored during crystallization and growth rates were determined by video microscopy. Finally, based on analyses of samples harvested after different times, the degree of silica incorporation to the forming crystal aggregates at distinct stages of growth is discussed.

6.3 Experimental Section

6.3.1 Synthesis of Silica-Witherite Biomorphs

Silica biomorphs can be grown either in silica gels or dilute sols, with no essential differences discernible concerning final aggregate structure and morphology.[23] In this work, both methods were employed, depending on their suitability for the respective type of analysis. Concentration and pH measurements were performed with solution samples, while growth in gels was chosen for video microscopy. All experiments were conducted using fresh commercial water glass (Sigma-Aldrich, reagent grade,

containing 13.8 wt% Na and 12.5 wt% Si, replaced at least monthly) as silica source and barium chloride dihydrate ($BaCl_2 \cdot 2H_2O$, Sigma-Aldrich, $\geq 99.0\%$) as soluble barium salt. Solutions were prepared using water of Milli-Q quality and stored in tightly stoppered plastic bottles so as to avoid, at the given high pH, undesired ingestion of both additional silica from glass walls and acidic carbon dioxide from the atmosphere prior to growth start.

Growth in solution was carried out following a protocol described previously.[26] First, a 1-350 (v/v) dilution of water glass is brought to a pH of about 11.3 using 0.1 M NaOH. The resulting solution is then combined with an equal volume of 0.01 M $BaCl_2$, to give a pH of 11.0 ± 0.1 and final species concentrations of 5.000 mM Ba, 8.426 mM Si and 8.905 mM Na (Na/Si ratio of 1.057). Subsequently, 2 mL portions of the reaction mixture are transferred quickly to cylindrical polystyrene wells of 1.7 cm in depth and 1.6 cm in diameter (Nunclon multiwell cell culture dishes). Samples are eventually allowed to stand under quiescent conditions in contact with the atmosphere at 20 ± 1°C. Continuous diffusion of atmospheric CO_2 into the alkaline system and concurrent conversion to carbonate species gradually triggers crystallization of barium carbonate and the formation of silica biomorphs. Growth of characteristic biomorphic architectures is usually terminated after a period of about 8-10 h, whereby discrete crystal aggregates are observed predominantly on the walls of the wells and the surface of the solution.

For growth in gels, the water glass stock was diluted 1-10 (v/v) with water and 3.25 mL of 1 M HCl were added to 10 mL of the resulting sol. This mixture was used to fill about half the volume of custom-designed rectangular crystallization cassettes, consisting of a rubber frame of 1-2 mm thickness sandwiched by two microscopy object slides or thinner coverslips as windows and sealed by grease, with needles inserted on the top and the side of the cassette enabling successive injection of reagents into the cell.[30,33] Alternatively, cylindrical glass capillaries with inner diameters between 1 and 2 mm (Hilgenberg GmbH, wall thickness: 0.01 mm, length: 80 mm) were charged with the acidified sol to a height of about 4-5 cm. In both cases, equilibration of the system for several days led to the formation of a homogeneous hydrogel having a pH of around 10.5. Subsequently, 0.5 M $BaCl_2$ solution was poured carefully on the gel slowly filling the residual volume of the cassette/capillary. Afterwards, the setups were closed to the atmosphere and left to evolve under quiescent conditions and room temperature. Diffusion of Ba^{2+} ions into the alkaline silica gel matrix provokes a decrease in pH and

causes, upon reaction with carbonate species present in the gel due to ingestion of atmospheric CO_2 by the silica sol prior to gelation, precipitation of barium carbonate. Concurrently, diffusion of silicate and hydroxide ions into the top metal salt solution increases its pH such that, after some delay, carbonate crystallization is also observed there. In this way, growth proceeds for periods of days and crystal aggregates with varying morphologies occur after different times in distinct regions of the setup, depending on the distance of the respective position from the gel-solution interface.[33] The most developed biomorphs are usually found far down in the gel, where diffusion is decelerated and gradual growth is possible. The small thickness of the gel layer in the cassettes and the capillaries ensured that the forming aggregates could easily be focused and followed during their evolution with an optical microscope.

6.3.2 Time-Lapse Video Microscopy

Once a promising aggregate at an apparently still early stage of growth was discerned, it was centered in the microscope at a suitable magnification and a series of micrographs was recorded from the selected region until no further essential change could be noted. The interval between the frames was varied between 1 s and 1 min. The used microscopes were a Nikon AZ100 and an Olympus BX51WI, both equipped with a CCD camera for imaging. Acquired image sequences were processed, evaluated and converted to movies with the ImageJ software. Radial growth rates of sheets were determined by drawing straight lines outwards normal to the tangent to the front of the sheet in the first frame. Then, the distance covered by the front within a predefined number of elapsed frames (and hence within a known time) was measured along the lines. Measurements were performed up to the point where radial growth either ceased by itself or was terminated by a curl. The rate with which curls are propagated along the perimeter of sheets was quantified in a similar manner, but using curved segments instead of straight lines for measuring.

6.3.3 pH Measurements

The pH of the samples was measured with the aid of a glass microelectrode from Mettler-Toledo (model InLab Micro) connected to a Schott laboratory pH meter (model CG-843). Monitoring the temporal evolution of the pH during growth of silica biomorphs in solution was accomplished by immersing the microprobe into the reaction mixture straight after transfer to the well and recording data in the following continuously over periods up to 20 h. pH values were thereby read automatically with

an interval of 5 s. Since the silica in solution may be suspected to contaminate the membrane of the glass electrode and therefore interfere with the pH measurements, a control experiment was performed in which the pH of a larger sample volume was followed with time using a common-size polymer-based electrode (Mettler-Toledo InLab Expert). When the surface-to-volume ratio of the sample was adjusted to that prevailing in the standard wells, identical results were obtained, thus ruling out potential disturbance of the employed glass microelectrode by the silica.

6.3.4 X-Ray Fluorescence Spectroscopy

The temporal evolution of the Ba concentration in solution was traced by means of X-ray fluorescence spectroscopy (XFS). Measurements were done at Beamline C of the storage ring DORIS III at the synchrotron radiation facility HASYLAB (DESY, Hamburg, Germany). Experiments were carried out at the Ba-K edge (37441 eV) using the Si(311) monochromator setup. Data were collected with a 6-channel detector positioned at 90° relative to the light path. For measurement, a single well was placed in the beam, filled with sample, and data acquisition was initiated as soon as possible. This delay was noted and later accounted for during evaluation. Beam dimensions were 6x1 mm. In the following, scans from 37110 to 37710 eV were performed continuously for up to 7 h, with a step width of 2 eV and an integration time of 1 s, resulting in an overall duration per scan and hence a time resolution of 10.5 min.

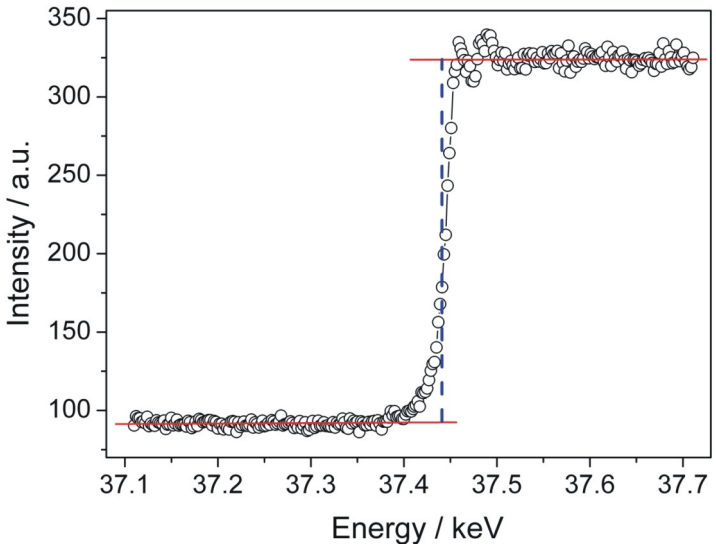

Fig. 6-1: Exemplary X-ray fluorescence spectrum acquired from a mother solution of silica-carbonate biomorphs. Red lines are linear fits to the pre- and post-edge region, respectively. The dashed blue line represents the edge jump.

The obtained spectra were first normalized for the incoming intensity. Edge jumps were then determined by fitting linear equations to both the pre- and post-edge region, and calculating the step at the inflection point of the curve (see Fig. 6-1). To be able to convert these edge jump values into concentrations, scans of a set of reference $BaCl_2$ solutions (1-10 mM) were conducted with the same routine, yielding a straight calibration line with good correlation (Fig. 6-2).

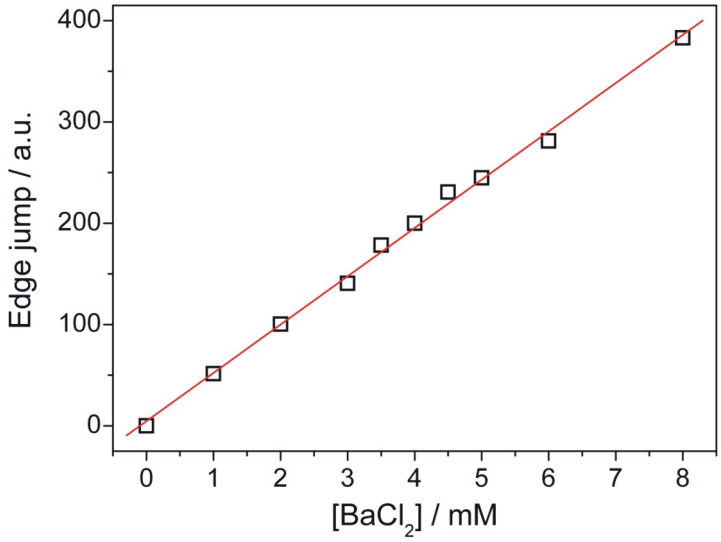

Fig. 6-2: Edge jump values determined for pure $BaCl_2$ solutions of different concentrations. A linear fit of the data (red line, R = 0.9984) was used to calculate the concentration of Ba^{2+} in the actual samples from the measured edge jump.

6.3.5 UV Spectroscopy

The only appropriate way to determine the silica concentration in solution under the given experimental conditions was found to be the molybdosilicate method. Low molecular weight siliceous species (primarily the mono- and dimer) are known to react under acidic conditions with molybdic acid to form a yellow silicomolybdate complex according to

$$12\ Na_2MoO_4 + Na_2SiO_3 + 26\ HCl \longrightarrow H_4SiO_4{\cdot}12MoO_3{\cdot}xH_2O + 26\ NaCl + 11\ H_2O$$

The rate of conversion of higher silica oligomers is in turn negligibly small.[34] Monitoring the absorbance of a sample thus allows for a distinct assessment of the silica speciation in solution. In the present work, this method was used to trace changes in the concentration of "reactive" silica during growth of silica biomorphs as a function of time. For analysis, samples were taken from individual wells at different times after growth start, passed through 200 nm syringe filters to remove colloidal silica, and then

rapidly acidified and converted to the silicomolybdate dye following a modified procedure described in literature.[35] To 0.4 mL of the filtered sample, 4.7 mL 0.128 M HCl and 0.2 mL of ammonium molybdate solution were given in rapid succession. The latter was prepared in direct advance to the experiments by dissolving 10 g ammonium heptamolybdate tetrahydrate ($(NH_4)_6Mo_7O_{24}\cdot 4H_2O$, Merck, ≥99.0%) in 100 mL water and subsequently adjusting the pH to 7-8 using powdered NaOH pellets (Merck, p.a.). After addition of the molybdate reagent, samples were left to stand for 5 min, before 0.15 mL of a 1 g/mL solution of oxalic acid dihydrate ($H_2C_2O_4\cdot 2H_2O$, Merck, ≥99.5%), meant to avoid side reactions, were added, effectuating a pH of about 1.3. The absorbance of the samples at 410 nm was read after waiting for another 6 min. Special care was thereby taken to maintain precisely the waiting times during the procedure, since the initially generated β-form of the silicomolybdate complex gradually transforms into the stable α-form and the two isomers show different absorption behavior.[36]

Eventually, the absorbance of the solution at 410 nm was determined with a Varian Cary 3E spectrophotometer using 1 cm disposable plastic cuvettes. Values for the silica concentration were obtained as an average of three independent experiments. For calibration, a series of water glass dilutions with known concentrations was subjected to the above procedure analogically, assuming that exclusively low molecular weight silica species exist in these dilute sols at their given high pH (> 11).

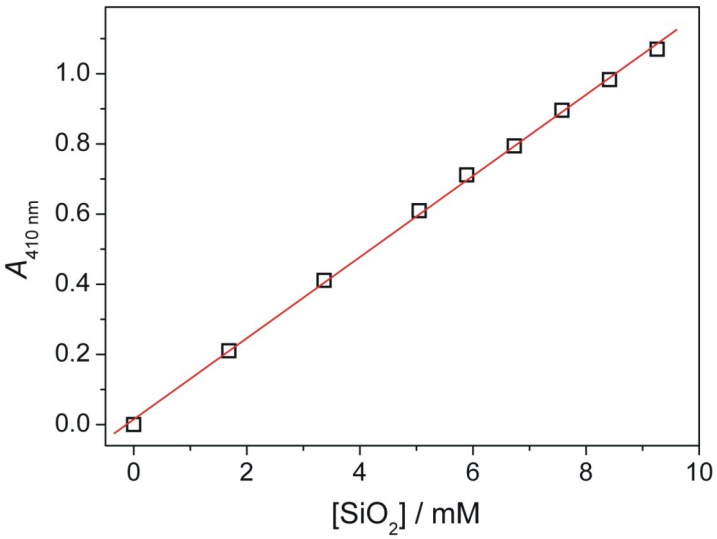

Fig. 6-3: Calibration curve for the UV measurements, obtained by converting different dilutions of water glass with the molybdate reagent and reading the absorbance at 410 nm. The correlation coefficient of the linear fit to the data (red line) is 0.9996.

A linear correlation was found (cf. Fig. 6-3), in agreement with the Lambert-Beer law, which was used to calculate concentrations from the measured absorbance values.

6.3.6 Electron microscopy

To study the incorporation of silica to the crystal aggregates during their development, solution-grown biomorphs were isolated and examined by means of field-emission scanning electron microscopy (FESEM) and energy-dispersive X-ray (EDX) analysis. Specimens for imaging were readily obtained by placing small glass coverslips on the bottom of the wells as growth substrates, on which the aggregates formed and remained stuck. The substrates were removed from the mother liquor after predefined times of growth and washed by careful rinsing with water and ethanol. Dried disks were fixed on aluminium stubs using conducting adhesive tape and coated with gold. SEM images were taken on a Zeiss LEO Gemini 1530 microscope at 3 kV. Selected aggregates on the coverslips were further investigated by atomic force microscopy (AFM), using a NanoWizard device from JPK Instruments and silicon cantilevers (Olympus, force constant: 42 N/m, typical frequency: 300 kHz). Images were acquired in tapping mode. For EDX studies, biomorphs grown in the wells were cleaned from excess salt by repeated replacing of the supernatant with water (5 x 10 mL), each time dispersing and withdrawing potentially occurring floccules of amorphous silica. Eventually, the wells were rinsed twice with 10 mL ethanol. Aggregates were then loosened gently from walls with the aid of a fine brush and promising candidates were transferred to the sample holder using micro-tools. Alternatively, a great deal of washed biomorphs was collected from a series of syntheses to obtain a practicable macroscopic powder, which was ground extensively in ethanol and dried in air. The remaining solid was pressed to give a flat and homogeneous tablet. A crucial advantage of this procedure is that the acquired EDX spectra, in particular when large areas are sampled, reflect the mean composition of numerous aggregates rather than of a single biomorph. In addition, the evenness of the specimens eliminates errors originating from the curved topology of the biomorphs as well as from the different height and orientation of structural segments relative to the X-ray detector, thus ensuring accurate quantitative analysis. Crushing and homogenizing moreover prevents interferences caused by the core-shell character of aggregates bearing an external silica skin, which may lead to disproportionately high counts for Si when probing intact architectures.[26] Unfortunately, this method could only be applied for biomorphs isolated at later stages of growth (usually $\geq$ 6 h), due to the limited amount of material available at earlier times. EDX measurements were carried

out at 10 kV using an Oxford INCA detector, recording spectra from several independent positions (both points and areas) in the samples and averaging results.

Individual crystallites of the carbonate core were investigated by transmission electron microscopy (TEM). Suitable samples were obtained on the one hand by grinding powdered aggregates in n-butanol to achieve a fine suspension, aliquots of which were loaded onto carbon-filmed copper grids and left to dry in air. On the other hand, unbroken biomorphs were embedded into Epon resin and thin-sectioned. For this purpose, an EMbed 812 kit from Electron Microscopy Sciences was used. Precursor solutions were prepared by mixing epoxy resin under moderate stirring in appropriate ratios with the hardeners DDSA (dodecenyl succinic anhydride) and MNA (methyl-5-norbornene-2,3-dicarboxylic anhydride) and adding, after 30 min, the accelerator DMP-30 (2,4,6-tris(dimethylaminomethyl) phenol). The final contents of the reagents (v/v) were 46 % epoxy resin, 28.5 % DDSA, 25.3 % MNA, and 0.2 % DMP-30. For embedding, a suspension of as-grown biomorphs in acetone (Merck, p.a.) was incubated with a 1-1 mixture of the Epon precursor and acetone for 2 h, and subsequently with a 2-1 mixture overnight. Eventually, the samples were infiltrated with pure resin solution and then cured for 48 h at 60°C. The resulting blocks were cut into slices of 70-200 nm in thickness with an ultramicrotome (Leica EM UC6, equipped with an Ultra 35 diamond knife from Diatome). Slices were taken up with copper grids carrying a Pioloform support film (Plano GmbH). TEM studies were performed on a Philips CM 12 and CM 30 ST microscope at 120 and 300 kV, respectively. Images were recorded with CCD cameras from Gatan. Single rods were characterized concerning their elemental composition by acquiring EDX spectra in nanoprobe mode with a Si/Li detector unit (Noran, Vantage System).

6.4 Results and Discussion

6.4.1 Temporal Progression of the Barium Concentration during Growth

Since conventional methods such as atomic emission spectroscopy or the use of an ion-selective electrode failed due to interferences caused by the silica and the high pH, the concentration of dissolved Ba^{2+} was determined *in situ* by monitoring its fluorescence upon irradiation of X-rays. As a crucial advantage of this technique, measurements are non-invasive and do not require perturbing sample drawing or conversion, but deliver data on-line in a highly reliable manner. Results obtained for a typical solution experiment are shown in Fig. 6-4. It is evident that the Ba^{2+} concentration decreases

linearly over the entire investigated period of time, with a slope of about 0.2 mM h^{-1}. When assuming that binding of Ba^{2+} ions to silicate species is negligible and that noticeable precipitation of barium silicate does not occur under the given conditions (both being supported by measurements of the silica concentration, cf. Section 6.4.5), this implies that the rate of $BaCO_3$ crystallization is constant during the formation of silica biomorphs.

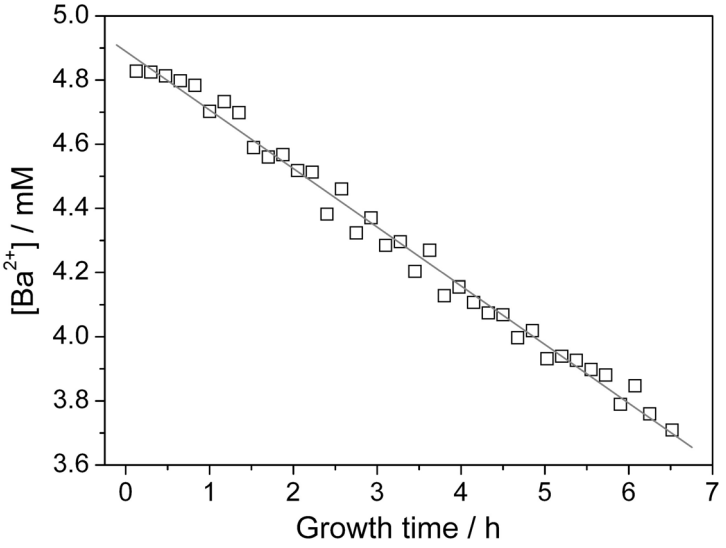

Fig. 6-4: Time-dependent profile of the Ba^{2+} concentration in solution during growth of silica biomorphs. The experimental data (squares) are well-described by a linear fit (full line). The maximum error in the values is estimated to ± 0.05 mM.

In addition, provided that the initially detected concentration (4.83 mM) as well as the intercept of the linear fit with the y-axis (4.89 mM) is lower than the analytical starting value of 5 mM, it seems as if the used silica sol already contains a certain, yet small amount of carbonate, indicating previous uptake of atmospheric CO_2 during preparation and storage. From optical microscopy studies it can be inferred that, in the present setup, the development of crystal aggregates is essentially completed after 8-10 h. However, according to Fig. 6-4, the barium concentration is still relatively high at that time (> 3 mM), hence precluding that termination of the characteristic growth behavior is due to a depletion or even quantitative consumption of the available Ba^{2+} ions.

6.4.2 Evolution of the Carbonate Concentration and the Bulk Supersaturation with Time

To estimate the actual concentrations of carbonate species in the system at distinct times, the bulk pH was recorded by immersing a glass microelectrode into the solution. The collected data reveal a slightly asymptotic decay (Fig. 6-5a), reflecting the diffusion-controlled uptake of CO_2 by the alkaline mixtures. Reference experiments

with non-glassy electrodes as well as discontinuous measurements confirm the traced evolution, and therefore ensure the functionality of the microprobe also in the long term despite the presence of silica. Apart from that, it is worth stressing that the small undulations seen in some sections of the curve (e.g. between 8 and 10 h), arousing the impression of an oscillating behavior, were identified as artifacts rather than true features of the sample.

Since the observed decrease in pH with time is caused by the conversion of CO_2 into carbonic acid and its subsequent deprotonation to bicarbonate and carbonate ions in solution, it is possible to derive (semi-)quantitative information on the concentrations of these species if the response of the system's pH to addition of acid is known. For this purpose, mother solutions of silica biomorphs were titrated with dilute HCl under carbonate-free conditions (see Appendix C.1). Interpolating the experimental titration curve yields equations with which the pH measured at a given time during growth can be translated to the number of protons which had to be generated by dissolution of CO_2 to establish that pH (cf. Fig. C-1, Fig. C-2, and Fig. C-3). Based on mass balance considerations and the distribution of carbonate species in solution as a function of pH, and taking into account the parallel removal of carbonate due to precipitation (as reflected by the measured linear decrease in the Ba^{2+} concentration), these data can be used to derive the apparent amounts of dissolved HCO_3^- and CO_3^{2-} ions present at a certain time (see Appendix C.1). Resulting concentration profiles are shown in Fig. 6-5b. The obtained values are in a reasonable order of magnitude and should hence at least qualitatively represent the evolution of the carbonate concentration in solution during growth of silica biomorphs. Generally, as expected, the total amount of carbonate in the system (i.e. both dissolved and precipitated carbonate species) rises with time, and its progression is inversely proportional to the pH of the solution. The concentration of dissolved CO_3^{2-} ions increases during the first 3 hours to reach a maximum at about 0.2-0.25 mM after 4-5 h, as a growing fraction of HCO_3^- ions exists in equilibrium at the already notably lowered pH.

Correspondingly, calculations of the relative supersaturation S show that the bulk solution becomes supersaturated with respect to barium carbonate after an initial period of 10-15 min, when enough carbonate has entered the system (Fig. 6-5c). As dissolution of atmospheric CO_2 proceeds while the Ba^{2+} concentration is still high, S increases steeply during the first hour to subsequently level off on a plateau of more or less constant values.

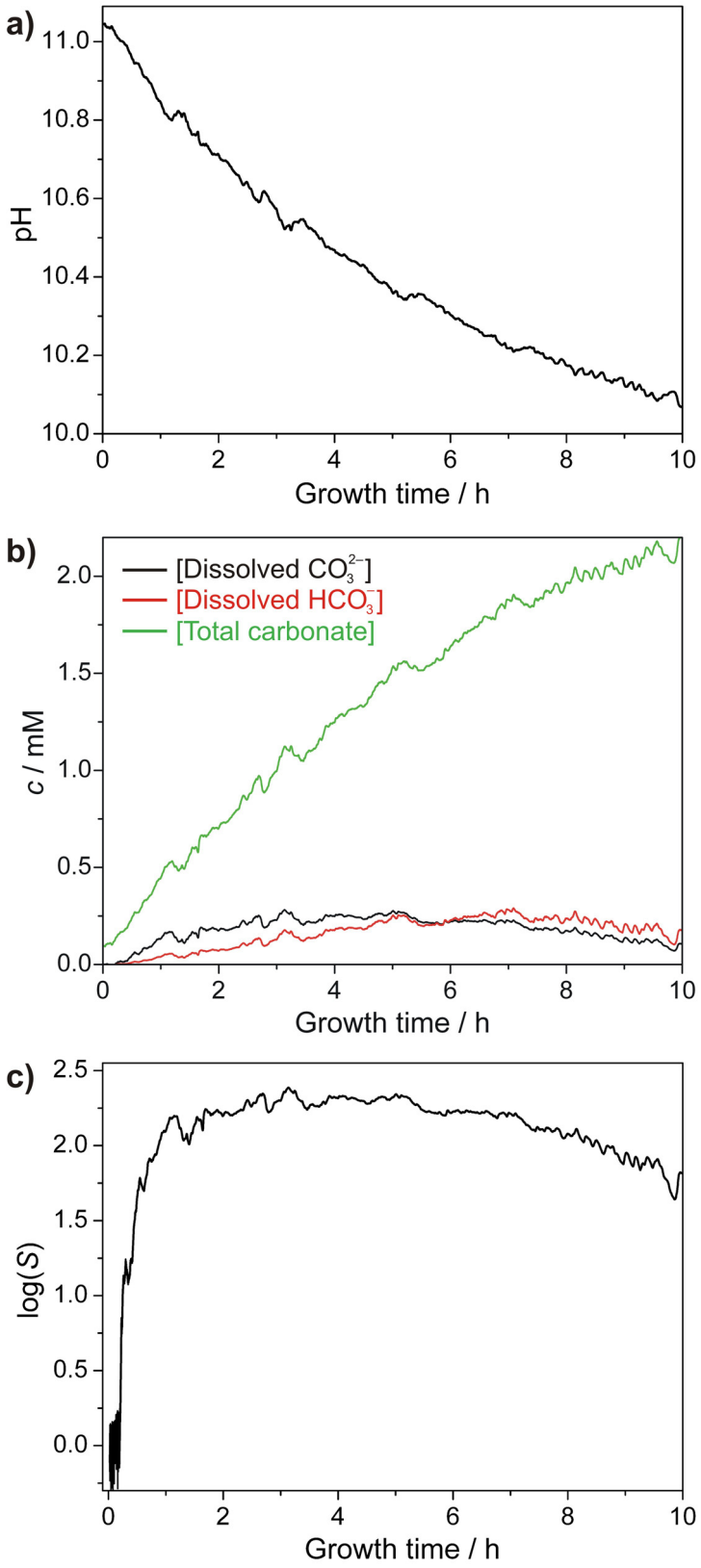

Fig. 6-5: (a) Variation of the bulk pH during growth of biomorphs from solution. (b) Calculated time-dependent progressions of the concentrations of dissolved carbonate and bicarbonate ions and the total amount of carbonate formed in the system. Note that the concentrations of dissolved CO_2 and carbonic acid can be neglected at the given high pH. (c) Logarithmic plot of the relative supersaturation of $BaCO_3$ in the bulk as a function of the growth time.

This indicates that any increment in *S* due to continued generation of carbonate ions is counterbalanced by the decrease in the Ba^{2+} concentration owing to precipitation. After roughly 7 h, a slight decrease in the supersaturation and the concentrations of dissolved CO_3^{2-} and HCO_3^- ions is observed, while the increase in the total amount of carbonate present is sensibly decelerated. This suggests that the rate of CO_2 uptake is markedly depressed under the meanwhile prevailing conditions. Nevertheless, the data demonstrate that throughout the time window in which growth of silica biomorphs is active (~2-10 h), the bulk mother solution is constantly supersaturated and thus provides only smoothly varying conditions for the development of complex crystal aggregates.

In light of these findings, the observed cessation of growth after around 10 h remains to be discussed, in particular because the system is at this stage obviously still supersaturated. Indeed, on continued ageing of the solutions, regular barium carbonate crystallites are occasionally seen to decorate the surface of existing biomorphs (see Fig. 6-6). This implies that crystallization does still occur, but coupled co-precipitation and the formation of nanocrystalline structures is no longer possible. In fact, it has been reported that growth of silica biomorphs takes place only locally at the active front, and that the front catalyzes precipitation of $BaCO_3$ by converting bicarbonate to carbonate ions and consequently raising supersaturation in its vicinity.[31] Therefore, the growth process should in principle be largely independent of the situation in the bulk, as long as the preconditions required for chemical coupling are fulfilled – which apparently is no more the case after 10 h. Perhaps, the restricted flow of CO_2 into the solution at the end of the experiment, the decreasing fraction of carbonate ions in equilibrium or the lower pH as such cause self-assembly to succumb. This shows that although biomorphs are quite flexible and can be grown in various environments, their formation inevitably necessitates proper starting conditions.

Eventually, it should be mentioned that the concentration profiles discussed here apply exclusively for growth in solutions. In gels, the found trends may be reversed, that is, the barium concentration should increase asymptotically due to diffusion into the gel whereas the concentration of carbonate, which is fully dissolved in the gel already at the beginning, decreases more or less linearly with time.

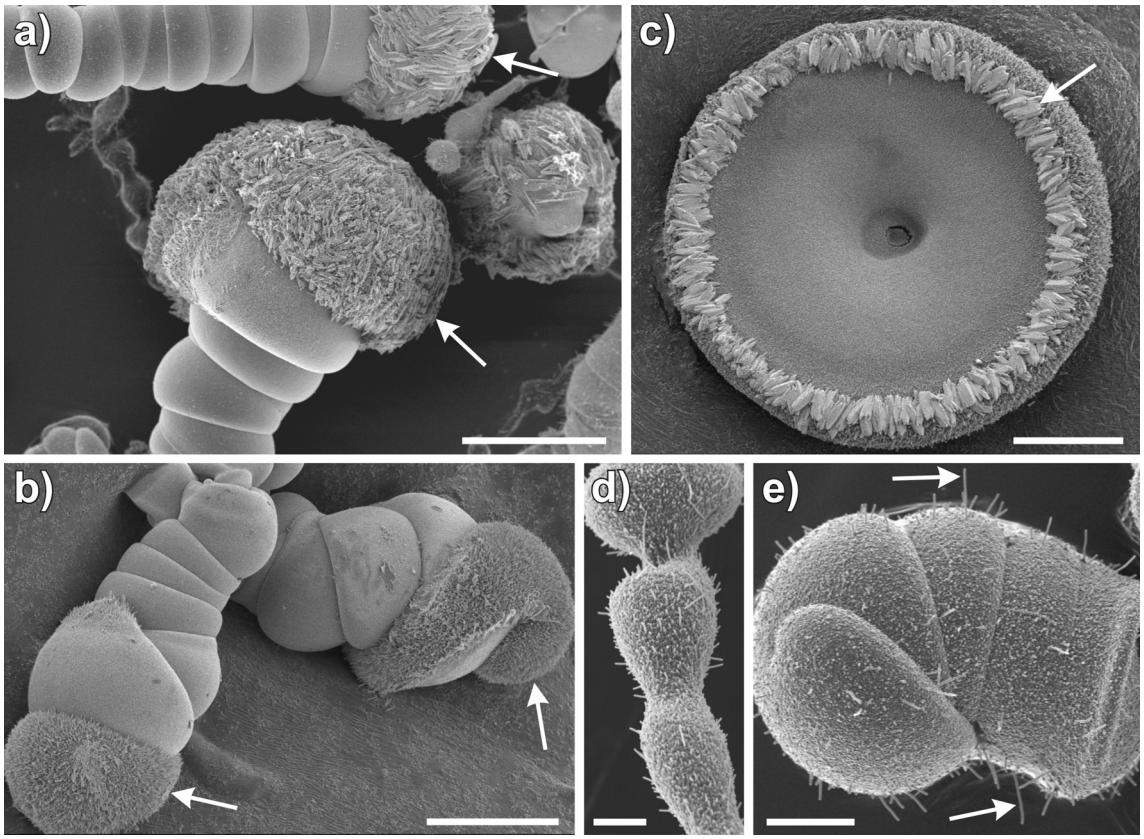

Fig. 6-6: Secondary crystallization: upon prolonged ageing, as-grown silica biomorphs frequently become covered by regular barium carbonate crystals. (a-b) Worms are often seen to carry a corona on their tip, which may consist either of blocky micron-sized subunits (a), or finer hairy individuals (b). (c) On sheets, elongated secondary crystals tend to form around the rim and usually share the preferred orientation of the nanorods in the aggregate underneath (i.e. are aligned radially outwards with respect to the center of the sheet). (d-e) In some cases, the surface of biomorphs – especially of those bearing an external silica skin – is decorated by spiky needle-like crystallites in the submicron range, which stick out of the aggregates at arbitrary angles. Scale bars: (a) 50 µm, (b) 20 µm, (c) 30 µm, (d) 3 µm, and (e) 10 µm.

6.4.3 Growth Rates of Individual Aggregates

For a further interpretation of the concentration data, the growth behavior of silica biomorphs was studied by acquiring series of optical images from evolving aggregates. In this work, only sheet-like morphologies were investigated since the movement of their growing front can easily be followed. Nevertheless, similar and kinetically consistent results can also be obtained for twisted forms. Exemplarily, a sequence of micrographs taken at different times from a suitable aggregate is shown in Fig. 6-7a. Growth rate analyses were performed by measuring the distance r the front has traveled after time t. Values for r are thereby given relative to the position of the front in the first frame which is set to $r = 0$, although in most cases the sheets had grown to notable dimensions already before acquisition was started. For radial growth, $r(t)$ was found to

be independent of the growth direction, i.e. the azimuthal angle of the chosen radial path. Therefore, values measured along the distinct measurement lines on a sheet were averaged for a given time *t*. In turn, this was not necessarily true for the propagation rate of different curls around the perimeter of the sheet. Plots of $r(t)$ demonstrate that the front advances linearly with time concerning both radial (Fig. 6-7b) and peripheral growth (Fig. 6-7c). On that basis, the mean radial and azimuthal propagation velocities, V_ρ and V_φ, can be derived from the slopes of linear fits to the $r(t)$ data.

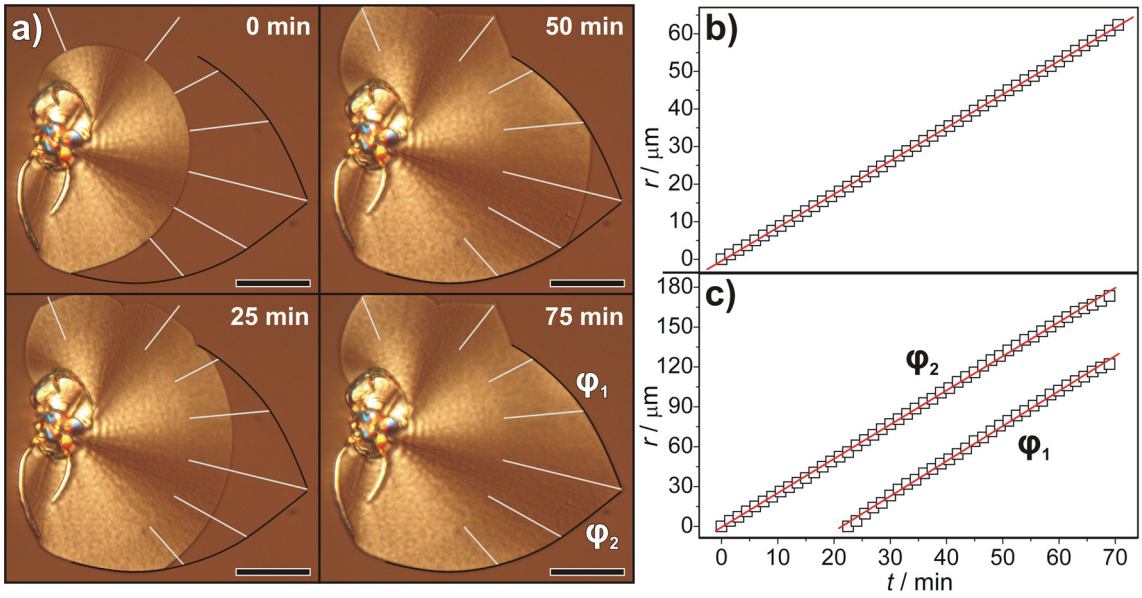

Fig. 6-7: (a) Temporal sequence of optical micrographs illustrating the development of a sheet-like biomorph in silica gel. The inserted lines depict the radial (white) and azimuthal (black) paths over which the advancement of the front with time was measured. Scale bars: 50 µm. (b, c) Plots of the distance r covered by the front within time t for radial (b) and azimuthal (c) growth, along with linear fits (red lines) to the experimental data (squares).

In the case of the sheet shown in Fig. 6-7a, the analyses yielded V_ρ = 0.89 ± 0.09 µm/min (radial growth), $V_{\varphi 1}$ = 2.6 ± 0.5 µm/min (upper curl), and $V_{\varphi 2}$ = 2.5 ± 0.3 µm/min (lower curl). Results agree well with values reported in a previous study for a sheet grown under similar conditions.[30] Evaluations of other image sequences (see Appendix C.2) confirm that biomorphs grow at a constant rate and, moreover, prove that the magnitude of the growth rate may vary from batch to batch within a typical range of about 0.1 to several microns per minute. Apart from the composition of the sample (i.e. concentration of species and pH), parameters like the position of an aggregate in the gel relative to the interface with the solution or the time at which it grows appear to be important in this context. For experiments conducted in solution, data usually exhibit a linear advancement of the front with time likewise. Here, the

surface-to-volume ratio of the sample has turned out to be, amongst others, crucial for the growth rate. For instance, using thin layers of solution drastically accelerates the increase of the carbonate concentration in the system and the decrease of the pH, therefore causing faster growth. In an extreme case, this may establish a situation in which the conditions at the growing front gradually adjust to those in the bulk, in that the locally generated supersaturations of barium carbonate and silica adopt consistently higher values as growth proceeds. Under such circumstances, the growth rate is found to be no longer constant, but increases with time (see Image Sequence C-5 in Appendix C.2).

The morphological evolution of the aggregates on the micron-scale can readily be understood on the basis of the measured growth velocities.[30] In the beginning, sheets spread radially with equal velocities in all directions and thus have rounded circular shapes (Fig. 6-7a, 0 min). Curling arrests radial enlargement and opens a new front which, in the following, advances orthogonally and competes with radial growth. Since, in the present and most other examples, multiple curls are created at similar times around the rim of a single sheet and their comparably high propagation rate allows for continuous overriding of radial growth, the initial circularity of the sheet becomes progressively distorted (Fig. 6-7a, 25 and 50 min). Eventually, when different curls approach on the perimeter of sheet, their relative height and handedness decide on whether intertwining can occur and twisted ribbons, helicoids, or worms emerge.[30] If, as in Figure 3a and Image Sequences C-1, C-2, C-4 and C-5 in Appendix C.2, the two curls are bent to the same side of the sheet (i.e. have opposite handedness) and display similar height, their convergence leads to the formation of a cusp (Fig. 6-7a, 75 min) at which growth is abandoned. The symmetry of the resulting leaf-like shape is essentially determined by the ratio of the corresponding azimuthal growth velocities; if both curls are propagated at a comparable rate ($V_{\varphi 1} \approx V_{\varphi 2} > V_{\rho}$), the sheet will exhibit bilateral symmetry and resemble a cardioid (cf. right-hand section of the sheet in Fig. 6-7a).

The finding that silica biomorphs grow linearly with time is in line with earlier observations made for sheets[30] as well as twisted structures.[30,37] Further, the microscopy data comply well with the measured progression of the barium concentration in solution. Since the latter depicts changes in the bulk whereas the former is representative of individual aggregates only, it may be presumed that temporally linear growth applies for all aggregates in a batch, although the particular rate might vary to a greater or lesser extent. In this regard, the concentration profile reflects the mean growth

velocity. Moreover, given that the barium concentration decreases linearly over the entire period of active growth while the development of individual aggregates is normally completed within less than 2-3 h (cf. Fig. 6-7 and Appendix C.1), it seems reasonable to infer that, in solution, biomorphs are formed within a certain window of time rather than growing simultaneously. Thereby, the growth rate appears to be independent from the time after mixing at which the formation of a crystal aggregate takes place, as evidenced by the concentration data. In view of these considerations, it is furthermore clear that the pH oscillations envisaged by the proposed model to occur at the growing front cannot be resolved by measurements of the bulk pH (cf. Fig. 6-5a). To that end, these oscillations would have to proceed largely in phase to be amplified to a detectable degree, for which there is no obvious reason.

6.4.4 Kinetics of Biomorph Formation

According to classical theories, the kinetics of crystal growth can be controlled either by the transport of ions to the growth site, i.e. diffusion from the bulk, or the incorporation of growth units to the lattice at the surface of the forming crystal.[38] Under diffusion-controlled conditions, the rate of the reaction is proportional to the bulk concentration of the reagents. Therefore, when only a certain amount is provided and no further reagents are dosed in the course of the reaction (as for Ba^{2+} during growth of biomorphs from solution), the overall growth rate of the crystal will decrease with time, describing a first-order exponential decay if the diffusion of one of the reagents is rate-determining. In turn, if the surface-integration step is significantly slower than the transport of reagents from the bulk, the process will become reaction-controlled. In this case, the growth rate may depend on the supersaturation at the crystal-solution interface, but no longer directly on that in the bulk, and will hence remain constant over time, provided that there are no drastic variations in the conditions and the crystal does not change its growth mode. Thus, the concentration of the reagents in the bulk is expected to decrease linearly with time, corresponding to a reaction of apparent order zero. For the crystallization of barium carbonate, both scenarios have been observed and the parameters influencing the kinetics were reported to be the bulk supersaturation, the pH, the morphology of the crystals, power input, as well as the type and design of the reactor used for precipitation.[39] Based on the concentration data and the measured growth rates, the kinetics of the formation of silica biomorphs is clearly identified as being reaction-controlled. Indeed, this finding is a logical consequence of the coupled co-precipitation mechanism proposed to account for morphogenesis. Since the growing

front by itself increases, relative to the bulk, the concentration of reactive species in its vicinity to elevate supersaturation and provoke nucleation, there will be no net transport of reagents to the growth site. Rather, carbonate ions and protonated silicate species will diffuse from the active region at the front into the bulk, along the generated concentration gradients. In this sense, the rate of the growth process can as such not be controlled by diffusion, but is limited by the production of new material for growth at the front and its incorporation to the aggregate. The latter involves on the one hand the autocatalytic transformation of reagents, i.e. the conversion of bicarbonate to carbonate ions upon precipitation of silica and the protonation of charged silicate species induced by the crystallization of carbonate, and, on the other, nucleation and growth of the respective component. Which of these steps is slowest and thus rate-determining, however, remains unknown.

6.4.5 Incorporation of Silica to the Crystal Aggregates at Distinct Stages of Growth

Finally, temporal changes in the concentration of silica occurring during growth from solution were investigated. Measurements were performed in a discontinuous manner, that is, samples were drawn at different times and the reaction was quenched by acidification prior to preparation for analysis. Results obtained by averaging values from multiply reproduced experiments are displayed in Fig. 6-8. Basically, the found progression of the silica concentration in solution can be subdivided into three intervals. Up to around 2.5 h, the amount of dissolved silicate species remains, with respect to the limits of experimental error, approximately constant and is only marginally lower than the initial analytical value. In the following, the silica concentration begins to decrease in a noticeable manner, yet still rather slowly and overall by merely about 0.4-0.5 mM after 7 h. At this time, a breakpoint can be discerned in the curve subsequent to which a much steeper and more or less linear decline until the end of the examined period is observed.

Earlier studies have repeatedly demonstrated that silica biomorphs are composite materials of alkaline-earth carbonates and silica.[19,21-28] The silica was thereby often reported to exist as an extended skin around the assembly of carbonate crystallites as a whole. Consistently, this skin was found to remain upon leaching with acid while the inner carbonate-rich core dissolved entirely.[23,25-28] However, it was further noted that not all crystal aggregates within a given batch exhibit this feature.[23,28] Other work provided evidence that significant amounts of silica occur also in the core part,

intertwined with the carbonate phase and possibly sheathing individual crystallites.[21,24] In order to investigate the presence of silica skins on the surface of the aggregates as well as inclusions in the core, and to interpret their origin with respect to the temporal profile of the concentration in the bulk, biomorphs were isolated from solution after distinct times and characterized by different techniques (cf. Fig. 6-9 to Fig. 6-14).

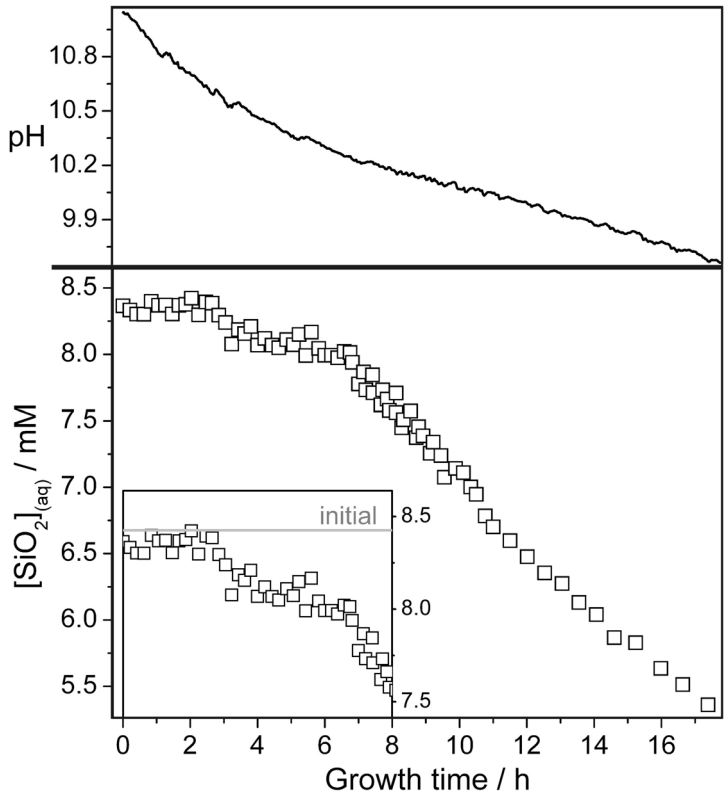

Fig. 6-8: The concentration of dissolved silica as a function of the growth time during the formation of silica biomorphs in solution, traced over a period of up to 18 h, along with a corresponding long-term pH profile (top). Inset: enlarged view on the first 8 hours after which growth of characteristic crystal aggregates is in most cases widely completed. The experimental error is estimated to ± 1.7 % of the respective value.

Although the fraction of aggregates sheathed by an outer silica skin is hard to quantify and varies substantially from batch to batch, the experiments performed in the present work strongly suggest that the growth time is a crucial parameter in this context. In FESEM images of biomorphs left to grow overnight, the occurrence of external skins can be clearly distinguished on occasion at some sites, especially when aggregates have cracks and thus permit insight to their interior. In such a case (Fig. 6-9c), it is evident that the silica membrane covering the inner carbonate core is composed of a quasi-monolayer of densely aggregated colloidal spheres with diameters in the range of 50-150 nm. EDX data confirm the presence of appreciable amounts of silica. Si/Ba atomic

ratios measured for biomorphs which obviously bear a silica skin were found to range from about 0.15 to 0.4, in good agreement with values reported previously for syntheses run under similar conditions.[40,41]

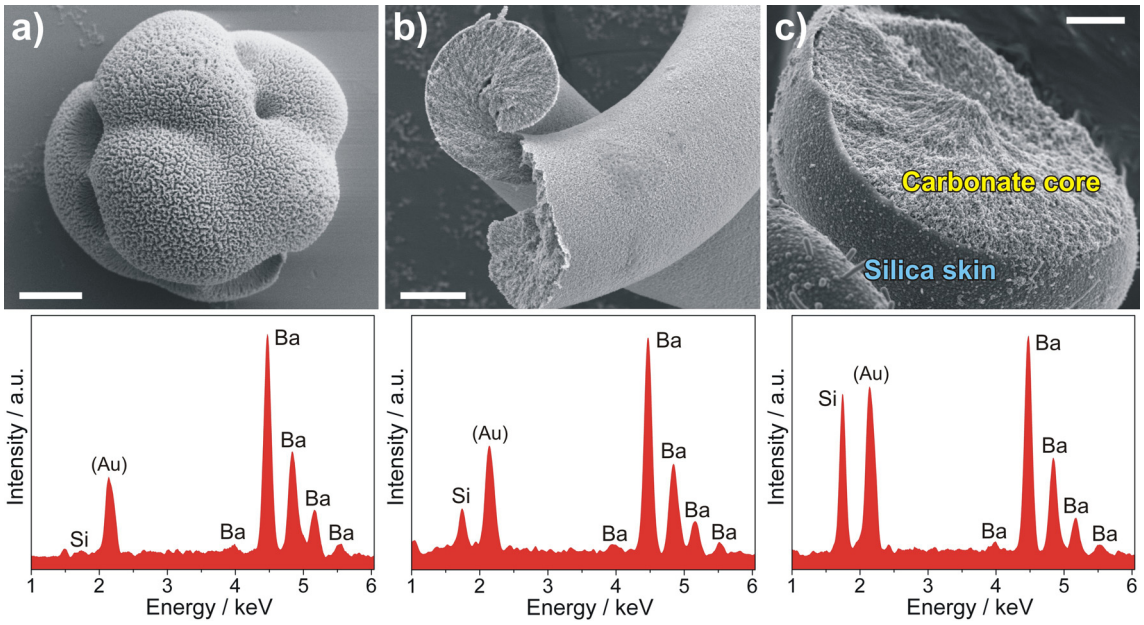

Fig. 6-9: FESEM micrographs of precipitates isolated after (a) 2, (b) 8, and (c) 14 hours of growth from solution, and EDX profiles collected from typical aggregates. Up to 8 h, there are no indications for the presence of silica neither on the surface nor in the core of the biomorphs in the images. Accordingly, the signal for silicon in the EDX spectrum after 2 h is negligibly low, while a distinct but still rather small peak is observed after 8 h. By contrast, aggregates grown for 14 h frequently exhibit a layer with different structure around the textured inner core, accompanied by a drastic increase in the relative intensity of the Si peak. The Si/Ba atomic ratios calculated from the shown spectra are (a) 0.009 ± 0.003, (b) 0.069 ± 0.008, and (c) 0.269 ± 0.009. Scale bars: 3 µm.

Coherent results were obtained when determining the average Si content of bulk samples prepared by homogenizing a great deal of aggregates. The mean composition of the biomorphs turned out to be sensitive, apart from the growth time (see below), also to the washing procedure and in particular the age of the used water glass lot. Inadequate washing may induce additional deposition of silica on the precipitates as an artifact during isolation, whereas prolonged leaching in water causes undesired superficial dissolution of components. On the other hand, upon ageing, concentrated silica stock solutions is expected to contain a higher fraction of condensed oligomeric species and small colloidal particles which enhances, at a given pH, the propensity to polymerization and coagulation. All these factors influence the final silica content of the aggregates in a delicate manner and consequently restrict the reproducibility of

experiments in terms of the Si/Ba ratio determined by EDX analysis. To minimize such parasitic effects, the syntheses of the present work were carried out utilizing fresh water glass only and applying a standardized cleaning protocol.

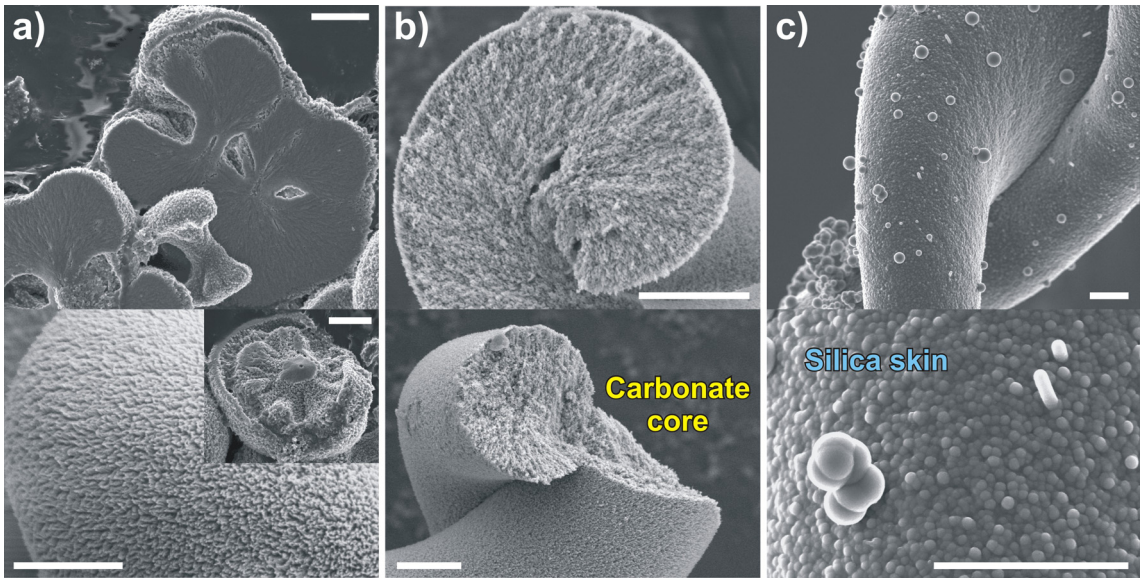

Fig. 6-10: The microstructure of aggregates grown for (a) 2 h, (b) 8 h, and (c) 14 h. (a) Views on the bottom and the cross-section of early fractal spherulites confirm that the formation of silica biomorphs starts from an elongated pseudohexagonal crystal which, via continuous splitting, successively undergoes a transition over a dumbbell-like morphology to eventually a closed sphere. These architectures grow attached to the substrate and are therefore flat on the bottom. Zooming into the surface reveals a perforated topology and pinnacled structure, which is typical for barium carbonate and argues for a high degree of branching. In turn, images do not support the presence of silica at this stage. (b) After 8 h, characteristic twisted forms have developed, but close-up views still show only a bare carbonate core and no distinct silica skin around it. (c) When left to evolve overnight, the aggregates have adopted a somewhat smoother appearance and are occasionally decorated by silica colloids as large as several hundreds of nm across. Higher magnifications of the surface demonstrate that the biomorphs are now covered by a layer of agglomerated spherical nanoparticles with diameters roughly ranging from 50 to 150 nm. Scale bars: 2 μm.

In any case, it seems clear that the precipitation processes leading to bulk Si percentages as high as 30-40% cannot occur until around 7 h after growth start, because the concentration in solution decreases only slightly during that period (Fig. 6-8). It must be stressed that the molybdosilicate method employed for measuring the silica concentration detects mainly mono- and dimers, while soluble oligomers and polymers hardly react with the molybdate ions (see Section 6.3.5). This implies that the factual concentration of dissolved silica in the samples at time *t* should be higher and the amount of precipitated silica even lower than indicated by the collected data. In this

regard, the extended silica layers observed on numerous aggregates in overnight batches are likely to be deposited at times greater than 7 h, when the concentration of silica decreases much more substantially. Since the development of characteristic curved architectures is however already widely completed at that stage (cf. Fig. 6-9b and Fig. 6-10b), the formation of external silica skins must be a secondary phenomenon not related to the very growth mechanism of silica biomorphs, as speculated in former work.[23,25,26] Probably, precipitation of silica on the surface of as-formed aggregates is caused by the continuous decrease of the pH with time (cf. Fig. 6-8) which, at a certain point, increases the bulk supersaturation of silica such that ample polymerization is initiated. Apart from distinct skins on the biomorphs, this becomes also manifest in suspended colloidal precipitates which becloud the solution towards the end of the experiment and eventually flocculate forming amorphous deposits on the bottom of the well (see Fig. 6-11).

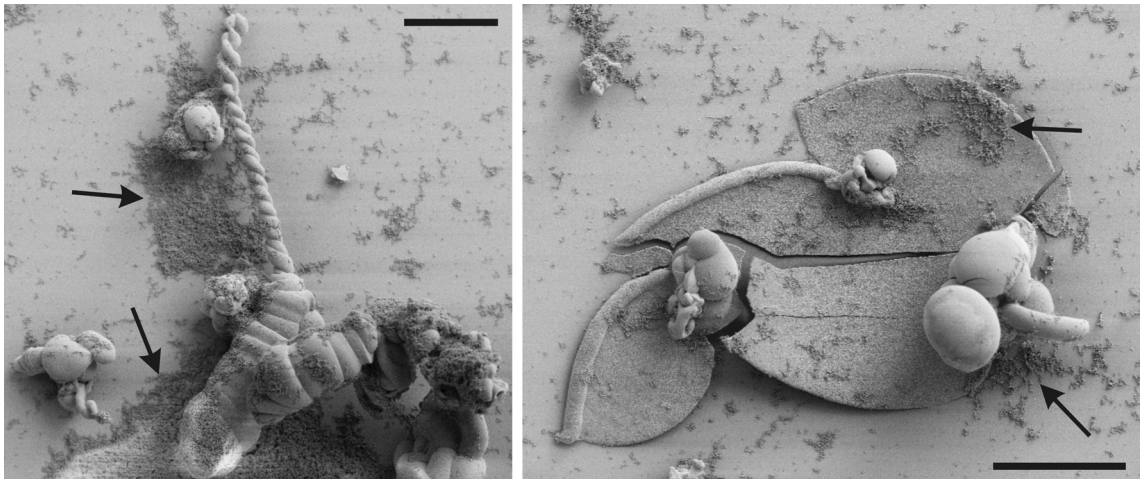

Fig. 6-11: Precipitation of colloidal silica on continued ageing of the solutions: when the system is left to evolve for periods longer than 12 h (in this case overnight, i.e. ~14 h), flocs of amorphous silica are often observed as deposits on fully developed biomorphs as well as aside on the used glass substrate (indicated by the arrows). Separate analyses on these precipitates have shown that the material contains only traces of barium and consists of uniform agglomerated silica nanospheres (50-200 nm in diameter). Flocculation results as a consequence of enhanced silica polymerization at lower pH. Condensation processes are further supported by charge-screening Ba^{2+} ions which, thereby, partly become occluded in the floccules. Scale bars: 50 μm.

These conclusions are supported by analyses of biomorphs harvested as soon as morphogenesis was apparently terminated (i.e. after ~8 h), which carry external silica skins much less frequently than their counterparts grown for longer periods. Accordingly, high-magnification images of corresponding aggregates reveal a bare

carbonate core instead of a smooth silica surface (Fig. 6-12), and EDX measurements prove that the amount of silica present is comparably low, with Si/Ba atomic ratios typically varying between 0.02 and 0.1 (Fig. 6-9b).

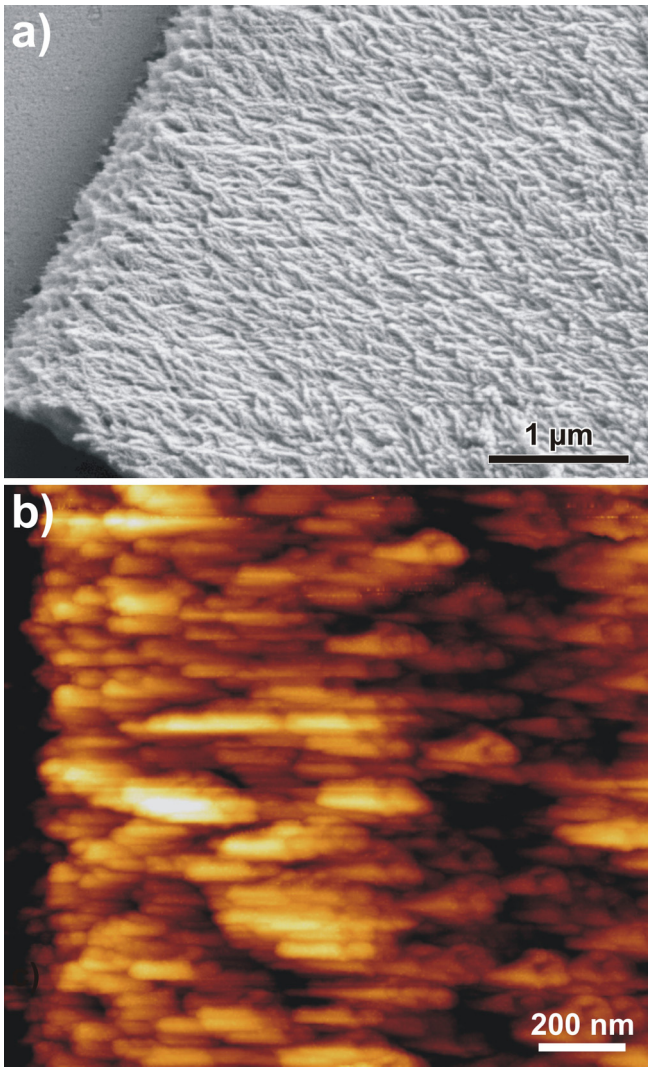

Fig. 6-12: (a) High-magnification FESEM and (b) AFM image showing the front of sheet-like biomorphs which were withdrawn from the mother solution after 8 hours of growth. In both cases, the aggregate consists of locally co-oriented elongated nanocrystals, with no evidence for an external silica skin coating the assembly.

The data further provide direct information on the role of the silica and the degree of its incorporation to the aggregates during the window of active growth (see inset in Fig. 6-8). Light microscopy and FESEM studies show that within the first 2-3 hours after mixing only globular particles are generated (Fig. 6-9a and Fig. 6-10a), which arise from non-crystallographic branching of a carbonate single crystal.[20,30] EDX spectra verify, in line with previous work,[41] that these fractal architectures contain, if any, only traces of silica (Si/Ba $\leq$ 0.01, cf. Figure 5a). This is in good agreement with the

measured constant silica concentration in this period. Minor percentages of silica in the particles may moreover originate from insufficient washing and consequent precipitation of actually dissolved species upon drying. Therefore, results demonstrate that although poisoning growth and provoking crystal splitting, the silica is not integrated to the forming aggregates to a significant extent during this first stage of morphogenesis.

In a second stage, laminar and curved morphologies begin to sprout from most of the globular precursors as the growth mode has changed from continuous fractal branching to the self-assembly of individual nanoscale crystallites.[30] The observed decrease in the concentration of dissolved silica and the concurrent increase of the bulk Si content in the aggregates indicate that silica is now noticeably co-precipitated with the carbonate. To investigate the presence of silica in the interior of the biomorphs, thin sections of the crystal aggregates were prepared for TEM studies. Micrographs disclose numerous rod-like particles with lengths in the range of ~200-400 nm and widths up to 50 nm (Fig. 6-13a-b), complying with values reported in literature.[21-23,26,27] The mutual arrangement of the rods in the slice supports orientational ordering (Fig. 6-13a) and thus shows that the structural integrity of the assembly was largely preserved during preparation, although voids in the film signify that some crystallites incidentally fell out.

Unfortunately, the poor stability of the slices in the electron beam at higher voltage prevented elemental analyses of the nicely exposed nanocrystals. Therefore, a different set of samples was prepared by grinding biomorphs and loading the resulting powder directly on TEM grids (see Fig. 6-14). EDX spectra of suitable intact crystallites exhibit a small peak for Si along with strong signals for Ba, C and O (Fig. 6-13b). Though varying, the Si/Ba atomic ratio found for the nanorods amounts to at most several percents in the majority of cases. Comparing the data with those determined for the bulk volume of aggregates lacking an outer silica skin (Fig. 6-9b) suggests that the typical Si content of single rods tends to be somewhat lower. This may hint that not all silica in the core is directly associated to the nanocrystals. Possibly, a certain fraction serves to connect neighboring rods by forming siliceous bridges between the particles which strengthen the crystal assembly.

Overall, experiments show that the quantity of silica accommodated by the aggregates during active growth is detectable and significant, but in total rather low. Further, we could not collect any evidence for distinct silica layers on individual rods, which one may suspect with regard to the postulated model of coupled co-precipitation.[30] If

cessation of growth and the stabilization of crystals with nanometric dimensions rely on induced precipitation of silica over their surface, then corresponding skins around the particles must be very thin.

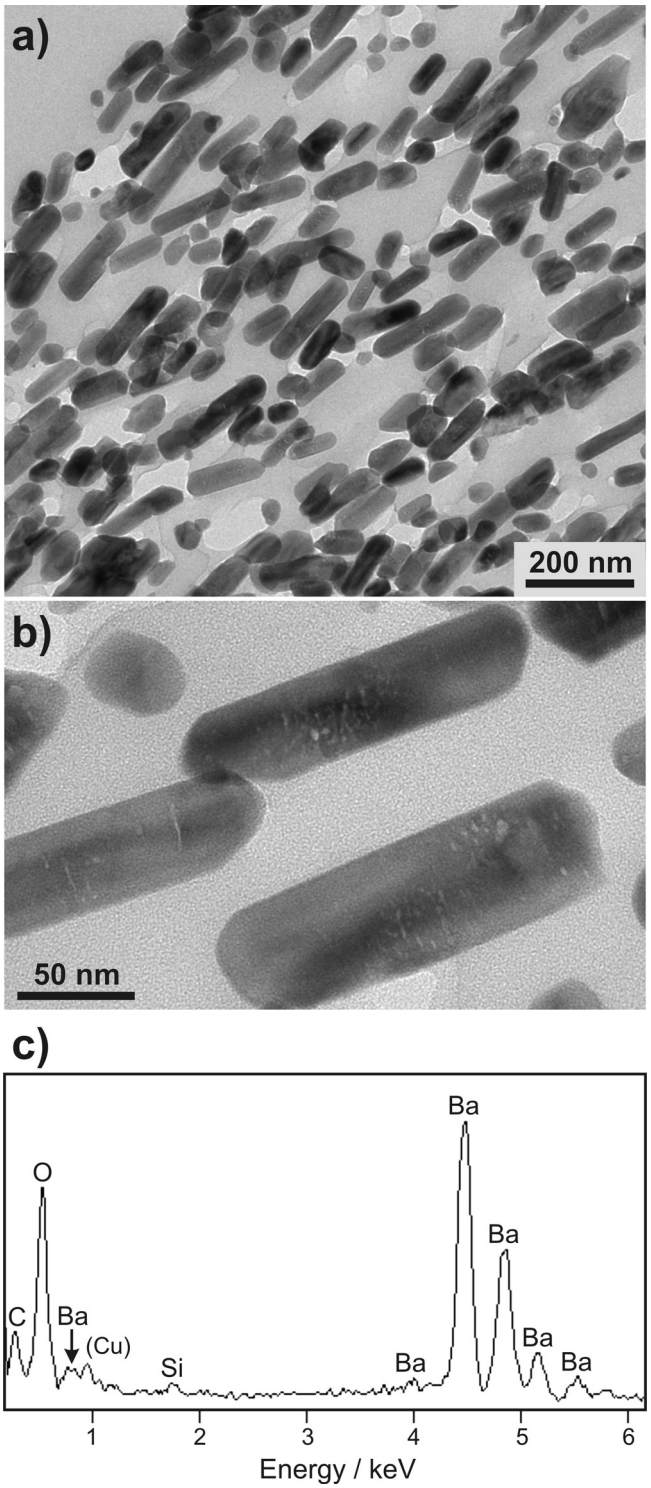

Fig. 6-13: (a-b) TEM images of the elongated nanocrystals making up the core of silica biomorphs, exposed by preceding thin-sectioning of as-grown aggregates. (c) EDX spectrum acquired from a single rod by point analysis, yielding a Si/Ba atomic ratio of 0.04 ± 0.01.

Alternatively, growth might become arrested by (specific) adsorption of more or less condensed silicate species on certain crystal faces, in analogy to the behavior of various organic polymers,[8,11] rather than a true coating of the particles. The latter scenario is tentatively supported by the present data.

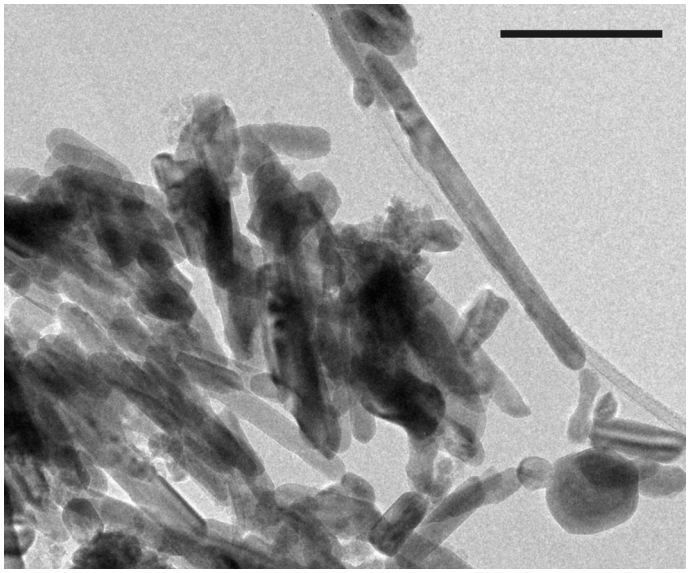

Fig. 6-14: TEM micrograph showing an accumulation of crystallites in a powder sample prepared by grinding biomorphs, which was used to acquire EDX spectra from individual crystallites. Scale bar: 200 nm.

Finally, it should be noted that the above findings partly contradict the results of previous work where, upon dissolution of the carbonate component in acid, a continuous silica phase still filling the entire volume of the former crystal aggregate remained.[21] Based thereon, the authors reasonably concluded that the nanocrystals were individually sheathed by a silica skin. Although these discrepancies cannot be explained certainly at the moment, it may be speculated that, since the mentioned experiments were performed exclusively in gels, there are yet some appreciable differences between the details of the growth process in the two media, in first instance apparently concerning the amount of silica incorporated to the forming aggregates.

6.5 Conclusion

In this chapter, temporal changes in the concentration of species relevant for growth during the formation of silica biomorphs from alkaline solutions were described and the obtained data were correlated with growth rates measured by video microscopy in gels as well as ex-situ analyses of samples at different stages of morphogenesis. In essence, results show that crystallization is in both media a reaction-controlled process which

occurs at a constant rate over the entire growth period and only at the surface of existing aggregates despite a homogeneously supersaturated bulk solution. This supports the proposed model of coupled precipitation at an active front that autocatalyzes the reaction by locally raising the supersaturation and thus renders the process independent from reagent diffusion and widely indifferent to the situation in the bulk, as long as certain prerequisites for the dynamic interplay are fulfilled. Mean growth rates measured in this work were found to vary in the range of few microns per minute, essentially being determined by the starting conditions and the particular experimental setup used. Further, the azimuthal propagation of curls on a given aggregate is commonly faster than its radial advancement, such that curved shapes emerge and twisted forms can be generated. Investigations of isolated aggregates evidence, in combination with measurements of the silica concentration in solution, that the presence of external silica skins on biomorphs can be reduced to secondary precipitation after completed growth due to the lowered pH, thereby excluding any morphogenetic role of a silica membrane as template. The amount of silica effectively integrated to the aggregates during growth from solution is in fact rather small, on the order of a few percents, and there is no distinct layer of silica around individual crystallites. This challenges existing ideas on the mode of particle stabilization by silica, and demonstrates that, although being synergistically co-mineralized with the carbonate phase, the silica yet retains the character of a true additive.

6.6 References

(1) (a) Addadi, L.; Weiner, S. *Angew. Chem. Int. Ed.* **1992**, *31*, 153. (b) Addadi, L.; Joester, D.; Nudelman, F.; Weiner, S. *Chem. Eur. J.* **2006**, *12*, 980.

(2) (a) Falini, G.; Albeck, S.; Weiner, S.; Addadi, L. *Science* **1996**, *271*, 67. (b) Belcher, A. M.; Wu, X. H.; Christensen R. J.; Hansma, P. K.; Stucky, G. D.; Morse, D. E. *Nature* **1996**, *381*, 56. (c) Checa, A. G.; Rodríguez-Navarro, A. B. *Biomaterials* **2005**, *26*, 1071. (d) Nudelman, F.; Gotliv, B. A.; Addadi, L.; Weiner, S. *J. Struct. Biol.* **2006**, *153*, 176.

(3) (a) Mayer, G. *Science* **2005**, *310*, 1144. (b) Bruet, B. J. F.; Qi, H. J.; Boyce, M. C.; Panas, R.; Tai, K.; Frick, L.; Ortiz, C. *J. Mater. Res.* **2005**, *20*, 2400.

(4) (a) Weiner, S.; Addadi, L. *J. Mater. Chem.* **1997**, *7*, 689. (b) Traub, W.; Arad, T.; Weiner, S. *Proc. Natl. Acad. Sci. U.S.A.* **1989**, *86*, 9822. (c) Beniash, E.; Metzler, R. A.; Lam, R. S. K.; Gilbert, P. U. P. A. *J. Struct. Biol.* **2009**, *166*, 133. (d) Jodaikin, A.; Weiner, S.; Traub, W. *J. Ultrastruct. Res.* **1984**, *89*, 324.

(5) (a) Mann, S. *Biomineralization: principles and concepts in bioinorganic materials chemistry*, Oxford University Press: New York, 2001. (b) Meldrum, F. C.; Cölfen H. *Chem. Rev.* **2008**, *108*, 4332.

(6) (a) Meldrum, F. C.; Hyde, S. T. *J. Cryst. Growth* **2001**, *231*, 544. (b) Mukkamala, S. B.; Powell, A. K. *Chem. Commun.* **2004**, 918.

(7) (a) Gower, L. B.; Tirrell, D. A. *J. Cryst. Growth* **1998**, *191*, 153. (b) Sugawara, A.; Ishii, T.; Kato, T. *Angew. Chem. Int. Ed.* **2003**, *42*, 5299.

(8) (a) Cölfen, H. *Top. Curr. Chem.* **2007**, *271*, 1. (b) Qi, L.; Cölfen, H.; Antionietti, M.; Li, M.; Hopwood, J. D.; Ashley, A. J.; Mann, S. *Chem. Eur. J.* **2001**, *7*, 3526. (c) Nassif, N.; Gehrke, N.; Pinna, N.; Shirshova, N.; Tauer, K.; Antonietti, M.; Cölfen, H. *Angew. Chem. Int. Ed.* **2005**, *44*, 6004.

(9) Hayashi, S.; Ohkawa, K.; Suwa, Y.; Sugawara, T.; Asami, T.; Yamamoto, H. *Macromol. Biosci.* **2008**, *8*, 46.

(10) Gower, L. B. *Chem. Rev.* **2008**, *108*, 4551.

(11) Yu, S.-H.; Cölfen, H.; Tauer, K.; Antonietti, M. *Nat. Mater.* **2005**, *4*, 51.

(12) (a) Kim, Y.-Y., Douglas, E. P.; Gower, L. B. *Langmuir* **2007**, *23*, 4862. (b) Cheng, Y.; Gower, L. B. *Biotechnol. Prog.* **2006**, *22*, 141.

(13) (a) Kim, Y. *Biomacromolecules* **2003**, *4*, 908. (b) Caruso, R. A. *Angew. Chem. Int. Ed.* **2004**, *43*, 2746.

(14) (a) Walsh, D.; Hopwood, J. D.; Mann, S. *Science* **1994**, *264*, 1576. (b) Walsh, D.; Mann, S. *Nature* **1995**, *377*, 320. (c) Thachepan, S.; Li, M.; Davis, S. A.; Mann, S. *Chem. Mater.* **2006**, *18*, 3557.

(15) Sheshadri, R; Meldrum, F. C. *Adv. Mater.* **2000**, *12*, 1149.

(16) Hall, S. R.; Bolger, H.; Mann, S. *Chem. Commun.* **2003**, 2784.

(17) Olszta, M. J.; Cheng, X.; Lee, S. S.; Kumar, R.; Kim, Y.-Y.; Kaufman, M. J.; Douglas, E. P.; Gower, L. B. *Mat. Sci. Eng. R* **2007**, *58*, 77.

(18) (a) Simon, P.; Rosseeva, E.; Buder, J.; Carrillo-Cabrera, W.; Kniep, R. *Adv. Funct. Mater.* **2009**, *19*, 3596. (b) Falini, G.; Fermani, S.; Gazzano, M.; Ripamonti, A. *Chem. Eur. J.* **1997**, *3*, 1807.

(19) García-Ruiz, J. M. *J. Cryst. Growth* **1985**, *73*, 251.

(20) García-Ruiz, J. M. *Geology* **1998**, *26*, 843.

(21) Imai, H.; Terada, T.; Miura, T.; Yamabi, S. *J. Cryst. Growth* **2002**, *244*, 200. (b) Terada, T.; Yamabi, S.; Imai, H. *J. Cryst. Growth* **2003**, *253*, 435.

(22) Hyde, S. T.; García-Ruiz, J. M. *Actual. Chim.* **2004**, *275*, 4.

(23) Hyde, S. T.; Carnerup, A. M.; Larsson, A. K.; Christy, A. G.; Garcia-Ruiz, J. M. *Physica A* **2004**, *339*, 24.

(24) Bittarello, E.; Aquilano, D.; *Eur. J. Mineral.* **2007**, *19*, 345.

(25) Voinescu, A. E.; Kellermeier, M.; Bartel, B.; Carnerup, A. M.; Larsson, A. K.; Touraud, D.; Kunz, W.; Kienle, L.; Pfitzner, A.; Hyde, S. T. *Cryst. Growth Des.* **2008**, *8*, 1515.

(26) Kellermeier, M.; Glaab, F.; Carnerup, A. M.; Drechsler, M.; Gossler, B.; Hyde, S. T.; Kunz, W. *J. Cryst. Growth* **2009**, *311*, 2530.

(27) García-Ruiz, J. M.; Hyde, S. T.; Carnerup, A. M.; Christy, A. G.; Van Kranendonk, M. J.; Welham, N. J. *Science* **2003**, *302*, 1194.

(28) García-Ruiz, J. M.; Carnerup, A. M.; Christy A. G.; Welham, N. J.; Hyde, S. T. *Astrobiology* **2002**, *2*, 353.

(29) Aizenberg, J.; Weaver, J. C.; Thanawala, M. S.; Sundar, V. C.; Morse, D. E.; Fratzl, P. *Science* **2005**, *309*, 275.

(30) (a) García-Ruiz, J. M.; Melero-García, E.; Hyde, S. T. *Science* **2009**, *323*, 362. (b) Kunz, W.; Kellermeier, M. *Science* **2009**, *323*, 344.

(31) Kellermeier, M.; Melero-García, E.; Kunz, W.; García-Ruiz, J. M. Local autocatalytic co-precipitation phenomena in self-assembled silica-carbonate materials. *J. Mater. Chem.* **2011**, submitted.

(32) Zaikin, A. N.; Zhabotinsky, A. M. *Nature* **1970**, *225*, 535.

(33) Melero-García, E.; Santisteban-Bailón, R.; García-Ruiz, J. M. *Cryst. Growth Des.* **2009**, *9*, 4730.

(34) Alexander, G. B. *J. Am. Chem. Soc.* **1953**, *75*, 2887.

(35) Clesceri, L. S.; Greenberg, A. E.; Eaton, A. D. *Standard methods for the examination of water and wastewater*, American Public Health Association: Washington, DC, 1982.

(36) Strickland, J. D. H. *J. Am. Chem. Soc.* **1952**, *74*, 868.

(37) García-Ruiz, J. M.; Moreno, A. *An. Quim. Int. Ed.* **1997**, *93*, 1.

(38) Nielsen, A. E.; Toft, J. M. *J. Cryst. Growth* **1984**, *67*, 278. (b) Söhnel, O.; Garside, J. *Precipitation*, Butterworth-Heinemann: Oxford, 1992. (c) Myerson, A. S. *Handbook of industrial crystallization*, Butterworth-Heinemann: Woburn, 2002.

(39) Kubota, N.; Sekimoto, T.; Shimizu, K. *J. Cryst. Growth* **1990**, *102*, 434. (b) Nore, P. H.; Mersmann, A. *Chem. Eng. Sci.* **1993**, *48*, 3083. (c) Chen, P.-C.; Cheng, G. Y.; Kou, M. H.; Shia, P. Y.; Chung, P. O. *J. Cryst. Growth* **2001**, *226*, 458. (d) Salvatori, F.; Muhr, H.; Plasari, E.; Bossoutrot, J.-M. *Powder Technol.* **2002**, *128*, 114.

(40) Voinescu, A. E.; Kellermeier, M.; Carnerup, A. M.; Larsson, A. K.; Touraud, D.; Hyde, S. T.; Kunz, W. *J. Cryst. Growth* **2007**, *306*, 152.

(41) Carnerup, A. M. *Biomorphs: morphology, chemistry and implications for the identification of early life*; PhD thesis, Australian National University, Canberra, Australia, 2007.

Chapter 7 The Possible Role of Surfaces During Morphogenesis of Silica Biomorphs

7.1 Abstract

Silica biomorphs are a unique example for higher-order self-organization in simple inorganic precipitation systems. Occurring when alkaline-earth carbonates are crystallized in moderately alkaline silica-containing media, their formation rests upon a spontaneously induced dynamic interplay between components which ensures continuous production of uniform silica-coated carbonate nanocrystals over extended frames of time. Crystallites assemble *in situ* following a specific long-range order and describing on global scales intricate shapes like flat sheets or periodically twisted filaments, the origin of which is still inadequately understood. This chapter reports on a series of experiments in which silica biomorphs were grown from solution under quiescent conditions as well as at different stirring speed using atmospheric CO_2 as carbonate source. Observed changes in the relative occurrence and size of distinct morphologies are correlated with the bulk pH and hence the supersaturation in the mixtures. Data evidence that although nucleation rates are strongly affected by agitation the fundamental growth behavior of the aggregates is widely indifferent to external convections, except for the fact that certain morphologies become favored over others. Based on these findings and further experiments with micropatterned substrates, it is proposed that morphogenesis takes crucial advantage of reduced nucleation barriers at both extrinsic and intrinsic surfaces, which may account for occasional quasi-2D growth and the striking expression of sinuous curvature in silica biomorphs. Eventually, results of studies on the effect of ultrasound and applied electric and magnetic fields are discussed.

7.2 Introduction

Although much has been learned in the past years about the mechanisms governing the morphogenesis of silica biomorphs (cf. Sections 1.4 and 6.2),[1-9] there are still fascinating questions left to answer.[10] For example, the reason why the polycrystalline assembly incipiently prefers to grow as flat sheets rather than any three-dimensional structure has so far not been sufficiently clarified. Beyond that, little is known about the

physical origin of smooth curvature in these plain inorganic systems, i.e. the actual circumstances which provoke curling of the sheets.

Interestingly, earlier studies have outlined that the formation of silica-witherite biomorphs is independent of the viscosity and diffusion properties of the surrounding medium.[11,12] Growth was found to proceed indistinctively in viscous silica gels and stagnant dilute solutions, with individual aggregates occasionally growing even through sol-gel interfaces. In turn, it was also noted that external convections imposed by stirring mother solutions and concurrent changes in mass transport noticeably perturb self-organization such that, if any, merely irregular sheets and pseudo-helicoids are obtained.[13]

In this part of the work, this latter observation by was critically revised investigating systematically the effect of stirring on the morphological behavior of silica biomorphs. To that end, barium carbonate was crystallized from silica-containing solutions under quiescent conditions and at varying stirring rates, respectively. The resulting precipitates were were analyzed quantitatively with respect to the occurrence of specific morphologies and their size. It is shown that agitation does not interfere with the very growth process itself, but rather affects the nucleation frequency and favors the formation of flat sheets over twisted structures. These findings are discussed in view of implications for possible mechanistic scenarios. Additionally, first results of experiments in which growth was carried out on micropatterned surfaces are presented. Based on the collected data, a scenario is proposed which might explain the evolution of the crystal aggregates towards complex curved shapes. In the second part of the chapter, results of experiments conducted under the influence of applied external electric and magnetic fields as well as ultrasound are reported.

7.3 Experimental Section

7.3.1 Crystallization Experiments

Syntheses of silica biomorphs from solution were carried out according to the protocol described in Section 6.3.1. In the reference experiment, the mother solution was left to evolve under stagnant conditions. Stirring was accomplished by adding a small Teflon-coated magnetic bar (15 mm long and 4.5 mm wide) to the well, placing the plate onto a magnetic stirrer (Heidolph MR 3001 K) and adjusting its speed to frequencies of 100, 300, 500 and 700 rpm, respectively. Care was taken to position the plate in a way that the stirrer bar rotated uniformly in the center of the well without noticeable nutation.

This was possible at all studied frequencies. The setup used for the stirring experiments is reproduced schematically in Fig. 7-1.

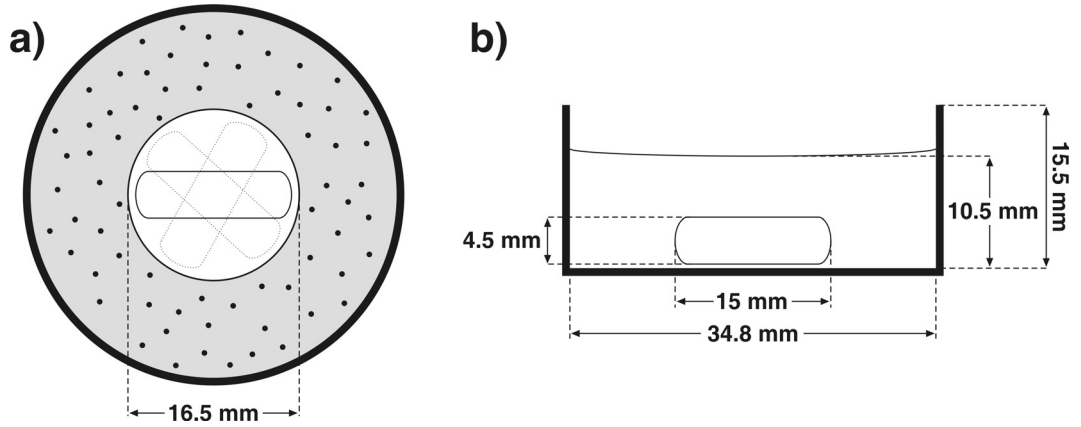

Fig. 7-1: Schematic representation of the experimental setup in (a) top and (b) side view. A stirrer bar (15 mm long and 4.5 mm wide) is added to the cylindrical crystallization well, which is then filled with reaction mixture to a height of 10.5 mm. Aggregates formed underneath the bar were all destroyed in the course of the experiment. Therefore, only the biomorphs located outside an inner circle of 16.5 mm in the gray-shaded area in (a), indicated as black dots, were investigated.

The wells were covered loosely with the lid of the plate to prevent contamination whilst still permitting contact to the atmosphere. Growth of mature biomorphs usually takes about 8-10 h at the chosen concentrations.[14] Aggregates are then seen to either float on the surface or adhere to the walls of the dishes. Here, all experiments were aborted after a reaction time of 8 hours by carefully removing the mother liquor and only the biomorphs formed on the bottom of the well were investigated. Due to the significant decrease of the bulk pH in the course of crystallization, amorphous silica also precipitated independently of the biomorphs and frequently buried the crystal aggregates. The amount of this fluffy material increases with the stirring rate, as the pH drops to lower values and nucleation of the amorphous phase is facilitated by the inhomogeneities and turbulence brought about by the stirring. However, biomorphic structures stuck on the well walls could easily be cleaned by repeatedly filling the wells with water, dispersing the silica floccules and withdrawing them with a pipette. Eventually, the aggregates were washed several times with ethanol (Baker, p.a.) and left to dry in air.

Growth in the presence of ultrasound was realized by mixing reagents in a well plate fixed in an ultrasonic bath from Branson Ultrasonics (model Bransonic 220) operating at 47 ± 3 kHz and 70 W, which was thermostatted at 20°C. Because solutions tend to

sprinkle out of the wells when ultrasound is applied, dishes were sealed with Parafilm through which a number of holes were punched with a needle. Ultrasonic waves were found to drastically accelerate the CO_2 flow into the mixtures, such that crystallization of carbonate sets in more or less instantaneously. Precipitation processes were visually completed already after roughly 2 h. Products were isolated by decanting the supernatant and washing with water and ethanol.

Experiments within an external electric field were performed by placing the wells between the horizontally arranged plates of a capacitor which was connected to a high voltage generator providing a variable output of 0-25 kV. At a plate distance of 2.2 cm, the accessible field strength was thus about 10^6 V/m. To investigate the effect of a magnetic field on the formation of silica biomorphs, wells were sandwiched between two permanent magnet plates having a flux density of roughly 0.1 Tesla. Alternatively, reaction mixture was filled in the cell of a custom-designed apparatus generating a helical field in the mT-range with adjustable handedness throughout the sample. In these and all of the above experiments, sufficient exchange with the atmosphere was ensured, such that any influence other than the applied fields can be ruled out.

7.3.2 Analytical Methods

In order to trace changes in the rate of CO_2 uptake induced by stirring and the presence of ultrasonic waves, the pH of the samples was monitored continuously during the first 6 hours of growth. For this purpose, a microelectrode (Mettler-Toledo InLab Micro) was immersed into the mixtures through a hole in the lid of the well plate or the Parafilm. Subsequently, the pH was read automatically every 5 seconds with the aid of a remote-controlled Schott laboratory pH-meter (model CG-843). Prior to measurement, the electrode was calibrated under the respective conditions using buffers of pH 7, 9 and 11 (Roth). Regeneration of the microprobe after each long-term run was achieved by successive treatment with 1 M solutions of NaOH and HCl, and eventual overnight equilibration in 3 M KCl.

The dried precipitates were studied first by means of polarized light microscopy directly in the wells. Images were taken with a Canon EOS 350D camera mounted on a Nikon Eclipse E400 transmission microscope. In a typical experiment, three principal morphologies can be discerned, namely flat sheets, helical filaments and thicker worm-like braids. All of these crystal aggregates are seen to emerge from globular objects or clusters thereof. Frequently, other such globules are observed from which none of the

mentioned characteristic structures has grown. To quantify the yield of the distinct morphologies, specific aggregates formed on the bottom of the wells were counted using a Wild macroscope (model M420) in a series of independent experiments. Overall, at least several hundreds of individuals were counted in the analyses, according to the relative occurrence of the respective type of morphology. The obtained values were averaged and normalized to the investigated area of the well. In parallel, the size of the aggregates was determined by measuring the length of helicoids and worms in optical images with the help of the Digital Micrograph 3.9 software package. Sheets were thereby approximated either by circles or ellipses; in the case of the latter, the apparent diameter was calculated as the arithmetic mean of the two radii. To gain good statistics, more than 200 specimens of each morphology were evaluated. Due to their high abundance, the amount of globular structures was estimated by counting particles in a set of micrographs and relating the average to the area of the image. Concurrently, the diameter of the globules was measured by fitting circles to their perimeter. As far as possible, individual spheroids were considered which, however, proved to be difficult in some cases owing to agglomeration or intergrowth. Analogous procedures were implemented also for the analysis of the stirred samples. However, due to the motion of the stirrer bar, the central area of the well became scrubbed in the course of the experiments and particles grown there were crushed. Therefore, this region was not investigated and only aggregates located in the surrounding unaffected part of the well bottom were considered for the analyses (see Fig. 7-1a). Reliable size distributions could not be established for spirals at stirring frequencies of 100 and 300 rpm because of their low number in the samples. At higher speed, no more helicoids and worms, and merely few minute sheets were observed. Therefore, only the globular objects were evaluated quantitatively concerning their occurrence and size at 500 and 700 rpm.

For scanning electron microscopy (SEM), samples of the unstirred reference were prepared readily by putting a small piece of conducting foil on the bottom of the well, rinsing the biomorphs grown on the substrate carefully and mounting the dried foil directly on a SEM stub. When solutions were stirred, the formed crystal aggregates were loosened from the walls gently with a brush and subsequently transferred to adhesive carbon tapes. Alternatively, to minimize damages to the crystal aggregates during manipulation and transfer, thin glass cover slips were fixed on the bottom close to the brink of the wells, on which the biomorphs grew indistinguishably. After gold- or

carbon-coating, specimens were inspected at 3 kV with a Jeol JSM 840 or a Zeiss LEO Gemini 1530 microscope.

7.3.3 Fabrication of Micropatterned Surfaces

Surfaces with defined periodic topology were obtained by manufacturing a polymeric replica of lithographically processed molds. For this purpose, silicon masters exhibiting different micron-scale structural motifs were purchased from GeSiM (Grosserkmannsdorf, Germany) and used to prepare stamps consisting of poly(dimethylsiloxane) (PDMS) following a procedure described in literature.[15] First, masters were hydrophobized by treatment with (heptadecafluoro-1,1,2,2-tetrahydrodecyl)-dimethylchlorosilane (ABCR Specialty Chemicals) to ensure removability of the PDMS stamp after completed preparation. Then, polymer precursor solution made by mixing Sylgard 184 (prepolymer received from Dow Corning) and a curing agent in a mass ratio of 10:1 was cast onto the masters and, after degassing in vacuum, samples were cured for 12 h at 60 °C. Eventually, the templated polymeric matrix was detached from the mold and hydrophilized in oxygen plasma for 45 sec at 0.2 mbar and an intensity of 80 W using a Flecto10 instrument from Plasma Technology.

Growth of silica biomorphs on as-prepared micropatterned surfaces was realized by placing the PDMS stamps into wells, filling with reaction mixture and withdrawing the substrate from the solution after the chosen growth period of 8 h with a pair of tweezers. Formed aggregates could readily be cleaned by careful rinsing with water and ethanol, and were studied by optical microscopy and SEM while still attached to the substrate.

7.4 Results and Discussion

7.4.1 pH Measurements

The pH-time profiles obtained for the stagnant mixture and those stirred at different speed are reproduced together with the corresponding curve from the ultrasound experiment in Fig. 7-2. Generally, the pH is found to decrease with time as atmospheric carbon dioxide diffuses into the solutions forming carbonic acid, which is subsequently deprotonated to give bicarbonate and carbonate ions in a certain ratio dictated by the current pH (see Section 6.4.2). Once the solubility product of barium carbonate is exceeded, precipitation removes carbonate ions from this equilibrium and thus further pushes absorption of CO_2. In the absence of external convections, a gradual lowering of

the pH can be noted which results in a final value of about 10.2 after the chosen growth period of 8 hours.

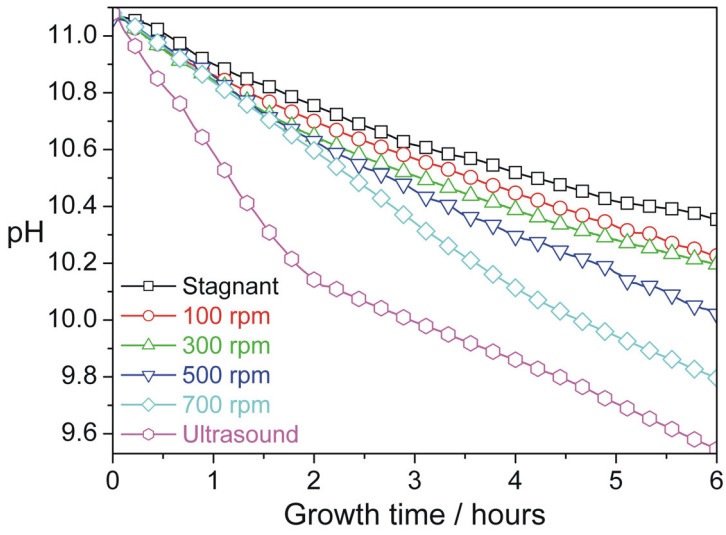

Fig. 7-2: Evolution of the bulk pH as a function of time in mother solutions of silica biomorphs under stagnant conditions, at different stirring rates (as indicated), and with applied ultrasound (50 Hz).

The findings of a recent study on the spatiotemporal development of the bulk pH during growth of silica-witherite biomorphs in gels have led to the conclusion that, in a common gel setup, the proposed coupled-precipitation mechanism and hence the construction of characteristic polycrystalline aggregates is only active at a pH of less than 9.8.[9] By contrast, the present data imply that, when conducted in dilute solutions, morphogenesis of typical biomorphic forms does also and preferentially occur at pH values well above 10 (see below). Indeed, experiments carried out at lower starting pH ($\leq$ 10.5) did not yield the desired crystal aggregates, but exclusively produced fractal dendrites as reported previously.[3] A possible reasoning for these apparent discrepancies is the following. In principle, the chemical feedback driving self-organization of nanoscale building units should be able to set in under all of the above conditions, provided that significant fractions of bicarbonate ions are present in equilibrium over the entire range of pH 9-11. However, it is not only the bulk pH and the feasibility of chemical coupling which determine whether biomorphs are formed or not, but in particular also the actual supersaturation of the system and its time-dependent changes. In gels, this latter parameter is largely governed by the diffusion of Ba^{2+} ions from a concentrated solution into the silica matrix already containing a given amount of pre-dissolved CO_2.[9] To trigger morphogenesis, enough Ba^{2+} must be transported to the growth site to establish proper conditions, which is inevitably accompanied by a

decrease in pH due to the acidity of the cations. Nevertheless, as long as the pH does thereby not fall below a certain threshold, fibrillation of fractal aggregates and the continuous production of silica-coated nanocrystals can still occur.[8] In solutions as those used in the present study, supersaturation is conversely regulated by diffusion of CO_2 into systems with evenly distributed Ba^{2+}. Unlike the situation encountered in gels, this process is not only driven by a concentration gradient, but does intimately depend also on the bulk pH. For the emergence of polycrystalline assemblies from the initial spherulites, the pH must in this case still be high to maintain sufficient CO_2 flow into the solution and hence adequate supersaturation. At lower starting pH values, this requirement is apparently no longer met and morphogenesis ceases at the end of the fractal route. In that sense, as already stated in earlier work,[9] there is no universal correlation between the bulk pH and the expected morphologies. Instead, within a distinct window allowing for coupled precipitation, the pH mainly reflects the conditions necessary to reach and sustain suitable supersaturation in a given setup producing regular silica biomorphs.

When comparing the progression of pH with time in samples at different stirring rates to the unstirred reference, it becomes obvious that increasing convection favors the uptake of CO_2 by the mixtures, resulting in a faster decrease of pH at higher speed. Correspondingly, fitting straight lines to the data of the first 2 hours yields slopes of -0.172, -0.188, -0.220, -0.232 and -0.245 h^{-1} for stirring rates of 0, 100, 300, 500 and 700 rpm, respectively. Likewise, the final pH measured after 8 hours of growth was found to be the lower the more intense samples were stirred (e.g. about 9.5 at 700 rpm). Taken together, it can thus be expected that the supersaturation prevailing throughout the experiments is consistently enhanced in stirred solutions.

An explicitly more pronounced effect on the evolution of pH in the system was detected when growth was performed in an ultrasonic bath. Here, an initially steep decline with a slope of -0.482 h^{-1} indicates extremely rapid ingestion of CO_2 and therefore a considerably high supersaturation from the very beginning on. A most striking feature of the curve is moreover the breakpoint observed at about 2 hours and pH 10.15, after which the decrease in pH is substantially slowed down (slope of -0.146 h^{-1}).

7.4.2 Growth in Stagnant Solutions

Crystal aggregates isolated from the unstirred experiment are widely identical in terms of morphology, size and structure to those described in previous studies dealing with

solutions at similar concentrations and pH.[3-5,8,11,16,17] A gallery of characteristic forms is shown in Fig. 7-3.

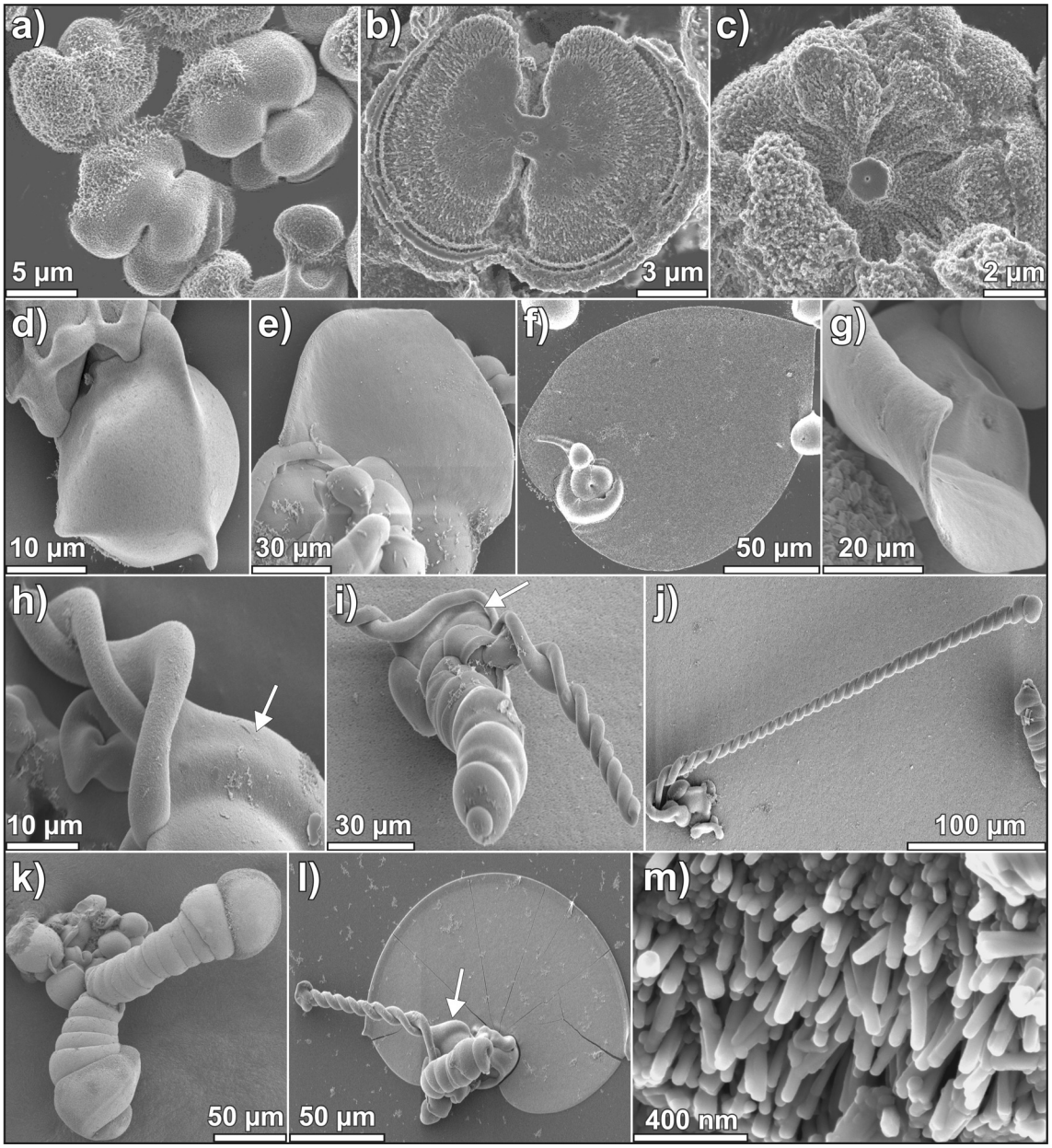

Fig. 7-3: SEM micrographs of silica-witherite biomorphs grown under quiescent conditions. (a-d): Early fractal architectures collected after 2 hours of growth. (e-l): Mature crystal aggregates exhibiting morphologies that fall into three major classes: extended flat sheets (f, g, l), helicoidal filaments (h-j, l), and worm-like braids (i, k, l), all of which emerge more or less directly from globular clusters. Larger sheets are always seen to adhere tightly to the substrate surface over their entire area. Arrows indicate small transitional laminar sections which sprouted freely into the solution without contact to a surface, thus curled and gave rise to a helicoid soon. (m) Zoom onto the edge of a sheet revealing uniform rod-like crystallites the aggregates are composed of.

Particles retrieved from their mother liquor already after a few hours of growth display primarily deformed globular or partially open spherulitic shapes (Fig. 7-3a), and frequently agglomerate to larger clusters. Dissecting the interior of the globules reveals that their core consists of an elongated pseudohexagonal single crystal, typically around 1-2 μm wide (Fig. 7-3b-c), which has suffered from non-crystallographic branching at both of its ends.[3,8] As a result, dumbbell-shaped structures are formed first, often with cauliflower-like appearance, which then become closed to more or less spherical architectures by continued splitting. With time, as the system passes into the stage where growth is based on the assembly of nanoscale units, crystallites happen to be attached preferably only along a quite thin path over the surface of the fractal clusters (Fig. 7-3d). In the following, flat sheets with thicknesses in the range of 1-3 μm are extracted from the initial globules, which grow radially in a quasi-two-dimensional fashion to adopt various rounded shapes (Fig. 7-3e-f). In line with the proposed phenomenological model, these sheets develop scrolled margins after some time and exhibit one or more cusps around their rim (Fig. 7-3f), owing to curling and the consequential competition between radial and tangential growth.[4,8] Helicoidal structures emerge when two such curls of equal handedness collide and intertwine, inducing a twist which is subsequently perpetuated by continued mutual winding (Fig. 7-3h). Along with these dainty filaments, a large number of tightly wound worm-like precipitates were obtained (Fig. 7-3k), which arise when a sheet curls and keeps on coiling on itself.[8] High-magnification SEM images (Fig. 7-3m) disclose that all sheets, spirals and worms are crystal aggregates consisting of oriented rod-like individuals about 200-300 nm long and 40-60 nm across, which is in fair agreement with values reported in literature.[5,11,16]

Indeed, a morphogenetic scenario comprising the formation of extended sheets from which helical strands emanate at later stages depicts well the growth behavior of silica biomorphs observed in gels.[6,9] However, there is some important deviance realized in the solution experiments of the present work which has not been mentioned to date and thus deserves attention.

First, it must be emphasized that virtually all flat sheets grew over their entire area in direct contact with either the surface of the wells or the solution-air interface (cf. Fig. 7-3f and l). In fact, leaves formed on the walls adhered so firmly that they could hardly be loosened without breaking them. When growing free in the solution without contact to an extrinsic surface, the sheets were in turn found to describe curved shapes

apparently trying to roll up on themselves (Fig. 7-3g). By contrast, most of the spirals and worms did not stick to surfaces but protruded at arbitrary angles into the solution (Fig. 7-3i-l).

Second, throughout the innumerous experiments performed, there was not a single case in which a twisted filament sprouted from a sheet larger than a few microns. Rather, the sheets that give rise to helical forms are those which grew independently of a surface and hence curled soon after emerging from the globular clusters (Fig. 7-3h-i). Very often, the transformation of the initial leaf to a twisted ribbon occurs almost instantaneously after polycrystalline growth has commenced such that a distinct sheet-like domain cannot be distinguished, thus arousing the impression that the spiral evolved straight from its parent fractal aggregate (Fig. 7-3i-j and l). This holds true also for any worm-like morphology sighted in the studies (Fig. 7-3i and k). Here, winding always proceeded right from the start leaving no space for an even section in-between.

Third, it is worth noting that by far not all fractal crystals develop a sheet, a worm or a helicoid. Instead, growth ends in many cases once non-crystallographic branching is terminated. Fig. 7-4 illustrates the relative occurrence of the different morphologies found in a typical experiment.

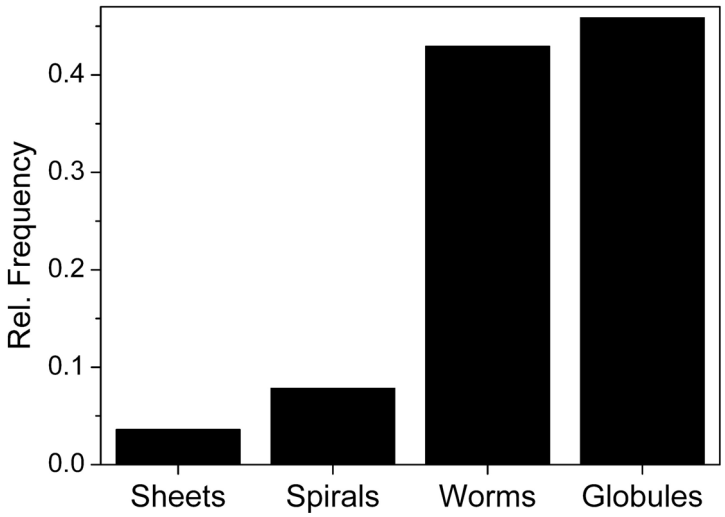

Fig. 7-4: Statistical distribution of morphologies displayed by silica biomorphs grown from stagnant solutions. Values were obtained by counting particles on a default area of the crystallization wells in a considerable number of independent experiments. “Spirals” signify all twisted morphologies (helical filaments, twisted ribbons, etc.). Note that only those sheets were counted which did not give rise to a helical filament.

The term “globules” thereby refers to any fractal aggregate which has not produced characteristic forms. Evidently, this applies to almost 50% of the counted precipitates.

Among the polycrystalline architectures, worms clearly make up the major fraction while the frequencies of sheets and spirals amount to less than 10%.

The observed morphological distribution can be rationalized when assuming that any laminar aggregate about to emerge from a fractal spherulite is prone to instant curling if it grows at noticeable distance from a surface. Reasonably, the probability for the initial outgrowth of a nanocrystal assembly should be equal all over the surface of a given globule. If this transition can yet only yield in extended flat sheets when taking place at the bottom of the globule and hence nearby the wall of the vessel, the relatively rare occurrence of that kind of morphology can readily be understood. By nature, this is different in gels since the silica matrix universally provides a surface to grow on throughout the sample. On the basis of the above hypothesis, it could be supposed that these circumstances are responsible for the consistent formation of large and often slightly sinuous sheets in gels, whereas their solution counterparts are generally flat and significantly less abundant and adhere to interfaces. Similar arguments can be put forward to explain the small number of spirals discerned in the present experiments as compared to worm-like structures. Worms are sheets which bend immediately after their initiation and wind around themselves constantly in the following. The formation of spirals, in turn, necessitates at least a short laminar domain which can curl and twist. However, since growth of even sheets seems to be generally unfavorable far off a surface and a leaf cannot curl downwards when growing flat in contact with an interface, the preconditions required for the generation of a helical filament are rather seldom fulfilled rendering worms the most frequent morphology. As opposed to that, practically all gel-grown aggregates have developed extended sheets before curling, such that the formation of helicoids becomes strongly favored and worms are hardly ever observed.

In light of these findings, one may speculate that the morphogenesis of silica biomorphs is intimately related to the presence of both extrinsic and intrinsic surfaces. As long as growth of the polycrystalline aggregate proceeds close to a foreign surface, like well walls in a solution experiment or the silica matrix in a gel setup, it will adopt the topology of the substrate by covering its surface with a thin layer of crystallites. The reason for this surface affinity and the concurrent quasi-2D growth behavior most likely relies on reduced nucleation barriers prevailing at interfaces (heterogeneous nucleation). In the absence of such a substrate, the only surface available for the aggregates to grow on is their own. This situation arises when a sheet is about to evolve freely in a solution

or once it encounters any discontinuity in the silica matrix during formation in gels. In this case, the crystal assembly prefers curved growth in order to fold back on itself and facilitate further nucleation. Depending on the actual conditions, the induced curling can affect either an emerging leaf as a whole, thus resulting in worm-like braids, or trigger ongrowth of a wave-like lip along the perimeter of the leaf potentially producing helicoidal filaments. In this sense, the incipient two-dimensionality as well as the origin of curvature and twisted structures characterizing silica biomorphs could derive to a greater or lesser extent from the beneficial impact of surfaces on nucleation scenarios.

7.4.3 The Effect of Stirring

When growth is carried out under stirring at moderate frequencies of 100 or 300 rpm, the observed morphologies are generally the same as those obtained from stagnant solutions (cf. Fig. 7-5). Still, almost perfectly flat sheets (Fig. 7-5a and d) as well as helicoids (Fig. 7-5a-b and e) and worms (Fig. 7-5d and f) can be discerned, yet next to a tremendously increased fraction of globular clusters not showing outgrowth of polycrystalline forms (see Fig. 7-6).

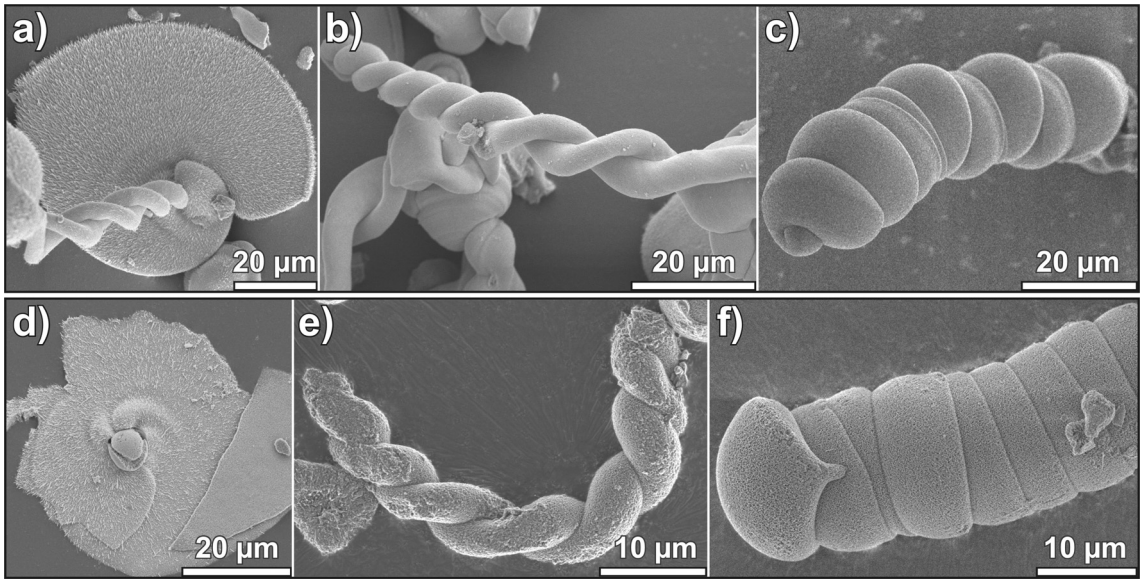

Fig. 7-5: SEM micrographs of precipitates isolated from experiments conducted at a stirring rate of (a-c) 100 rpm and (d-f) 300 rpm.

The regularity of twisted filaments did apparently not suffer from the applied external convections, in contrast to what was reported in earlier work.[13] Instead, it was found that many of the aggregates were overgrown heavily either with a thin layer of hairy crystallites or numerous larger, spiky rods up to several tens of microns in length (see Fig. 7-7). This results most probably as a consequence of secondary crystallization of

regular barium carbonate on top of preformed biomorphic architectures, owing to the higher supersaturation caused by the stirring. Interestingly, the secondary crystallites covering sheets happen to be aligned radially outwards from the center along the former growth direction (Fig. 7-5a and d), and thus maintain a certain co-orientation to the nanorods within the crystal aggregate. This suggests an epitaxial relation between already existing crystallites and those nucleated thereupon after the very growth process has been terminated.

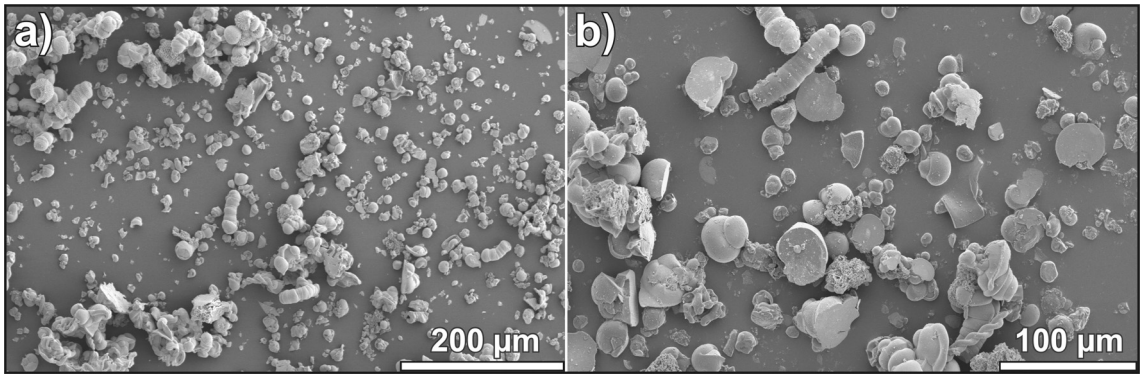

Fig. 7-6: SEM images granting an overview of particles formed in experiments at a stirring rate of (a) 100 and (b) 300 rpm. Note that the lack of a higher number of sheets is due to the fact that they were stuck firmly on the walls of the wells and could thus hardly be transferred onto the SEM stub. Apart from that, some of the aggregates seem to be broken, likely because of the mechanical stress imposed by either the stirring or manipulation during sample preparation.

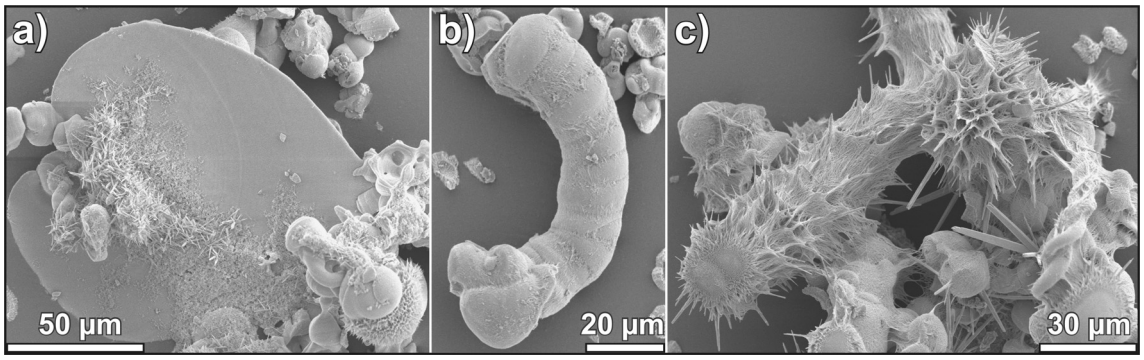

Fig. 7-7: Secondary crystallization in samples at stirring frequencies of (a-b) 100 and (c) 300 rpm. Due to the enhanced rate of CO_2 uptake by stirred solutions and the consequently increased degree of supersaturation, as-formed biomorphs frequently become overgrown by regular barium carbonate towards the end of the experiments. Secondary crystals may occur as conglomerates of small needles on the surface of the biomorphs (a), as spiky rods sticking out of them (b), or in the form of a fine, hairy film coating the aggregates (b).

The most important changes provoked by stirring become manifest in optical micrographs of the as-grown precipitates (Fig. 7-8). While under quiescent conditions

sheets occur sporadically over the surface of the wells along with a great deal of worms and some spirals (Fig. 7-8a), they populate in abundance large areas in experiments conducted at 100 and 300 rpm (Fig. 7-8b-c).

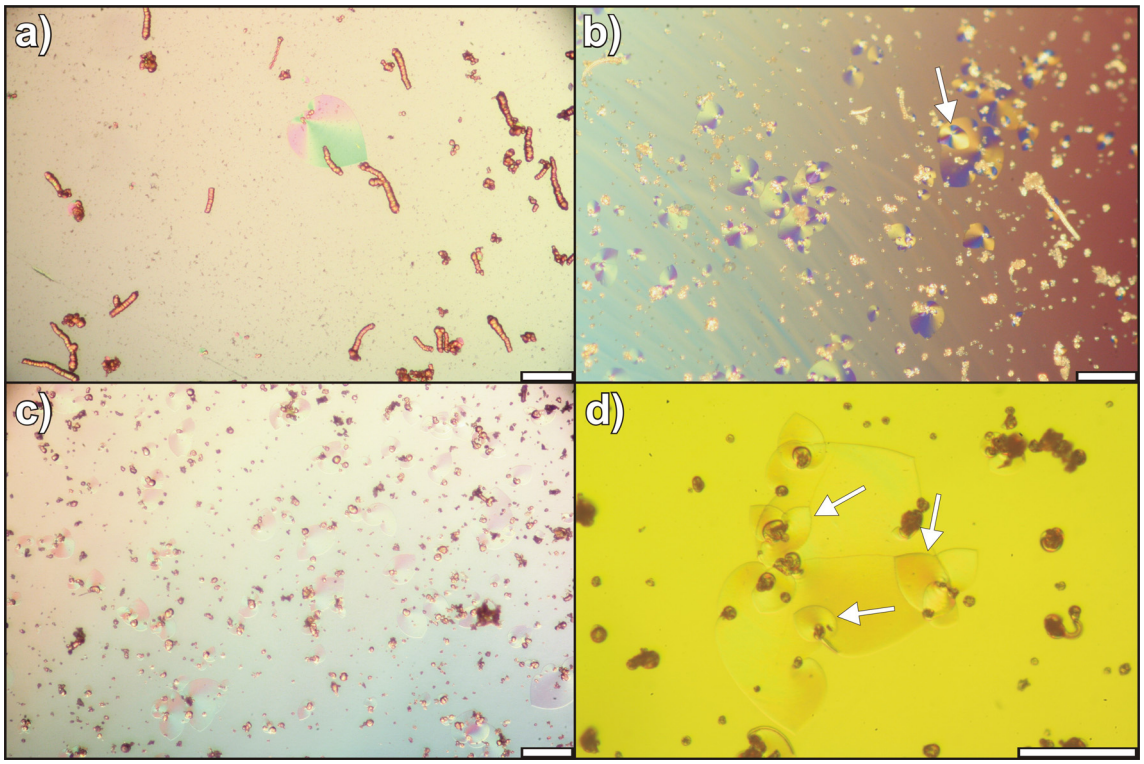

Fig. 7-8: Polarized optical micrographs representing the occurrence of distinct morphologies at stirring frequencies of (a) 0, (b) 100, and (c) 300 rpm. In (d), a conglomerate of sheets found at 300 rpm is shown, with several small second-generation leaves (indicated by the arrows) growing on top of a larger "mother" sheet. Scale bars are 200 µm in (a-c) and 100 µm in (d).

In turn, there are consistently less helicoids and worms when raising the stirring rate, whereas simultaneously the amount of undefined globular aggregates increases considerably. All observed sheets display characteristic Maltese cross-like extinction patterns when viewed between crossed polarizers, indicating radial orientation of the nanorods with respect to their long axis.[11] This means that stirring does not affect the growth behavior of the biomorphs in terms of their microstructure and orientational ordering, in agreement with SEM analyses performed in our previous study.[27] Further, the overall optical anisotropy of the sheets, as deduced from the degree of coloration, was explicitly diminished when solutions were stirred, signifying that the thickness of the sheets decreases with increasing speed. Another essential finding is that in many cases novel fractal crystals were generated upon already formed sheets and subsequently developed leaves growing flat in close contact with the aggregate underneath (Fig. 7-8d). This proves on the one hand that morphogenesis is active in a

fairly wide window of both time and pH. On the other, since the orientation of crystallites in the second-generation leaves often differs clearly from that in the subjacent sheet, it can be concluded that the ongrowth of crystal aggregates onto others does not necessarily require epitaxial matching. Nevertheless, it is evident that silica biomorphs favor their own surface as a growth substrate.

At stirring rates of 500 and 700 rpm, the formation of specific polycrystalline aggregates is markedly repressed. Rather, a multitude of fractal globules hallmark the appearance of the samples (Fig. 7-9a-b). In some instances but quite rarely, small sheets are seen to protrude from the particles which, within 8 hours, have grown to dimensions usually not exceeding 20 μm (Fig. 7-9c). Both worms and helicoids were never observed in experiments at a speed equal to or higher than 500 rpm.

The above observations can be verified quantitatively by counting individuals of a given morphology on a predefined area of the crystallization wells at the various studied stirring frequencies. The resulting statistical distributions are illustrated in Fig. 7-10. Within the range of speed where growth of typical biomorphic aggregates still occurs (i.e. up to 300 rpm), the stirring evidently leads to a shift in the morphological distribution in favor of sheets and at the expense of worms and spirals. In parallel, the amount of globular structures first escalates when switching from 0 to 100 rpm, and subsequently further increases exponentially with the stirring rate. The latter finding most likely derives from the enhanced supersaturation induced by the stirring. As a consequence, nucleation of witherite is propelled and a growing quantity of crystal seeds are generated which become subject to fractal branching. It is interesting to note that despite the intense convections prevailing at 700 rpm, nucleation does still take place exclusively in a heterogeneous way on walls or surfaces. This seems to be a principal property innate to growth of biomorphs in solutions. Generally, it could be thought that higher supersaturation and nucleation frequency should result in the formation of a larger number of smaller crystals. In fact, this holds true for globular particles, the size of which scales inversely with their relative occurrence (see Fig. 7-11, and Fig. D-1 in Appendix D for size distributions). Further, one may assume that when morphogenesis is initiated at an increasing number of sites, growth will proceed in average to a minor extent leading to less developed crystal aggregates. This applies for samples at stirring rates of 500 and 700 rpm, where so many fractal architectures are produced that the overall supply with reagents only suffices to form few and rather small leaves.

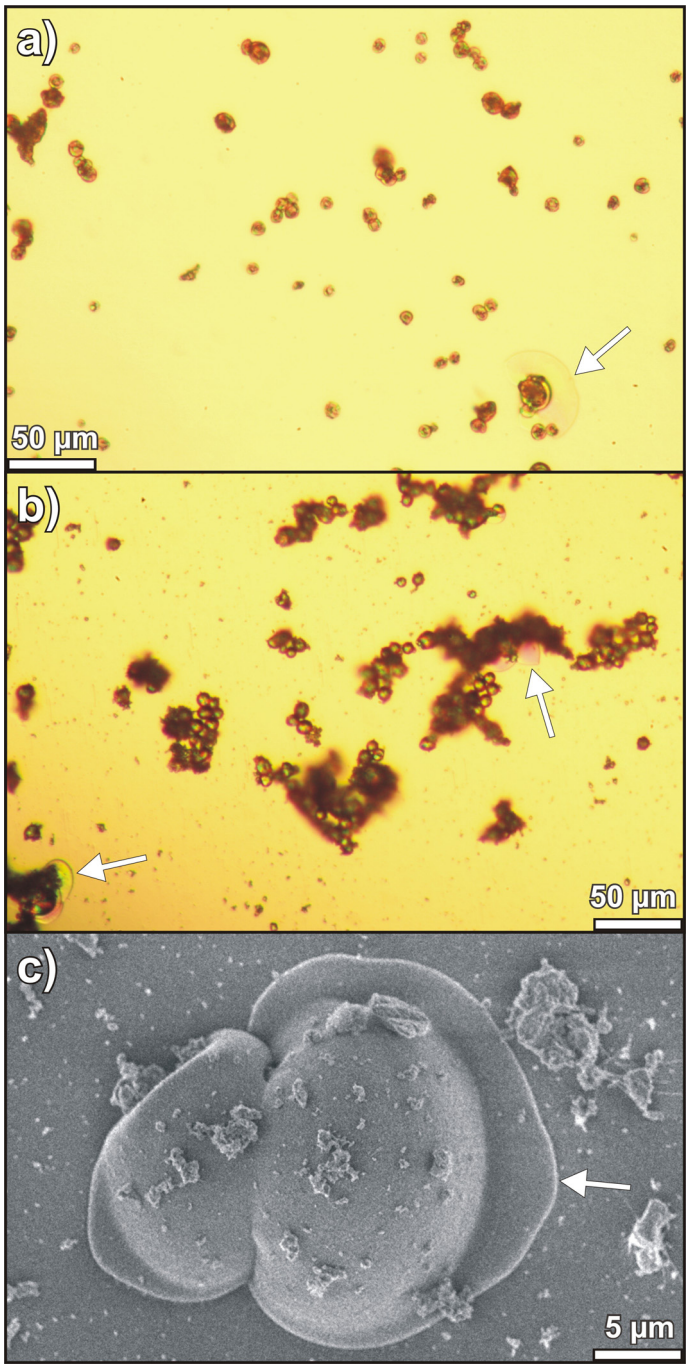

Fig. 7-9: (a-b) Light microscopy images of precipitates grown from solutions stirred at (a) 500 and (b) 700 rpm. The overall picture is in both cases dominated by more or less agglomerated globular objects, from which tiny sheets emerge occasionally (highlighted by the arrows). The dark shades concealing some of the particles in (b) originate from tenacious silica floccules. (c) SEM micrograph showing a closed fractal architecture from which laminar segments measuring less than 5 µm have sprouted after 8 hours of growth at 500 rpm.

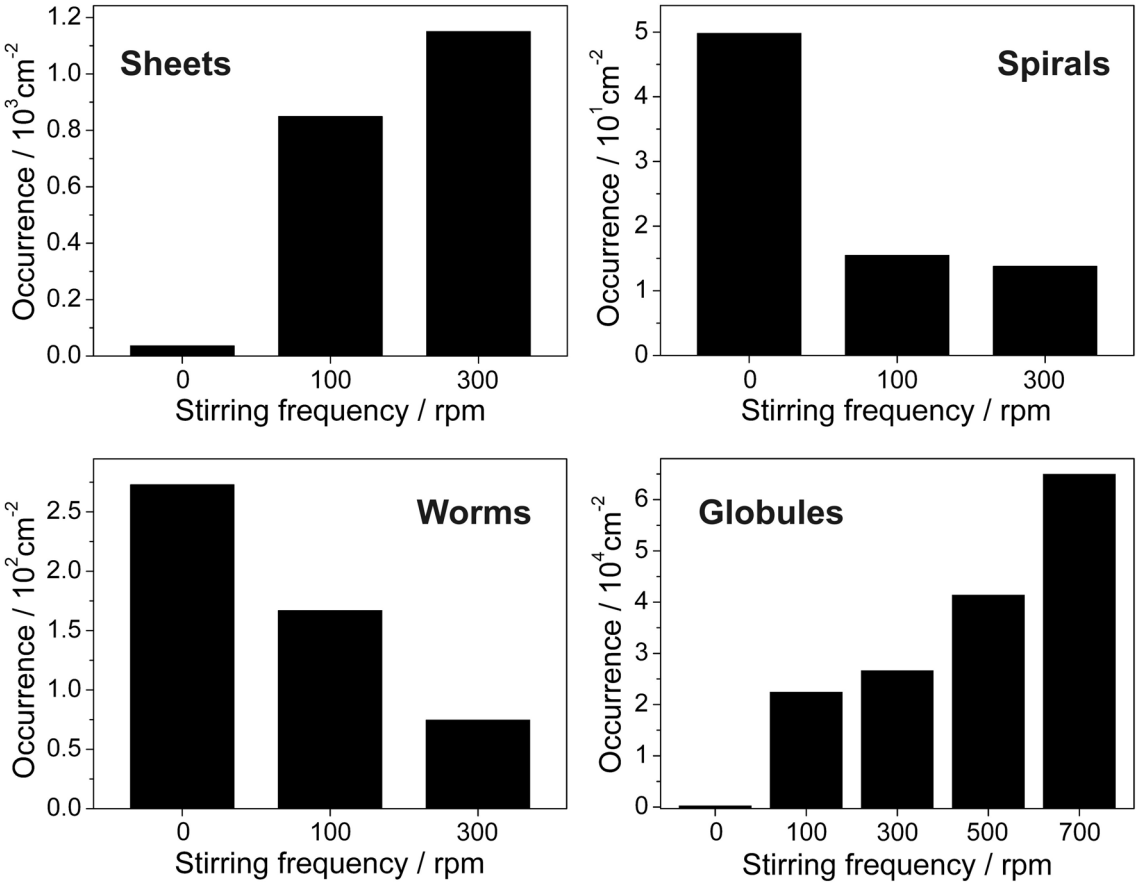

Fig. 7-10: Bar plots of the normalized occurrence of the different morphologies as depending on the applied stirring rate. Worms and spirals could no longer be distinguished at 500 and 700 rpm. Moreover, the number of minute sheets traced at these frequencies was negligibly small as compared to the values at lower speed.

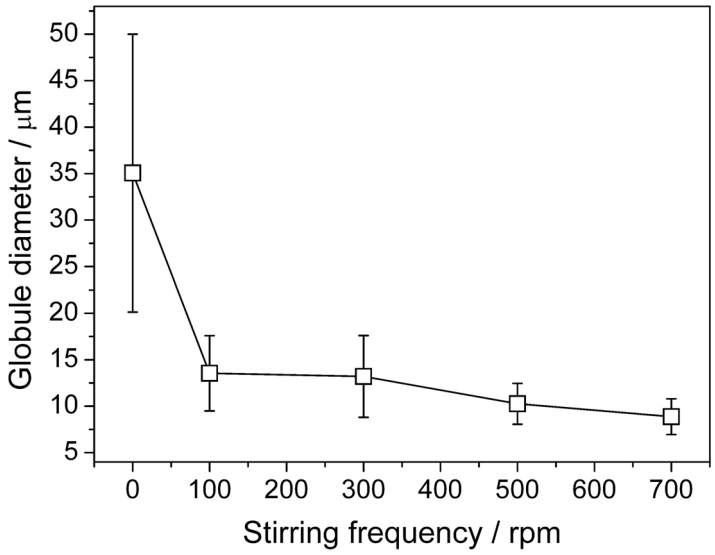

Fig. 7-11: Derived mean diameters of the globules with corresponding standard deviations outlined as a function of the applied stirring frequency.

At 100 and 300 rpm, a similar tendency is observed concerning sheets whose diameters are clearly reduced relative to the unstirred reference (see Fig. 7-12 and Fig. D-2 in Appendix D).

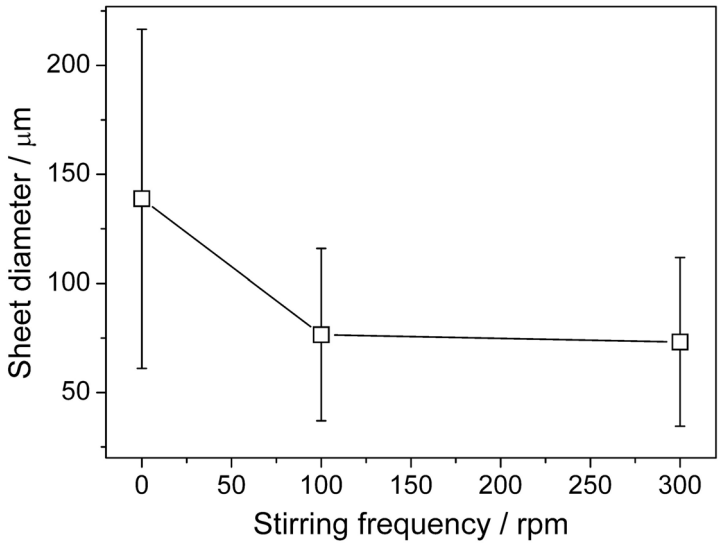

Fig. 7-12: Average diameters of sheets isolated from experiments conducted at different stirring frequencies.

Size distributions and mean lengths determined for worms at 0, 100 and 300 rpm (Fig. 7-13 and Fig. D-2 in Appendix D) as well as corresponding values measured for spirals (Fig. D-3 in Appendix D) confirm that these morphologies grow in average also to smaller dimensions in stirred solutions as compared to stagnant conditions, although differences do not exceed the estimated limits of error.

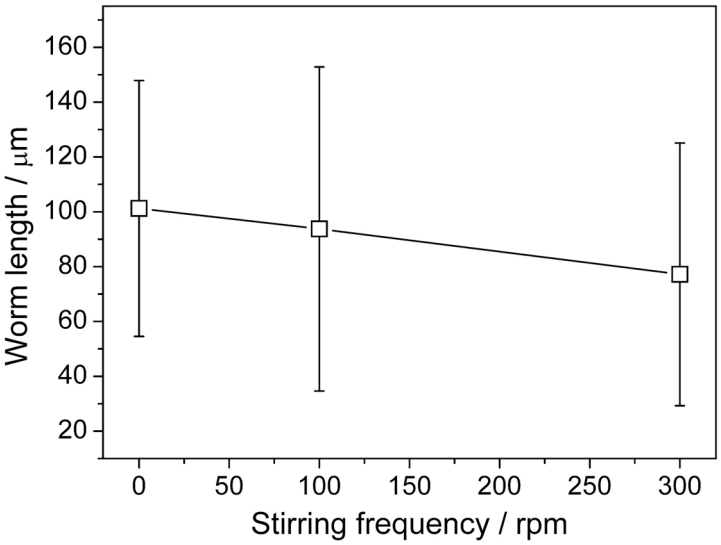

Fig. 7-13: Mean lengths of worms formed during growth under stagnant conditions and from solutions stirred at 100 and 300 rpm.

A possible explanation for the missing essential changes in the size of the aggregates at moderate stirring speed relies on the effective yield of the experiments. Precise weighing of a well before and after growth, including meanwhile alkaline leaching of the aggregates to remove incorporated silica, revealed that at most about 20-25% of the total molar amount of Ba present crystallized over a period of 8 hours from stagnant solutions (see also Section 6.4.1). Since the uptake of CO_2 is amplified in agitated systems, the overall quantity of material precipitated during the experiments should increase with the stirring rate, which is in fact observed. Up to 300 rpm, the resulting higher concentration of carbonate species multiplies the nucleation frequency while still leaving enough reagents for the formation of well-developed biomorphs. Therefore, the total number of polycrystalline aggregates found at 100 and 300 rpm is higher than in stagnant solutions (Fig. 7-14).

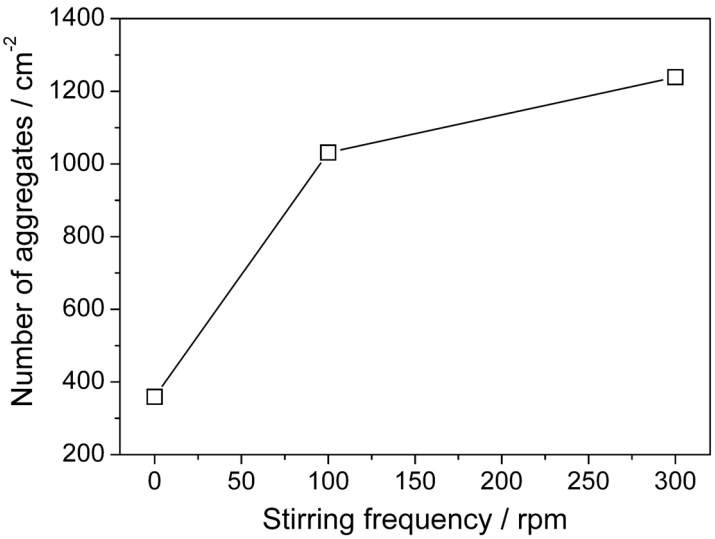

Fig. 7-14: Plot of the total number of polycrystalline aggregates (i.e. the sum of observed sheets, helicoids and worms) as a function of the stirring frequency.

On the other hand, under reinforced stirring at 500 and 700 rpm adequate supersaturation is no longer provided at the end of the fractal route due to precedent exhaustive consumption of reagents, and coupled co-precipitation cannot be excited or succumbs soon after being initiated. This shows that silica biomorphs can in principle be grown under conditions of forced convection. However, alterations of the CO_2 flow into the solutions and related variations in the time-dependent supersaturation profiles of the system provoke distinct nucleation frequencies and growth rates, such that morphogenesis becomes arrested at earlier stages when stirring is intensified.

Finally, the shift in the distribution of morphologies traced from 0 to 300 rpm remains to be discussed. As already put forward above, the outgrowth of nanocrystalline aggregates from a fractal architecture nucleated at an interface should be equally likely to occur in any available direction. However, this assumption might only be valid for stagnant solutions. Readily, one may envisage that a mineralization process which relies on its own dynamics and locally changing conditions will disfavor turbulence at its growth site (see Chapter 8 for more details).[18] In this respect, it is of particular interest to note that in a stirred vessel there always exists a boundary layer at the liquid-wall interface within which the solvent remains more or less stagnant.[19] This layer of "unstirred" water usually extends to dimensions in the μm-range. Sheets with their typical thicknesses of some microns could thus form free of any convectional perturbation in this zone – provided that they grow flat and very close to the surface. Hypothesizing further that worms and helicoids are only generated when the crystal assembly curls onto itself owing to the absence of a reachable foreign surface, the detected decrease in their relative abundance appears reasonable. For the formation of these morphologies, growth has to proceed freely in the solution far off the wall and hence in regions where detrimental turbulent flow is expected. As a consequence, the material precipitated during the polycrystalline stage is preferentially used for the production of sheets, such that their relative frequency increases with the applied stirring rate on the account of worms and spirals. The fact that the latter are still sighted and do not vanish completely in stirred experiments might moreover be related to the observation that both morphologies form predominantly nearby the corners of the wells. There, convection should basically be to some degree lowered as compared to the residual area of the well, leading to a higher probability for outgrowth distant from the wall surface. Furthermore, it is well-known that the quasi-quiescent zone at interfaces becomes thinner upon increasing the stirring rate.[19] This explains the observed decrease in the thickness of sheets with growing speed, and therefore strongly supports the notion that stagnant boundary layers play a decisive role for the morphological selection in stirred mixtures (see Chapter 8). Taken together, these experiments corroborate that sheets form in direct contact with the well walls whereas helicoids and worms grow at certain angles into the solution. Results thus confirm the purported idea that the formation of sheets and the associated two-dimensional growth behavior may derive from a crucial involvement of extrinsic surfaces during morphogenesis, while curling and twisting originate when growth occurs at sites without contact to a foreign surface.

7.4.4 Growth on Micropatterned Surfaces

Such a morphogenetic scenario inevitably implies that biomorphs should be sensitive to the properties and condition of the surface they grow on. To verify this hypothesis, experiments were performed with substrates having a defined and non-even topology. Fig. 7-15 shows aggregates which formed on a surface characterized by a line-pattern microstructure comprising periodically arranged, rectangular division bars, each 5 µm in both height and width.

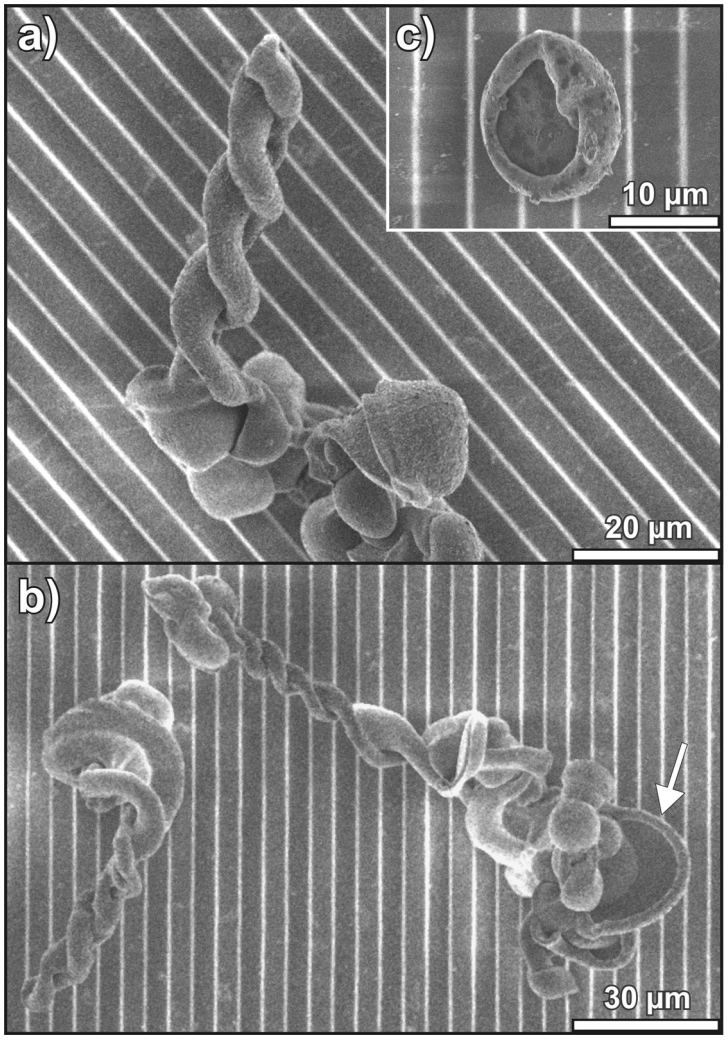

Fig. 7-15: SEM images of biomorphs grown on a polymeric substrate exhibiting regular line-pattern topology. The uneven relief of the surface on the micron-scale impedes the formation of extended flat sheets and causes emerging leaves to curl soon. Consequently, helicoids and worms emanating from the surface represent the major fraction of aggregates observed in the experiments.

Detailed studies of the samples prove that growth starts by nucleation of a crystal seed on top of the bars, presumably due to the limited space in the gaps in-between and the poor accessibility of the enclosed volume. Subsequent fractal branching produces

variously shaped and intergrown globular clusters, which often extend over several bars bridging the indents (cf. Fig. 7-15a-b). The distribution of polycrystalline morphologies occurring on the patterned substrate drastically differs from what is usually found on even surfaces. In fact, we could not discern a single sheet which grew flat over distances larger than 10 μm, but almost exclusively observed worms and helicoids protruding steeply from the surface (Fig. 7-15a-b). The few laminar segments sighted were in turn all heavily scrolled around their rim (see arrow in Fig. 7-15b). Comparable results were obtained when a pattern with distinct geometry, but similar structural dimensions was used (see Fig. 7-16).

These findings are perfectly in line with the proposed model of surface-assisted mineralization. A sheet which emerges from its fractal precursor may spread over the top face of the bar but, when arriving at the gap, starts to curl (Fig. 7-15c). The abrupt vertical change of the topology can at this point obviously not be followed by crystal assembly, such that curved growth back towards the own surface is preferred. Likewise, the distance between the bars is apparently too large to be covered by the sheet without an underlying substrate, although this seems to be sporadically possible in some cases (Fig. 7-15b). As a consequence, twisted morphologies and worm-like braids become strongly favored over extended flat sheets on the micropatterned surface. Thus, by modifying the structural constitution of the growth substrate, the formation of silica biomorphs and in particular the yield of specific morphologies can be deliberately influenced.

It should be emphasized that the described differences in the growth behavior are not related to the chemical nature of the surface. Indeed, spacious sheets were found in unstructured parts of the polymeric base, occasionally right next to patterned regions (see Fig. 7-16a-b and d). Additional experiments with other materials as substrates (distinct polymers, glasses and metals) proved that the surface composition has no noticeable effect on the morphogenesis of the crystal aggregates. This confirms that the given topologies alone provoked the observed changes.

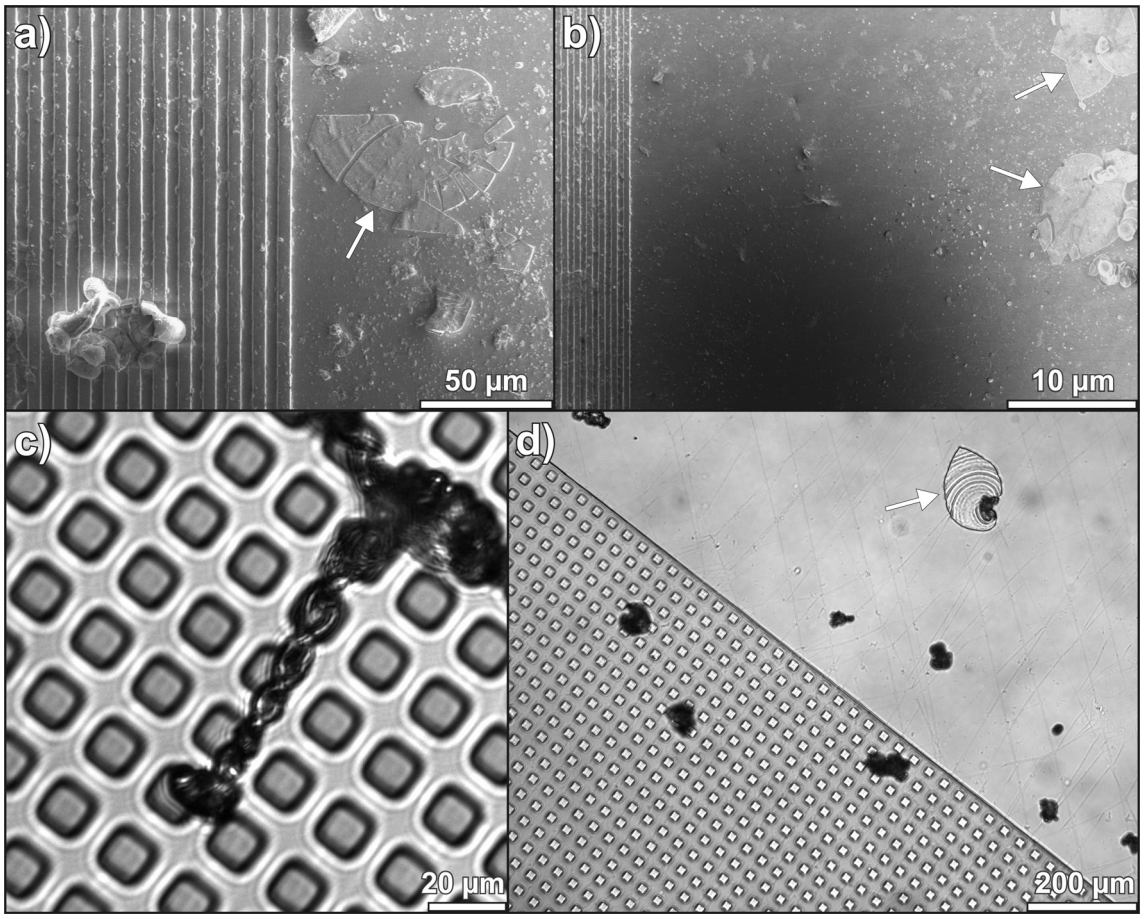

Fig. 7-16: (a-b) SEM images showing the borderline between the patterned (left) and unpatterned (right) areas of the PDMS substrate. It is evident that expanded sheets can develop in even regions of the substrate (arrows), while flat morphologies exceeding sizes of few microns were never observed on the stepped surface. (c-d) Optical micrographs of biomorphs grown on a different microstructured surface (a regular square mesh of islands with an area of 10x10 µm^2 and a height of ~5 µm, arrayed at a mutual distance of 10 µm). Again, only globular particles, worms and twisted morphologies protruding from the substrate into the solution were found on the pattern, whereas sheets could very well form on the same surface in the absence of a bumpy topology (arrow in (d)).

7.4.5 Growth in the Presence of External Electric and Magnetic Fields

In a further set of experiments, possible effects of externally applied electric and magnetic fields were investigated. These studies were intended to test whether the assembly of silica-coated witherite nanorods and especially their mutual co-orientation can be influenced and modified by that means. For this purpose, silica biomorphs were grown between the plates of a conventional capacitor at various electric field strengths as well as within the simple field of two permanent magnets. Collected precipitates were subsequently examined by optical and electron microscopy, with special focus on

their microstructure. However, in all cases there were no perceptible changes noted neither regarding the global morphology nor the internal texture.

In general, silica skins ought to inflict a negative charge on the particles at the given high pH, which can yet be counterbalanced by cation screening and interparticle silica condensation reactions.[8] The resulting net forces clearly have to be attractive enabling compact aggregation. Nevertheless, the characteristic misalignment between neighboring crystallites does also suggest a certain contribution of repulsive interactions. A feasible reason for the tilted arrangement of adjacent rods might in that sense be based on varying overall charge densities over the surface of the particles, likely driven by the shape anisotropy of the building blocks, which could in an extreme case cause some sort of dipolar properties.[10] If so, the orientation of the rods should be deranged to a greater or lesser extent by a suitably strong electric field, which was yet not observed. This indicates that the interactions between the crystallites are fairly weak, merely expressed at the contact sites of particles, or as such not governed by electrical forces. For a profound understanding of the circumstances leading to orientational order in the aggregates, a central question to be answered is whether individual rods are consistently and over their entire surface covered by siliceous mantles (see Section 6.4.5). Only then, well-grounded considerations can be made concerning possible interactions. In principle, these may include electrostatic or van-der-Waals forces and, if free carbonate surface proves to be still available, potentially also epitaxial relations or intrinsic electrical anisotropies of the crystal lattice. Alternatively, the relative orientation of the crystallites might be a sheer consequence of the current local growth direction of the assembly. In sheets, rods arrange with their long axis radially outwards from the origin and hence always lie perpendicular to the advancing front. In the course of coupled precipitation, nucleated witherite crystals grow fastest along the c-axis towards regions of high supersaturation, that is, into the gradient surrounding the front of the aggregate (see Chapter 8). If mineralization proceeds so rapidly that any re-orientation due to specific interparticle interactions cannot occur (which appears reasonable when recalling the typical growth rates reported in Section 6.4.3), the textural field described by the rods may simply reflect the growth direction and its delicate variations in both time and space. In this case, the striking microstructure of silica biomorphs does not result from distinct particle aggregation processes, but rather directly from the crystallization conditions brought about by chemical coupling.

Apart from that, attempts were made to impact the handedness of twisted filaments and thus induce chirality by exposing the growing aggregates to a special magnetic field which circulates in a helical manner through the sample. Despite much effort with diversely chosen field parameters and also upon adding traces of different paramagnetic ions, no such effect could ever be discerned and racemic mixtures of left- and right-handed species were obtained in all batches, as in earlier work.[4] The curling of sheets which gives rise to helicoidal structures is evidently by nature a random phenomenon producing stochastically about equal numbers of opposite twists in a significant number of events. Accordingly, the formation of spirals requires a fortunate accident during morphogenesis that can be steered deliberately neither by the magnetic fields used in the present study nor by chiral molecular additives.[8]

7.4.6 Growth under the Influence of Ultrasound

Eventually, modifications to the growth behavior of silica biomorphs provoked by ultrasonic waves were explored. As shown by the pH measurements, the uptake of CO_2 is drastically accelerated in the presence of ultrasound (cf. Fig. 7-2). Correspondingly, a white precipitate formed in the mixtures soon after the experiment had been started, which settled gradually with time until after about 2 hours no more visual changes were observed. Strikingly, SEM analyses of samples quenched at times between 0.5 and 5 h disclose that the deposited material does not at all contain biomorphic architectures, but instead consists of numerous undefined island-like chunks (Fig. 8).

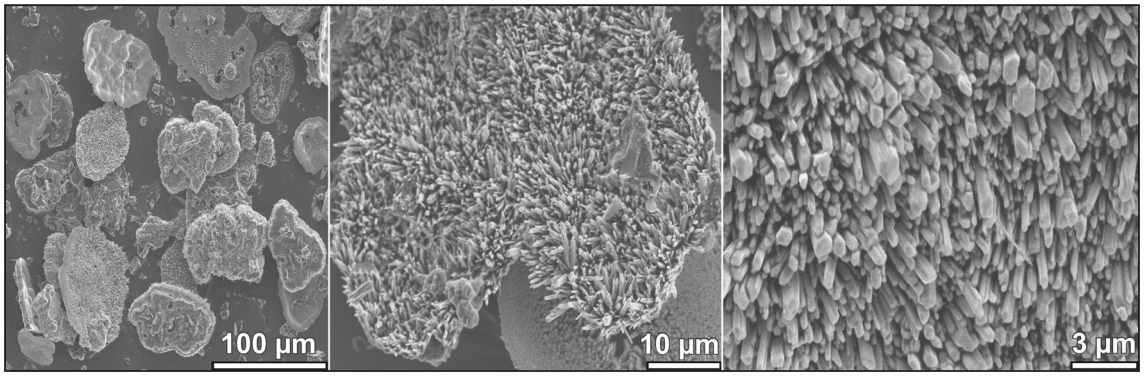

Islands of rod-like microcrystallites obtained after 2 hours when growth was conducted in an ultrasonic bath with a frequency of 47 kHz.

These islands appear to be composed of multiple elongated crystals exhibiting the common pseudohexagonal habit of witherite. The size distribution of these rods is found to be quite broad, with diameters averaging 440 ± 160 nm and lengths in the range of

1-2 μm, thus rendering the crystallites markedly larger than the nanorods making up the core fraction of the aggregates isolated from stagnant solutions. Further, although there is a general preference for parallel alignment, no pronounced long-range order of individuals can be identified.

Another important finding is the absence of any non-crystallographic branching and bifurcation at the tips of the rods. This implies that silicate poisoning did not noticeably act upon the crystals during growth. All in all, results strongly suggest that the crystallization of barium carbonate takes place exempt from the otherwise distinct influence of silica when ultrasound is applied. In fact, nanoscale crystalline witherite has previously been prepared by an ultrasonic method based on the diffusion of atmospheric CO_2 into alkaline solutions of barium acetate with no explicit additive.[20] The reported crystallites were considerably smaller than those distinguished here, presumably due to the higher Ba^{2+} concentration used. Most probably, the enormous increase in supersaturation accounts for the formation of regular elongated crystals rather than fractal architectures and curved polycrystalline assemblies in the present case. As the amount of carbonate species rises steeply from the very beginning on, the nucleation frequency becomes boosted and a multitude of nuclei are generated homogeneously throughout the solution, the latter being additionally mediated through the micro-heterogeneities created by the ultrasonic waves. Subsequent growth occurs so rapidly that specific adsorption of silica and crystal splitting is substantially suppressed. On the whole, crystallization seems to be completed quantitatively in this way already after 2 hours. Termination of precipitation is indicated by the breakpoint in the pH-time profile (cf. Fig. 7-2), after which diffusion of CO_2 is not anymore fuelled by conversion to $BaCO_3$ and hence appreciably slowed down.

In essence, the origin of miniaturized crystallites relies mainly on the elevated bulk supersaturation under the given conditions, unlike the situation encountered in biomorphs where concerted dynamic interactions lead to the stabilization of nanosized units. Nevertheless, the possibility that silica adsorbs more or less non-specifically on the crystal nuclei cannot be excluded, thus favoring separate growth of individuals and avoiding fusion as described formerly for organic additives like polyvinyl alcohol.[20] Indeed, varying but significant portions of silica were repeatedly detected in the products, as a consequence of either direct co-precipitation or simple deposition after exhausted crystallization. Howsoever, exposure to ultrasound is obviously found to be the only effective means to prevent ordinary morphogenesis of silica biomorphs from

solutions at ambient temperature and suitable concentrations and pH. Heavily altered supersaturation values do thereby not allow for extensive chemically coupled precipitation as observed at high stirring rates, and beyond that also prohibit the earlier stage of fractal branching by impeding prolonged continuous crystal growth.

7.5 Conclusion

Silica biomorphs resemble polycrystalline biominerals in terms of structural hierarchy, oriented texture and smoothly curved morphologies without being biomimetic in the true sense, as their formation does not require complex organic matrices or polymeric additive molecules. Given the ease of preparation and the simplicity of the involved reagents, these materials yet serve as model systems for studying the directed self-organization of nanoscale building units in general. Understanding the mechanisms that trigger structure evolution in this case could help to gain deeper insight to the concepts at work during biomineralization and may devise advanced strategies for laboratory morphosynthesis.

The results presented in this chapter have shed novel light on the development of the crystal aggregates on global scales and led to a feasible explanation for the characteristic quasi-two-dimensionality of sheets and the actual origin of curvature. First, it was affirmed that, unlike previously thought, the obtained morphologies do not universally correlate with the adjusted bulk pH. Instead, while ranging in a distinct corridor where coupled precipitation is permitted, the pH may adopt virtually arbitrary values which appear to be determined widely by the diffusion processes necessary to establish appropriate supersaturation in a given experimental setup. Accordingly, the generation of well-developed crystal aggregates premises a higher pH in solution than in gels.

Further, the collected data strongly suggest that growth of silica biomorphs is closely linked to the presence of surfaces which facilitate nucleation. In solutions, aggregates form exclusively via heterogeneous nucleation at interfaces, and sheets expand to larger dimensions only when growing flat in contact with for instance a wall. Curved structures like helicoids and worms emerge by contrast when polycrystalline growth is initiated far from an interface, such that the assembly needs to turn back in order to use, for lack of an extrinsic surface, its own as substrate. These considerations are supported by syntheses conducted in stirred solutions which yielded well-developed biomorphs despite enhanced bulk convections as a direct consequence of their propensity to grow

on interfaces, where fluid flow is reduced. In line with the proposed scenario, statistical analyses revealed that stirring induces a marked shift in the distribution of morphologies for the benefit of leaf-like shapes, which evolve in the stagnant boundary layer at vessel walls. As an essential implication of these findings, it should be possible to control, or least affect, morphogenesis of silica biomorphs by varying the topology of the growth substrate. Experiments with microstructured patterns proved that surfaces having profiles with periodically changing height effectively prevent larger sheets from forming when the length scale of the structural motif is small as compared to the common dimensions of the aggregates. In this case, the amount of curved morphologies is increased relative to reference samples – as opposed to the effect of stirring. This confirms the crucial role of extrinsic surfaces in the growth process and shows for the first time that the fractions of distinct morphologies in a given batch can be tuned concertedly. Further, it can be envisaged that by means of different substrates – for example surfaces with smooth, wavy profiles or patterns with larger dimensions enabling growth also in the indents – the shape and curvature of the aggregates, in particular of sheets, can be forthright molded.

Finally, crystallization in an ultrasonic bath failed to produce typical biomorphic forms, since the window of admissible supersaturation is supposedly left under these conditions. In turn, applied external electric and magnetic fields had no traceable effect on the morphogenesis and structure of the crystal aggregates.

7.6 References

(1) (a) García-Ruiz, J. M.; Amoros, J. L. *J. Cryst. Growth* **1981**, *55*, 379. (b) García-Ruiz, J. M. *J. Cryst. Growth* **1985**, *73*, 251.

(2) Baird, T.; Braterman, P. S.; Cheng, P.; García-Ruiz, J. M.; Peacock, R. D.; Reid, A. *Mater. Res. Bull.* **1992**, *27*, 1031.

(3) García-Ruiz, J. M. *Geology* **1996**, *26*, 843.

(4) García-Ruiz, J. M.; Carnerup, A. M.; Christy, A. G.; Welham, N. J.; Hyde, S. T. *Astrobiology* **2002**, *2*, 353.

(5) García-Ruiz, J. M.; Hyde, S. T.; Carnerup, A. M.; Christy, A. G.; Van Kranendonk, M. J.; Welham, N. J. *Science* **2003**, *302*, 1194.

(6) Terada, T.; Yamabi, S.; Imai, H. *J. Cryst. Growth* **2003**, *253*, 435.

(7) (a) Imai, H.; Terada, T.; Miura, T.; Yamabi, S. *J. Cryst. Growth* **2002**, *244*, 200. (b) Voinescu, A. E.; Kellermeier, M.; Bartel, B.; Carnerup, A. M.; Larsson, A. K.; Touraud, D.; Kunz, W.; Kienle, L.; Pfitzner, A.; Hyde, S. T. *Cryst. Growth Des.* **2008**, *8*, 1515.

(8) García-Ruiz, J. M.; Melero-García, E.; Hyde, S. T. *Science* **2009**, *323*, 362.

(9) Melero-García, E.; Santisteban-Bailon, R.; García-Ruiz, J. M. *Cryst. Growth Des.* **2009**, *9*, 4730.

(10) Kunz, W.; Kellermeier, M. *Science* **2009**, *323*, 344.

(11) Hyde, S. T.; Carnerup, A. M.; Larsson, A. K.; Christy, A. G.; García-Ruiz, J. M. *Physica A* **2004**, *339*, 24.

(12) García-Ruiz, J. M.; Moreno, A. *An. Quim. Int. Ed.* **1997**, *93*, 1.

(13) Bittarello, E.; Aquilano, D. *Eur. J. Mineral.* **2007**, *19*, 345.

(14) Kellermeier, M.; Glaab, F.; Carnerup, A. M.; Drechsler, M.; Gossler, B.; Hyde, S. T.; Kunz, W. *J. Cryst. Growth* **2009**, *311*, 2530.

(15) Pretzl, M.; Schweikart, A.; Hanske, C.; Chiche, A.; Zettl, U.; Horn, A.; Böker, A.; Fery, A. *Langmuir* **2008**, *24*, 12748.

(16) Hyde, S. T.; Garcia-Ruiz, J. M. *Actual. Chim.* **2004**, *275*, 4.

(17) Voinescu, A. E.; Kellermeier, M.; Carnerup, A. M.; Larsson, A. K.; Touraud, D.; Hyde, S. T.; Kunz, W. *J. Cryst. Growth* **2007**, *306*, 152.

(18) Kellermeier, M.; Melero-Garcia, E.; Kunz, W.; Garcia-Ruiz, J. M. *Local autocatalytic co-precipitation phenomena in self-assembled silica-carbonate materials*, submitted to *J. Mater. Chem.*

(19) Malone, D. M.; Anderson, J. L. *AlChE J.* **1977**, *23*, 177.

(20) Alavi M. A.; Morsali, A. *Ultrason. Sonochem.* **2008**, *15*, 833.

Chapter 8 Local Autocatalytic Co-Precipitation Phenomena in Silica Biomorphs

8.1 Abstract

Precipitation of barium carbonate into alkaline silica-rich environments affords unusual polycrystalline aggregates exhibiting complex curved shapes and hierarchical structuring. The formation of these silica biomorphs is thought to result from a coupling of chemical equilibria which allows evolving aggregates to synthesize constituents on their own at growing fronts. By evaluating semi-quantitatively the effect of fluid motion on morphogenesis outlined in the previous chapter, it is shown that these autocatalytic processes occur only locally on a short length scale within a so-called active region nearby the surface, the characteristic dimension of which is estimated based on the collected data. Results suggest that growth of silica biomorphs is essentially independent of mass transport from the bulk and thus support the proposed formation mechanism.

8.2 Introduction and Basic Concept

Silica-carbonate biomorphs constitute a remarkable example of self-assembled materials in which the delicate interplay between their two inorganic components in solution results in exceptional crystalline structures with morphologies void of any symmetry constraints.[1-6] Consisting of a myriad of partially oriented alkaline-earth carbonate nanocrystals embedded in a matrix of amorphous silica,[7] these purely abiotic aggregates imitate textures and shapes so far only encountered in biomineralized parts of living organisms,[8-13] or in bio-inspired artificial organic-inorganic hybrid materials.[14-22] Recently, the formation of the manifold morphologies displayed by silica biomorphs was described explicitly at the micrometer level, and a model based on a coupled co-precipitation of silica and carbonate was put forward to explain the chemistry behind the growth mechanism.[23] This chemical coupling, schematically depicted in Fig. 8-1, takes place under alkaline conditions (pH 9-11) and relies on the inverse trends in solubility of the two components with pH and, in particular, on changes in the speciation of each of the components induced by the precipitation of the other. As crystallites of barium carbonate (red bars in Fig. 8-1) nucleate and grow at the front of a developing aggregate (Stage 1), the local decrease in carbonate ions induces dissociation of nearby

bicarbonate ions to re-establish the point-perturbed HCO_3^-/CO_3^{2-} speciation equilibrium (Stage 2). This leads to a local release of protons which are rapidly consumed by reaction with dissolved silicate species (such as $Si(OH)_3O^-$). Enhanced protonation raises the local concentration of silicic acid (Stage 3) and thus the supersaturation of amorphous silica at the front. As a consequence, silica (indicated in blue) polymerizes and precipitates around the carbonate crystallites (Stage 4), preventing further growth. Continued silica oligomerization reactions cause a net removal of protons and seek to re-elevate the local pH nearby the precipitation site (Stage 5). This affects the local carbonate speciation by increasing the amount of CO_3^{2-} ions in equilibrium (Stage 6) and hence the supersaturation of barium carbonate, such that a novel nucleation event can occur and the cycle is reiterated. It is crucial to note that this sequential description only serves to illustrate the process in a simplified manner. Since both proton diffusion and protonation/deprotonation reactions are extremely fast, co-precipitation of carbonate and silica is likely to proceed close in space and more or less simultaneously in time.

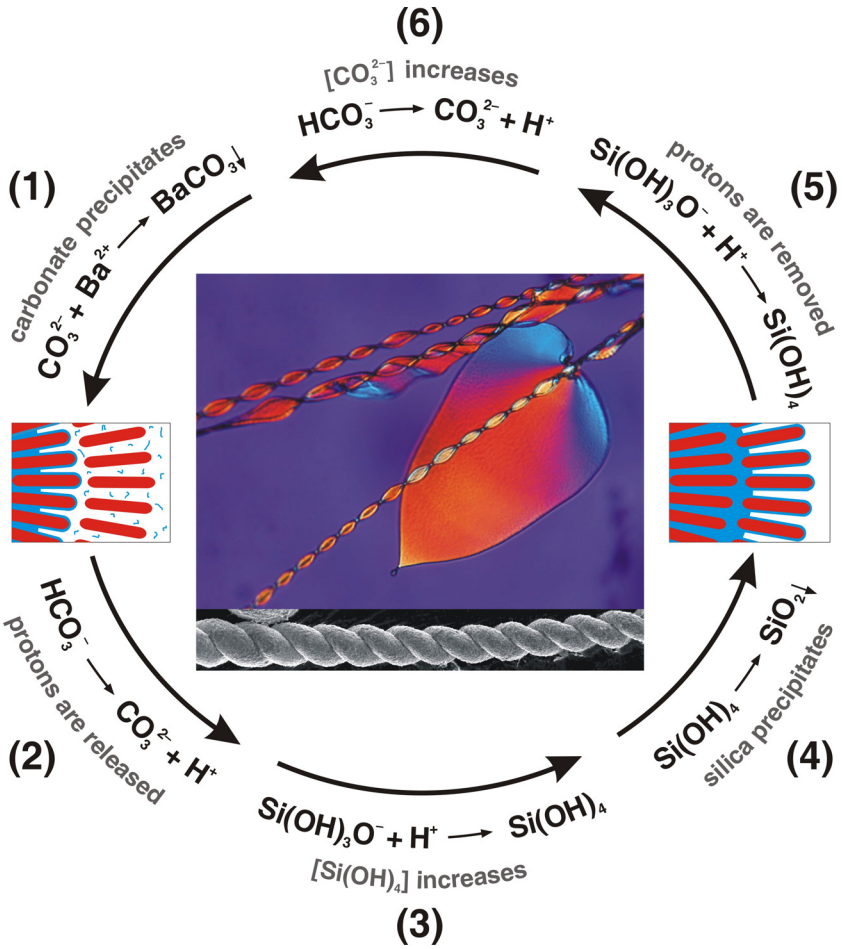

Fig. 8-1: Scheme of the proposed coupled co-precipitation mechanism for the formation of silica-carbonate biomorphs, with inserted images showing typical morphologies.

Although the postulated model helps to interpret many of the observations gathered over the years about these fascinating materials, it has not yet been directly proven. The main reason for this is the small scale on which the envisaged mechanism is expected to operate, rendering experimental access highly difficult. In this chapter, evidence is provided which confirms that growth of silica biomorphs is a local phenomenon occurring only at and around the front of evolving aggregates and, in doing so, sustains the theory proposed to account for their formation.

The rationale of the approach is as follows. In view of the reaction sequence indicated in Fig. 8-1, the growing front of biomorphs can be regarded as a catalyst for the conversion of bicarbonate and charged silicate ions, both being abundant in the bulk solution under typical growth conditions,[23] into the actually precipitating species, carbonate ions and neutral $Si(OH)_4$ molecules. Protonation/deprotonation processes drive both transformations and tend to re-establish the chemical equilibria locally altered by the precipitation of silica and barium carbonate. Their combined action should increase the concentrations of both reactants nearby the growing front (hereinafter referred to as the active region) and therefore create a region (hereinafter referred to as the active region) in which the supersaturation of the components is markedly higher than that in the bulk (S_{bulk}), thus leading to a profile of supersaturation with growing distance from the front as outlined in Fig. 8-2a. The notion of a locally elevated supersaturation arises naturally from the proposed formation mechanism and is moreover fully coherent with experimental findings: while the great number and small size of the carbonate crystallites constituting the biomorphs suggest growth under conditions of high supersaturation, the absence of corresponding crystals in the mother solution at any stage and the relatively rare occurrence of aggregates in the experiments hint at low bulk supersaturation.

Such a scenario would have two essential implications. First, the autocatalytic action of the front should render the growth process independent of mass transport from the bulk, as the concentrations of the two reagents are in fact highest at the precipitation site. This is in stark contrast to classical crystal growth where diffusion of reagents to the surface plays an important role and, commonly, forced convection results in a faster growth rate as supersaturation is maximized due to a more efficient transport of growth units from the mother solution.[24] Second, due to the presumed small dimension of the active region around the forming biomorphs, self-assembly should be indifferent to particular hydrodynamic circumstances in the surrounding bulk medium, like the characteristics

and strength of fluid motion, at least up to a certain degree. In stagnant solutions, where syntheses of silica biomorphs are usually carried out, the excess CO_3^{2-} and $Si(OH)_4$ species generated in the active region will partly diffuse *into* the bulk due to the existing concentration gradients, and be lost there by re-equilibration. Nevertheless, the increased supersaturation close to the surface of the aggregates is maintained in time as the growing front continuously produces new reagents inside the active region.

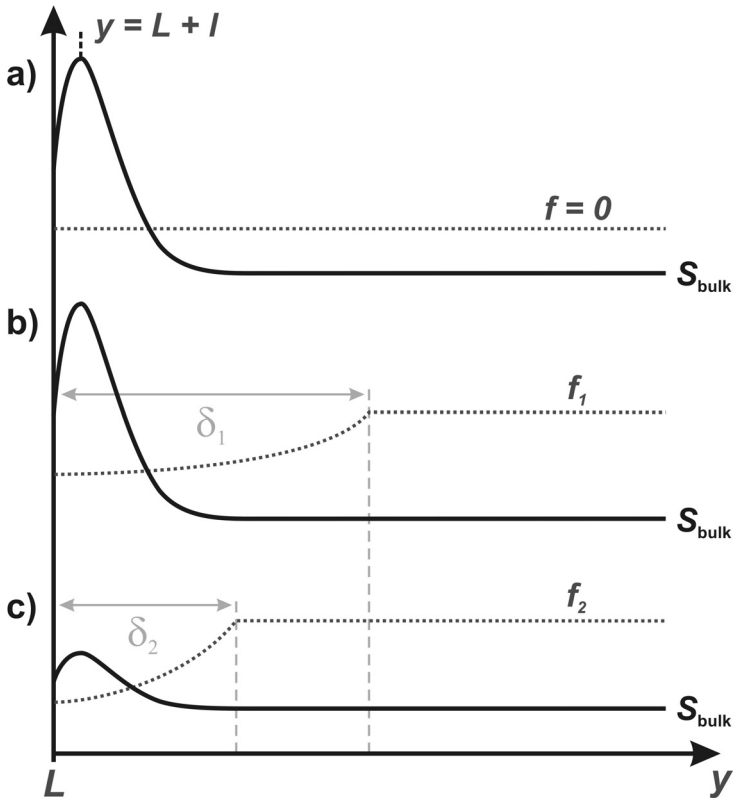

Fig. 8-2: Qualitative profiles expected for the supersaturation of barium carbonate and silica (full lines) and the fluid velocity (dotted lines) as a function of the distance y from the front of a biomorph (with length L) growing in a purely diffusive environment (a), and perpendicular to the wall of the vessel (located at $y = 0$) in solutions stirred at distinct frequencies f_1 and f_2 (b and c), with $f_2 > f_1$. In case of moderate stirring (f_1) and a boundary layer with correspondingly large thickness (δ_1), the fluid is almost stagnant across the active region and the supersaturation profile remains unaffected (b). In turn, a thinner boundary layer (δ_2) expected at higher stirring rates (f_2) implicates significant fluid motion in the active region, which alters the profile (c) and eventually – when advection is strong enough – interferes with the coupled precipitation mechanism.

The same should be true for a situation in which the bulk solution is subject to reinforced convections – as long as there is no significant change in fluid flow across the length of the active region. Thus, the complex shapes and textures typically obtained in quiescent environments should be able to form also in agitated systems. In turn, when

the imposed convections are strong enough to provoke appreciable fluid motion also inside the active region, transport of reagents to the bulk will be enhanced and the local supersaturation diminished until, eventually, autocatalysis can no longer compensate the depletion caused by advection and coupled precipitation ceases. In this manner, a resilience of the formation mechanism to fluid motion would confirm the existence of a localized active region, while the intensity of forced flow required to completely suppress morphogenesis would be a measure for its characteristic dimension.

Here, these predictions were tested by growing silica biomorphs in solutions stirred at different rates, in full analogy to the experiments described in the preceding chapter, but with special focus on whether typical crystal aggregates can in principle form under the chosen conditions rather than on changes in the relative occurrence of distinct morphologies. For sufficiently large bulk Reynolds number, order-of-magnitude analysis of the Navier-Stokes equations for incompressible fluids yields that a thin boundary layer exists on fixed surfaces in the flow. Within this layer, the fluid cannot be considered inviscid and the fluid velocity decreases from its bulk value to zero at the surface (for non-slip conditions). For laminar flow and flat surfaces, the thickness of the boundary layer δ (i.e. its length perpendicular to the surface and the flow) can be approximated according to the Blasius solution as defined in Eqn. 8-1, where υ is the kinematic viscosity of the fluid, U_∞ the free fluid velocity in the bulk, and x a spatial coordinate along the surface in direction of the flow.[25]

$$\delta \approx 5\sqrt{\frac{\upsilon x}{U_\infty}} \qquad \text{(Eqn. 8-1)}$$

Increasing the rate of stirring results in a decrease of δ and, therefore, in a steeper variation of the fluid velocity across the boundary layer (Fig. 8-1b). Since biomorphs usually grow attached to the walls of the used vessel, the boundary layer formed there will essentially determine the regime of fluid motion experienced by the aggregates during growth. Higher stirring frequencies lead to pronounced advection at smaller distances from the walls such that, beyond a certain threshold, noticeable fluid flow will occur across the characteristic length of the active region. The resulting convection should finally lead to a decoupling of carbonate and silica precipitation and hence inhibit ordinary morphogenesis of silica biomorphs (Fig. 8-1c).

8.3 Results and Discussion

8.3.1 Morphology and Microstructure of Aggregates Grown from Stirred Solutions

In Fig. 8-3 and Fig. 8-4, SEM images of typical crystal aggregates obtained at different stirring rates are shown. Up to 300 rpm, the isolated biomorphs exhibit shapes, textures (Fig. 8-4), and morphologies identical to those in the control experiment at 0 rpm, as opposed to the results of an earlier study where the regularity of the aggregates was reported to deteriorate when syntheses were performed in stirred media.[5]

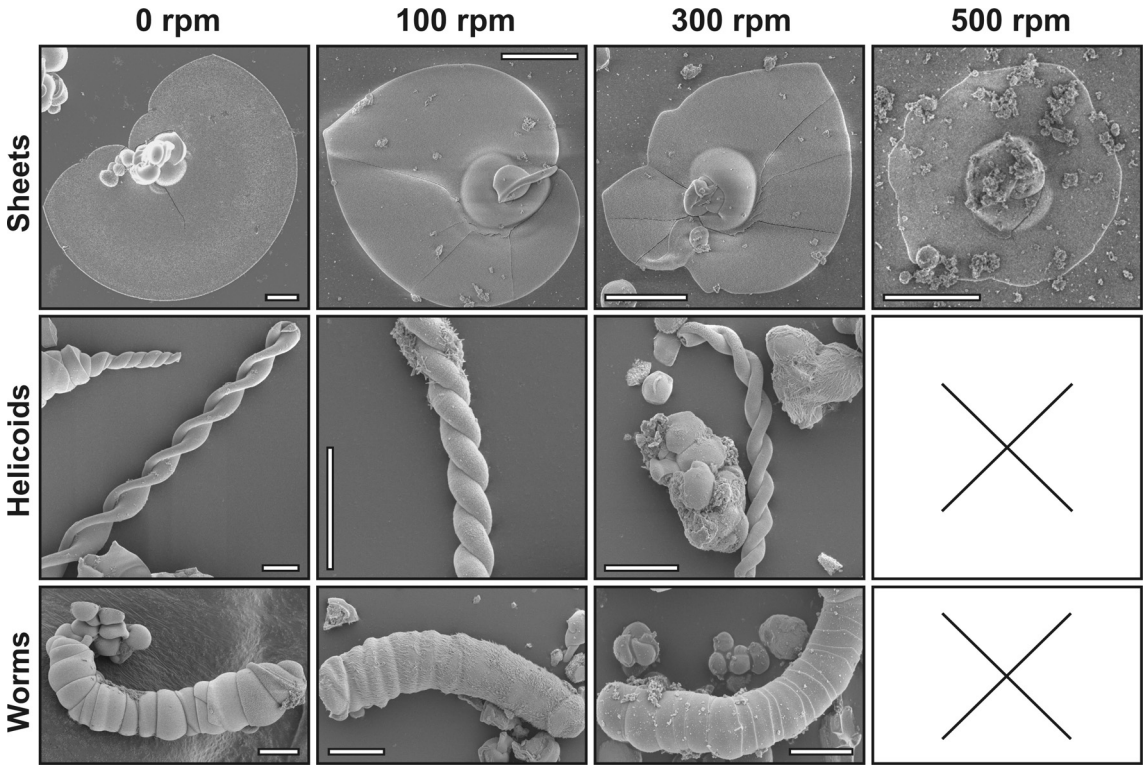

Fig. 8-3: Comparative chart of the three most distinctive morphologies commonly displayed by silica biomorphs grown in solution at different stirring rates. Helicoids and worms occurred only at rates of up to 300 rpm, whereas sheets were formed also at 500 rpm. Scale bars are 20 μm.

Under stagnant conditions, flat sheets always form and grow parallel to the walls of the wells, while twisted morphologies commonly protrude into the liquid (cf. Section 7.4.2). This was true also in solutions stirred at moderate frequencies, although the length and relative occurrence of worms and helicoids decreased with increasing stirring rate (see Fig. 7-10, Fig. 7-13, and Appendix D). By contrast, at 500 rpm all twisted morphologies were absent (Fig. 7-10) and only the leaf-like aggregates adhering to the

walls were observed, though thinner than at lower frequencies. Moreover, the central globular structures from which the sheets emerged were smaller (cf. Fig. 7-11).

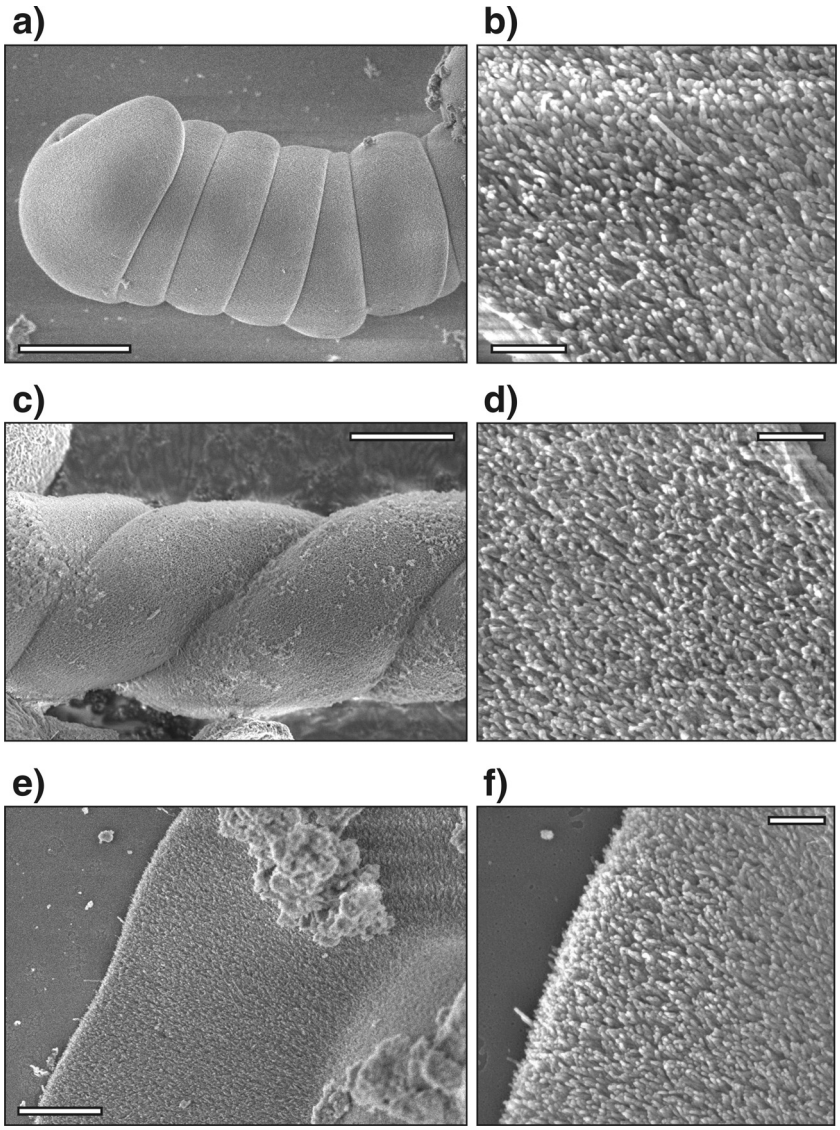

Fig. 8-4: SEM micrographs of silica biomorphs isolated after 8 h from solutions stirred at a nominal frequency of (a-b) 100 rpm, (c-d) 300 rpm, and (e-f) 500 rpm. Both worms (a) and helicoids (b) exhibit morphologies and a regularity indistinguishable from corresponding counterparts formed under quiescent conditions. Close-up views of selected regions (b, d, and f) reveal that the aggregates consist of uniform elongated witherite nanocrystals in all cases, as reported previously for silica biomorphs obtained from stagnant solutions.[26] Obviously, stirring does not change the microstructure of the precipitates. Scale bars are 10 μm in (a), 5 μm in (b), 2 μm in (c), and 500 nm in (b), (d) and (f).

8.3.2 Prevention of Biomorph Formation at High Stirring Rates

In a further experiment, growth was carried out in solutions stirred at the maximum frequency accessible with the used setup (1250 rpm). In order to avoid that, due to the

stirring, the pH of the system decreases very fast and the window of appropriate conditions is passed too quickly, the inflow of CO_2 was reduced by sealing the well with Parafilm through which three holes were punched. The resulting temporal pH profile (Fig. 8-5a) exhibits a slope and progression comparable to curves recorded for samples at 100 rpm which were covered only loosely with the lid (see Fig. 7-2). Therefore, it can be concluded that with respect to the rate of CO_2 uptake and the bulk pH, it should be possible to grow biomorphs under the given conditions (see Section 7.4.1 for details). In turn, observed changes in the growth behavior originate clearly from the applied stirring.

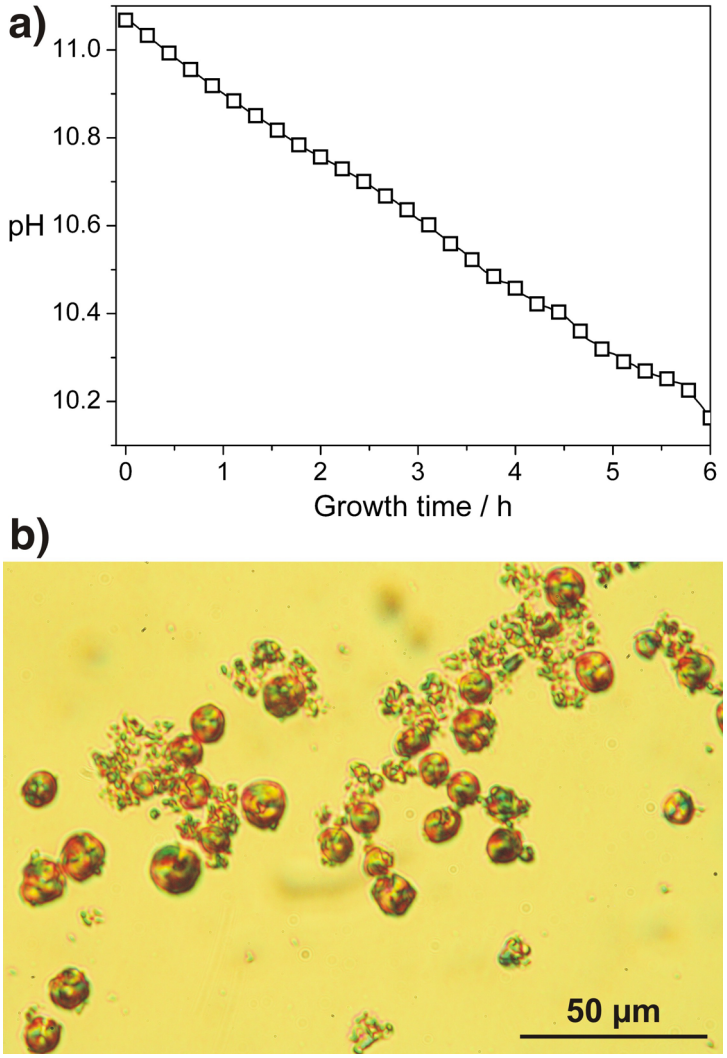

Fig. 8-5: Growth of silica biomorphs at a stirring frequency of 1250 rpm. (a) Temporal evolution of the bulk pH in the sample. (b) Optical micrograph of the globular aggregates formed in the experiment.

Typical precipitates found after a period of 8 hours are shown in Fig. 8-5b. It is evident that mainly globular aggregates with diameters in the range of 5-10 µm were formed at 1250 rpm, while none of the characteristic morphologies usually displayed by silica

biomorphs could be discerned in the well. As described previously, these fractal aggregates are precursors of the more complex morphologies, which arise due to silica-induced non-crystallographic branching of a carbonate single crystal, rather than coupled co-precipitation.[23] Obviously, coupled co-precipitation of the components and the concurrent development of self-assembled polycrystalline architectures are effectively suppressed at high stirring rates. Thus, the above findings clearly show that increased convection progressively affects the morphogenesis of silica-carbonate biomorphs in accordance to what can be expected from the proposed model.

8.3.3 Numerical Estimation of the Boundary Layer Thickness

In order to estimate the thickness of the boundary layer under the different stirring conditions, it was assumed that the Blasius solution for the laminar boundary layer established over a flat plate is valid for the walls of the wells in the experiments. Since the walls are curved and the bottom, being flat, is subjected to a flow which is also curved, the Blasius solution can only be applied for length scales x (see Eqn. 8-1) at which the curvature of the walls and the flow can be neglected. For the present setup, x was assumed to be 1 mm and υ was taken as the kinematic viscosity of pure water at 20°C. For the bulk velocity of the flow, U_∞, the maximum possible value at each stirring frequency was used. This value corresponds to the linear velocity v of the edges of the stirrer bar. For a given stirring rate f, v can be calculated according to Eqn. 8-2, where r equals half the length of the stirrer bar (15 mm, cf. Section 7.3.1) and ω is its angular velocity.

$$U_\infty \equiv v = r \cdot \omega = 7.5 \cdot 10^{-3} \cdot \frac{2\pi}{60} \cdot f(\text{rpm}) \ \text{ms}^{-1} \qquad \text{(Eqn. 8-2)}$$

The values thus obtained for δ (see Table 8-1) are clearly approximations of upper limits, but should nevertheless give an idea of the correct order of magnitude.

f / rpm	U_∞ / ms^{-1}	δ / µm
100	0.08	564
300	0.24	323
500	0.39	272[a]
1250	0.98	167[a]

Table 8-1: Calculated free fluid velocities U_∞ and maximum boundary layer thicknesses δ at different nominal stirring rates f. [a] Note that at 500 and 1250 rpm, the equation for the thickness of the laminar boundary layer may not be fully valid.

In view of the rather small variation of δ when going from 300 to 500 rpm, the radical shift in the observed morphology distribution indicates a significant change in the characteristics of fluid motion inside the boundary layer. One may suspect that in this frequency range a transition from a laminar to a turbulent boundary layer occurred. Such a transition would cause higher fluid velocities closer to the wall, so that any biomorph growing out into the solution, even when protruding at a small angle to the surface, would suffer too strong convections and would therefore not form or cease to grow soon. In this case, only flat sheets of typically few microns in height can evolve safely inside the thin viscous sublayer existing beneath the turbulent boundary layer, where the fluid velocity is markedly reduced.[25] At 1250 rpm, the thickness of this sublayer is smaller than the height of the sheets, such that these aggregates become also exposed to pronounced convection and can no longer form.

8.3.4 Order-of-Magnitude Evaluation of the Characteristic Length of the Active Region

In general, the effect of fluid motion on the transport of reactants and, therefore, the degree of perturbation of the proposed supersaturation profile depends on the relative orientation between the growth direction and the fluid flow. In the worst case, the front grows parallel to the velocity gradient (i.e. perpendicular to the wall of the vessel) and thus progressively becomes exposed to higher and higher velocities. Growth will then be abandoned at a distance from the wall where the fluid velocity exceeds a certain critical value u_c and ample convection prevents continued coupled precipitation. For hypothetical aggregates growing perfectly perpendicular to the wall, this distance can be written as the sum of the final aggregate length L and the distance between the front and the maximum of supersaturation l, i.e. $u_c = u(L+l)$ (see Fig. 8-2). Within a laminar boundary layer, the vertical velocity profile $u(y)$ can be described reasonably well by a second-order polynomial of the form:

$$u(y) = U_\infty \cdot \left[2\left(\frac{y}{\delta}\right) - \left(\frac{y}{\delta}\right)^2 \right] \qquad \text{(Eqn. 8-2)}$$

where y is the coordinate perpendicular to the flat surface and therefore to the flow.[25] Then, for a certain velocity profile $u_i(y)$ corresponding to a stirring rate f_i, it follows that

$$u_c = u_i(L_i + l) = u_i(L_i) + \left.\frac{du_i}{dy}\right|_{y=L_i} \cdot l \qquad \text{(Eqn. 8-3)}$$

When assuming that u_c and l are independent of the stirring rate, the unknown critical velocity can be eliminated by writing Eqn. 8-3 for two distinct frequencies, e.g. 100 and 300 rpm. Combining these equations and using Eqn. 8-2 and its first derivative results in an expression for l (Eqn. 8-4) in which the only unknown parameter remaining is the final aggregate length L_i.

$$l = \frac{u_{100}(L_{100}) - u_{300}(L_{300})}{\left.\frac{du_{300}}{dy}\right|_{y=L_{300}} - \left.\frac{du_{100}}{dy}\right|_{y=L_{100}}} = \tag{Eqn. 8-4}$$

$$= \frac{U_{\infty,100} \cdot \left[\frac{2L_{100}}{\delta_{100}} - \left(\frac{L_{100}}{\delta_{100}}\right)^2\right] - U_{\infty,300} \cdot \left[\frac{2L_{300}}{\delta_{300}} - \left(\frac{L_{300}}{\delta_{300}}\right)^2\right]}{U_{\infty,300} \cdot \left[\frac{2}{\delta_{300}} - \frac{2L_{300}}{\delta_{300}^2}\right] - U_{\infty,100} \cdot \left[\frac{2}{\delta_{100}} - \frac{2L_{100}}{\delta_{100}^2}\right]}$$

Since worms and helicoids usually grow protruding from the wall into the solution it is reasonable, for the given purpose, to take L_i as the typical length of those morphologies. While the rare occurrence of helicoids in stirred solutions did not permit a determination of their size with statistical significance, measuring the length of the more frequent worms in optical micrographs led to mean values of 94 and 77 μm at 100 and 300 rpm, respectively (cf. Fig. 7-13).

However, given that the aggregates in practice develop at arbitrary angles from the normal to the walls, these values do not represent the length of a biomorph growing perfectly parallel to the velocity gradient. Rather, when presuming that growth is terminated once the front reaches a certain distance from the wall, the shortest worms formed under the respective conditions should be those which grew perpendicular to the wall. Hence, to estimate L_{100} and L_{300} the lowest values reproducibly measured for the length of worms at 100 and 300 rpm were used, which were roughly 50 and 30 μm. With the values for U_∞ and δ listed in Table 8-1, this yields:

$$l \approx \frac{0.014 - 0.043}{1348 - 259}\,\mathrm{m} = -2.66 \cdot 10^{-5}\,\mathrm{m} \tag{Eqn. 8-5}$$

Eqn. 8-4 is valid for hypothetical aggregates which grow exactly at a right angle to the wall. This criterion is apparently not met by the worms in the present experiments. Therefore, and considering the assumptions made for deriving Eqn. 8-4 and calculating

U_∞ and δ, the negative sign of the result received for l is judged to be physically meaningless and a consequence of the implemented approximations. Nonetheless, its absolute value allows for estimating the order of magnitude of l which is, according to Eqn. 8-5, several tens of microns. However, due to the used upper limits for U_∞, it is expected that the true value for the characteristic length of the active region is in the lower range of the predicted magnitude, that is, between few and few tens of microns.

8.4 Conclusion

The presented results provide an indirect proof for the major assumption of the mechanism proposed to underlie the morphogenesis of silica-carbonate biomorphs: the localness of speciation changes. The notion that out-of-equilibrium concentrations and critical supersaturations required for nucleation occur, as a consequence of autocatalysis, only in the close vicinity of growing fronts is strongly supported by the growth behavior traced in stirred solutions. In line with predictions formulated on the grounds of the postulated model, the performed experiments have shown that growth of biomorphs is resilient to forced bulk convections at moderate stirring frequencies and that fluid motion does in this case not affect the morphology and texture of the crystal aggregates. Further, it was verified that there is a threshold in the stirring frequency (between 300 and 500 rpm in the present setup) above which the formation mechanism becomes progressively perturbed, such that first only flat sheets growing in direct contact with vessel walls are obtained before, eventually, self-assembly of complex forms succumbs entirely. These experimental findings and the fact that nucleation is not observed in the bulk solution can be rationalized when admitting that coupled co-precipitation takes place only within an active region of limited dimension at the front which, based on the collected data and semi-quantitative calculations, is estimated to extend over a length scale on the order of microns.

The possibility to grow the delicate biomorphic ultrastructures even under pronounced fluid motion as well as the envisaged virtual independence of mass transport from the bulk underline the singularity of their formation mechanism. On the other hand, exposure of mother solutions to ultrasound was found to provoke ample ingestion of CO_2 and a rapid increase of the carbonate concentration and decrease of pH, which triggered homogeneous nucleation and avoided the formation of biomorphs (see Section 7.4.6). This demonstrates that local autocatalytic growth yet premises certain

requirements in terms of the bulk chemistry of the system,[27] such as slowly varying conditions and overall fairly low supersaturation.

The interplay leading to the morphogenesis of these biomorphs is featured by another peculiarity: the silica as an additive prompting structure formation behaves dynamically during growth and is able to react instantly on local changes in conditions due to the flexibility of its speciation. This is in contrast to typical organic polymers used for biomimetic syntheses, which have a fixed chemical constitution. Here, crystallizing mineral and structure-directing agent influence each other *in situ*, and thereby excite synergetic co-organization which enables the design of complex architectures also in simple inorganic environments. These particular characteristics render silica biomorphs such interesting laboratory systems for the study of self-assembly processes in micron- and nanoscale crystalline composite materials.

8.5 References

(1) (a) García-Ruiz, J. M.; Amorós, J. L. *J. Cryst. Growth* **1981**, *55*, 379. (b) García-Ruiz, J. M. *J. Cryst. Growth* **1985**, *73*, 251.

(2) (a) García-Ruiz, J. M. *Geology* **1998**, *26*, 843. (b) García-Ruiz, J. M.; Hyde, S. T.; Carnerup, A. M.; Christy, A. G.; Van Kranendonk, M. J.; Welham, N. J. *Science* **2003**, *302*, 1194.

(3) (a) Voinescu, A. E.; Kellermeier, M.; Carnerup, A. M.; Larsson, A. K.; Touraud, D.; Hyde, S. T.; Kunz, W. *J. Cryst. Growth* **2007**, *306*, 152. (b) Voinescu, A. E.; Kellermeier, M.; Bartel, B.; Carnerup, A. M.; Larsson, A. K.; Touraud, D.; Kunz, W.; Kienle, L.; Pfitzner, A.; Hyde, S. T. *Cryst. Growth Des.* **2008**, *8*, 1515. (c) Kellermeier, M.; Glaab, F.; Carnerup, A. M.; Drechsler, M.; Gossler, B.; Hyde, S. T.; Kunz, W. *J. Cryst. Growth* **2009**, *311*, 2530.

(4) Imai, H.; Terada, T.; Miura, T.; Yamabi, S. *J. Cryst. Growth* **2002**, *244*, 200.

(5) Bittarello, E.; Aquilano, D. *Eur. J. Mineral.* **2007**, *19*, 345.

(6) Bittarello, E.; Massaro, F. R.; Aquilano, D. *J. Cryst. Growth* **2010**, *312*, 402.

(7) (a) Hyde, S. T.; Carnerup, A. M.; Larsson, A. K.; Christy, A. G.; García-Ruiz, J. M. *Physica A* **2004**, *339*, 24. (b) Terada, T.; Yamabi, S.; Imai, H. *J. Cryst. Growth* **2003**, *253*, 435.

(8) García-Ruiz, J. M.; Carnerup, A.; Christy, A. G.; Welham, N. J.; Hyde, S. T. *Astrobiology* **2002**, *3*, 353.

(9) Addadi, L.; Weiner, S. *Angew. Chem. Int. Ed.* **1992**, *31*, 153.

(10) Mann, S. *Biomineralization: Principles and Concepts in Bioinorganic Materials Chemistry*; Oxford University Press: Oxford, 2001.

(11) Cusack, M.; Freer, A. *Chem. Rev.* **2008**, *108*, 4433.

(12) Su, X.; Belcher, A. M.; Zaremba, C. M.; Morse, D. M.; Stucky, G. D.; Heuer, A. H. *Chem. Mater.* **2002**, *14*, 3106.

(13) Aizenberg, J.; Weaver, J. C.; Thanawala, M. S.; Sundar, V. C.; Morse, S. E.; Fratzl, P. *Science* **2005**, *309*, 275.

(14) (a) Mann, S.; Ozin, G. *Nature* **1996**, *382*, 313. (b) Mann, S. *Nat. Mater.* **2009**, *8*, 781.

(15) (a) Meldrum, F. C. *Int. Mater. Rev.* **2003**, *48*, 187. (b) Cölfen, H. *Curr. Opin. Colloid Interface Sci.* **2003**, *8*, 23. (c) Meldrum, F. C.; Cölfen, H. *Chem. Rev.* **2008**, *108*, 4332.

(16) Falini, G.; Fermani, S.; Gazzano, M.; Ripamonti, A. *Chem. Eur. J.* **1998**, *4*, 1048.

(17) (a) Tlatlik, H.; Simon, P.; Kawska, A.; Zahn, D.; Kniep, R. *Angew. Chem. Int. Ed.* **2006**, *45*, 1905. (b) Rosseeva, E.; Buder, J.; Simon, P.; Schwarz, U.; Frank-Kamenetskaya, O. V.; Kniep, R. *Chem. Mater.* **2008**, *20*, 6003.

(18) Tian, Z. R.; Voigt, J. A.; Liu, J.; Mckenzie, B.; Mcdermott, M. J. *J. Am. Chem Soc.* **2002**, *124*, 12954.

(19) Grassmann, O.; Müller, G.; Löbmann, P. *Chem. Mater.* **2002**, *14*, 4530.

(20) Donners, J. J. J. M.; Nolte, R. J. M.; Sommerdijk, N. A. J. M. *J. Am. Chem. Soc.* **2002**, *124*, 9700.

(21) Kulak, A. N.; Iddon, P.; Li, Y.; Armes, S. P.; Cölfen, H.; Paris, O.; Wilson, R. M.; Meldrum, F. C. *J. Am. Chem. Soc.* **2007**, *129*, 3729.

(22) Guo, X.-H.; Yu, S.-H. *Cryst. Growth Des.* **2007**, *7*, 354.

(23) (a) García-Ruiz, J. M.; Melero-García, E.; Hyde, S. T. *Science* **2009**, *323*, 362. (b) Kunz, W.; Kellermeier, M. *Science* **2009**, *323*, 344.

(24) (a) Chernov, A. A. *Modern Crystallography III: Crystal Growth*; Springer:Berlin, 1984. (b) Sunagawa, I. *Crystals: Growth, Morphology and Perfection*; Cambridge University Press: Cambridge, 2005.#

(25) Fox, R. W.; McDonald, A. T. *Introduction to Fluid Dynamics*, 4th Ed., Ch. 9; Wiley-VCH: Wilmington, 1992.

(26) Hyde, S. T.; García-Ruiz, J. M. *Actual. Chim.* **2004**, *275*, 4.

(27) Melero-García, E.; Santisteban-Bailón, R.; García-Ruiz, J. M. *Cryst. Growth Des.* **2009**, *9*, 4730.

Chapter 9 Morphological Tuning of Silica Biomorphs

9.1 Abstract

In this chapter, the influence of selected additives on the formation process and in particular the final morphology of silica biomorphs is described. The chosen additives include a cationic surfactant (CTAB), a cationic polymer (pDADMAC), a salt of a trivalent metal cation ($LaCl_3$), and sodium chloride as a means to vary the ionic strength. Further, results of experiments performed in the absence of additives, but at elevated temperature or high barium concentration are presented. It is shown that any of the modifications imparted to the regular synthesis protocol provoked substantial changes in the course of crystallization. Isolated precipitates were characterized not only concerning their morphology, but also with respect to texture and composition. While high ionic strengths effectively prevented growth of characteristic polycrystalline architectures, already minor amounts of CTAB, pDADMAC and $LaCl_3$ shifted the appearance of the crystal aggregates from helicoids and worms towards floral spherulites. Similar and in addition coral-like forms were generated at high Ba^{2+} content, whereas raising the temperature led to a variety of cup-, trumpet- and flower-like shapes. The observed effects are discussed in terms of the impact of the distinct additives and precipitation conditions on the chemistry of silica, its interplay with growing carbonate crystals and the rate of $BaCO_3$ crystallization under the given circumstances. It is proposed that the found morphologies are essentially determined by the particular branching behavior of an initial crystal seed, which appears to be governed largely by the state of silica in solution. The collected data evidence that the evolution of complex curved form in silica biomorphs can be manipulated by introducing suitable additives or simply by adjusting experimental parameters. This may pave the way to a concerted synthesis of polycrystalline materials with diversified shapes.

9.2 Introduction

The synthesis of “biomimetic” materials has aroused a great deal of interest throughout the last decade.[1-6] In most cases, the influence of organic additives or template structures on the crystallization (or precipitation) of inorganic matter is exploited, modeled on the principles of nature, to build up microstructures with extraordinary and elaborate shapes which potentially provoke superior macroscopic material properties.[7,8]

The presence of suitable organic molecules or networks modifies the mineralization process leading to morphologies beyond crystallographic restraints. For instance, gelatin hydrogels and films have been employed as matrices for biologically inspired growth of calcium carbonate crystal assemblies.[9] Polymeric membranes were used to imprint desired morphologies on single $CaCO_3$ crystals.[10] Moreover, specifically designed double-hydrophilic block copolymers have proven to be versatile additives for directing non-classical structure formation of various inorganic materials.[11]

The self-assembly of alkaline-earth metal carbonates in the presence of silicate is an outstanding example in this context, as *purely inorganic* precursors cooperate in this case to constitute hierarchical structures and shapes strongly reminiscent of biological forms.[12-14] Precipitation of barium carbonate from alkaline silica solutions or gels yields a variety of complex curved, non-crystallographic ultrastructures, some of which closely mimic the morphology of certain putative microfossils.[15-18] The resulting silica biomorphs consist of a crystalline phase of quite monodisperse, defect-free aragonite-type carbonate nanorods in a compact array exhibiting liquid crystal-like long-range orientational ordering with a constant mutual twist between neighboring rods.[19-21] The whole assembly of crystallites is often surrounded by an outer amorphous silica skin which is composed of densely aggregated siliceous nanospheres.[19,20] Composite architectures with identical shape and structure were observed when strontium was substituted for barium,[22] while transferring the structural concept of biomorphs onto calcium carbonate (aragonite phase) required either higher synthesis temperatures[23] or seeding of the solutions.[24] Reported morphologies were thereby different from those obtained with the higher alkaline-earth homologues, and typically comprised coral- and floral dumbbell-like forms. Interestingly, spiral-shaped superstructures consisting of $BaCO_3$ nanocrystals, though on a smaller global scale than in the case of silica biomorphs, were prepared using a racemic block copolymer as additive.[25] Selective adsorption of the polymer onto specific faces of the primary building blocks and subsequent particle self-assembly in a preferentially staggered arrangement were suggested to facilitate helix formation in these experiments. Helical $CaCO_3$ aggregates (vaterite phase) were moreover obtained by Gower *et al.* upon growth in the presence of polyacrylates.[26]

This chapter is meant to illustrate that the panoply of morphologies displayed by silica biomorphs is not at all limited to those mentioned in the previous sections, and to disclose how the growth process can be influenced such that distinct novel shapes are

generated. Earlier studies evidenced that variations of synthesis parameters like the bulk pH,[13,27,28] temperature,[15,21,29,30] or species concentrations[19,21] can intimately affect the development of the crystal aggregates in both time and space. In the present work, morphological tuning was sought to be achieved predominantly with the aid of certain "secondary" additives which will interact with the "primary" additive, silica, and thus modify the progress of self-organized mineralization. To that end, numerous experiments were performed using a broad variety of substances, ranging from simple salts over diverse alcohols to different kinds of surfactants and polymers. The observed effects were manifold and pronounced to quite distinct degrees. In the following, selected examples will be discussed. On the one hand, the influence of two organic additives is described, namely a common cationic surfactant, cetyltrimethylammonium bromide (CTAB), and a cationic polymer consisting of monomers with a quaternary ammonium functionality, poly(diallyldimethylammonium chloride) (pDADMAC, see Fig. 9-1).

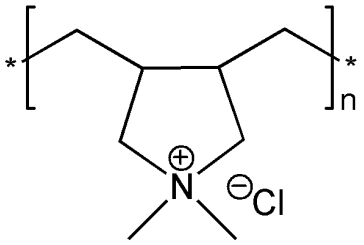

Fig. 9-1: Molecular structure of the repetitive unit of poly(diallyldimethylammonium chloride) (pDADMAC).

Both compounds are known to maintain strong interactions with silicate species in solution. For example, CTAB templates the famous mesoporous silica materials.[31,32] During their formation process, anionic silicate species adhere to the cationic head of the surfactant and subsequently mineralize the structure of supramolecular surfactant assemblies in solution. The polymeric additive pDADMAC has also been successfully employed to create mesopores in siliceous material,[33] thus indicating marked interactions with silica also in this case. Cooperative effects of two distinct additives on the crystallization of inorganic matter have been reported in literature. For instance, CTAB was added during precipitation of $CaCO_3$ from solutions of certain block copolymers[34] or dendrimers,[35] resulting in uniform pine-cone shaped calcite crystals and calcite rhombohedra covered with vaterite discs, respectively.

On the other hand, the role of the ionic strength in the formation of silica biomorphs is elucidated by experiments in which different amounts of excess sodium chloride were

introduced to the standard preparation recipe. To further explore the impact of salts on morphogenesis, growth was carried out also in mother solutions that were doped with trivalent lanthanum cations. Moreover, insight is provided into the influence of parameters intrinsic to the regular synthesis protocol – herein the barium concentration and the temperature – and the morphologies accessible *via* their variation. Finally, traced changes are evaluated primarily in view of the solution speciation of silica expected under the different conditions, and a phenomenological model is suggested to rationalize the experimental observations.

9.3 Experimental Section

9.3.1 Materials

Silica-witherite biomorphs were obtained by gradually precipitating barium carbonate from dilute alkaline mixtures of barium chloride and sodium silicate upon prolonged exposure to the atmosphere. Syntheses were performed by the procedure and at the concentrations specified in Section 6.3.1, except for the experiments at increased Ba^{2+} content where the silica sol was combined with a 0.5 M instead of a 0.01 M $BaCl_2$ solution. Cetyltrimethylammonium bromide was purchased from Fluka ($\geq$ 99%) and used without further purification. Poly(diallyldimethylammonium chloride) was received as a powder ("Magnafloc 368") from Ciba Specialty Chemicals (Lampertheim, Germany), with a purity specification of 90-100% due to varying water content. The product was dried in a vacuum oven at 60°C for at least 48 h before use. The average molecular weight of the polymer was ~ 750 kDa, corresponding to about 4640 monomer units per polymer chain. The main field of application of "Magnafloc 368" is its use as primary coagulant inducing flocculation of colloidal suspensions of negatively charged particles. Sodium chloride was obtained from Merck (p.a.), lanthanum chloride heptahydrate from Sigma ($LaCl_3 \cdot 7H_2O$, $\geq$ 99.9%). All solutions and dilutions were freshly prepared using exclusively water of Milli-Q quality.

9.3.2 Biomorph Syntheses

Additives were generally introduced by dissolving proper amounts of the respective substance in the $BaCl_2$ solution prior to mixing. This required vigorous overnight stirring in case of the polymer. The resulting virtually clear solution still contained traces of suspended solid, which were removed by filtration. Final concentrations of the

surfactant and the polymer in the mother liquor were varied between 0.1 and 10 mM (referred to total monomer concentrations for the polymer), while those of NaCl ranged between 50 and 500 mM. The optimum amount of $LaCl_3$, in terms of a structuring influence, was found to be 1 mM.

The initial pH of the mixtures was determined using a Metrohm combined glass electrode (model 6.0238.000) connected to a Schott laboratory pH-meter (model CG-843). The presence of the surfactant and polymer did not affect the starting pH to a noticeable extent in the studied concentration regime (i.e. $pH_{initial} \approx 11$). The same held true for the samples to which NaCl was added (at least in the range of ionic strengths for which the pH can be measured with a glass electrode). In turn, addition of La^{3+} ions and increasing the Ba^{2+} concentration both led to a significant decrease of the pH, giving initial values of about 10.4 and 10.5, respectively. This can likely be ascribed to the acidity of multivalent cations.

Crystallization at elevated temperatures (here exemplarily 50°C) was carried out in the absence of additives at "standard" concentrations (5 mM Ba^{2+} and 8.9 mM SiO_2), using pre-heated reagent solutions. After mixing, the well plate was covered with its lid and placed in a thermostatted cabinet.

Growth was allowed to proceed over a period of around 9 hours in case of the reference without any additives and at ambient temperature, both at 5 and 250 mM Ba^{2+}. The time required for the formation of mature crystal aggregates was reduced to ~6 h in the presence of CTAB and pDADMAC, to ~7 h in La^{3+}-doped solutions, and to about 5 h at 50°C. In these samples, continued diffusion of atmospheric CO_2 led to heavy overgrowths with regular $BaCO_3$ crystals on the biomorphs, indicating that the conditions for chemically coupled co-precipitation were no longer met after the respective timeframe. Regarding the surfactant, the polymer, and the trivalent cations, this behavior is probably due to their promotional effect on silica condensation processes,[36] which have substantially altered its speciation after a certain time producing a high fraction of polymerized fragments. Raising the temperature in turn results in a decrease of the solubility of $BaCO_3$,[37] such that precipitation will overall be faster. By contrast, crystallization from solutions enriched in NaCl took considerably longer than under "standard" conditions. Typical periods elapsed before no further growth occurred ranged from about 12 h at 50 mM NaCl to 20 h at 500 mM. Decelerated mineralization at increased ionic strengths presumably originates from the known decrease in the Henry constant of CO_2 and hence its concentration in solution in equilibrium with the

gas phase at higher salinities.[38] Moreover, the solubility of alkaline-earth carbonates was reported to be enhanced when the ionic strength of the system is incremented.[39]

Experiments were terminated after the stated times by withdrawing the mother liquor, repeatedly filling the wells with water and sucking off flocculated silica and partially gelled matter (especially in the presence of La^{3+}). The amount of amorphous silica particles or gel-like clumps formed independently of the biomorphs was thereby found to be noticeably increased in additive-containing samples as well as at raised Ba^{2+} content and higher temperature. Likewise, all these mixtures – except for those at comparably low ionic strength ($c_{NaCl} \leq 100$ mM) – turned cloudy soon after combining reagents, suggesting that silica oligomerization was drastically reinforced under the given circumstances. In part, precipitated silica floccules served as substrates on which biomorphic structures grew in addition to the well walls. This complicated isolation of the aggregates. To collect the desired crystalline architectures, the fluffy sediments had to be carefully torn into pieces and dispersed several times in water, such that they eventually released the biomorphs which then settled to the bottom of the well. Finally, the crystal aggregates were rinsed successively with water and ethanol, and left to dry in air.

9.3.3 Characterization Techniques

Isolated specimens were examined by optical microscopy using a Wild microscope (Model M420). Selective dissolution of the silica skin and the carbonate core of the as-prepared biomorphs were achieved by immersion of the aggregates in 0.1 M NaOH and 0.01 M acetic acid (Merck), respectively. Thereby, time-lapse image sequences were acquired from the samples with the aid of an attached Canon Powershot A640 digital camera, choosing intervals between the frames of 10-60 s.

Promising aggregates were mounted on carbon adhesive tabs and gold- or carbon-coated for electron microscopy (Polaron E5200 SEM autocoating sputter unit and Balzers MED 010 sputter coater, respectively). Scanning electron microscopy (SEM) was performed using a Jeol JSM-840 microscope operated at 5 kV. Field-emission scanning electron microscopy (FESEM) studies were done using either a Zeiss LEO Gemini 1530 or a Hitachi S4500 microscope, both working at 0.1-30 kV. Cryogenic transmission electron microscopy (cryo-TEM) was carried out using a Zeiss EM922 EF microscope working at an acceleration voltage of 200 kV. Samples were prepared by placing a small drop of solution on a plain carbon grid, removing subsequently excess

liquid with a filter paper and finally plunging the grid into liquid ethane. TEM studies were performed at temperatures around 90 K. Images were recorded with a CCD camera (Gatan Ultrascan 1000) and processed using the Digital Micrograph 3.10 software package.

The elementary composition of as-synthesized biomorphs was determined by means of energy-dispersive X-ray (EDX) analysis. Therefore, a number of specimens was collected and subsequently crushed and pressed to give a flat layer of material for proper analysis. EDX measurements were performed at a working voltage of 15 kV using an EDAX microanalyser installed on a FEI Quanta 400T scanning electron microscope, or at 10 kV by means of an Oxford INCA detector attached to the LEO 1530 instrument.

For X-ray diffraction (XRD) studies, selected biomorphs were fixed individually on cryo-loops (Hampton Research). Diffraction was thus taken from single aggregates in this work. Measurements were done at beamline XRD1 of the synchrotron radiation facility ELETTRA in Trieste, Italy. Data were collected under rotation at a fixed wavelength of 0.1 nm, using a two-dimensional CCD detector from Mar Research having 2048x2048 pixels with a pixel size of 78.1 μm. The size of the incident beam was about 300x400 μm. Alternatively, patterns were recorded on a Bruker X8 Proteum laboratory diffractometer, as described in Section 3.3.2.4.

9.4 Results

9.4.1 Control Experiments

In a first reference experiment, barium carbonate was precipitated from dilute aqueous solutions at high pH in the absence of both silicate species and other additives. Upon continued diffusion of atmospheric CO_2 into the system, characteristic microcrystalline $BaCO_3$ dendrites and spherulitic bundles of needles were found in the growth cells after several hours (see Fig. 9-2a), as reported previously for $BaCO_3$ grown by gas diffusion reactions.[11c] The presence of sufficiently high amounts of silica during precipitation generally led to micron-scale curved morphologies with non-crystallographic symmetries at silica and barium concentrations ranging between about 7-15 mM (as SiO_2) and 5-500 mM, respectively, and at starting pH values between about 9.5 and 12. For a typical composition of 8.9 mM silica, 5 mM $BaCl_2$, $pH_{initial}$ = 11, and without any secondary additives, self-assembly results in racemates of regularly wound helical

filaments (Fig. 9-2b), curvilinear sheets as well as thicker croissant-like braids (worms), as described in the previous chapters and documented in detail in earlier work.[13,14,16,19,20] Since the influence of the cationic surfactant CTAB and the cationic polymer pDADMAC on the morphology of barium carbonate biomorphs is discussed in the following, a series of control experiments were performed in which $BaCO_3$ was crystallized in the presence of varying amounts of both substances at pH 11, with no added silica. Within the investigated additive concentration range (0.1-5 mM for CTAB, 0.1-10 mM as monomer for pDADMAC), there was little pronounced effect on the morphology of the crystals discernible in both cases, with classical faceted forms found in all batches. The presence of the surfactant resulted in a larger number of smaller crystals, most of them being single pseudo-hexagonal witherite needles. The latter finding might be due to noticeable adsorption of CTAB on the surface of the crystals, as reported for calcium carbonate.[40]

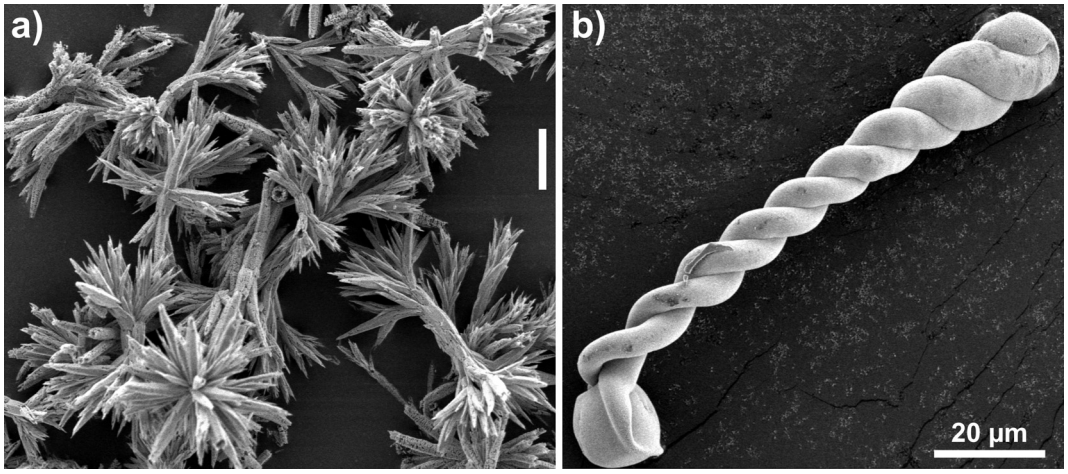

Fig. 9-2: SEM images of (a) dendritically branched and spherulitic witherite microcrystals grown in the absence of any additives under gas diffusion-controlled conditions ([$BaCl_2$] = 5 mM, pH = 11, T = 20°C), and (b) a twisted-ribbon silica biomorph grown from solutions containing silica but no further additives ([$BaCl_2$] = 5 mM, [SiO_2] = 8.9 mM, pH = 11, Growth time: 9 h, T = 20°C). Scale bar in (a): 10 µm.

9.4.2 Influence of Organic Additives on the Growth Behavior of Silica Biomorphs

9.4.2.1 Effect of the Cationic Surfactant CTAB

By contrast, adding CTAB to alkaline mixtures of barium chloride and silicate provoked significant morphological changes in the forming crystal aggregates at sufficiently high additive concentrations. First, when increasing the CTAB concentration from 0.1 to

about 0.4 mM, typical biomorph forms such as spirals and worms are replaced by an increasing fraction of less regular clusters, mainly aggregates of globules with scrolled braid-like excrescences in most cases. Helical filaments were rarely observed in these and all other experiments with additives as well as at higher temperature and Ba^{2+} concentration. For CTAB, uniformly twisted aggregates were never observed in growth media containing more than 0.5 mM of the surfactant. Instead, increasing areas of rather flat, sheet-like regions appeared in the precipitates, with (hemi)spherical overall aggregate shape becoming more and more predominant. At 1 mM CTAB, floral spherulites reminiscent of cloves are found in the growth cells after about 6 hours. A second major fraction of particles formed under these conditions were spherulitic aggregates composed of straight filaments emanating radially from a common core, resembling to some degree certain sea anemones. Aggregate diameters vary roughly between 50 and 150 µm in both cases. Fig. 9-3 shows typical biomorphic forms grown in the presence of CTAB.

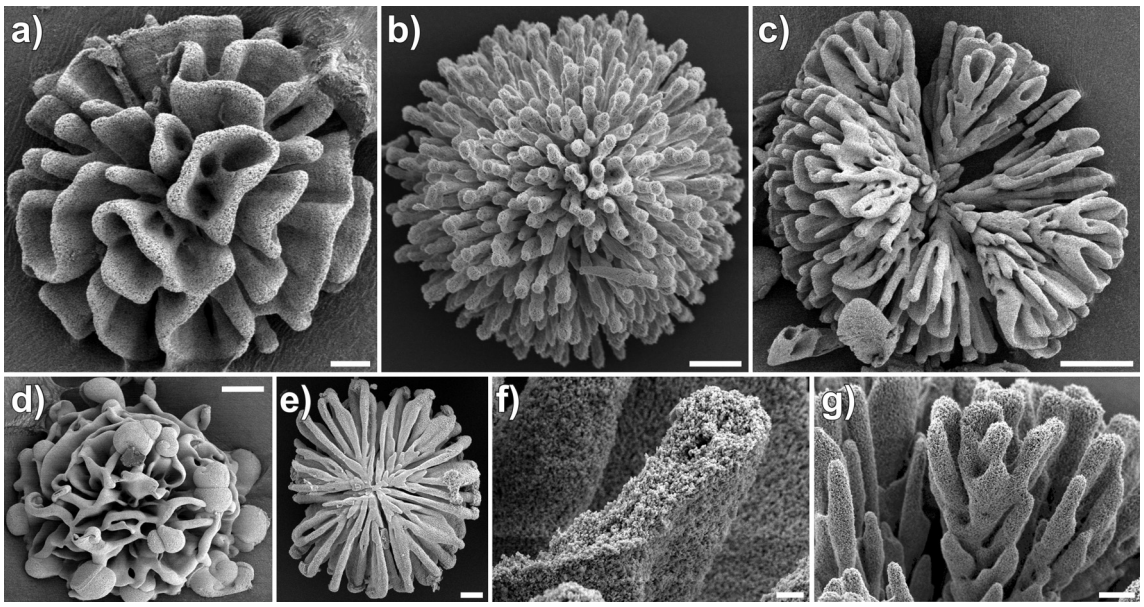

Fig. 9-3: FESEM images of crystal aggregates grown in the presence of both silica and the cationic surfactant CTAB ([$BaCl_2$] = 5 mM, [SiO_2] = 8.9 mM, [CTAB] = 1 mM (except for (d)), pH = 11, Growth time: 6 h, T = 20°C). (a) and (c) "Floral spherulites". (b) "Anemone-like" spherulite. (d) "Transitory" morphology obtained at 0.5 mM CTAB. (e) Bottom view of a floral spherulite. (f) and (g) Higher magnifications taken from sections of a floral spherulite. Scale bars: (a) 10 µm, (b) 10 µm, (c) 25 µm, (d) 25 µm, (e) 10 µm, (f) 1 µm, and (g) 5 µm.

The aggregate displayed in Fig. 9-3d, obtained at 0.5 mM CTAB, is representative for the morphological transition observed when adding the surfactant: globular domains, typical for rather low CTAB fractions, co-exist with branched petalloid sheet-like

regions. The latter form predominates at higher CTAB concentrations, giving floral spherulites. It is also worth noting that virtually all spherulites grown at 1 mM CTAB have flat bases exhibiting a central origin that is presumably the initial nucleation point, from which aggregate segments appear to radiate outwards (see Fig. 9-3e). These flat faces are likely to be cast from the walls of the plastic growth wells or the surface of the solution, since the aggregates frequently adhere to these interfaces. Similar observations were reported previously for coralline calcium carbonate biomorphs.[23]

9.4.2.2 Effect of the Cationic Polymer pDADMAC

Introducing the cationic polymer pDADMAC during the synthesis of silica-witherite biomorphs also induced significant changes in terms of the morphology of the final crystal aggregates. Fig. 9-4 illustrates typical forms found after 6 h when adding 1 mM pDADMAC to the mother solution.

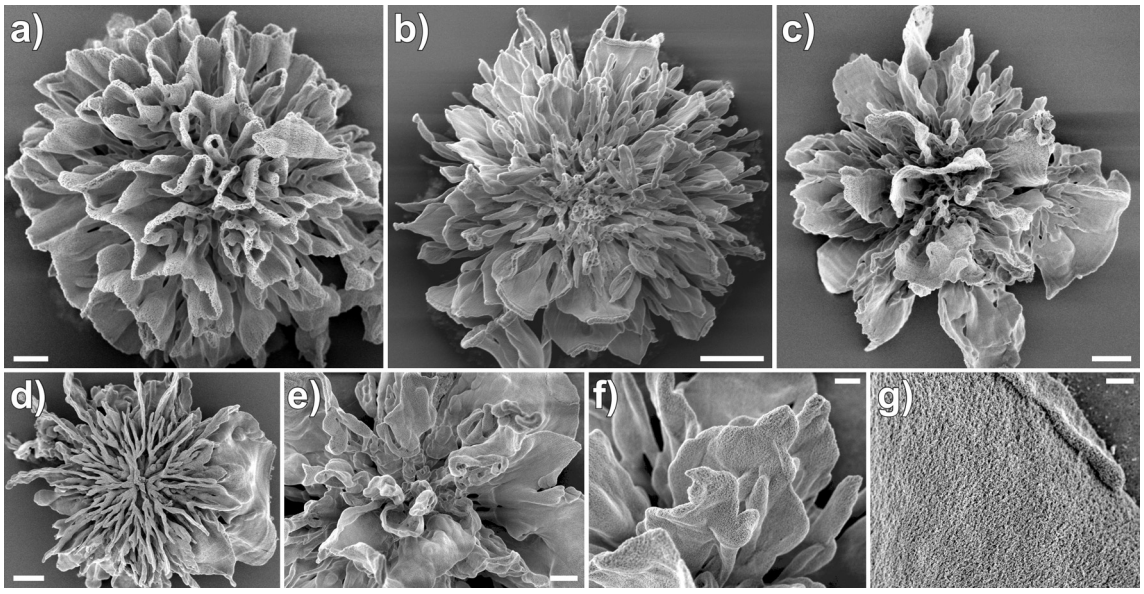

Fig. 9-4: FESEM images of $BaCO_3$ aggregates formed under the influence of both silica and the cationic polymer pDADMAC ([$BaCl_2$] = 5 mM, [SiO_2] = 8.9 mM, [pDADMAC] = 1 mM (monomer concentration), pH = 11, Growth time: 6 h, T = 20°C). (a-c) "Flower-like" spherulites. (d) Bottom view of an aggregate. (e-g) Zoom sequence into a typical flower-like spherulite. Scale bars: (a) 10 μm, (b) 20 μm, (c) 20 μm, (d) 10 μm, (e) 20 μm, (f) 4 μm, and (g) 2 μm.

As in the case of added CTAB, a gradual morphological transition from regularly wound helices and worms (no added polymer) to flower-like shapes (1 mM) can clearly be discerned. Overall, biomorphs generated on addition of the polymer are somewhat more irregular than those grown the presence of the surfactant, resembling (slightly

withered) petaloid flowers. In turn, aggregates obtained in the presence of pDADMAC are slightly bigger than their CTAB counterparts, with diameters typically between about 100 and 200 µm. The bases of these flower-like architectures are likewise flat, as observed for the CTAB-induced spherulites, which is again probably due to the affinity of the crystal assemblies with the walls of the plastic wells. Thus, nucleation appears to be favored on interfaces, in analogy to "regular" silica biomorphs as highlighted in Chapter 7.

With both organic additives, another type of morphology is frequently found throughout most batches, which may be referred to as "cauliflower-like" aggregates. Fig. 9-5 shows examples of such architectures, grown in the presence of 1 mM of the respective additive. These ultrastructures are almost exclusively encountered at the surface of the reaction mixture after several hours of growth, in contrast to the flower-like morphologies that predominantly nucleate and grow on the walls.

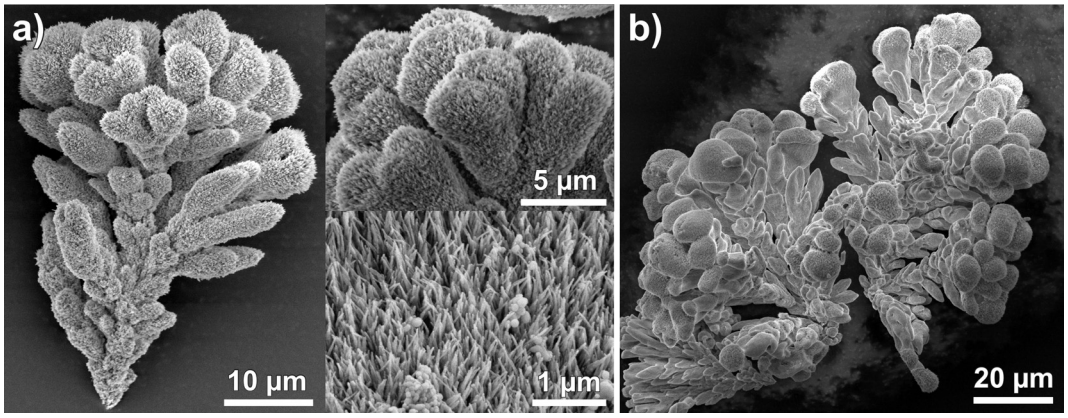

Fig. 9-5: FESEM images of "cauliflower-like" architectures grown in the presence of 8.9 mM silica and 1 mM of (a) the cationic surfactant CTAB, and (b) the cationic polymer pDADMAC. [$BaCl_2$] = 5 mM, pH = 11, Growth time: 6 h, T = 20°C. In both cases, "cauliflowers" are found exclusively at the surface of the reaction mixture.

The distinct morphological discrepancy between the aggregates formed on the cell walls and those grown at the surface can likely be ascribed to different reaction kinetics prevailing deep down in the solution and at its surface. The fractal character of the particles in Fig. 9-5 suggests that they have a similar origin as the globular precursors of biomorphs formed in the "standard" experiment, that is, they result from branching at non-crystallographic angles.[13,41] When assuming that the flower-like spherulites observed at the bottom of the wells grow likewise from an initial crystal seed which underwent fractal branching, this implies that morphogenesis proceeded to a minor extent at the surface of the solution, possibly because the supersaturation was too high

there and hence more and in average less developed aggregates were generated (cf. Section 7.4.3). In the following discussion, only the flower-like morphologies depicted by Fig. 9-3 and Fig. 9-4 will be addressed in more detail.

9.4.2.3 Variation of Species Concentrations

For both additives investigated, the optimal (monomer) concentration regarding a structuring effect was found to be around 1 mM. Lesser amounts of additive also affected the final aggregate morphology, however their primary effect was simply to contort the regular helical or worm-like silica biomorphs. These "intermediate" morphologies can still be classified as non-crystallographic witherite biomorphs, not least due to their internal microstructure (see below). Increasing the additive concentration above 1 mM does initially not change the final product of the precipitation reaction. However, above a certain threshold, biomorphic forms were no longer observed in the growth cells. Rather, classical witherite microcrystals are obtained, as grown in the absence of both silica and organic additive (cf. Fig. 9-2a). Obviously, high fractions of surfactant and polymer effectively prevent the silica from interacting with carbonate, thus resulting in "regular" crystallization. This finding can be attributed to the strong interactions between silica and both additives in alkaline solutions. In other words, increased concentrations of CTAB and pDADMAC virtually remove "active" silica from the solution, probably by driving condensation of lower oligomers into polymeric species and colloidal particles.[36] Recall that free (excess) additive likewise has little effect on conventional witherite crystallization.

Varying the silica concentration, while maintaining the content of organic additive, also changes the situation under certain conditions. Increasing significantly the amount of silica present during the syntheses suppresses of the influence of the additives. For example, regular silica biomorphs with familiar morphologies including spirals, sheets and worms were formed at 15 mM SiO_2 and 1 mM additive. Presumably, the excess silica efficiently locks up the organic additives in this case, leaving additional silica exempt from their influence to exert its specific effect on $BaCO_3$ crystallization, resulting in usual silica biomorphs. When decreasing the effective silica concentration, at first no noticeable change is observed, until finally biomorph formation succumbs, giving way to conventional $BaCO_3$ crystals. The lower silica limit necessary for the formation of biomorphic aggregates in the presence of CTAB and pDADMAC was found to be somewhat higher than in additive-free experiments (about 4 mM SiO_2).[19]

Consequently, it can be concluded that both additives compete with carbonate species for interaction with the silica in solution.

9.4.2.4 Effect of the Nature of the Added Cationic Surfactant

In a further suite of experiments, the nature of the added cationic surfactant was varied both in terms of chain length and headgroup type. It was found that morphologies as shown in Fig. 9-3 are generated when the number of carbon atoms in the hydrophobic chain is equal to or higher than 13. Below this threshold, no noticeable effect of the additives on the morphology and structure of silica biomorphs could be discerned at comparable concentrations (i.e. helices and worms are formed). Significantly higher amounts of the additive (50 mM or more) in turn affect aggregate morphology in a similar manner to simple salts such as sodium chloride (see Section 9.4.4). All investigated surfactants with chains longer than C_{13} (up to C_{20}) appeared to have essentially the same influence during biomorph growth, with flower-like shapes being predominant in all cases. A number of experiments were also carried out with distinct surfactant headgroups. The methyl moieties in CTAB were replaced by ethyl groups, and imidazolium was substituted for the quaternary ammonium. In addition, the bromide counter-ion of CTAB was exchanged by chloride and tetrafluoroborate. None of these changes imparted significant influence on the resulting morphologies.

9.4.2.5 Microstructure of Flower-Like Spherulites

The microstructure of the flower-like morphologies produced with the aid of CTAB and pDADMAC is generally the same as that of silica biomorphs grown without any additives.[14,19,20] The interior of the aggregates is composed of an array of single elongated witherite nanorods, with a preferred orientation of the rods over the image area. The whole crystallite assembly is in turn occasionally sheathed by an outer amorphous silica skin, which consists of densely agglomerated siliceous nanospheres, as evidenced by the high-magnification FESEM images displayed in Fig. 9-6. The nanorods constituting the carbonate core were found to be about 300-400 nm in length and 50-100 nm in width, in good agreement with earlier work.[17,20] The diameter of the silica spheres establishing the outer skin is around 100 nm. The witherite nanorods are roughly aligned along the growth direction of the aggregates, i.e. radially outwards from the central origin, and appear to share a similar, but still slightly varying vector regarding their long axis. However, the long-range orientation field, characteristic of

silica biomorphs, appears to be less regular here than reported elsewhere.[19] More detailed FESEM analysis and selected-area X-ray diffraction might clarify this question. Nevertheless, given the nanometric microstructure as well the observed complex curved ultrastructures, crystal aggregates grown in the presence of modest amounts of organic additives can unambiguously be classified as "silica-carbonate biomorphs" due to their composite microstructures, with intimate intergrowths of nanocrystalline witherite and amorphous silica.

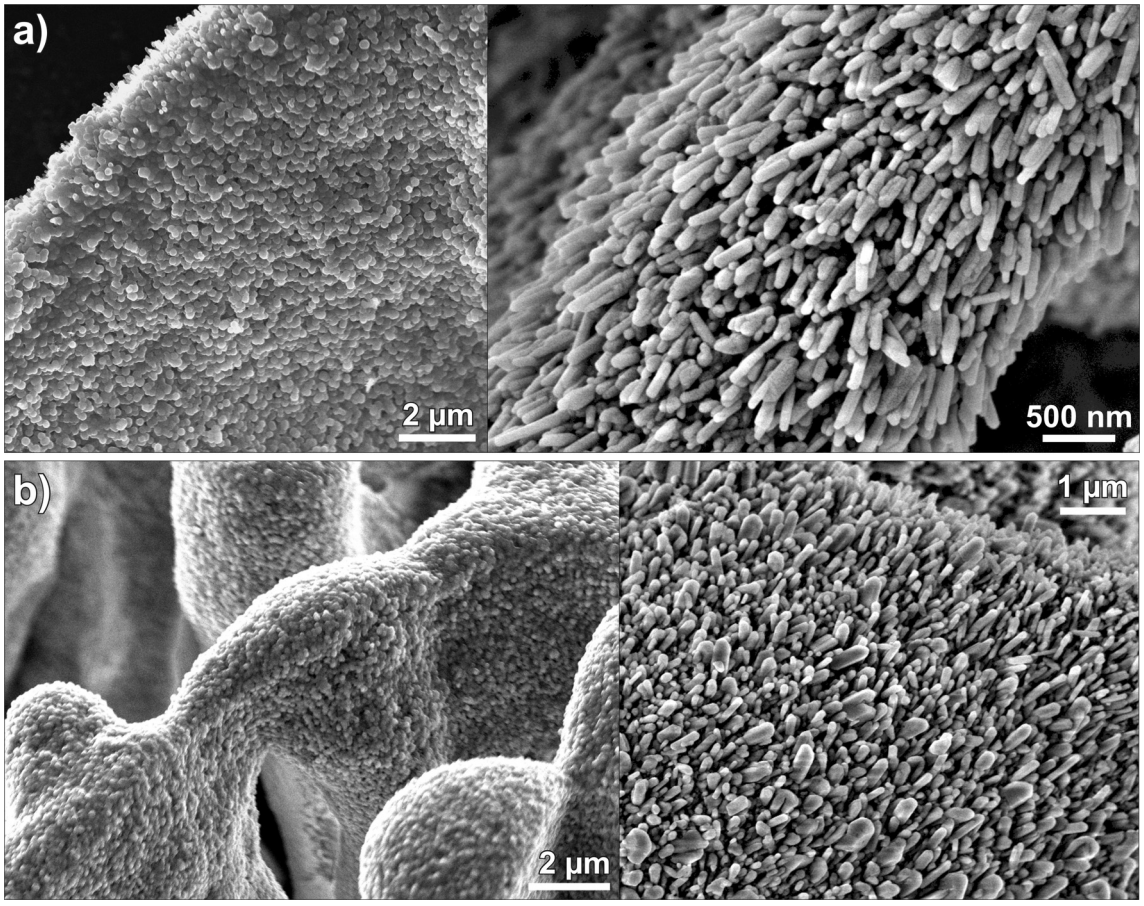

Fig. 9-6: The microstructure of flower-like morphologies produced by introducing (a) CTAB and (b) pDADMAC into the synthesis of silica biomorphs. Aggregates consist of an inner carbonate core which is constituted by single elongated $BaCO_3$ crystallites (right), and an outer amorphous silica skin composed of aggregated colloidal spheres (left). In order to reveal the inner core (rightward panels), samples were leached in 0.1 M NaOH prior to FESEM studies.

9.4.2.6 Leaching Experiments

The composite nature of such biomorphs can further be clearly visualized by selective dissolution of single components. On the one hand, immersion in dilute base removes the outer silica sheath, leaving an intact silica-free carbonate core (see Fig. 9-6). On the

other, leaching with dilute acid has shown to be effective to dissolve any carbonate material, resulting in a hollow silica "ghost" whose ultrastructure thereby remains unchanged.[16,17,19,23] A typical time-lapse sequence of optical micrographs showing the dissolution of the carbonate core from flower-like aggregates grown in the presence of pDADMAC is given in Fig. 9-7. However, it should be noted that many aggregates in a single batch do not exhibit distinct silica skins; the fraction of sheathed aggregates varies from batch to batch. Comparative carbonate dissolution studies with additive-induced morphologies and additive-free biomorphs (helices and worms) give the impression that silica skins are less frequently found on the former than on the latter.

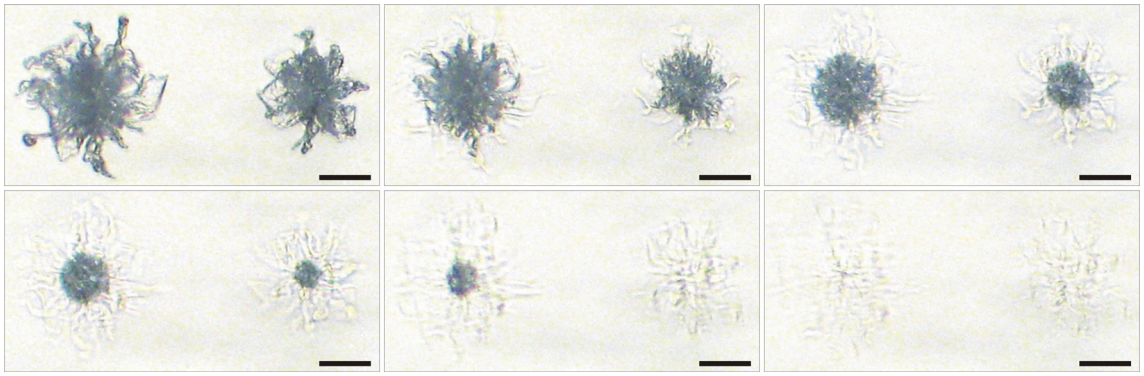

Fig. 9-7: Time-lapse sequence of carbonate dissolution from pDADMAC-induced flower-like aggregates by leaching in 0.01 M acetic acid (from top left to bottom right), leaving a structurally intact silica "ghost". Time interval between frames: 220 s. Scale bars: 100 µm.

Irrespective of this, there were no differences in sheathed fractions across distinct morphologies induced by the same additive (e.g., between floral and anemone-like spherulites in the case of CTAB). Finally, it became obvious over the course of these studies that on average a lower fraction of particles possess an outer silica skin when using pDADMAC as additive than with CTAB. This finding is also reflected in the EDX data (cf. Section 9.4.5).

9.4.2.7 Mesoporous Silica Nanoparticles as a By-Product of Biomorph Formation in the Presence of CTAB and pDADMAC

The repeated lack of external silica skins on the organic additive-induced architectures as well as the fact that both the surfactant and the polymer are not incorporated to the forming crystal aggregates (as verified by the EDX analyses in Section 9.4.5) may be explained on the basis of washing processes, which could have removed silica and organics after growth. However, cryo-TEM studies of samples taken from solutions at different times suggest an alternative "sink" for the additives and the silica in the course

of the experiments. Images reveal nanoscale mesoporous silica particles in both systems (Fig. 9-8), which must have formed during or parallel to growth. The size distribution of these particles is overall quite narrow, with diameters ranging approximately from 100-200 nm and 30-50 nm for CTAB and pDADMAC, respectively. The mesoporosity of the particles is in both cases clearly seen in the micrographs. Pore sizes were determined roughly from fast Fourier transforms (FFT) of the images (cf.i in Fig. 9-8a). In the case of the surfactant, regular pores arranged mostly in a hexagonal or lamellar lattice could be discerned, with pore dimensions around 4.5 nm, which is in good agreement with previously described materials of the M41S family.[32] The pores found in the nanoparticles generated in the presence of the polymer are not staggered in a regular manner, but seem to be interconnected, establishing a sponge-like structure with pore diameters of around 2.5 nm. Particles of similar morphology, size and internal structure were found in aqueous dispersions of certain lipid mesophases.[42] Recent studies on porous silica materials based on pDADMAC as structuring agent (Beta-H zeolite) reported both hierarchical mesopores of 5-20 nm in diameter and ordered micropores in the range of 0.8 nm in the samples.[33]

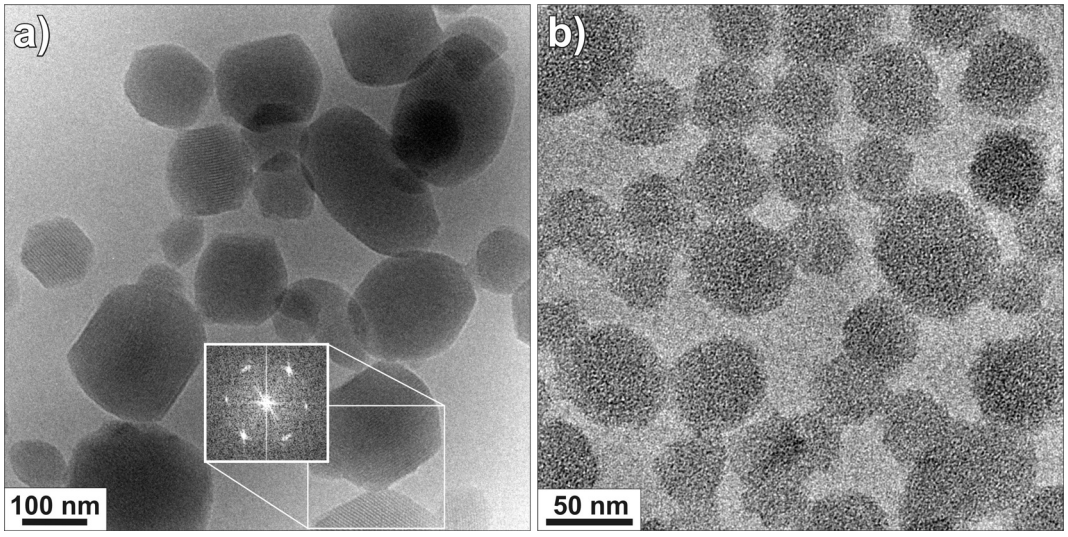

Fig. 9-8: Cryo-TEM micrographs of isolated particles of mesoporous silica found in mother solutions of silica biomorphs growing in the presence of (a) the cationic surfactant CTAB, and (b) the cationic polymer pDADMAC. Samples were taken after 80 min of growth. Particles grown in the presence of CTAB exhibit domains of mesopores in regular arrays, as seen from Fourier transforms of the images (inset in (a), taken from the area marked in white, reveals regular hexagonal arrangement of pores).

Reasons for the apparent discrepancies as well as structural details concerning both pore systems will not be discussed further here. Nonetheless, it is worth noting that isolated

nanoparticles of mesoporous silica were observed in the present work, whereas most other syntheses of such materials yield at least micron-scale, or larger, bulk phases. Furthermore, these particles have proven to be stable in the reaction mixtures for a minimum of 6 hours, remaining suspended in solution instead of aggregating or even flocculating, and thereby imparting a slightly turbid, blueish appearance to the samples. Moreover, it appears as if mesoporous particles form continuously over a certain frame of time. Particles of sizes and shapes similar to those shown in Fig. 9-8a have been described in previous work on CTAB-induced mesoporous silicas.[43] Both the dilution of the reaction mixtures and their pH have proven to be crucial parameters for particle size distributions in mesoporous silica materials (rather than the presence of alkaline-earth cations, as one might suppose).

There is a remarkable congruency in size of the mesostructured particles shown in Fig. 9-8 and those establishing the silica sheath of biomorphs (cf. Fig. 9-6). However, despite explicit efforts, no noticeable difference between the silica particles composing the skin in the absence and in the presence of the additives could be detected (though in particular the CTAB-induced particles are clearly featured by angled edges rather than being round). The observed size consistency may simply arise due to the tendency of silica to form colloids of such dimensions under the governing physicochemical conditions in solution, regardless of the presence of additives.

The formation of these monodisperse mesoporous particles seems to be a process occurring parallel to the steps decisive for biomorph growth. In a set of control experiments, silica and additives were mixed in the absence of barium and carbonate species under otherwise identical conditions. It was found that particles as shown in Fig. 9-8 form nonetheless, with virtually identical size, structure and number (as evidenced by cryo-TEM and DLS data, not shown). Also, the kinetics of particle formation remain more or less unchanged when removing barium and carbonate ions from the mixture. These findings suggest that the formation of mesoporous particles indeed is a process uncoupled from biomorph growth.

9.4.3 Effect of Added Multivalent Cations

Precipitates isolated from mother solutions doped with lanthanum cations also exhibited morphologies quite distinct from those obtained in a regular biomorph synthesis. A gallery of typical aggregates is shown in Fig. 9-9. At first glance, it is evident that the formed structures are widely similar, if not identical, to some of the architectures found

in samples to which the surfactant CTAB was added (compare Fig. 9-9b with Fig. 9-3a). However, the floral spherulites produced in the presence of La^{3+} are on the one hand somewhat smaller (ca. 30-80 µm in diameter) than counterparts generated by CTAB (50-150 µm).

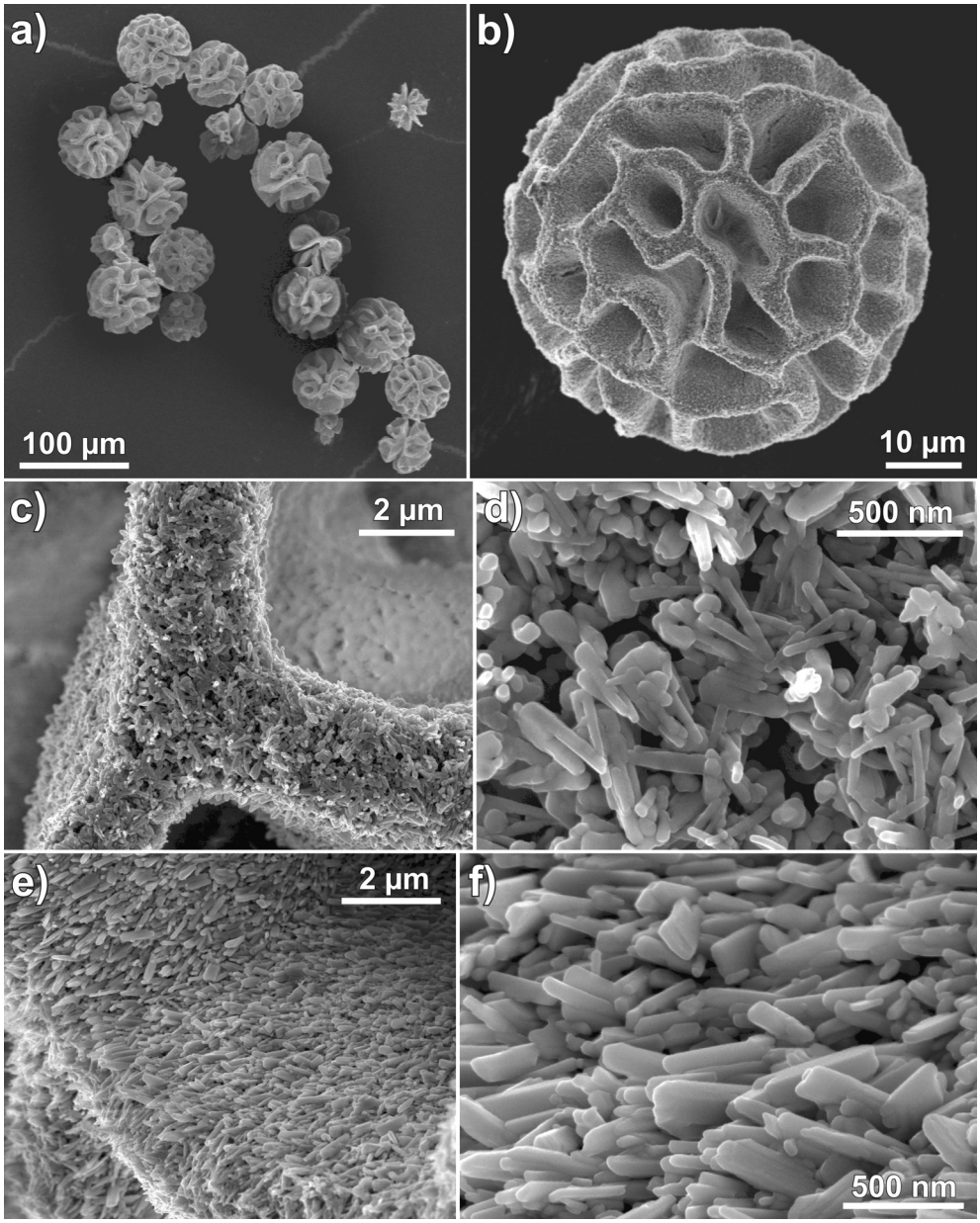

Fig. 9-9: Polycrystalline aggregates of $BaCO_3$ with floral structures prepared by adding La^{3+} cations to the conventional synthesis protocol of silica biomorphs. (a) FESEM image granting an overview on formed precipitates and illustrating that most aggregates display quite uniform morphology. (b) Close-up view of a floral spherulite. (c-d) Zooms into the aggregate shown in (b), revealing textural details of at a junction site where three different sheet-like domains meet. (e-f) Higher magnifications of the surface of a leaf-like section, disclosing numerous nanoscale crystallites with some degree of preferred orientation. [$BaCl_2$] = 5 mM, [SiO_2] = 8.9 mM, [$LaCl_3$] = 1 mM, pH = 10.4, Growth time: 7 h, T = 20°C.

On the other hand, aggregates grown by addition of La^{3+} display much higher morphological uniformity, that is, apart from certain reasonable deviations, virtually all precipitates share a spheroidal flower-like appearance (see Fig. 9-9a). Nevertheless, the striking similarity of the morphologies observed with CTAB and La^{3+} (and to some extent also with pDADMAC) strongly suggests that they originate from the same morphogenetic scenario. In turn, the floral structures obtained with $LaCl_3$ as additive differ from those shown in Fig. 9-3 and Fig. 9-4 in that they appear to be overall spherical and do not have flat bases, indicating that the aggregates did at least in most cases not grow on the walls of wells or the surface of the solution. This finding can be understood when recalling that added La^{3+} cations induced partial gelation of the silica and that many of the biomorphs developed within gelled entities. As outlined in Section 7.4.2, the growth behavior of silica biomorphs in gels is distinguished from that in solution by the universal presence of surfaces, provided by the gel matrix, which render morphogenesis less dependent on foreign interfaces. Thus, nucleation of the initial crystal seed does not have to occur necessarily on the walls, but is more or less equally favored throughout the gelled volume. Subsequent growth in the gel body may then proceed in all directions, and the aggregates can moreover evolve free from restrictions imposed by nucleation barriers, resulting in curved leaf-like domains rather than flat sheets or filaments which wind around themselves to use their own surface as substrate.

Another interesting feature worth noticing refers to the microstructure of the aggregates grown under the influence of La^{3+} ions. While the length and width of the crystallites constituting the assemblies (Fig. 9-9f) are comparable to those spotted in the core of precipitates generated with CTAB and pDADMAC (cf. Fig. 9-6), their textural arrangement agrees only partially with what has been described in Section 9.4.2.5. In fact, when investigating the surface of a leaf-like domain in the spherulites, the nanorods locally point with their long axis into a more or less common direction (presumably the actual direction of growth, Fig. 9-9e-f), in line with the behavior found for regular silica biomorphs and CTAB- or pDADMAC-induced crystal aggregates. By contrast, higher magnifications of the cross-section of these sheet-like segments reveal that the crystallites are highly disordered there and do not exhibit any kind of preferential orientation (Fig. 9-9d). This observation may be due to artefacts caused during isolation and manipulation of the precipitates, but could also indicate that the core of biomorphs is generally featured by a lesser degree of textural order. Apart from that, SEM analyses of the samples proved that the vast majority of aggregates retrieved

from La^{3+}-containing solutions did not carry a noticeable external silica skin. This appears reasonable when considering that the presence of the trivalent cations provoked ample silica polymerization and the formation of gelled sediments, due to their high charge density and thus the ability to screen electrostatic repulsions in-between siliceous species.[36] As a consequence, a great deal of the available silica is expected to be coagulated already before or during morphogenesis of the biomorphs such that, afterwards, minor amounts are present and the deposition of skins on the aggregates is markedly restricted.

9.4.4 Variation of the Ionic Strength

Addition of sodium chloride as a means to raise the ionic strength of the growth medium did at first, that is, at concentrations between 1 and 10 mM not have a significant effect on the observed morphologies. In turn, a distinct and consistent influence can be noted at higher NaCl content (see Fig. 9-10). From solutions containing 50 mM extra salt, no more sheets and helical filaments crystallized. In fact, a substantially increased amount of globular particles and variously shaped, colony-like clusters of interpenetrating spheroids were observed. Frequently, worms were seen to emerge from these clusters and grow to lengths of often more than 100 μm (Fig. 9-10a). Strikingly, none of the characteristic polycrystalline morphologies formed in the experiments when ≥ 100 mM NaCl were added to the mother solution. Instead, exclusively globular architectures were found after growth was completed (Fig. 9-10b), with typical morphologies reminiscent of the shape of raspberries or cauliflower (Fig. 9-10c and e).

Indeed, such fractal architectures occur also during the formation of silica biomorphs in the absence of additives.[41] However, they are usually less developed in this case, mostly consisting of single or twinned spheroids which sometimes are not even closed and rather display dumbbell-like morphologies (cf. Fig. 7-3, in particular panels a-d). Further, the fractal precursors observed under “standard” conditions are commonly much smaller (5-20 μm) than the particles obtained at high ionic strength (> 100 μm). Fairly akin dendritic cauliflower-like crystal forms were moreover reported to yield from $BaCO_3$ precipitation in silica-rich solutions at lower pH (9.3-10), though again with appreciably smaller sizes (~30 μm in diameter).[13] As already stated above, these structures arise due to the poisoning effect of silicate oligomers and polymers on carbonate crystal growth, which causes a single crystal core to split into a radiating

array of fibers that, subsequently, branch by themselves at non-crystallographic angles and thus undergo continuous bifurcation. Likely, this scenario accounts for the morphologies retrieved from syntheses at elevated NaCl content as well. This is supported by close-up views of the surface of the spheroids (Fig. 9-10d and f), which reveal myriads of nanoscale projections and hence suggest a large degree of branching. These subunits are hairy (or spiny in some cases) and consequently to a certain extent distinct from the thicker rod-like crystallites making up the core of typical polycrystalline forms (see for example Fig. 9-9f).

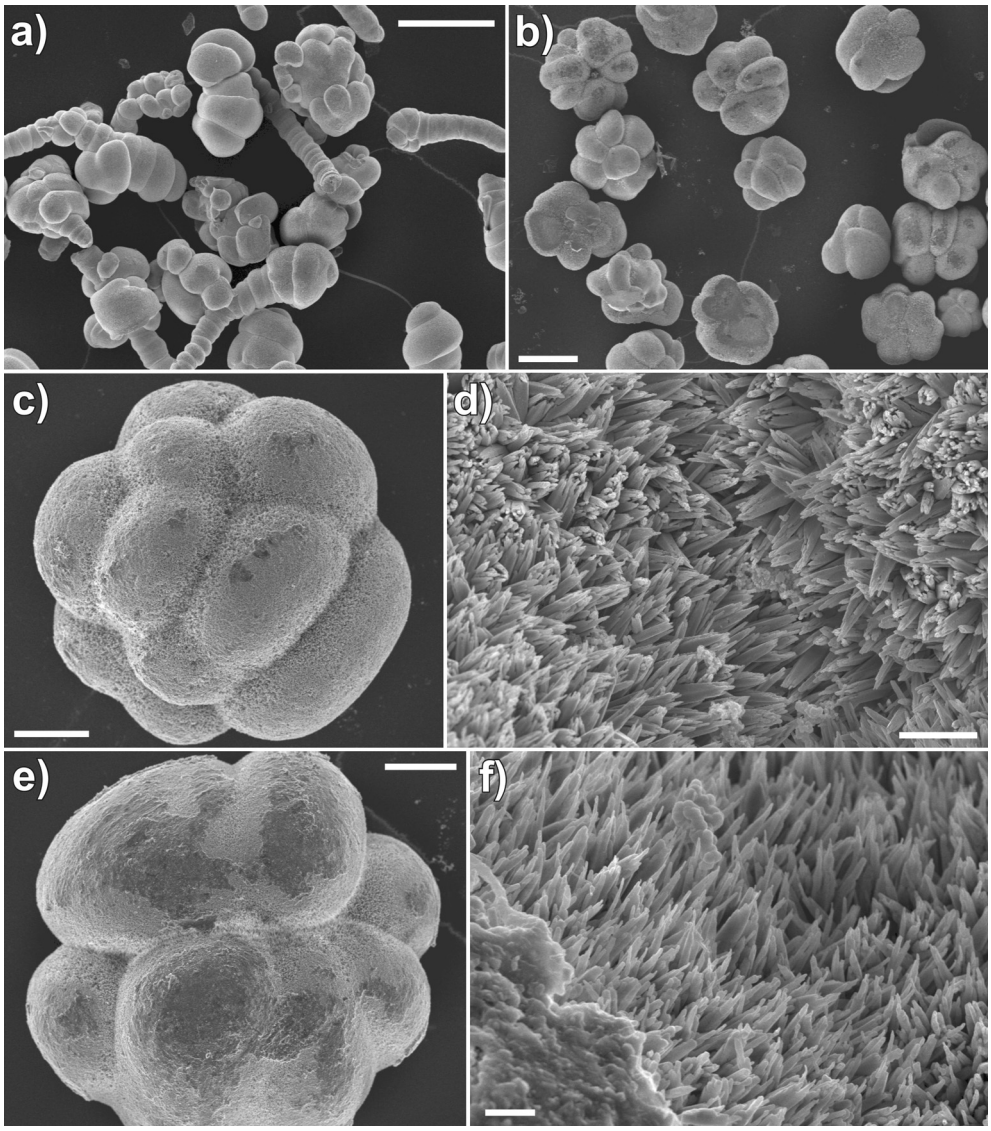

Fig. 9-10: Biomorphic crystal architectures generated from Ba^{2+}-containing alkaline silica sols to which (a) 50, (b-d) 250, and (e-f) 500 mM NaCl were added. [$BaCl_2$] = 5 mM, [SiO_2] = 8.9 mM, pH = 11, Growth time: (a) 12 h, (b-d) 15 h, (e-f) 20 h, T = 20°C. Scale bars: (a) 100 µm, (b) 100 µm, (c) 30 µm, (d) 3 µm, (e) 30 µm, and (f) 1 µm.

Essentially, the presence of high amounts of salt prevents fibrillation of the branched, but still single-crystal front and the transition into a growth mode based on the perpetual production and incorporation of individual building blocks. Therefore, the system responds to proceeding CO_2 diffusion and carbonate precipitation by continuing non-crystallographic branching such that, eventually, the fractal architectures grow to markedly larger dimensions.

9.4.5 Composition of Additive-Induced Morphologies

The crystal structure and elemental composition of the morphologies prepared with the different additives was investigated by means of X-ray diffraction (XRD) and energy-dispersive X-ray (EDX) analysis. For the former technique, suitable and representative specimens were selected, mounted individually in the setup and diffraction images were collected while rotating the sample. For EDX studies, a collection of biomorphs were ground and subsequently pressed to give a flat layer on the SEM stub. This preparation procedure was applied to ensure accurate quantitative EDX analysis, avoiding erroneous effects caused by locally varying sample height. Fig. 9-11 and Fig. 9-12 provide typical EDX spectra of flower-like aggregates obtained with CTAB/pDADMAC, floral structures grown with $LaCl_3$, and fractal spheroids produced at high NaCl content, together with XRD patterns for each sample type.

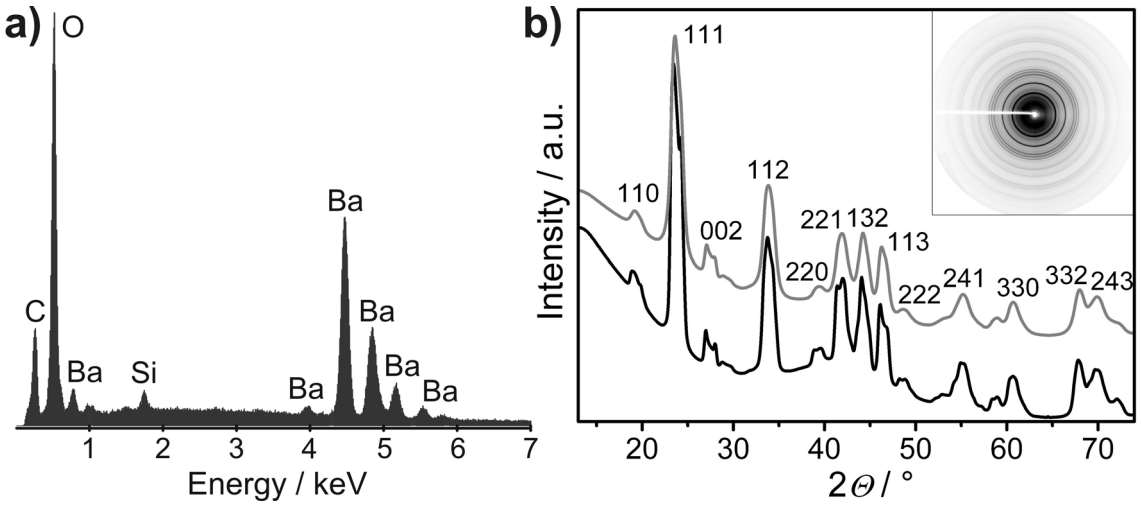

Fig. 9-11: (a) EDX spectrum of flower-like spherulites grown in the presence of pDADMAC (cf. Fig. 9-4). (b) X-ray diffraction data acquired from single floral spherulites produced with pDADMAC (grey) and CTAB (black), confirming the witherite crystal lattice (corresponding Miller indices are outlined above the peaks). The shown diffractograms were calculated by averaging over all angles in the original diffraction image (see inset).

The XRD data prove the presence of crystalline aragonite-type barium carbonate (witherite structure) inside the samples. Furthermore, the diffraction images of the flower-like architectures shown in Fig. 9-3, Fig. 9-4, and Fig. 9-9 display complete rings rather than discrete reflections or arcs (see insets in Fig. 9-11b and Fig. 9-12b). This indicates that the aggregates consist of multiple crystallites whose orientation must be isotropic in average throughout the assembly, as opposed to previous results on sheet-like silica-witherite biomorphs which revealed to some degree preferred orientation of the crystallites within whole aggregates.[16] These discrepancies can be ascribed to the different biomorph fractions sampled by the beam during XRD measurements. In particular, the floral structures consist of several (intergrown) sheets with distinct orientations within the aggregate, which leads to multiple overlapping patterns caused by individual sheets, giving rise to powder-like diffraction images. Indeed, local orientational ordering of the crystallites is also observed in biomorphs grown in the presence of additives (cf. Fig. 9-6 and Fig. 9-9), though the length scale of that ordering is comparably small.

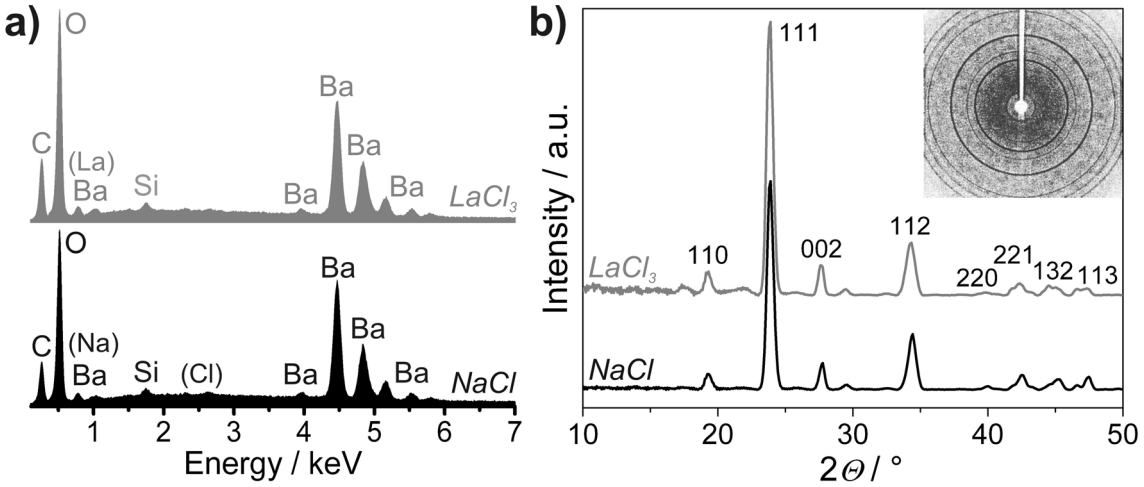

Fig. 9-12: (a) EDX spectra and (b) XRD patterns of individual crystal architectures formed from solutions containing 500 mM NaCl and 1 mM $LaCl_3$, respectively. Theoretical peak positions of added elements are indicated in brackets, as they do not show noticeably increased counts. The 2-D diffraction image shown as inset in (b) corresponds to the $LaCl_3$ sample and corroborates that the precipitates are polycrystalline aggregates. The occurrence of full diffraction rings implies that the sampled volume comprised crystallites arranged in all directions of space.

The EDX data confirm the presence of barium carbonate, and further identify certain amounts of silica in the precipitates. Quantitative elemental analysis averaged over several independent positions in the samples yielded the aggregate compositions listed

in Table 9-1. The Si content of the aggregates was determined to be 13.4, 7.6, 3.8 and 3.4% relative to the Ba atomic count for typical morphologies obtained with CTAB, pDADMAC, NaCl and $LaCl_3$, respectively. Previous studies on the Si/Ba ratio in silica biomorphs led to a diverse range of values, depending on the type of morphology as well as on the investigated position within an aggregate. For instance, Si/Ba percentages of 15-29 % were reported for biomorph helices, while 6-35 % was found for worms.[14,30] Coralline $CaCO_3$ biomorphs were claimed to contain 35-40 % Si relative to Ca.[23] However, as all these analyses were performed on intact biomorphic architectures rather than ground and pressed powders, it is hardly possible to directly compare the present results to those reported in earlier work. Further, the composite nature of biomorphs with their frequently occurring outer silica skin calls direct EDX studies on intact architectures into question, considering the limited penetration depth of the method.

Additive	C (K)	O (K)	Si (K)	Ba (L)	Si/Ba	Na (K)	Cl (K)	La (M)
CTAB	34.73	45.16	2.37	17.73	0.134	n.d.	n.d.	n.d.
pDADMAC	37.64	45.13	1.22	16.02	0.076	n.d.	n.d.	n.d.
NaCl	26.99	52.41	0.73	19.30	0.038	0.34	0.25	n.d.
$LaCl_3$	32.63	48.11	0.65	17.92	0.036	0.36	0.15	0.19

Table 9-1: Elemental compositions (in at%) and the silicon-barium atomic ratio of flower-like aggregates grown in the presence of 1 mM CTAB or pDADMAC, raspberry-shaped fractal architectures obtained at 500 mM NaCl, and a floral spherulite produced with 1 mM $LaCl_3$. Carbon, oxygen, silicon, sodium and chlorine contents were calculated based on the K edge, while the L and M edge was used for barium and lanthanum, respectively. Values for the fractions of C and O are less reliable due to background contributions.

In any case, the traced trends in the silica content of the aggregates agree reasonably well with observations made by optical and electron microscopy. Within the limits of error, the amount of silica detected in flower-like morphologies grown with the aid of CTAB and pDADMAC is comparable to values measured for mature biomorphs formed without any additives (see Section 6.4.5). FESEM analyses have yet suggested that the number of CTAB- and pDADMAC-induced aggregates carrying an external silica skin is somewhat lower than when biomorphs are synthesized in the absence of additives. This apparent inconsistency is attributed to a possibly interfering influence of the applied washing procedure and the fact that the samples discussed in Section 6.4.5 were prepared with a different lot of water glass than those described here. Thus, it seems plausible to assume that addition of the surfactant and the polymer led to slight decrease

in the amount of silica incorporated to the evolving crystal aggregates. When La^{3+} cations are introduced to the system, the final silica content in the precipitates is in turn clearly reduced. This is well in line with FESEM images, where a distinct layer of amorphous silica could never be discerned (cf. Fig. 9-9). The Si/Ba atomic ratio determined for the fractal architectures retrieved at high ionic strength is equally low. This finding corroborates the notion that poisoning of silica does not implicate marked integration of the siliceous species into the split crystal, as evidenced also by the data collected for the fractal precursors of biomorphs in regular syntheses (see Section 6.4.5) and values reported in literature.[30]

It is worth emphasizing that none of the studied additives is incorporated to a noticeable degree into the forming aggregates. In the case of CTAB and pDADMAC, EDX spectra verify the absence of nitrogen peaks, although particular efforts were made to look for them during the analyses. Additional IR measurements confirm this finding, as all detected bands can be assigned to either silica or carbonate and no organic vibrations were observed (data not shown). Samples prepared with $LaCl_3$ and NaCl as additive do likewise not show significantly increased counts of La, Na and Cl in the EDX data. Indeed, quantitative evaluations assign non-zero fractions to all three elements, but the calculated values are generally only slightly above or even below the detection limit of the technique (~0.2 wt%). For instance, more or less equal percentages of Na and Cl were obtained for the precipitates grown in the presence of 500 mM NaCl and 1 mM $LaCl_3$ (cf. Table 9-1), despite the drastically higher concentrations of both ions in the former system. These results suggest that the added species do not interact directly with the crystallizing carbonate phase (which constitutes the major component in the final aggregates), but rather affect the growth process indirectly by influencing the silica in solution. The latter scenario would further imply that the interactions between the additives and dissolved silica do not rest upon an effective binding (which would lead to certain amounts of the additives in the silica skins), or that the silica to which the added species bind is not co-precipitated with the forming biomorphs.

9.4.6 Growth at High Barium Concentrations

Apart from introducing appropriate additives, the morphology of silica biomorphs can also be intimately modified by varying intrinsic parameters of the regular synthesis protocol. When, for example, the concentration of barium ions present during growth is increased beyond a certain threshold, common forms are replaced by highly delicate

ultrastructures, as visualized by the images reproduced in Fig. 9-13. The isolated biomorphs are open and more or less perfectly spherical architectures, which consist of a network of interpenetrating sheet-like domains.

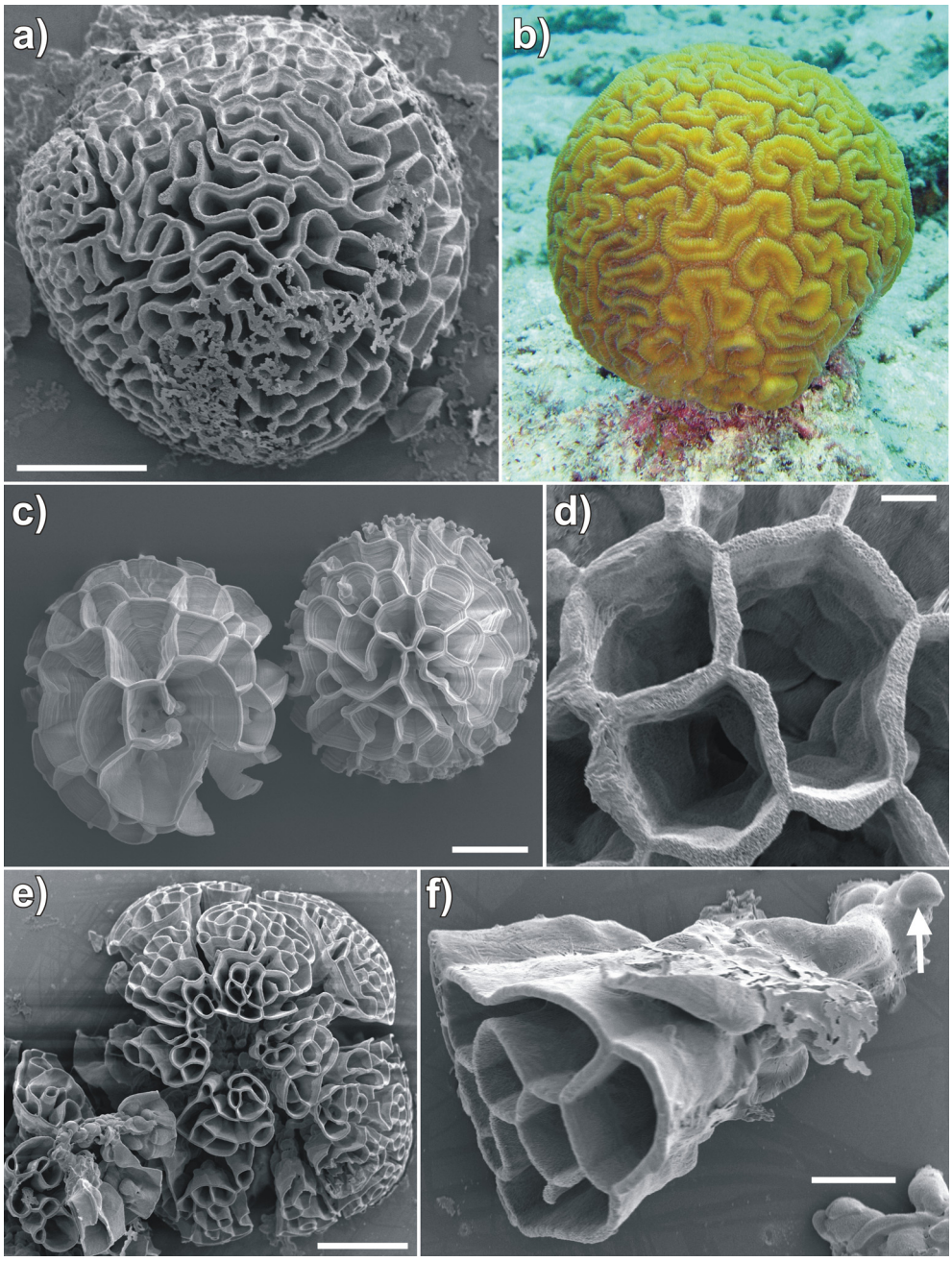

Fig. 9-13: Coral-like forms (a, e, f) and floral spherulites (c-d) synthesized in the absence of additives at high barium concentration. (b) is a photograph of a living brain coral in its marine environment.[44] The arrow in (f) indicates the globular clusters from which the cone-shaped aggregates seems to emerge. [$BaCl_2$] = 250 mM, [SiO_2] = 8.9 mM, pH = 10.5, Growth time: 10-15 h, T = 20°C. Scale bars: (a) 50 µm, (c) 50 µm, (d) 10 µm, (e) 100 µm, and (f) 20 µm.

Overall, the observed shapes are widely similar but nevertheless exhibit slight differences, which suggest a classification into three distinct types of morphology. The

first class represents fairly large spherulitic aggregates (diameters of 100 to more than 200 μm) which are featured by rather elongate and randomly shaped voids separated by walls of about 5 μm in thickness (Fig. 9-13a). These architectures have a coral-like appearance and thus, when compared to suitable (though magnitudes larger) living organisms (Fig. 9-13a), nicely illustrate the capability of silica biomorphs to imitate forms actually innate to the animate nature. The second group of morphologies encountered at high Ba concentration are floral spherulites (Fig. 9-13c) resembling those produced at 1 mM CTAB (Fig. 9-3) or $LaCl_3$ (Fig. 9-9), and aggregates reported previously for syntheses conducted at 500 mM Ba^{2+}.[19] Here, the voids characterizing the structure are generally wider and not as elongate as in case of the coral-like forms, while their walls tend to be slightly thinner. In fact, the surface of the aggregates can be described by relatively regular adjacent holes with a more ore less rectangular shape (Fig. 9-13d). The mean diameter of this kind of morphology ranges from around 50 to 150 μm, which complies with sizes found for CTAB counterparts but is yet notably smaller than the dimensions of typical coral-like aggregates. Finally, a third class can be noted which is distinguished by the large size of corresponding architectures (up to 500 μm) and the fact that the morphologies are no longer uniformly spherical (Fig. 9-13e). Rather, the ultrastructure is composed of several cone-like subunits (Fig. 9-13f), which appear to be connected to each other at their apexes in the center of the aggregate. This arrangement results in small voids inside the cones, whereas larger cavities exist in-between the different segments. Detailed FESEM analyses moreover showed that the bottom sides of the spherulites generated at 250 mM Ba^{2+} are generally flat (Fig. 9-14). In combination with observations made by light microscopy, this confirms that these biomorphs grew in contact with the walls of the wells, in line with the behavior found for aggregates formed in the presence of CTAB. It is interesting to note that the number of aggregates isolated at high barium content was not noticeably greater than at lower concentrations. Indeed, even less particles were counted, all being relatively huge in size. This may be ascribed to the decreased starting pH of the system, which could cause low levels of supersaturation at the beginning of the experiments, such that less seeds are nucleated which then grow to large dimensions. Close inspection of the architectures moreover suggests that morphogenesis of these peculiar forms involves, in analogy to the mechanism proposed to account for the formation of biomorphs under regular conditions,[41] an initial stage of non-crystallographic branching

of a single-crystal core. The latter is likely to be situated in the core of the floral structures (see arrow in Fig. 9-14), or at the apex of the cones (Fig. 9-13f).

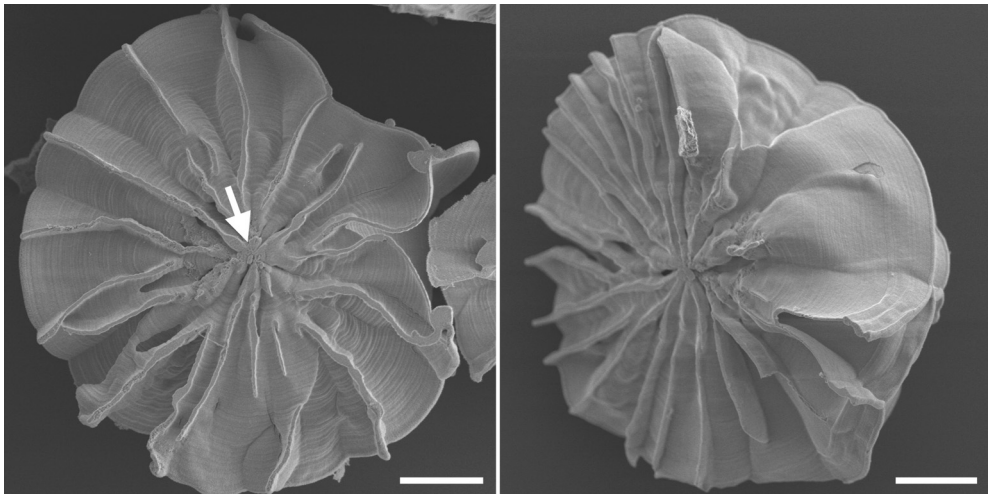

Fig. 9-14: Bottom views of floral spherulites grown at 250 mM Ba^{2+}. The arrow points to the core of the architecture, where the initial crystal seed is suspected. Scale bars: 30 μm.

9.4.7 Influence of Temperature

Further intriguing alterations of aggregate morphology can be provoked when the temperature at which growth occurs is incremented, under otherwise unchanged conditions. In the following, observations made for syntheses conducted at 50°C will be summarized exemplarily, although additional and again fundamentally different crystal architectures can be obtained at higher temperatures, as described in detail elsewhere.[30,45]

Generally, the morphologies characterizing silica biomorphs grown from solution at ambient temperature (i.e. helicoids, worms, and flat sheets) prove to be fully absent when the mixtures are heated. Instead, a broad variety of novel shapes lacking any sort of crystallographic symmetry are generated. Many of the precipitates isolated after growth at 50°C exhibit cup- or trumpet-like forms (Fig. 9-15). These include rather small and hollow chalice-like morphologies (typically 5-20 μm in length) which usually display convex curvature (Fig. 9-15a) and often reveal circular ring patterns on their surface (Fig. 9-15b). When growing further, the cups appear to transform into trumpets that eventually reach dimensions far beyond 100 μm (Fig. 9-15c-h) and, on occasion, exhibit concave curvature (Fig. 9-15c-d). Both the trumpet- and chalice-like architectures can be symmetric (cf. Fig. 9-15c-e) or, at some point, grow preferentially along a certain segment of their rim (cf. Fig. 9-15b and f-h).

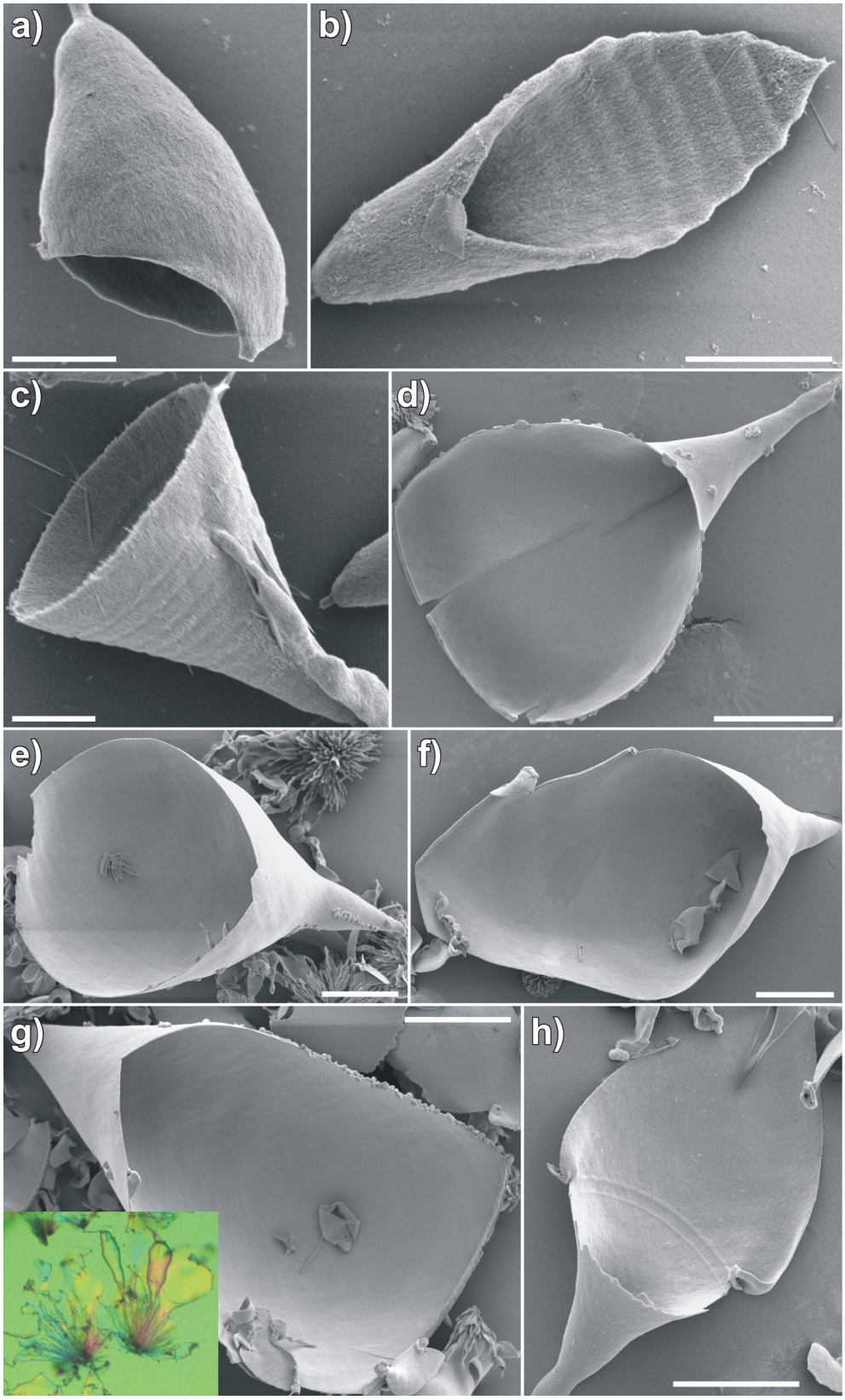

Fig. 9-15: Chalice- and trumpet-like morphologies (both symmetric and asymmetric) obtained at a synthesis temperature of 50°C. The arrow in (h) indicates banding on the rim of an initially symmetric trumpet, which subsequently began to grow asymmetrically. [$BaCl_2$] = 5 mM, [SiO_2] = 8.9 mM, pH = 11, Growth time: 5 h. Scale bars: (a-c) 5 µm, (d-g) 50 µm, and (h) 30 µm.

This leads to the emergence of frequently sinuous sheet-like outgrowths, which ultimately form a cusp on their perimeter. These cusps happen to be located in the middle axis defined by the narrow cone from which the trumpets arose (Fig. 9-15b and h), but can likewise be situated elsewhere around the rim and thus impart the appearance of an asymmetrically rolled-up sheet of paper to the aggregate (Fig. 9-15g). In some cases, the transition from a symmetric trumpet into such asymmetric structures seems to be accompanied by ring-shaped bumps on the surface relief (indicated by the arrow in Fig. 9-15h).

The microstructure of these architectures is hallmarked by reams of nanocrystals which are densely packed so that individuals can hardly be recognized (Fig. 9-16). The size and shape of the building units appear to be less uniform than in aggregates formed at 20°C. In general, the crystallites are not as clearly featured by the classical rod-like form of $BaCO_3$. Typical dimensions range from 100-200 nm in length and 20-50 nm in width.

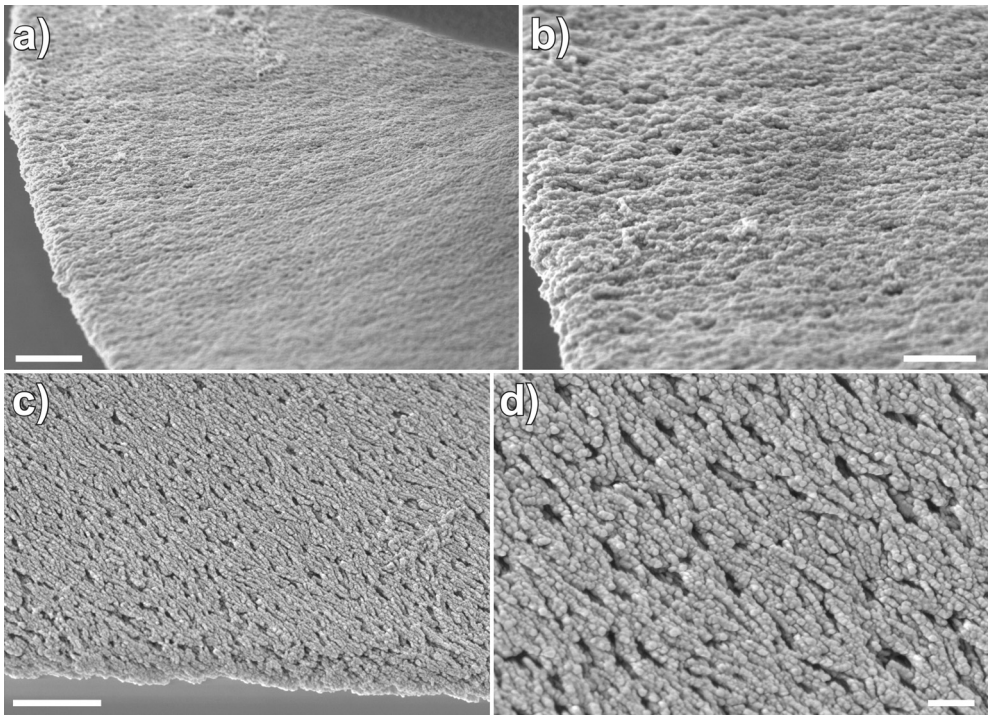

Fig. 9-16: High-magnification FESEM images of cup- and trumpet-like aggregates grown at 50°C, revealing the texture of the carbonate assembly. Scale bars: (a) 1 µm, (b) 500 nm, (c) 1 µm, and (d) 200 nm.

Indeed, some degree of orientational order is evident from the images, but the alignment of the crystallites is relatively poor. The observed texture may be described as a kind of disordered herringbone pattern. Moreover, the walls of the cups are about 300-600 nm thick and therefore much thinner than the sheets formed at 20°C (cf. Section 7.4.2).

A second type of morphology often seen at 50°C are floral-like biomorphs (Fig. 9-17). These aggregates adopt overall predominantly spherical shapes (cf. Fig. 9-17a and c), as observed in experiments with the additives CTAB, pDADMAC and $LaCl_3$ as well as at higher barium concentrations. However, there are also non-symmetrical aggregates (Fig. 9-17b) and the architectures tend to be smaller, rarely reaching diameters of more than 50 μm.

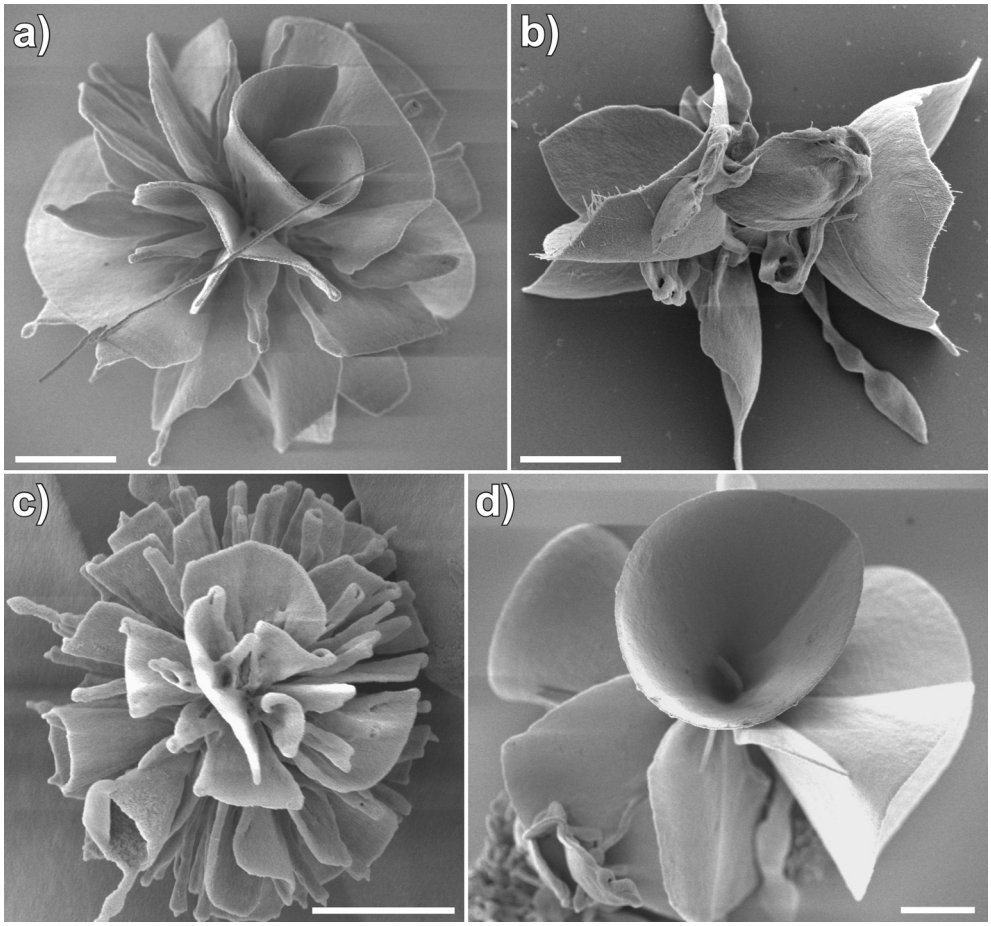

Fig. 9-17: Flower-like silica biomorphs isolated along with cup- and trumpet-like forms from experiments conducted at 50°C. [$BaCl_2$] = 5 mM, [SiO_2] = 8.9 mM, pH = 11, Growth time: 5 h. Scale bars: 10 μm.

Apart from that, floral structures produced at 50°C clearly display a higher diversity of shapes than those synthesized with the additives or by increasing the concentration of Ba^{2+}. Generally, the morphologies are more open and seem to consist of widely separate laminar subunits, all of which sprout from a common origin. These subunits can be single sheets with curvatures ranging from slightly sinuous over bent to heavily curled or scrolled (Fig. 9-17a and c), or individual cups and trumpets (Fig. 9-17b and d).

As a third and final class of structures, crystallization at 50°C furnished spherulitic aggregates composed of narrow elongate strings radiating outwards from the growth

center, which closely resemble the anemone-like morphologies described as a by-product of floral architectures in the presence of CTAB (see Section 9.4.2.1 and Fig. 9-3b). Fig. 9-18a shows such a spheroid; it consists of two almost identical hemispheres that broke apart as they were connected only at a single central point. A closer look at the emanating projections reveals occasional, though not frequent branching.

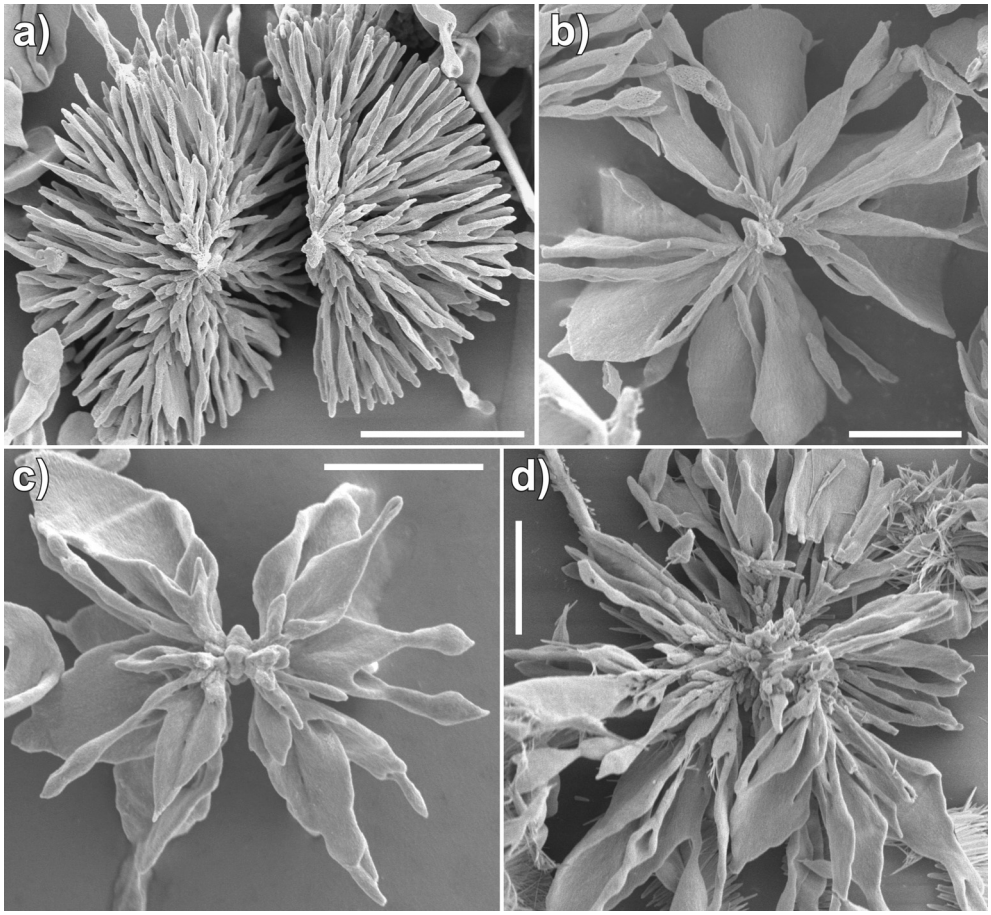

Fig. 9-18: Precursor and intermediate structures during the development of floral architectures at 50°C. Scale bars: (a) 20 µm, and (b-d) 10 µm.

Interestingly, there were further intermediate morphologies observed at 50°C in which multiple string-like projections can still be recognized, but are apparently extended in width, mutually bridged, or decorated at their tips by sheet-like excrescences (Fig. 9-18b-d). This indicates that fractal architectures as seen in Fig. 9-18a are precursors of the more complex floral superstructures, which is supported by an approximate congruency in size between these forms.

9.5 Discussion

The collected data have evidenced that the range of morphologies accessible with silica biomorphs can be appreciably extended by simple means such as introducing suitable additives or changing experimental conditions for example in terms of reactant concentrations or the synthesis temperature. This is clearly of interest from the viewpoint of materials science. However, for a concerted design of novel shapes, the influence of a chosen additive or varied parameter must be understood on a mechanistic basis. Therefore, some ideas on possible morphogenetic scenarios shall be discussed in the following.

When sufficient amounts of sodium chloride were added to the mother solution, the growth process was found to be arrested at the end of the fractal stage, such that merely dendritic cauliflower-like architectures were obtained. Apparently, fibrillation and chemically coupled co-precipitation were not possible under these circumstances. In principle, high ionic strength is expected to screen electrostatic repulsions in-between negatively charged silicate species and thereby favor condensation reactions.[36] This implies that the speciation of silica will shift towards higher oligomers and polymers in the system, which becomes manifest in a clouding of the mixtures as colloidal silica particles are generated and start to precipitate. These colloids may consist of pure silica or, especially at higher NaCl content, also of sodium silicate or mixed sodium/barium silicates. Decreasing the pH is known to have a related effect on the distribution of silicate species in solution and, in fact, similar growth behavior was reported for silica biomorphs in less alkaline environments.[13] Possibly, enhanced oligomerization at higher salinity prevents the pH-based coupling from being initiated by reducing the effective concentrations of available silicate monomers (and dimers) – provided that the latter are the active species in the interplay. This is in line with studies performed on the crystallization of $BaCO_3$ in the presence of lowered amounts of silica, which likewise gave only globular architectures.[30] A second feasible explanation refers to the supply of the system with carbonate ions. As mentioned already in Section 9.3.2, high ionic strengths depress the rate of CO_2 uptake by the solutions due to a decrease of its solubility in water.[38] It seems likely that coupled co-precipitation premises a constantly high concentration of carbonate species to be present during mineralization. This criterion may not be met in media of elevated salinity, and could furthermore be one of the reasons for the growth behavior traced at low pH.[46] Finally, the occurrence of increased concentrations of different ions might affect directly the development of the

carbonate crystals in time and space, for example by adsorption on specific planes. Poisoning of growth and the observed branching of crystal seeds may not only be directed by silicate oligomers, but can in principle be induced in an analogical manner by any other sort of “impurity”, such as simple ions like Na^+, Cl^-, or also HCO_3^-. However, since the structures obtained at high NaCl content closely resemble those found at low pH, a distinct effect of the added ions on the branching pattern can probably be excluded. Beyond that, the absence of increased counts of Na and Cl in the EDX spectra of the precipitates renders adsorption of the ions on or in the witherite lattice and a corresponding influence on relative growth rates unlikely. This applies equally well for the other additives investigated.

The presence of CTAB, pDADMAC and La^{3+} cations in the reaction mixtures had a comparable bearing on the generated morphologies. Relative to sodium chloride, where at least 50 mM were required to provoke noticeable changes, these additives operate in an effective fashion already at much lower concentrations and a content of around 1 mM was confirmed to be ideal to achieve distinct beautiful structures. In fact, a clear shift in the morphology of the aggregates from helices and worms in experiments without additives to predominantly flower-like forms at 1 mM was verified. Despite this variation in global shape on the multi-μm scale, the typical mesoscale texture of the biomorphs apparently remained widely unaltered, with single elongated witherite nanocrystallites describing a more or less strictly ordered orientational field throughout the assemblies. On occasion, the aggregates produced with CTAB and pDADMAC were sheathed by an outer siliceous skin, yet by trend less frequently than counterparts grown in the absence of additives, whereas the architectures formed on addition of $LaCl_3$ did hardly ever carry such skins. The morphologies obtained from syntheses at elevated temperature as well as high barium concentration in general seem to fall into the same category, that is, spherulites with floral appearance were often isolated from the batches. Admittedly, there are certain profound differences in the detailed shape, curvature and arrangement of sheet-like domains in the ultrastructures compared to the additive-induced aggregates, as is most evident from the coral- and trumpet- or cup-like forms occurring at 250 mM Ba^{2+} and 50°C, respectively. Nevertheless, it may be assumed that all these architectures have a related physical origin.

Based on the existing data, the phenomenology and mechanism of growth under the various conditions can most readily be explained for the case of increased temperature

(see Fig. 9-19). As stated in Section 9.4.7 and illustrated by Fig. 9-18c, open fractal spherulites lacking any characteristic floral features were frequently observed in the experiments, which are judged to be ancestors of the flower-like morphologies. The formation of biomorphs at 50°C thus seems to start from a micron-sized crystal seed (Fig. 9-19a) located in the center of the later spherulites, which becomes subject to splitting at both ends and develops daughter generations of fibers that continue branching at non-crystallographic angles (Fig. 9-19b).

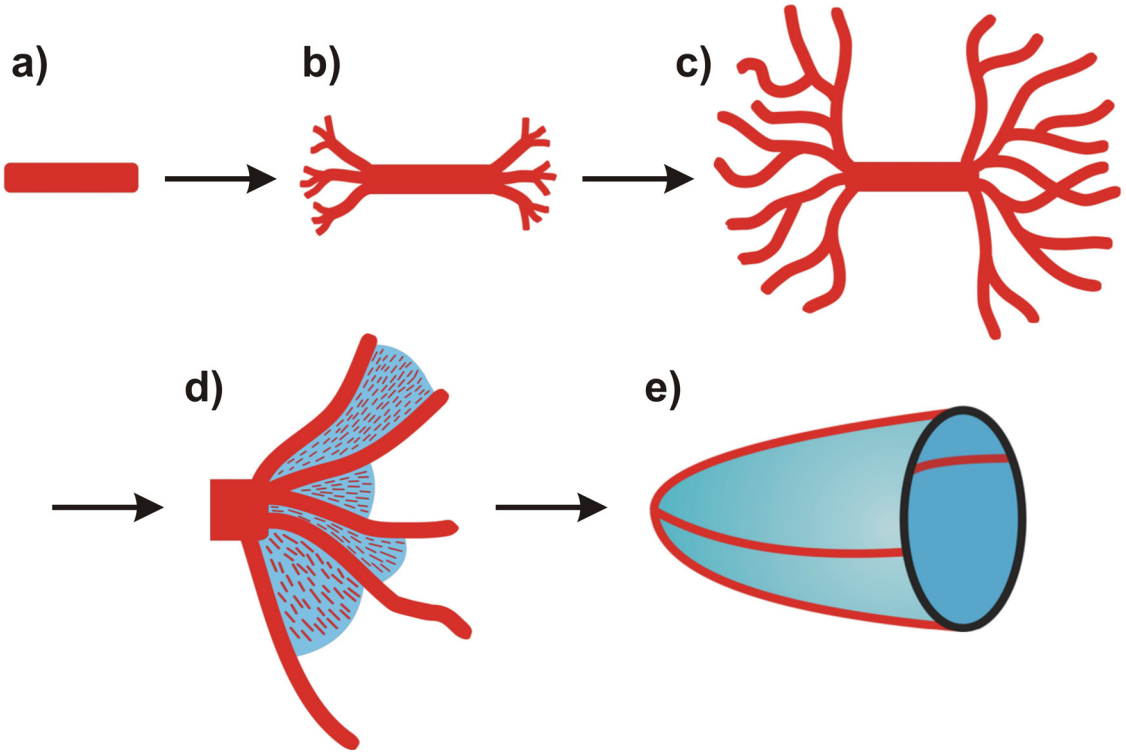

Fig. 9-19: Scheme depicting the envisaged growth mechanism at 50°C. (a) First, a classical elongated $BaCO_3$ crystal seed is nucleated and grows. (b) Fractal branching is initiated at both ends of the crystal. (c) A rather small number of comparably thick projections emerge from the initial crystal exhibiting a distinct branching pattern. (d) Lamellar polycrystalline growth occurs in-between the branches of the fractal aggregate, leading to sheet-like linkages. (e) Depending on the relative orientation of branches, the connecting sheets give rise to architectures with curved surfaces like cups (red lines represent the branches of the initial fractal crystal) and floral aggregates.

Thereby, a self-similar branching process is initiated, driven by crystal poisoning due to silica oligomers and causing fractal patterns as depicted in Fig. 9-19c. To this point, morphogenesis thus proceeds in the same manner as proposed for growth under ambient conditions.[41] At elevated temperature, successive splitting does however neither lead to dense structures nor to closed spheres. Rather, open architectures emerge, as branching occurs less frequently and at different, that is, significantly larger angles than observed

during the early stages at room temperature. This results in the formation of a smaller number of considerably thicker and well separated fibers. As crystal growth and splitting take place primarily on both ends of the rod-like seed, open dumbbell-shaped morphologies often characterize immature aggregates. At this stage, the precipitates consequently happen to display some sort of mirror symmetry (cf. Fig. 9-18c and Fig. 9-19c). Another significant difference between the fractal aggregates observed at 50°C and those found at 20°C is their typical size, the former (~50 μm) being notably bigger than the latter (~5 μm). In this regard, changes in the development of the crystal architectures during the early stages of growth at 50°C may derive from the effect of temperature on the kinetics of both carbonate crystallization and silica polymerization. Generally, the solubility of barium carbonate decreases with temperature,[37] while the rate of silica condensation processes commonly increases.[47] This means that both carbonate crystallization and silica polymerization should be faster at 50°C. In turn, it is obvious that the poisoning influence of silica on carbonate crystal growth becomes less pronounced when the temperature is raised. A straightforward explanation for the traced growth behavior would thus be that accelerated carbonate crystallization is the determining factor simply by leaving less time for the silica to intervene. In this case, regular crystal growth would compete more and more with fractal branching. On the other hand, enhanced silica condensation under these conditions implicates a different solution speciation than at room temperature, which could likewise readily account for a modified poisoning action of the silica towards less branched structures, as observed.

Nonetheless, growth is not restricted to such fractal shapes at 50°C, in contrast to the samples at high NaCl content. The transition to a stage where silica-stabilized nanocrystals are continuously produced and mineralized takes place in this case, though the volume fraction of polycrystalline segments decreases significantly as compared to that of the fractal precursors (which are notably bigger than at room temperature). This is most likely due to the fact that silica needs more time to effectively abandon the fractal route on a relative scale, so that less material is left for the polycrystalline route. The development of sheet-like domains occurs at first in-between the branched projections (Fig. 9-19d), thereby closing the gaps between neighboring fibers. This could be induced by lateral growth of single members, which ends in fusion and may be driven by a slow turnover of high to low line energy, given that the tips of the projections represent a short growth front whereas the laminar sections have a much longer boundary. Such a scenario would suggest changes in the chemical affinity of the

growing edge for the mother solution. In any case, depending on the number as well as the relative position and orientation of the different branches, surfaces with various curvatures are generated. Cross-linking of multiple projections can finally trigger morphogenesis of forms like cups (Fig. 9-19e) or floral spherulites. On that basis, the mirror symmetry displayed by some of the aggregates (Fig. 9-18c) and the initial absence of growth along the mirror plane can also be understood. Sheet-like outgrowths from the branched projections of the seed crystal develop first on both sides of the plane, before continued crystallization yields more or less space-filling spherulitic structures as those shown in Fig. 9-17.

The most important implication of the above considerations is that the final morphology adopted by silica biomorphs in experiments at 50°C relies on the detailed way in which the seed crystal is branched and, essentially, the geometry of the resulting fractal architecture. In this sense, since the crystal aggregates obtained with CTAB, pDADMAC, $LaCl_3$ and high barium concentration exhibit similar shapes, the influence of the additives and the excess Ba^{2+} ions has to be discussed primarily with respect to their role in the branching process.

Addition of La^{3+} cations and raising the Ba^{2+} content are expected to have a related effect, as in both cases the amount of multivalent cations present in the system is increased. Certainly, the Ba^{2+} concentration will also determine the actual supersaturation of $BaCO_3$, together with the flow of CO_2 into the solution. However, given that the number of crystal aggregates formed at 250 mM Ba^{2+} does not markedly exceed the frequency of biomorphs at 5 mM, it can be assumed that a considerable fraction of the cations is not involved in crystallization and rather acts as dissolved, additive-like species. Multivalent cations are known to be much more efficient agents in the coagulation of silica sols than simple salts like NaCl, as they can bridge negatively charged colloids instead of merely shortening the Debye screening length.[36] This explains why the presence of only 1 mM La^{3+} already provoked partial gelation, whereas more than 100 mM NaCl were necessary for a notable clouding of the solutions to occur. It is worth noting that lanthanum (and to a minor degree also barium) ions will not prevail in their triply (or doubly) charged state in the alkaline media. In fact, such cations tend to form complexes with hydroxide (or in the present case potentially also carbonate and silicate) ions at high pH, which reduces their effective charge.[48] Nevertheless, the observed macroscopic behavior of the samples strongly suggests that

the distribution of silica will substantially shift to higher oligomers when La^{3+} is added or the concentration of Ba^{2+} is incremented. In the case of $LaCl_3$, there should be no drastic changes in the rate of carbonate crystallization, given that the overall ionic strength is only slightly increased and no significant adsorption of La^{3+} ions in the witherite lattice could be detected (which may inhibit growth[49]). Therefore, modified branching characteristics can only arise as a consequence of the altered speciation of silica under these conditions. This holds true also for the samples at elevated Ba^{2+} content. In principle, one may suspect that the higher Ba^{2+} concentration raises the supersaturation and thus fuels crystallization. However, the presence of 250 mM $BaCl_2$ implies as well that the salinity of the system is dramatically increased, which will hamper CO_2 uptake as described for NaCl. On this account, and clearly also because of the lower pH, the rate of crystallization and the final amount of precipitates are not enhanced in this case, rendering different properties of the silica in solution the only reasonable explanation for the experimental findings. It should be emphasized that the decrease in the initial pH of the mixtures brought about by addition of $LaCl_3$ and excess $BaCl_2$ is not alone responsible for the discerned morphological variations. As already mentioned, low pH usually entails the formation of cauliflower-like fractal dendrites rather than floral structures.

Taken together, the above argumentation leads to the conclusion that added trivalent cations and excess divalent Ba^{2+} ions influence the growth process predominantly by changing the speciation of silica in solution, which in turn affects non-crystallographic branching during the first stage of morphogenesis presumably promoting open fractal architectures. In this yet still theoretical model, the resulting separate projections subsequently become interconnected by sheet-like domains, eventually giving rise to the found flower- or coral-like morphologies. Interestingly, such a scenario would furthermore rationalize previous observations made for the crystallization of calcium carbonate in silica-containing environments. Indeed, biomorphic forms could be generated when the formation of aragonite was favored, but only coral-like and no helicoidal or worm-shaped aggregates were obtained.[23,24] Corresponding syntheses were carried out on the one hand at high temperature,[23] which may by itself account for the lack of common morphologies, in agreement with the experiments performed at 50°C in the present work. On the other, precipitation of $CaCO_3$ in silica gels seeded with aragonite crystals failed to produce helical structures also under ambient conditions.[24] This finding indicates that the replacement of barium by calcium must have further

implications, apart from the problem that the formation of silica biomorphs necessitates the aragonite modification and $CaCO_3$ usually crystallizes as calcite at room temperature. In light of the effects discerned in syntheses with $LaCl_3$ as additive and at high Ba^{2+} concentration, the interactions between dissolved calcium ions and silicate species should be considered in this context. Ca^{2+} is smaller than Ba^{2+} and therefore has a higher charge density (or, in other words, it is a "harder" cation). Consequently, it binds more strongly than for instance Ba^{2+} to charged silica surfaces[50] and causes pronounced "salting-out" of silicate species.[51] Thus, in a regular reaction mixture which would yield (among others) helicoidal biomorphs when Ba^{2+} is used, the presence of the same amount of Ca^{2+} ions is expected to reinforce silica condensation and thereby, according to the model outlined above, alter the mode of fractal branching and hence the final morphology. If Ca^{2+} acts in a similar manner as La^{3+} or higher concentrations of Ba^{2+}, preferentially flower- or coral-like aragonite-based aggregates should be obtained, which is fully coherent with the results described in earlier work.[23,24]

Finally, the role of the investigated organic additives during morphogenesis of silica biomorphs remains to be discussed. As in the presence of $LaCl_3$ and at elevated temperature or Ba^{2+} content, most of the inspected precipitates showed overall roughly spherical geometry and exhibited flower-like forms. These were very similar to the morphologies generated with La^{3+} in the case of the surfactant CTAB, whereas somewhat unique shapes were induced by the polymer pDADMAC. Since the pH was not affected by both additives and control experiments without silica proved that there is no distinct influence on carbonate crystal growth (see Section 9.4.1), it seems safe to assume that the organics influence the formation of biomorphs by interacting with the silica in solution.

It is well-known that both CTAB and pDADMAC tend to flocculate silica sols, though usually at higher silica concentrations than in the present experiments. Indeed, Iler reported that addition of relatively small amounts of cetyltrimethylammonium chloride (CTAC) to dispersed silica colloids can give rise to more or less flat, sheet-like aggregates silica particles at high pH.[36] It was proposed that charge screening and simultaneous bridging of the colloids by cationic micelles promotes agglomeration. Layer formation was ascribed to preferential particle adhesion at the sheet edges, where the surfactant is predominantly adsorbed and hence lowers electrostatic repulsions relative to the sheet faces. Similar bridging effects in-between silica colloids were envisaged for cationic polymers. This concept is schematically reproduced in Fig. 9-20.

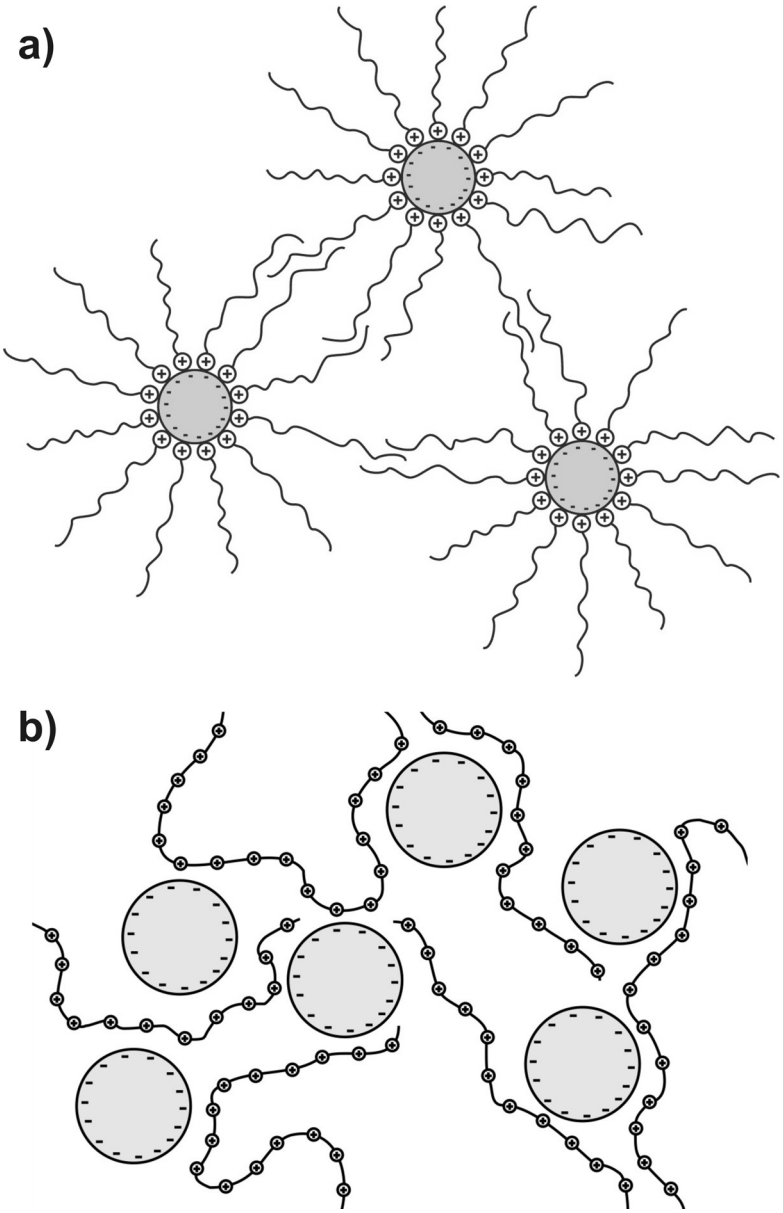

Fig. 9-20: Bridging and consequential aggregation of negatively charged colloidal silica spheres induced by the presence of (a) a cationic surfactant, and (b) a cationic polymer. Note that structures are not drawn to scale.

Silica coagulation will be favored by a combination of electrostatic and hydrophobic interactions in the case of CTAB, while a substantial gain in entropy (due to the release of water molecules) may additionally contribute to the binding of pDADMAC to silicate species. The affinity of the two organic additives for the silica in solution is reflected in the instant turbidity of the samples which, as evidenced by the cryo-TEM analyses presented in Section 9.4.2.7, can be attributed to the formation of colloidal silica particles with mesoporous structure. The latter are likely to be generated in parallel to growth of biomorphs by polymerization of silica around supramolecular assemblies of the surfactant (obviously a hexagonal phase) and analogous pDADMAC

aggregates (such as polymer coils). It is worth stressing that the expected concurrent decrease in the amount of dissolved silica cannot account for the observed morphological variation, as lower silica concentrations were reported to result in fractal architectures, and not floral aggregates.[30] To which degree the additives are co-precipitated with the mesoporous particles is uncertain. Howsoever, the silica remaining in solution must likewise experience a change in its speciation to explain the traced growth behavior. Single polymer molecules may readily be regarded as cross-linkers promoting condensation of silicate species, due to their high charge density. In the case of the surfactant, the situation is more complicated because it is not clear whether it forms micelles under the given circumstances or not. The cmc of CTAB is around 0.9 mM in pure water, but the presence of salt will decrease this value markedly.[52] Silica condensation reactions might hence be assisted by true surfactant micelles or, more generally speaking, by bridging of silicate oligomers and polymeric fragments in an arrangement involving a "pseudo-hydrophobic phase" as indicated in Fig. 9-20.
In any case, it can be anticipated that addition of CTAB and pDADMAC shifts the chemistry of silica towards a state of more condensed species and, in doing so, should influence fractal branching in a similar fashion as high temperatures and barium concentrations or the presence of multivalent cations do. This is fundamentally supported by the occurrence of "anemone-like" morphologies in the course of crystallization from CTAB-containing solutions (cf. Fig. 9-3b). These architectures are thought to originate from a crystal seed which develops a comparably small number of projections that radiate outwards to establish a quasi-spherical overall shape, possibly as a consequence of isotropic growth rates around the central core. Once this fractal stage is completed, laminar polycrystalline segments develop in-between the branches (as illustrated for example by the intermediate morphology shown in Fig. 9-3c and schematically depicted in Fig. 9-19) and, with time, grow to eventually give the found flower-like forms.

In essence, the argumentation put forward above explains the morphogenesis of floral and coralline structures on a satisfactory level and suggests that the role of all studied additives as well as the influence of temperature and the barium concentration can be reduced to promotional effects on silica condensation processes and concurrent modifications of fractal branching phenomena. However, this is clearly a simplistic view, and compelling objections remain.

For example, it is surprising that a NaCl content of 250 mM leads to dense fractal architectures and prevents polycrystalline growth, while a completely different branching pattern and well-developed biomorphic shapes should occur in systems at the same concentration of $BaCl_2$ and hence a higher net ionic strength. The fact that polycrystalline aggregates do not form in the presence of high amounts of NaCl is likely to be related to the reduced flow of CO_2 into the solution; this effect could be counterbalanced to some extent by the additional Ba^{2+} which might raise the supersaturation to sufficient levels. Nevertheless, addition of more than 100 mM NaCl provokes significant silica condensation (as manifest in a clouding of the mixtures) and should therefore also be capable of altering the branching behavior. One may speculate that the ability of multivalent cations and the two organic additives to bridge and link silica colloids is a decisive factor for establishing a state of the silica in solution which is suitable to account for a less dense and open branching motif. This is tentatively supported by the finding that surfactants with shorter chains (e.g. dodecyltrimethyl-ammonium bromide) behaved like simple salts (see Section 9.4.2.4). In this case, the growth mode at elevated temperature would yet have to be distinct from that in the other samples, possibly resting upon accelerated carbonate crystallization rather than distinct changes in the silica speciation.

Further, the morphologies observed under the various conditions are indeed generally similar, but still exhibit clearly discernible differences in terms of the frequency, shape, and curvature of polycrystalline segments, which allows for classifying them into flowers, corals, trumpets and the like. Parameters governing the detailed evolution of the aggregates on global scales can hardly be identified based on the current knowledge. This applies as well for “regular” silica biomorphs, which adopt diverse particular forms in a seemingly accidental manner. An important point to stress is that the sheet-like domains constituting the three-dimensional floral and coral-like spherulites described in this chapter have apparently grown free from an underlying substrate and nonetheless did in many cases not coil onto themselves. This is in conflict with the claim formulated in Chapter 7 of this work, i.e. that the formation of biomorphs is intimately related to the presence of surfaces. In the case of the experiments with La^{3+}, this contradiction is remedied by the observation that the crystal aggregates developed within chunks of gel segregated from solution upon reinforced condensation. In turn, noticeable gelation could not be verified for the other samples. The exposure of large surface areas in the morphologies, without a beneficial substrate underneath, tempts to suspect that the

surface is somehow stabilized in the solutions. When assuming that multivalent cations as well as cationic surfactants and polymers can induce bridging of silica particles (which they generated before by promoting condensation) into more or less extended layers, as described by Iler for CTAC,[36] the resulting colloidal networks could deposit on or in front of growing sheets, thereby facilitating nucleation and explaining their virtual two-dimensionality. This would partially lead us back to the formerly proposed membrane-templating model for silica biomorphs,[19] or respectively a combination of bottom-up self-assembly driven by chemically coupled co-precipitation and top-down shaping of the emerging aggregate by colloidal silica membranes. A potentially fatal flaw in this model is the lack of a visible skin on many of the aggregates, although re-dispersion of colloids after mineralization and upon changes in conditions with time may afford an account for this. However, this hypothetical scenario can only be argued for crystallization in the presence of the organic additives (or La^{3+}) and at higher Ba^{2+} concentration, while the formation of flat laminar segments must have different reasons in syntheses performed at 50°C. Again we can only speculate, but it is feasible that homogeneous nucleation becomes possible at elevated temperature and even prevails under these circumstances, such that the aggregates are no longer dependent on the advantage of heterogeneous nucleation at interfaces.

Eventually, it should be noted that a discussion of morphological variations based on changes on the global multi-µm scale may paint a comprehensible and consistent picture of the underlying mechanisms, but it fully neglects alterations in the interactions between the silica-associated nanocrystals on short length scales. Although the present work has demonstrated that individual rods do not carry a distinct skin of silica (see Section 6.4.5), there will yet be some sort of silica adsorption on the crystallites which might be different when additives are present and/or the silica speciation is modified. Likewise, repulsive and attractive forces in-between the building blocks should change when the chemistry of silica shifts. These factors likely determine the final shape and dimensions of the crystals, as well as their conformation and co-orientation, thus potentially influencing the evolution of the aggregates also in terms of global morphology. The present experiments confirmed that the size and form of the nanocrystals were not noticeably affected when CTAB, pDADMAC or La^{3+} was introduced to the syntheses, whereas the mutual arrangement did show some differences and overall less order. At high temperature, both the appearance of individual crystals and their orientational field were in turn substantially distinct (cf. Fig. 9-16). This

underlines the importance of considering variations in the short-range interactions between the building blocks in these materials and their implications for the development of curved ultrastructures. With the currently available information, such effects are however still utterly difficult to assess.

9.6 Conclusion

The presented results have demonstrated that the formation of silica biomorphs is sensitive to changes in experimental parameters as well as to the presence of certain additives. Nevertheless, in all cases except for syntheses at high ionic strength, crystallization of barium carbonate from alkaline silica sols produced polycrystalline aggregates with extraordinary morphologies and structure. This underlines the ability of this self-assembling system to respond to the given conditions by slightly modifying the mode of growth and thus adopting somewhat distinct global shapes, rather than fully abandoning self-organization as observed frequently in biomineralization or biomimetic approaches of morphosynthesis using delicate substances such as proteins.

Another essential finding in this part of the work is that the concentration of an additive required to provoke sensible morphological variations can be very low, given proper choice of the compound in question. Indeed, it has previously been recognized that already trace amounts of for instance foreign ions are capable of interfering noticeably with the crystallization of carbonate minerals regarding, among others, precipitation kinetics and crystal morphology.[49,53] However, it can be inferred from the present data that the role of the investigated additives should rather be interpreted with respect to their interactions with the “primary” structuring agent, that is, the silica in solution. The aqueous chemistry of silica involves a highly delicate combination of protonation-deprotonation and dissolution-precipitation processes as well as adsorption/desorption and complexation phenomena, all of which depend intimately on various factors such as the pH or the kind and concentration of salts present. These circumstances principally enable the birth of fascinating materials like silica biomorphs, and at the same time provide a means to direct self-assembly in a more or less deliberate manner. Due to the inherent complexity of the system and the many parameters evolving simultaneously on distinct time and length scales, the effects achieved with a certain additive are yet far from being understood and still impossible to predict. An interesting approach for future work would be to use an additive that is assumed to be indifferent to the presence of silica and will only or mainly interact with the carbonate, ideally a substance which by

itself induces structured carbonate crystallization. This could establish a situation in which two different additives compete for interaction sites on the growing crystals, potentially giving rise to novel mineralized patterns and permitting further insight to the mechanisms of self-organization. Promising candidates in this context may be anionic polymers like polyacrylates, which have proven to be versatile auxiliaries in $CaCO_3$ morphosynthesis.[26,54]

The additives discussed in this chapter appeared to all exert a related influence on dissolved silica, namely shift its state in solution towards more condensed species. Oligomerization processes affecting the silica involved in the formation of biomorphs were confirmed to be triggered predominantly by colloidal interactions rather than a true binding or precipitation of the additives with silica, given that none of the introduced ions could be detected in the final crystal aggregates. A sheer increment in the ionic strength realized by addition of considerable amounts of sodium chloride did not lead to significant changes in the growth behavior of barium carbonate, but arrested morphogenesis at the end of the fractal route presumably as a consequence of restricted CO_2 uptake at high salinities. By contrast, multivalent cations as well as the cationic surfactant CTAB and the polymer pDADMAC provoked growth of spacious flower-like ultrastructures which, from a morphological perspective, resemble typical aggregates isolated from syntheses at elevated temperature or high barium concentration and those previously produced with calcium carbonate.[23,24] These analogies and analyses of premature aggregates led to the conclusion that a distinct branching behavior of the initial crystal seed accounts for the formation of the observed floral- and coralline-type biomorphs. In this scenario, splitting occurs less frequently as a consequence of either the altered speciation of silica or modifications in the relative rates of carbonate crystallization and silica polymerization. Eventually, open spherulitic architectures are obtained which consist of well-separated, radially emanating branches. Laminar polycrystalline segments then develop primarily in-between these projections, generating individual curved leaves. The growth mechanism envisaged under these conditions thus bears a fundamental difference to morphogenesis in a “standard” experiment: in the latter case, the fractal stage yields in closed globular particles from which, upon fibrillation, the emerging crystal assembly sprouts and in the following evolves independently of its precursor whereas, in the former case, the branched structure pre-determines at least to a certain extent the shape of the final aggregate. This notion and further achievements made in this work (cf. in particular Chapter 7) may

help to design nanocrystalline materials with virtually tailor-made shapes using the concept of silica biomorphs in the future, but at the moment tuning of morphologies still rests upon an essentially empirical basis.

9.7 References

(1) Mann, S. *Angew. Chem. Int. Ed.* **2000**, *39*, 3392.

(2) Busch, S.; Dolhaine, H.; DuChesne, A.; Heinz, S.; Hochrein, O.; Laeri, F.; Podebrad, O.; Vietze, U.; Weiland, T.; Kniep, R. *Eur. J. Inorg. Chem.* **1999**, 1643.

(3) Cölfen, H. *Curr. Opin. Colloid Interface Sci.* **2003**, *8*, 23.

(4) Champ, S.; Dickinson, J.; Fallon, P. S.; Heywood, B. R.; Mascal, M. *Angew. Chem. Int. Ed.* **2000**, *39*, 2716.

(5) Yu, J. G.; Zhao, X. F.; Liu, S. W.; Li, M.; Mann, S.; Ng, D. H. L. *Appl. Phys. A* **2007**, *87*, 113.

(6) Bigi, A.; Boanini, E.; Walsh, D.; Mann, S. *Angew. Chem. Int. Ed.* **2002**, *41*, 2163.

(7) Addadi, L.; Weiner, S. *Angew. Chem. Int. Ed.* **1992**, *31*, 153.

(8) Mann, S. *Biomimetic materials chemistry*; VCH Publishers: New York, 1996.

(9) (a) Grassmann, O.; Müller, G.; Löbmann, P. *Chem. Mater.* **2002**, *14*, 4530. (b) Falini, G.; Fermani, S.; Gazzano, M.; Ripamonti, A. *J. Chem. Soc., Dalton Trans.* **2000**, 3983.

(10) Park, R. J.; Meldrum, F. C. *Adv. Mater.* **2002**, *14*, 1167.

(11) (a) Antonietti, M.; Breulmann, M.; Göltner, C. G.; Cölfen, H.; Wong, K. K. W.; Walsh, D.; Mann, S. *Chem. Eur. J.* **1998**, *4*, 2493. (b) Qi, L.; Cölfen, H.; Antonietti, M.; Li, M.; Hopwood, J. D.; Ashley, A. J.; Mann, S. *Chem. Eur. J.* **2001**, *7*, 3526. (c) Yu, S. H.; Cölfen, H.; Antonietti, M. *J. Phys. Chem. B* **2003**, *107*, 7396.

(12) (a) García-Ruiz, J. M.; Amorós, J. L. *J. Cryst. Growth* **1981**, *55*, 379. (b) García-Ruiz, J. M. *J. Cryst. Growth* **1985**, *73*, 251.

(13) García-Ruiz, J. M. *Geology* **1998**, *26*, 843.

(14) Voinescu, A. E.; Kellermeier, M.; Carnerup, A. M.; Larsson, A. K.; Touraud, D.; Hyde, S. T.; Kunz, W. *J. Cryst. Growth* **2007**, *306*, 152

(15) García-Ruiz, J. M. *Origins Life Evol. Biosphere* **1994**, *24*, 451.

(16) García-Ruiz, J. M.; Carnerup, A.; Christy, A. G.; Welham, N. J.; Hyde, S. T. *Astrobiology* **2002**, *3*, 353.

(17) García-Ruiz, J. M.; Hyde, S. T.; Carnerup, A. M.; Christy, A. G.; Van Kranendonk, M. J.; Welham, N. J. *Science* **2003**, *302*, 1194.

(18) Carnerup, A. M.; Christy, A. G.; García-Ruiz, J. M.; Hyde, S. T.; Larsson, A. K. *The record of early life: in search of biosignatures*; in: *Life as we know it. Cellular origin, life in extreme habitats, and astrobiology*; Seckbach, J., Ed., Springer: Dordrecht, 2006.

(19) Hyde, S. T.; Carnerup, A. M.; Larsson, A. K.; Christy, A. G.; García-Ruiz, J. M. *Physica A* **2004**, *339*, 24.

(20) Hyde, S. T.; García-Ruiz, J. M. *Actual. Chim.* **2004**, *275*, 4.

(21) Bittarello, E.; Aquilano, D. *Eur. J. Mineral.* **2007**, *19*, 345.

(22) Terada, T.; Yamabi, S.; Imai, H. *J. Cryst. Growth* **2003**, *253*, 435.

(23) Voinescu, A. E.; Kellermeier, M.; Bartel, B.; Carnerup, A. M.; Larsson, A. K.; Touraud, D.; Kunz, W.; Kienle, L.; Pfitzner, A.; Hyde, S. T. *Cryst. Growth Des.* **2008**, *8*, 1515.

(24) Imai, H.; Terada, T.; Miura, T.; Yamabi, S. *J. Cryst. Growth* **2002**, *244*, 200.

(25) Yu, S. H.; Cölfen, H.; Tauer, K.; Antonietti, M. *Nature Mater.* **2005**, *4*, 51.

(26) Gower, L. A.; Tirrell, D. A. *J. Cryst. Growth* **1998**, *191*, 153.

(27) Baird, T.; Braterman, P. S.; Cheng, P.; Garcia-Ruiz, J. M.; Peacock, R. D.; Reid, A. *Mater. Res. Bull.* **1992**, *27*, 1031.

(28) Melero-Garcia, E.; Santisteban-Bailon, R.; Garcia-Ruiz, J. M. *Cryst. Growth Des.* **2009**, *9*, 4730.

(29) García-Ruiz, J. M.; Moreno, A. *An. Quim. Int. Ed.* **1997**, *93*, 1.

(30) Carnerup, A. M. *Biomorphs: morphology, chemistry and implications for the identification of early life*; PhD thesis, Australian National University, Canberra, Australia, 2007.

(31) Beck, J. S.; Vartuli, J. C.; Roth, W. J.; Leonowicz, M. E.; Kresge, C. T.; Schmitt, K. D.; Chu, C. T. W.; Olson, D. H.; Sheppard, E. W.; McCullen, S. B.; Higgins, J. B.; Schlenker, J. L. *J. Am. Chem. Soc.* **1992**, *114*, 10834.

(32) Ying, J. Y.; Mehnert, C. P.; Wong, M. S. *Angew. Chem. Int. Ed.* **1999**, *38*, 56.

(33) Xiao, F. S.; Wang, L.; Yin, C.; Lin, K.; Di, Y.; Li, J.; Xu, R.; Su, D. S.; Schlögl, R.; Yokoi, T.; Tatsumi, T. *Angew. Chem. Int. Ed.* **2006**, *45*, 3090.

(34) Qi, L. M.; Li, J.; Ma, J. M. *Adv. Mater.* **2002**, *4*, 300.

(35) Donners, J. J. J. M.; Heywood, B. R.; Meijer, E. W.; Nolte, R. J. M.; Sommerdijk, N. A. J. M. *Chem. Eur. J.* **2002**, *8*, 2561.

(36) Iler, R. K. *The chemistry of silica*, Wiley: New York, 1979.

(37) Busenberg, E.; Plummer, L. N. *Geochim. Cosmochim. Acta* **1986**, *50*, 2225.

(38) Zeebe, R. E.; Wolf-Gladrow, D. *CO_2 in seawater: equilibrium, kinetics, isotopes*. Elsevier Oceanography Series, Vol. 65, pp. 346, Elsevier: Amsterdam, 2001.

(39) Miller, J. P. *Am. J. Sci.* **1952**, *250*, 161.

(40) Suhara, T.; Esumi, K.; Meguro, K. *Bull. Chem. Soc. Jpn.* **1983**, *56*, 2932.

(41) (a) García-Ruiz, J. M.; Melero-García, E.; Hyde, S. T. *Science* **2009**, *323*, 362. (b) Kunz, W.; Kellermeier, M. *Science* **2009**, *323*, 344.

(42) Barauskas, J.; Misiunas, A.; Gunnarsson, T.; Tiberg, F.; Johnsson, M. *Langmuir* **2006**, *22*, 6328.

(43) (a) Cai, Q.; Luo, Z. S.; Pang, W. Q.; Fan, Y. W.; Chen, X. H.; Cui, F. Z. *Chem. Mater.* **2001**, *13*, 258. (b) Nooney, R. I.; Thirunavukkarasu, D.; Chen, Y.; Josephs, R.; Ostafin, A. E. *Chem. Mater.* **2002**, *14*, 4721. (c) Ikari, K.; Suzuki, K.; Imai, H. *Langmuir* **2006**, *22*, 802.

(44) www.orange-metropolis.de/ink/wp-content/uploads/2011/01/Brain_coral.jpg

(45) Fleischmann, M. *Synthesis and characterization of self-assembled silica-carbonate biomorphs under various experimental conditions*; Bachelor Thesis, University of Regensburg, Regensburg, Germany, 2009.

(46) Eiblmeier, J.; Kellermeier, M.; Kunz, W. *Effect of the initial bulk pH on the growth behavior of silica-witherite biomorphs in alkaline solution*. To be submitted to *J. Cryst. Growth*.

(47) (a) Alexander, G. B. *J. Am. Chem. Soc.* **1953**, *76*, 2094. (b) Greenberg, S. A.; Sinclair, D. *J. Phys. Chem.* **1955**, *59*, 435. (c) Belton, D. J.; Deschaume, O.; Patwardhan, S. V.; Perry, C. C. *J. Phys. Chem. B* **2010**, *114*, 9947.

(48) Holleman, A. F.; Wiberg, E. *Lehrbuch der Anorganischen Chemie*; 101. Auflage, de Gruyter Verlag: Berlin/New York, 1995.

(49) Tsuno, H.; Kagi, H.; Akagi, T. *Bull. Chem. Soc. Jpn.* **2001**, *74*, 479.

(50) Dove, P. M.; Craven, C. M. *Geochim. Cosmochim. Acta* **2005**, *69*, 4963.

(51) Marshall, W. L.; Warakomski, J. M. *Geochim. Cosmochim. Acta* **1980**, *44*, 915.

(52) Mukerjee, P.; Mysels, K. J. *Critical micelle concentrations of aqueous surfactant systems*; US Government Printing Office: Washington, DC, 1971.

(53) (a) Reddy, M. M.; Nancollas, G. H. *J. Cryst. Growth* **1976**, *35*, 33. (b) Reddy, M. M.; Wang, K. K. W. *J. Cryst. Growth* **1980**, *50*, 470. (c) Gutjahr, A.; Dabringhaus, H.; Lacmann, R. *J. Cryst. Growth* **1996**, *158*, 310.

(54) Sims, S. D.; Didymus, J. M.; Mann, S. *J. Chem. Soc., Chem. Commun.* **1995**, 1031.

Chapter 10 Summary and Outlook

In essence, the work performed in the framework of this thesis has clearly demonstrated that the interplay of purely inorganic species can lead to fascinating phenomena in conventional crystallization experiments. The effects provoked by silica include

- distinct interactions with different precursor or intermediate phases occurring in the course of polymorphic precipitation and corresponding alterations of transformation rates,
- modulations of the growth behavior of single crystals by specific adsorption,
- as well as stabilization of nanoparticle building units and their concerted arrangement into higher-order superstructures with remarkable texture and morphology.

In this regard, the silica is obviously capable of interfering with the crystallization of alkaline-earth carbonates on multiple time and length scales. The delicate influence achieved in this manner may very well be compared to processes identified both in biological and biomimetic mineralization. There, however, control over the various factors determining the final appearance, composition and structure of a mineral is usually retained by the action of fairly complex organic polymers, supramolecular assemblies and/or templating surfaces or matrices. Thus, the conclusions drawn from the present investigations, together with previous studies on silica-directed carbonate crystallization, could pave the way towards an alternative strategy to design novel advanced materials based on chemically simple inorganic compounds.

A general concept most probably underlying many of the effects observed throughout this work is the pH-mediated coupling of the speciations of carbonate and silicate in alkaline media, initially proposed by García-Ruiz and co-workers. The main implication of this paradigm is that the precipitation of one of the components intimately affects the state of the other in solution. Such a dynamic feedback is only possible because the silica is by itself inherently reactive under the prevailing conditions and can factually co-precipitate. This is another key point distinguishing the studied systems from conventional approaches to manipulate the progress of crystallization, where substances with defined constitution are typically employed as additives and their role can be considered with respect to given molecular or colloidal aspects. Silica, by contrast,

responds to both bulk and local changes in conditions by more or less instantly adjusting its chemistry. This enables synergetic self-assembly in combination with suitable partners such as carbonates, but at the same time renders ongoing processes often highly difficult to assess. Nevertheless, from the evaluation and discussion of the data collected during this thesis, it seems evident that spontaneous coating of growing carbonate particles by silica due to pH- (or cation-) induced polymerization is a characteristic feature innate to these systems, which either replaces or cooperates with effects caused by classical (selective) adsorption phenomena.

Calcium Carbonate Precipitation

In particular, the studies carried out in the field of calcium carbonate precipitation have shown that the presence of silica allows for arresting crystallization at virtually any desired stage or, in other words, at any rung of the energetic ladder down from the dissolved ions to thermodynamically stable calcite (cf. Fig. 1-16 and Fig. 1-20). This can be accomplished essentially by a mere tuning of experimental parameters and, *per se*, has great potential not only for the concerted synthesis of a designated $CaCO_3$ polymorph, but also as an analytical tool for the capture and investigation of different transient precursors.

At modest carbonate supersaturations and low to medium contents of silica, the interplay between the species became manifest in the stabilization of ACC nanoparticles which were generated initially upon nucleation (**Chapter 2**). Analyses of the samples proved that local silica precipitation was effective to produce extended siliceous layers with thicknesses of up to 10 nm around the particles under these circumstances. This was ascribed to a decrease in pH nearby growing carbonate surfaces, thus serving as direct evidence for the validity of the envisaged theory of chemical coupling. In this way, core-shell particles of ACC and silica were obtained by a straightforward one-step mixing procedure, while hollow spheroids of silica could be prepared by subsequent immersion of the composites in acid. Both types of material are interesting from the viewpoint of practical applications (e.g. as filler), and future work should be focused on testing their actual performance. Beyond that, it was shown that particle sizes, shell dimensions and, above all, the extent of protection against energetically favored transformation of the enclosed ACC phase sensibly depend on the amount of silica added. When left in solution, decelerated gradual conversion to calcite was observed at low silica concentrations, suggesting that the sheathing skins acted as pervious barriers

delimiting but not fully suppressing exchange with the surrounding medium and re-dissolution of ACC. Higher concentrations in turn led to the formation of thicker and less porous shells conserving the metastable precursor for prolonged periods before, above a certain threshold, complete and quantitative inhibition of transformation was realized. These findings illustrate the superior degree of control achievable over the temporal stability of ACC by means of silica. Preliminary experiments using barium instead of calcium carbonate moreover verified that such effects are not restricted to $CaCO_3$, but may be generalized to any kind of (amorphous) particles which tend to lower the pH in their vicinity during growth. In this context, minerals comprising anions of di- or multibasic acids, such as sulfates or phosphates, appear most promising.

Further remarkable observations were made when following the crystallization of calcite from silica-coated ACC in the regime of concentrations where protection was of transitory nature (**Chapter 3**). Owing to the fact that silica shells re-dissolved in the mother liquor after having released their carbonate core, a progressive influence of soluble silicate species on the morphological evolution of calcite single crystals could be discerned, mainly originating from preferential adsorption of oligomers or polymers on selected faces. This provoked rhombohedra with rounded corners and edges at overall low silica content (adsorption dominated by electrostatic interactions), while intricate three-pointed star-like forms were generated at slightly higher concentrations due to successive elongation and splitting of a basal crystal (enhanced contribution of sterical matching in adsorption processes). Another increment in the amount of silica added eventually gave rise to polycrystalline aggregates of needle-shaped calcite nanocrystals exhibiting non-crystallographic morphologies (dumbbells, porous spheroids, trunks) and showing some degree of orientational order. These architectures may readily be regarded as “calcite biomorphs”. The formation of elongate nanoscale building units was explained by a combination of specific adsorption (accounting for elongation) and precipitation (stabilizing nano-sized individuals) of silica, whereas reasons for the ordered arrangement of the crystallites remained obscure. Certainly, the origin of these peculiar aggregates deserves further exploration, and structural details of the nanocrystals should be revealed for instance by leaching experiments or EDX and HR-TEM measurements. In any case, the traced delicate growth behavior of calcite in these samples teaches an important lesson: temporary storage of $CaCO_3$ as silica-stabilized ACC and subsequent controlled release of growth units allows for the development of complex crystal architectures under precipitation conditions – a feature

commonly associated with experiments at rather low supersaturation. This is, again, in full analogy to supposed concepts in biomineralization and non-classical *in-vitro* crystallization, hence re-emphasizing the biomimetic character of these completely abiotic systems.

When the silica concentration was considerably increased at a constant $CaCO_3$ content, the progress of crystallization could, for the first time, be brought to a stop already before nucleation took place (**Chapter 4**). This provided novel insight to the pre-nucleation stage of $CaCO_3$ precipitation and enabled the detection of single ion clusters even in heavily supersaturated solutions. Here, the influence of the silica was interpreted to rely on a colloidal stabilization of the clusters against nucleation due to binding of negatively charged silicate species in their periphery (rather than a true coating), which was proposed to cause mutual electrostatic repulsion and thus hinder cluster aggregation. In turn, when the pH was lowered step-wise, the clusters could be gradually allowed to aggregate such that the crystallization process was continued incrementally to "later" stages, eventually resulting in the nucleation of ACC. These results have two essential implications. On the one hand, since the clusters could be transferred into dry state without apparent structural changes (as evidenced by subsequent TEM analysis), silica-mediated inhibition of nucleation represents a valuable strategy for the isolation of these species in large amounts, thus possibly facilitating detailed investigations with conventional methods. Corresponding work might be done using solid-state NMR, extended X-ray absorption fine-structure (EXAFS), or fluorescence spectroscopy. On the other hand, the presence of silica and concurrent variations of the pH were shown to distinctly slow down homogeneous nucleation, and hence permit monitoring of otherwise extremely short-lived transient states. By this means, the processes underlying nucleation were elucidated and a model based on cluster aggregation and successive coalescence was established, which contributes to the currently emerging body of knowledge on non-classical nucleation-growth pathways and could be of interdisciplinary relevance. Nevertheless, more experiments are necessarily required to confirm the drawn conclusions and, in particular, to shed light on the actual step of phase separation, that is, when a true interface between the initially solute-like clusters and the solution is generated. Moreover, although the acquired data paint a thoroughly consistent picture, a direct proof for the observed clusters in fact consisting of $CaCO_3$ is still missing. TEM/EDX studies under carefully regulated low-dose conditions or coupled AFM-IR

measurements with high spatial resolution might serve this purpose. Finally, it is worth pointing out that the prevention of crystallization accomplished by the interference of silica in the pre-nucleation stage and, likewise, the long-term stabilization of colloidal amorphous particles found at lower concentrations obviously depict feasible concepts for scale inhibition. However, the alkaline pH needed for corresponding effects to operate will probably limit applicability in practical settings, although concrete and systematic test runs are surely necessary to estimate the true potential of this approach.

Tracing crystallization with the aid of on-line diffraction analysis in brines of dramatically higher supersaturation showed that precipitation of $CaCO_3$ proceeded in this case *via* metastable crystalline polymorphs rather than a direct conversion of (intermittently silica-stabilized) ACC to calcite (**Chapter 5**). The conducted experiments confirmed that this additional intermediate phase is vaterite under ambient conditions and aragonite at elevated temperature. Introduced silica was found to exert marked effects already at quite low $SiO_2/CaCO_3$ ratios as compared to the results obtained for more dilute systems. Recorded diffraction patterns suggested a considerable retardation or full hindrance of the vaterite/aragonite-to-calcite transformation, leading to a steady co-existence of varying fractions of distinct polymorphs in the suspensions. This behavior was attributed to adsorption and/or precipitation of silica around kinetically formed particles of the respective metastable phase and concurrent inhibition of transformation, which turned out to be particularly pronounced in the case of aragonite. To assess whether such phenomena are caused by local pH gradients and how the silica interacts in detail with the occurring phases, precipitates should be isolated and examined by electron microscopy and elemental analysis. Surprisingly, an increase in the silica content eventually prompted the system to directly crystallize as calcite and no longer involve vaterite as an intermediate at both room temperature and 50°C. This finding was explained on the basis of a competing promotional influence of silica on calcite growth rates. Here, noticeable stabilization of amorphous precursors could be deduced from the diffraction data, thus highlighting the multiple roles of silica during $CaCO_3$ polymorphic precipitation in a single set of experiments. From a general perspective, these results demonstrate that synchrotron EDXRD is a powerful technique to monitor and quantify the progress of $CaCO_3$ crystallization *in situ*, as well as to elucidate the impact of foreign species on transformation scenarios. Such methodology may help to develop non-empirical strategies for, among others, scale prevention and the synthesis of $CaCO_3$ powders with

defined properties for technical applications. Clearly, it would be interesting to investigate the effect of other additives with the described setup. In fact, corresponding data for substances previously reported to have a significant bearing on $CaCO_3$ precipitation (e.g. Mg^{2+} ions or polycarboxylates as typical antiscalant agents) were acquired already in the course of the measurements carried out in this work, and their evaluation is currently underway.

On the whole, the experiments summarized above have outlined that the interplay between precipitating calcium carbonate and added silica can be exploited to control the crystallization process on different levels and, at the same time, gain fundamental information on the distinct steps decisive for nucleation, growth, and polymorphic transformations. Apart from the mentioned implications, the results presented in this part of the thesis may be relevant for the geochemistry of carbonates and silica – especially with regard to their frequent common occurrence in geological scales – and could moreover devise novel routes to an efficient sequestration of atmospheric CO_2 by combined precipitation and cementation in silica.

Silica Biomorphs

The studies conducted in the field of silica biomorphs have addressed various aspects of these exceptional self-assembled materials. The most central goals were evidently to substantiate and advance the existing picture of their formation mechanism and to seek answers to so far unresolved questions concerning morphogenesis. Time-dependent profiles of the barium concentration in solution verified that the kinetics of the growth process is essentially reaction-controlled under typical synthesis conditions (**Chapter 6**). This could be supported by and correlated with growth rates determined for individual aggregates from optical image sequences which, in most cases, showed a linear advancement with time. On the other hand, progressions of the actual carbonate content in the system, derived from pH measurements and considerations of the underlying equilibria, indicated slight but permanent bulk supersaturation, which yet appeared to be insufficient to trigger homogeneous nucleation. These findings are in line with a situation in which precipitation takes place only nearby an evolving aggregate, and thus corroborate the proposed model of chemical coupling. Nevertheless, further measurements of species concentrations including a systematic variation of experimental parameters should be performed in order to ascertain whether reaction-limited growth applies in general, or predominantly, for the formation of biomorphs. It

is also evident that video microscopy represents a precious tool enabling time-resolved investigations of the morphological behavior on global scales, which will presumably continue to promote our understanding of this peculiar system in the future. Beyond that, data on the evolution of the silica concentration in solution pointed out that the amount of the additive in fact co-precipitated with carbonate during the crucial stages of morphogenesis is merely on the order of few percents – as opposed to previous reports on the composition of mature crystal aggregates. This unexpected observation was confirmed by *ex-situ* characterizations of specimens extracted after different times of growth, revealing that the major fraction of silica associated with the final biomorphs and especially the skins covering the assemblies in some instances were the result of secondary deposition owing to the decreased bulk pH at the end of carbonate crystallization. Thus, the existence of a pre-formed colloidal silica membrane and its feasible templating influence during growth could be disproven. In turn, inspection of crystallites exposed by a novel thin-sectioning procedure argued for the absence of a true silica shell also around individual carbonate building blocks in the core. This calls the notion of particle stabilization by pH-induced silica polymerization in their vicinity to a certain degree into question and, tentatively, renders a scenario involving adsorption rather than extensive co-precipitation more likely. To clarify this issue and decide whether one or perhaps both mechanisms may operate during the construction of silica biomorphs, single crystallites of independently and maybe differently prepared aggregates (e.g. gel- and solution-grown samples) must be analyzed concerning the presence of an outer silica skin. It would be interesting to know if a growing $BaCO_3$ rod can in principle excite silica condensation on its surface and induce spontaneous coating by silica in analogy to what was found for ACC particles. To that end, concerted precipitation experiments must be designed that yield gradually growing nanosized carbonate crystals in silica-containing solutions.

Investigations devoted to tracing the phenomenology of biomorph formation on the micron-scale basically gave results in good agreement with the meanwhile published work of García-Ruiz *et al.* (**Chapter 7**). It was verified that growth starts from an initial crystal seed and proceeds at first by non-crystallographic branching towards variously shaped fractal architectures. The subsequently emerging polycrystalline aggregates were shown to adopt morphologies falling into three categories under “standard” preparation conditions, and relative frequencies of the distinct forms in a typical experiment were determined by statistical analysis. Based on these data and the empirical observation

that sheets always grow in contact with surfaces in solution while twisted forms protrude into the liquid, it was suggested that the morphological evolution relies on the beneficial impact of extrinsic or intrinsic interfaces on the growth process. Such a scenario would furnish possible answers to two of the most important and still open questions regarding morphogenesis: the 2D character of the incipient laminae as well as the origin of curvature or, in other words, the reason for sheet curling. In the realm of the proposed model, two-dimensionality arises as a consequence of reduced nucleation barriers on well walls or the surface of the solution, causing the crystal assembly to progress in thin layers along the respective interface. In turn, when evolving freely in solution and far from foreign interfaces, the aggregates will prefer to fold back on themselves to use their own, already existing surface as growth substrate. This line of thought was indeed supported by the morphological selection traced in stirred solutions, where the occurrence of sheets was strongly favored over that of twisted structures. Nevertheless, certain objections remain. For example, it has been demonstrated that worms and especially helicoids originate from a small initial leaf which rapidly becomes scrolled in the medium and coils in the following. However, the formation of such a laminar domain far off an interface can hardly be understood. Furthermore, even if the driving force for curling rests upon the gain in energy achieved by the subsequent possibility of heterogeneous nucleation, one may wonder how the developing crystal aggregates “know” about these circumstances and why they would hence begin to grow in a curved manner. In that sense, the ideas on these delicate steps in the morphogenesis of silica biomorphs put forward in this part of the work should be considered as a starting point for future studies and clearly leave space for refinement. In spite of this, the affinity of the aggregates to surfaces seems evident and delineates an exciting concept towards a deliberate shaping of biomorphs: as illustrated by the conducted preliminary experiments with patterned substrates, growing sheets can readily adapt their morphology to the boundaries of a confined volume in which they are forced to form. Consequently, the combination of top-down templating by prefabricated moulds and bottom-up self-assembly based on the dynamic interplay between carbonate and silica might allow for the synthesis of polycrystalline architectures with virtually arbitrary shapes. By contrast, relatively few information could be gathered on the origin of the orientational ordering of crystallites characterizing the microstructure of silica biomorphs. Syntheses carried out in the presence of external electric and magnetic fields did not show significant effects in terms of the mutual orientation of the rods (nor with

respect to the fractions of left- and right-handed helices when chiral fields were applied). This may hint at electrostatic interactions in-between the silica-bearing nanocrystals being of minor importance in their arrangement. Using thin-sectioning techniques as those developed in the present work, future studies should try to decipher whether some kind of siliceous bridges exist between individuals in the core and if there are any differences concerning the detailed nature of the tips and lateral faces of the rods, which would potentially account for the observed slight misalignment.

Aside from sustaining the surface affinity of sheets, the growth behavior of silica biomorphs discerned when stirring their mother solutions was elaborated to serve as an indirect proof for the dynamic chemical processes believed to drive their formation (**Chapter 8**). In principle, this section of the thesis was grounded on the assumption that precipitation and crystallization are local phenomena widely independent of bulk conditions, as the front of evolving aggregates is capable of synthesizing constituents on its own and hence elevate in an autocatalytic manner the supersaturation of the components in its vicinity. Self-assembly was thus expected to be indifferent to agitation and enhanced fluid motion, as long as no reinforced convections occur across the localized dimension where the supposed coupling is at work. These considerations were verified in the experiments and, by relating the morphology and size of aggregates formed at different stirring rates to flow characteristics envisaged for the corresponding circumstances, the length scale of the active region was estimated to be on the order of microns. A most intriguing implication of the introduced rationale is the fundamental insignificance of reagent diffusion from the bulk to the growth site, which likely distinguishes silica biomorphs from the vast majority of other self-organized materials. In turn, as it is typical for systems operating far from equilibrium, proper starting conditions and critical parameters (such as the flow of CO_2 into the solution) nonetheless need to be chosen to allow dynamic self-assembly to be initiated and maintained in both time and space. This was, for instance, apparently not the case in syntheses performed under the influence of ultrasound or at very high rates of stirring. Although the implemented approach sheds novel light on the extraordinary mechanistic features associated with the formation of silica biomorphs, direct experimental evidence still has to be provided to fully validate the model of local autocatalytic growth. A milestone in this context would be to image the front of a growing aggregate *in situ* – which certainly is a highly non-trivial task. Sophisticated techniques such as X-ray microscopy or solution AFM could be suitable for this purpose. Another strategy to

experimentally access the processes leading to structured mineralization might be to measure the pH in the close vicinity of developing biomorphs, for example by employing special (fluorescent) dyes and using a spectrometer with sufficient spatial resolution. Sensible changes or, ideally, oscillations of the pH with time would be an ultimate proof for the concept of coupled co-precipitation and moreover enable a quantification of reaction kinetics on a microscopic level.

In a final set of experiments, the role of distinct synthesis parameters and selected additives on the phenomenology of growth and final morphologies displayed by silica biomorphs under these conditions was explored (**Chapter 9**). By raising the temperature, increasing the effective Ba^{2+} concentration, and dissolving small amounts of trivalent cations, cationic surfactants or cationic polymers in the mixtures, a variety of complex forms were generated that included cup-, trumpet-, flower- and coral-like shapes. High concentrations of sodium chloride were in turn found to arrest morphogenesis at the end of the fractal stage, yielding raspberry-like branched architectures. Indeed, similar results were reported in part already in previous work but, with regard to the considerable progress made in recent years concerning the formation mechanism of silica biomorphs, it is certainly worth and even necessary to re-evaluate former observations based on the meanwhile existing knowledge. This applies not only for the influence of the parameters studied herein. Further effort should in this sense be spent for instance to re-analyze the detailed impact of factors like the bulk pH of mother solutions, the morphological development of both strontium and calcium carbonate biomorphs, or the outcome of growth experiments conducted with mixtures of Ca and Ba or Sr. In the present case, the discerned effects were interpreted primarily with respect to alterations in the rate of carbonate crystallization and the degree or fashion of silica condensation provoked by the modified conditions and the action of the additives, respectively. In particular, high ionic strength was judged to markedly decelerate uptake of CO_2 from the atmosphere and hence prevent adequate time-dependent species concentrations required for fibrillation and coupled co-precipitation to be excited. On the other hand, the chosen additives were confirmed to encroach upon the crystallization process *via* their interaction with silica, inducing a shift in the speciation towards larger oligomers and colloidal particles. A similar influence was ascribed also to excess Ba^{2+} ions and elevated temperature. As a consequence, the branching behavior of the initial crystal seed during the fractal stage was apparently affected and gave open architectures rather than closed spherulites. Polycrystalline growth in the second stage of

morphogenesis was then seen to fill the gaps between the emanating projections, causing the observed morphologies. This model would assign a somewhat templating role to the fractal precursor and awaits confirmation or rebuttal by further experiments.

Taken together, it is evident that the lessons learnt from biomorphs will help to shed more light on the strategies Nature uses to design hierarchical architectures and, at the same time, might set a landmark from which controlled syntheses of complex materials based on the synergy of the involved components could be conducted. An interesting challenge will surely be to look for other reagent pairs that would incur a similar coupled interplay when conditions are properly regulated. This search for generalization may begin with straightforward substitutions such using phosphates instead of carbonates, but should certainly be extended also to phenomena across disciplines and processes not necessarily related to pH effects or precipitation, yet possibly relying on an analogous principle. The present work has contributed to a deeper understanding of the concepts being at the heart of self-assembly in silica biomorphs and simultaneously highlighted fascinating questions left to be answered, which may stimulate and inspire future studies.

Appendices

A. Effect of pH on the Speciation and Solubility of the Components

A.1 Theoretical Background

The pH essentially determines the distribution of both carbonate and silicate species in aqueous media and thus has strong influence on occurring precipitation processes. The speciation of carbonate in solution is well described by the dissociation equilibria of carbonic acid according to

$$H_2CO_3 \overset{K_1}{\rightleftharpoons} HCO_3^- + H^+ \overset{K_2}{\rightleftharpoons} CO_3^{2-} + 2H^+$$

where K_1 and K_2 are the first and second dissociation constant of carbonic acid. In the case of silica, the situation is substantially more difficult due to the possibility of condensation reactions and hence the occurrence of diverse soluble oligomeric species. Considering in a first approximation only neutral silicic acid and the corresponding singly and doubly charged anions, the relevant equilibria can be written in analogy to carbonate as:

$$Si(OH)_4 \overset{K_1}{\rightleftharpoons} SiO(OH)_3^- + H^+ \overset{K_2}{\rightleftharpoons} SiO_2(OH)_2^{2-} + 2H^+$$

Based on the principle of mass preservation and assuming ideality for the dilute systems, the following equations for the concentrations of the different species can be derived:

$$[H_2A] = \frac{[H^+]^2 \cdot [A]_0}{K_1 \cdot K_2 + K_1 \cdot [H^+] + [H^+]^2} \qquad \text{(Eqn. A-1)}$$

$$[HA^-] = \frac{K_1 \cdot [H^+] \cdot [A]_0}{K_1 \cdot K_2 + K_1 \cdot [H^+] + [H^+]^2} \qquad \text{(Eqn. A-2)}$$

$$[A^{2-}] = \frac{K_1 \cdot K_2 \cdot [A]_0}{K_1 \cdot K_2 + K_1 \cdot [H^+] + [H^+]^2} \qquad \text{(Eqn. A-3)}$$

where A represents either CO_3 or $Si(OH)_2O_2$ and $[A]_0$ is the overall analytical concentration of the carbonate and silicate, respectively. Distributions obtained on the basis of Eqns. A-1 to A-3 are outlined as a function of the pH in Fig. A-1. The values

used for the constants during calculation, valid for $T = 25°C$ and infinite dilution, were $K_1 = 4.47 \cdot 10^{-7}$ mol/L and $K_2 = 4.68 \cdot 10^{-11}$ mol/L for carbonic acid,[1] and $K_1 = 1.44 \cdot 10^{-10}$ mol/L and $K_2 = 3.72 \cdot 10^{-14}$ mol/L for silicic acid.[2]

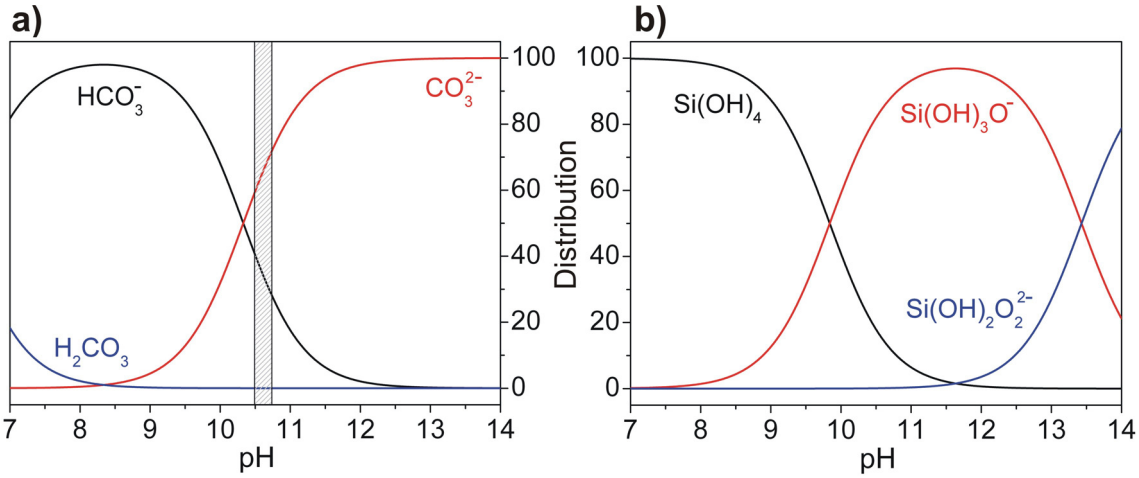

Fig. A-1: Distribution profiles for the different chemical species of (a) carbonate and (b) monomeric silicate existing in solution at different pH. The shaded area in (a) marks the pH range in which precipitation was carried out in the present experiments.

It is evident that the fractions of the distinct species vary sensibly with the pH of the solution. For the silica, this has a particular consequence: starting from about pH 9, where significant dissociation of silicic acid sets in and anionic silicates are formed, the solubility increases dramatically with the pH.[3,4] Since precipitation of amorphous silica ($SiO_2^{(A)}$) proceeds via condensation of silanol groups (Si-OH) between saturated $Si(OH)_4$ molecules into siloxane bonds (Si-O-Si),[3] the solubility of silica is regulated by the concentration of silicic acid in equilibrium with the solid phase, according to:

$$SiO_2^{(A)} + 2\,H_2O \rightleftharpoons^{K_{Diss}} Si(OH)_4\big|_0$$

with $pK_{Diss} = 2.714$ for $T = 25°C$ and $p = 1$ bar.[5] Correspondingly, the solubility of silica is rather low around pH 7 and amounts to $[Si(OH)_4]_0 \approx 1.9$ mM (≈ 116 ppm). However, due to dissociation, $Si(OH)_4$ will be removed from the above equilibrium at elevated pH and more amorphous silica will dissolve. Over the relevant range of pH, the total solubility of silica ($[SiO_2]_{total}$) is equal to the sum of the concentrations of all present silicate species which, using Eqns. A-1 to A-3, can be written as

$$\begin{aligned}[SiO_2]_{total} &= [Si(OH)_4]_0 + [SiO(OH)_3^-] + [SiO_2(OH)_2^{2-}] \\ &= [Si(OH)_4]_0 \cdot \left(1 + \frac{K_1}{[H^+]} + \frac{K_1 \cdot K_2}{[H^+]^2}\right)\end{aligned} \qquad \text{(Eqn. A-4)}$$

The progression of the silica solubility with increasing pH calculated in this way is displayed in Fig. A-2a.

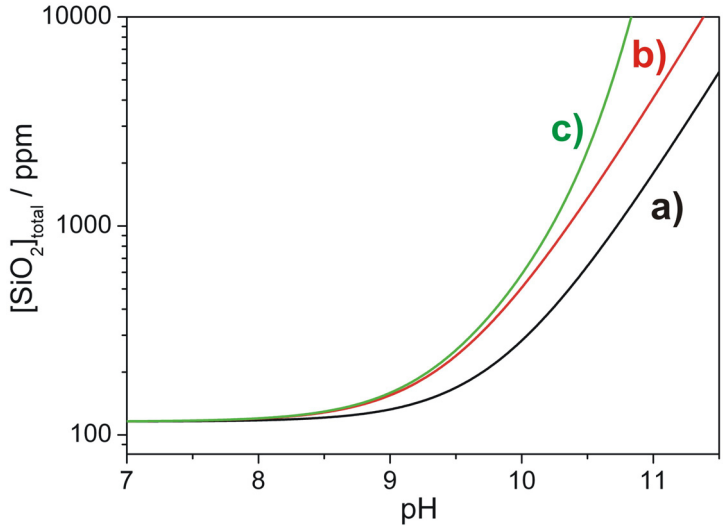

Fig. A-2: Total solubility of silica as a function of the pH. (a-b) Profiles were calculated under the assumption that only silica monomers ($Si(OH)_4$, $SiO(OH)_3^-$ and $SiO_2(OH)_2^{2-}$) are present in solutions at an ionic strength of (a) 0 and (b) 0.6 M. (c) Solubility curve obtained when admitting, at I = 0.6 M, apart from the dissociation of the monomer also the formation of the singly ($Si_2O_2(OH)_5^-$) and doubly charged ($Si_2O_3(OH)_4^{2-}$) dimer as well as the triply charged linear ($Si_3O_5(OH)_5^{3-}$) and cyclic ($Si_3O_6(OH)_3^{3-}$) trimer. The formation and dissociation constants of the different species used for the calculations were those reported by Sjöberg for T = 25°C.[8]

Although taking into account only monomeric neutral and ionic species at infinite dilution yields curves that reflect well qualitative changes in the solubility with pH, absolute values thus obtained usually differ noticeably from factual solubilities. This is because, on the one hand, silica solutions with concentrations higher than 10 mM (≈ 600 ppm) contain an appreciable amount of diversely charged oligomeric and polymeric species, including linear, cyclic and cage-like structures,[6] which form by condensation of monomers and hence promote solubility. On the other hand, the particular formation and dissociation constants of the distinct species vary sensibly with the ionic strength.[7] To give an idea on the order of magnitude of corresponding effects, the total solubility of silica was evaluated exemplarily for systems at an ionic strength of I = 0.6 M in which only monomers (Fig. A-2b) or in addition also dimers and trimers (Fig. A-2c) exist in equilibrium. Obviously, the assumed higher ionic strength and the consideration of oligomers increase the predicted solubility. In practice, the distribution of species is by far more complicated than indicated here,[8] and other polynuclear compounds (such as cyclic tetramers or cubic octamers) further reinforce the overall solubility. Moreover,

a certain fraction of the silica may occur in the form of finely dispersed nanoscale particles,[3,9] thus imparting a higher apparent solubility to the sol.

A.2 Evaluations for ACC Particle Formation in Silica-Containing Solutions

Based on the above considerations and with respect to the pH data shown in Section 2.4.5 (cf. Fig. 2-18), it is possible to estimate the fractions of carbonate and bicarbonate ions existing in equilibrium in the course of ACC formation in the presence of silica. Exemplarily, percentages of the two ions were calculated using Eqns. A-1 to A-3 for the pH detected after 2 min. Results for mixtures of various silica contents are listed in Table A-1, evidencing that significant amounts of both ions occur in the systems during precipitation.

ppm SiO_2	pH after 2 min	% HCO_3^-	% CO_3^{2-}
0	10.69	30.19	69.81
135	10.64	32.77	67.23
270	10.56	36.79	63.21
375	10.57	36.05	63.95
540	10.54	37.65	62.35
750	10.51	39.40	60.60
1230	10.57	36.26	63.74
1870	10.71	29.37	70.63

Table A-1: pH values measured 2 min after mixing in samples at different silica concentrations and the corresponding molar percentages of carbonate and bicarbonate ions theoretically expected in equilibrium.

Concerning the solubility of silica, theoretical evaluations suggest a limit of about 2000-3000 ppm at the pH values determined for the samples (cf. Fig. A-2). However, the used water glass dilutions in fact proved to be stable and optically isotropic solutions at concentrations of up to at least 4000 ppm, both at their given native pH (10.8-11.2) and at that effected upon successive addition of Na_2CO_3 and $CaCl_2$ (10.5-11.0). Light scattering measurements moreover confirmed that the silica solutions did not contain traceable amounts of nanocolloids. It can thus be inferred that silica is soluble under the bulk conditions of the experiments. This has an essential implication: precipitation of silica on the carbonate particles must be related to the local circumstances prevailing at their surface. The removal of carbonate ions due to the formation of ACC is expected to cause a substantial amount of bicarbonate ions to dissociate, in order to re-establish

equilibrium speciation at the given pH (see shaded area in Fig. A-1a). The associated production of protons in the vicinity of the particles should lead to a decrease of the silica solubility in this region (Fig. A-2) and consequently favor polymerization. However, this does not necessarily imply that the local pH around the particles has to drop below a certain critical value (e.g. < 9) to trigger precipitation. Alternatively, on a molecular level, the released protons may react instantly with silicate anions to $Si(OH)_4$ species (Fig. A-1b) which then rapidly condense and trigger precipitation of amorphous silica.

References

(1) Andersen, C. B. *J. Geosci. Edu.* **2002**, *50*, 389.

(2) Dove, P. M.; Rimstidt, J. D. *Rev. Mineral. Geochem.* **1994**, *29*, 259.

(3) Iler, R. K. *The chemistry of silica*, Wiley: New York, 1979.

(4) Alexander, G. B.; Heston, W. M.; Iler, R. K. *J. Phys. Chem.* **1954**, *58*, 453.

(5) Rimstidt, J. D.; Barnes, H. L. *Geochim. Cosmochim. Acta* **1980**, *44*, 1683.

(6) (a) Lentz, C. W. *Inorg. Chem.* **1964**, *3*, 574. (b) Harris, R. K.; Knight, C. T. G.; Hull, W. E. *J. Am. Chem. Soc.* **1981**, *103*, 1577. (c) Cary, L. W.; De Jong, B. H. W. S.; Dibble, W. E. Jr. *Geochim. Cosmochim. Acta* **1982**, *46*, 1317. (d) Sjöberg, S.; Öhman, L.-O.; Ingri, N. *Acta Chem. Scand.* **1985**, *A39*, 93. (e) Svensson, I. L.; Sjöberg, S.; Öhman, L.-O. *J. Chem. Soc. Faraday Trans. 1* **1986**, *82*, 3635. (f) Bass, J. L.; Turner, G. L. *J. Phys. Chem. B* **1997**, *101*, 10638. (g) Felmy, A. R.; Cho, H.; Rustad, J. R.; Mason, M. *J. Solution Chem.* **2001**, *30*, 509.

(7) (a) Engelhardt, G.; Zeigan, D.; Jancke, H.; Hoebbel, D.; Wieker, W. *Z. Anorg. Allg. Chem.* **1975**, *418*, 17. (b) Sjöberg, S.; Hägglund, Y.; Nordin, A.; Ingri, N. *Mar. Chem.* **1983**, *13*, 35. (c) Icopini, G. A.; Brantley, S. L.; Heaney, P. J. *Geochim. Cosmochim. Acta* **2005**, *69*, 293.

(8) Sjöberg, S. *J. Non-Cryst. Solids* **1996**, *196,* 51.

(9) Bergna, H. E. *The colloid chemistry of silica*, Advances in chemistry, Volume 234, American Chemical Society: Washington, DC, 1994.

B. Results of EDXRD Measurements

In the following, the full set of EDXRD data discussed in this work is reproduced. Successively, time-dependent diffraction patterns of samples with increasing silica content are illustrated for reaction temperatures of 20, 50 and 80°C in the form of 2-D contour plots (left) as well as by means of 3-D representations (right), in which the occurring reflections are assigned to families of planes in the calcite (C), vaterite (V), or aragonite (A) lattice.

20°C

0 ppm SiO_2

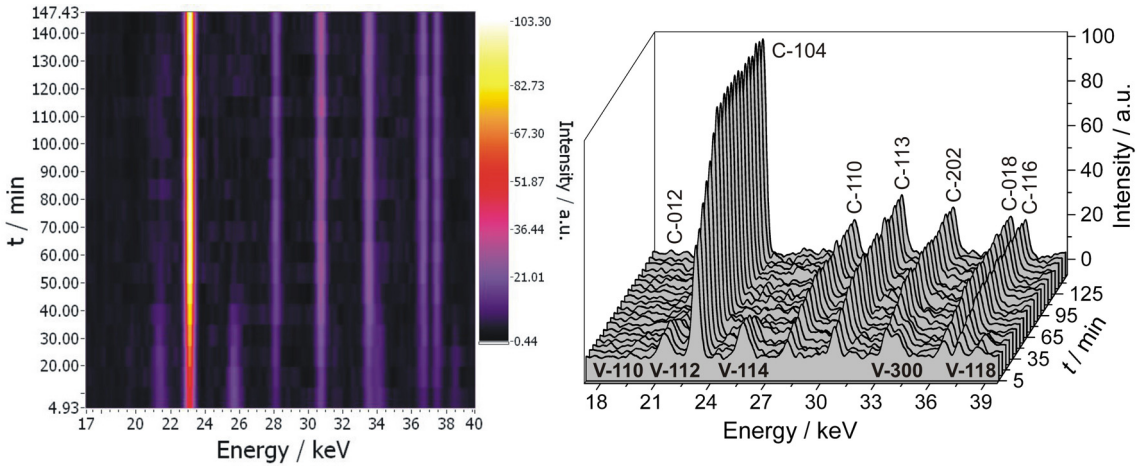

200 ppm SiO_2

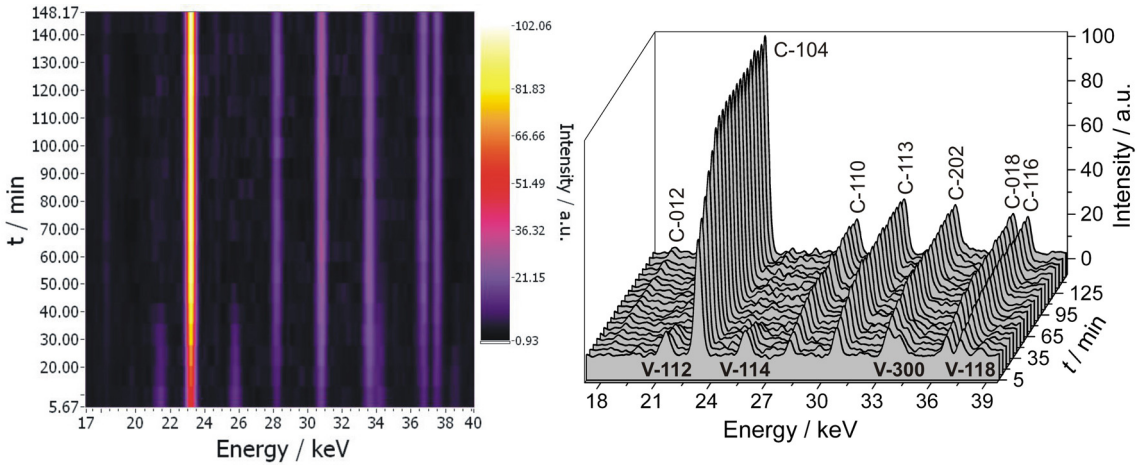

600 ppm SiO_2

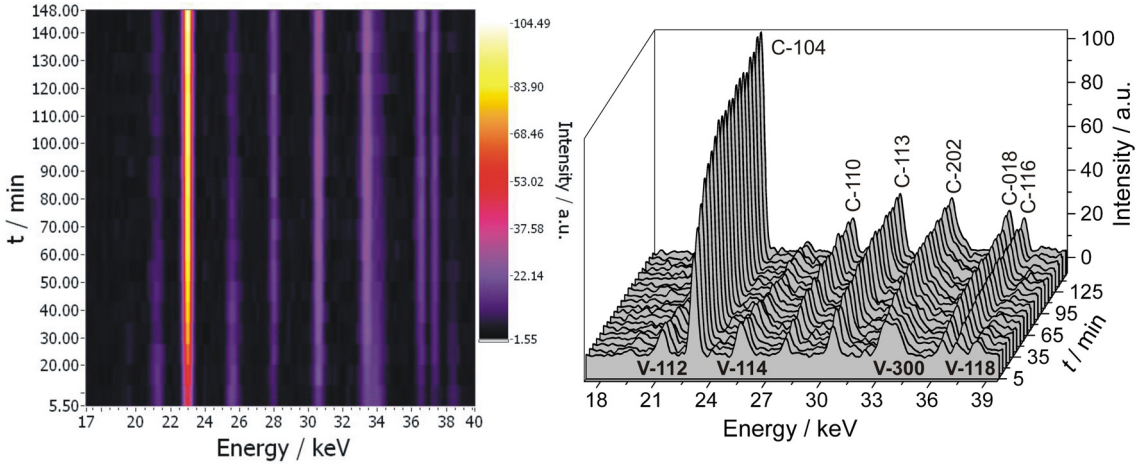

1200 ppm SiO_2

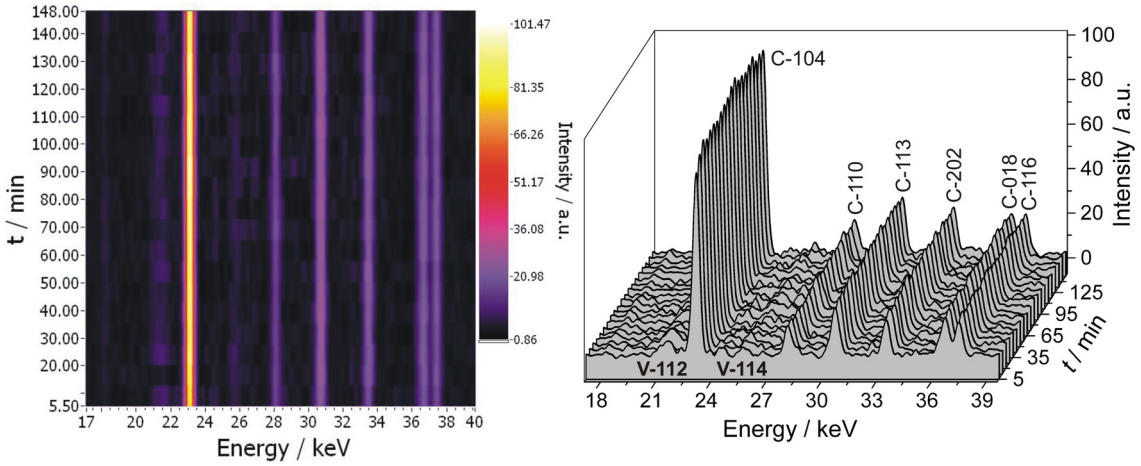

2000 ppm SiO_2

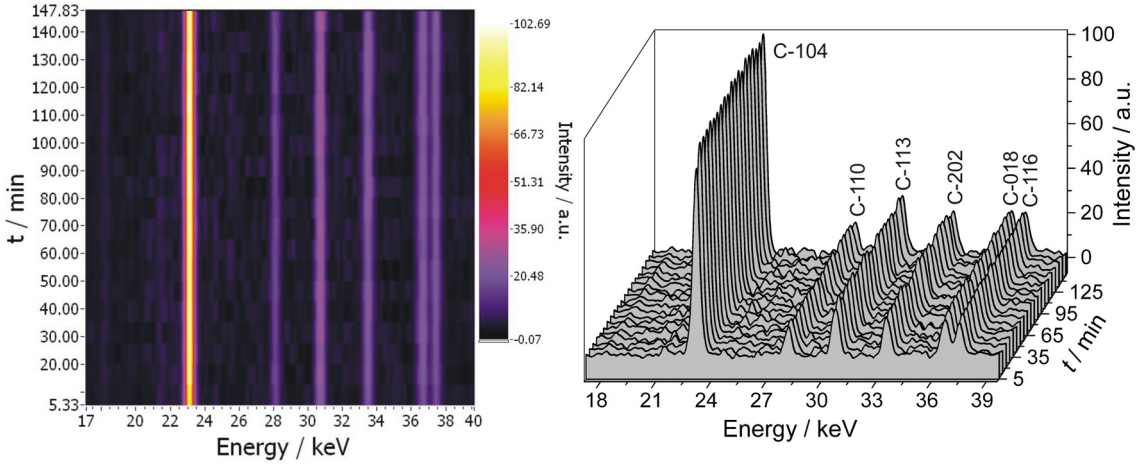

5000 ppm SiO_2

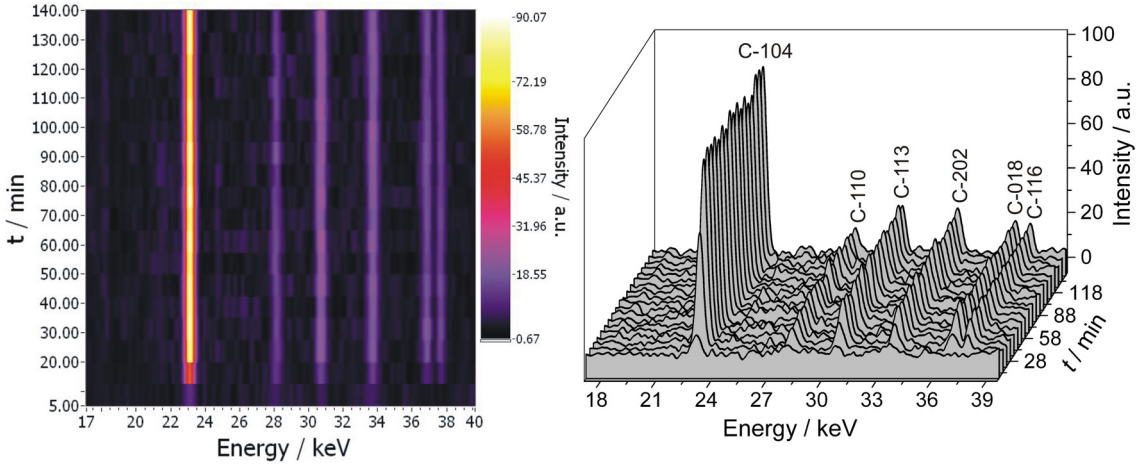

10000 ppm SiO_2

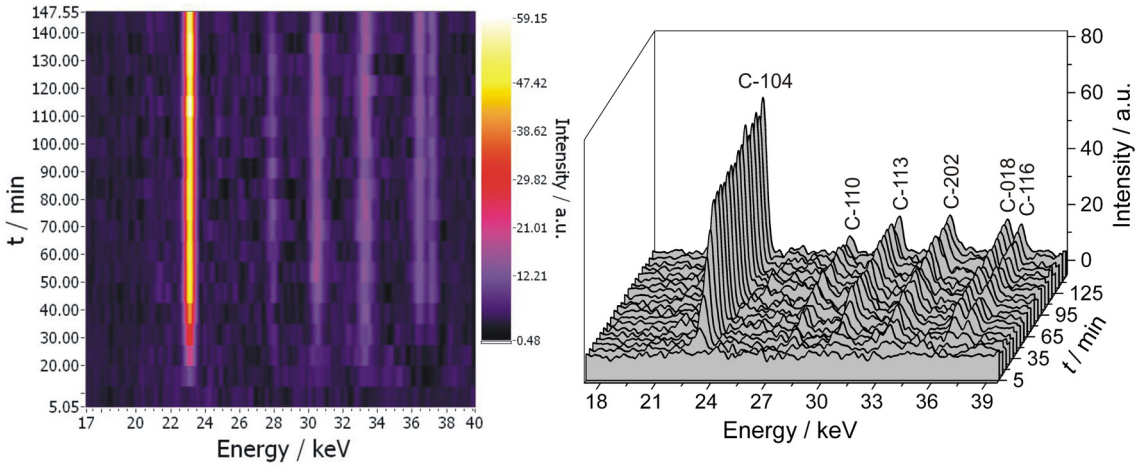

20000 ppm SiO_2

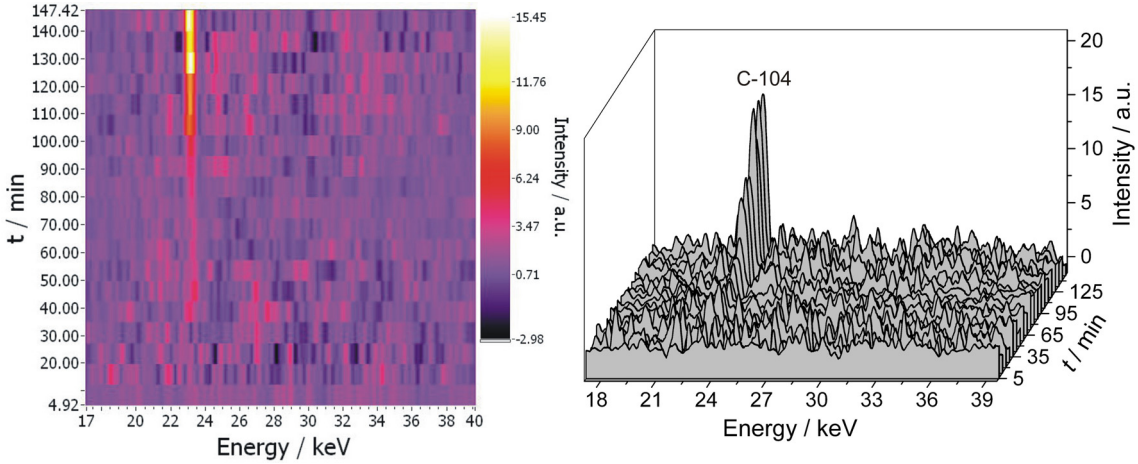

50°C

0 ppm SiO_2

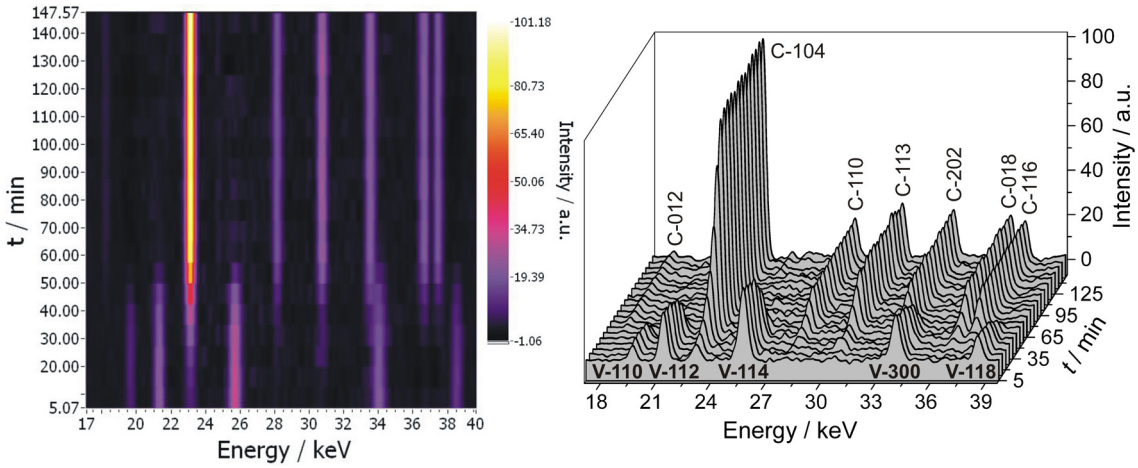

200 ppm SiO_2

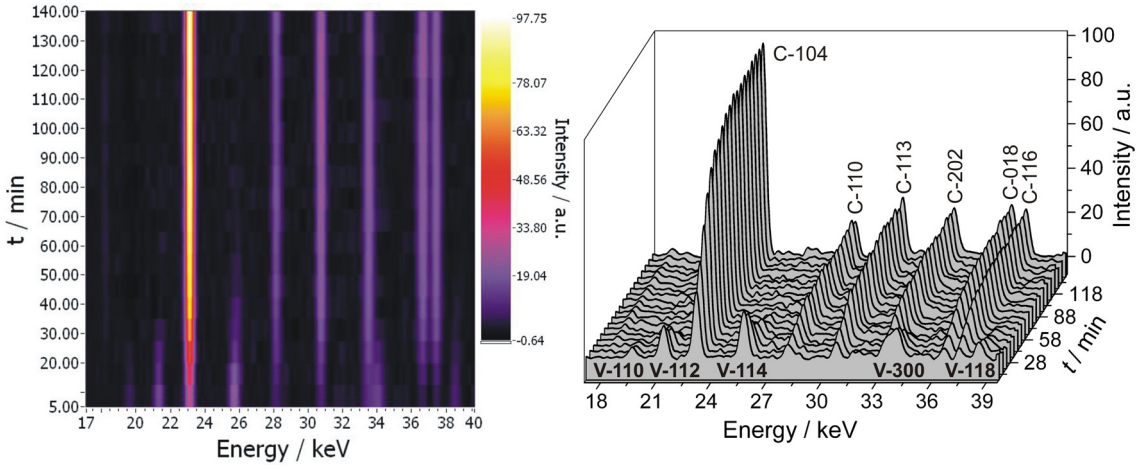

600 ppm SiO_2

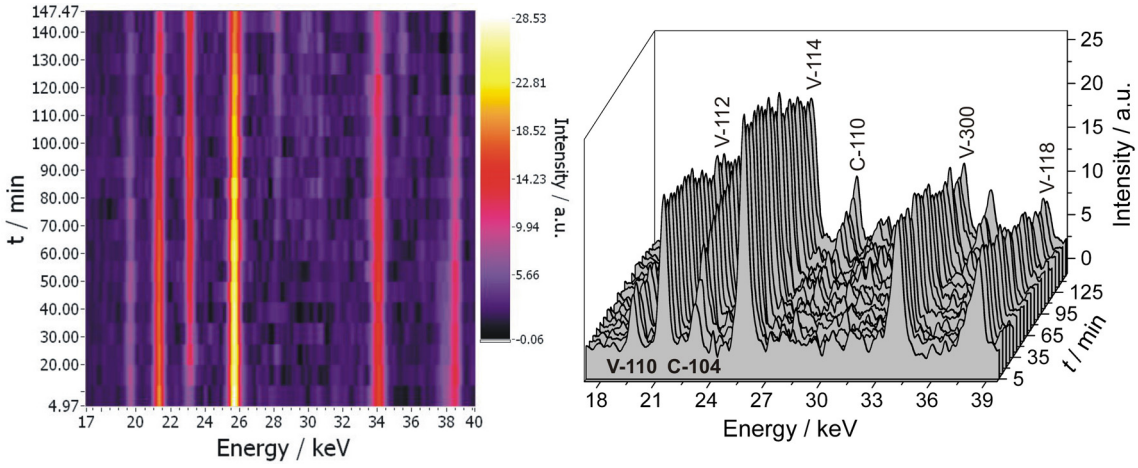

1200 ppm SiO_2

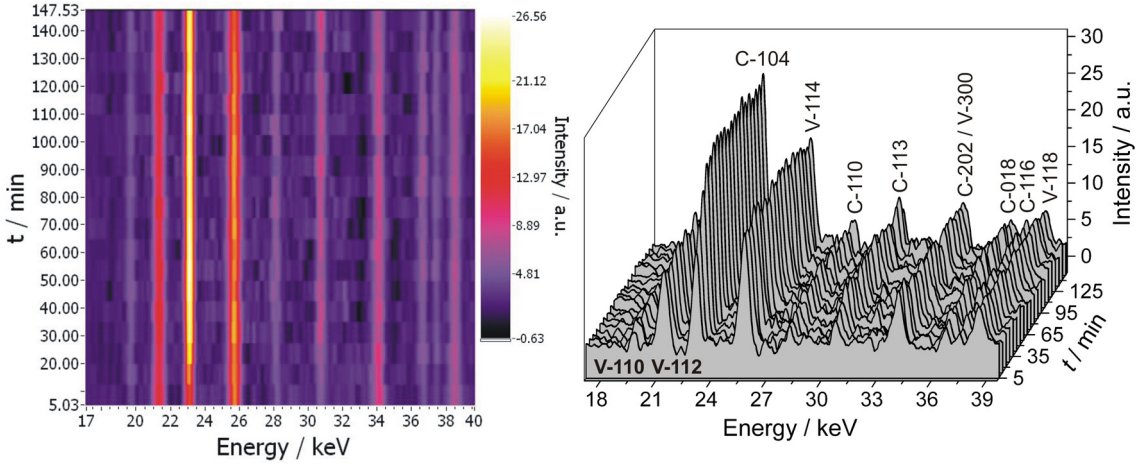

2000 ppm SiO_2

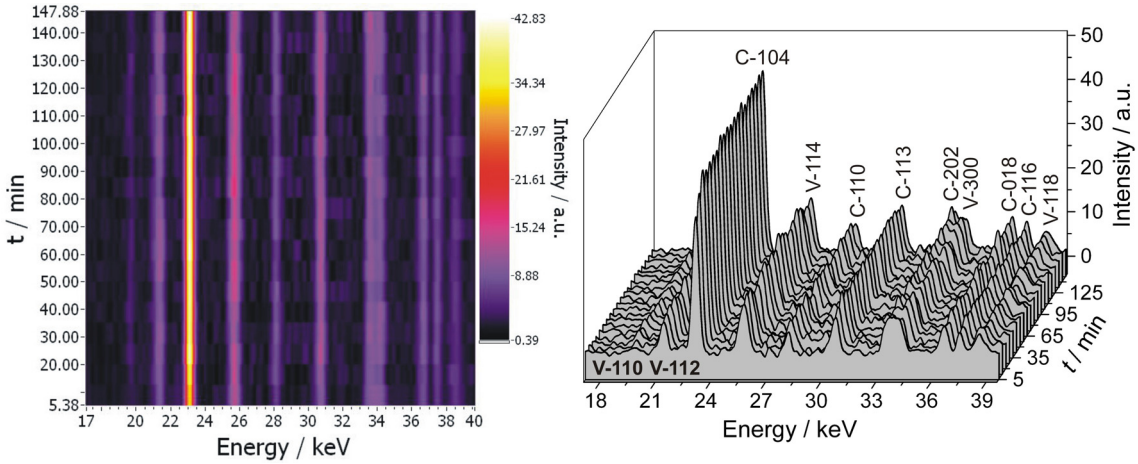

5000 ppm SiO_2

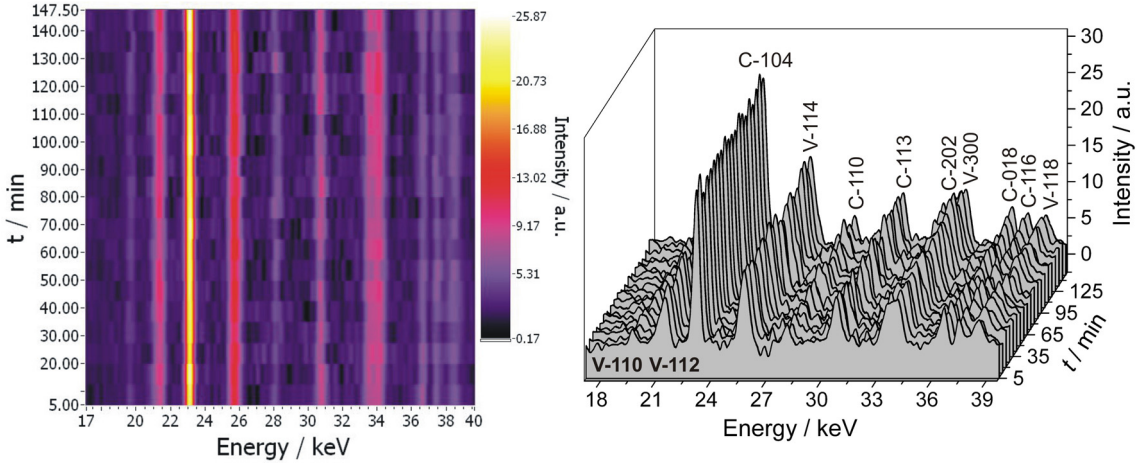

10000 ppm SiO_2

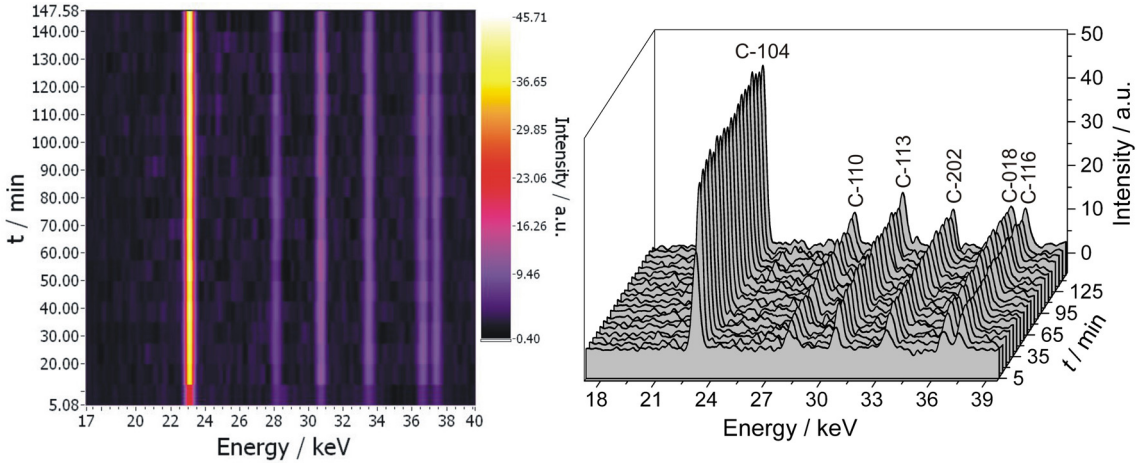

80°C

0 ppm SiO_2

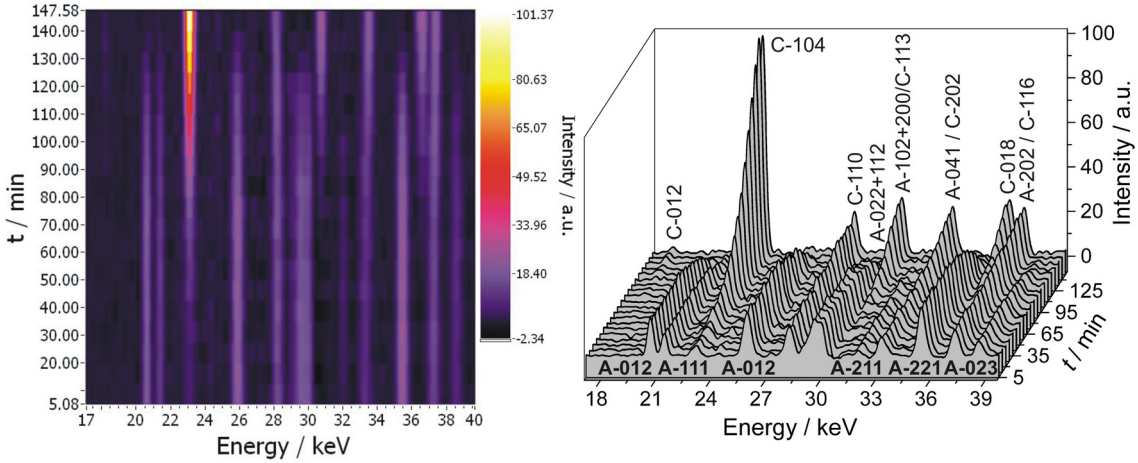

200 ppm SiO_2

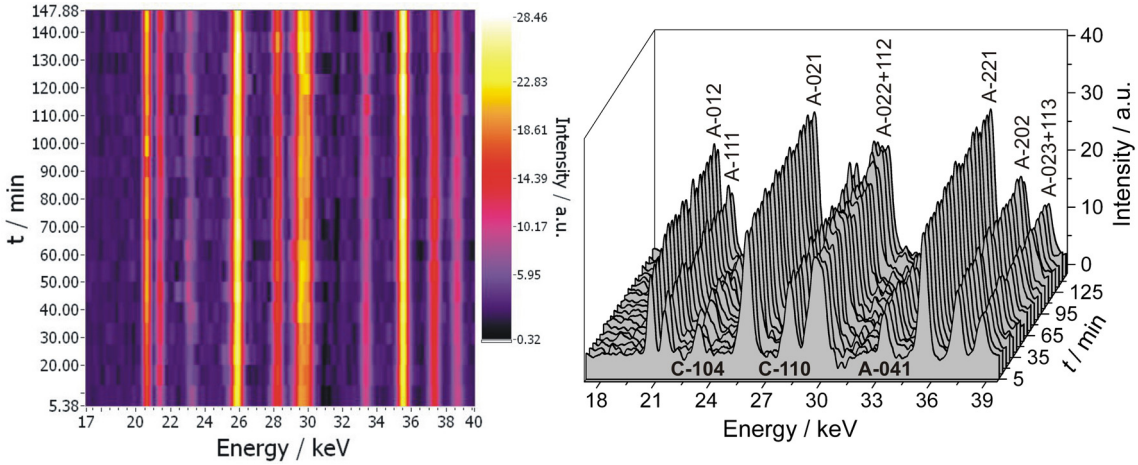

600 ppm SiO_2

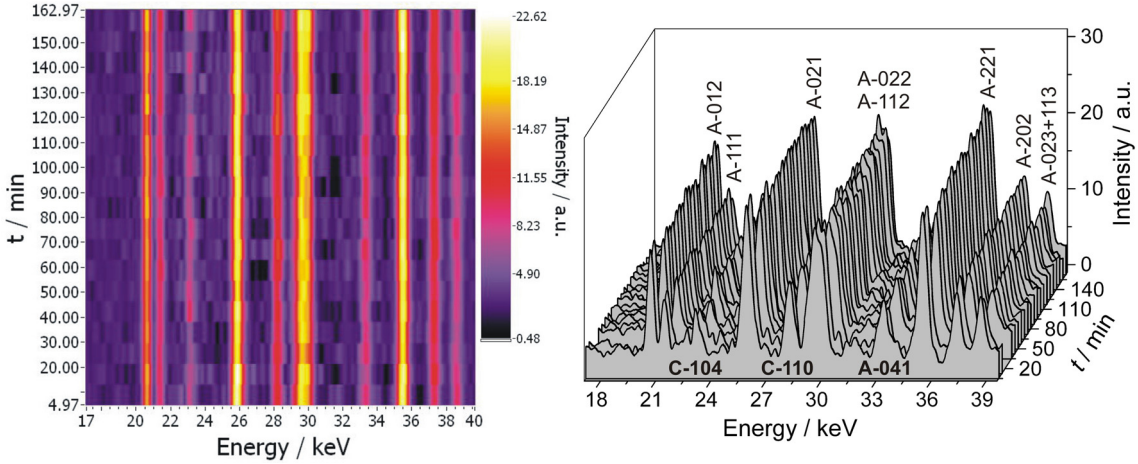

1200 ppm SiO_2

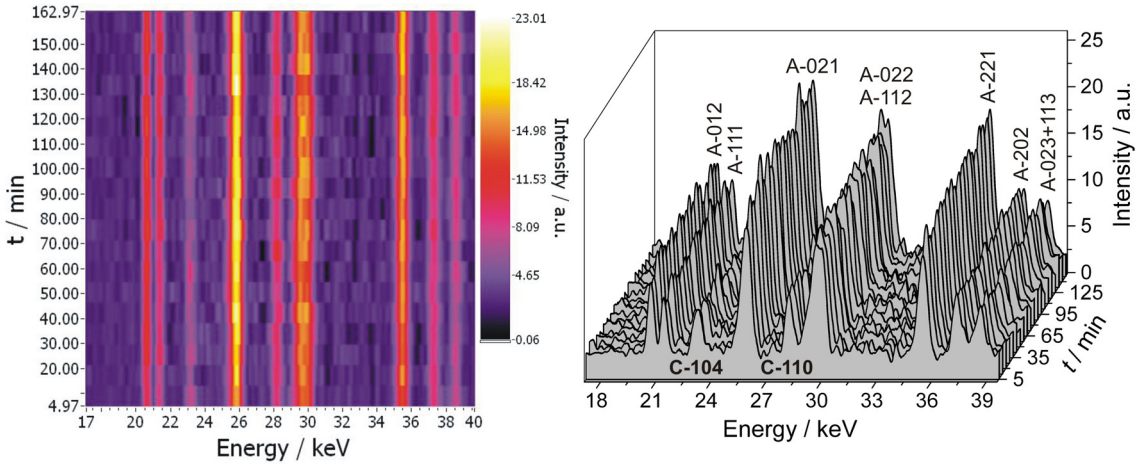

2000 ppm SiO_2

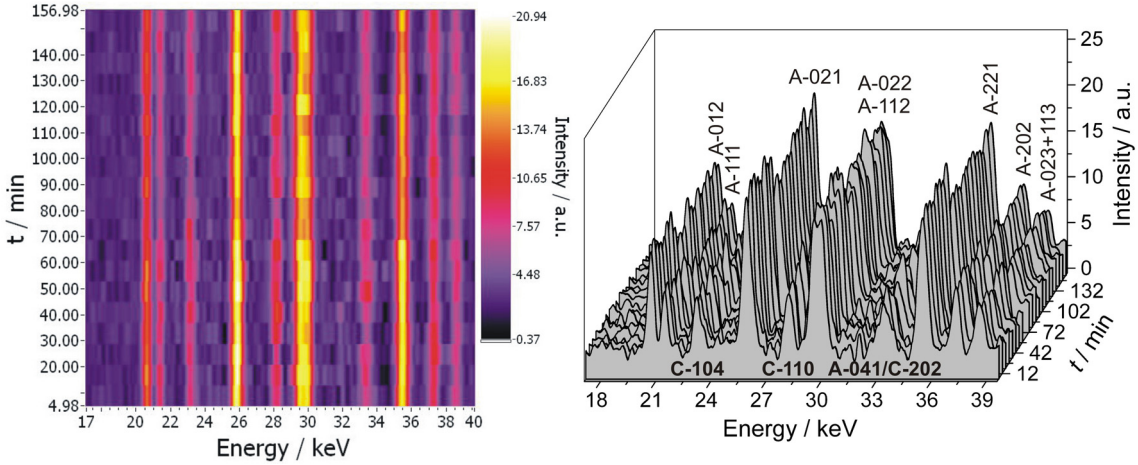

5000 ppm SiO_2

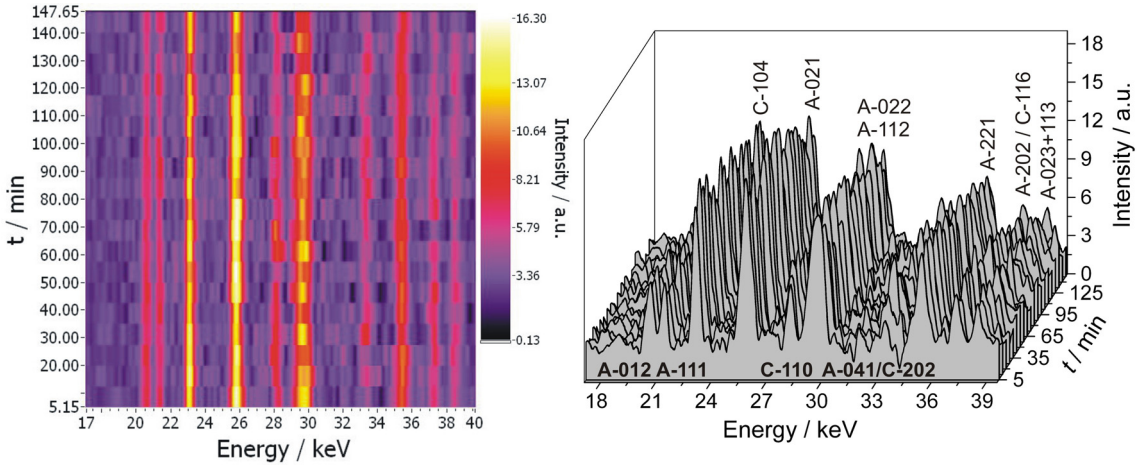

10000 ppm SiO_2

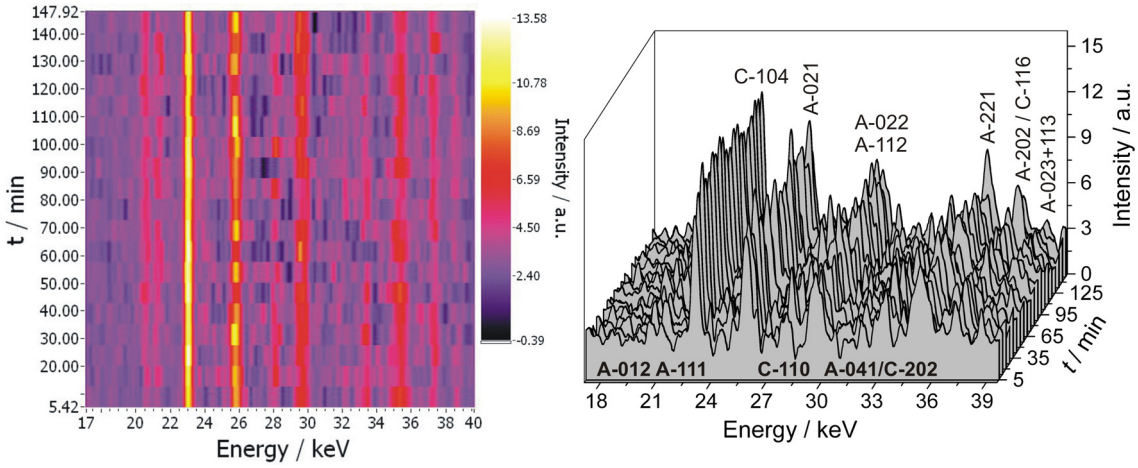

C. Growth Kinetics of Silica Biomorphs

C.1 Estimation of the Actual Carbonate Concentration from Measured pH Profiles

Titrations of silica biomorph mother solutions were performed by adding aliquots of 0.01 M hydrochloric acid to moderately stirred mixtures of equal volumes of 0.01 M $BaCl_2$ and a 1-350 silica dilution (with added NaOH) and reading the pH after equilibration. These experiments were carried out under water-saturated nitrogen atmosphere with solutions previously freed from dissolved CO_2 by purging with N_2 for several hours, so as to preclude the presence of any carbonate. A typical titration curve thus obtained is shown in Fig. C-1.

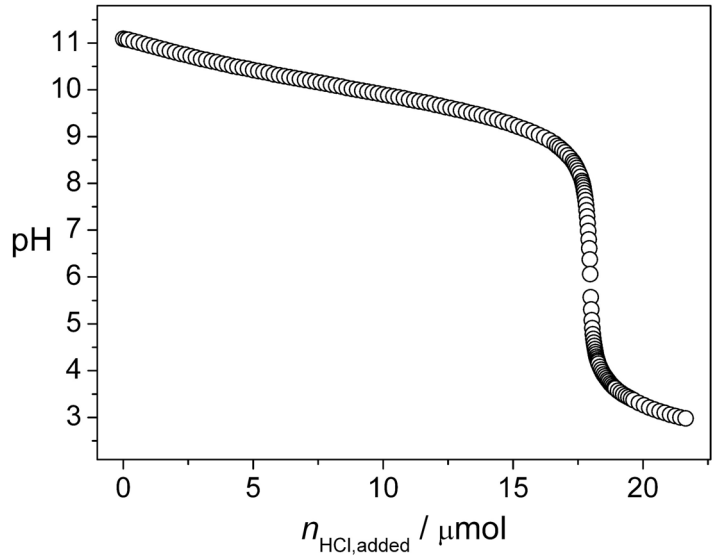

Fig. C-1: The pH of 2 mL silica biomorph mother solution as a function of the amount of added acid, as determined by titration with dilute HCl under CO_2-free conditions.

The initial pH of the reaction mixture measured in the absence of carbonate is slightly higher (about 0.05 units) than under regular growth conditions in contact with the atmosphere. This is again evidence for the presence of pre-dissolved carbonate in the silica sols used for the syntheses, in line with the barium concentration detected by XFS straight after mixing (cf. Section 6.4.1). Further, the titration data suggest that the silica has a marked buffering effect on the pH of the system over a pH interval of about 9-10.5. Calculations of the buffering capacity of the solutions (not shown) reveal a maximum at around pH 10, which roughly coincides with the pK_a value of silicic acid (9.9).[1]

The observed progression of the pH with the amount of added HCl during titration, respectively the inverse function $n_{HCl,added}$ = f(pH), was fitted by describing the data with a spline interpolation in the software Maple (version 7.0) (Fig. C-2).

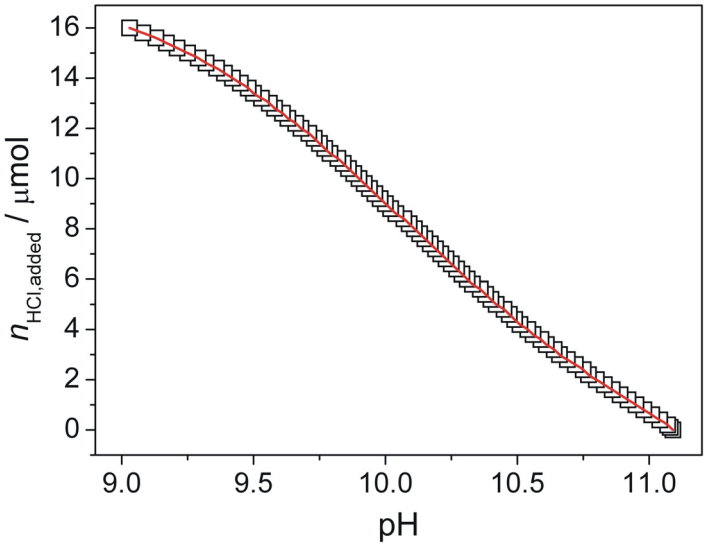

Fig. C-2: Plot of the mole number of titrated HCl versus the corresponding measured pH within the range of pH relevant for biomorph growth. The red line is a fit of data achieved by interpolating the experimental data with a spline routine

The resulting equations were then used to convert the pH values of growth to apparent quantities of generated protons, as depicted in Fig. C-3.

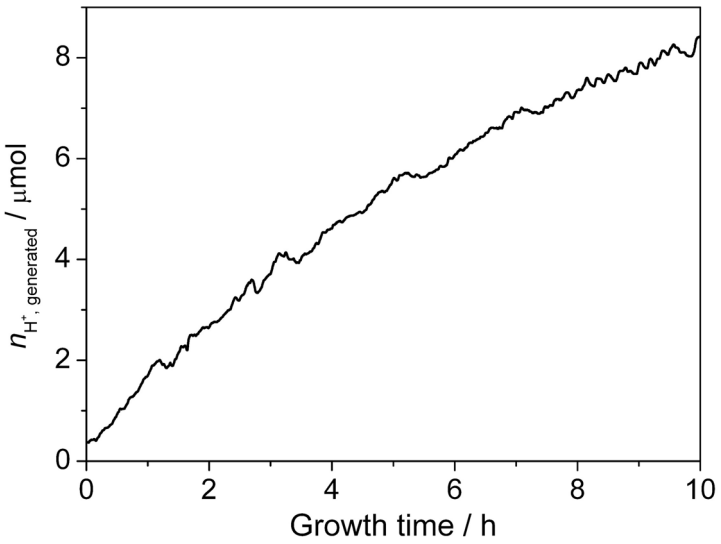

Fig. C-3: Molar amounts of protons generated in solution as a function of the growth time.

The continuous uptake of CO_2 by the system and its successive conversion to bicarbonate and carbonate lead to a steady increase in the amount of generated protons.

In molar terms, the latter is related to the amounts of bicarbonate and carbonate dissolved and barium carbonate precipitated at time *t* according to

$$n_{\mathrm{H^+generated}}(t) = n_{\mathrm{HCO_3^-}}(t) + 2\,n_{\mathrm{CO_3^{2-}}}(t) + 2\,n_{\mathrm{BaCO_3\ precipitated}}(t) \qquad \text{(Eqn. C-1)}$$

With the definition for the mole fraction of carbonate ions existing in equilibrium

$$x_{\mathrm{CO_3^{2-}}}(t) = \frac{n_{\mathrm{CO_3^{2-}}}(t)}{n_{\mathrm{CO_3^{2-}}}(t) + n_{\mathrm{HCO_3^-}}(t)} \qquad \text{(Eqn. C-2)}$$

it follows that

$$n_{\mathrm{HCO_3^-}}(t) = \frac{1 - x_{\mathrm{CO_3^{2-}}}(t)}{1 + x_{\mathrm{CO_3^{2-}}}(t)} \cdot \left(n_{\mathrm{H^+generated}}(t) - 2\,n_{\mathrm{BaCO_3\ precipitated}}(t) \right) \qquad \text{(Eqn. C-3)}$$

The term $x_{\mathrm{CO_3^{2-}}}$ represents the distribution of carbonate species in solution which, when assuming ideality for the dilute systems, is determined solely by the bulk pH. Based on the dissociation equilibria of carbonic acid

$$\mathrm{H_2CO_3} \underset{}{\overset{K_1}{\rightleftharpoons}} \mathrm{HCO_3^-} + \mathrm{H^+} \overset{K_2}{\rightleftharpoons} \mathrm{CO_3^{2-}} + 2\,\mathrm{H^+}$$

the mole fraction of carbonate ions can be written as

$$x_{\mathrm{CO_3^{2-}}}(t) = \frac{K_1 \cdot K_2}{K_1 \cdot K_2 + K_1 \cdot 10^{-\mathrm{pH}(t)} + \left(10^{-\mathrm{pH}(t)}\right)^2} \qquad \text{(Eqn. C-4)}$$

where K_1 and K_2 are the first and second dissociation constant of carbonic acid. The amount of precipitated barium carbonate can be derived from the temporal change in the concentration of dissolved Ba^{2+} observed by XFS. Since a linear decrease was found (cf. Fig. 6-4), a corresponding fit yields a straightforward equation for the calculation of $[Ba^{2+}]$ at time *t*:

$$[\mathrm{Ba^{2+}}] = \left(4.889 - 0.183 \cdot \frac{t}{\mathrm{h}} \right) \mathrm{mM} \qquad \text{(Eqn. C-5)}$$

The difference between $[Ba^{2+}](t)$ and the analytical initial Ba^{2+} concentration is equal to the quantity of carbonate ions consumed by precipitation of $BaCO_3$, such that $n_{\mathrm{BaCO_3\ precipitated}}(t)$ can readily be obtained according to

$$n_{\mathrm{BaCO_3\ precipitated}}(t) = \left[\left(5\ \mathrm{mM} - [\mathrm{Ba^{2+}}](t)\right) \cdot 0.002\,\mathrm{L}\right]\ \mathrm{mmol} \qquad \text{(Eqn. C-6)}$$

Thus, with Eqns. C-3, C-4 and C-6 and the values for $n_{\mathrm{H^+\ generated}}(t)$ shown in Fig. C-3, the amount of dissolved bicarbonate ions present in the mixtures at a given pH and time can be calculated and taken to determine the amount of carbonate ions via Eqn. C-1. When neglecting the fractions of carbonic acid and dissolved CO_2 in equilibrium at high pH, the total amount of carbonate in the system is given as the sum of bicarbonate and carbonate ions:

$$n_{\mathrm{Total\ carbonate}}(t) = n_{\mathrm{HCO_3^-}}(t) + n_{\mathrm{CO_3^{2-}}}(t) + n_{\mathrm{BaCO_3\ precipitated}}(t) \qquad \text{(Eqn. C-7)}$$

Eventually, the obtained time-dependent data for the concentration of dissolved Ba^{2+} and CO_3^{2-} ions were used to evaluate the supersaturation ratio *S*, which is defined as

$$S = \frac{[\mathrm{Ba^{2+}}] \cdot [\mathrm{CO_3^{2-}}]}{K_{\mathrm{sp}}(\mathrm{BaCO_3})} \qquad \text{(Eqn. C-8)}$$

where $K_{sp}(BaCO_3)$ is the solubility product of barium carbonate.

Apart from ideality, another major assumption underlying the above-described methodology is that the pH is dominated by the buffer equilibria of silica, and that there is no distinct influence on the pH exerted by those of carbonate. Otherwise, the titration data could not be used to relate the measured pH to a number of generated protons, as they were collected under carbonate-free conditions. However, since the concentration of silica in the solutions is significantly higher ($\geq$ 8 mM within the first 8 h, cf. Fig. 6-8) than that of carbonate species ($\leq$ 0.5 mM at all times), this approximation can be considered to hold true at least within the given limits of error.

Calculations on the basis of Eqns. C-1, C-3 and C-6 occasionally yielded negative values for $n_{\mathrm{HCO_3^-}}$ and $n_{\mathrm{CO_3^{2-}}}$ during the first 10-15 min, when there is hardly any carbonate present in the system. These unreasonable results are likely to originate from the fact that the input data, i.e. the time-dependent pH and $[Ba^{2+}]$ profiles, were recorded in two independent experiments. Slight differences in the amount of pre-dissolved CO_2 (affecting the initial pH and the y-axis intercept of $[Ba^{2+}](t)$) or the mean rate of precipitation (altering the progress of $n_{\mathrm{H^+\ generated}}(t)$ and the slope of $[Ba^{2+}](t)$) could readily account for large relative errors when the total concentrations are small.

However, such discrepancies between the two experiments can partly be corrected for by introducing certain boundary conditions. When $BaCl_2$ solution is added to the silica sol, that is, at time $t = 0$, the presence of pre-dissolved carbonate species is expected to provoke instant precipitation of $BaCO_3$. Consequently, as long as diffusion has not delivered further CO_2 from the atmosphere, the amount of CO_3^{2-} ions in the system should correspond to the equilibrium value $n^{eq}_{CO_3^{2-}}$ set by the solubility product of barium carbonate and thereby, at a given pH, also determine the concentration of co-existing bicarbonate ($n^{eq}_{HCO_3^-}$). Thus, it follows that

$$n_{BaCO_3\,precipitated}(t=0) = \frac{1}{2}\left(n_{H^+generated}(t=0) - n^{eq}_{HCO_3^-} - 2n^{eq}_{CO_3^{2-}}\right) \quad \text{(Eqn. C-9)}$$

Obviously, the amount of initially precipitated $BaCO_3$ can under these circumstances be determined directly from the number of protons generated at $t = 0$. This was achieved by an iteration routine in Maple. The obtained value represents the concentration of Ba^{2+} ions consumed by instant precipitation as indicated by the pH data, and was found to be 0.09 mM. This implies a concentration of 4.91 mM for dissolved Ba^{2+} at $t = 0$ which, when compared to the value of ~4.89 mM obtained from the XFS measurement (cf. Eqn. C-6), suggests that either slightly more carbonate was pre-dissolved or precipitation occurred somewhat faster in the latter experiment, although differences are within the error bars determined for the intercept of the $[Ba^{2+}](t)$ curve. Nevertheless, the value for the y-axis intercept in Eqn. C-5 was substituted by that computed using the pH data, in order to correlate the experiments. Indeed, molar amounts obtained on that basis for both carbonate and bicarbonate ions in solution during the first 10-15 min were almost exclusively positive and close to the respective values expected in equilibrium with solid $BaCO_3$, consequently giving supersaturation ratios around 1. In turn, concentrations of the species during the later stages of growth were not affected to a noticeable degree. This shows that the applied procedure adequately eliminates errors caused by imperfect reproducibility of the experiments.

The eventually resulting temporal progressions of distinct species concentrations and the supersaturation ratio are displayed in Fig. C-4 and Fig. 6-5b. The values used for K_1, K_2, and $K_{sp}(BaCO_3)$ during the calculations were $4.47 \cdot 10^{-7}$ mol/L, $4.68 \cdot 10^{-11}$ mol/L, and $5.01 \cdot 10^{-9}$ mol^2/L^2, respectively.[2,3]

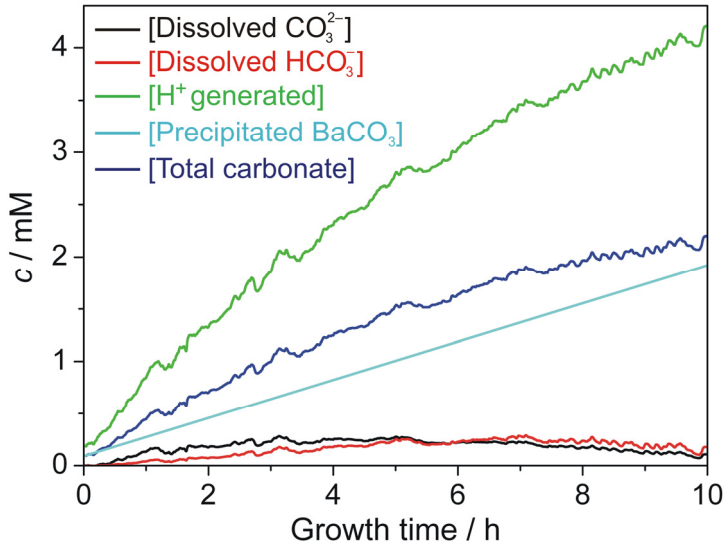

Fig. C-4: Calculated concentrations of dissolved carbonate and bicarbonate ions as a function of time during growth of silica biomorphs, together with the estimated quantities of generated protons and precipitated barium carbonate as well as the total amount of carbonate species present in the system.

References

(1) Iler, R. K. *The chemistry of silica*, Wiley: New York, 1979.

(2) Andersen, C. B. *J. Geosci. Edu.* **2002**, *50*, 389.

(3) Chen, P. C.; Cheng, G. Y.; Kou, M. H.; Shia, P. Y.; Chung, P. O. *J. Cryst. Growth* **2001**, *226*, 458.

C.2 Determination of Growth Rates from Further Optical Image Sequences

Sequence C-1

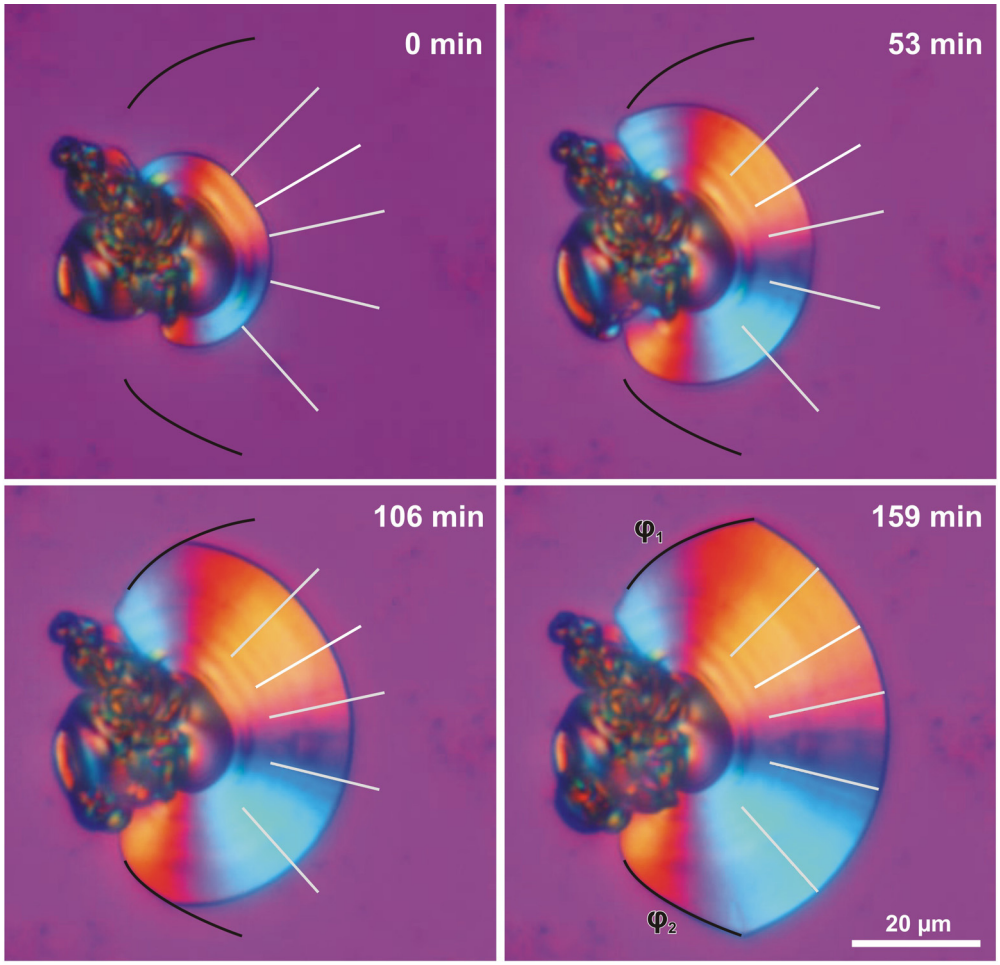

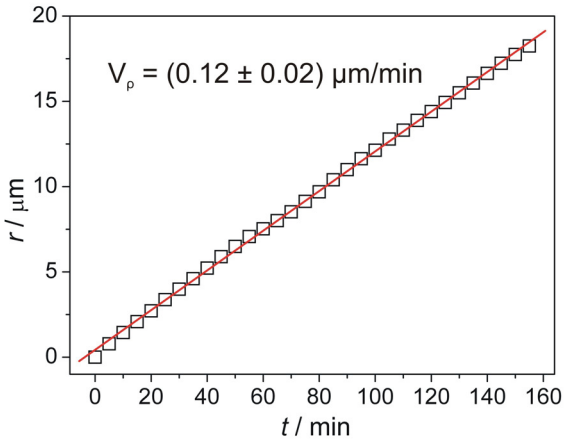

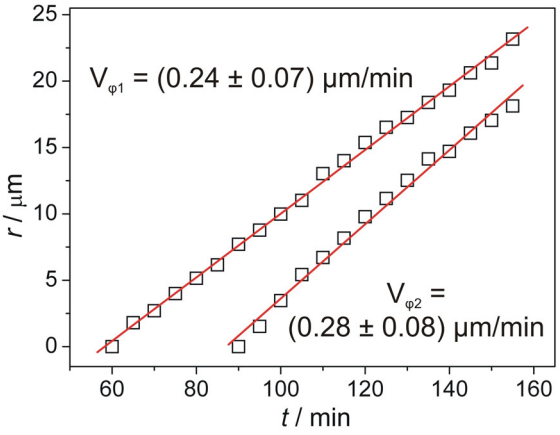

Sequence C-2

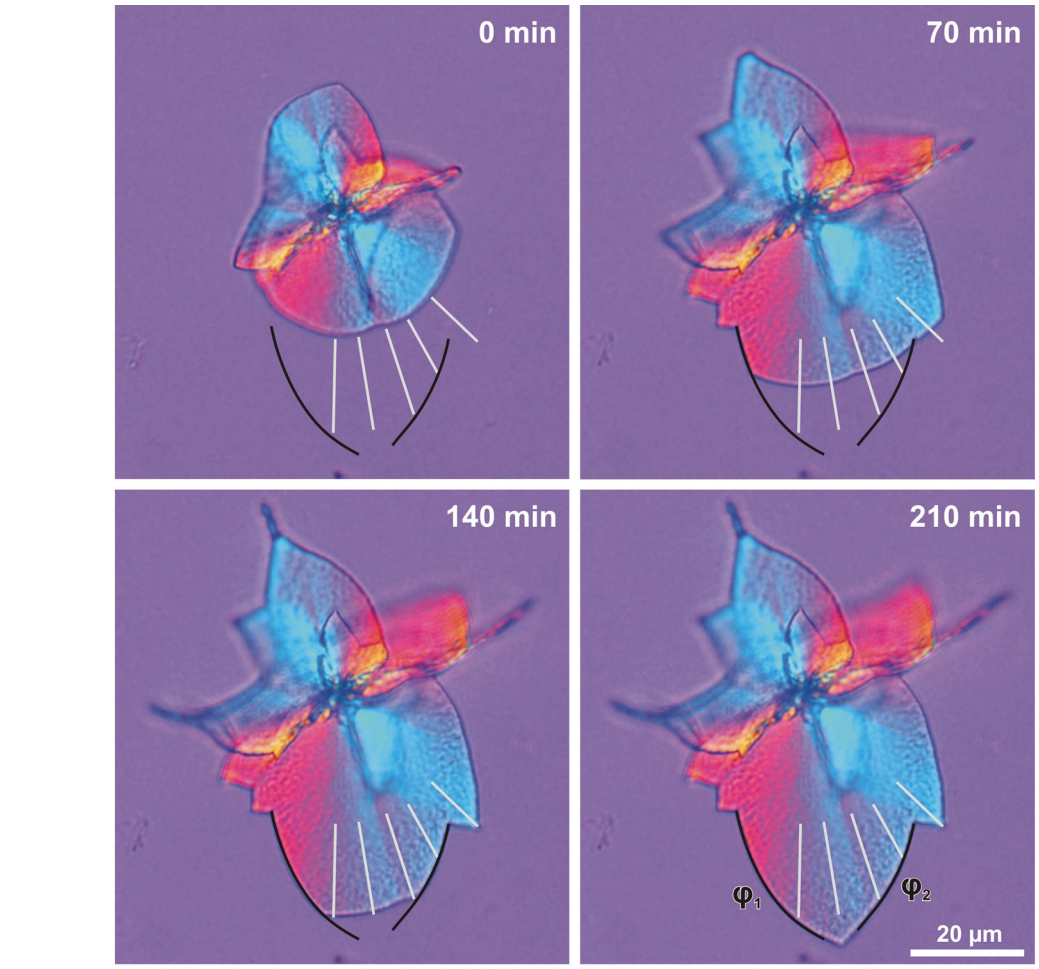
0 min
70 min
140 min
210 min
φ1
φ2
20 µm

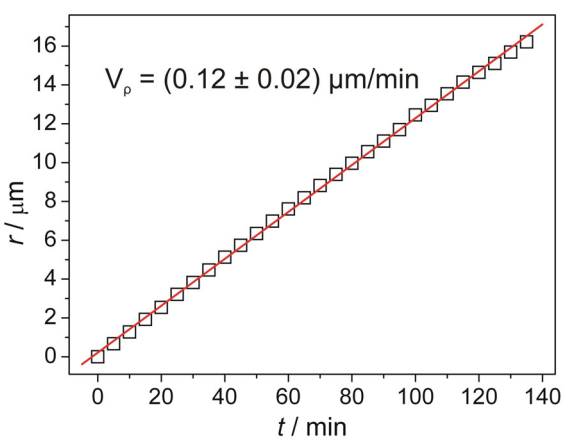
Vρ = (0.12 ± 0.02) µm/min
r / µm
t / min

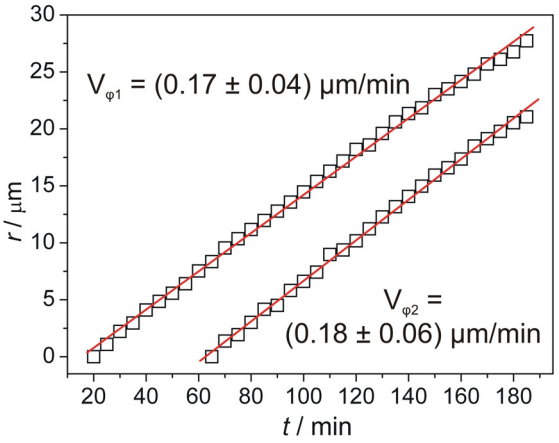
Vφ1 = (0.17 ± 0.04) µm/min
Vφ2 =
(0.18 ± 0.06) µm/min
r / µm
t / min

Sequence C-3

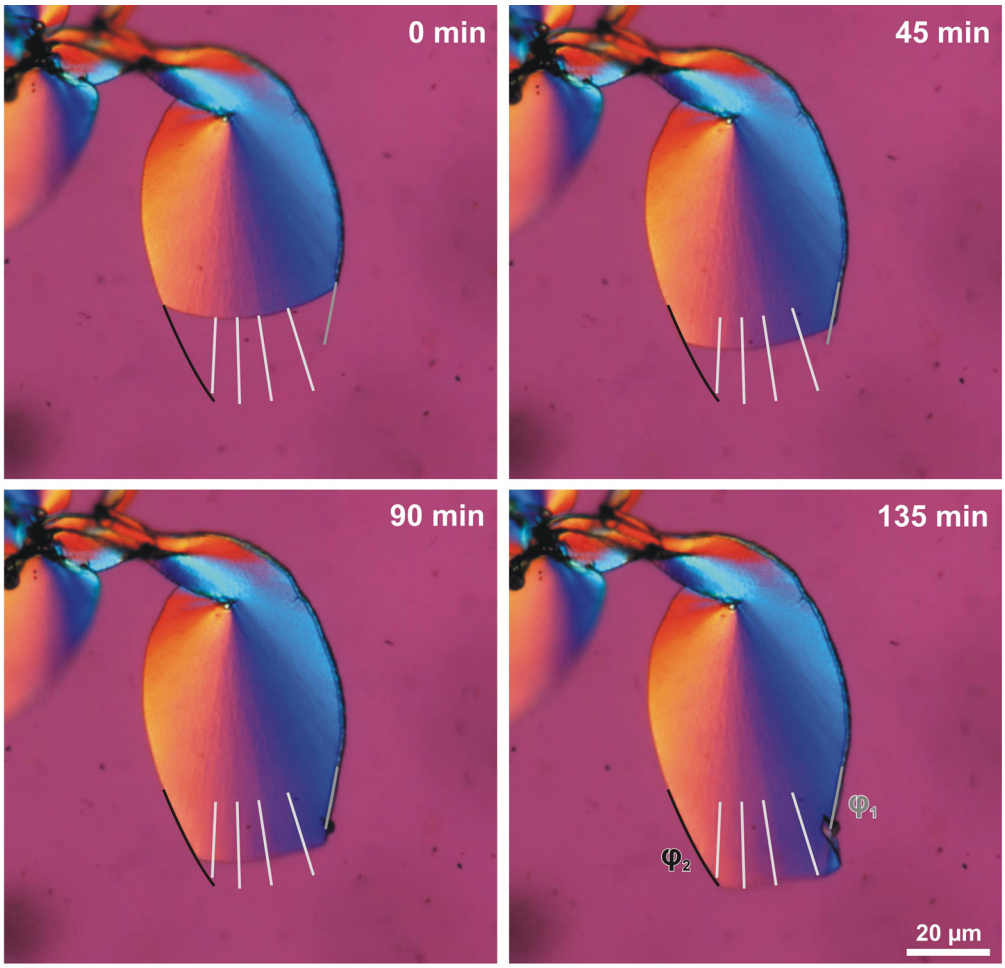
0 min
45 min
90 min
135 min
φ1
φ2
20 µm

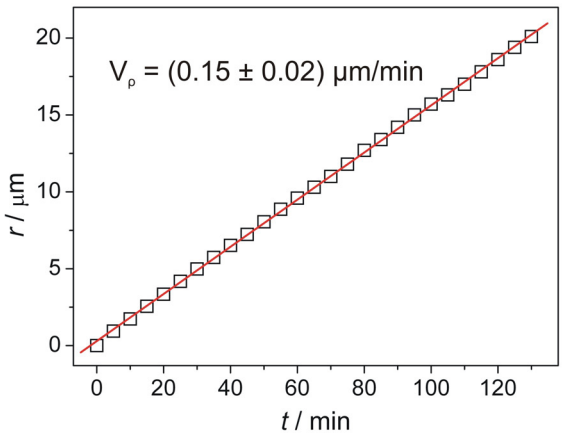
V_ρ = (0.15 ± 0.02) µm/min
r / µm
t / min

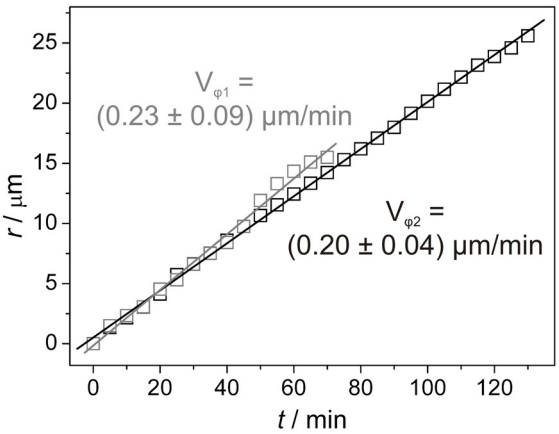
V_φ1 =
(0.23 ± 0.09) µm/min
V_φ2 =
(0.20 ± 0.04) µm/min
r / µm
t / min

Sequence C-4

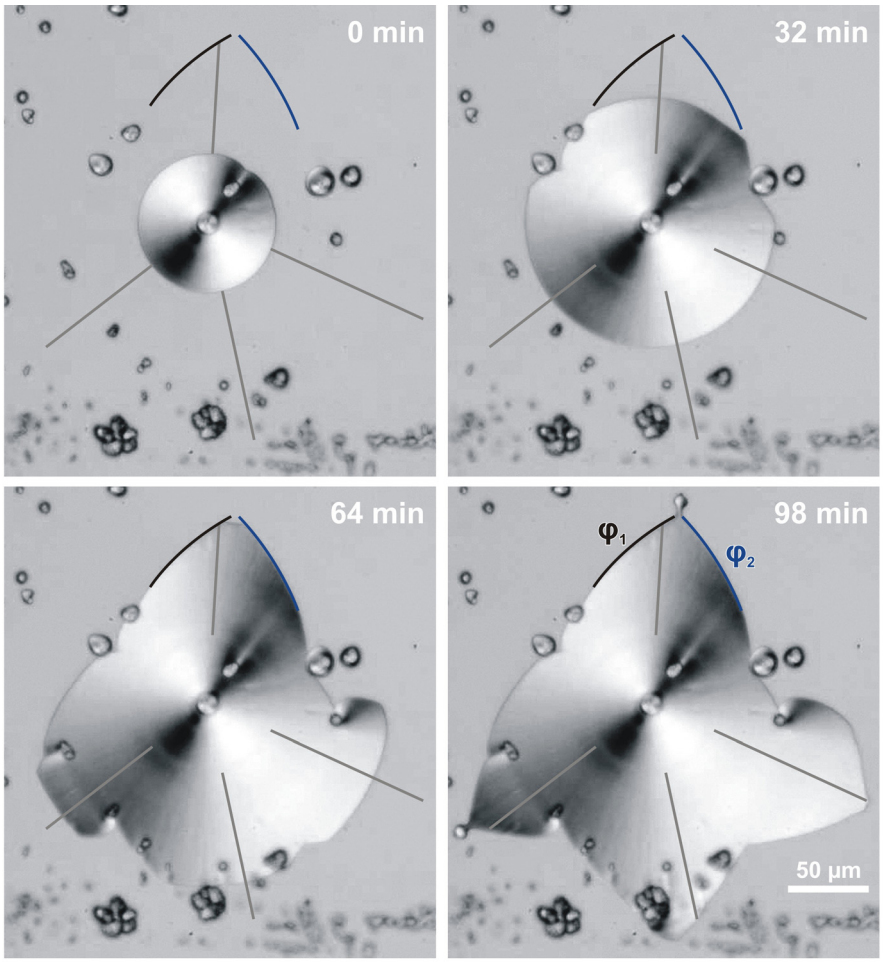
0 min
32 min
64 min
98 min
φ1
φ2
50 µm

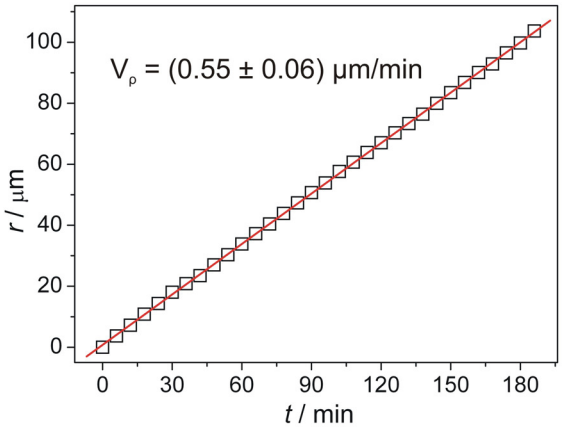
Vρ = (0.55 ± 0.06) µm/min
r / µm
t / min
0
20
40
60
80
100
0
30
60
90
120
150
180

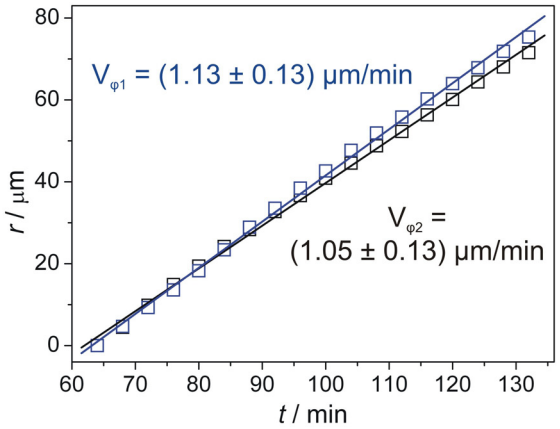
Vφ1 = (1.13 ± 0.13) µm/min
Vφ2 =
(1.05 ± 0.13) µm/min
r / µm
t / min
0
20
40
60
80
60
70
80
90
100
110
120
130

Sequence C-5

Occasionally, and in particular when growth is carried out from solution in vessels with high surface-to-volume ratio, image sequences yield $r(t)$ profiles which slightly deviate from linearity. This video shows a sheet which developed in the interval between 2 and 3 hours after mixing reagents in a flat well filled with solution up to only few millimeters in height, which was used to monitor growth with an inverted microscope (Zeiss Axiovert 200).

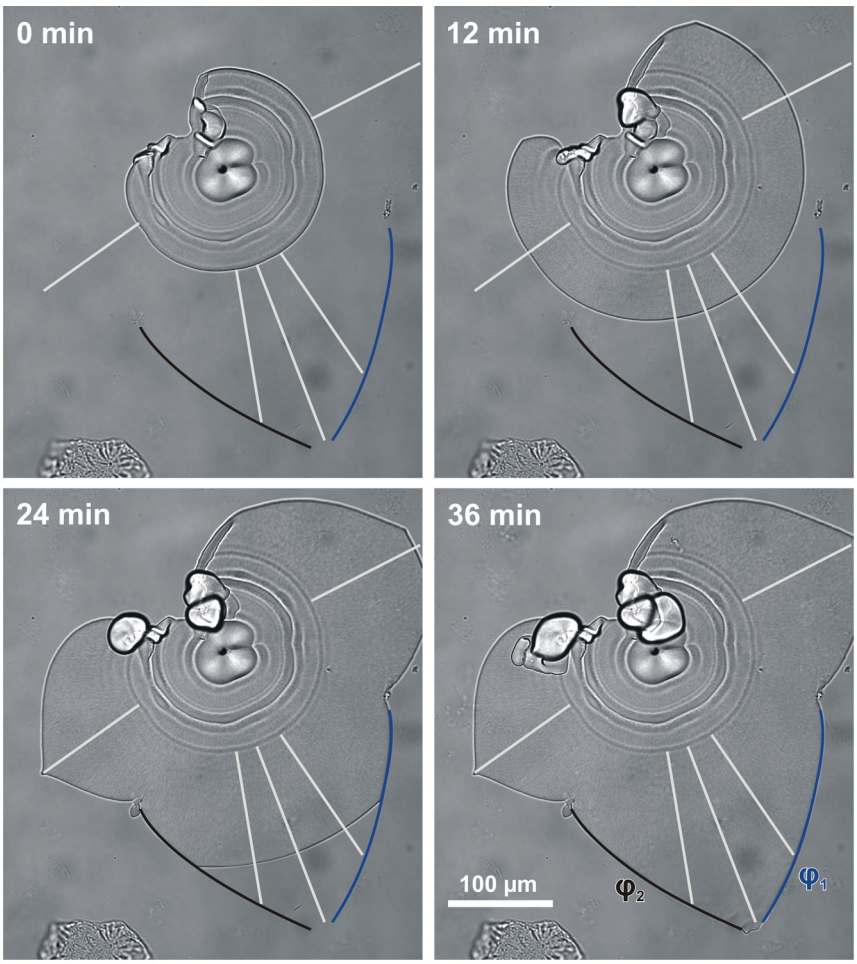

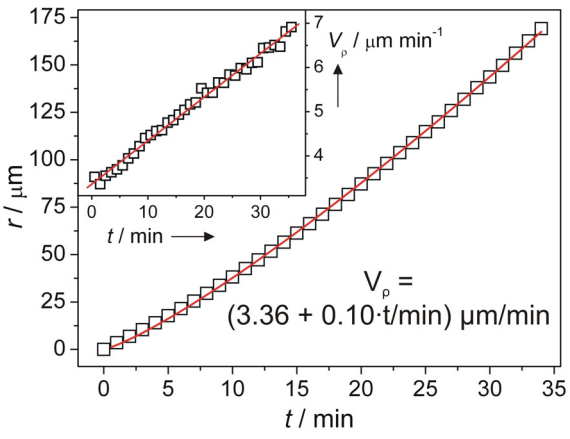

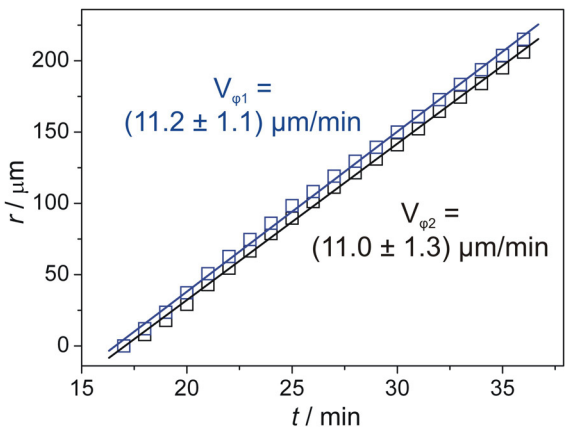

Data evidence that the radial advancement of the front can be described properly by a power law with a scaling exponent of 1.22, rather than a simple straight line. This implies that, in contrast to the other videos, the radial growth rate is not constant in this case but in fact increases linearly with time. Likely, this finding can be ascribed to the geometry of the cell, which causes an accelerated rate of CO_2 uptake and thus a faster decline of the bulk pH and silica solubility. Consequently, the supersaturation of both carbonate and silica should be higher and change much more distinctly during growth than in the standard wells for solution experiments or the gel setups used otherwise throughout this study. The processes occurring at the growth front now appear to be no longer independent of variations in the bulk conditions. The autocatalytic precipitation cycle rather winds itself up such that local supersaturation values and hence the overall growth rate increase continuously with time.

Notably, this does not apply for the propagation of the curls along the perimeter of the sheet, for which linear relations are found. This demonstrates that radial and azimuthal growth of a given aggregate can not only differ in terms of the absolute values of their rates, but also concerning their kinetics as such.

D. Size Distributions of Silica Biomorphs Grown from Stirred Solutions

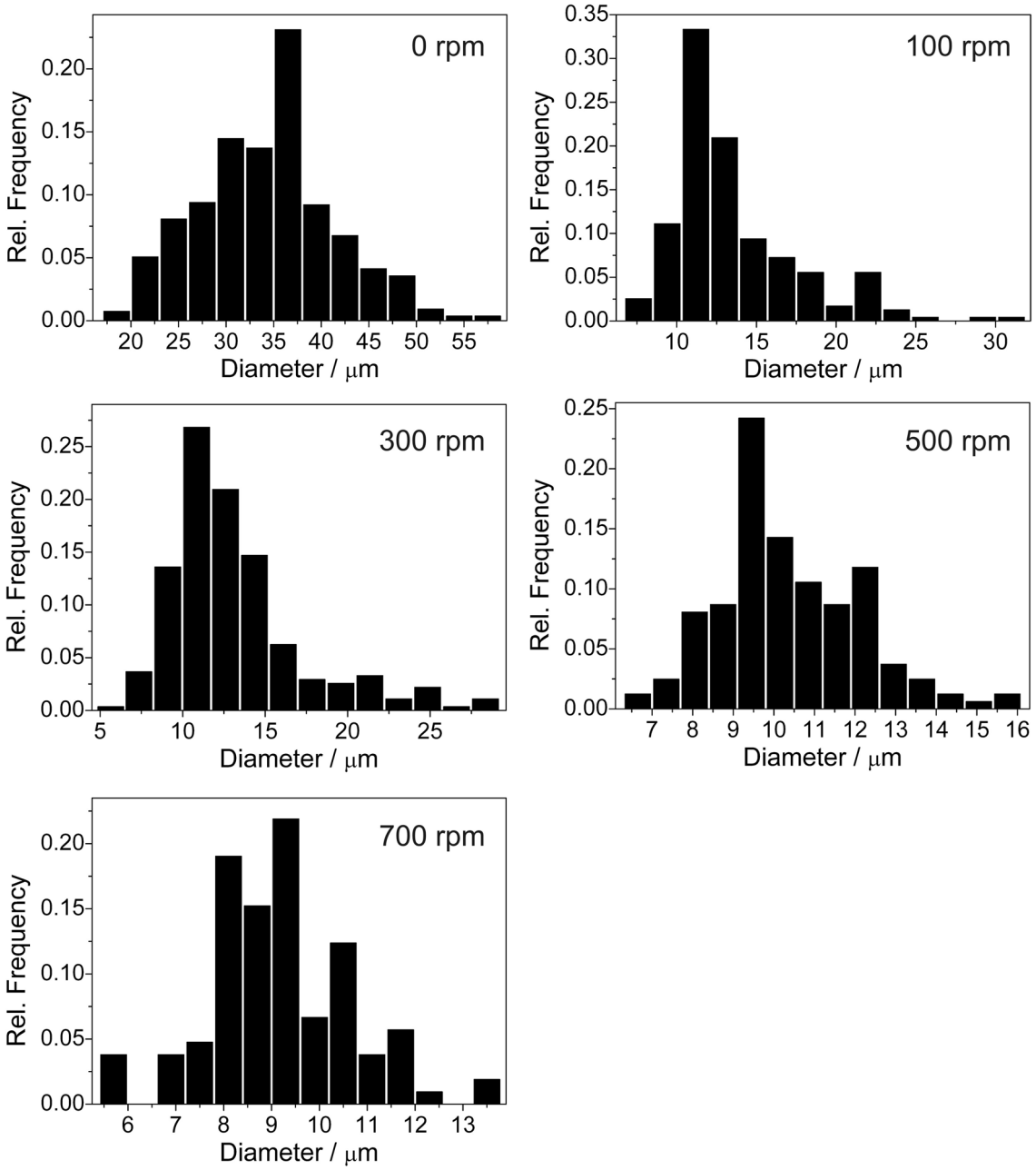

Fig. D-1: Size distributions for globular structures observed upon growth at various stirring rates. In case of agglomeration or intergrowth (particularly occurring at higher speed), the diameter of individual particles was measured.

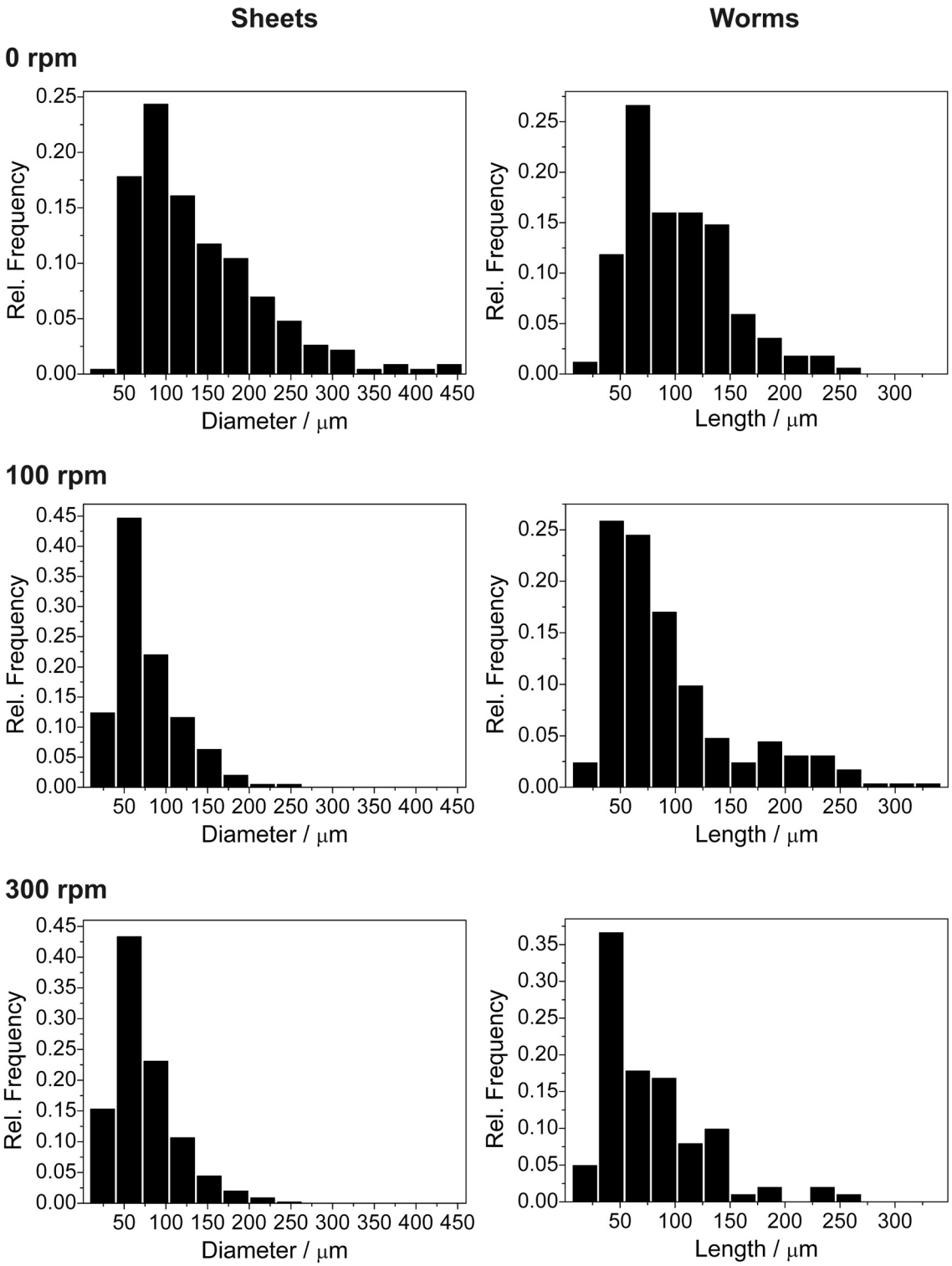

Fig. D-2: Size distributions of sheets (left) and worms (right) grown at stirring rates of 0, 100, and 300 rpm. Data were obtained by measuring more than 200 specimens in each case.

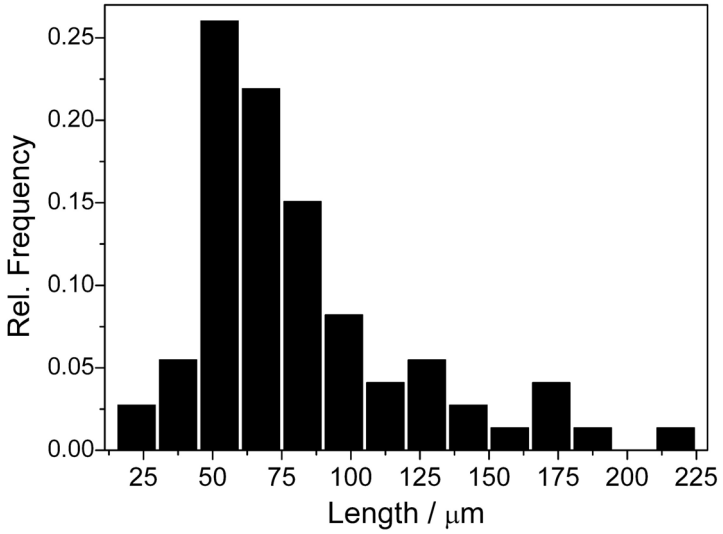

Fig. D-3: Size distribution of helicoidal filaments (expressed in terms of their length) found for growth under quiescent conditions. Analogous diagrams for helicoids formed in stirred solutions were not established due to their relatively rare occurrence and thus the lack of statistical significance. Nevertheless, the collected data suggest that stirring leads to a slight decrease in the length of the filaments.

List of Figures

List of Tables

List of Publications and Patents

(1) **Kellermeier, M.**; Melero-García, E.; Glaab, F.; Klein, R.; Drechsler, M.; Rachel, R.; García-Ruiz, J. M. "Stabilization of Amorphous Calcium Carbonate in Inorganic Silica-Rich Environments". *Journal of the American Chemical Society* **2010**, *131*, 17859-17866. (Chapter 2)

(2) **Kellermeier, M.**; Melero-García, E.; Kunz, W.; García-Ruiz, J. M. "Biomimetic Crystallization in Purely Inorganic Precipitation Systems". To be submitted to *Crystal Growth and Design*. (Chapter 3)

(3) **Kellermeier, M.**; Gebauer, D.; Melero-García, E.; Drechsler, M.; Talmon, Y.; Kienle, L.; Cölfen, H.; García-Ruiz, J. M.; Kunz, W. "Calcium Carbonate Pre-Nucleation Processes Revealed by Stabilization of Transient States with Silica". To be submitted to *Nature*. (Chapter 4)

(4) **Kellermeier, M.**; Glaab, F.; Melero-García, E.; Klein, R.; Kunz, W.; García-Ruiz, J. M. "The Effect of Silica on Calcium Carbonate Polymorphic Precipitation: An In-Situ Synchrotron X-Ray Diffraction Study". To be submitted to *Angewandte Chemie International Edition*. (Chapter 5)

(5) **Kellermeier, M.**; Melero-García, E.; Glaab, F.; Eiblmeier, J.; Kienle, L.; Kunz, W.; García-Ruiz, J. M. "Growth Behavior and Kinetics of Self-Assembled Silica-Carbonate Biomorphs". To be submitted to *Chemistry of Materials*. (Chapter 6).

(6) **Kellermeier, M.**; Melero-García, E.; Eiblmeier, J.; Pretzl, M.; García-Ruiz, J. M.; Kunz, W. "The Possible Role of Surfaces During Morphogenesis of Silica Biomorphs". To be submitted to *Crystal Growth and Design*. (Chapter 7).

(7) **Kellermeier, M.**; Melero-García, E.; Kunz, W.; García-Ruiz, J. M. "Local Autocatalytic Co-Precipitation Phenomena in Self-Assembled Silica-Carbonate Materials". To be submitted to *Journal of Materials Chemistry*. (Chapter 8)

(8) **Kellermeier, M.**; Glaab, F.; Carnerup, A. M.; Drechsler, M.; Gossler, B.; Hyde, S. T.; Kunz, W. "Additive-Induced Morphological Tuning of Self-Assembled Silica-Barium Carbonate Crystal Aggregates". *Journal of Crystal Growth* **2009**, *311*, 2530-2541. (Chapter 9)

(9) Glaab, F.; **Kellermeier, M.**; Kunz, W.; García-Ruiz, J. M. "Chemical Gradients and Potential Differences Across Self-Assembling Inorganic Membranes". To be re-submitted to *Angewandte Chemie International Edition*.

(10) Eiblmeier, J.; **Kellermeier, M.**; Kunz, W. "Effect of the Initial Bulk pH on the Growth Behavior of Silica-Witherite Biomorphs in Alkaline Solutions". To be submitted to *Journal of Crystal Growth*.

(11) Kunz, W.; **Kellermeier, M.** "Beyond Biomineralization". *Science* **2009**, *323*, 344-345.

(12) Voinescu, A. E.; **Kellermeier, M.**; Bartel, B.; Carnerup, A. M.; Larsson, A. K.; Touraud, D.; Kunz, W.; Kienle, L.; Pfitzner, A.; Hyde, S. T. "Inorganic Self-Assembled Silica Aragonite Biomorphic Composites". *Crystal Growth and Design* **2008**, *8*, 1515-1521.

(13) Voinescu, A. E.; **Kellermeier, M.**; Carnerup, A. M.; Larsson, A. K.; Touraud, D.; Hyde, S. T.; Kunz, W. "Co-Precipitation of Silica and Alkaline-Earth Carbonates Using TEOS as Silica Source". *Journal of Crystal Growth* **2007**, *306*, 152-158.

(14) Glaab, F.; **Kellermeier, M.**; Kunz, W. "Chiral Polymer Helices with Shape Identical to Previously Reported Helical Calcium Carbonate Morphologies". *Macromolecular Rapid Communications* **2007**, *28*, 1024-1028.

(15) Klein, R.; Zech, O.; Maurer, E.; **Kellermeier, M.**; Kunz, W. "Oligoether Carboxylates – Task-Specific Room-Temperature Ionic Liquids". *Submitted to Journal of Physical Chemistry B*.

(16) Klein, R.; **Kellermeier, M.**; Drechsler, M.; Touraud, D.; Kunz, W. "Solubilisation of Stearic Acid by the Organic Base Choline Hydroxide". *Colloids and Surfaces A: Physicochemical and Engineering Aspects* **2009**, *338*, 129-134.

(17) Zech, O.; **Kellermeier, M.**; Thomaier, S.; Maurer, E.; Klein, R.; Schreiner, C.; Kunz, W. "Alkali Oligoether Carboxylates – A New Class of Ionic Liquids". *Chemistry – A European Journal* **2009**, *15*, 1341-1345.

(18) Eljaouhari, A. A.; Müller, R.; **Kellermeier, M.**; Heckmann, K.; Kunz, W. "New Anisotropic Ceramic Membranes from Chemically Fixed Dissipative Structures". *Langmuir* **2006**, *22*, 11353-11359.

(19) Kunz, W.; **Kellermeier, M.**; Klein, R.; Maurer, E.; Touraud, D. "Biologically Acceptable Choline Compounds and Their Use as Tensides". *EP 2010-152626* (University of Regensburg), 2010.

(20) Kunz, W.; Thomaier, S.; Maurer, E.; Zech, O.; **Kellermeier, M.**; Klein, R. "Onium Salts of Carboxyalkyl-Terminated Polyoxyalkylenes for Use as High-Polar Solvents and Electrolytes". *WO 2008-135482* (BASF SE), 2008.

Declaration

Hereby, I declare that I have composed this work on my own and using exclusively the quoted references and resources. Literally or correspondingly adapted material has been marked accordingly.

Erklärung

Hiermit erkläre ich, dass ich die vorliegende Arbeit selbständig und nur mit den angegebenen Quellen und Hilfsmitteln angefertigt habe. Wörtlich oder sinngemäß übernommenes Gedankengut habe ich als solches kenntlich gemacht.

Ort, Datum

Matthias Kellermeier